UNIVERSITÉ DE TOURS

ÉCOLE DOCTORALE : EMSTU

Laboratoire E.A 6293 GéoHydrosystème Continentaux (GéHCO)

THÈSE présentée par :

Hanieh Seyedhashemi

Soutenance prévue le 8 février 2022

pour obtenir le grade de : **Docteur de l'université de Tours**

Discipline/ Spécialité : Science de la Terre

Influence des retenues d'eau et du changement climatique sur la température des cours d'eau :

modélisation à haute résolution et application au bassin de la Loire

THÈSE dirigée par :

Mme Moatar Florentina	Directrice de recherche, INRAE

Co-directeur :

M. Vidal Jean-Philippe	Chargé de recherche HDR, INRAE

RAPPORTEURS :

Mme Ducharne Agnès	Directrice de Recherche CNRS, Paris
M. St-Hilaire André	Professeur à l'INRS, Québec

JURY :

Mme Ducharne Agnès	Directrice de Recherche CNRS, Paris (rapporteur)
M. St-Hilaire André	Professeur à l'INRS, Québec (rapporteuse)
Mme Moatar Florentina	Directrice de recherche, INRAE (directrice)
M. Vidal Jean-Philippe	Chargé de recherche HDR, INRAE (co-directeur)
Mme Grosbois Cécile	Professeure, Université de Tours (présidente du jury)
M. Hannah David	Professeur, Université de Bermingham (examinateur)
Mme Thomas Zahra	Maître de conférences HDR, AgroCampus Ouest, Rennes (examinatrice)
M. Maire Anthony	Ingénieur - Chercheur, Électricité de France (invité)

Acknowledgements

This doctoral project has been conducted with the help of many people. First of all, I would like to thank Agnès Ducharne and André St-Hilaire for agreeing to be the reporters of this work. I would like also thank Cécil Grosbois, David Hannah and Zahra Thomas for accepting to be part of my thesis jury. I am deeply grateful to Florentina Moatar and Jean-Philippe Vidal for giving me this PhD opportunity. Without their persistent encouragement, help and guidance, this project would not have materialized. They have been extraordinarily tolerant and supportive.

I owe a very important debt to Aurelien beaufort for helping me to understand the T-NET thermal model and to work with it. He gave me many insightful comments and suggestions.

I would like to express my gratitude to Dominque Thiery (BRGM) who ran the EROS hydrological model and provided us with daily stream flows over the past and future.

Andre Chandesris' support, encouragement, suggestions and comments were invaluable. Special thanks to him for helping me with the integration of riparian shading into the T-NET thermal model and his valuable contribution on my first article.

I would like to show my greatest appreciation to Jake Diamond (UR RiverLy, INRAE) for his collaboration on my articles. His meticulous comments were always an enormous help to me during the project.

I owe my deepest gratitude to Anthony Maire (EDF) for his collaboration on my second article. He always gave me constructive comments and warm encouragement.

I have greatly benefited from Yann Jullian from the University of TOURS who helped me a lot with working with T-NET thermal model and modifying it.

I would like also to thank Herve pella (UR RiverLy, INRAE), Nicolas lamouroux (UR RiverLy, INRAE) and Maxime Morel for providing me with the required materials for integrating the new hydraulic geometry model into the T-NET thermal model.

I would like to offer my special thanks to Laurent valette (UR RiverLy, INRAE) for providing me with the surface waters data and his collaboration on my first article.

I would also thank Celin Monteil (EDF) for providing me with naturalized stream flows for the Loire and Allier, and her collaboration on my second article.

I would like also thank Coline picard for providing me with the data about the density of brown trout over the Loire River. Moreover, her support and encouragement were invaluable.

I would also like to express my gratitude to French electricity (EDF) and university of Tours for their financial support.

Finally and importantly, I owe my deepest gratitude to my husband. Without his persistent and warm encouragement, support and help, this project would not have been possible. I have also greatly benefited from his comments and suggestions on my first article.

I would like to dedicate this work to my husband.

Abstract

Stream temperature (Tw) is a critical parameter for water quality, aquatic communities, and socio-economic activities, but our understanding of its spatio-temporal variability induced by anthropogenic impoundments and climate change at a large scale is limited. These issues have been addressed here using both observed Tw data and Tw simulated by the T-NET physical process-based thermal model coupled with the EROS semi-distributed hydrological model at the scale of the entire Loire River basin in France (10^5 km^2 with 52 278 reaches).

First, observed Tw data are rarely available to identify the influence of impoundments, and novel “thermal signatures” based on observed stream-air temperature relationships are introduced here. These thermal signatures highlighted two dominant modes of thermal alteration induced by dams and ponds in the basin. Large dams decrease summer Tw by 2 °C and delay the annual Tw peak by 23 days relative to the natural regimes. In contrast, the cumulative effects of upstream ponds increase summer Tw by 2.3 °C and increase the synchronicity with air temperature regimes.

Natural Tw stations identified through the thermal signature analysis were then used to assess T-NET performance over the Loire basin. Improvements related to hydraulic geometry and riparian shading led to a decrease in model bias. Moreover, the difference between simulated (natural) and observed (influenced) Tw at altered stations were used to quantify the influence of dams and ponds. Results showed that the impacts of impoundments in a hot year could be 2-4 times larger than in a cool year.

The improved T-NET model was then used to reconstruct Tw over the 1963-2019 period to estimate the magnitude of past trends in natural Tw, and assess their relation with hydroclimate changes and landscape characteristics. Results revealed that Tw increased for almost all reaches in all seasons (+0.38 °C/decade) with the largest increases in spring and summer. Rates of stream temperature increases were larger than for air temperature across seasons for the majority of reaches. Spring and summer increases were typically the greatest in the southern headwaters (up to +1 °C/decade) and in the largest rivers. Importantly, the largest Tw increases were accompanied by similar trends in air temperature (up to +0.71 °C/decade) and the largest decreases in streamflow (up to 16%/decade). Critically, riparian vegetation shading mitigated stream temperature increases in smaller streams by 0.16 °C/decade.

Finally, the T-NET model was used to project Tw under different future climate projections over the whole 21st century from 3 climate modeling chains under three emissions scenarios. A consistent increase in future Tw towards the end of the century was projected over the whole Loire River basin. The median Tw changes are in the range of [+0.72 °C ; +2.68 °C] across climate projections and seasons in the middle of the century, and in the range of [+0.47 °C ; +4.95 °C] at the end of the century, and the largest future summer Tw was found for the largest rivers. The largest Tw anomalies synchronized with the largest negative Q anomalies regardless of the season. Moreover, positive Tw changes and negative Q changes were concomitant in the majority of the reaches, mostly in the southern headwaters. Importantly, riparian vegetation shading could mitigate the increase in future summer Tw by [+3.3 °C ; +4.6 °C]. These findings underscore that there is a need to grow and maintain Tw sensor networks. They can also help assess the various stresses on freshwater habitat sustainability due to human impacts and develop appropriate management strategies to mitigate extreme thermal events induced by such human impacts and conserve thermal refugia.

Résumé

La température des cours d’eau (Tw) est un paramètre critique affectant la qualité de l’eau, des communautés aquatiques et les activités socio-économiques. Cependant, notre compréhension actuelle de sa variabilité spatio-temporelle induite par les retenues d’eau et le changement climatique à grande échelle est documentée. Ces problèmes ont été abordés ici en utilisant à la fois les données Tw observées et les Tw simulées par le modèle thermique basé sur les processus physiques T-NET couplé au modèle hydrologique semi-distribué EROS à l’échelle de l’ensemble du bassin de la Loire en France (10^5 km^2 avec 52 278 tronçons).

Premièrement, les données Tw observées sont rarement disponibles pour identifier l’influence des aménagements anthropiques, et de nouvelles « signatures thermiques » basées sur les relations observées entre la température des cours d’eau et de l’air sont introduites ici. Ces signatures thermiques ont mis en évidence deux modes dominants d’altération thermique induits par les barrages et les étangs du bassin. Les grands barrages diminuent la Tw estivale de 2 °C et retardent le pic annuel de la Tw de 23 jours par rapport aux régimes naturels. En revanche, les effets cumulatifs des étangs en amont augmentent la Tw estivale de 2,3 °C et augmentent la synchronicité avec les régimes de température de l’air.

Les stations Tw naturelles identifiées grâce à l’analyse de la signature thermique ont ensuite été utilisées pour évaluer les performances du T-NET sur le bassin de la Loire. Les améliorations liées à la géométrie hydraulique et à l’ombrage de la végétation rivulaire ont entraîné une diminution du biais du modèle. De plus, la différence entre la Tw simulée (naturelle) et observée (influencée) aux stations modifiées a été utilisée pour quantifier l’influence des barrages et des étangs. Les résultats ont montré que les impacts des retenues pendant une année chaude pourraient être 2 à 4 fois plus importants que pendant une année froide.

Enfin, le modèle T-NET a été utilisé pour projeter Tw sous différentes projections climatiques futures sur l’ensemble du 21e siècle à partir de 3 chaînes de modélisation climatique sous trois scénarios d’émissions. Une augmentation constante du futur Tw vers la fin du siècle a été projetée sur l’ensemble du bassin de la Loire. Les changements médians de Tw sont de l’ordre de [+0,72 °C ; +2,68 °C] selon les projections climatiques et les saisons au milieu du siècle, et de l’ordre de [+0,47 °C ; +4,95 °C] à la fin du siècle, et la plus grande Tw estivale a été trouvé pour les plus grands fleuves. Les plus grandes anomalies Tw synchronisées avec les plus

grandes anomalies Q négatives quelle que soit la saison. De plus, des changements positifs de Tw et des changements négatifs de Q étaient concomitants dans la majorité des tronçons, principalement dans le cours supérieur sud. Il est important de noter que l'ombrage de la végétation rivulaire pourrait atténuer l'augmentation de la future Tw estivale de [+3,3 °C -; +4,6 °C].

Ces résultats soulignent qu'il est nécessaire de développer et de maintenir les réseaux de capteurs Tw. Ils peuvent également aider à évaluer les divers stress sur la durabilité de l'habitat d'eau douce dus aux impacts humains et développer des stratégies de gestion appropriées pour atténuer les événements thermiques extrêmes induits par de tels impacts et conserver les refuges thermiques.

Contents

List of Figures

List of Tables

Notations

Tw	stream (water) temperature
Ta	air temperature
Q	stream flow
DJF	December, January, February
MAM	March, April, May
JJA	June, July, Auguest
SON	September, October, November
IRI	Impounded Runoff Index
GCM	Global climate model
RCM	Regional Climate Model
RCP	Representative Concentration Pathways
GHG	Greenhouse gases
RMSE	Root mean square error
IQR	Interquartile range
W	river width
H	river depth
SF	riparian shading factor
vc	vegetation cover density

CHAPTER 1

State of art and objectives

1.1 Stream temperature in a changing world

Stream (water) temperature (Tw) is a critical parameter affecting the eutrophication of water bodies (Minaudo et al., 2018; Le Moal et al., 2019; Zhao et al., 2022), water quality, and the distribution of aquatic communities (Cox and Rutherford, 2000; Poole and Berman, 2001; Caissie, 2006). Changes in natural thermal conditions affect metabolism, the life cycle (Elliott and Elliott, 2010) and spatial distribution of aquatic organisms (Comte et al., 2013; Morales-Marín et al., 2019), and a wide range of biogeochemical processes (Ouellet et al., 2020). In addition to these consequences, changes in the natural thermal regime of rivers can also have economic and social impacts (Van Vliet et al., 2012b; Ouellet et al., 2020). Recently, alterations induced by impoundments (e.g., lakes, reservoirs, and ponds) along the river continuum have come to light as a critical factor in nitrogen removal (Harrison et al., 2009; Schmadel et al., 2018), and storage of phosphorus (Grantz et al., 2014) and sediments (Vörösmarty et al., 2003). An emerging concern is the cumulative effects of impoundments on thermal regimes (Olden and Naiman, 2010). Indeed, it is important to develop a more general understanding of these effects since the global change will likely exacerbate them if the number of future dams or ponds or the capacity of current ones increases. For instance, in some countries, recurrent droughts have led to a recent increase in the number of small farm dams storing water for later use in irrigation (Habets et al., 2018).

There is also growing evidence that stream warming is occurring around the world (e.g., Isaak et al., 2012; Orr et al., 2015; Michel et al., 2020; Wilby and Johnson, 2020), decreasing dissolved oxygen, increasing phytoplankton biomass during the growth period, and reducing it afterward (Ducharne, 2008). Stream warming also affects freshwater ecosystems through structural and functional changes in biological communities throughout the food web (Woodward et al., 2010; O'Gorman et al., 2012; Scheffers et al., 2016). Deleterious warming effects are documented from bottom-dwelling microorganisms (e.g., Romaní et al., 2016; Majdi et al.,

2020) up to macroinvertebrates (e.g., Floury et al., 2013; Bruno et al., 2019) and fish communities (e.g., Maire et al., 2019; Stefani et al., 2020). Moreover, more frequent and severe droughts (Mantua et al., 2010; Giuntoli et al., 2013; Prudhomme et al., 2014) and earlier low flows due to climate change (van Vliet et al., 2013; Michel et al., 2020) can lead to a more synchronous timing of maximum temperature and low flow (Arismendi et al., 2013b; van Vliet et al., 2013; Arevalo et al., 2020), doubling the trouble for cold-water biota.

These intense and fast changes do not let organisms adapt to the new environment, leading to a decline in aquatic species' population and ultimately their extinction. There is thus a need for larger-scale assessments of spatio-temporal variability in thermal regimes, especially in light of confounding factors like land use, hydro-climate forcings, and hydraulic conditions. Such assessments could also have implications for understanding the freshwater habitat sustainability, and the spatial distribution and persistence of aquatic organisms. To address these issues, large-scale ecological studies typically use air temperature (Ta) as a proxy for Tw due to a lack of Tw data (e.g., Buisson et al., 2008; Buisson and Grenouillet, 2009; Tisseuil et al., 2012; Domisch et al., 2013). However, Ta can be an imprecise surrogate for Tw (Caissie, 2006). Indeed, many natural drivers (e.g., stream discharge (Q), streambed, morphology, topography, and vegetation cover) (Hannah and Garner, 2015), as well as anthropogenic drivers (e.g., lakes, reservoirs, ponds, and climate change) contribute to the spatio-temporal variability of Tw (Figure 1.1). In the following sections, the influence of these drivers on thermal regimes will be explained.

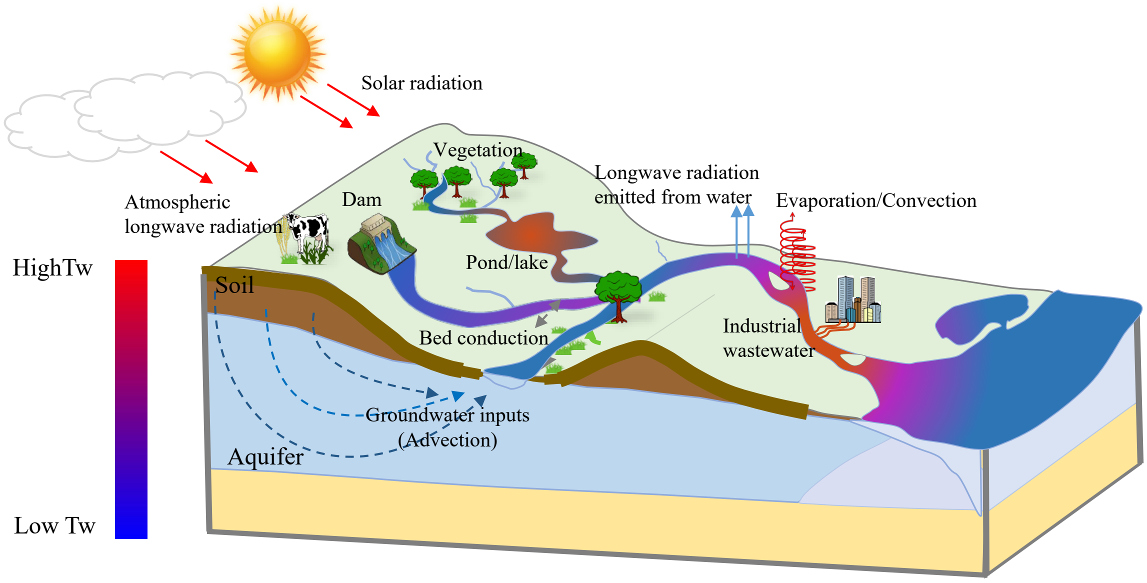

Figure 1.1: The natural and anthropogenic drivers of thermal regimes over the summer period at a large scale. The heat fluxes at the water-air and water-stream bed interface are also presented.

1.2 Natural drivers of thermal regimes

Cumulative effects of multivariate and nested at macro-, meso- and micro scales natural drivers produce dynamics of natural thermal regimes (Hannah and Garner, 2015; Dugdale et al., 2017, and see Figure 1.1). The first-order driver is climate, which drives the magnitude and seasonal variability in Tw at the regional scale (Ward, 1985; Garner et al., 2014). The second-order drivers are basin characteristics, which moderate the influence of climate and modify thermal regimes. The third-order drivers are reach-specific factors (or local factors) such as topography, riparian vegetation shading, hyporheic exchanges, and groundwater inputs, which further moderate the influence of climate on thermal regimes.

For instance, riparian vegetation may obstruct solar radiation –which is the dominant heat flux at the water-atmosphere interface (Hannah et al., 2004; Caissie, 2006), decreasing Tw response to Ta (Johnson, 2004; Loicq et al., 2018). At midday in July, about 74% decrease can be observed in net energy from an open reach under full sun to a full shaded reach (Johnson, 2004). It should be noted that riparian vegetation shading can greatly decrease the temperature of small rivers (Moore et al., 2005; Loicq et al., 2018), whereas it has a limited effect on larger rivers since only a small part of their width can be shaded. However, Loicq et al. (2018) showed that the cooling effect can remain above 1 °C even for medium rivers with width larger than 40 m. Johnson and Wilby (2015) showed that approximately 0.5 km of complete shade is necessary to offset stream temperature by 1 °C at midday in July in headwaters whereas 25 km downstream, 1.1 km of shade is required. Riparian clear-cutting can also increase maximum daily water temperature by up to 8 °C (Johnson and Jones, 2000; Gomi et al., 2006), which can gradually return to pre-harvest temperature after a 15-year regrowth period (Caissie, 2006). The riparian shading may decrease not only the maximum daily Tw but also the amplitude of the diurnal cycle (Moore et al., 2005; Imholt et al., 2010; Loicq et al., 2018). It can also mitigate the heating effects in thermal regimes induced by ponds (Maxted et al., 2005). Nevertheless, the efficacy of riparian planting and riparian shading is also highly dependent upon the type and structure of forest stands (Dugdale et al., 2018), channel orientation, canopy density, and within-reach residence times (Garner et al., 2017).

In addition to the riparian shading, groundwater inputs can also moderate the influence of climate, and disrupt the Tw-Ta relationship. The linear relationship between the stream and air temperature over the year (Kinouchi et al., 2007; Ducharne, 2008) is strong ($R^2 > 0.8$) for large rivers, and becomes weaker for headwaters or rivers with groundwater inputs (Caissie, 2006; O'Driscoll and DeWalle, 2006; Kelleher et al., 2012; Beaufort et al., 2020a). Indeed, streams with high groundwater discharge are less sensitive to climate change than streams with low groundwater discharge (Chu et al., 2008). Groundwater mainly affects rivers thermal regime through summer cooling and winter warming. In fact, the groundwater temperature has a weaker amplitude than stream temperature, but it keeps a seasonal cycle similar to that of stream temperature (Hannah et al., 2009). The geological composition of the substrate (Karst) and the geometry of the watercourse can affect the amount of such groundwater inputs into the river and modify energy intake or loss (O'Driscoll and DeWalle, 2006; Garner et al., 2014).

Figure 1.2 shows the parsed effects of natural drivers over the Loire River basin (10^5 km^2), a temperate region. First of all, as it can be seen in the figure, Tw has a sinusoidal pattern with the lowest temperatures occurring in winter and the highest ones in summer (Caissie, 2006) following the same intra-annual fluctuations as Ta. This figure clearly shows that Ta is an imprecise proxy for Tw since Ta has a lower variability than Tw at a large scale, indicating the influence of other drivers on Tw. Indeed, streams altered by both the groundwater inputs and the riparian shading are the most moderated thermal regimes. These streams are thus less sensitive to Ta. The annual amplitude of Tw in these streams is half of the annual amplitude of Ta. Conversely, stations located on large streams with a large distance from the source have the closest regimes to Ta regimes. In fact, these streams are less sensitive to moderating drivers such as groundwater inputs and riparian shading due to their larger conveyed volumes and greater thermal inertia (Smith and Lavis, 1975; Webb and Walling, 1993; Caissie, 2006; Kelleher et al., 2012). This highlights the importance of large-scale assessments to parse the effects of natural drivers on thermal regimes. However, the paucity of detailed and long-term time series of Tw (Webb and Walling, 1996; Nelson and Palmer, 2007; Webb et al., 2008; Arora et al., 2016), has impaired such assessments to date.

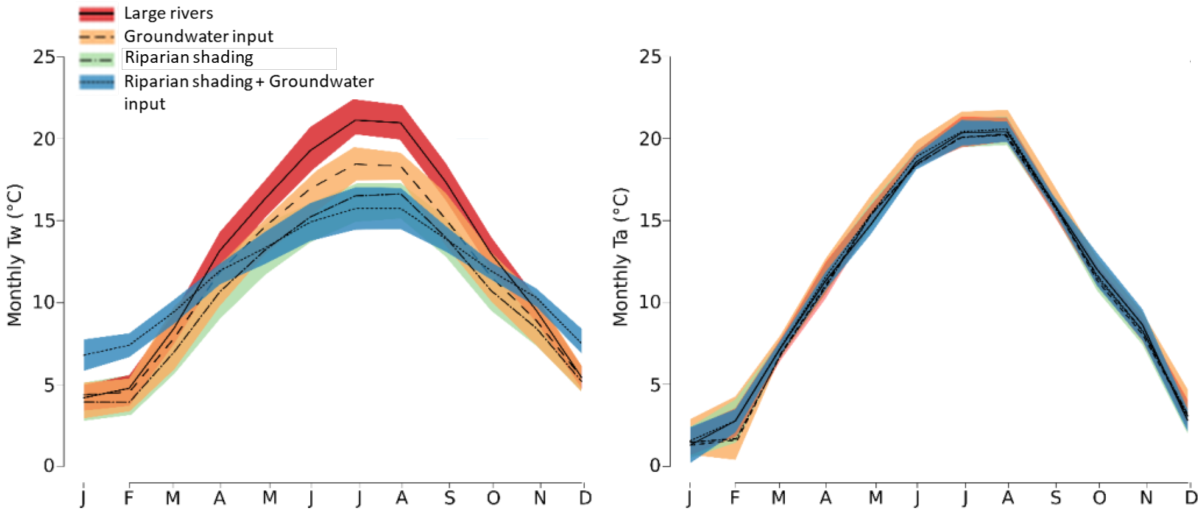

Figure 1.2: The monthly regimes of Ta and Tw, and the parsed effects of natural drivers of Tw at the scale of the Loire River basin (10^5 km^2). The Tw stations are on natural thermal regimes. This figure is adopted from Beaufort et al. (2020a).

1.3 Anthropogenic drivers of thermal regimes

In addition to natural drivers, the variation in stream temperature can be the result of anthropogenic drivers such as urbanization (LeBlanc et al., 1997; Nelson and Palmer, 2007), industrial wastewaters (Kinouchi et al., 2007), effluents from power plants (Prats et al., 2012; Bae et al., 2016), deforestation (Moore et al., 2005; Caissie, 2006), impoundments, and reservoirs (e.g., for irrigation and hydroelectricity) (Sinokrot et al., 1995; Lowney, 2000; Preece and Jones, 2002; Olden and Naiman, 2010; Maheu et al., 2016c; Chandesris et al., 2019), and climate change (see van Vliet et al., 2013; Wanders et al., 2019, at a global scale). However, among these drivers, the cumulative effects of impoundments on thermal regimes are poorly understood. Such effects are expected to be exacerbated if the number of future dams or ponds or the capacity of current ones increases in order to satisfy water demand in the context of climate change. Moreover, recently, there is more impetus to investigate alterations in thermal regimes associated with climate change for assessing future needs for thermal resilience of river ecosystems (Ouellet et al., 2020).

1.3.1 Impacts of impoundments

The impacts of impoundments on thermal regimes depend strongly on their individual characteristics and overall spatial distributions, complicating the scales of inference and prediction. For example, anthropogenic features like dams and ponds appear to have contrasting effects on stream temperature, which itself mainly depends on the reservoir volume, stream order, distance from the dam, and mode-of-operation (Webb, 1996; Webb et al., 2008; Olden and Naiman, 2010; Kędra and Wiejaczka, 2018, and see Figure 1.3 for different impoundments). The preponderance of studies on the regional scale effects of anthropogenic structures uses physical process-based models that are highly parameterized (Van Vliet et al., 2012a; Niemeyer et al., 2018; Yearsley et al., 2019; Cheng et al., 2020), limiting their broad applicability (Dugdale et al., 2017). Hence, there is a need for simpler, data-based tools that can identify and predict such anthropogenic effects on stream temperature and subsequent consequences to ecosystems, particularly at large scales relevant to water management.

Large dams tend to reduce stream temperature and shift annual cycles

The effects of large dams on river thermal regimes are well studied at the site scale (Webb and Walling, 1993, 1996, 1997; Lowney, 2000; Preece and Jones, 2002; Casado et al., 2013). These studies typically compare observed stream temperature regimes above and below the dam, before and after dam construction, or in regulated and unregulated streams, with unregulated streams being located nearby regulated streams with a similar climate. Results provide

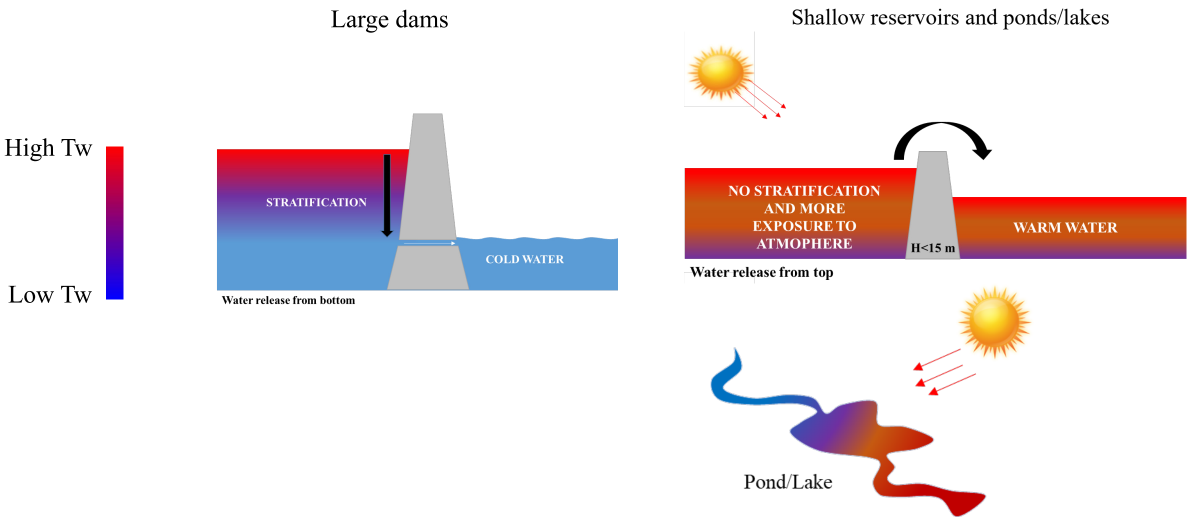

Figure 1.3: Schematic representation of different impoundments with different mode-of-operation regulating thermal regimes.

strong evidence that large dams generally reduce downstream temperatures by releasing cold, hypolimnetic water in summer (Olden and Naiman, 2010), and that they delay the annual cycle of both flow (Lehner et al., 2011) and stream temperature regimes (Webb and Walling, 1993; Webb, 1996). Additionally, through discharge regime regulation (Petts and Gurnell, 2005), large dams may also modify stream temperature by affecting thermal capacity without necessarily modifying the components of the heat budget (Webb and Walling, 1996; Poole and Berman, 2001). While some subsequent works have used physical process-based models to upscale these effects across river networks and regions (Van Vliet et al., 2012a; Niemeyer et al., 2018; Cheng et al., 2020; Daniels and Danner, 2020), large-scale empirical assessments remain scarce (but see Steel and Lange, 2007; Hill et al., 2013; Maheu et al., 2016c). Hence, there is still a major gap in our regional scale understanding of dam-induced alterations.

Ponds and shallow reservoirs tend to increase stream temperature

Pond and shallow (<15 m in height based on ICOLD (2011)) reservoirs and their effects on stream temperature differ from those of large dams due to their mode of downstream water release. A global review of the impacts of these kinds of impoundments Mbaka and Wanjiru Mwaniki (2015) revealed that the majority of studies on small impoundments (73%) show no significant influence of small impoundments on downstream Tw. However, a few studies (26%) suggest that the surficial water release from these structures – as opposed to hypolimnetic release from large dams (Figure 1.3) – tends to increase downstream stream temperature (e.g., Sinokrot et al., 1995; Maxted et al., 2005; Bae et al., 2016; Maheu et al., 2016b; Chandesris et al., 2019; Zaidel et al., 2020). Indeed, these anthropogenic features increase water travel time, leading to more exposure of water to the atmosphere and an increase in downstream Tw (Maheu et al., 2016c). The greatest increase in stream temperature occurs during low-flow periods due to their smaller conveyed volumes and greater sensitivity to alteration (Webb and Nobilis, 1995).

Specifically, these structures increase not only the average stream temperature but also its diurnal range and the frequency and duration of high temperatures (Maheu et al., 2016c,b; Chandesris et al., 2019). Furthermore, the increase in downstream temperature induced by ponds and shallow reservoirs is weakly compensated by natural processes, leading to minimal downstream recovery to baseline temperature (Boon and Shires, 1976; Fraley, 1979; Maxted et al., 2005; Dripps and Granger, 2013). However, thermal alterations from small impoundments are far less studied than those of large dams, and their cumulative effects on river thermal regimes at the regional scale are barely known.

1.3.2 Impacts of climate change

As Ta increases worldwide due to climate change, Tw is expected to follow a similar trajectory (Mohseni et al., 1999; Kaushal et al., 2010; Van Vliet et al., 2011; Isaak et al., 2012; Arora et al., 2016). Few studies have shown a clear trend in Tw at a large scale over the last decades (but see Orr et al., 2015; Arora et al., 2016; Wanders et al., 2019; Michel et al., 2020). This Tw warming was also anticipated to continue and be more pronounced for the extreme scenarios and toward the end of the century (Mantua et al., 2010; Selbig, 2015; Michel et al., 2021). Moreover, rising groundwater temperature (Taylor and Stefan, 2009; Gunawardhana et al., 2011; Kurylyk et al., 2013, 2014) and reduced groundwater flows (Gunawardhana et al., 2011; Kurylyk et al., 2014) due to climate change may further contribute to upward Tw trends (Meisner, 1990; Arora et al., 2016), leading to asymmetric controls (vis-à-vis Ta) on Tw (Moatar and Gailhard, 2006), especially in headwaters (Caissie, 2006; Kelleher et al., 2012; Mayer, 2012).

Finally, the intensification of the water cycle (Huntington, 2006), with more frequent and severe droughts (Mantua et al., 2010; Giuntoli et al., 2013; Prudhomme et al., 2014), as well as more intense and sudden floods (Blöschl et al., 2019) can decouple Ta-Tw trends, exacerbating Tw increases that will most likely be evident during summer low flows when thermal capacity and flow velocity are at their minima (Webb, 1996; Webb et al., 2008). For instance, van Vliet et al. (2013) and Michel et al. (2021) found that an increase in Tw happened where an increase in Ta and a decrease in Q occurred coincidentally. This may also lead to the synchronicity of high temperatures and low flows, doubling the problem for cold-water aquatic communities (Arismendi et al., 2013b; Arevalo et al., 2020). There is thus a clear need to improve our estimates of Tw changes to assess how stream ecosystems will respond in the face of a changing climate. Unfortunately, extrapolating trend estimates and changes derived from short time series may lead to paradoxical results, e.g., cooling streams in a warming world (Arismendi et al., 2012).

This discrepancy in short- and long-term dynamics is likely due to confounding influences of Ta and hydrology, with implications for the persistence of specialized aquatic organisms (e.g., for cold-water biota, as shown by Arismendi et al., 2013b) and the completion of their life cycle (e.g., for diadromous fish, Arevalo et al., 2020). Hence, from an ecological perspective, it will be critical to understand and deconvolve the joint influence of changing Tw and Q regimes from the past to the future using long-term time series.

1.4 Longitudinal profile of stream temperature

The cumulative effects of both natural and anthropogenic drivers on thermal regimes lead to the propagation of the thermal signal from low upstream Tw to high downstream Tw at a whole basin scale (see Figure 1.1). Indeed, Tw starts with some upstream temperature (T0) and then undergoes some changes as the result of heat exchange with ambient conditions. After traveling some time, it tends towards an equilibrium temperature (Te) (Figure 1.4; cf. Mohseni and Stefan, 1999). Te is the temperature at which the heat exchange between Tw and the atmosphere is null. There are two types of T0 (see Figure 1.4): 1) T0 may be warm and similar to the groundwater temperature in winter or the temperature of released water from the top of small impoundments (see Figure 1.3). 2) T0 may be cool and similar to groundwater temperature in summer or the temperature of released water from the bottom of large reservoirs (see Figure 1.3). Indeed, the temperature of water released from the bottom of a large reservoir is cool due to the stratification phenomenon, and it can reduce downstream Tw (Olden and Naiman, 2010, and see Figure 1.3). Such cool T0 can be also due to snowmelt in spring.

Our understanding of the longitudinal variation of Tw is improving thanks to programmable digital thermometers (Webb et al., 2008; Steel et al., 2017). In recent years, the non-invasive method of thermal infrared remote sensing (TIR) has provided measurements for unshaded medium and large rivers (Handcock et al., 2006; Lalot et al., 2015). Such method however remains limited, costly, complex, and temporally limited as well as being sensitive to cloud cover (satellite), or weather conditions (airborne) (Handcock et al., 2012). Thus, we still have a limited understanding of longitudinal variations of Tw at a large scale.

1.5 Modeling stream temperature

To better understand the impacts of impoundments and global climate changes on Tw at a large scale, and in the absence of more robust data sources, modeling Tw is an indispensable tool. Models can provide us with detailed, long-term data over a large scale. However, model selection entails important considerations. For example, Tw can be estimated through a statistical (or stochastic) model based on multiple independent drivers (Benyahya et al., 2007), a common

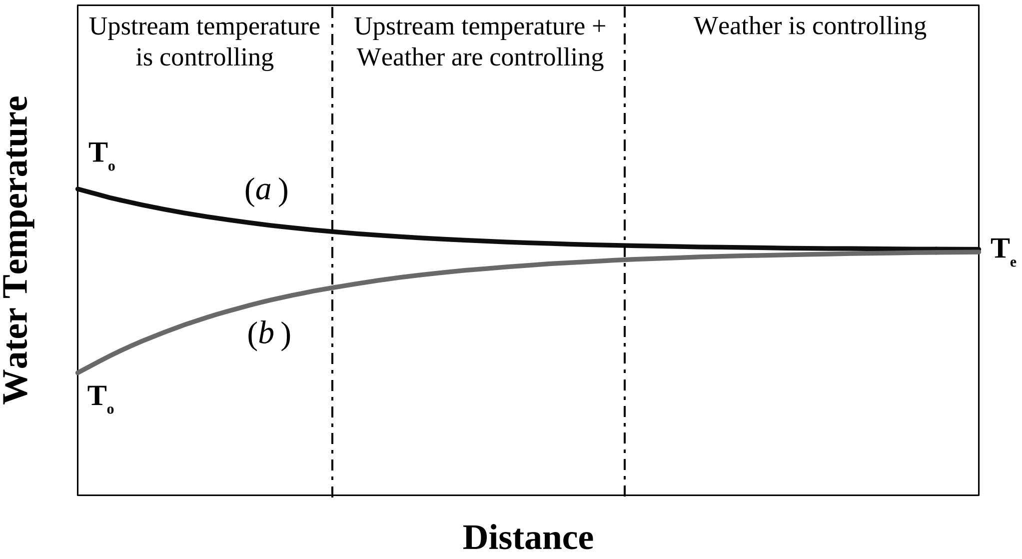

Figure 1.4: Schematic representation of the influence of the upstream Tw on the longitudinal profile. This figure is adopted from Mohseni and Stefan (1999). Tw after some travel time tends towards an equilibrium temperature: (a) a warm upstream Tw (e.g., groundwater input in winter or released water from small impoundments); (b) a cold upstream Tw (e.g., groundwater in summer, hypolimnetic water from a reservoir), or snowmelt in spring.

practice for large scale studies (e.g. Mantua et al., 2010; Isaak et al., 2012, 2017; Jackson et al., 2017, 2018). However, such statistical models lack mechanisms. In fact, they cannot reveal specific energy transfer mechanisms that are responsible for the spatio-temporal patterns of Tw (Dugdale et al., 2017). They are also unable to predict Tw for periods other than those used for their calibration, due to a non-stationary relationship between Ta and Tw (Arismendi et al., 2014).

Alternatively, physically-based (or deterministic) models are entirely mechanistic. They predict Tw dynamics over time and space through a heat budget, accounting for energy exchanges at the water-air and water-stream bed interfaces (see Figure 1.1), and the cumulative effects of controlling factors on energy transfer (Sinokrot et al., 1995; Webb and Walling, 1997; Yearsley, 2009; van Vliet et al., 2013). There are five heat fluxes at the water-air interface (Hannah et al., 2008; Dugdale et al., 2017): 1) net solar radiation, which is typically the largest heat flux (Webb and Zhang, 1997), 2) atmospheric longwave radiation, 3) long-wave radiation emitted from the water, 4) convection, and 5) evaporation. At the water-stream bed, the heat is exchanged through advection (groundwater inputs or tributary inflows) and conduction.

The physical process-based thermal models face some limitations like their statistical counter partners. For instance, they can be data-intensive. They may also lack routines representing the heat flux from snowmelt, precipitation, soil water, and in-stream chemical and biological process. They may also disregard the influence of impoundments and reservoirs (Dugdale et al., 2017). Nevertheless, they can be used not only to reconstruct past time series but they can be used in forecasting or predicting Tw response to projected climate or land-use changes (Caissie et al., 2007; Dugdale et al., 2017). A range of physical process-based thermal models have already been developed and published, but they may differ in terms of representation of each heat flux component, output resolution/output storage, complexity, coupling with other models (i.e., hydraulic or hydrological models), applicability to other regions, accessibility, and finally and importantly, spatial and temporal resolution (Dugdale et al., 2017). Such consideration should be taken into account by users when selecting a thermal model.

1.6 Objectives of the dissertation

The main objective of this study is to understand and explain current and future Tw changes under the impact of impoundments and climate change at a large scale. For this aim, the Loire river basin (10^5 km^2) is selected as the study area since it presents several advantages: 1) it is one of the largest European basins; 2) it covers contrasting land use/land cover and climatic conditions (Moatar and Dupont, 2016); 3) it hosts contrasting impoundments (i.e., dams and ponds); 4) many Tw measurements data are available for this region; and 5) finally, a high-resolution physical process-based thermal model (T-NET, Temperature-NETworkT-NET) (Beaufort et al., 2016a; Loicq et al., 2018) coupled with a semi-distributed hydrological model (EROS) has already been developed over this basin (Thiéry, 1988; Thiéry and Moutzopoulos, 1995; Thiéry, 2018).

The most important challenge in this effort is to identify the influence of dams and ponds on stream temperature. Indeed, firstly, the T-NET thermal model is a process-based thermal model that does not consider the influence of impoundments on thermal energy balance and thus could only produce “natural” thermal regimes. Therefore, the thermal model can not be used at this point. Secondly, observed Tw data above and below the impoundments, and before and after impoundments construction are not available for comparing thermal regimes and addressing the impacts of dams and ponds, a traditional practice favored by existing literature.

Consequently, the first objective of this dissertation is to distinguish between altered and natural regimes and to identify the influence of dams and ponds without prior information on the source of modification or upstream water temperature conditions using a simple and data-based approach. The second objective of this work is to make some modifications to the T-NET thermal model (to improve hydraulic geometry and riparian shading). The third objective is to use the modified T-NET thermal model outputs to infer and quantify the impacts of dams and ponds at the altered stations identified through the first objective. The fourth objective is to reconstruct Tw over the past decades using the T-NET thermal model outputs to estimate the magnitude of past trends in simulated Tw and to assess the variation in such trends in relation to hydroclimate changes and landscape diversity. Finally, the last objective is to use the T-NET thermal model to project Tw under different future climate projections, estimate the magnitude of changes in projected Tw under such projections over the 21st century, and assess the influence of hydroclimate changes and landscape diversity on such changes. The schematic diagram illustrating these dissertation objectives is given in Figure 1.5.

1.7 Chapters of the dissertation

This doctoral project is constituted of 3 articles. One of these articles has already been published, one is under revision and the last one is in progress. The dissertation is structured as follows:

- **Chapter 2** presents the characteristics of the Loire River basin as well as surface waters, datasets of meteorological variables, observed Tw data, and observed Q data.
- **Chapter 3** presents a simple and data-based approach to distinguish between altered and natural thermal regimes. Here, borrowing the concept of hydrological signatures, we introduce the novel "thermal signatures" based on observed stream-air temperature linear regression and seasonality analysis to identify the influence of dams and ponds, and to determine their spatial distribution at a regional scale without prior information on the source of modification or upstream water temperature conditions. The content of this chapter was published in the journal of *Science of Total Environment*: Seyedhashemi, H., Moatar, F., Vidal, J.-P., Diamond, J. S., Beaufort, A., Chandesris, A., and Valette, L. (2020). Thermal signatures identify the influence of dams and ponds on stream temperature at the regional scale. Science of The Total Environment, page 142667.
- **Chapter 4** presents the principles and input datasets for both the EROS hydrological model and the T-NET thermal model. In this chapter, the modifications to the T-NET thermal model i.e. modifications to hydraulic geometry and to the riparian vegetation shading are described. Then, the performance of both the EROS and T-NET models is assessed at near-natural hydrometric and Tw stations. For assessing the performance of the T-NET thermal model, the natural stations identified in the previous chapter are used. Finally, the thermal model bias (i.e., the difference between simulated Tw and observed Tw) at influenced stations identified in the previous chapter is used to infer and quantify the influence of dams and ponds.
- **Chapter 5** deals with the reconstruction of natural Tw and Q time series over the past 57 years (1963–2019) at the scale of the Loire River basin and at the reach resolution by using the EROS and the T-NET models. The ability of both the EROS and the T-NET models to capture long-term temporal trends is assessed by using a few long-term

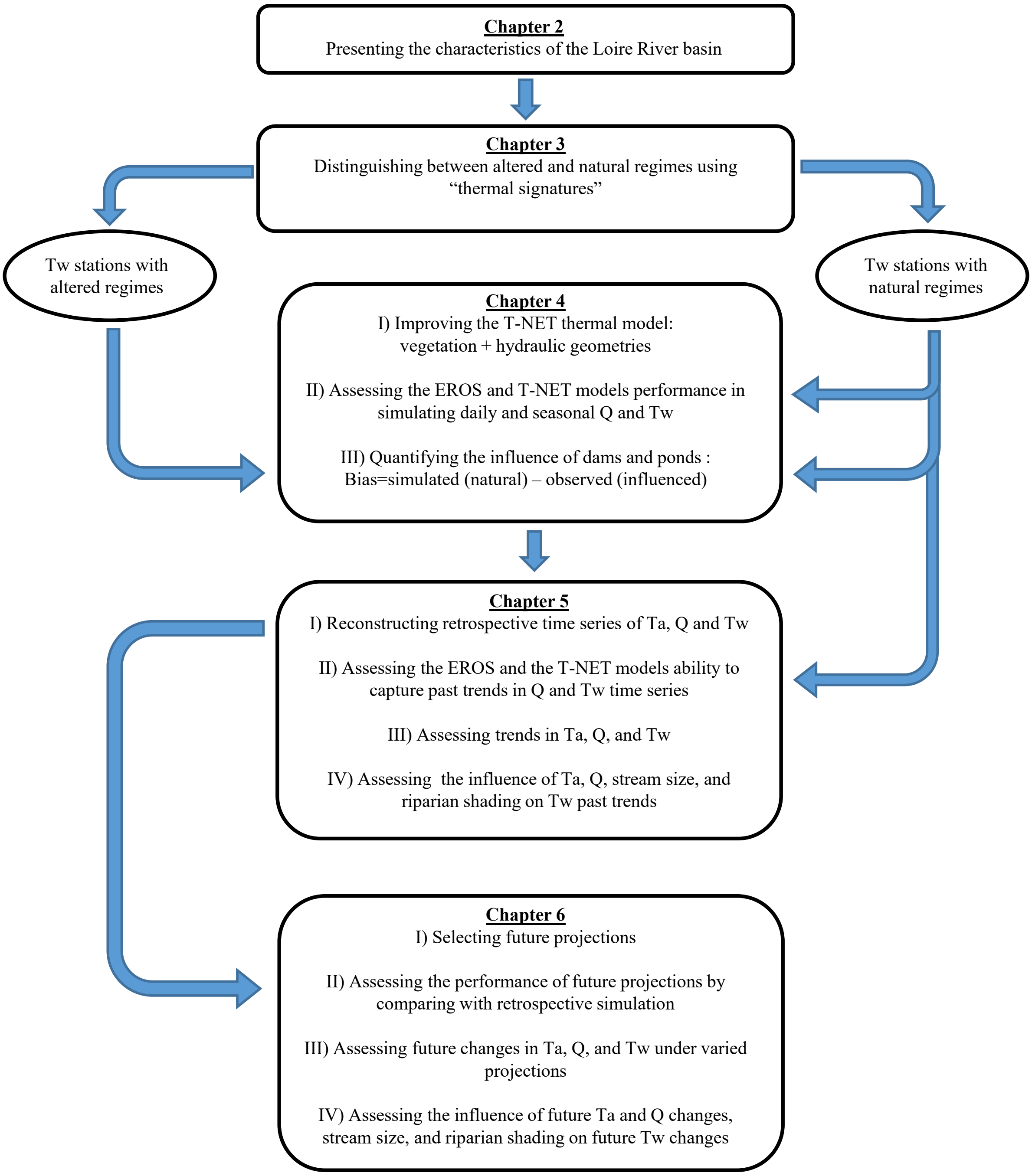

Figure 1.5: Schematic diagram illustrating dissertation objectives.

observations, with continuous daily data. The magnitude of trends in Tw (reconstructed by the T-NET thermal model), Q (reconstructed by the EROS hydrological model), and Ta (provided by the SAFRAN reanalysis data described in Chapter 2) are then estimated over the past 57 years. Finally, variations of decadal trends in seasonal and annual simulated Tw are discussed in relation to hydro-climatic changes (i.e., trends in Ta and Q), network size, spatial heterogeneity in the landscape, and riparian shading. The content of this chapter is published as a preprint in the journal of *Hydrology and Earth System Science* and is under review: Seyedhashemi, H., Vidal, J.-P., Diamond, J. S., Thiéry, D., Monteil, C., Hendrickx, F., Maire, A., and Moatar, F. (2021). Regional, multi-decadal analysis reveals that stream temperature increases faster than air temperature. Hydrology and Earth System Sciences Discussions, pages 1–31.

- **Chapter 6** first presents the state-of-the-art for future climate projections used in the present study. Natural Tw and Q time series are then projected under selected varied future climate projections over the 21st century at the scale of the Loire River basin and at the reach resolution by using the EROS and the T-NET models. The magnitude of Tw, Ta, and Q changes under different future climate projections is estimated, and the spatial and temporal links between Tw changes and hydro-climate changes are studied. The performance of projections is assessed beforehand by comparing meteorological variables and Tw in projections with those in the retrospective simulation (obtained from Chapter 5) over the recent decades. Finally, future Tw is studied as a function of stream size and riparian shading.

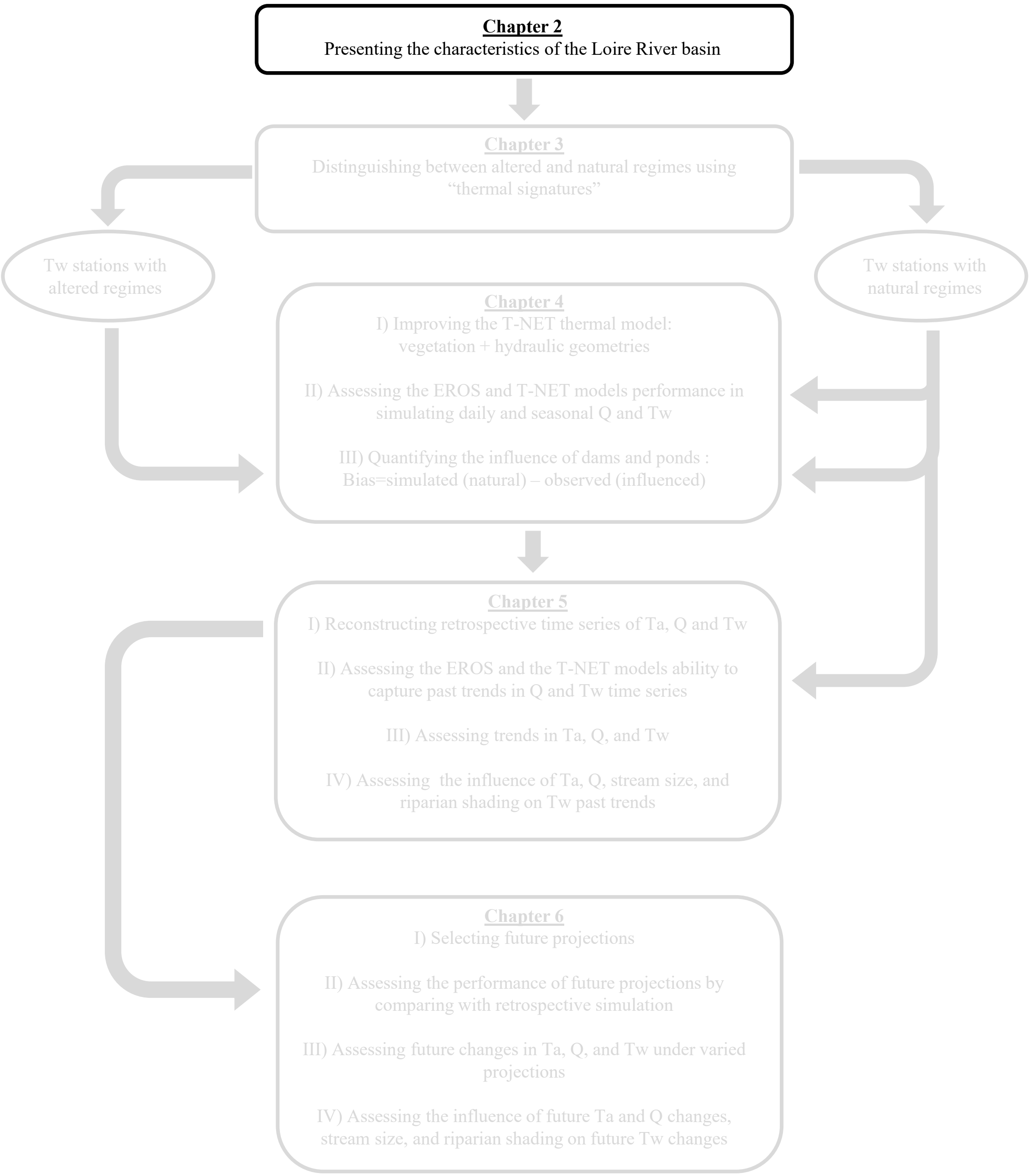

Schematic diagram illustrating thesis objectives.

CHAPTER 2

The Loire River basin and data

2.1 General information

The Loire River basin is one of the largest in Europe (10^5 km^2, 1 012 km), and represents 20% of French territory. This basin includes five main tributaries: Allier (18 700 km^2), Cher (13 700 km^2), Indre (4 000 km^2), Vienne (20 000 km^2), and Maine (21 300 km^2). It encompasses an area with contrasting land use/land cover, climatic conditions (Moatar and Dupont, 2016), and anthropogenic impoundments (Figure 2.1)– characteristics that make it an ideal case study to disentangle the drivers of the spatio-temporal heterogeneity in Tw. The variability in mean annual precipitation (P) (549–2130 mm), mean annual potential evapotranspiration (PET) (550–850 mm), mean annual Ta (6.0–12.5°C) (Figure 2.2) and altitude (10–1850 m) (Figure 2.1, right panel) provide spatial heterogeneity in Tw regimes.

There are five main HydroEco Regions (hereafter referred to as "HER") in this basin, which were previously categorized based on climate, lithology, and relief (Wasson et al., 2002). Since two of these HERs are very small compared to the other ones, they are merged with the nearest HER (see Figure 2.3). Thus, three main HERs are considered in this study (Figure 2.1). This is consistent with a previous study on this basin conducted by Beaufort (2015).

Granite and basalt dominate the south headwaters of the catchment in HER A (mostly in the Massif Central; 45 600 km^2) (Figure 2.1, left panel). The lower values of mean annual Ta (Median=10 °C) and PET, and higher values of mean annual liquid (median=824 mm) and solid (median=35 mm) P are found in this HER (Figure 2.2). The high-altitude areas are also in this part of the basin (Figure 2.1, right panel). Sedimentary rocks occupy the middle reaches in HER B, with a potential for groundwater input (53 200 km^2), followed by granite and schist in the lower reaches in HER C (11 200 km^2). The higher values of mean annual Ta (median=11.5 °C) and PET ($>$ 750 mm), and lower values of mean annual liquid (median=740 mm) and solid (median=12 mm) P are found in these two HERs. The percentage of riparian vegetation cover (mean over both sides of a river bank at a buffer of 10 m, Valette et al., 2012) is more important in HER A (median=73%) and in HER B (median=68%) (Figure 2.1, middle panel). In HER C, the presence of riparian vegetation is quite heterogeneous (median=50%). These HERs are considered the main controls of landscape diversity and are used to explain spatial heterogeneity in Tw in the following chapters.

2.2 Surface waters

There are 13000 impoundments (reservoirs, lakes, and ponds) in the Loire River basin. These surface waters cover approximately 0.8% of the Loire River basin (obtained from BD CARTHAGE® , IGN, 2006), and include 11 natural lakes and numerous artificial ponds, shallow reservoirs ($6 \text{ m} < \text{height} < 15 \text{ m}$), and large dams ($\text{height} \geqslant 15 \text{ m}$) (Figure 2.1, right panel). Unfortunately, there is no information about mode-of-operation of reservoirs and ponds, and the dimensions of all ponds. Therefore, reservoirs with the $\text{height} \geqslant 15 \text{ m}$ are considered large reservoirs and are called "dams" in the current study. Dams constitute 0.5% of surface waters, and therefore, over 99% of surface waters are actually shallow reservoirs ($6 \text{ m} < \text{height} < 15$ m), natural lakes, and ponds. Up to 70% of surface waters have a surface area of less than 10 ha, and less than 0.6% of the surface waters (by number) are shallow reservoirs and natural lakes. Hence, over 98% of surface waters are artificial ponds, commonly dedicated to irrigation or recreation. Based on these observations, this study considers surface waters that are not dams to be “ponds”, while recognizing that a small proportion of these so-called ponds may indeed be shallow reservoirs or natural lakes. Height and volume estimates are unavailable for most of these artificial ponds.

In addition to ponds and natural lakes, the Loire River basin houses 73 large dams (total storage capacity=999 Mm^3; see Figure 2.1, right panel), which are used for hydroelectricity (734 Mm^3), drinking water (57 Mm^3), recreation (32 Mm^3) and navigation (234 Mm^3). The two largest dams in the basin are: 1) Naussac dam (190 Mm^3, height=50 m), and 2) Villerest dam (138 Mm^3, height=59 m). These large dams are located in the upstream part of the basin (HER A), with granite and basalt lithology, and little influence of groundwater input. The data on dams’ characteristics (location, height, and volume) are provided by the Loire-Bretagne water agency (AELB) (Chandesris and Pella, 2006).

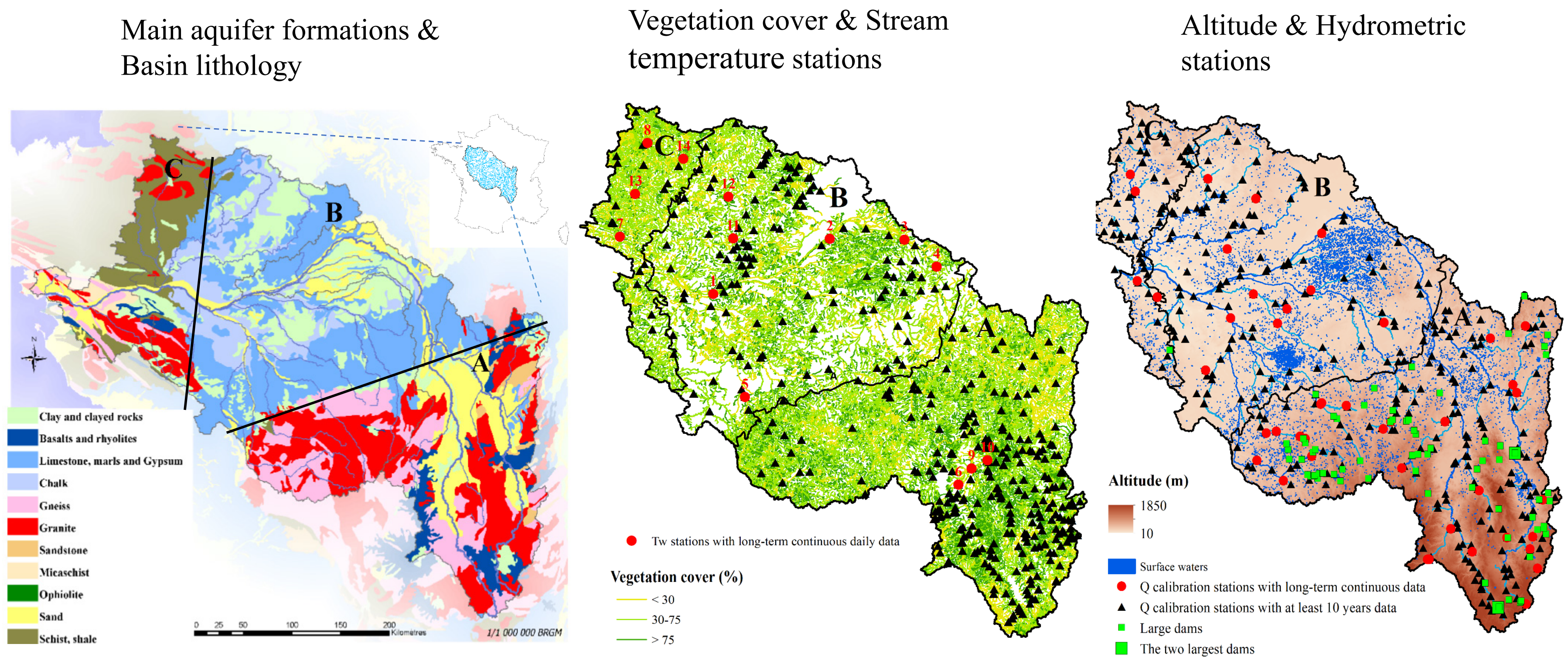

Main aquifer formations & Basin lithology

Vegetation cover & Stream temperature stations

Altitude & Hydrometric stations

Figure 2.1: Maps of the Loire River basin and characteristics. Left panel: main aquifer formations and lithology. The lithology map is adopted from Moatar and Dupont (2016), based on original data from BRGM (French Geological Survey). Middle panel: vegetation cover (Valette et al., 2012) and Tw stations. The 14 Tw stations in red in the middle panel have the long-term Tw data (see Table 2.1). These 14 stations are used to assess the ability of the T-NET model to capture long-term trends (see section 5.2, p. 133). The numbers in red in the middle panel correspond to the ID of long-term Tw stations in Table 2.1. Right panel: altitude (IGN, 2011), surface waters (IGN, 2006), and hydrometric stations (extracted from French national Banque Hydro database: http://www.hydro.eaufrance.fr/). All hydrometric stations (in black) are used for calibrating the EROS hydrological model (see section 4.1, p. 85). 44 hydrometric stations on the French Reference Hydrometric Network (RHN) (in red) are used for assessing the ability of the EROS model to capture long-term trends (see section 5.2, p. 133). Small green square points in the right panel show the large dams (height > 15 m), and big green square points show the two largest dams in the basin. The data on dams' characteristics (location, height, and volume) are provided by the Loire-Bretagne water agency (AELB) (Chandesris and Pella, 2006).

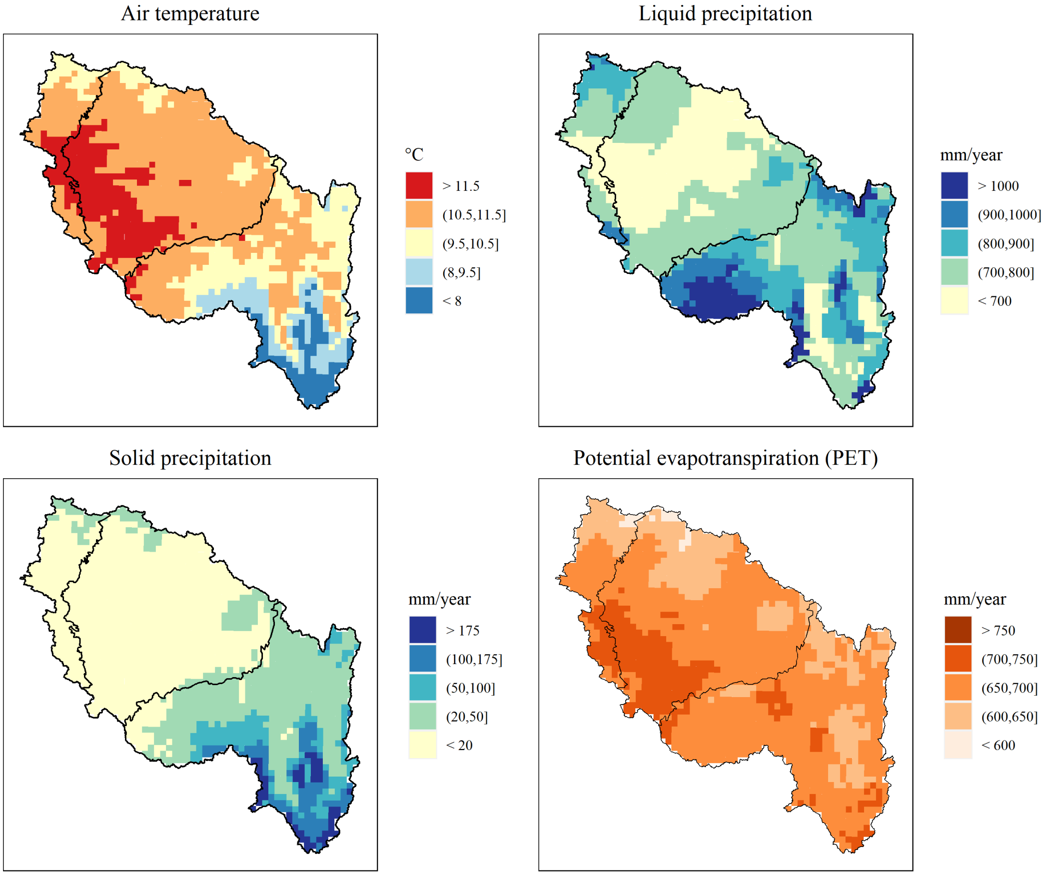

Air temperature

Liquid precipitation

Solid precipitation

Potential evapotranspiration (PET)

Figure 2.2: Annual mean Ta, liquid and solid P, and PET over the 1958–2019 period. These data are derived from the SAFRAN reanalysis data (Quintana-Segui et al., 2008; Vidal et al., 2010, and see section 2.3.1).

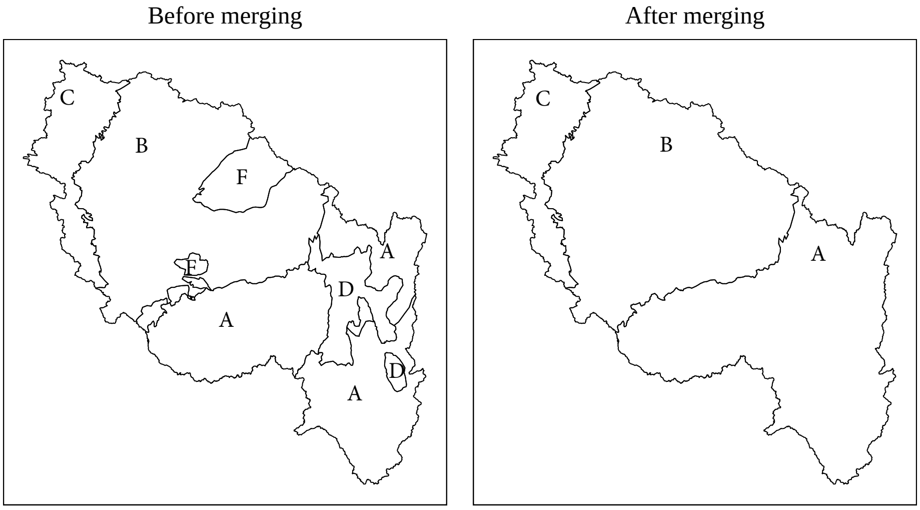

Before merging

After merging

Figure 2.3: The HydroEco Regions (HER) in the Loire basin. Two of these HERs (left panel) are merged with the nearest HER (right panel).

2.3 Meteorological and hydrological data

The following sections describe all the datasets of meteorological variables, observed Tw data, and observed Q used in the next chapters.

2.3.1 Meteorological data

Hourly Ta (°C), specific humidity (g.kg^{-1}), wind velocity (m.s^{-1}), shortwave radiation (W.m^{-2}), longwave radiation (W.m^{-2}) (see Le Moigne et al., 2020, for more information about the recent changes and biases), solid and liquid precipitation (P) (mm), and potential evapotranspiration (PET) (mm, and calculated using Penman-Monteith equation, Allen et al., 1998) are provided by the 8 km gridded SAFRAN atmospheric reanalysis data released by Météo France over the 1958–2019 period (Vidal et al., 2010). SAFRAN is a mesoscale analysis system for atmospheric variables near the surface. It uses surface observations, combined with global meteorological models to produce hourly variables at the French national scale through data assimilation with an optimal interpolation algorithm (Quintana-Segui et al., 2008). The first guess of SAFRAN comes from ERA-40 (Uppala et al., 2005), a reanalysis of the global atmosphere and surface conditions produced by ECMWF (European Centre for Medium-Range Weather Forecasts). These meteorological variables are used in Chapter 4 as the input data of both the EROS and T-NET models. The daily Ta is used in Chapter 3, and Ta at each Tw station is derived from the daily-averaged data of the closest SAFRAN grid cell to the Tw station.

2.3.2 Observed stream temperature

Daily observed Tw data are available at 694 stations (which are scattered over the Loire River basin, and include natural and influenced thermal regimes) over the 2000–2018 period. Most of these stations are managed by the French Agency for Biodiversity (http://www.naiades.eaufrance.fr) and the National Fishing Federation (https://www.federationp-eche.fr) (22% and 67% of the stations, respectively). These data were collected in the “TIGRE” project (Beaufort et al., 2020b, and see https://thermie-rivieres.inrae.fr/). In that project (conducted at the national scale), hourly temperature measurements were considered to be outliers when they exceeded a certain threshold or when the variation between two hours (at the hourly time step), intraday, or between two consecutive days (at the daily time step) seemed too strong to be considered natural. Then, the resulting hourly data were screened visually before being averaged into the mean daily stream temperature (Beaufort et al., 2020b).

In the current study, corrected hourly Tw times series from the TIGRE project over the Loire River basin are averaged into mean daily stream temperature. Here, these daily Tw time series are again checked visually before being used. This visual analysis allows for the diagnosis of measurement errors in some of the daily time series (see Figure 2.4 as an example), through the comparison of daily Tw with daily Ta. Indeed, Tw is expected to be close to Ta, and no big difference between the daily time series of these variables (like the ones displayed in Figure 2.4) should be observed. In our visual assessment, 6 % of the original 694 Tw stations are removed due to the diagnosed errors. Finally, after removing measurement errors, stations with at least one complete year of daily Tw data are retained. The data availability of the final stations with complete-year data over the 2000–2018 period is presented in Figure 2.5.

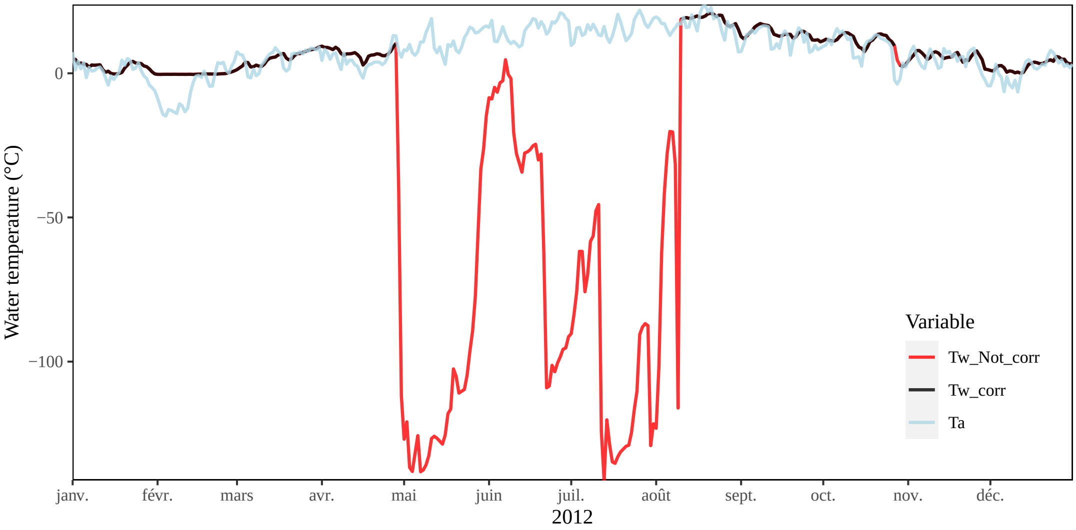

Figure 2.4: One example of the errors found in observed Tw data. Tw–Not–cor: Tw before correction; Tw–corr: Tw after correction; Ta: air temperature.

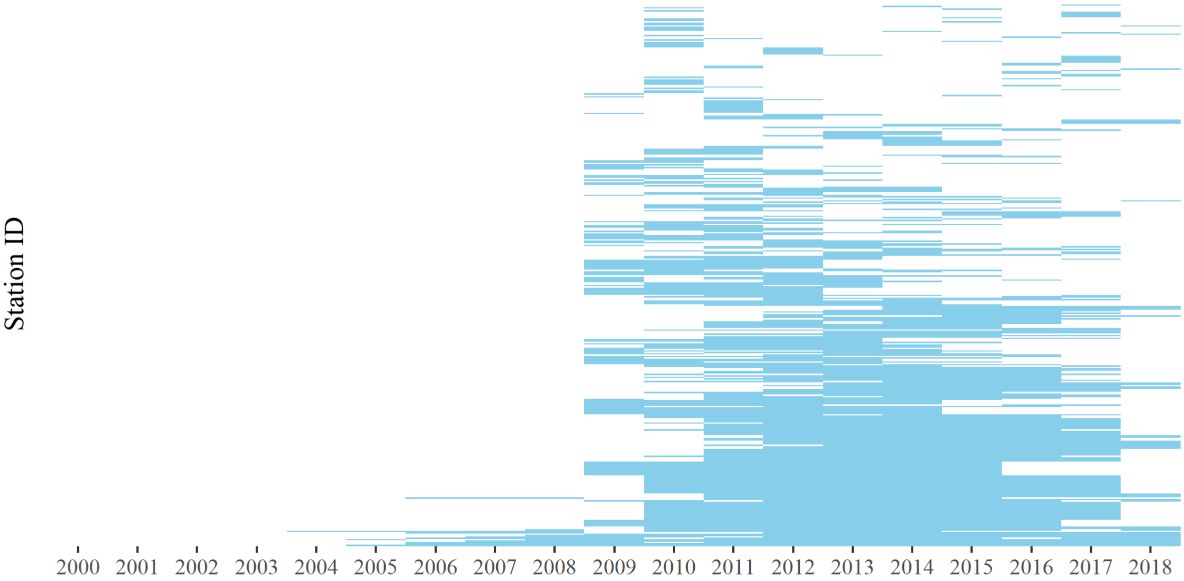

Figure 2.5: Data availability of observed daily Tw over the 2000–2018 period, from 392 stations with at least one complete year of daily data.

Indeed, there are very few stations with complete-year daily data over the 2000–2007 period (see Figure 2.5). Thus 392 stations with missing years over the 2008-2018 period are retained. These Tw stations are scattered homogeneously around the Loire river basin (see Figure 2.1, middle panel). 14 stations of these 392 Tw stations have the long-term continuous daily (≥ 8 years) data between 1977 and 2019, most of which are located on medium and large rivers (Table 2.1; see red points in Figure 2.1, middle panel). These 14 stations with long-term continuous daily data are mainly used in Chapter 5 for assessing the ability of the T-NET thermal model to capture the long-term temporal trends.

Table 2.1: The 14 Tw stations with long-term data. See red points in Figure 2.1, middle panel for the position of these stations. The ID of each station corresponds to the numbers (in red) shown in the Figure 2.1, middle panel.

ID	River (Location)	Catchment area (km^2)	Record period	Total years	Source of data
1	Loire (Chinon)	57043	1977–2019	43	EDF
2	Loire (St-Laurent)	38088	1977-2019	43	EDF
3	Loire (Dampierre)	36212	1977–2019	43	EDF
4	Loire (Bellevile)	35172	1979–2019	41	EDF
5	Vienne (Civaux)	5795	1997–2017	21	EDF
6	Artière (Clermont-Ferrand)	48	2005–2017	13	DREAL Auvergne
7	Oudon (Segré)	1342	2004–2014	11	DREAL PDL
8	Mayenne (Ambrières-les-Vallées)	825	2004–2014	11	DREAL PDL
9	Bedat (Saint-Laure)	419	2008–2017	10	DREAL Auvergne
10	Credogne (Puy-Guillaume)	84	2008–2017	10	DREAL Auvergne
11	Loir (Flée)	6215	2010–2017	8	DREAL PDL
12	Huisne (Montfort-le-Gesnois)	1931	2010–2017	8	DREAL PDL
13	Jouanne (Forcé)	413	2010–2017	8	DREAL PDL
14	Merdereau (Saint-Paul-le-Gaultier)	123	2010-2017	8	DREAL PDL

Most of these 392 Tw stations (50%) have at least 5 years of data, with only 1.7% having complete 11 years of temperature data and 33% having less than 3 years of data (see Figure 2.5). 64% of these stations are located in HER A, 29% are situated in HER B, and the remaining stations belong to HER C. These stations represent a wide range of river discharge (mean annual discharge 72–1050 mm.y^{-1}) and width (1.5–181 m), with 75% of the stations located on rivers with a Strahler order from 2 to 4. The mean annual Tw (over the 2008–2018 period) varies mainly between 8 °C in the upstream part of the basin and 14 °C in the western downstream part (Figure 2.6). The vegetation cover (mean over both sides of a river bank at a buffer of 10 m; Valette et al., 2012) at these stations ranges between 0% and 100%.

2.3.3 Observed streamflow

There are 352 hydrometric stations with at least 10 years of daily observations available between 1971 and 2018 in the Loire River basin (range=40-1600 km^2; mean=300 km^2). Observed daily Q data at these stations are extracted from the French national Banque Hydro database (http://www.hydro.eaufrance.fr/). Stations along the main Loire and Allier rivers are highly

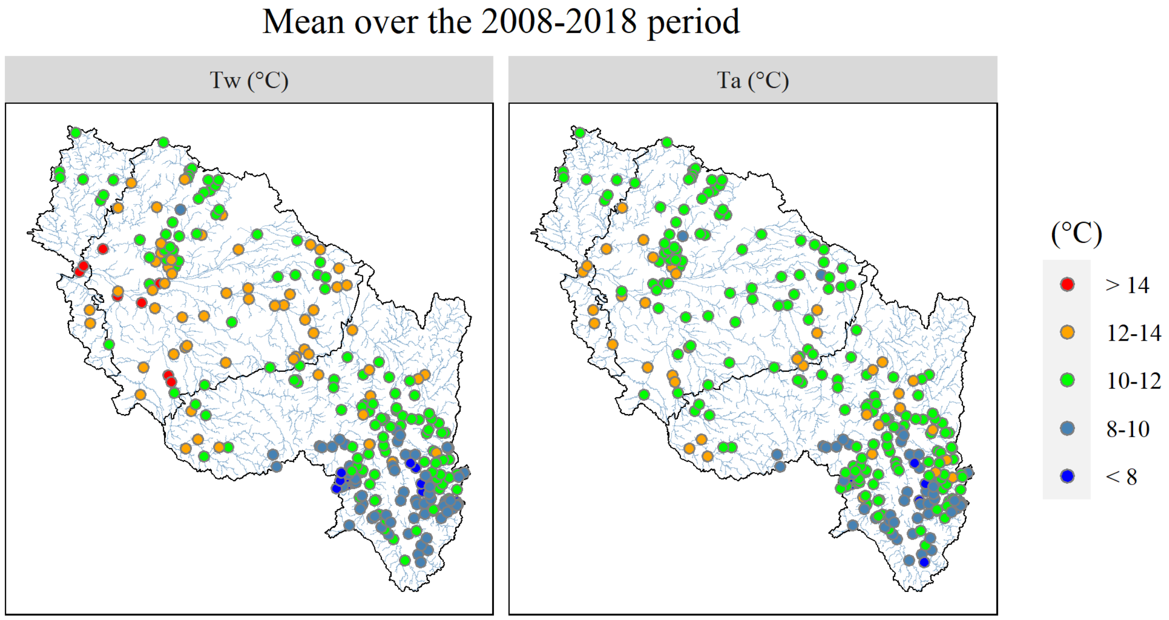

Figure 2.6: The interannual mean of Tw and Ta over the 2008–2018 period at 392 Tw stations. The daily Ta at each Tw station is derived from the daily-averaged data of the closest SAFRAN grid cell to the Tw station (see section 2.3.1).

influenced by the management of large dams, notably through summer releases to sustain low-flows (https://www.eptb-loire.fr/). Time series for these stations have been naturalized by EDF (electricity producer) by taking into account dam storages and releases. These naturalized Q time series are provided by Céline Monteil (from EDF). The list of these stations can be found in Table A.3 in Appendix A. These 352 stations are mainly used in Chapter 4 for calibrating the EROS hydrological model.

Of these 352 hydrometric stations, 44 are part of the French Reference Hydrometric Network (RHN) described by Giuntoli et al. (2013), which gathers stations with long-term continuous high-quality data gauging near-natural catchments. These 44 RHN stations with long-term continuous daily data are mainly used in Chapter 5 for assessing the ability of the EROS hydrological model to capture the long-term temporal trends. These 352 and 44 hydrometric stations are presented with black and red points, respectively, in Figure 2.1 (right panel). The list of all hydrometric stations can be found in Tables A.1 and A.2 in Appendix A.

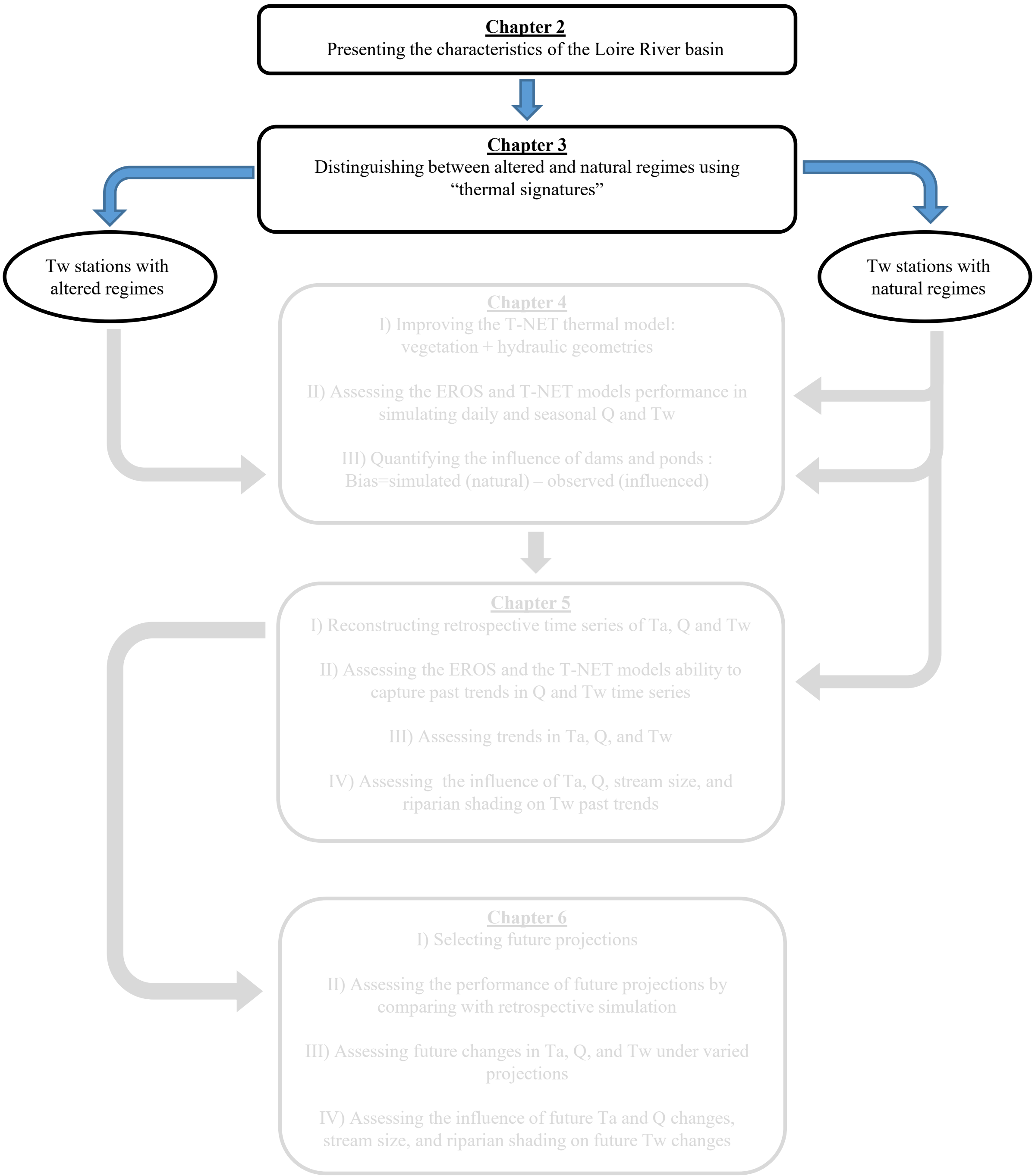

Schematic diagram illustrating thesis objectives.

CHAPTER 3

Thermal signatures identify the influence of dams and ponds on stream temperature

Anthropogenic impoundments (e.g., large and small reservoirs, and ponds) are expanding in number globally, influencing downstream temperature regimes in a diversity of ways that depend on their structure and position along the river continuum. However, there has been a paucity of studies characterizing the cumulative effects of these impoundments on thermal regimes at the catchment scale, and differentiating regimes altered by them from natural ones. This issue is due to the lack of detailed information about the heat budget in large-scale assessments (Webb and Zhang, 1997). To overcome the lack of Tw data, Ta is commonly used as a proxy for computing the river heat budget. Simple linear regression between water and air temperature is a common proxy technique to infer stream thermal regimes (Stefan and Preud'homme, 1993; Pilgrim et al., 1998; Mohseni et al., 1999; Erickson and Stefan, 2000; Caissie et al., 2004), but regression parameters are highly spatially variable. For instance, the river reaches without groundwater input typically have steep regression slopes with low intercepts, but opposite relations can emerge for groundwater-dominated reaches (Caissie, 2006; O'Driscoll and DeWalle, 2006; Kelleher et al., 2012). The relationship between Tw and Ta may also be altered by different types of anthropogenic disturbances, leading to a weaker correlation and/or a smaller regression slope (Erickson and Stefan, 2000; Webb et al., 2008; Bae et al., 2016).

These spatially variable relationships can therefore be used to infer the controls and drivers of stream temperature. Here, such relationships between observed Tw and Ta are also used to distinguish between altered and natural regimes. To do so, stations subject to alterations induced by impoundments are first selected. Then, analogous to "hydrological signatures" (Gupta et al., 2008), some "thermal signatures" based on the Tw-Ta relationship are defined to identify the influence of dams and ponds through a clustering approach. The derived clusters are validated in different ways. Finally, the characteristics of altered regimes are compared with natural ones.

Note that, in this chapter, the observed Tw data at the 392 stations with missing years between 2008 and 2018 described in section 2.3.2 (p. 46) are used.

3.1 Selecting stream temperature stations sensitive to alterations induced by impoundments

Stations are selected based on their potential to be influenced by anthropogenic structures. This effectively eliminates large rivers from the dataset because they are weakly sensitive to thermal regime alterations due to their larger conveyed volumes and their greater thermal inertia (Smith and Lavis, 1975; Webb and Walling, 1993; Caissie, 2006; Kelleher et al., 2012). Moreover, because large river temperatures are approximately in equilibrium with air temperature (Moatar and Gailhard, 2006; Bustillo et al., 2014), information extracted from regression-type analyses is often equivocal. Therefore, this study focuses on smaller rivers to identify altered regimes.

To subset the original dataset to focus on smaller rivers, stations that are in equilibrium with air temperature are removed using a distance-from-source threshold. To calculate this threshold, the interannual summer (June–August, referred to as “JJA” throughout) temperature average is regressed for both stream and air temperature on distance from headwater source (as derived from the Theoretical Hydrographic Network for France (RHT), Pella et al., 2012), and the intersection of the two regression lines is selected (Figure 3.1, left panel). Sites above the distance-from-source value at this intersection are then removed from further analysis.

The distance-from-source analysis exhibits that a distance of 100 km approximately delineates the designation between small and large rivers (Figure 3.1). Large rivers in this sense are rivers with stream temperature in equilibrium with air temperature and less sensitive to the human-induced alterations (Figure 3.1, right panel). These stations are therefore excluded, resulting in 330 stations with a median catchment area of 232 km^2 (range = 3–1600 km^2) and median width of 7m (range=1.5–34 m) (as derived RHT, Pella et al., 2012).

The majority of these 330 stations ($\sim$80%) have artificial ponds in their contributing area. There are 38 stations downstream of large dams (median distance = 6 km). However, no information on the mode-of-operation (e.g., peaking, run-of-river, storage, etc.) of these dams is available. Only four stations are located downstream of natural lakes (median distance = 4.15 km).

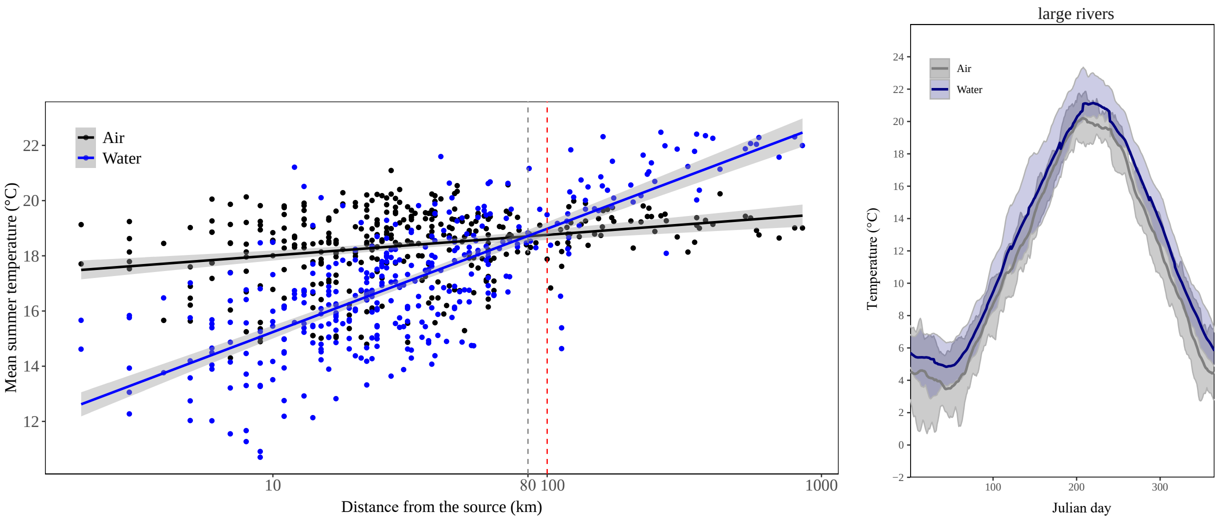

Figure 3.1: (left) Interannual mean summer Tw and Ta versus the distance from the source for 392 observed Tw stations. 38 stations with a large upstream dam are excluded in this preselection to avoid incidentally removing them. Indeed, in this step, it is assumed that all large dams alter downstream thermal regimes. Solid lines represent linear regression lines with a 95% confidence interval. The dashed grey line shows the exact intersection value, 80 km. It was decided to round this value to 100 km based on our judgment of the stations, and the objective of including as many stations as possible. Note that there are only nine stations with a distance from the source between 80 km to 100 km (the selected threshold for the rest of the work). (right) Annual air and stream temperature regimes of stations on large rivers. Shaded areas represent the 10th-90th percentile band, and the solid line represents the median value.

3.2 Defining “thermal signatures” of altered regimes

Typically, upstream reference conditions are used to identify the downstream thermal alterations of anthropogenic structures (Webb and Walling, 1993, 1996, 1997; Lowney, 2000; Preece and Jones, 2002; Casado et al., 2013; Chandesris et al., 2019). Since such information is in practice rather limited, the air temperature may be used as a proxy for the heat budget reference conditions. As such, a novel concept of “thermal signatures” based on air-water temperature relationships is suggested here to characterize regimes altered by anthropogenic influences. The choice of the name thermal signatures derives from the analogous concept of “hydrological signatures” (Gupta et al., 2008), which uses a statistical analysis of flow regimes to provide information about broader controls on hydrological behavior (e.g., dominant flow processes, strength, and spatiotemporal variability of the rainfall-runoff response; see Berhanu et al., 2015; McMillan et al., 2017). Hydrological signatures may also be based on soil moisture (Branger and McMillan, 2019) and snow data (Horner et al., 2020). Similarly, thermal signatures capitalize on indicators extracted from the statistical structure of local stream-air temperature relationships to identify the dominant processes (e.g., anthropogenic influences) that generate the observed stream temperature time series.

The choice of thermal signatures in the current study is based on a preponderance of literature evidence on the known impacts of dams and ponds and visual assessments. For instance in section 1.3.1 (p. 30), we saw that large dams delayed the annual cycle of thermal regimes, and ponds increased downstream Tw. Examples of visual assessments are also provided in Figures 3.2 and 3.4. Figure 3.2 compares the parameters of summer stream-air linear regression (slope and coefficient of determination) at two different stations. One of these stations (Figure 3.2, left panel) is downstream of a large dam, Queuille dam (5.9 Mm^3, height =28 m). The other (Figure 3.2, left panel) is downstream of a lot of ponds on Vincou stream (with 1.3 % ponded upstream catchment area; see Figure 3.3). The linear regression parameters (slope and coefficient of determination) at the station influenced by ponds (Figure 3.2, right panel), are greater than those at the station influenced by a dam (left panel) (slope=0.45 vs 0.19; and R^2= 0.5 vs 0.2).

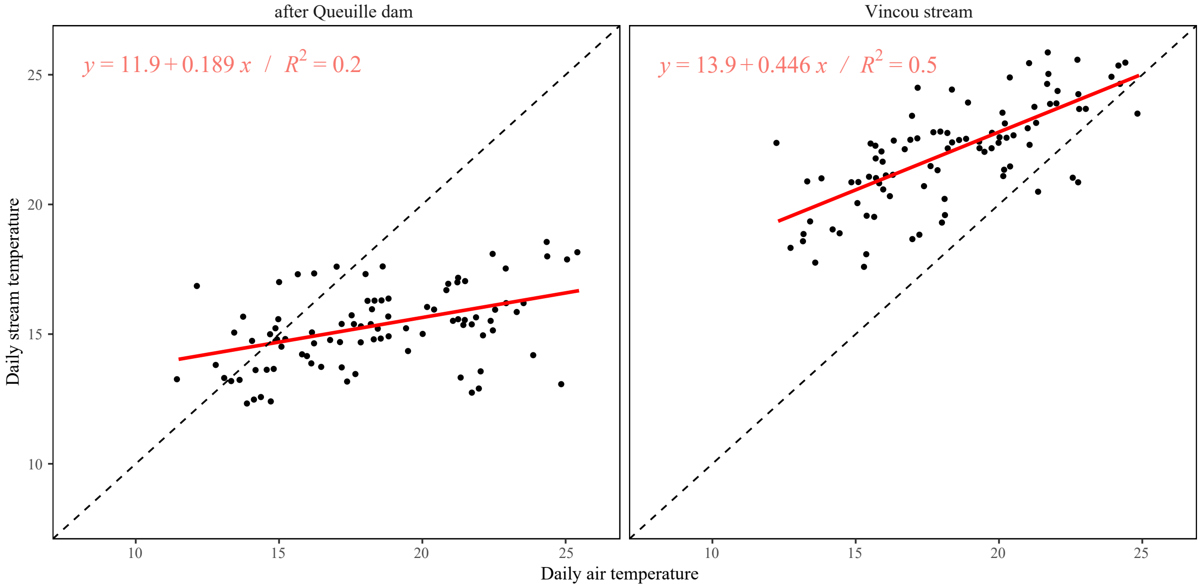

Figure 3.2: Examples of summer stream-air temperature regressions over a single year (left panel) downstream the large Queuille dam (5.9 Mm^3, height=28 m), and (right panel) downstream the highly ponded Vincou stream (with 1.3 % ponded upstream catchment area). Ponds lead to a higher stream-air temperature slope and coefficient of determination than the large dam.

Other examples of impacts of dams and ponds are provided in Figure 3.4, which depicts the time series of two groups of stations: 1) (top) stations influenced by an upstream dam, and 2) (bottom) stations influenced by ponds. Figure 3.4 (top left and top middle panels) shows the 30-days moving average of Tw and Ta time series upstream and downstream of Sidiailles dam (5.6 Mm^3, height = 22 m) in 2009. There is no difference between the annual peak of Tw and Ta in the upstream part of the Sidiailles dam. However, downstream part of this dam, the annual peak of Tw is shifted compared to that of Ta. Figure 3.4 (top right panel), downstream of Queuille dam (5.9 Mm^3, height = 28 m), also shows a shift in the annual peak of Tw compared to that of Ta in 2012. Unfortunately, there is no year with concomitant Tw data upstream and

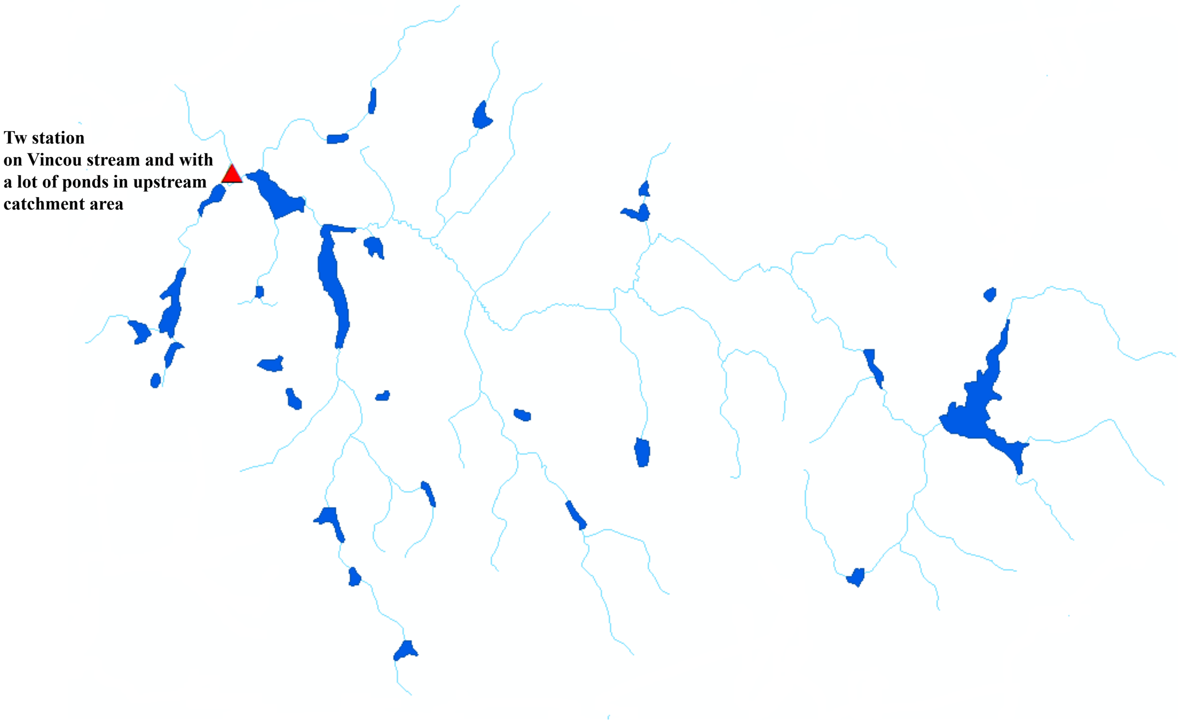

Figure 3.3: The Tw station downstream of the highly ponded Vincou stream (with 1.3 % ponded upstream catchment area). The blue polygons show the surface waters.

downstream of the dam.

Figure 3.4 (bottom left and bottom middle panels) shows the 30-days moving average of Tw and Ta time series upstream and downstream of the natural Chambon lake in 2014. There is no difference between the annual peak of Tw and that of Ta upstream and downstream of this lake. However, Tw regime is shifted up by 4 °C compared to Ta regime in the downstream part of the lake. Such a shift can also be seen at a station downstream of a lot of ponds on the Vincou stream in 2009 (see Figure 3.4, bottom right panel). Therefore, our thermal signatures can be defined based on these relationships.

Five thermal signatures are proposed to identify the dominant process of a thermal regime (Figure 3.5 and Table 3.1). The first two signatures are based on daily, summertime stream-air temperature linear regressions (see Figure 3.5, top panels). Stream-air temperature linear regression analysis may be conducted on annual data (Kelleher et al., 2012; Beaufort et al., 2020a) or summer data only (Mayer, 2012). The summer period is selected in the current study to capture the higher influence of large dam operations on stream temperature during these months.

The first derived thermal signature is the regression slope between the stream and air temperature, which is termed "thermal sensitivity", or TS (°C.$°C^{-1}$, or unitless [-]), because it indicates how sensitive stream temperature is to changes in air temperature (Kelleher et al., 2012). In natural streams, TS is greater when the climate is the main control on stream temperature, but

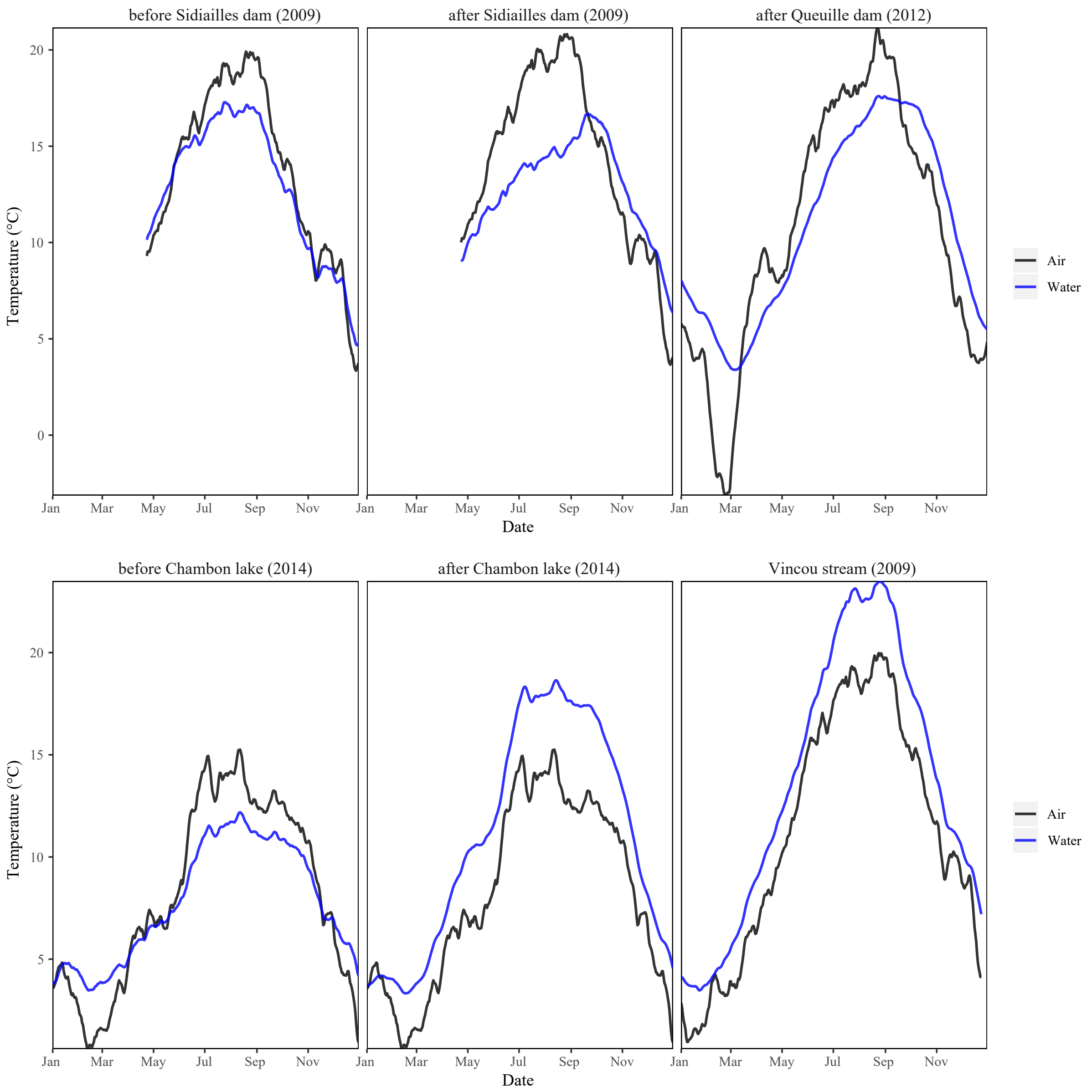

Figure 3.4: Examples of impacts of (top) dams and (bottom) ponds on stream temperature time series with respect to air temperature time series. (top left and middle) Influence of Sidiailles dam (5.6 Mm^3, height =22 m) with both upstream and downstream Tw data, and (top right) influenced of Queuille dam (5.9 Mm^3, height =28 m) with only downstream Tw data. (bottom left and middle) Influence of the natural Chambon lake with both upstream and downstream Tw data, and (bottom right) impact of the highly upstream ponded Vincou stream (with 1.3 % ponded upstream catchment area) with only downstream Tw data.

TS is lower where groundwater inputs are large (Caissie, 2006; Mayer, 2012; Beaufort et al., 2020a) or when dams reduce the temporal coupling between the stream and air temperature (like in Figure 3.2, left panel).

The second thermal signature is the coefficient of determination (R^2) of the regression between the stream and air temperature, which indicates the predictive capacity of air temperature on stream temperature, and therefore shows how strongly these variables are coupled (Kelleher et al., 2012). In natural streams, R^2 is high, whereas in streams with an upstream dam, R^2 is low, similar to TS (like in Figure 3.2, left panel).

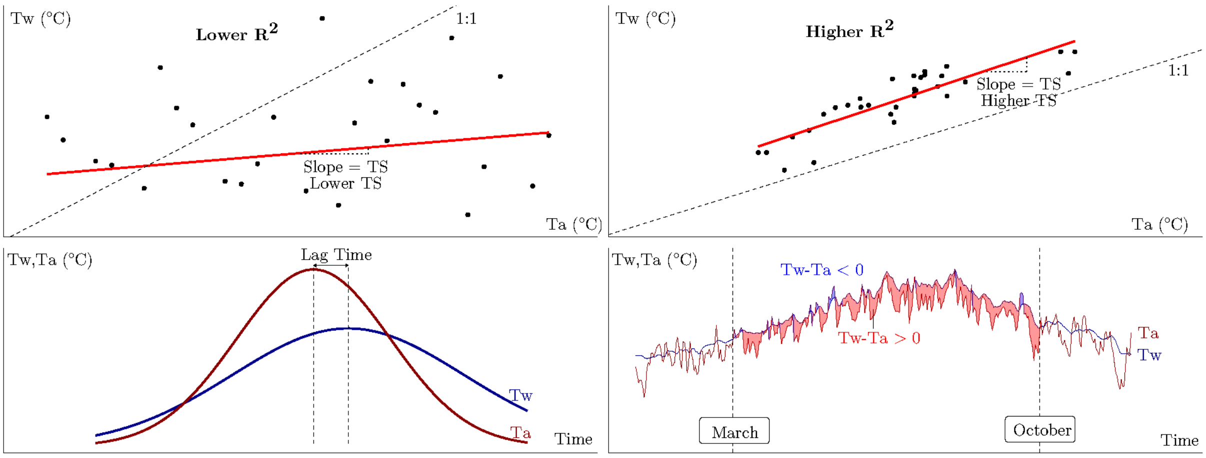

Dam Impact

Pond Impact

Figure 3.5: Conceptual representation of thermal signatures. Top row: daily stream-air temperature linear regression showing (left) lower TS (Thermal Sensitivity) and lower R^2 downstream of a dam, and (right) higher TS and higher R^2 downstream of ponds. Bottom row: stream and air temperature regimes showing (left) the lagged annual cycle of stream temperature relative to air temperature downstream of a dam, and (right) greater heating effect and thermal effect occurring more often downstream of ponds. See Table 3.1 for the detailed description of thermal signatures.

Table 3.1: Signatures used to identify altered and natural thermal regimes. Signatures are grouped into two groups based on their hypothesized ability to detect thermal effects from their respective anthropogenic structures: dam signatures and pond signatures. Note that these signatures are calculated based on interannual averages.

Signatures	Definition	Rationale
	Dam signatures	
Thermal sensitivity (TS)	Daily JJA stream-air temperature linear regression slope	Dams reduce TS
R^2	Daily JJA stream-air temperature coefficient of determination	Dams reduce R^2
Lag time	Lag time between the annual peak in 30-days moving average Tw and Ta regimes	Dams increase lag time
	Pond signatures	
Heating effect	Mean positive difference of daily stream-air temperature (Tw-Ta) from March to October	Ponds increase distributed energy storage, leading to heating
Thermal effect	Mean overall difference of daily stream-air temperature (Tw-Ta) from March to October	Ponds increase energy storage, even in the presence of natural cooling

The remaining three thermal signatures are derived from daily stream and air temperature time series (see Figure 3.5, bottom panels). The first one is the “lag time” (in days) between the annual peak of the two 30-days moving average time series. This signature detects how dams delay the annual cycle. The next signature, which is termed the “heating effect” (°C), is the mean positive difference of daily stream-air temperature (Tw-Ta) from March to October. This period is selected to avoid any snowmelt effect on stream temperature and to have the greatest increase in stream temperature due to ponds during the low-flow period. This heating effect indicates how energy storage in ponds increases downstream stream temperature. The last signature, which is termed the “thermal effect” (°C), is the mean overall difference of daily stream-air temperature (Tw-Ta) from March to October. The thermal effect indicates the overall temperature effects of ponds on downstream waters, accounting for potential natural cooling and mitigation of heating effects.

As presented in Table 3.1, it is hypothesized that because TS, R^2, and lag time would be able to capture the impacts of managed dams (indeed, dams would decrease TS and R^2 (Webb et al., 2008), and delay the annual cycle (Webb and Walling, 1993; Webb, 1996)), they would reveal dam signatures on thermal regimes. Similarly, It is hypothesized that the remaining two signatures (namely, the heating effect and the thermal effect) would detect the influence of energy storage observed in the presence of artificial ponds (Dripps and Granger, 2013; Chandesris et al., 2019), and thus reveal ponds signature on thermal regimes (Table 3.1). These thermal signatures are calculated for 330 stations over the basin. The five signatures are calculated at each station for each year with data and their interannual means are computed for further analysis.

Over the basin, thermal signature distributions tend to group together based on their hypothesized thermal signature (i.e., dam or pond; Figure 3.6). TS is spatially variable across the region and lacks clear patterning although most low TS (i.e., $TS < 0.2$) stations are located in the upstream part of the basin (Figure 3.6). In contrast, spatial distributions of R^2 and lag time vary much less, covary with each other, and are more spatially homogeneous. Indeed, 83% of stations have both high R^2 (i.e., > 0.6), and short lag times (i.e., < 20 days). Visual inspection reveals that stations with low TS coincide with lower values of R^2 (< 0.6), and higher values of lag time (> 30 days) in the upstream part of the basin. Ranges of heating and thermal effects are 0.05 °C to 4 °C and -4.9 °C to 3.7 °C, respectively, but the interquartile ranges are much narrower: 0.54 °C to 1.14 °C and -1.58 °C to 0.16 °C, respectively. Stations with larger heating effects (e.g., > 1 °C), tend to exhibit greater thermal effects (e.g., > 1 °C) as well (r=0.9).

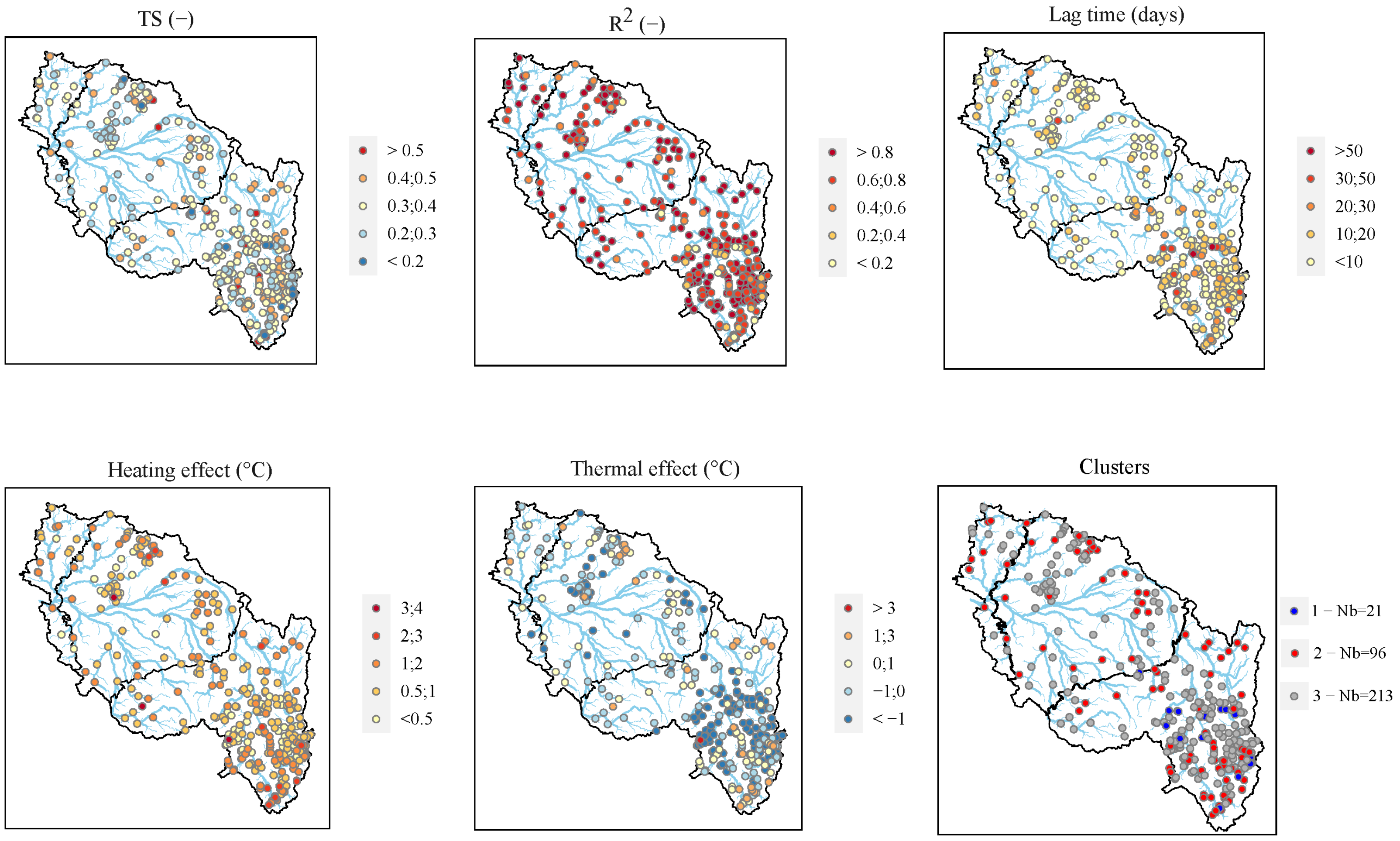

Figure 3.6: Spatial distribution of the five thermal signatures at 330 stations over the Loire River basin. The top row is expected dam signatures and the bottom row (i.e., heating and thermal effects) are expected pond signatures. bottom right panel: the spatial distribution of the stations in three obtained clusters (see section 3.3).

3.3 Identifying altered regimes through clustering

The objective of this step is to cluster stations using the scaled values of the five thermal signatures defined in Table 3.1. For this aim, K-means clustering (with Euclidean distance) is used. This method is an unsupervised learning algorithm that partitions n observations into k clusters, where each observation belongs to the cluster with the nearest mean, serving as a representative of the cluster. In theory, thermal regimes that are in the same group should have similar catchment properties and/or features, while thermal regimes in different groups should have highly dissimilar catchment properties and/or features. The optimal number of clusters is obtained using the NbClust R package (Charrad et al., 2014; R Core Team, 2013). This package provides 30 popular indices that determine the number of clusters in a dataset by using the k-means clustering method and offers the user the best clustering scheme based on different results. The number of clusters suggested by the majority of these indices is selected.

The greatest proportion of indices (11 out of 30) suggests an optimal number of three clusters based on the five thermal signatures. Figure 3.7 represents these clusters as the colors of individuals/stations on the principal component map. Indeed, this map shows there is a clear difference between the 3 obtained clusters. Furthermore, Figure 3.6, bottom right panel shows the different spatial distributions of the obtained clusters. Stations in cluster 1 are located in the upstream part of the basin (HER A). Stations in cluster 2 are scattered over the basin, and 60% of the stations in cluster 3 tend to be found in the upstream part of the basin.

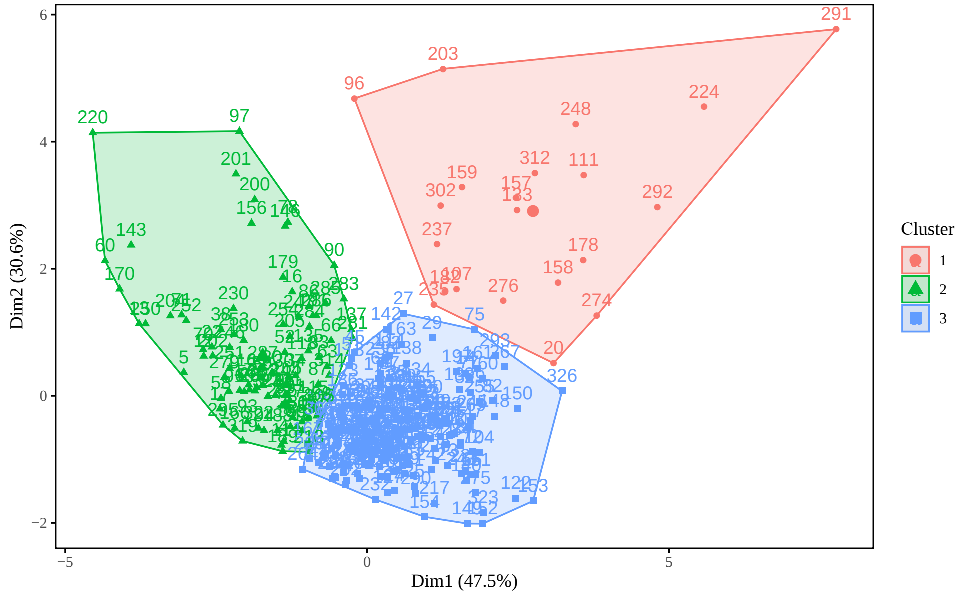

Figure 3.7: Representation of individual stations on the principal component map and their corresponding cluster. The numbers are showing ID of each station.

At this point, the question arises which clusters are showing altered regimes. To answer this question, first, the obtained clusters are labeled. The statistical distribution of thermal signatures within each cluster suggests the proper labeling of the obtained clusters with regard to the underlying physical processes (Figure 3.8).

First, the lowest median values of TS (0.22) and R^2 (0.23) are observed in cluster 1, along with the greatest median value of lag time (26 days). Therefore, cluster 1 is labeled as “dam-like". Second, the greatest median values of TS (0.42), heating effect (1.38°C), and thermal effect (0.65°C) are found in cluster 2. The second cluster is thus labeled as “pond-like". Finally, the median value of TS in stations that belongs to cluster 3 (0.34) is closer to the median value of TS in the stations in the pond-like cluster than that of the stations in the dam-like cluster. Stations in cluster 3 also exhibit the highest median value of R^2, and the smallest median values of heating effects. In this regard, cluster 3 is labeled as “natural-like".

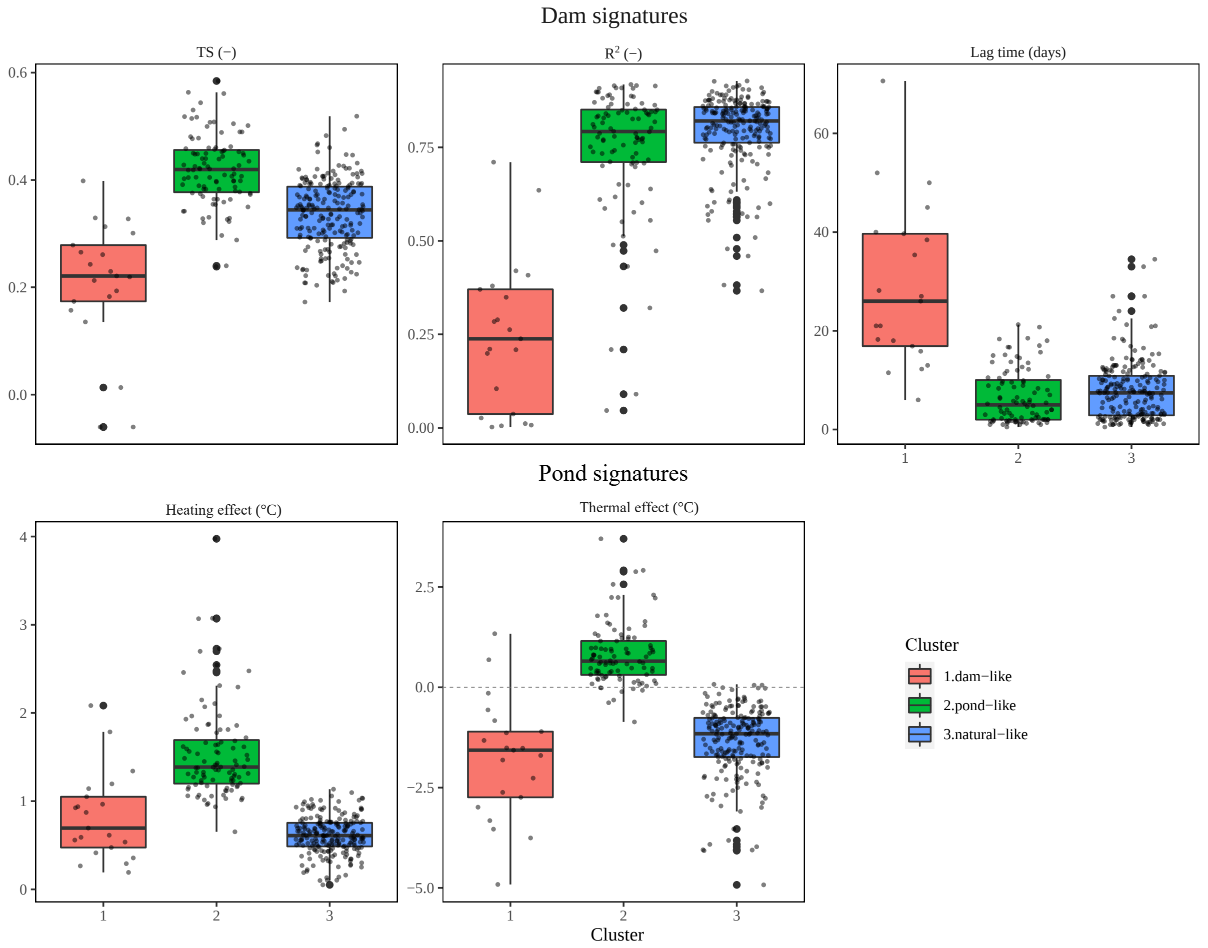

Figure 3.8: Statistical distribution of thermal signatures in each cluster: 1.dam-like with 21 stations; 2.pond-like with 96 stations; 3.natural-like with 213 stations.

3.4 Cross validating derived clusters

The derived clusters are validated in three ways, each based on the expectation that stations clustered together would have similar catchment properties and anthropogenic features.

3.4.1 Presence-absence test

In a first step, a simple presence/absence test is used for upstream human constructions (i.e., to answer whether the station has an upstream pond or dam). The odds ratios are then calculated for each cluster from the presence/absence counts of upstream dams or ponds to determine the strength of the association between the clustering based on thermal signatures and known anthropogenic influence. For example, for a cluster with dam thermal signatures, the ratio is calculated between the odds of being in that cluster given the presence of a dam and the odds of being in the cluster given the absence of a dam.

In support of the chosen labeling scheme, 71 % of stations (15 out of 21) in the dam-like cluster have an upstream dam, and if a site contains an upstream dam, it is 31.1 times more likely ($p < 0.001$) to be in the dam-like cluster than if it does not have an upstream dam. Similarly, 94 % of stations (90 out of 96) in the pond-like cluster (N=96) have ponds in their catchment and if a site contains an upstream pond, it is 6.5 times more likely ($p < 0.001$) to be in the pond-like cluster than if it does not have an upstream pond. The lower odds ratio for the pond-like cluster is due to the high proportion of stations (49 % of all stations) outside of this cluster that does have upstream ponds (i.e., false negatives). Indeed, 72 % of stations in the natural-like cluster (153 out of 213) have ponds in their catchment.

The presence/absence test of dams and ponds is the first and simple validation. Indeed, the presence of dams and ponds in the upstream part of a station does not by itself prove that the regime is altered, and so more validation is needed.

3.4.2 Dam and pond characteristic distributions

To test how well the clusters align with specific anthropogenic features, statistical distributions of dam and pond characteristics, described in Table 3.2, are compared among the clusters using ANOVA and the post-hoc Tukey's Honestly Significant Difference t-test with Bonferroni adjustment. Prior to any analysis, the homogeneity of variances and normality is ensured by using log-transformation when necessary. Because the cross-validation data rely on measured dam and pond characteristics, these analyses are conducted on subsets of stations with known dams (n=38) and ponds (n=253). It is hypothesized that stations from the respective dam- or pond-like clusters would have greater or lower values of their respective feature characteristics. For example, it is expected that stations from the dam-like cluster would have a much smaller distribution of distance to the closest dam than the other clusters, or stations from the pond-like cluster are expected to have a higher proportion of ponded surface area than the other clusters. Hence, this provides a more detailed validation than the simple presence/absence test.

Results show that the statistical distribution of dam descriptive variables differs from one cluster to another—IRI (p=0.01), d_{dam} (p=0.005), and IRI/d_{dam} (p=0.035). This provides strong support for the clustering results (Figure 3.9). Dam-like stations are located closer to their upstream dam (median=4.8 km) compared to pond-like stations (median=10 km; p=0.001) and natural-like stations (median=6.5 km; p=0.014). Similarly, dam-like stations have upstream dams that are an order of magnitude larger (implied by larger values of IRI, median=14.3 %) than dams upstream of pond-like stations (median=0.36 %; p=0.003) and natural-like stations (median=3.7 %; p=0.012).

The mean values of pond descriptive variables also differ from each other among the clusters, but the differences are less pronounced than for dam descriptive variables—$f_{pond,reach}$ (p=0.97), $\bar{f}_{pond,reach}$ (p=0.854), and $f_{pond,catchment}$ (p=0.003) (Figure 3.10). Although statistically non-significant, pond-like stations have over twice as much ponded reach area than natural like stations at both the local reach scale (median $f_{pond,reach}$=1.4% versus 0.6%; p=0.578) and the catchment scale (median $\bar{f}_{pond,reach}$=6.5% versus 3.0%; p=0.815). These results are mirrored by the overall proportional ponded area at the catchment scale (i.e., not just along reaches) for pond-like and natural-like stations (median $f_{pond,catchment}$=0.14% versus 0.07%; p=0.001). The dam-like cluster is not analyzed with t-tests because it is assumed that the stream temperature regime resets at the dam position and the cumulative effects of ponds will be lost.

Table 3.2: Descriptive variables tested for assessing the links between thermal signatures and dam/pond characteristics. Mean and standard deviation values (SD) are shown for the 330 stations selected in the study.

Notation	Variable	Mean	SD	Unit
Dam characteristics [a]				
d_{dam}	Distance from the closest upstream large dam	6.6	4.2	km
IRI	Impounded Runoff Index of the closest large dam [b]	11	16	%
IRI/D_{dam}	IRI/distance from the closest large dam [c]	10	25.5	%/km
Pond characteristics [d]				
$f_{pond,reach}$	Fraction of station's reach surface area that is ponded [e]	7.5	12	%
$\bar{f}_{pond,reach}$	Fraction of station's reach surface area that is ponded; averaged over all upstream reaches	1.6	2.7	%
$f_{pond,catchment}$	Fraction of the catchment area that is ponded [f]	0.17	0.8	%
Catchment characteristics [g]				
Ta	Annual mean Ta at station	12	1.5	°C
$A_{catchment}$	Catchment area	232	300	km^2
Alt	Altitude at station	399	290	m
S	Upstream mean slope	0.037	0.03	m/km
D	Distance from the source	30	20	km
W_q	Width for median discharge [h]	8.7	6.3	m
D_q	Depth for median discharge [h]	0.3	0.16	m
q	Mean annual specific discharge [i]	10	4.9	$l/s/km^2$
CI	Concavity index [j]	0.4	0.08	-
Veg	Rate of vegetation cover [k]	83	22	%

[a] The data on dams' characteristics (location, height, and volume) are provided by the Loire-Bretagne water agency (AELB) (Chandesris and Pella, 2006).

[b] Ratio of dam volume to mean annual runoff.

[c] To capture the interaction between the dam characteristic and the position of a station from the dam.

[d] The surface areas of ponds are extracted from BD CARTHAGE® (IGN, 2006).

[e] Extracted from SYRAH-CE database (Valette et al., 2012). The final nodes of each considered river segment are at important confluences and topologically important places.

[f] A proxy of cumulative effects of upstream ponds.

[g] These variables are available on the Theoretical Hydrographic Network for France (RHT, Pella et al., 2012).

[h] From the ESTIMKART empirical model developed by Lamouroux et al. (2010).

[i] Based on geostatistical interpolation on the Theoretical Hydrographic Network for France (RHT, Pella et al., 2012). (Sauquet et al., 2000; Pella et al., 2012).

[j] CI: (Q10-Q99)/(Q1-Q99); represents the shape of the dimensionless flow duration curve. This descriptor is a measure of the contrast between low-flow and high-flow regimes. Values close to 1 are observed where there are large aquifers or storage in snowpacks. Values close to 0 are related to catchments exposed to contrasting weather (Sauquet and Catalogne, 2011).

[k] Derived from remote sensing on both sides of reaches with a buffer of 10 m at the station, as reported in SYRAH-CE database (Valette et al., 2012).

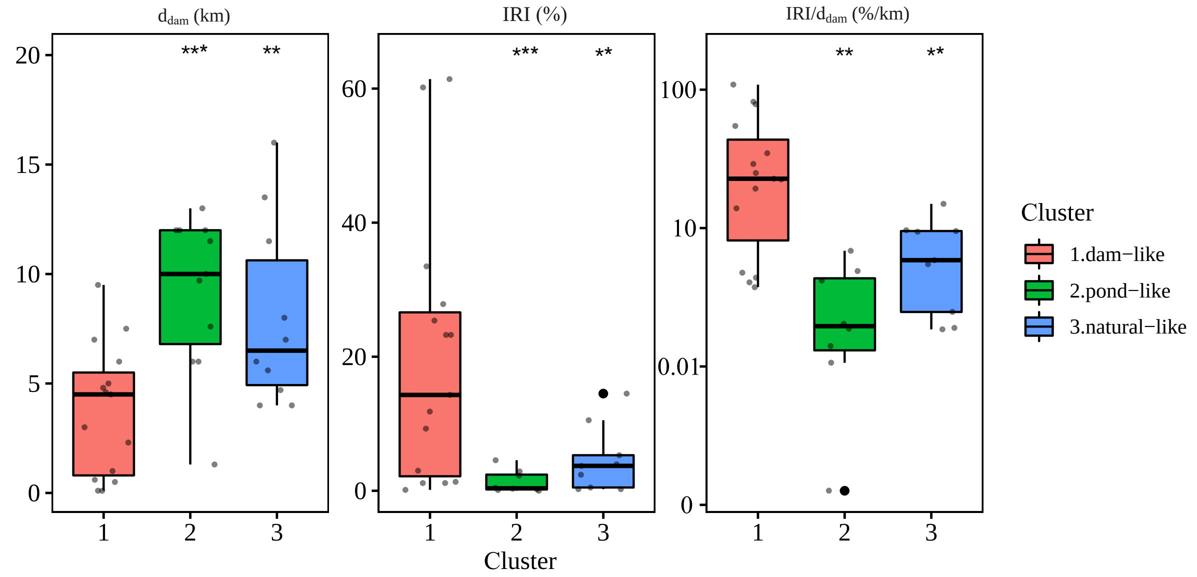

Figure 3.9: Boxplots of dam descriptive variables for all 38 stations with an upstream dam. The information about the volume of six of these stations is missing. The t-test has been done with the reference group of the dam-like cluster. ***, **, and * indicates that the dam characteristics for the group of the dam-like cluster are significantly different from those in the other two clusters at the 1, 5, and 10% confidence levels, respectively.

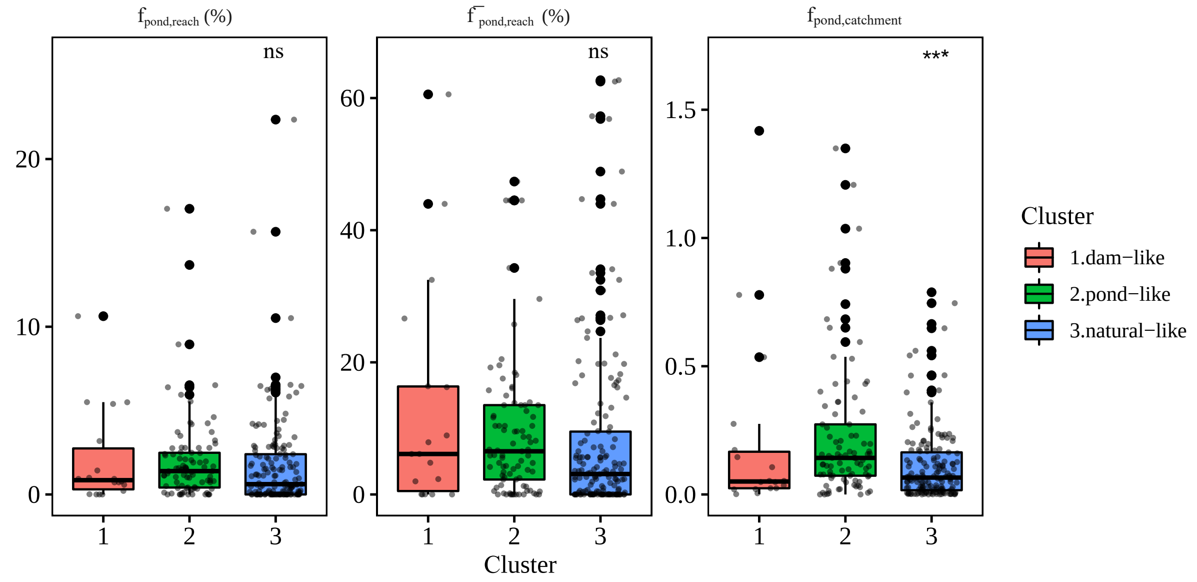

Figure 3.10: Boxplots of pond descriptive variables for all 253 stations that have upstream ponds. For dam-like stations, the impounded surface water by an upstream dam is removed from the calculations wherever there is information on it. ***, **, and * indicates that the pond characteristics for the group of pond-like cluster is significantly different from natural-like cluster at the 1, 5 and 10% confidence levels, respectively. The “ns” shows the pond characteristics for the group of pond-like cluster is non-significantly different from the natural-like cluster.

3.4.3 Multiple regression with catchment variables

The dam/pond thermal signatures clustering is also validated by using catchment-specific dam and pond characteristics in the presence of other natural landscape predictors as controlling factors. To do so, forward and backward stepwise linear regression is used (MASS package in R; Venables and Ripley, 2002) to select the catchment, dam, or pond characteristics (Table 3.2) that best explain their respective thermal signatures. The catchment descriptive variables are selected based on hypothesized controls on thermal regimes, and a preliminary multi-collinearity assessment using various diagnostic tests from the mctest R package (Imdadullah et al., 2016). Note that the most contributive predictors i.e. ones leading to significant performance improvement to the model are selected at the end.

The stepwise multiple regression procedure broadly supports the clustering results and indicates that dam and pond characteristics are the strongest controls on thermal signatures. Indeed, of the 10 considered catchment variables (see Table 3.2), only two arise as being important predictors of or controlling factors on thermal signatures (Table 3.3). Please note that the descriptive variables (see Table 3.2) that do not appear in Table 3.3 are not selected by the algorithm (stepwise linear regression), and are thus irrelevant.

Table 3.3: Stepwise multiple linear regression results for cross-validation approach relating descriptive variables for dam and pond thermal signatures. ***, **, and * denote significance at the 1, 5, and 10% confidence levels, respectively. Scaled coefficients are shown in parentheses for comparison among predictor variables.

Dam signatures			
Descriptive variable	TS (−)	R^2 (-)	lag time (days)
S $[m/km]$	−	−	232.85±92.891** (0.377±0.151)
$d_{dam}[km]$	0.015±0.005*** (0.458±0.140)	0.029±0.010** (0.385±0.141)	-1.6±0.560*** (-0.425±0.151)
IRI [%]	-0.002±0.001** (-0.306±0.145)	-0.009±0.002*** (-0.484±0.146)	−
Adjusted R^2	0.43	0.482	0.3
F statistic (df)	12.37 (29)	15.43 (29)	7.64 (29)
p-value	< 0.001	< 0.001	0.002
Pond signatures			
Descriptive variable	Heating effect (°C)	Thermal effect (°C)	−
Veg [%]	-0.003±0.002* (-0.164±0.102)	−	−
$f_{pond,catchment}$ [%]	0.62±0.211*** (0.296±0.102)	0.762±0.305** (0.257±0.102)	−
Adjusted R^2	0.1	0.060	−
F statistic (df)	5.442 (87)	3.872 (87)	−
p-value	0.006	0.024	−

For dam thermal signatures, only lag time is influenced by the catchment slope, and for the pond signature, the heating effect is reduced by vegetation. More important are dam characteristics: the closer a station is to a dam (low d_{dam}), and the bigger the dam (high IRI), the lower the TS and R^2 are. Lag time also increases at stations that are closer to a dam. The influence of d_{dam} on TS is approximately 50% stronger than IRI, but d_{dam} influence on R^2 is approximately 20% weaker than IRI (based on scaled regression coefficients, Table 3.3). For lag time signature, the influence of d_{dam} is 13% stronger than the catchment slope. For ponds, ponded catchment area ($f_{pond,catchment}$) is the most important predictor variable of both heating and thermal effects, but percentage vegetation cover (Veg%) appears to partially mitigate heating effects (at approximately half the influence of $f_{pond,catchment}$).

Finally, the significant relationship between dam thermal signatures and dam descriptive variables as well as the significant relationship between pond thermal signatures and pond descriptive variables (see Table 3.3) demonstrate the derived clusters correspond to their considered label. Therefore, thermal signatures helped to distinguish between altered and natural regimes and to identify the influence of dams and ponds. Note that Tw stations and their corresponding clusters are presented in Table B.1.

3.5 Characterizing identified thermal regimes

3.5.1 Variability of thermal metrics for altered and natural thermal regimes

At this point, the altered thermal regimes are sought to be placed in the context of widely used ecological metrics. In fact, thermal metrics are the components of a thermal regime that help describe it in terms of magnitude, amplitude, frequency, duration, and timing (Olden and Naiman, 2010; Maheu et al., 2016a; Steel et al., 2017). There is a diversity of metrics, which can be used depending on the user's purpose. In Figure 3.11, some examples of these metrics are presented.

For instance, monthly mean Tw (in orange), mean of Tw over the hottest month (in red), annual maximum or minimum Tw (in blue), and finally annual mean Tw (in black dashed line) are describing the magnitude feature of a thermal regime. The time corresponding to the maximum or minimum Tw (in brown) can be considered as the metric that describes the timing feature of a thermal regime. The solid horizontal lines (referred to as high and low thresholds) in Figure 3.11 correspond to lethal temperatures of aquatic communities, and the frequency and duration of days below or above these thresholds can be applied as the descriptors of a thermal regime (Olden and Naiman, 2010).

In the current study, a group of metrics is gathered from biodiversity and stream ecology (Verneaux et al., 1977; Buisson et al., 2008; Steel et al., 2017) to quantitatively evaluate the

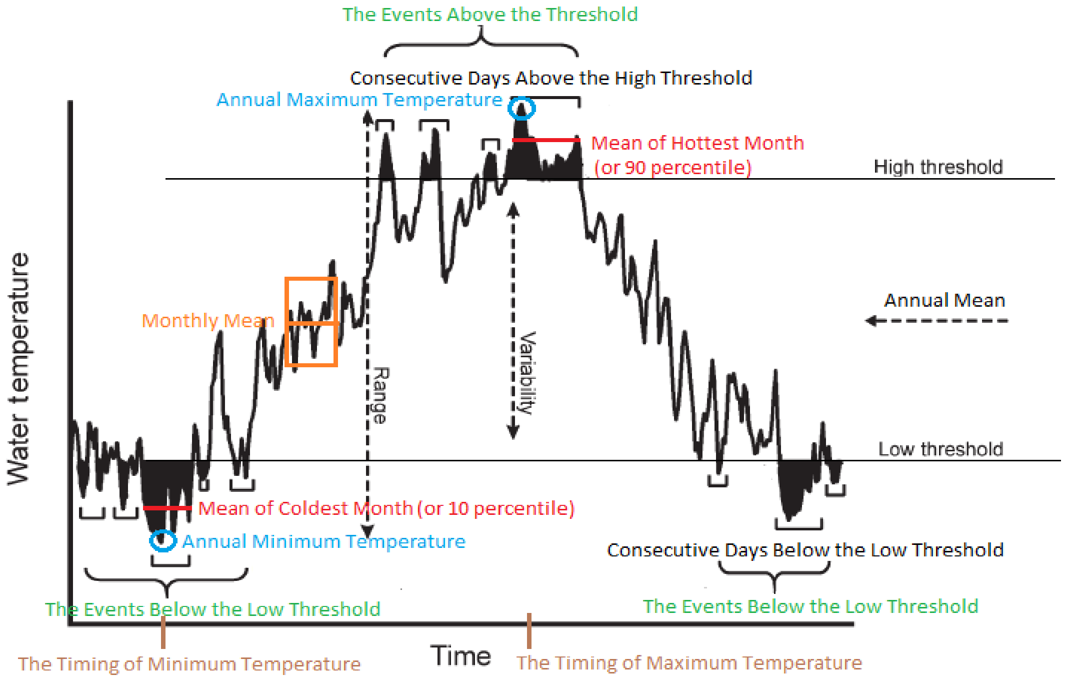

Figure 3.11: Examples of thermal metrics that can describe a thermal regime in terms of magnitude, amplitude, frequency, duration, and timing. The original figure can be found in Olden and Naiman (2010).

anthropogenic effects in altered regimes compared to natural ones. The means of these thermal metrics are compared from the altered regimes to those from natural regimes using ANOVA and the post-hoc Tukey's Honestly Significant Difference t-test with Bonferroni adjustment (natural regimes are used as the reference group). False-positives (e.g., stations that are identified in the dam-like cluster, but do not have a dam) are excluded from this analysis to avoid misinterpretation of true anthropogenic effects.

Figure 3.12 shows that altered thermal regimes (i.e., dam- and pond-like) clearly separate from natural regimes along ecological metrics: $\bar{T}_{w,summer}$ (p<0.001), max($T_{w,monthly}$) (p<0.001), $N_{Tw}>20$ (p<0.001), $D_{Tw}>15$ (p<0.001), and $max(\Delta Tw)$ (p<0.001). Magnitude and frequency ($\bar{T}_{w,summer}$ and $N_{Tw}>20$) thermal metrics are lower for dam-like stations than for natural-like stations (by 2 °C, p=0.02; and 4 days, p=0.001), but frequency, duration and rate of change thresholds are equivocal.

Furthermore, altered thermal regimes from ponds also differ from natural regimes along every thermal metric considered here, with:

- a 2.3°C increase in average $\bar{T}_{w,summer}$ (p<0.001),
- a 2.5 °C increase in max($T_{w,monthly}$) (p<0.001),
- a 15-day increase in $N_{Tw}>20$ (p<0.001),
- a 39-day increase in $D_{Tw}>15$ (p<0.001), and

Table 3.4: Selected ecologically-relevant thermal metrics for comparison between altered regimes and natural ones. The biological importance (last column) is adopted from Steel et al. (2017).

Regime feature	Metric	Description	Biological importance
Magnitude	$\bar{T}_{w,summer}$	Mean Tw in summer (June–August)	Differences in mean temperature across river systems contribute to determining which species are present and which are absent
Magnitude	$\max(T_{w,monthly})$	Maximum of the 30-day moving average daily mean Tw	Used in the biotypology according to the formula proposed by Verneaux et al. (1977)
Frequency	$N_{Tw} > 20$	Number of days that daily mean Tw > 20 °C	Species-specific differences in response to high temperatures provide preferential advantages to particular species
Duration	$D_{Tw} > 15$	Duration of consecutive days with mean Tw > 15 °C	Accumulated stress may trigger migration and other major life-history transitions
Rate of change	ΔTw	Difference between mean Tw in August and February	The competitive advantage of one species over another may be determined by conditions in both summer and winter

- a 2.6 °C increase in ΔTw ($p<0.001$).

3.5.2 Annual thermal regime at altered and natural stations

Finally, the thermal regimes of the derived clusters are characterized by comparing their aggregate stream and air temporal behaviors and comparing the natural regime with altered regimes together. The goal is to create a portrait of how the respective cumulative effects of dams and ponds modulate stream temperature relative to air temperature and relative to so-called “natural” regimes. In this step, as it is expected that large dams to be responsible for altered regimes partitioned in the dam-like cluster, we consider stations (N=15) with an upstream dam for the dam-like cluster. Similarly, we consider stations with upstream ponds (N=90) for the pond-like cluster.

The annual regimes from the three clusters depicted in Figure 3.13 support the current understanding of how anthropogenic structures influence stream and river thermal regimes. Compared to natural regimes, temperatures of dam-like stations exhibits a downshifted regime (by 2°C) and a lag in summer thermal peaks (by 23 days), with less clear differences in winter (Figure 3.1, left panel). In contrast, the stream temperature of pond-like stations remains above air temperature over the whole year and is nearly synchronous with air temperature, mimicking the regime of large rivers (Figure 3.1, right panel). Indeed, the annual stream temperature am-

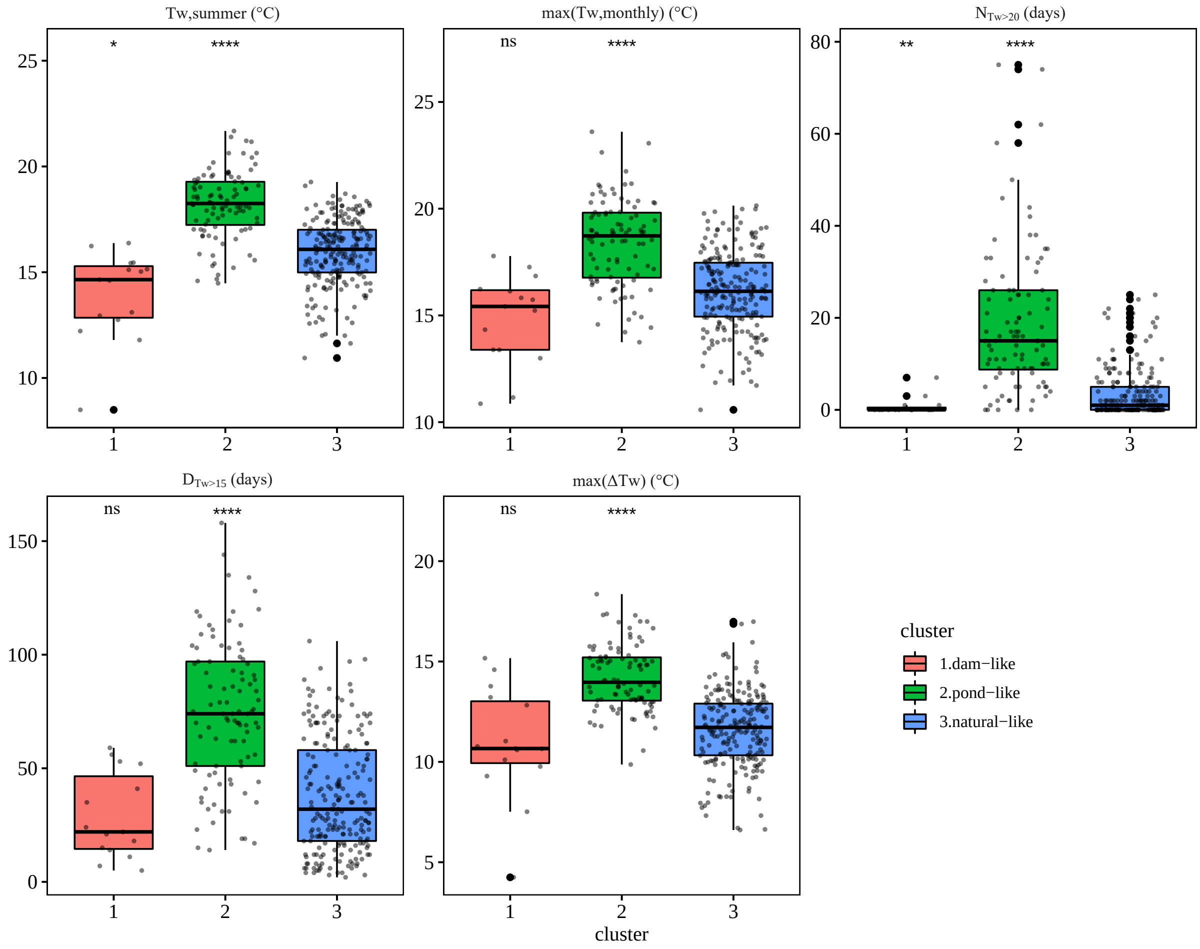

Figure 3.12: Statistical distribution of ecologically-relevant thermal metrics in each cluster: 1) dam-like with 15 stations that have a large upstream dam, 2) pond-like with 90 stations, and 3) natural-like with 213 stations. The t-test is conducted with the reference group of the natural-like cluster. ***, **, and * indicate that the metric for the group of altered regimes is significantly different from natural regimes at the 1, 5, and 10% confidence levels, respectively. The "ns" shows that the metric for the group of the altered regime is non-significantly different from natural regimes.

plitude of pond-like stations is 14 °C, 2.5 °C less than that of large rivers (16.5°C), but 2-4 °C greater than that of dam-like or natural stations. Natural-like stations stand out in that their summer peaks are cooler than pond-like stations, but are warmer and more synchronous with air temperature than dam-like stations.

3.6 Discussion

The above results demonstrate that five simple signatures derived from stream-air temperature time series are capable of identifying the extent and characteristics of both altered and natural thermal regimes. Using these signatures, it is possible to accurately parse the divergent thermal regimes.

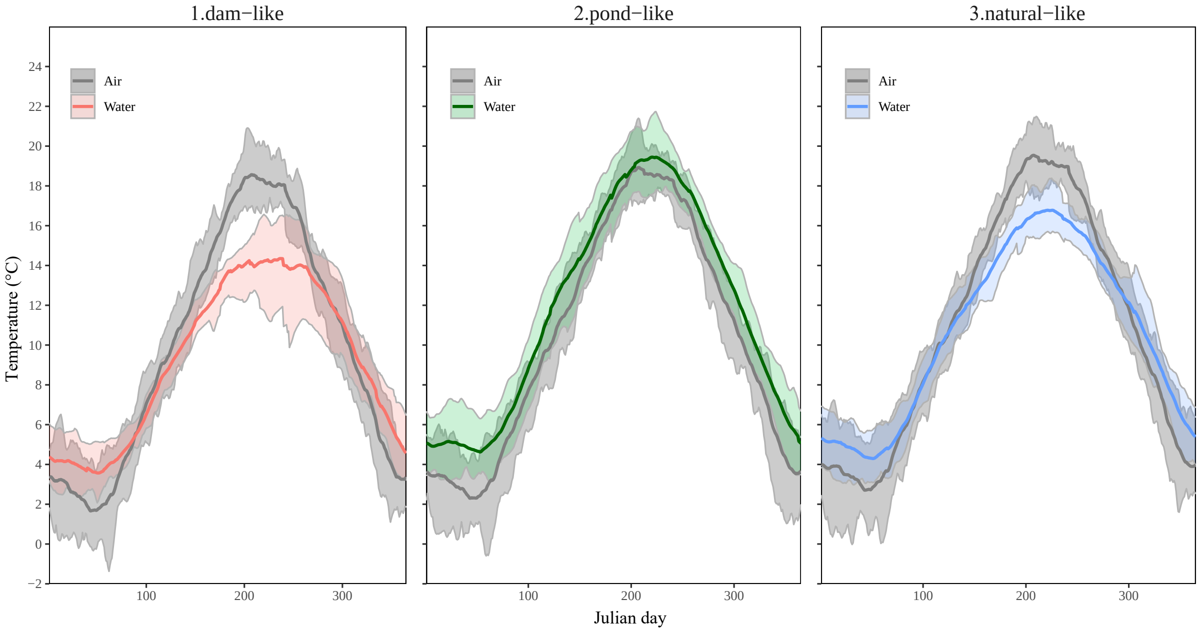

Figure 3.13: The annual air and water temperature regimes of altered (by dams and ponds) and natural streams. Shaded areas represent the 10th-90th percentile band over all stations in each cluster, and solid lines represent the median value: 1.dam-like with 15 stations that have a large upstream dam; 2.pond-like with 90 stations that have upstream ponds; 3.natural-like with 213 stations.

3.6.1 Large dam thermal signatures

Spatial clustering of dam thermal signatures in the upstream part of the Loire River basin aligns with the known distribution of dams there (Figure 2.1 (right panel), p. 44). This thermal signature approach may therefore be useful in identifying areas with the strong thermal alteration from dam proliferation, like in the Amazon headwaters (Anderson et al., 2018).

The mode of operation of dams affects its degree of effect in the downstream thermal regime (Olden and Naiman, 2010; Maheu et al., 2016c) and should be reflected in its emergent thermal signatures. Observed dam thermal signatures are based on hypothesized cooling effects from hypolimnetic release, and although most stations downstream of large dams exhibit this signature, many do not. This suggests alternative modes of operation. Hence, in future works, using alternative thermal signatures to capture other modes of operation may be explored. Even dams with similar purposes could have different modes of operation (Maheu et al., 2016c).

The interannual variability driven by climate adds an additional layer of complexity that may be difficult to assess with this method. To see the influence of interannual variability, in the present study, the 10th percentile of (Tw-Ta) is taken as a measure of dam regulation. This measure is much more variable from one year to another in dam-like stations (median=1.95°C) than in the other stations due to the interannual variability of dam operations (median of 0.74°C and 0.97°C for pond-like and natural-like clusters, respectively) (see Figure 3.14). Therefore, even the relatively simple approach adopted here is largely successful in identifying altered thermal regimes. For instance, along with other studies, it is observed that dams that release hypolimnetic water disrupt the stream-air temperature relationship (R^2) (Buendía et al., 2015), and delay the annual stream temperature peak (Olden and Naiman, 2010) (Figures 3.8 and 3.13).

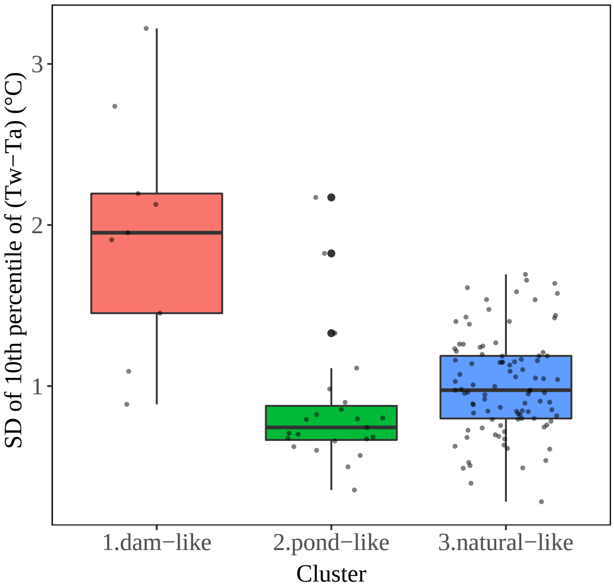

Figure 3.14: Interannual variability of the 10th percentile of (Tw-Ta) in each cluster. Only 130 stations with more than 6 years of available data are considered here to insure a robust estimation of the interannual variability.

The extent of a dam thermal alteration depends on the reservoir volume, the stream order, and the distance from the dam (Webb et al., 2008; Batalla et al., 2004). Here, the channel slope is an important confounding factor on dam influence, which appears to amplify lag time effects (Table 3.3): the steeper the channel, the smaller water exposure time to air, and the greater the lag time between the stream and air temperature. Cross-validation results also highlight the critical effect of dam volume on thermal regimes, underscoring previous works that identified a critical impoundment threshold of 5–20% of the mean annual runoff (Buendía et al., 2015; Maheu et al., 2016c). Importantly, It is found that IRI$>$20% (see Figure 3.15, left panel) completely erase stream-air temperature correlation (cf. Buendía et al., 2015; Maheu et al., 2016c). Stations with the weakest dam signatures are far from large dams, supporting the known reduction of dams influence on thermal regimes (an increase of TS) with distance (see Figure 3.15, right panel) due to the heat exchange with ambient conditions (cf. Preece and Jones, 2002; Buendía et al., 2015). The coupling of greater distance from dam and lower IRI of upstream dam lead to weaker downstream alteration induced by an upstream dam. This may provide additional explanation as to why 17 stations with known dams do not cluster into our dam-like thermal signature. Indeed, the smaller ratio of IRI/D_{dam} (Figure 3.9, right panel) of stations with an upstream large dam in the other clusters also confirms not only that these stations are located further from the upstream dam, but also that the volume of the dam is not large enough relative to the stream annual runoff to cause the downstream alteration.

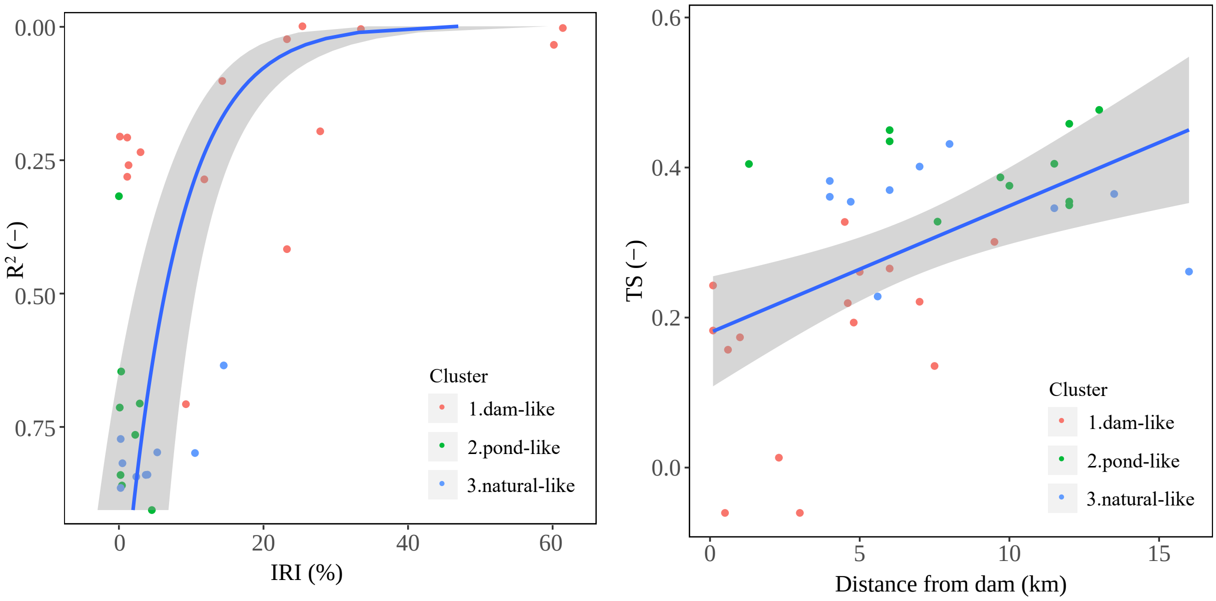

Figure 3.15: Examples of the influence of dams on thermal signatures based on dam descriptive variables. (left) R^2 with respect to Impounded Runoff Index (see Table 3.2), and (right) TS (thermal sensitivity) with respect to the distance from the dam. The three colors correspond to the stations in each cluster. Solid lines represent logarithmic/linear regressions with a 95 % confidence interval. Please note that the information about the volume of six of these stations is missing, limiting us to calculate IRI.

Changes induced by dams in ecologically-relevant thermal metrics on downstream temperature are moderate. We observe the effects of a decreased summer stream temperature and a decrease in the frequency of high temperature, in accordance with previous works (Olden and Naiman, 2010; Maheu et al., 2016c). Nevertheless, little evidence for the effects of other ecologically-relevant thermal metrics is found compared to natural systems. However, the focus of selected ecologically-relevant thermal metrics in the current study is biased towards increased thermal alterations, and further metrics and analyses would benefit future inference.

3.6.2 Pond thermal signatures

Ponds and shallow reservoirs impound water for different purposes that depend on location and local needs. Ponds are evenly distributed throughout the Loire River basin, with no clear clustering of sizes (Figure 2.1 (right panel), p. 44). In support of this observation, pond-like thermal signatures are evident throughout the basin (Figure 3.6), located mostly on medium-size streams (median of distance from source = 40 km).

Ponds typically release warm water from overflow, increasing downstream temperature synchronically with air temperature (Dripps and Granger, 2013; Maheu et al., 2016b). The pond thermal signatures identified here align with other empirical results (Chandesris et al., 2019;

Zaidel et al., 2020) and the general conceptual model (Figures 3.5 and 3.13).

Stations influenced by small dams experience a small reduction in R^2 compared to natural stations (cf. Bae et al., 2016, and see Figure 3.8). The extent of the change induced by ponds depends mostly on the surface area and residence time (Maxted et al., 2005; Chandesris et al., 2019). The lack of data on the depth of the pond/shallow reservoirs at this scale prevented us from using residence time. A larger surface area, or a larger residence time increases the time of exposure to air temperature and incoming solar radiation, leading to a greater sensitivity of stream temperature to air temperature (increased TS) (Maheu et al., 2016b; Michel et al., 2020). Here, a greater TS (thermal sensitivity) for pond-like stations is also detected (see Figure 3.8). Moreover, Figure 3.16 shows that the heating effect of more than 1 °C and positive thermal effect can clearly partition pond-like stations from natural-like ones. The single best signature of the pond thermal alteration is the proportion of a station's catchment that is ponded ($f_{pond,catchment}$), strongly implying that ponds have an emergent, cumulative effects on stream temperature regimes. Indeed, two other descriptors based on reach-scale characteristic (at the station and averaged over upstream), could not differentiate the thermal signatures (see Table 3.3 and Figure 3.10). However, reach scale metrics are defined based on recorded surface waters in 2011 and are perhaps not temporally aligned with stream and air temperature measurements used here. Importantly, the cross-validation (see Table 3.3) suggests that the thermal influence of ponds may be mitigated by vegetation cover (Maxted et al., 2005), suggesting the strategic planting of canopy cover species in thermal restoration efforts.

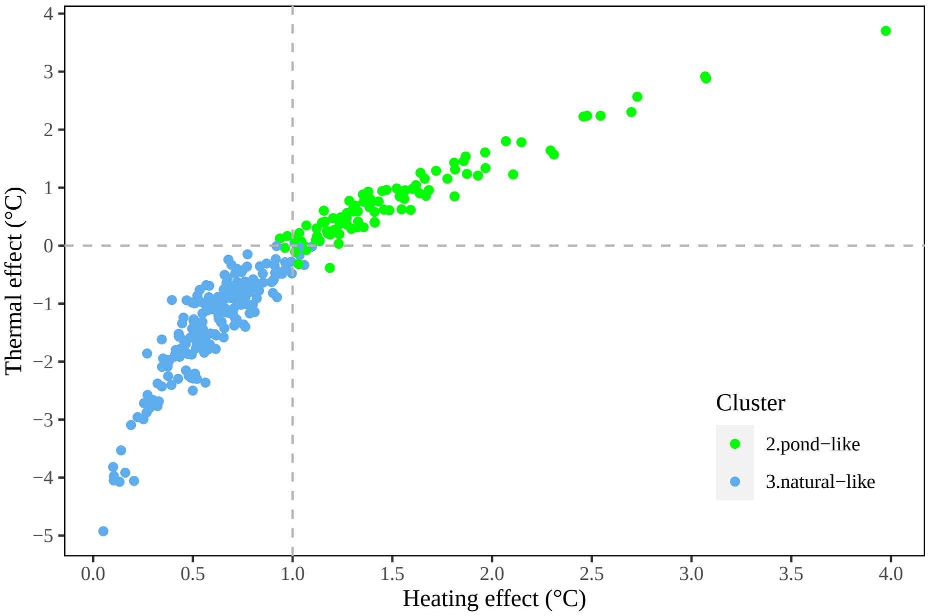

Figure 3.16: Heating effect and thermal effect at the whole natural-like and pond-like stations over the Loire River basin (see Figure 3.8).

Finally, ponds can have substantial effects on ecologically-relevant thermal metrics. They increase the summer temperature and the frequency and duration of high temperature values (cf. Lessard and Hayes, 2003; Maheu et al., 2016c,b; Chandesris et al., 2019, and see Figure 3.12).

3.6.3 Natural regimes

The thermal regimes of natural-like stations are those that are most strongly driven by natural factors like climate, topography, vegetative shading, and stream discharge (Poole and Berman, 2001; Kelleher et al., 2012; Hannah and Garner, 2015). These natural regimes should therefore arise in regions with minimal anthropogenic influence, which is observed in their spatial distribution. They are predominately located in the upstream part of the Loire River basin, HER A, where there is the largest proportion of vegetation cover (cf. Beaufort et al., 2020a, and see Figure 2.1 (middle panel), p. 44). These natural-like stations are located on small streams (median of distance from source = 24 km) and have typically a larger proportion of vegetation cover (median of vegetation cover within a 10-meter buffer = 100%).

Natural-like regimes, unlike altered ones, have a strong correlation with air temperature (cf. Webb et al., 2008) and exhibit minimal lag time, heating, or thermal effects (see Figure 3.8). In accordance with Beaufort et al. (2020a) those who studied the natural controlling factors of natural regimes of the Loire River basin, TS at stations located on large rivers (median=0.43) (where the climate is the key driver of stream temperature) is greater than TS in natural-like stations (median=0.34). However, TS in the current study is smaller than the TS values reported by Beaufort et al. (2020a), since the present study focused on summer TS values. A similar result (median of TS=0.45) was obtained in an analysis focused on August stream temperature by Mayer (2012). In the current study, TS of the stations located in HER B – which has the greatest potential for groundwater input – is lower than TS in stations located in HER A and C (median TS=0.29 versus 0.35). Mayer (2012) also attributed a lower summer TS to groundwater input (Mayer, 2012). Supporting the thermal signature approach, the annual amplitude for stations with natural thermal regimes (median=11°C) was in direct accordance with observations in Beaufort et al. (2020a) for natural Tw stations (9–14°C; and see Figure 1.2, p. 29).

3.6.4 Limitations of the study

The obtained results show that stations can be clearly partitioned into three clusters without information on the upstream catchment characteristics and water temperature, and by only using thermal signatures that compare stream and air temperature time series. The lack of long-term continuous data forces us to use all existing observed stream temperature stations, despite the heterogeneity of data availability between years during the 2008-2018 period (see Figure 2.5, p. 47). However, there is a concern about the sensitivity of thermal signatures to interannual data heterogeneity (i.e., years with gaps over the study period) since the five thermal signatures are based on interannual means.

Figure 3.17 shows that the mean values of all thermal signatures are however reasonably constant with respect to the number of years used for their computation. The only exception is lag time signature, which can be heavily influenced by year-to-year variations in both climate and upstream reservoir management. Here, stations with complete annual data are used, but, the other concern may be within-year data availability. Less complete databases may be less adequate for the outlined approach, which should be assessed further.

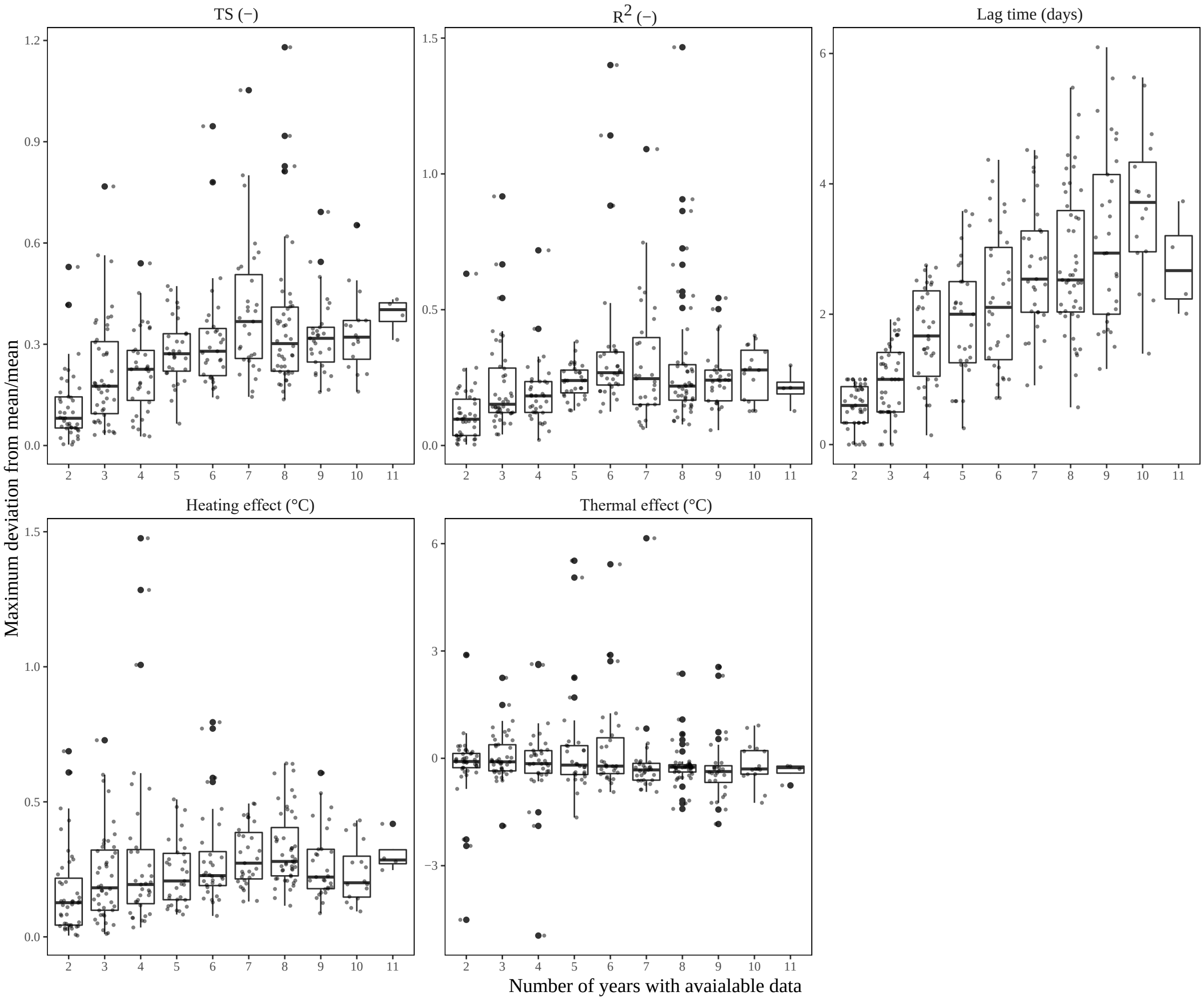

Figure 3.17: Maximum of the normalized yearly absolute deviation of thermal signatures from the interannual mean for all stations, with respect to the number of years with available data. For calculating the maximum deviation (y-axis), the deviation of desired signatures is calculated from the interannual mean (considered in the calculations) at each station for each year (if the data is available). Then, the maximum observed deviation for each station is considered. Then, it is divided by the interannual mean (considered in the calculations) to get a normalized value which let compare the different stations. The x-axis shows the number of years with available data for each station from 2008 to 2018.

The large sample size used in the present study, the presence of different types of reservoirs over the study area, and the blind-eye toward dam operations may have some implications for generalizing our findings. For example, in regions with more variable dam operations, different clusters may arise, or it may be difficult to perform a cluster analysis without additional thermal signatures.

In this study, there is a low possibility of station pseudo-replication due to the high resolution of SAFRAN data (8 km): only 20% of the SAFRAN grid cells include more than one station, and only 12% of the grid cells include the stations from the same cluster. However, it is imperative to verify and cross-validate this approach when applied to new datasets.

3.6.5 Implications and perspectives

The proposed thermal signature approach allows a simple, rapid, and accurate workflow to identify river reaches that are highly influenced by dams and ponds. The methodology is inherently regional, aligning in scale with the jurisdictions of most environmental agencies and working groups. The thermal signature results can be used to identify hotspots and target specific reaches for restoration and further investigation and to more broadly design strategic measurement networks (Jackson et al., 2016). Thermal signatures can also identify natural reaches as benchmarks for restoration or aquatic species habitat protection. Indeed, there is much interest in predicting the phenological and spatial diversity for species of interest or their prey (Steel et al., 2017). Moreover, because climate change will likely exacerbate the degree of thermal alterations (Michel et al., 2020) through increasing air temperature, decreasing streamflow, and increasing demand for ponds and dams (Webb and Walling, 1996; Moatar and Gailhard, 2006), the thermal signature framework could be used to plan pond and dam placement to minimize cumulative downstream effects.

The proposed thermal signatures may also be used by modelers to develop a reference-condition model by using natural regimes (Hill et al., 2013), or to assess the performance of distributed water temperature models that do not take into account anthropogenic activities. The difference between simulated and observed thermal signatures at altered stations can serve to correct biases found in simulations by using a known dam or pond descriptive variables. Such implications will be explored in the next chapter to assess the performance of the T-NET thermal model at natural stations identified in this chapter. The T-NET thermal model bias (i.e., the difference between simulated and observed Tw) at altered regimes identified in this chapter, will also be used to infer and quantify the influence of dams and ponds.

The thermal signature approach is flexible and can easily be reimagined for purposes other than detection and characterization of altered regimes from anthropogenic impoundments. For example, the stream-air temperature linear regression calculated on annual data could identify varied thermal regimes of natural streams (with a focus on TS and the intercept) like Kelleher et al. (2012); Maheu et al. (2016a); Beaufort et al. (2020a) (see also Figure 1.2, p. 29). In addition to parsing the natural drivers of thermal regimes, spots with the potential of inputs from shallow groundwater may be traced by using the lag time signature (Briggs et al., 2018). Identifying such streams is important since shallow groundwater will warm in response to climate change (Kurylyk et al., 2015) and increase Tw. Moreover, the synthesis of thermal signatures and hydrological signatures could be applicable to analyzing fish and macroinvertebrate communities.

3.7 Conclusion on the impacts of dams and ponds on stream temperature

The cumulative effects of anthropogenic impoundments on stream temperature at a large scale are barely known. To address this issue, five thermal signatures based on the stream-air temperature relationship are defined in this chapter. These signatures enable a rapid way to distinguish between altered and natural regimes and to identify the influence of dams and ponds without prior information about the source of the modification and upstream Tw condition through a clustering approach. The derived thermal regimes or clusters are then cross-validated with several known catchment characteristics. The results demonstrate that five simple signatures are capable of identifying the extent and characteristics of both altered and natural thermal regimes.

The results further reveal that the thermal regimes altered by dams arise in the upstream part of the basin where there are mostly large dams, and the degree of induced alteration depends on the dam's IRI (Impounded Runoff Index) and distance from the upstream dam. Along with the other studies, dams with IRI>20% completely erase stream-air temperature correlation. Nevertheless, alterations induced by dams disappear when moving further downstream from the dam. On the other hand, the degree of alteration induced by ponds depends on the proportion of a station's catchment that is ponded, strongly implying that ponds have cumulative effects on stream temperature regimes. Nevertheless, such effects of ponds can be mitigated by vegetation cover, suggesting the strategic planting of canopy cover species in thermal restoration efforts.

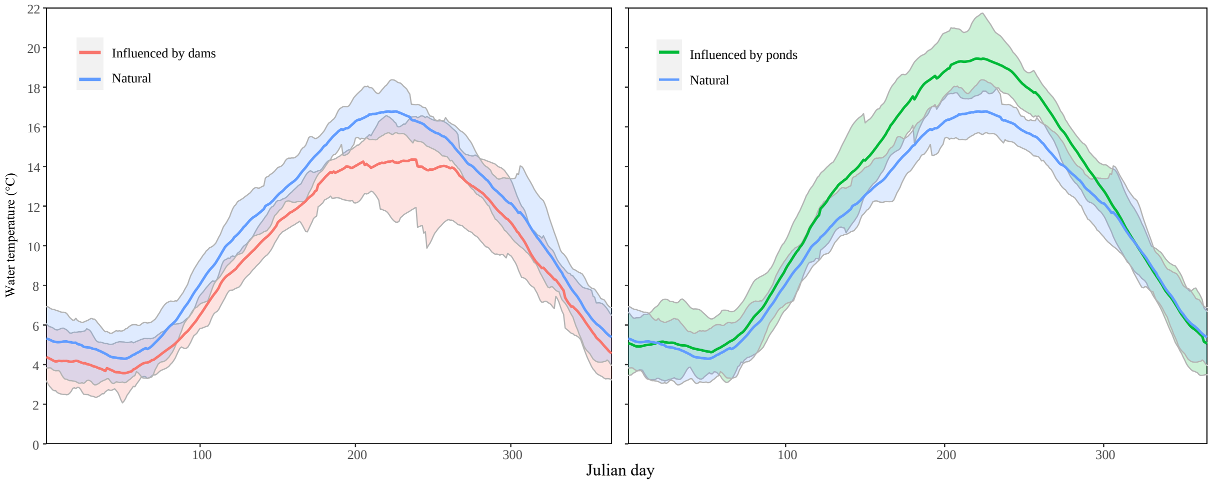

Figure 3.18: Altered regimes vs natural regimes.

Moreover, comparing Tw regime of altered stations with those of natural ones exhibits that large dams decrease summer temperature by 2 °C, and delay the annual stream temperature peak by 23 days at local scales (Figure 3.18, right panel). In contrast, the cumulative effects of upstream ponds increase summer stream temperature by 2.3 °C, and increase the synchronicity with air temperature regimes (Figure 3.18, left panel).

Therefore, due to the wide availability of air temperature data and the rapid growth of water temperature datasets, thermal signatures can be applied at large scales, facilitating regional assessments of stream temperature variability. Thermal signatures further allow tracing of systematic changes introduced by anthropogenic structures like dams or ponds, and identification of highly influenced reaches at a large scale.

In the next chapter, the implications of the parsed thermal regimes will be explored. Tw at the identified natural stations will be used to assess the performance of the T-NET thermal model. Furthermore, the T-NET thermal model bias (i.e., the difference between simulated (natural) and observed (influenced) Tw) at the identified altered stations will be used to infer and quantify the influence of dams and ponds.

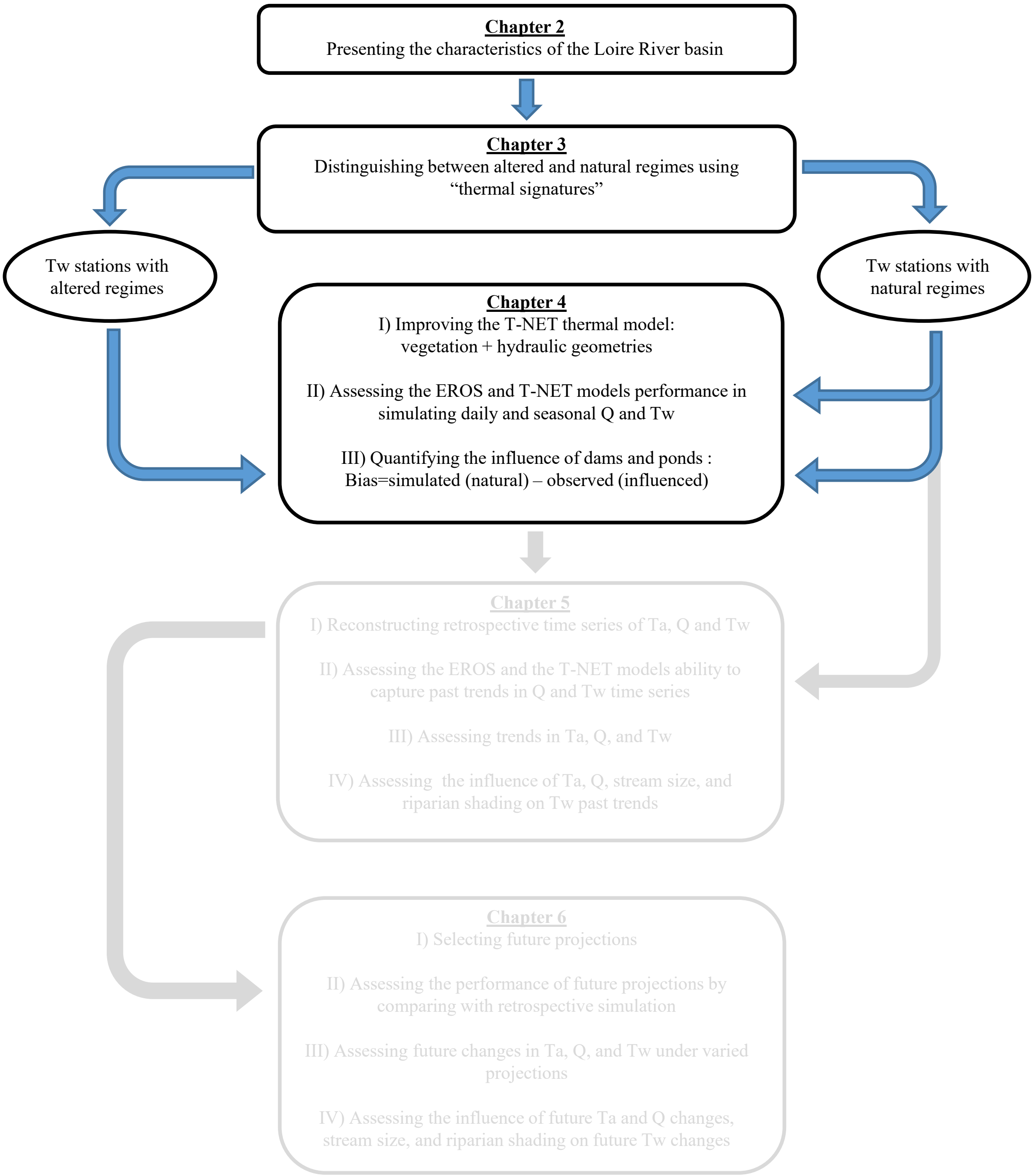

Schematic diagram illustrating thesis objectives.

CHAPTER 4

The hydrological and thermal models

To overcome the lack of Tw data, large scale studies commonly use Ta as a proxy of Tw (e.g., Buisson et al., 2008; Tisseuil et al., 2012; Domisch et al., 2013). However, Ta is a not a good surrogate for Tw (Caissie, 2006), and other drivers (e.g., stream discharge (Q), streambed, morphology, topography, and vegetation cover) contribute to the spatio-temporal variability of Tw (Hannah and Garner, 2015). Moreover, recently, Kirk and Rahel (2021) showed that using Ta instead of Tw led to over-predicting changes to stream fish assemblages with climate warming. Thus, modeling Tw with considering not only Ta but also other drivers is needed to have long-term and detailed Tw data at a large scale.

Here, the T-NET physical process-based thermal model coupled with the EROS semi-distributed hydrological model is used over the Loire River basin (Beaufort et al., 2016b; Loicq et al., 2018) to produce Q and Tw data at a large scale and a high spatial resolution. The inputs of these models are provided by the SAFRAN reanalysis data (section 2.3.1, p. 46). In this chapter, the principles and input data of both the EROS and T-NET models are first presented. Then, some improvements are made to the T-NET thermal model. The first improvement is related to hydraulic geometry (river width and depth) for which a recently developed model is considered. This new hydraulic geometry model is based on catchment physical characteristics, and uses a Random Forest approach (Morel et al., 2020). The next improvement is the implementation of dynamic riparian shading as a function of tree height, river width, solar elevation angle, vegetation density (using the approach proposed by Li et al., 2012), and phenology instead of considering a constant riparian shading.

Afterwards, the performance of both the EROS and the T-NET models is assessed at weakly influenced stations since both models produce natural outputs. For the EROS model, two types of stations are considered: calibration stations with data between 1971 and 2018 (N=352), and stations from the Reference Hydrometric Network (RHN) with long-term continuous daily data (N=44) (see section 2.3.3, p. 48). The performance of the T-NET model with new features in simulating daily Tw is assessed at stations with a natural thermal regime identified in the previous chapter (see Figure 3.8, p. 62) with missing years over the 2008–2018 period (N=275). The performance of the T-NET thermal model in simulating seasonal Tw is also assessed at stations with continuous daily data over the 2010–2014 period (N=67). Note that, these 67 Tw stations are derived from the Tw stations with missing years over the 2008–2018 period. Then, the ability of the T-NET model to derive longitudinal profile of stream temperature, and to capture alterations resulting from groundwater inputs is also investigated at the Loire River. Finally, the bias of the T-NET thermal model i.e. the difference between simulated Tw (provided by the T-NET model) and observed Tw at altered stations identified in the previous chapter (see Figure 3.8, p. 62), is used to infer and quantify the influence of dams and ponds.

4.1 The EROS hydrological model

The EROS semi-distributed hydrological model simulates daily discharge (Thiéry, 1988; Thiéry and Moutzopoulos, 1995; Thiéry, 2018). This model is made up of a network of sub-basins in which each sub-basin is subjected to rainfall, snowfall and potential evapotranspiration. The water balance in the sub-basin is modeled by a lumped model using three reservoirs (Figure 4.1) as follows:

1. the first reservoir represents the soil that is subjected to evapotranspiration and precipitation;
2. the second non-linear reservoir represents the vadose zone, models the percolation time, and determines the partition between runoff and infiltration;
3. the third reservoir represents the underlying aquifer characterized by a recession time, and characterizes the groundwater flow.

The contribution flow of each sub-basin is the sum of the runoff and the groundwater flow. The total flow at the outlet of each sub-basin is the sum of its contribution and the total flow of the upstream sub-basins (delayed by a transfer function representing their propagation time).

Water abstractions, dams and ponds are not considered in the EROS model, and the hydro-meteorological balance in each sub-basin is carried out at a daily time step. This hydrological model was already used in several studies on the impacts of climate change (Ducharne et al., 2011; Moatar et al., 2013; Habets et al., 2013; Bustillo et al., 2014).

The EROS hydrological model uses Ta (°C), solid and liquid precipitation (mm), and reference evapotranspiration (ET_0, mm) to produce daily Q and groundwater flows over the Loire River basin (Thiéry, 1988; Thiéry and Moutzopoulos, 1995). Meteorological inputs are provided by the SAFRAN atmospheric reanalysis data (Vidal et al., 2010, see section 2.3.1, p. 46). ET_0 is computed from the SAFRAN variables with the Penman-Monteith equation (Allen et al., 1998).

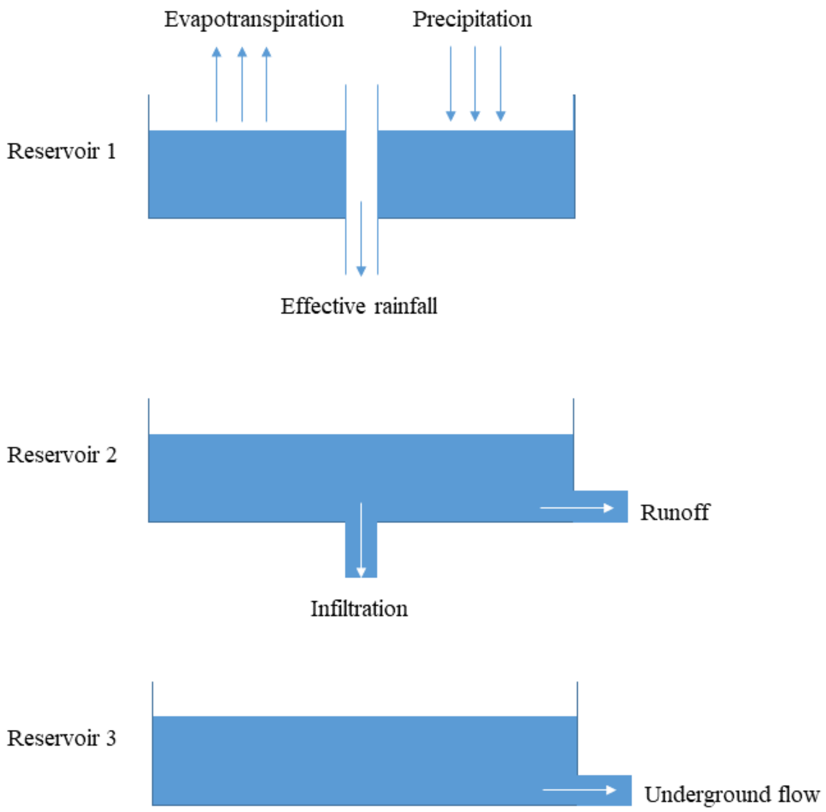

Figure 4.1: Schematic figure of the EROS model operation for each sub-basin.

In the Loire River basin, there are 368 sub-basins within which the climate, land use and geology are quite homogeneous (Figure 4.2). The EROS model is calibrated at 352 out of the 368 sub-basins over the 1971–2018 period where observed Q is available (see section 2.3.3, p. 48). Time series at these calibration stations have been naturalized by EDF (electricity producer) by taking into account dam storages and releases (see section 2.3.3, p. 48).

A 3-year warm-up period (1971-1974) is discarded from the calibration period. The calibration aims at adjusting all unknown parameters (soil capacity, recession times and propagation times) in each sub-basin by maximizing the Nash-Sutcliffe efficiency (NSE) criterion (Nash and Sutcliffe, 1970) on the square root of sub-basin streamflow, and minimizing the sub-basin absolute value of the relative bias. The relative bias is the average streamflow bias divided by the mean streamflow. The square root of the streamflow is a classic transformation (Oudin et al., 2006; Garcia et al., 2017) that helps reducing the heteroscedasticity of model residuals. Maximizing the NSE criteria on the untransformed streamflow favors the goodness of fit of the hydrograph for high flows. Using the NSE criterion on the square roots of the flows provides an estimate of model performance without favoring either high or low flows.

The simulation is then carried out for all 368 sub-basins. Although meteorological variables are available over the 1958–2019 period (see section 2.3.1, p. 46), the first years are discarded from the outputs of simulation for the sake of the EROS model's convergence, and thus daily simulations at the outlet of 368 sub-basins is considered over the 1963–2019 period. Figure 4.3 presents in summary different periods considered for the EROS model in different steps.

Note that the EROS model is calibrated and executed by Dominique Thiéry from BRGM (French Geological Survey). We only provide him with meteorological input data for each sub-watershed.

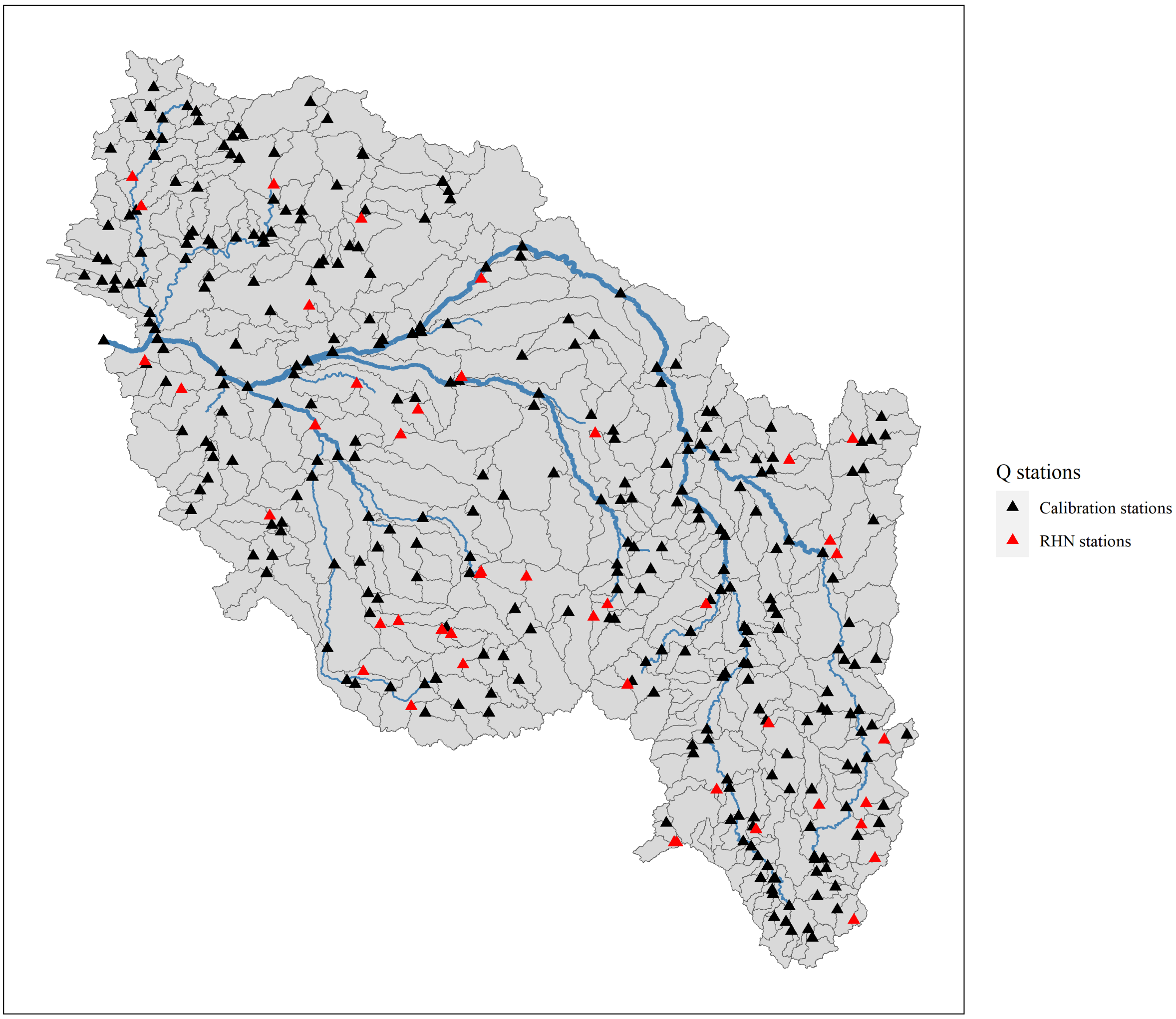

Figure 4.2: The 368 sub-basins over the Loire River basin. The climate, land use and geology are quite homogeneous within each sub-basin.

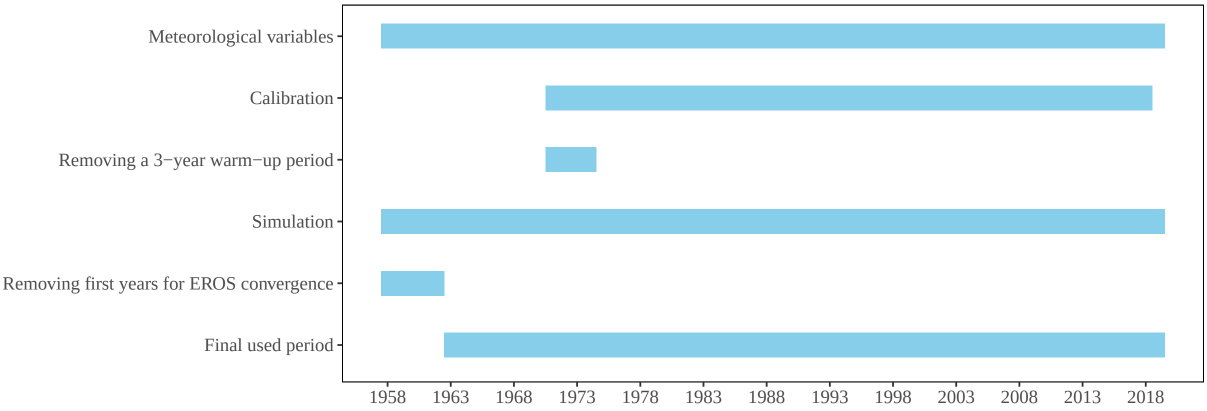

Figure 4.3: Summary of considered period in each step for the EROS model.

The majority of 44 RHN stations (see section 2.3.3, p. 48) do not have detailed data before 1968 (see Figure 4.4). They mostly have long-term continuous high-quality data over the 1968–2019 period. Indeed, they have data for more than 90% of days in each year, and more than 84% of years over the 1968–2019 period (see Figure 4.4). Thus, the 1963–1967 period is discarded from the study period of 44 RHN stations. The performance of the EROS hydrological model is assessed at both 352 calibration stations (between 1971 and 2018) and 44 RHN stations (over the 1968–2019 period).

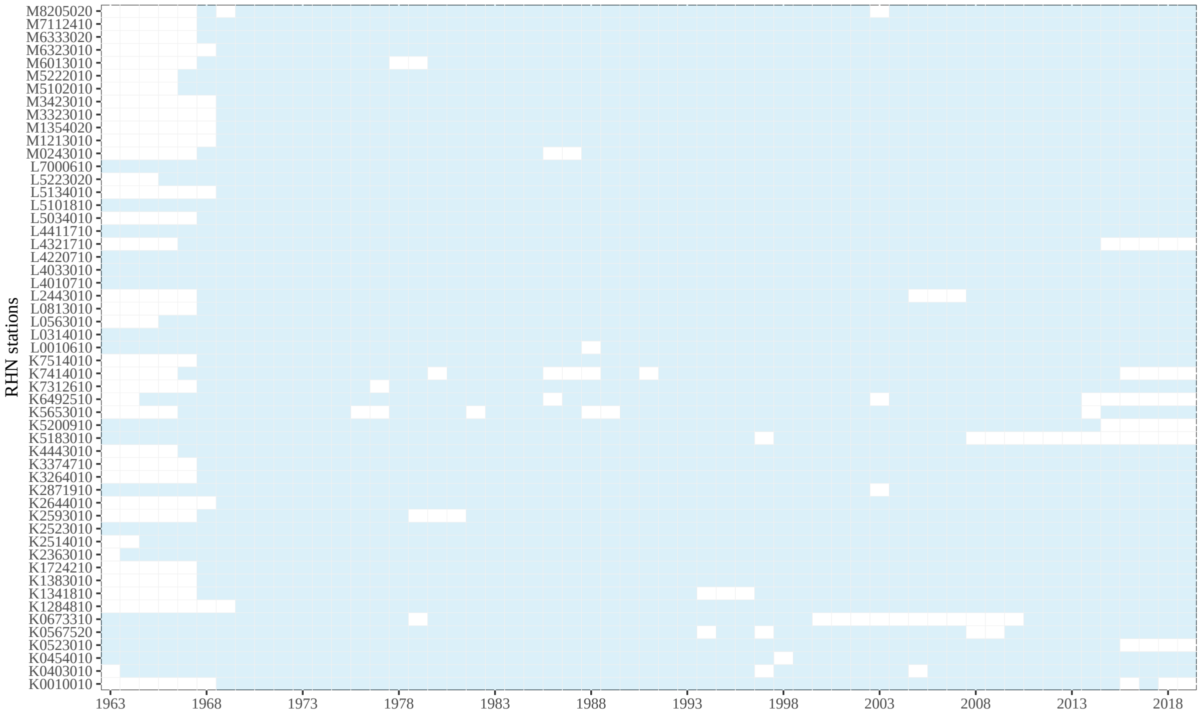

Figure 4.4: The data availability of RHN stations over the 1963–2019 period. Colored years have data >90% of days.

4.2 The T-NET thermal model

4.2.1 Principles of the T-NET model

The T-NET (Temperature-NETwork) thermal model is a physical process-based model developed by Beaufort et al. (2016b) and Loicq et al. (2018) over the Loire River basin. This model computes Tw along the longitudinal dimension of the hydrographic network (a GIS polyline) of the Loire River basin based on two main steps: 1) computation of equilibrium temperature (Te), and 2) upstream-downstream propagation of the thermal signal. The combination of these two steps makes it possible to take into account the thermal propagation and spatio-temporal variations of the heat energy balance as well as hydraulic conditions.

The thermal propagation approach is based on a hydrographic network of the Loire River basin adopted from the BD CARTHAGE® (IGN, 2006). This network was modified by removing all unconnected watercourses as well as all braided channels. The final hydrographic network of the model (see Figure 4.5) consists of 52 278 reaches delimited either by confluences of two streams or a headwater source (i.e., first-order reaches). Therefore, each reach is prioritized according to Strahler's classification knowing that the Strahler order of a reach without a tributary is 1, and that the Strahler order of the Loire at the outlet is 8. The median (resp. mean) reach length in the model is 1.3 km (resp. 1.7 km), and 74% of the reaches have a Strahler order lower than 3. In the following, the two main steps of the the T-NET model are explained.

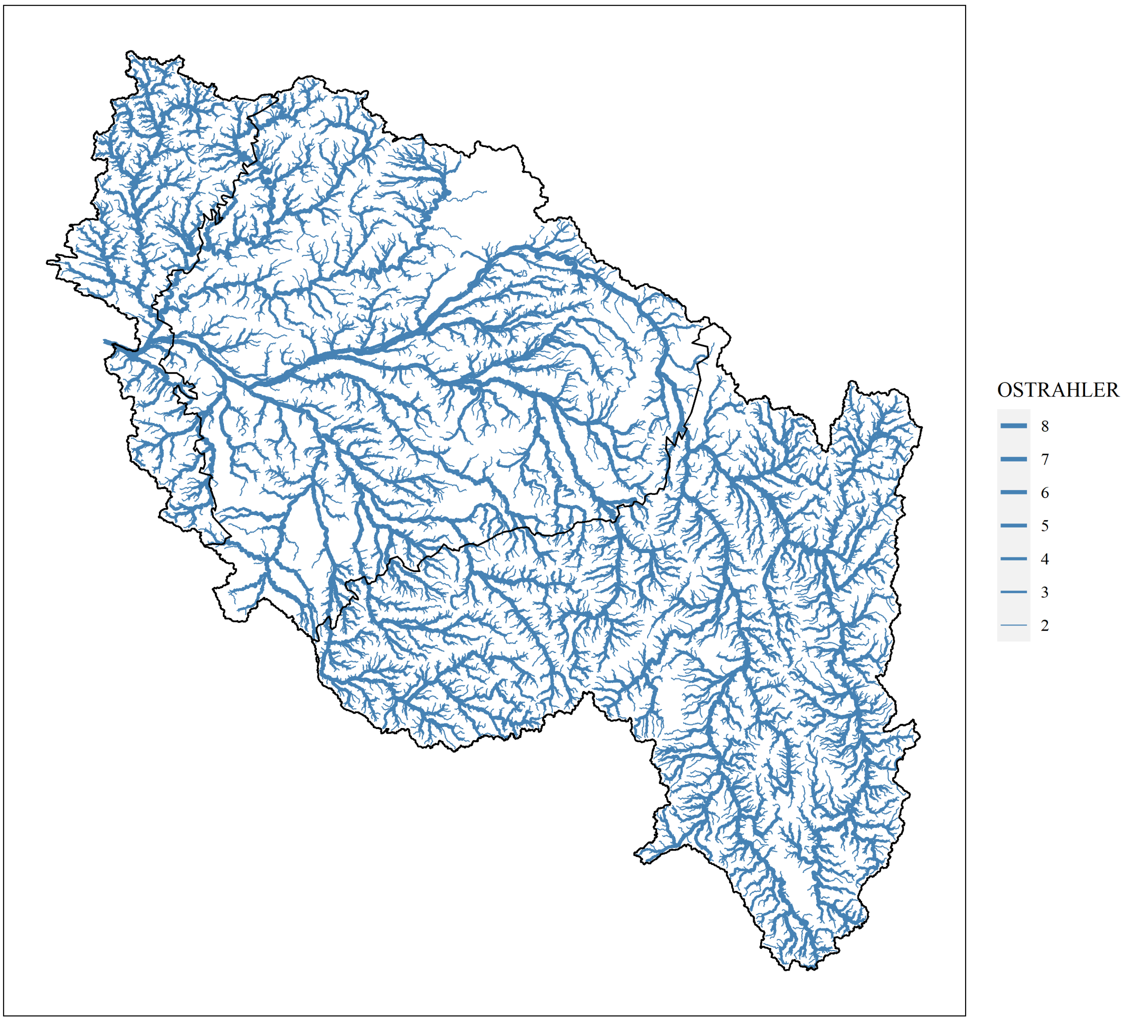

Figure 4.5: The hydrographic network of the Loire River basin. For sake of the readability, small reaches with Strahler order (OSTRAHLER) < 2 are not shown. Solid black lines show the Hydro-Ecoregion delineation (see Figure 2.1, p. 44).

4.2.1.1 Computation of equilibrium temperature (Te)

The 1D heat equation for vertically well-mixed streams (Sinokrot and Stefan, 1993) is written as:

$$\frac{\partial T}{\partial t} + V\frac{\partial T}{\partial x} + D_L\frac{\partial^2 T}{\partial x^2} = \frac{\Sigma H_i(t)}{\rho_w.c_{pw}.D} \tag{4.1}$$

with D: the river dpeth (m), V: water velocity (m.s^{-1}), Tw: the water temperature (°C), c_{pw}: the specific heat of water, ρ_w: the water density, H_i: the sum of energy heat fluxes at the water-air interface and the water-stream bed interface (see Figure 4.6).

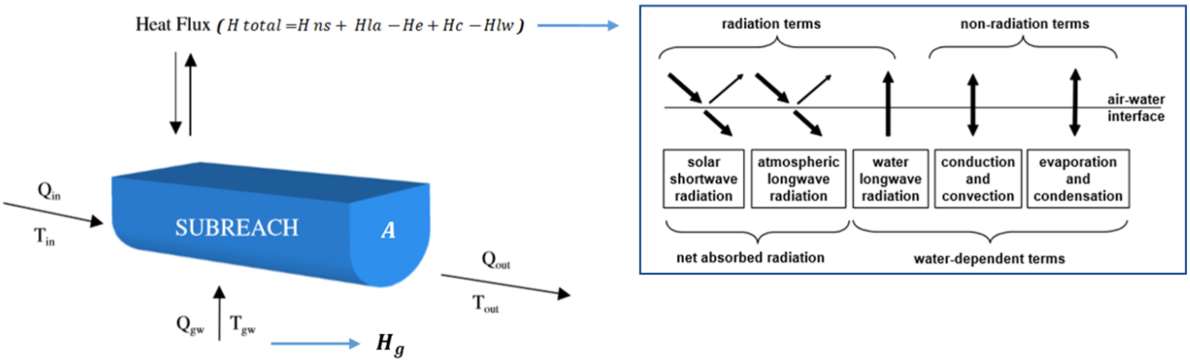

Figure 4.6: The heat exchanges at the water-air and water-stream bed interfaces.

By considering steady condition ($\frac{\partial T}{\partial t} \approx 0$) and assuming negligible diffusion at the basin scale ($D_L\frac{\partial^2 T}{\partial x^2} \approx 0$), the 1D heat equation for a rectangular channel ($V = \frac{Q}{D*B}$) can be written as:

$$\frac{\partial T}{\partial x} = \frac{\Sigma H_i(t).B}{\rho_w.c_{pw}.Q} \tag{4.2}$$

To solve Equ. 4.2 in a simple way, the concept of equilibrium temperature (Te) is used (Edinger et al., 1968). Te is the temperature at which the net heat exchange at the body of water is null ($\Sigma H_i = H_{ns} + H_{la} - H_{lw} + H_c - H_e + H_g = 0$). All the parameters required for calculating the six energy fluxes and the net heat exchange at the body of water are detailed in Table 4.1. It is also assumed that the net heat exchange is proportional to the difference between Tw and Te (Edinger et al., 1968). Therefore, the net heat exchange can be linearized by establishing a proportional relationship between the difference of Te and Tw:

$$\Sigma H_i = K_e(T_e - T_w) \tag{4.3}$$

By substituting Equ. 4.3 in Equ. 4.2:

$$\frac{\partial T}{\partial x} = \frac{K_e.B}{\rho_w.c_{pw}.Q}(T_e - T_w) \tag{4.4}$$

Table 4.1: Formulas and parameters used to determine heat fluxes at the water-air and water-stream bed interfaces (Brutsaert and Stricker, 1979; Sridhar et al., 2004; Bustillo et al., 2014; Beaufort et al., 2016a). These heat fluxes were presented before in Figure 1.1, p. 27.

Heat flux (W.m^{-2})	Formulas	Parameters	Assumptions
Net solar radiation (H_{ns})	$H_{ns} = (1 - Alb).R_g.(1 - SF)$	Alb: surface water albedo Rg: shortwave radiation (W.m^{-2}) SF: shading factor (see section 4.2.2.3)	$Alb = 0.6$
Long wave radiation (H_{la})	extracted from the Safran reanalysis data		
Long wave emitted radiation (H_{lw})	$H_{lw} = \varepsilon_w.(\sigma)(T_w + 273.15)^4$	ε_w: water emissivity T_w: water temperature (°C)	$\varepsilon_w = 0.96\sigma$
Convection (H_c)	$H_c = B.f(x).(T_a - T_w)$	B: Bowen's coefficient $f(w) : aw + b$: wind function w :wind speed at 2 m (m.s^{-1})	B= 0.62 mb.k^{-1} a=4 w.m^{-3}.mb^{-1} b=7.4 w.m^{-2}.mb^{-1}
Evaporation (H_e)	$H_e = f(x).(e_s - e_a)$	e_s : water vapour pressure in air (mb) e_s :saturation vapour pressure for Tw (mb)	Magnus–Tetens approximation: $e_s = 6.11 \exp \frac{17.27Tw}{237.3Tw}$
Groundwater inputs (H_g)	$H_g = \rho_w.C_{pw}.\frac{Q_g}{A}(T_g - T_w)$	ρ_w: density of water (kg.m^{-3}) C_{pw}: specific heat capacity (J.kg^{-1}.°K^{-1}) Q_g: groundwater flow m^3.s^{-1} A: exchange area between groundwater and river (m^2) T_g: groundwater temperature (°C) (approximated by adding 1°C to the moving average of Ta over 365 days (Todd and Mays, 2004))	

In this equation, K_e is rate at which the Tw responds to different heat exchange processes and is expressed in W/m^2/K. It is determined using a theoretical formula (Poulin, 1980; Bustillo et al., 2014; Beaufort et al., 2016b) as the partial derivative of heat fluxes (ΣH_i) with respect to Te:

$$K_e = \frac{-\Sigma \partial H_i}{\partial T_e}$$

$$\mathrm{K}_e = 4\varepsilon\sigma(T_w + 273.15) + f(w)(0.62 + 6.11\frac{17.27\times 2371.3}{(237.3+Tw(t))^2)} \times \exp\frac{17.27Tw(t)}{237.3+Tw(t)}) + \rho_w.C_{pw}.\frac{Q_g(t)}{A} (4.5)$$

The parameters in this equation can be found in Table 4.1.

4.2.1.2 Upstream-downstream propagation of the thermal signal

The headwater temperature, or in other words, boundary condition (Tw of a reach with a Strahler order 1), is considered as groundwater temperature (Tg) approximated by adding 1°C to the moving average of Ta over 365 days (Todd and Mays, 2004). To satisfy the steady condition ($\frac{\partial T}{\partial t} \approx 0$), each reach is cut into segments (Δx) that water travels in 1h (Figure 4.7, left panel), a period of time for which the model's inputs data i.e. the meteorological variables (at the hourly time step) and discharges (at the daily time step, but are considered constant over 24h) are constant (see sections 2.3.1, p. 46 and 4.1 for more detailed information about these inputs data).

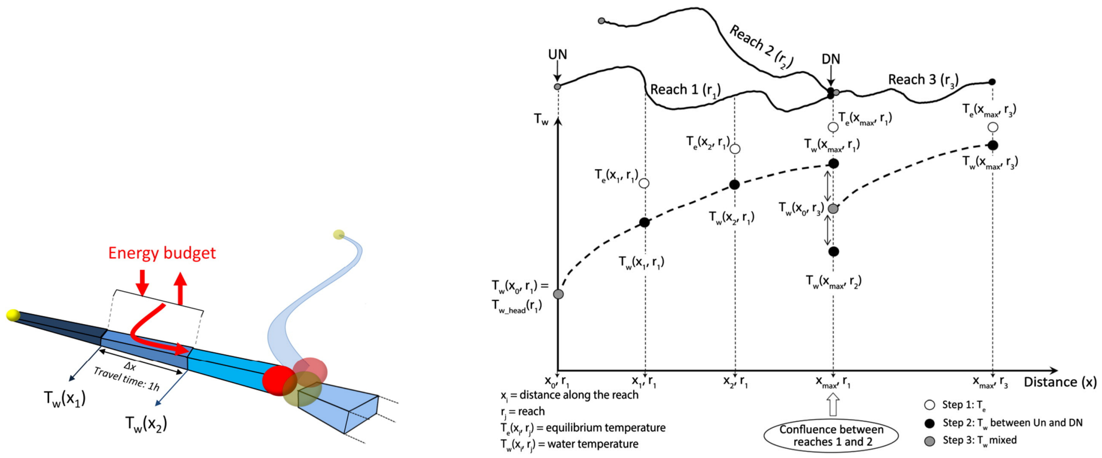

Figure 4.7: The upstream–downstream propagation of thermal signal. Source of figure: Beaufort et al. (2016a).

The segments (Δx) of each reach have the same length, and are determined after calculating the travel time (TTj , j=1 to 52 278 reaches) for the reach. TTj is calculated by dividing the reach length (Lj) by the water velocity of the reach (Vj). Therefore, the number of segments (Δx) with the same length in the reach (j) will be n=TTj/Δt (Δt=1 hr here). This leads to the calculation of Tw at the initial (Δx_i) and final node (Δx_{i+1}) of each segment (Δx) (see Figure 4.7, left panel) by rearranging Equ. 4.4, and using the final equation as below:

$$T_w(x_{i+1}, r_j) = T_e(x_{i+1}, r_j) + [T_w(x_i, r_j) - T_e(x_{i+1}, r_j)].\exp[\frac{-B(r_j).K_e(x_{i+1}, r_j)}{\rho_w.C_{pw}.Q(r_j)}] \tag{4.6}$$

Indeed, this equation calculates Tw at the final node of each segment, which is indeed Tw at the initial node of the next segment (except for a reach with a Strahler order 1). Thus, executing such an equation for all segments of a reach gives Tw at the final node of the last segment of the reach (see Figure 4.7, left panel).

Finally, the thermal signal of two reaches at a confluence are mixed with respect to their discharges (Equ. 4.7, and see Figure 4.7, right panel):

$$T_w(x_{initial}, j) = T_w(x_{final}, j) \times \frac{Q(x_{final}, j)}{Q(x_{final}, j) + Q(x_{final}, j+1)} + T_w(x_{final}, j+1) \times \frac{Q(x_{final, j+1})}{Q(x_{final}, j) + Q(x_{final}, j+1)} \tag{4.7}$$

It should be noted that outputs of the T-NET model are only available at the initial and final nodes of each reach. In the current study, outputs at the final node of each reach are used.

4.2.2 Input data of the T-NET thermal model

To compute the six heat fluxes (see Table 4.1) and the water travel time (TTj) for each reach, various input data are needed, and they are summarised in Figure 4.8. They are furthermore explained in detail below.

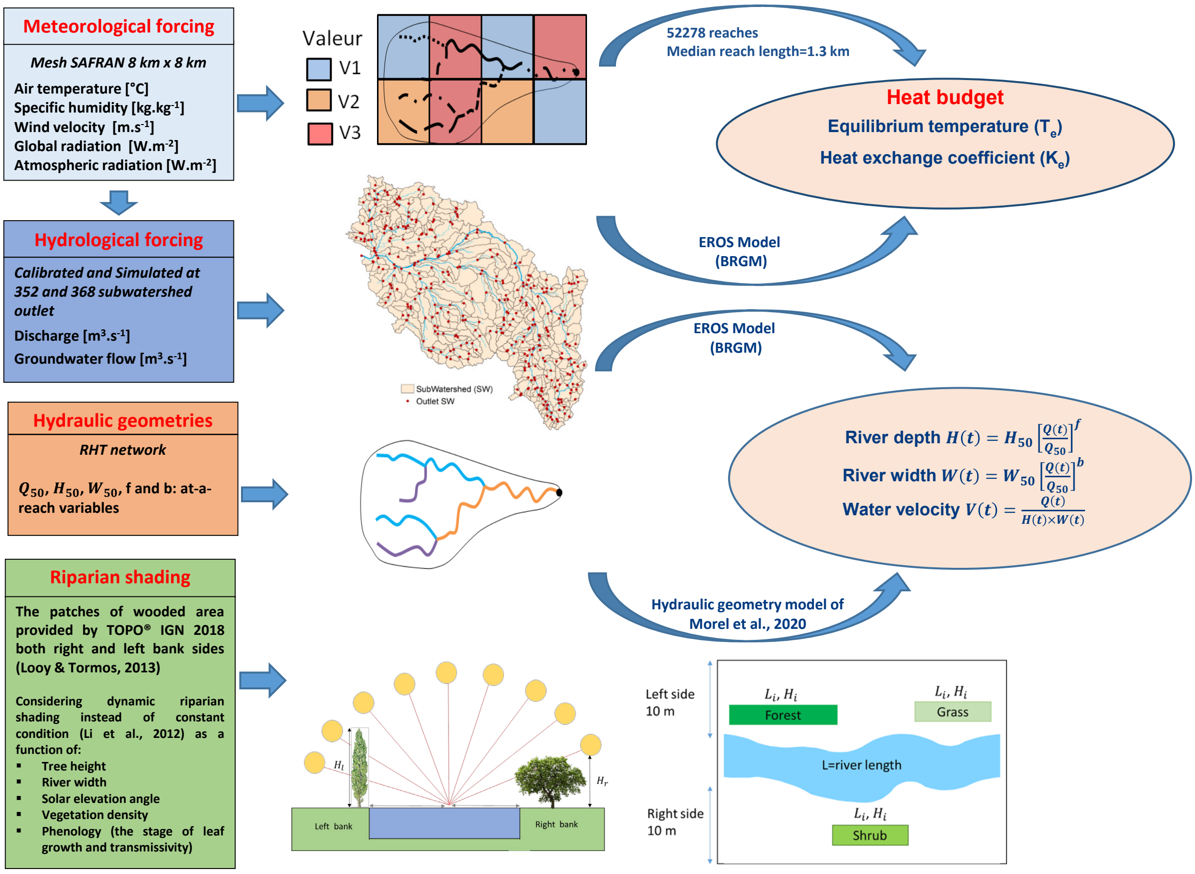

Figure 4.8: The summary of inputs data of the T-NET model (Beaufort et al., 2016b; Loicq et al., 2018).

4.2.2.1 Meteorological and hydrological variables

Hourly Ta (°C), specific humidity (g.kg^{-1}), wind velocity (m.s^{-1}), shortwave radiation (W.m^{-2}), and longwave radiation (W.m^{-2}) are provided by the SAFRAN reanalysis data (see section 2.3.1,

p. 46). All the reaches located within a grid cell of SAFRAN (8×8 km) are assigned the values of the meteorological variables of the grid cell. For the reaches flowing through more than one grid cell, the values of the meteorological variables are weighted by the relative length of the reach in each grid cell.

The daily streamflow simulated at the outlet of 368 homogeneous sub-basins (see section 4.1) are redistributed along the river network inside each sub-basin according to the reach drainage area for informing the T-NET model at the reach scale. The ratio of sum of the lengths of all reaches upstream of a reach to the sum of the lengths of all reaches located in a sub-basin is used as the proxy of the drainage area of a reach. Q is considered to be constant over the 24 hours to have hourly Q.

4.2.2.2 Hydraulic geometry

Standard version

In the previous version of the T-NET model used by Beaufort (2015) and Loicq (2018), a hydraulic geometry model, ESTIMKART, depending on river slope, watershed area and reach Strahler order, was used (Lamouroux et al., 2010). Morel et al. (2020) recently developed a new hydraulic geometry model using Random Forest (hereafter referred to as RF) approach. They used RF models to develop and test international empirical models of reach-scale hydraulic geometries that can be applied across entire stream networks. Since Morel et al. (2020) showed better performance for this new hydraulic geometry model (referred to as RF model) at observed stations (mainly for small and medium rivers) over France and New Zealand, this hydraulic geometry model (RF model) is used in the current study. Compared to the ESTIMKART model, the RF model better predicts river depth (H) (median bias=-0.003 m, and RMSE=0.07 m) and width (W) (median bias=-0.121 m, and RMSE=1.29 m) at the stations over the Loire River basin (see Figure 4.9). Indeed, the ESTIMKART model underestimates river width and depth.

Modified version

Therefore, here, hydraulic geometry (river width and depth) are calculated by using RF model and assuming a rectangular river section being constant over 24 hours (Morel et al., 2020):

$$D(t) = D50 \times \left[\frac{Q(t)}{Q50}\right]^{f} \tag{4.8}$$

$$W(t) = W50 \times \left[\frac{Q(t)}{Q50}\right]^{b} \tag{4.9}$$

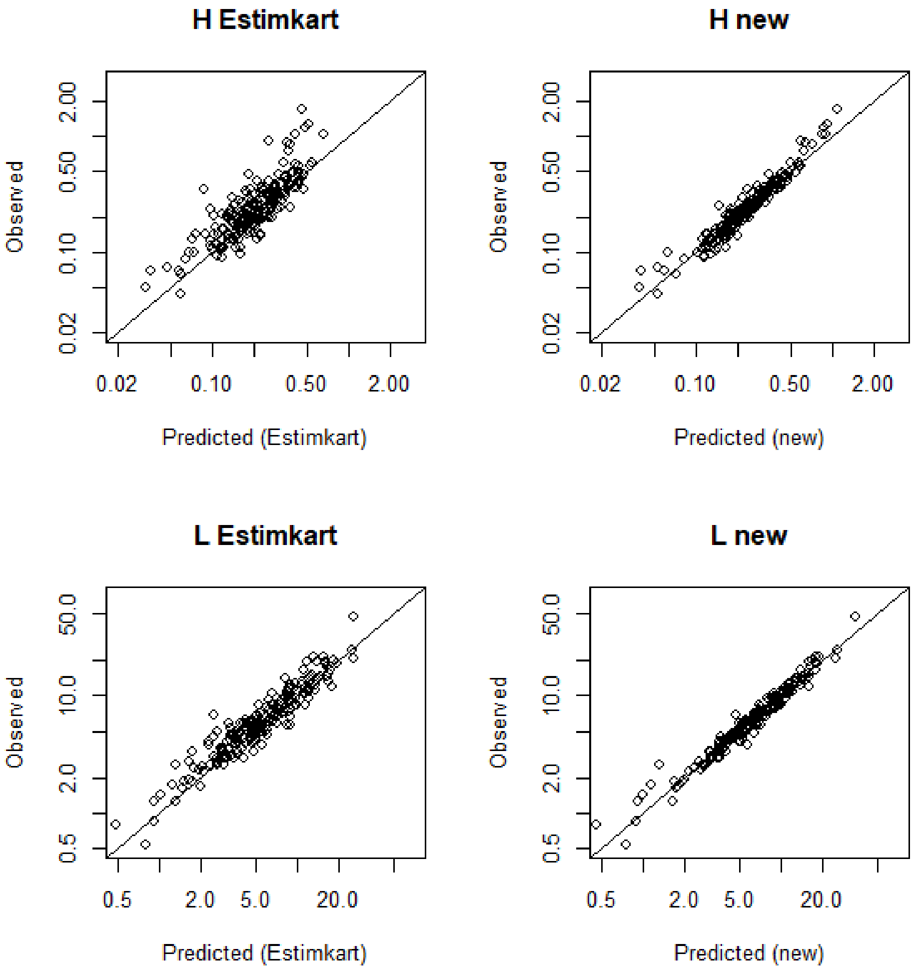

Figure 4.9: The performance of the RF (new) and the ESTIMKART (old) geometry models in predicting river width and depth at 203 field measurements over the Loire River basin. H: river depth and L: river width. This figure is provided by Maxime Morel.

with f and b being at-a-reach exponents previously derived from climate, hydrological, topographic and land use descriptors (Morel et al., 2020). Q (t) is the daily mean streamflow provided by the EROS hydrological model (see section 4.1). The Q50, W50, D50 (the median of Q, width and height, respectively) and the exponents are available on the Theoretical Hydrographic Network for France (RHT, Pella et al., 2012). There is about 50% correspondence between reaches of the T-NET and RHT networks. For the remaining reaches, required hydraulic geometry variables for T-NET reaches are extrapolated from the nearest RHT reach. The calculation related to this extrapolation is done by Herve Pella and Nicolas Lamouroux (EcoFlowS team, UR RiverLy, INRAE). This river hydraulic geometry allows for computing the water velocity by the ratio of Q (t) to rectangular wetted cross-section. Lastly, the travel time is also calculated by the ratio of water velocity to the reach length (TTj=Vj/Lj, j=1 to 52 278 reaches).

In section 4.3.2.1, the performance of the T-NET thermal model in simulating daily Tw by using each of these hydraulic geometry models (ESTIMKART and RF) is assessed.

4.2.2.3 Riparian shading

Standard version

In the previous version of the T-NET model developed by Beaufort (2015), a constant method was used in a first attempt for calculating the riparian shading factor (SF) over the whole Loire River basin. In this approach, vegetation density (vc) was computed at the reach scale in a buffer of 10 m around the reach from remote sensing (Valette et al., 2012). In order to take into account the influence of reach width on shading area, vegetation density (vc) was then weighted linearly by a coefficient linked to the Strahler order ranging from 1 (for a river reach with Strahler order 1) to 0 (for a reach with Strahler order 8).

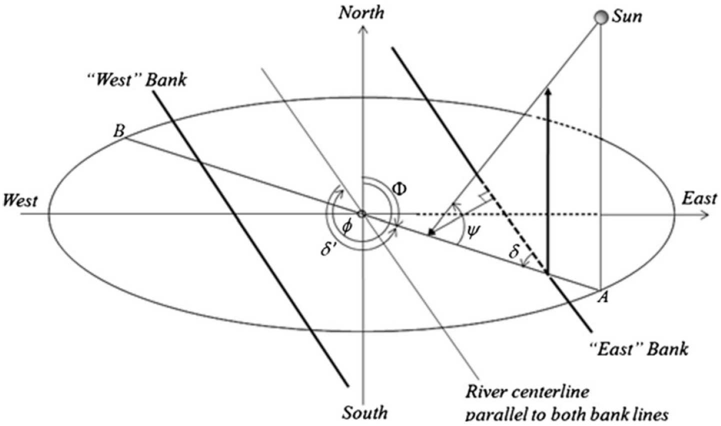

Figure 4.10: Representation of the shading method proposed by Li et al. (2012). The black lines show channel banks. The vertical line and the orthogonal area on the right bank show a tree and its effective shading. Ψ is the solar altitude angle; ϕ is the stream azimuth angle from the north; Φ is the solar azimuth angle from the north; $\delta\prime$ is the difference between solar azimuth angle and stream azimuth angle ($\delta\prime = \Phi - \phi$); δ is the angle between bank line and solar beam at horizontal plane. Source of figure: Li et al. (2012).

In a second attempt, Beaufort (2015) tried to describe the dynamics of riparian shading in the T-NET thermal model by calculating shading factor through the variable method proposed by Li et al. (2012) (see Equ. 4.10 and Figure 4.10). This method calculates SF as a function of tree height, river width, solar elevation angle and vegetation density in each side of a river bank as following:

$$W_{\text{shaded}} = \frac{H_{\text{left/right}} \times \cot\Psi \times \sin\delta}{W} \tag{4.10}$$

$$SF_{\text{right}} = (W_{\text{shaded}})_{\text{right}} \times (vc)_{\text{right}} \tag{4.11}$$

$$SF_{\text{left}} = (W_{\text{shaded}})_{\text{left}} \times (vc)_{\text{left}} \tag{4.12}$$

$$SF = Max(SF_{\text{right}}, SF_{\text{left}}) \tag{4.13}$$

where H is average tree height, W is the river width (see Equ. 4.8), Ψ is the solar altitude angle, δ is the angle between solar azimuth and the mean azimuth of T-NET reach (see Equ. 4.20), and vc is the vegetation density (%). The solar altitude angle, Ψ (rad), is calculated using the following equation (Li, 2006):

$$\sin\Psi = \sin\alpha.\sin\beta - \cos\alpha.\cos\beta.\cos\omega t \tag{4.14}$$

where β is the site latitude (rad), negative for south hemisphere, and γ is the earth angular velocity ($\frac{\pi}{day}$) and t is the true solar time (day). α is the solar declination angle (rad), which is negative for south hemisphere, and is calculated as below (Bourges, 1985; Garg and Datta, 1993):

$$\alpha = 2.45\frac{\pi}{180}.\sin(\frac{2\pi(N+2384)}{365.25}) \tag{4.15}$$

where N is the Julian day. The true solar time, t, which is the time in a time reckoning system that the sun returns to the local meridian at exactly 12:00 noon, was computed by adding the Equation of Time (EOT) to the Mean Solar Time (MST):

$$t = MST + EOT \tag{4.16}$$

The MST is the average time as indicated by well-regulated clocks. For a specific given location, the MST was computed from the local clock time and the location longitude using the following formula:

$$MST = T_{Local} + \frac{\lambda^\circ - TimeZone \times 15^\circ}{361^\circ} \tag{4.17}$$

where MST and T_{Local} are in numerical format (e.g., 0 = 12:00 midnight, 0.5 = 12:00 noon, etc.), λ is the observed longitude of the location (in degree) (negative for west hemisphere), Time Zone is the zone on which the local clock time is based (negative for west hemisphere), and 361° is the approximate rotation angle of the Earth in a day. If daylight saving time is in practice in the local clock time, we simply add 1 to the time zone or subtract 1 hour from the local clock time. The EOT is the difference between the true solar time and the Mean Solar Time calculated as below:

$$EOT = 9.87\sin 2\beta - 7.53\cos\beta - 1.5\frac{\sin B}{60\times 24} \tag{4.18}$$

where EOT is in numerical day, $B = (2\pi/364)\times(N-81)$, and N is the Julian day.
The solar azimuth, Φ, defined as clockwise from north in radius (Figure 4.10), is calculated using the following equation (Li, 2006):

$$\Phi = \frac{\pi}{2} \pm \arccos(\frac{\cos\alpha\times\sin\omega t}{\cos\Psi}) \tag{4.19}$$

The plus sign is used when the sun moves from azimuth 90° to azimuth 270°, and the minus sign is used in the very early morning ($<$ 90° to 90°) and late evening (270° to $>$ 270°). In a rare case, the solar altitude, Ψ, should be exactly 90° or 270°, a very small angle is added so that the above equation would still work. Then, for calculating the angle (δ) between solar azimuth and the mean azimuth of T-NET reach, the difference between the solar azimuth angle and the stream orientation angle ($\delta\prime$) is calculated as follows:

$$\delta\prime = \Phi - \phi \begin{cases} \text{–for the "east" bank:} & \\ \delta = \pi + mod(|\delta\prime|, 2\pi) & \text{if } \delta\prime < 0 \\ \delta = \pi + mod(\delta, 2\pi) & \text{otherwise} \\ \text{–for the "west" bank it is the reverse of the "east" bank:} & \\ \delta = \delta + \pi & \text{if } \delta > \pi \\ \delta = \delta - \pi & \text{otherwise} \end{cases} \tag{4.20}$$

To implement this variable method, as seen in Equ. 4.10, it is first needed to calculate the average tree height and vegetation density for both right and left sides of a river bank. For this aim, Beaufort (2015) considered the mean vegetation cover in a buffer of 10 m around the reach as the vegetation density of both sides of a river bank. In other words, the vegetation density was the same for both sides of a river bank. Moreover, he considered the constant height of 15 m for all vegetation species. He also considered the phenology by applying an assumed coefficient varying with season.

Beaufort (2015) compared biases produced by these two different vegetation methods, namely variable and constant methods over the Loire River basin (see Figure 6.14, p. 208 of Beaufort, 2015). He mostly found a weaker performance for the variable method compared to the constant method in producing daily Tw. Indeed, for rivers with less than 100 km distance from the source, the T-NET model with the variable method overestimated daily Tw by more than 1 °C in winter. This model also underestimated daily Tw by 2 °C in summer for medium and large rivers. The root mean square error (RMSE) of Tw at the annual scale for the variable method (2.1 °C) was also greater than that for the constant method (1.7 °C). Moreover, no significant difference between RMSE of these methods was observed over the summer.

The sensitivity analyses (testing different heights) conducted by Beaufort (2015) for the variable method also showed that tree height had little effect on monthly Tw, and maximum and minimum daily Tw of streams with less than 100 km distance from the source especially on small ones (see Figure 6.17, p. 212 of Beaufort, 2015). Beaufort (2015) explained that this could be due to the small average width of this type of streams, and the fact that above a certain tree height, the shaded area covers the entire surface of the watercourse regardless of the tree height. Finally, he also found a $\pm$ 50% change in the river width of the streams in the T-NET thermal model had very little influence on the monthly Tw of the stations located on small and medium rivers (see Figure 6.18, p. 213 of Beaufort, 2015).

In the second version of the T-NET model, Loicq (2018) used vegetation cover extracted from the LiDAR data within a single buffer of 10 m around 270 km of river over the Maine basin. He used a new vegetation method for the T-NET model (referred as LiDAR method here). This model is a spatially-explicit method that computes riparian shading factor from a LiDAR-derived digital surface model (Loicq et al., 2018). The performance of the T-NET model in simulating maximum daily Tw in the middle Loire from April to September was improved by using the LiDAR method (Bias=-0.82 °C, RMSE=1.95 °C) compared to the variable method (Bias=-1.86 °C, RMSE=2.55 °C) and constant method (Bias=-1.44 °C, RMSE=2.17 °C) (see Table 5.3, p. 122 of Loicq, 2018).

Loicq (2018) also used vegetation density and tree height extracted from LiDAR data in the variable method (Equ. 4.10), and investigated the performance of the T-NET model in simulating the longitudinal profile of maximum daily Tw (13 to 31 August 2009 average). At first, he only used vegetation density of LiDAR data in the variable method (Equ. 4.10), and kept the tree height as 15 m. He found that the mean bias of this version of the variable method (-1.19 °C) was less than mean bias of original variable method (-1.86 °C), and it was close to the mean bias of the LiDAR method (-0.94 °C) (Loicq et al., 2018). Afterwards, he used both tree height and vegetation density extracted from LiDAR data. He found much an improvement in mean bias of the variable method (-0.78 °C). Therefore, the poor performance of the T-NET model with the variable method (height=15) found by Beaufort (2015) could be due to the poor representation of vegetation density and tree height in each side of a river bank.

Consequently, Beaufort (2015) found that the variable method with considering constant height and the same vegetation density for both sides of a river bank could not improve the T-NET model performance. However, Loicq (2018) showed in the Maine basin that differentiating between vegetation density of each sides of a river bank, and considering different tree heights can lead to better results. In this regard, in the current study, the variable method with vegetation density for each side of a river bank is considered. Moreover, tree height corresponding to vegetation species are taken into account.

Modified version

As mentioned before, the variable method was already integrated into the T-NET thermal model, but some of its inputs are updated in the current study to have vegetation density and tree height for each side of a river bank. To do so, first, patches of wooded area provided by the BD TOPO® (IGN, 2008) database are used as a proxy of vegetation. The vegetation species and length of each wooded patch in a buffer of 10 m are extracted for both right and left sides of a river bank by using the approach proposed by van Looy and Tormos (2013). The vegetation density (vc) is then calculated as the ratio of patch length to reach length for both right and left sides of a river bank. In case of multiple wooded patches in any side of a river bank, the average vegetation density of the patches is considered. This vc is then used in Equ 4.10. Since the information about tree height is not available at this scale, it is approximated by knowing the vegetation species (see Table 4.2).

Table 4.2: Vegetation species and their approximated height (extracted from: Otto (1998); Aulinger et al. (2005); Allaby (2019); https://cms.geobretagne.fr; www.polebocage.fr).

specie	height (m)
Wood forest	25
Coniferous forest	25
Deciduous forest	25
Open forest	20
Mixed forest	25
Poplar grove	25
Hedge	15
Mixed vegetation	20
Shrub	10
Grass	0

In the presence of different vegetation species, the average tree height (m) for each side of a river bank is used (Equ. 4.21).

$$H = \frac{1}{n}\Sigma_{i=1}^{n} H_i \frac{L_i}{L} \tag{4.21}$$

Where L_i (in m) is the length of each wooded patch in a buffer of 10 m, and L is the length of reach (in m). Finally, this average height, H, is also used in Equ 4.10.

To take into account the phenology and stages of leaf growth, a coefficient corresponding to each season and transmissivity is applied to SF to calculate the final shading factor: $SF_{final} = SF \times (1 - \text{transmissivity})$. The transmissivity in leafless months (Jan, Feb, Nov and Dec), months of leaf growth (Mar and Apr), and full-leaf months (May-Sep) is fixed to 0.3, 0.2 and 0, respectively, following Hutchison and Matt (1977). The shortwave radiation is lastly regulated by a factor of $1 - SF_{final}$ (see Table 4.1). Considering this kind of phenology seems logic, even though there is ever-green vegetation species (Coniferous forest) in the basin since a small proportion of vegetation in the basin ($\approx 10\%$) belongs to this kind of vegetation species. Moreover, the regulation of riparian shading is more important in summer period for which 0 transmissivity for all kinds of species is considered (including evergreen species).

In section 4.3.2.1, the performance of the T-NET thermal model in simulating daily Tw for both the constant method developed by Beaufort (2015) and the new version of the variable method (developed in the current study) is assessed over the Loire River basin. Since Beaufort (2015) already showed that his version of variable method had a poor performance compared to the constant method, only his constant method is considered here.

4.3 Model performance

4.3.1 Daily and seasonal streamflow

To assess the performance of the EROS model, first, at both calibration (N=352) and RHN (N=44) stations, the Nash-Sutcliffe efficiency (NSE) for Q, $\sqrt{Q}$ and Ln(Q) are calculated as following:

$$NSE = \begin{cases} 1 - \frac{\Sigma_{t=1}^{T}(Q_m^t - Q_o^t)^2}{\Sigma(Q_o^t - \overline{Q_o})^2} \\ 1 - \frac{\Sigma_{t=1}^{T}(\sqrt{Q_m^t} - \sqrt{Q_o^t})^2}{\Sigma(\sqrt{Q_o^t} - \overline{\sqrt{Q_o}})^2} \\ 1 - \frac{\Sigma_{t=1}^{T}(\ln Q_m^t - \ln Q_o^t)^2}{\Sigma(\ln Q_o^t - \overline{\ln Q_o})^2} \end{cases} \tag{4.22}$$

where $\bar{Q}$ is the mean of observed daily streamflow, and Q_m^t is the modeled daily streamflow at time t, and Q_o^t is observed daily streamflow at time t. The NSE criterion for $\sqrt{Q}$ was also used for calibrating the EROS model (see section 4.1).

In addition to NSE, seasonal and annual relative biases are computed for both calibration (over the 1971–2018 period) and RHN (over the 1968–2019 period) stations. Seasonal and annual Q are important since they will be used later in the next chapters.

The map of NSE of simulated daily Q shows that at least 75 % of the calibration stations have a NSE > 0.7 for all formulations considered (Figure 4.11, top panel). The majority of stations with a low NSE values are found in the upstream part of the basin, in HER A. The NSE criteria for Q, $\sqrt{Q}$ and $\ln Q$ at the majority of RHN stations (83 %) are also > 0.7 (Figure 4.11, bottom panel).

The EROS model performs well at the 352 calibration stations at the annual scale with a median relative bias close to 0 (see Figure 4.12, left panel). It slightly underestimates winter Q (median relative bias (across stations)=-6.27%) and spring Q (-3.47%), and overestimates summer Q (+34.7%) and fall Q (+20.9%). The overestimation in summer and fall could be due to the fact that the EROS model does not take into account water abstractions.

The EROS model also performs well at 44 RHN stations with long-term continuous daily data at the annual scale with a median relative bias of 0.37% (see Figure 4.12, right panel). It slightly underestimates winter Q (median relative bias (across stations)=-7.26%) and spring Q (-6.79%), and overestimates summer Q (+37.7%) and fall Q (+24.7%).

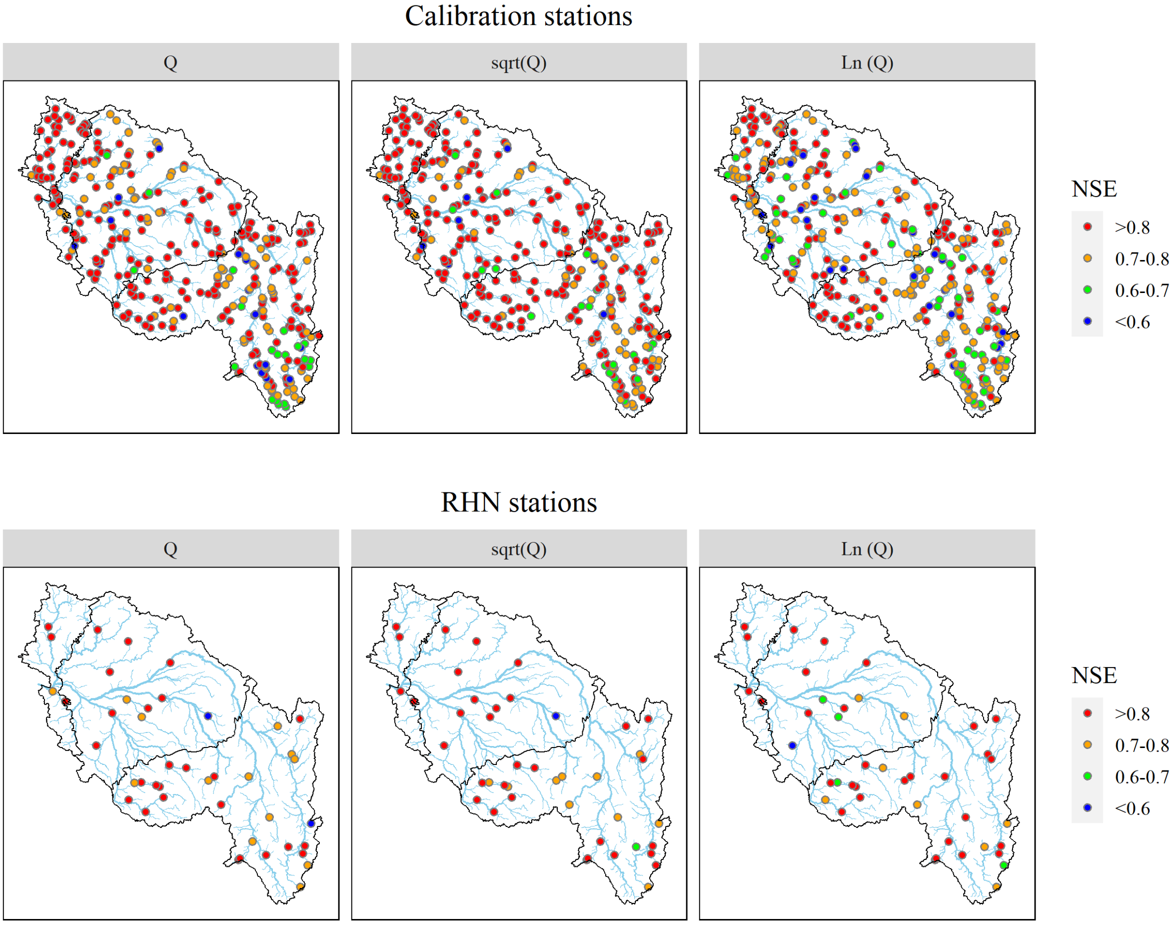

Figure 4.11: NSE values of simulated daily Q for Q, $\sqrt{Q}$ (sqrt(Q)) and $\ln Q$ at (top) 352 calibration stations between 1971 and 2018, and at (bottom) 44 RHN stations over the 1968–2019 period.

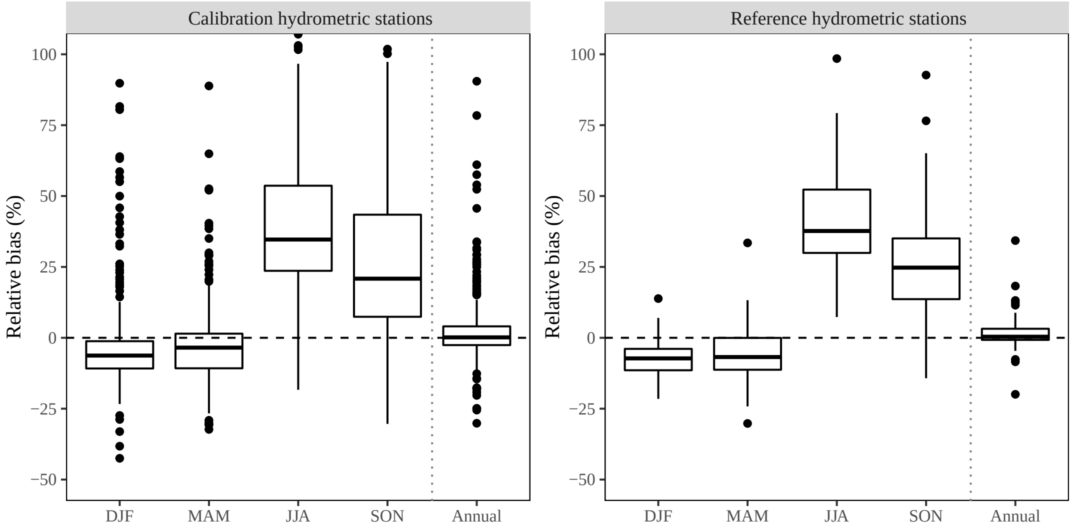

Figure 4.12: Relative bias of the EROS hydrological model in simulating the seasonal and annual Q at (left) 352 stations between 1971 and 2018, and at (right) 44 RHN stations with long-term continuous daily data over the 1968–2019 period.

Figure 4.14 shows the good performance of the EROS model in reconstructing daily Q at three different hydrometric stations in three different years. These stations are located in the upstream, the middle, and the downstream part of the Loire River basin. Position of these stations are presented in Figure 4.13. The annual regime of simulated Q at 44 RHN stations (Figure 4.15) also shows the good performance of the EROS hydrological model in simulating Q regimes.

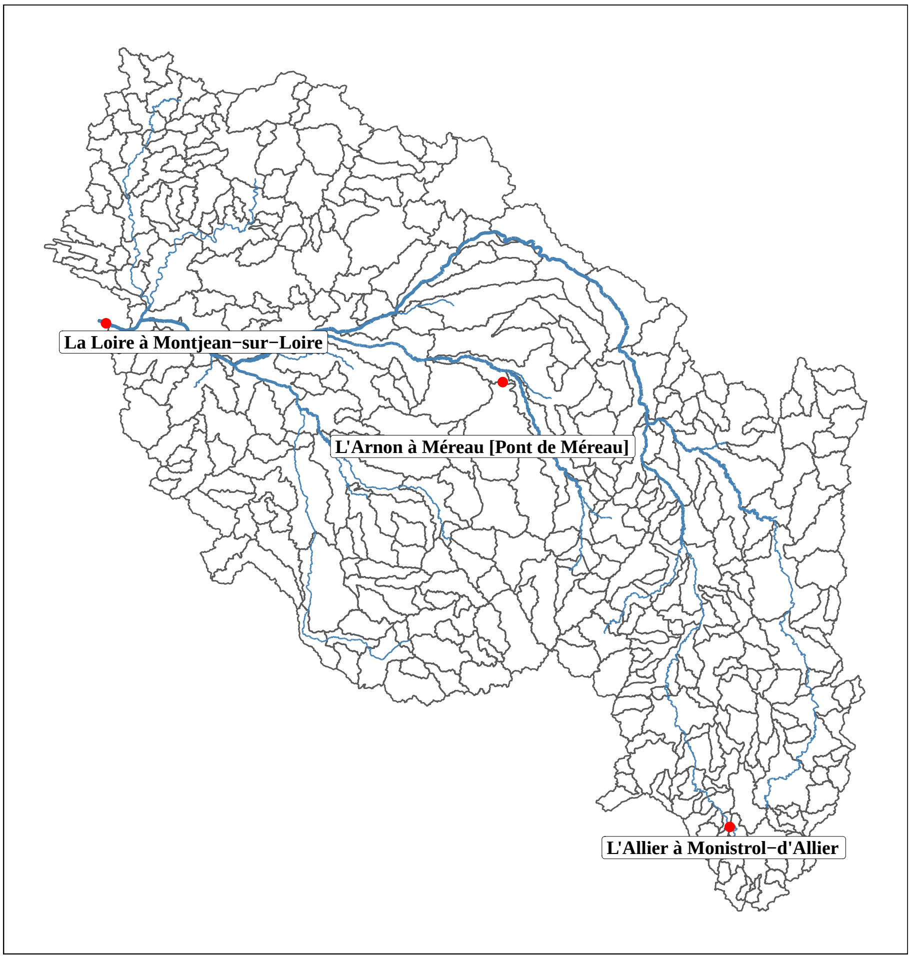

Figure 4.13: Position of sub-watersheds shown in Figure 4.14.

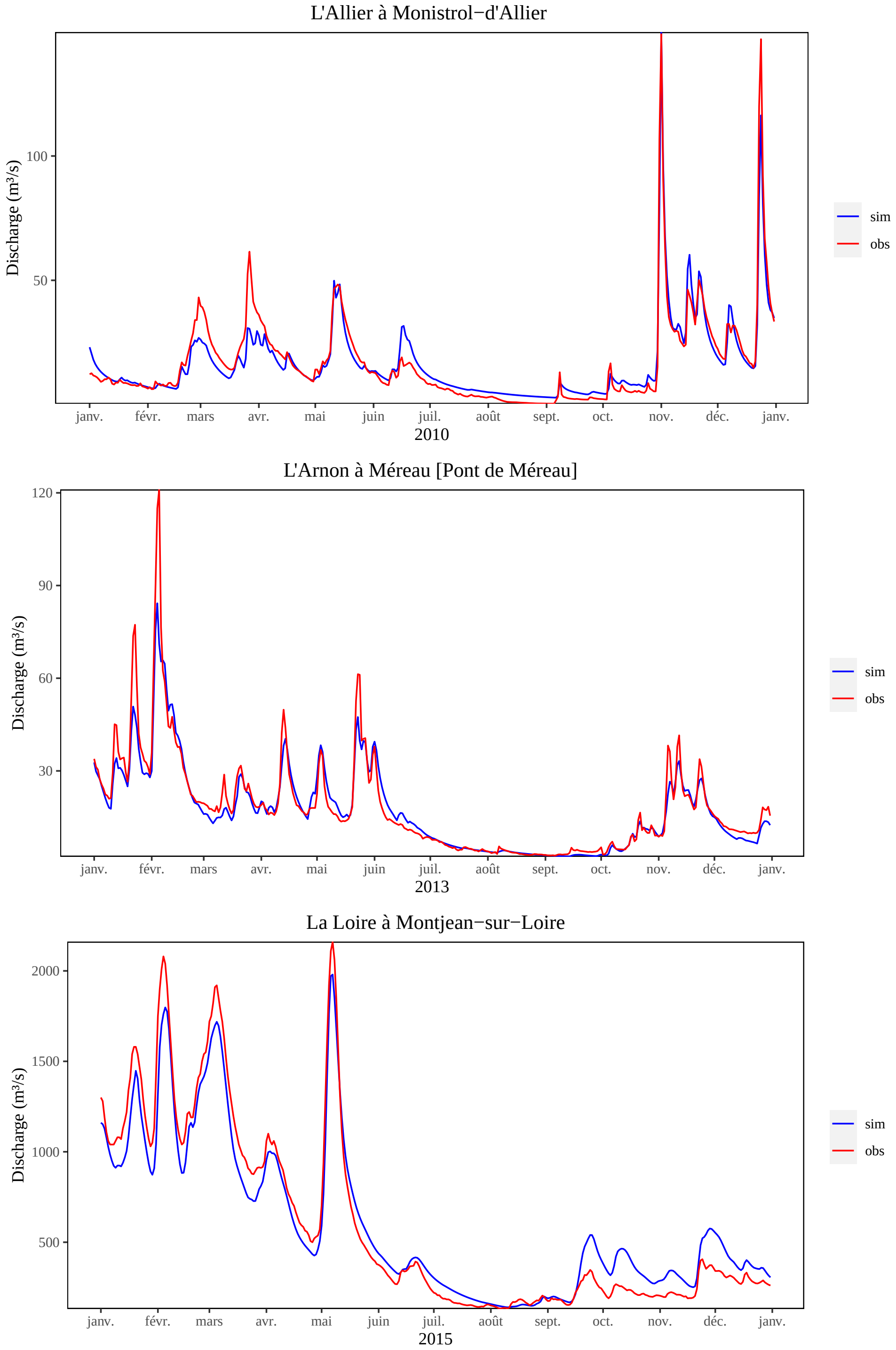
L'Allier à Monistrol−d'Allier

L'Arnon à Méreau [Pont de Méreau]

La Loire à Montjean−sur−Loire

Figure 4.14: Simulated and observed daily Q at three different hydrometric stations: (top) in the upstream part (L'Allier à Monistrol-d'Allier), (middle) in the middle part (L'Arnon à Méreau [Pont de Méreau]), and (bottom) in the downstream part (La Loire à Montjean-sur-Loire) of the Loire River basin.

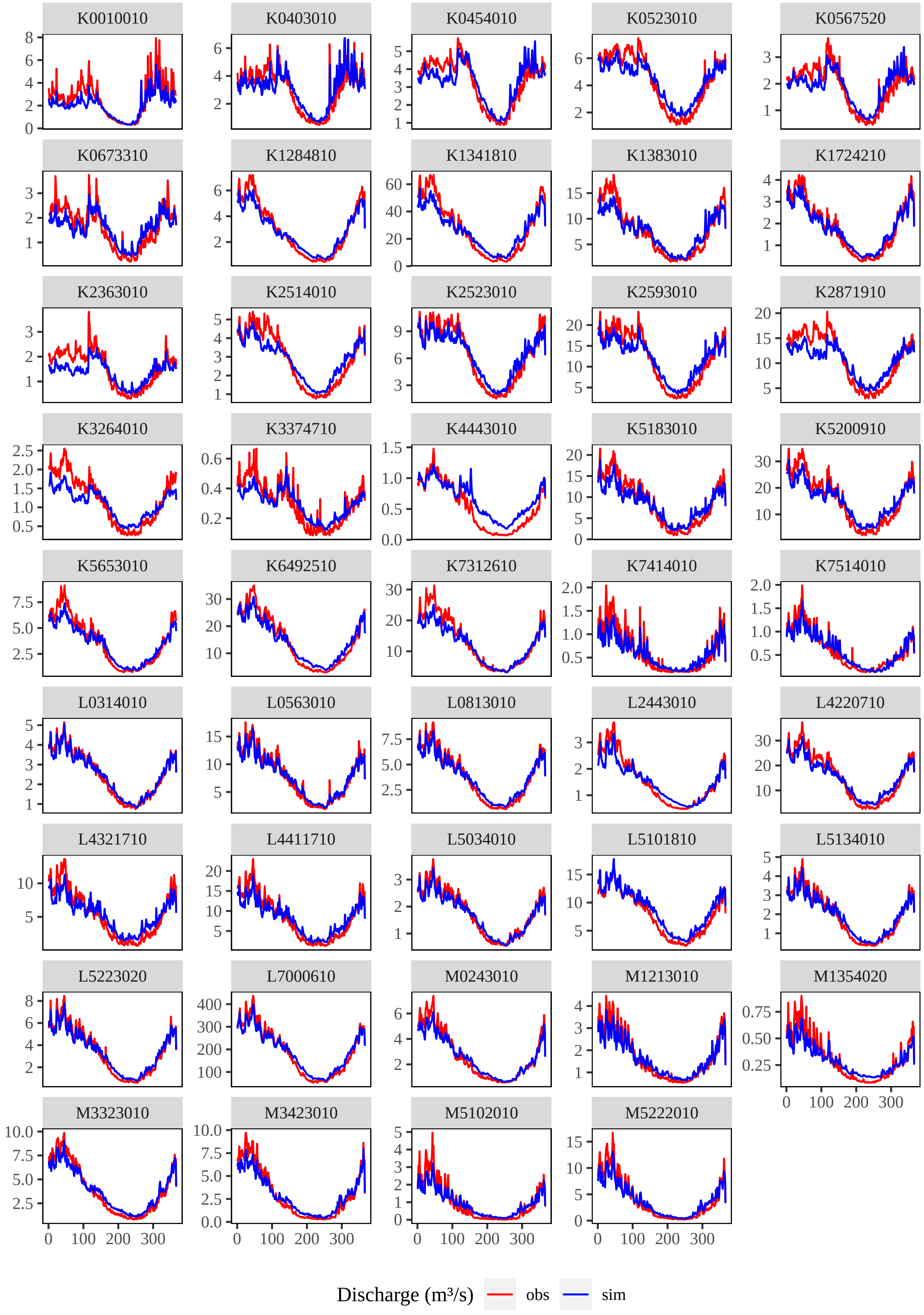

Figure 4.15: Annual regime of simulated and observed Q at 44 RHN stations. For each day, the average of Q over the 1968–2019 period is calculated.

4.3.2 Daily and seasonal Tw

Both Beaufort (2015) and Loicq (2018) assessed the performance of the T-NET thermal model. Beaufort (2015) used 128 stations with missing years over the 2008–2012 period over the Loire River basin to assess the model performance in simulating daily Tw. He showed that the RMSE of the T-NET model (with the constant vegetation method and the ESTIMKART hydraulic geometry model) in simulating daily Tw was on average 1.6 °C at these 128 stations. Loicq (2018) assessed the model performance in simulating mean, maximum, and minimum daily Tw as well as daily amplitude at 44 stations with missing years over the 2008-2015 period over the middle Loire River, the Maine catchment. He showed that the RMSE of the T-NET model (with the constant vegetation method and the ESTIMKART hydraulic geometry model) in simulating mean daily (resp. maximum, and minimum daily Tw, and daily amplitude) was 1.84 °C (resp. 2.05 °C, 2.03 °C, and 1.65 °C) at 44 stations over the Maine catchment.

In contrast to the these previous studies, the current study is considering a new hydraulic geometry model and a new variable vegetation method. It also uses more Tw stations and stations with Tw data in a more recent period to assess the performance of the T-NET thermal model in simulating daily, seasonal and annual Tw over the Loire River basin. The model performance is also assessed at stations with continuous daily data. Moreover, none of these previous studies has assessed the ability of the T-NET thermal model to capture the long-term temporal trends in Tw, which will be further studied in the current study in the Chapter 5.

4.3.2.1 Daily Tw at natural stations over the 2008–2018 period

The T-NET model does not consider the influences of impoundments on the thermal energy balance, and thus produces “natural” thermal regimes. Therefore, the model performance should be assessed at natural Tw stations. 275 near-natural Tw stations (including stations on large rivers) with gap years between 2008 and 2018 are used, which were identified as natural regimes using the thermal signatures approach in the previous chapter (Figure 3.8, p. 62). Please note that in the previous chapter, stations on large rivers were removed from the analysis due to their weak sensitivity to thermal regime alterations induced by impoundmenst (see section 3.1, p. 53), but they are used here. 213 near-natural Tw stations are located on small/medium streams (with distance from the source < 100 km) whereas the remaining are located on large rivers (distance from source > 100 km). The average catchment area is 150 km^2 for small/medium streams, and 10 582 km^2 for large rivers.

In the following, first, the performance of the T-NET model with the new hydraulic geometry model (the RF model) is compared with the previous hydraulic geometry model (the ESTIMKART model) in terms of both bias and RMSE at 275 near natural stations with missing years between 2008–2018. Note that, for this assessment, the constant vegetation method is considered. Then, the performance of the T-NET model with the new version of the variable vegetation method developed in the current study (see section 4.2.2.3), is compared with the constant vegetation method used by Beaufort et al. (2016b). At this step, the performance of the T-NET model in simulating daily Tw is assessed.

Hydraulic geometry model

Figure 4.16 shows no significant difference between the two hydraulic geometry models in simulating daily Tw. Nevertheless, the median bias (across stations) of the RF model is lower (up to 0.53 °C) than that of the ESTIMKART model over the winter months in small and medium streams (Figure 4.16, left panel). Compared to the ESTIMKART model, the median RMSE for the RF model is also slightly lower (up to 0.27 °C) over the winter months in small and medium streams (Figure 4.16, right panel). In these streams, the median bias of the RF model is slightly greater (up to 0.25 °C) than that of the ESTIMKART model in summer months. Moreover, in these streams, the median RMSE for the RF model is slightly higher (up to 0.17 °C) over the summer months compared to the ESTIMKART model. 85% (resp. 83%) of the stations have the annual mean of daily bias in range of -1 °C and 1 °C when the RF (resp. ESTIMKART) model is used. 77% (resp. 80%) of the stations, have an annual RMSE$<$ 2°C when the RF (resp. ESTIMKART) model is used.

Although the performance of the T-NET model in simulating daily Tw does not change significantly when the RF hydraulic geometry model is used, the RF model is used from now on in the T-NET model since, firstly, this hydraulic geometry model has a better performance in prediction of river width and depth (see Figure 4.9). Secondly, it improves the T-NET model performance in winter months in small and medium rivers.

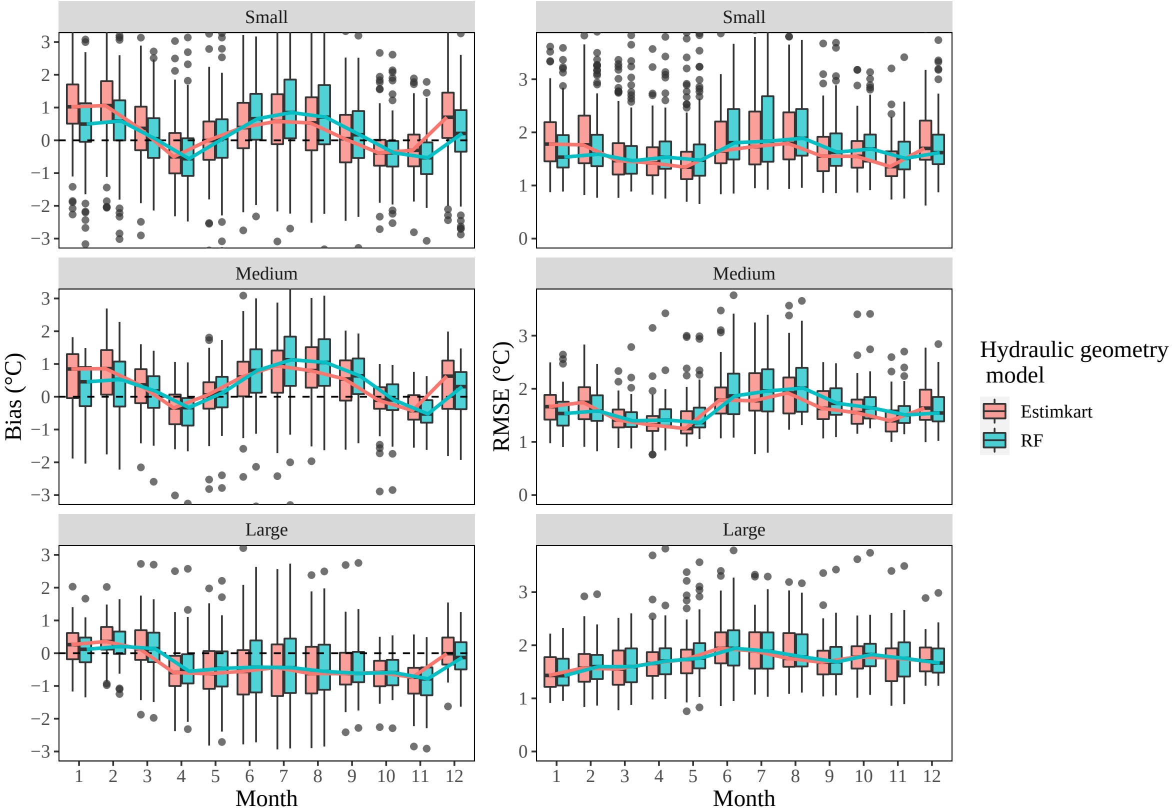

Figure 4.16: Monthly mean of daily Tw bias, and monthly RMSE of daily Tw for the RF and ESTIMKART hydraulic geometry models at 275 natural stations with regard to reach size between 2008 and 2018. Small=distance from the source < 30 km; Medium=30 < distance from the source < 100 km; Large=distance from the source > 100 km.

Riparian shading factor

An improvement in simulating daily Tw by the variable method is observed in summer months in small and medium streams (Figure 4.17). The median bias (across stations) of the variable method is lower (up to 1.25 °C) than that of the constant method over the summer months in small and medium streams (Figure 4.17, left panel). Moreover, in these streams, the median RMSE for the variable method is lower (up to 0.5 °C) over the summer months compared to that for the constant method (Figure 4.17, right panel). In medium streams, the interquartile range (IQR) of RMSE for the variable method is smaller (up to 0.5 °C) over the summer months compared to that for the constant method (Figure 4.17, right panel). Unsurprisingly, no difference between the biases and the RMSE of the two vegetation methods is observed at stations on large rivers since their large width makes the influence of shading less pronounced. 63% (resp. 52%) of the stations have the summer mean of daily bias in the range of -1 °C and 1 °C when the variable (resp. constant) method is used. 80% (resp. 77%) of the stations have an annual RMSE$<$ 2°C when the variable (resp. constant) method is used.

The variable vegetation method is used from now on in the T-NET model as it improves the performance of the T-NET model in simulating daily Tw over the summer months in small and medium streams.

Note that in Figure 4.17, left panel, shows an underestimation (median bias up to -1 °C) in daily Tw at large rivers. We hypothesize that such an underestimation is due to poor simulation of river width by hydraulic geometry model used in the T-NET thermal model since the hydraulic geometry model was developed using measurements mainly on small and medium rivers (see Morel et al., 2020). To confirm that, we do few validations on measured river width and depth over the middle Loire River (measurements provided by Valverde et al., 2013). The results show that there is 50% underestimation in simulating river width. Such underestimation was also found by Beaufort et al. (2016a). To compensate for this underestimation in width (which leads to underestimation in Tw) in the middle Loire River, 50 % is added to simulated river width.

Finally, as mentioned before, Beaufort (2015) showed that the RMSE of the T-NET model (with the constant vegetation method and the ESTIMKART hydraulic geometry model) in simulating daily Tw was on average 1.6 °C at 128 stations with missing years over the 2008–2012 period over the Loire River basin. Moreover, Loicq (2018) showed that the RMSE of the T-NET model (with the constant vegetation method and the ESTIMKART hydraulic geometry model) in simulating mean daily Tw was 1.84 °C at 44 stations with missing years over the 2008-2015 period over the Maine catchment. The current study shows that the RMSE of the T-NET model (with the RF hydraulic geometry model and the variable vegetation vegetation method) in simulating mean daily is 1.80 °C at 275 stations with missing years over the 2008-2018 period over Loire River basin.

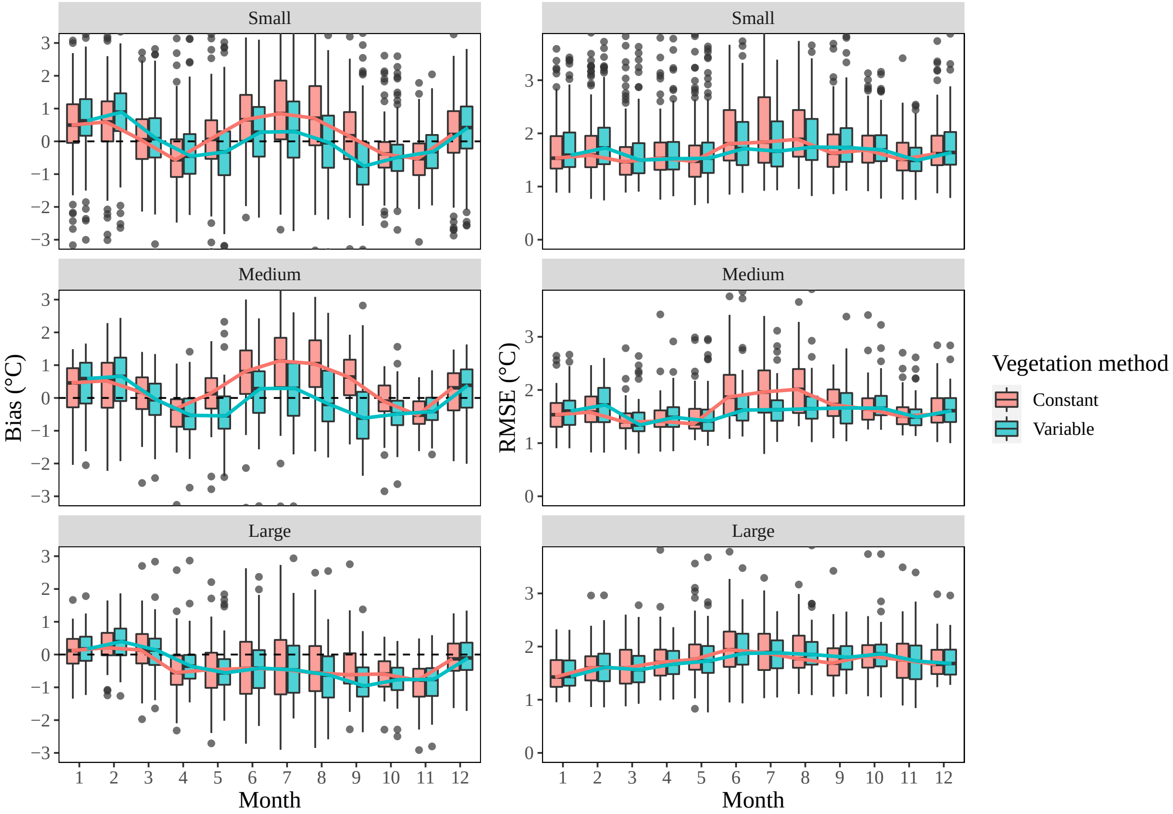

Figure 4.17: Monthly mean of daily Tw bias, and monthly RMSE of daily Tw for the variable and the constant vegetation methods at 275 natural stations with regard to reach size between 2008 and 2018. Small=distance from the source < 30 km; Medium=30 < distance from the source < 100 km; Large=distance from the source > 100 km.

Figure 4.18 shows the good performance of the T-NET model with the RF hydraulic geometry model and the variable vegetation method in reconstructing daily Tw at three stations on natural rivers with different sizes.

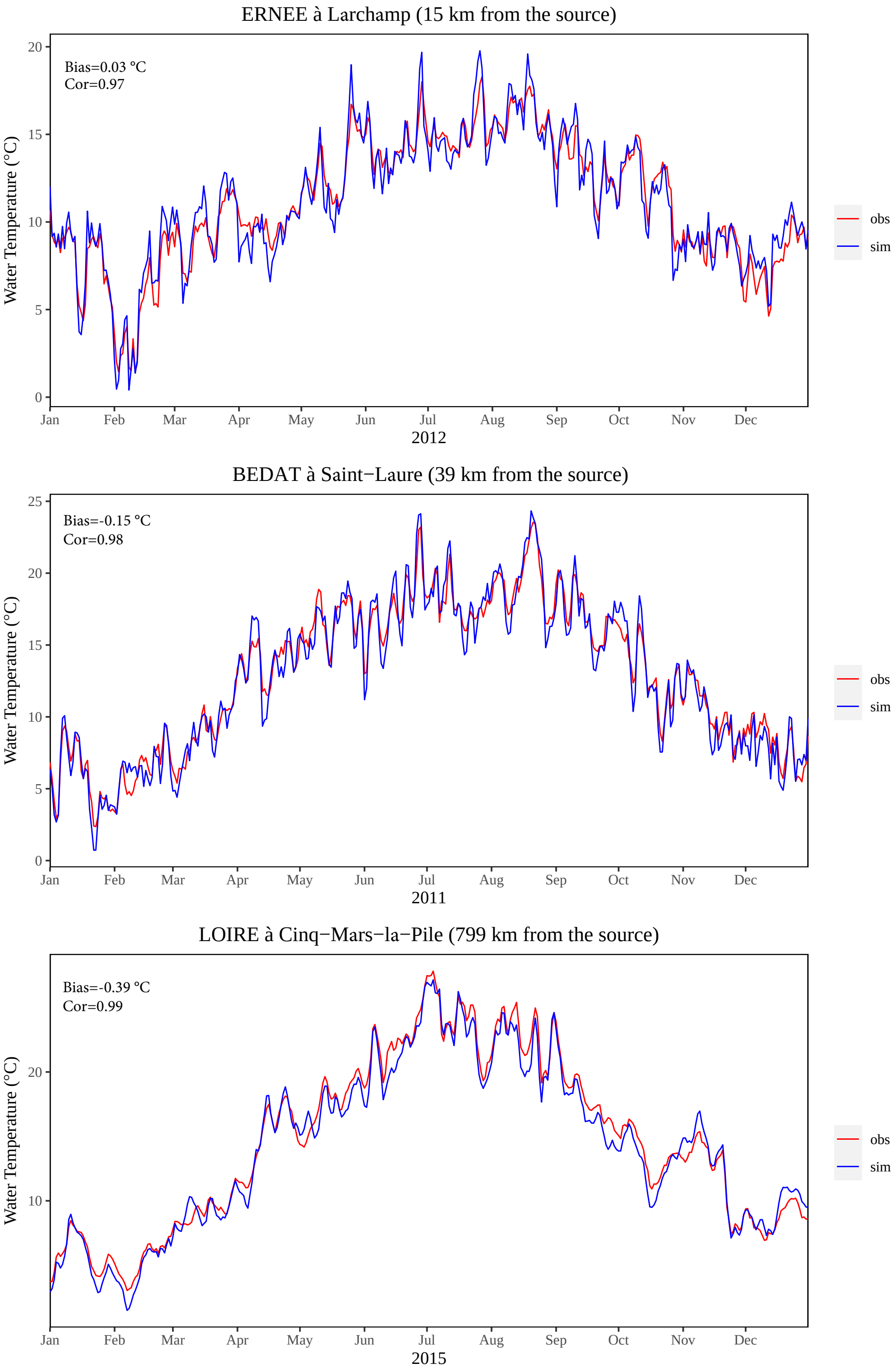

ERNEE à Larchamp (15 km from the source)

BEDAT à Saint−Laure (39 km from the source)

LOIRE à Cinq−Mars−la−Pile (799 km from the source)

Figure 4.18: Simulated and observed Tw at three Tw stations on natural rivers with different sizes. Small=distance from the source $<$ 30 km; Medium=30 $<$ distance from the source $<$ 100 km; Large=distance from the source $>$ 100 km.

4.3.2.2 Seasonal and annual Tw at natural stations with continuous daily data over the 2010–2014 period

At this point, the performance of the T-NET model in simulating seasonal and annual Tw is assessed at 67 near-natural stations with continuous daily data over the 2010–2014 period (Figure 4.19). These stations are among the natural stations used in the previous section (section 4.3.2.1). They are selected by finding a trade-off between the maximum number of stations with at least 5 years (our choice) of continuous daily data over a period of time, and an homogeneous spatial distribution of such stations over the basin. 55 out of these 67 stations with continuous daily data are located on small/medium streams whereas the remaining are located on large rivers. The average catchment area is 151 km^2 (range=7-1 342 km^2) for small/medium streams, and 18 926 km^2 (range=1 931-57 043 km^2) for large rivers.

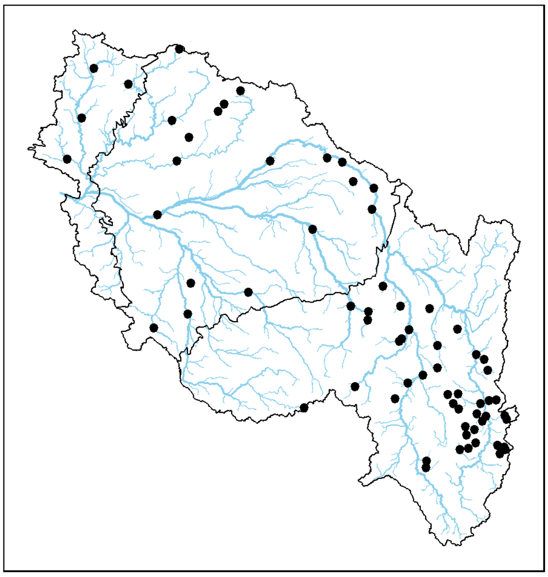

Figure 4.19: The 67 stations with continuous daily observed Tw data over the 2010–2014 period.

For these stations, no systematic bias is observed for the seasonal and annual Tw at the stations on small and medium rivers (Figure 4.20, top left panel). The median Tw bias ranges from -0.26 °C (in fall) to 0.8 °C (in winter). Large rivers exhibit a small Tw underestimation (Figure 4.20, top right panel), with a median bias ranging from -0.29 °C (in fall) to +0.15 °C (in winter), and the overall biases are still quite small across seasons (IQR=0.4–0.7 °C across seasons).

The median RMSE of the T-NET thermal model, for small and medium rivers, ranges between 0.52 °C (Annual) and 0.91 °C (DJF and JJA) across seasons with IQR in range of 0.5 °C (annual) and 0.86 °C (JJA and SON) across seasons (Figure 4.20, bottom left panel). For large rivers, the median RMSE of the T-NET thermal model ranges between 0.38 °C (annual) and 1.11 °C (JJA and SON) across seasons with IQR in range of 0.2 °C (DJF) and 0.85 °C (MAM)

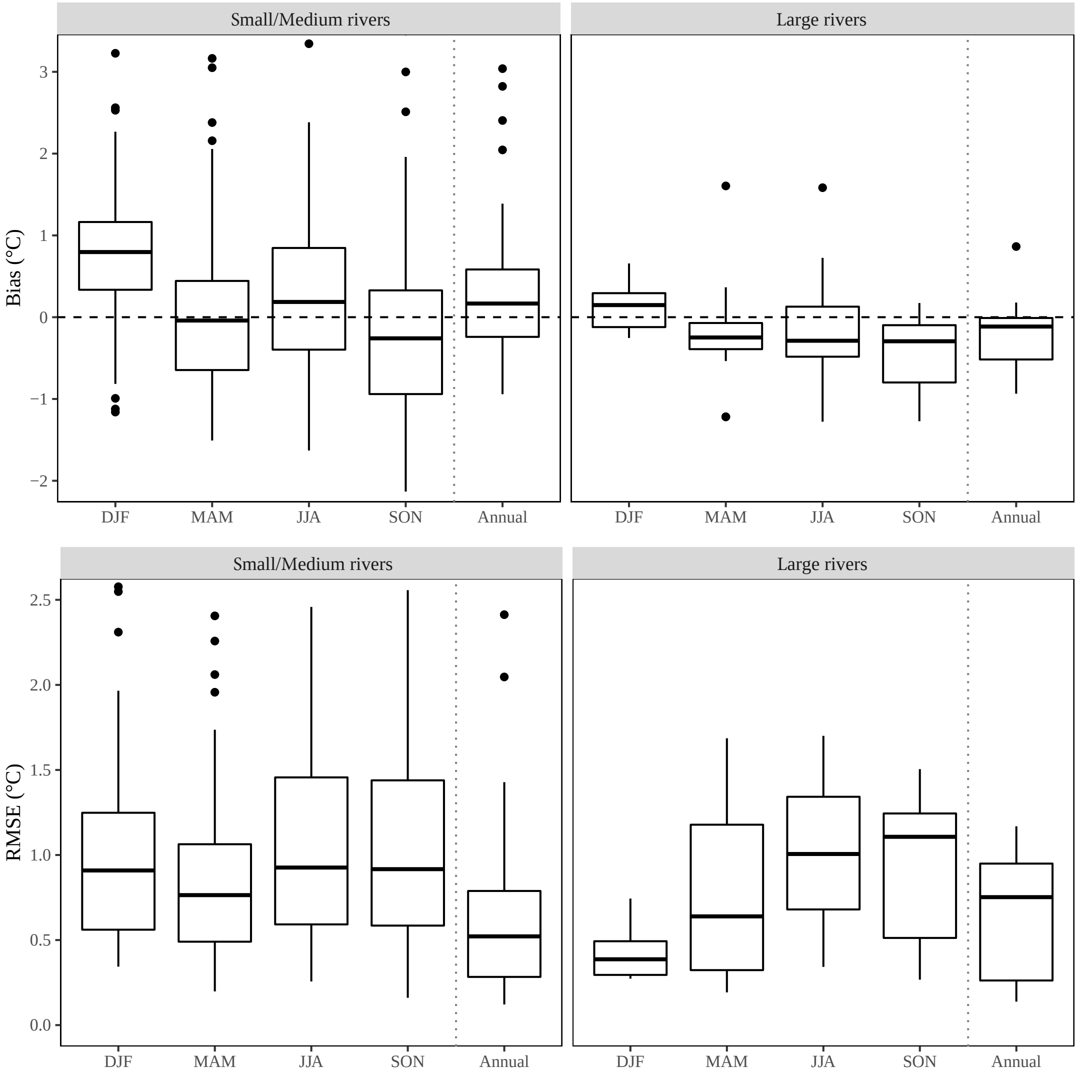

Figure 4.20: Bias and RMSE of the T-NET thermal model in simulating the seasonal and annual Tw at 67 observed Tw stations (55 on small and medium rivers, left; 12 on large rivers, right) with continious daily data over the 2010–2014 period.

across seasons (Figure 4.20, bottom right panel). Overall, the T-NET thermal model shows a good performance in terms of RMSE at these 67 stations (median range= 0.2-1.11 °C across rivers and seasons). Indeed, 53-83% stations (resp. 50-100%) on small and medium (resp. large) rivers have a RMSE<1 °C across seasons.

A visual comparison of observed and simulated Tw time series at seasonal and annual scale at stations with long-term data (> 20 years) between 1977 and 2019 (see Table 2.1, p. 48) suggests a strong coherence and agreement between observations and simulations for all seasons (Figure 4.21). The bias at these stations (black numbers in bottom right corner of Figure 4.21) ranges between -0.54 °C to 0.59 °C depending on the season and station. The annual regime of simulated Tw at 67 stations with continuous daily data over the 2010–2014 period also shows the good performance of the T-NET thermal model (see Figure C.1).

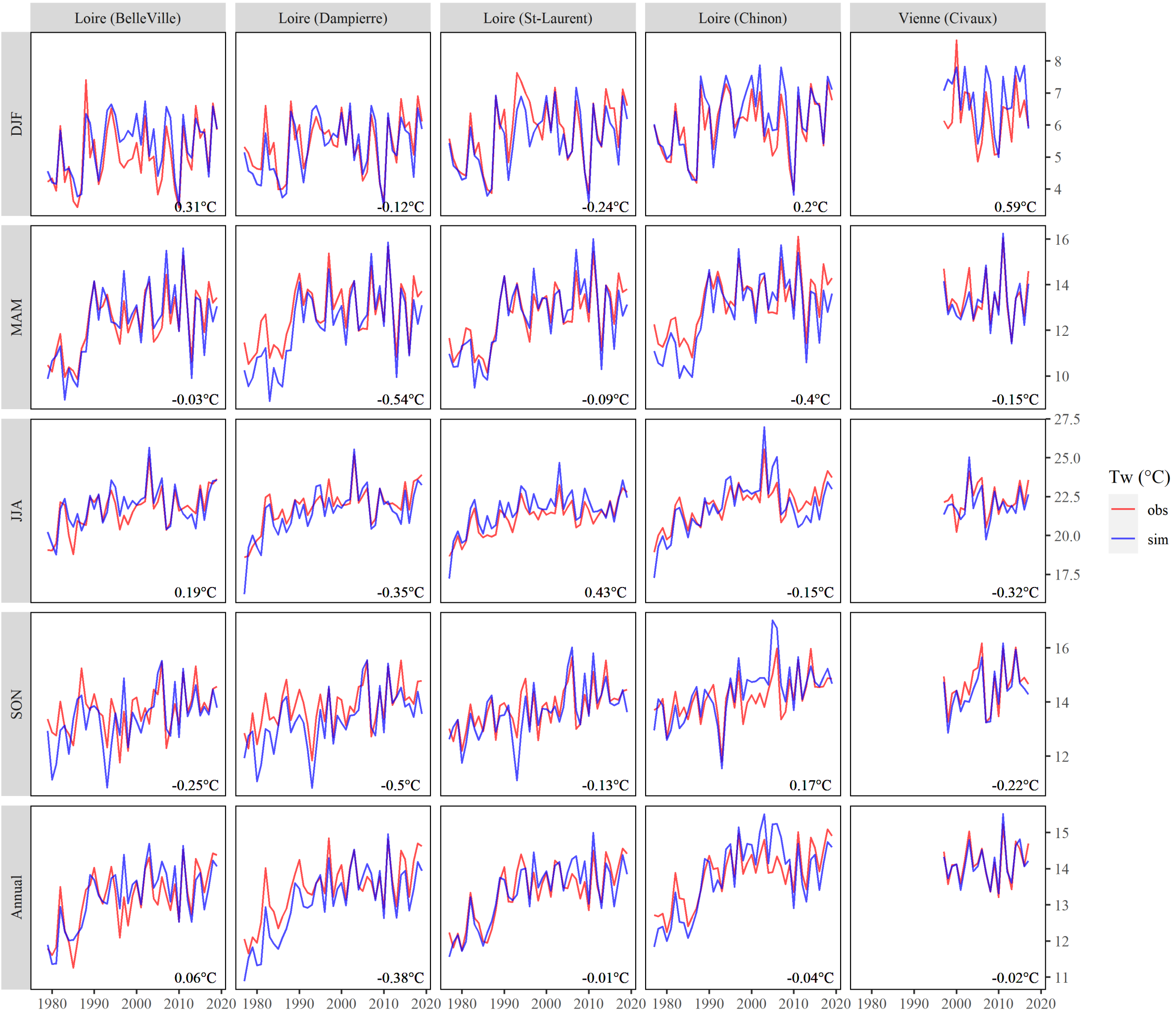

Figure 4.21: Seasonal and annual time series of observed and simulated Tw at stations with long-term continuous data (> 20 years) between 1977 and 2019 (see Table 2.1, p. 48) . Numbers in black in the bottom right corner of each graph show the mean bias of the reconstruction.

4.3.2.3 Longitudinal profile of the Loire River

The Loire River basin is the longest river in France (1012 km), and it has a large longitudinal thermal gradient (Beaufort, 2015). Lalot et al. (2015) used thermal infrared remote sensing (TIR) to provide data on longitudinal variation of Tw along the Loire River. Moreover, Lalot et al. (2015) provided maps of the longitudinal variation of Tw starting from 500 km distance from the source. Nevertheless, this technique provides a snapshot of Tw at a given point in time. Thus, there is still a weak understanding of longitudinal variations of Tw at a large scale.

Here, the T-NET thermal model can address this issue, and provides us with longitudinal variations of Tw for the whole Loire River. In contrast to TIR, the Tw simulated by the T-NET thermal model is not limited in time and space. The simulated Tw can also be compared with observed Tw at four stations with long-term daily data along the Loire River (see Table 2.1, p 48). A good agreement between observed and simulated Tw at seasonal and annual scale was already found at these stations between 1977 and 2019 (see Figure 4.21).

Figure 4.22 shows the longitudinal profile of seasonal simulated Tw in 2003 for the Loire River. This year is exceptional in the recent period since it was very hot and dry (Moatar and Gailhard, 2006; Bustillo et al., 2014). There is a good agreement between observed (in points) and simulated seasonal Tw at the stations along the Loire River.

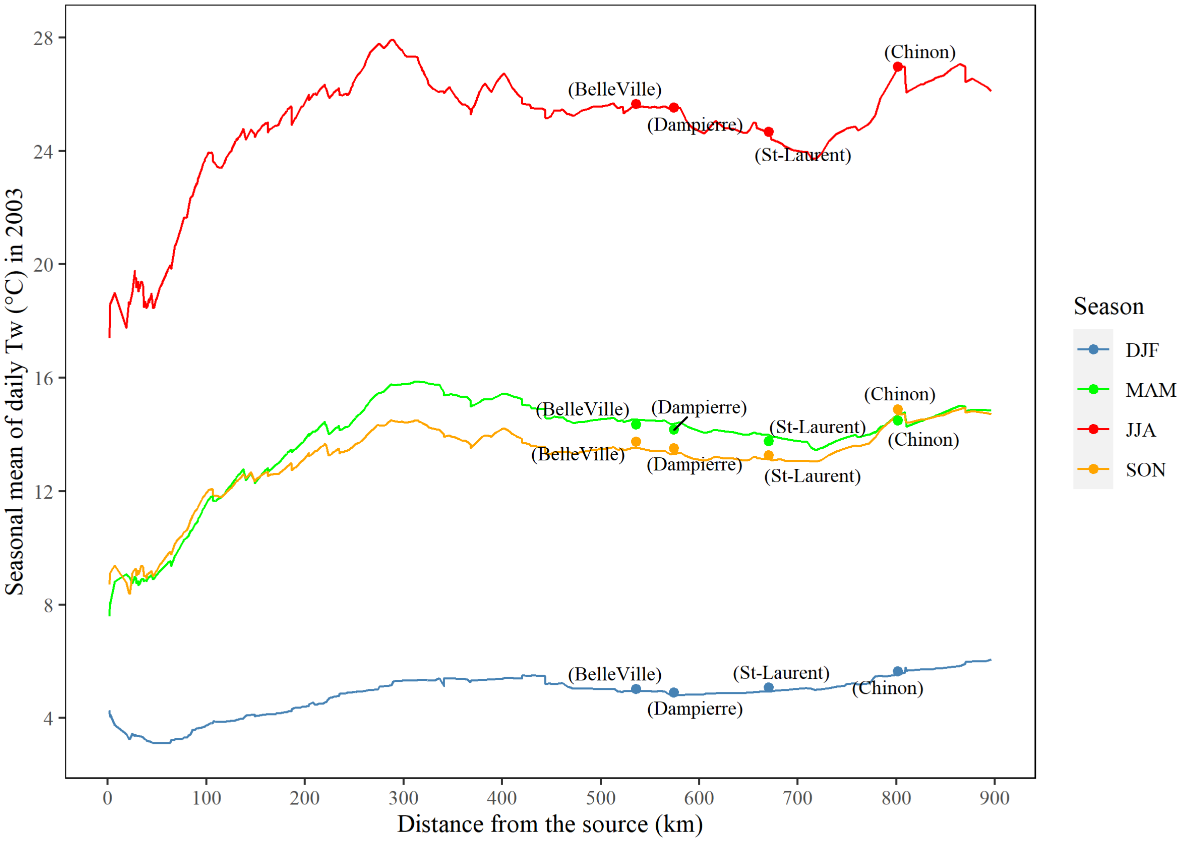

Figure 4.22: Longitudinal profile of seasonal Tw in 2003 for the Loire River, the longest river in France. Lines and points are showing the simulated and observed Tw, respectively.

Along with the schematic longitudinal profile observed in introduction (Figure 1.4, p 34), Tw starts with a cool spring (7.6 °C), fall (8.4 °C) and summer (17.4 °C) or a warm winter (6 °C) upstream temperature. Then, Tw tends to increase since the influence of upstream conditions decreases as water moves away from the upstream. Moreover, the longer distance from the source, the more Tw is influenced by atmospheric conditions (cf. Caissie, 2006). Finally, after travelling some distance (here 290 km), Tw reaches an equilibrium temperature (DJF=5.3 °C, MAM=15.8 °C, JJA=28 °C and SON=14.5 °C). In winter, due to larger conveyed volume and a greater thermal capacity, water travels faster and there is less time for water-air temperature equilibrium.

Along this longitudinal Tw variation, a cooling at Saint-Laurent is observed for both simulated and observed Tw in spring, fall and summer compared to the Tw at Dampierre. Moatar and Gailhard (2006) already found that observed Tw at this station (Saint-Laurent) was cooler in summer (1.4 °C on average in Aug over the 1976–2003 period) and warmer in winter (0.3 °C on average in January over the 1976–2003 period) compared to the other stations located on Loire River. They explained this cooling effect by the inflow of groundwater from the Beauce limestones aquifer, which was computed by the energy balance on the basis of a constant water discharge of 10 m^3/s from the underground Beauce aquifer at a temperature of 13.5 °C. Loicq (2018) also found that the thermal impact of this groundwater input is significant (up to ±2.5 °C for a station in the Beauce area, monthly average on 2008–2013). Along with these studies, here, average Tw over the 1977–2019 period shows that Tw is cooler in summer (by 0.6-0.9 °C) at Saint-Laurent compared to three other stations on the Loire River basin.

The T-NET model is able to capture the cooling effect of groundwater inputs, since along with observed Tw in 2003, a decrease in simulated Tw is also observed at the Saint-Laurent in spring, summer and fall compared to Tw at Dampierre. This cooling effect is more pronounced in summer (1.8 °C decrease in Tw compared to Tw at Dampierre) than that in spring and fall (0.18-0.4 °C decrease in Tw compared to Tw at Dampierre). There is also a slight warming effect of groundwater input in winter (0.15 °C) at Saint-Laurent for both simulated and observed Tw.

4.4 Difference between simulated and observed Tw quantifies the influence of dams and ponds

Since the T-NET thermal model does not consider the influence of impoundments, it was expected that it performs well at natural stations. Along with that, in section 4.3, it was observed that the T-NET model could perform well at the natural stations identified in section 3.3 (p. 61) through thermal signatures, showing its capability in producing natural regimes. According to the good performance of the T-NET model at natural stations, it is also expected that this model provides the natural condition of the altered regimes identified in section 3.3 (p. 61).

Therefore, here, the difference between simulated (natural) and observed (influenced) Tw (i.e., T-NET bias) at some altered stations is used to quantify and illustrate the influence of dams and ponds. To do so, first, a region with a lot of ponds, and another region with several large dams in the Loire River basin are selected. The first choice is the Vienne catchment and its surrounding area, one of the most ponded catchments in the Loire River basin. The second choice is the upstream part of the Loire River basin in which there is a considerable number of large dams (see Figure 2.1, right panel, p. 44). Then, the difference between simulated (natural) and observed (influenced) Tw (i.e., T-NET bias) at some selected stations in these regions is used to quantify the influence of impoundments.

Ponds

In Figure 3.6 (p. 60), it was seen that some of Tw regimes altered by ponds were located in the Vienne catchment and its surrounding area. Figure 4.23 shows the Vienne catchment and its surrounding area, ponds and the corresponding cluster of each Tw station in this region (obtained in section 3.3, p. 61). The pond thermal signatures, the heating effect (mean positive difference of daily Tw-Ta from March–October) and thermal effect (mean overall difference of daily Tw-Ta from March–October) used to identify the influence of ponds in the previous chapter (see Table 3.1, p. 58) are also presented here.

In the Vienne catchment and its surrounding area, there are only two clusters, natural-like and pond-like, because there is not probably a large-enough dam in this region to alter the Tw regime. The influence of ponds on Tw regime is also clear. For instance, the heating effect at stations influenced by pond-like stations can reach up to 3 °C, while it is lower at natural-like stations (up to 1 °C). Besides the heating effect, the thermal effect at pond-like stations can reach up to 2.7 °C, and it is again lower at natural-like stations (up to 0.07 °C). Moreover, the annual Tw regime at altered stations is shifted up by +2.5 °C (over August month) compared to that at natural stations (Figure 4.24). Indeed, Figure 4.24 shows that the median of influenced thermal regimes remains warmer than median of natural thermal regimes from April to October. Such an annual thermal regime was also found in Figure 3.13, p. 72 at the scale of the Loire River basin.

To illustrate that the T-NET model can produce the natural version of an altered regime, two close stations in this region (see Figure 4.23), which were partitioned into pond-like and natural-like clusters in the previous chapter, are selected and compared. Here, Vonne river (pond-like), and Benaize river (natural-like) are selected (see Figure 4.23). These two stations have a similar distance from the source and a similar surface area (260 km^2), and they have observed Tw data over 2012. As they are located in the same region, the climate for both stations are similar. If Tw regime at both selected Tw stations were natural, it was expected that Tw simulated by the T-NET model would be close to the observed Tw at both of these stations. However, with the current condition, it is expected that simulated Tw will be close to observed Tw at the natural station (Benaize river) whereas simulated Tw will be shifted down compared to observed Tw at the station altered by ponds (Vonne river).

First of all, to understand better difference between these selected stations, in Figure 4.25 values of their heating effect and thermal effect are shown with respect to such values for the whole natural-like and pond-like stations over the Loire River basin identified in the previous chapter. In this representation, the heating effect of more than 1 °C and positive thermal effect can partition clearly pond-like stations from natural-like ones.

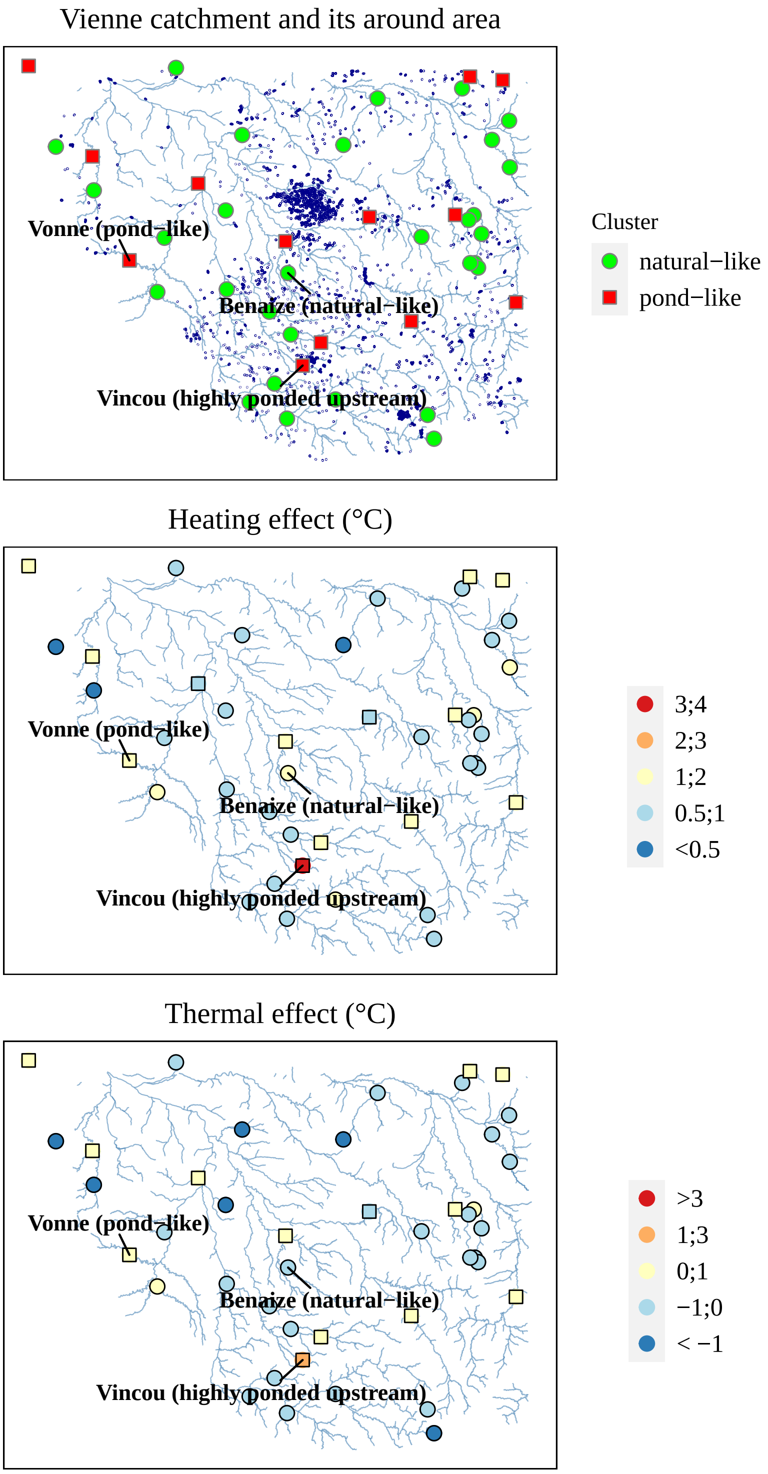

Figure 4.23: Vienne catchment and its surrounding area and the stations identified as natural or influenced by ponds (see Figure 3.8, p. 62). The arrows are showing Benaize river with natural regime, Vonne river with the influence of upstream ponds, and Vincou stream with a lot of upstream ponds. The heating effect (mean positive difference of daily Tw-Ta from March–October) and thermal effect (mean overall difference of daily Tw-Ta from March–October) were used to identify the influence of ponds in the previous chapter (see Table 3.1, p. 58). The shape of each point corresponds to the cluster of Tw station identified in the previous chapter. Please note that the surface waters (dark blue polygons in top panel) are not repeated in each panel for the sake of readability.

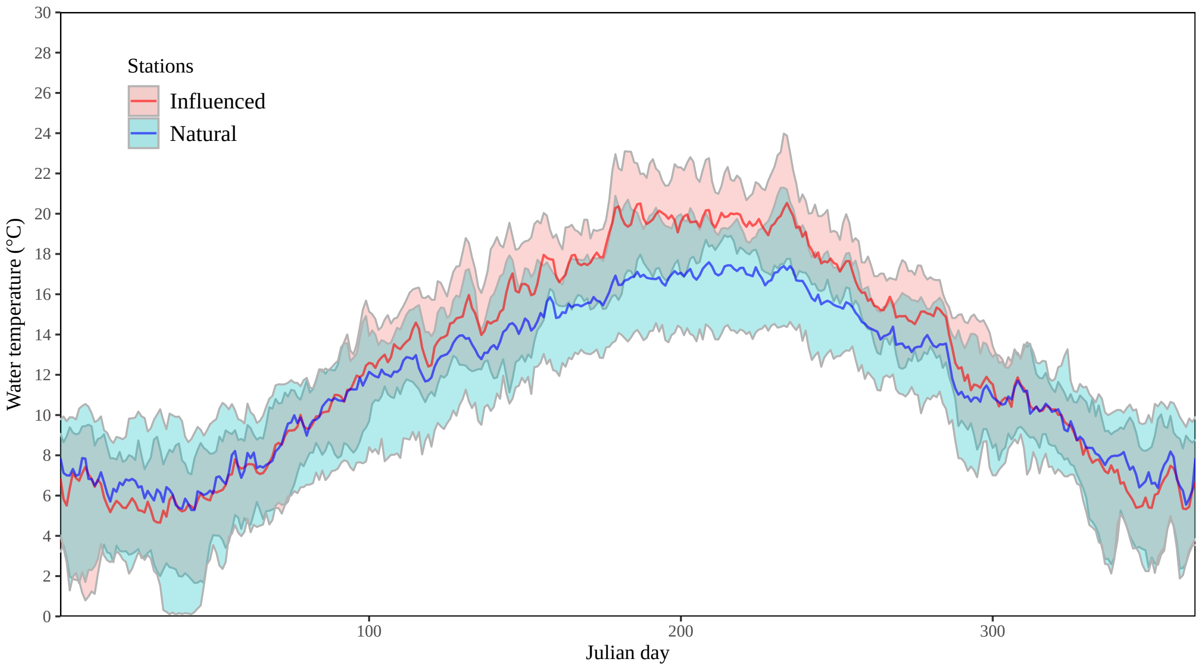

Figure 4.24: The annual Tw regime of the altered stations by ponds and the natural ones over the Vienne catchment and its surrounding area (see Figure 4.23, top panel) over the 2008–2018 period. Shaded areas represent the 10th-90th percentile band, and solid lines represent the median value.

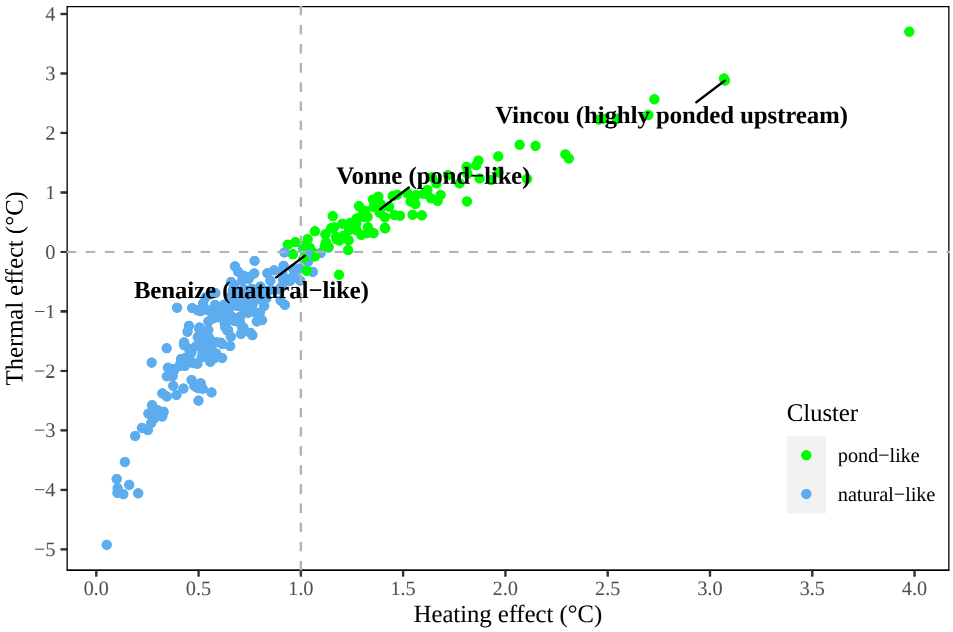

Figure 4.25: The heating effect and thermal effect at the whole natural-like and pond-like stations over the Loire River basin identified in the previous chapter (see Figure 3.8, p. 62).

Figure 4.26 (left panel) shows that, as it is expected, at the natural station (Benaize river), the simulated Tw regime follows the closely observed Tw. However, at the altered station (Vonne river) (Figure 4.26, right panel), the observed Tw regime is shifted up by +2 °C from March–October (the period considered for capturing the influence of ponds; see Table 3.1, p. 58). Moreover, the daily bias of the T-NET model, i.e. the difference between simulated (natural) and observed (influenced) Tw at this altered station (-1.5 °C) is twice greater than that at the natural station (-0.7 °C).

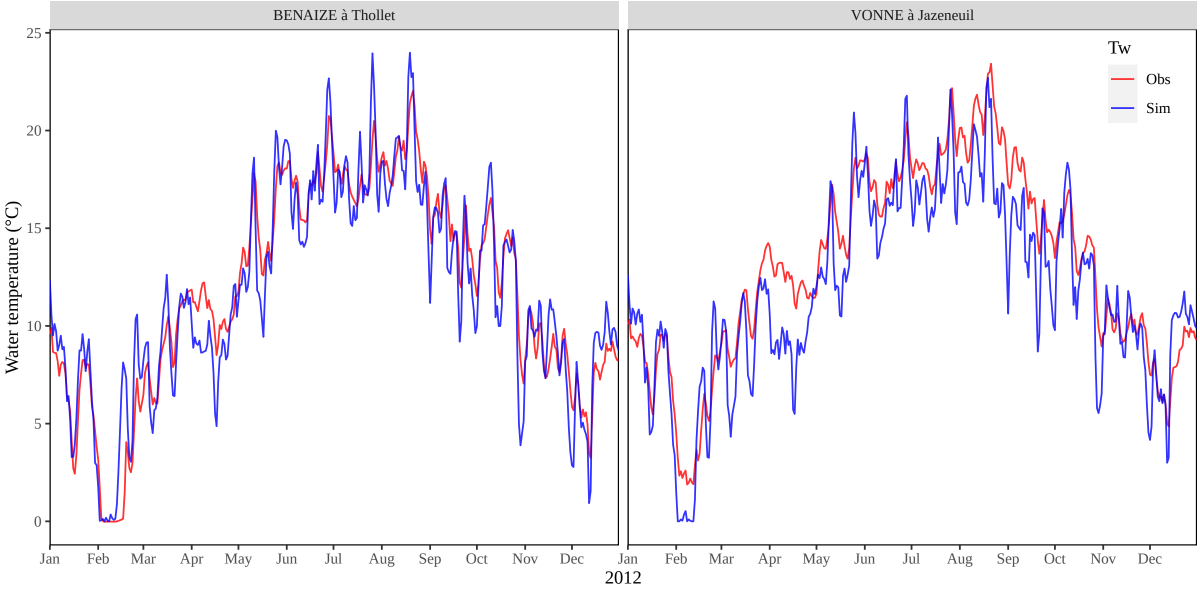

Figure 4.26: Simulated (natural) and observed (influenced) daily Tw at a natural station (Benaize river) and at an altered station (Vonne river) located in the same region and with the same catchment area (260 km^2), over 2012.

To understand and quantify the relationship between the impacts of ponds in a hot year, the difference between simulated (natural) and observed (influenced) Tw (i.e., T-NET bias) in two hot and cool years are compared at a station on the Vincou stream, which is the most ponded station in the Vienne basin (with 1.3 % ponded of a catchment area of 62 km^2). It has the highest heating effect and thermal effect among the pond-like stations over the Loire River basin (see Figure 4.25). The years 2011 and 2009 with spring Ta anomalies of 2.8°C and 0.83°C (with respect to the 1963–2019 period), are selected as the hot and cool (relatively) years, respectively. The other reason for choosing these years is the availability of observed Tw data in these years at the selected station on the Vincou stream.

The results reveal that in the Vincou stream, the difference between simulated (natural) and observed (influenced) Tw over the spring in 2011 is -4.5°C, which is two times greater than the bias in 2009 (-2.24°C) showing greater impacts of ponds in a hot year (Figure 4.27).

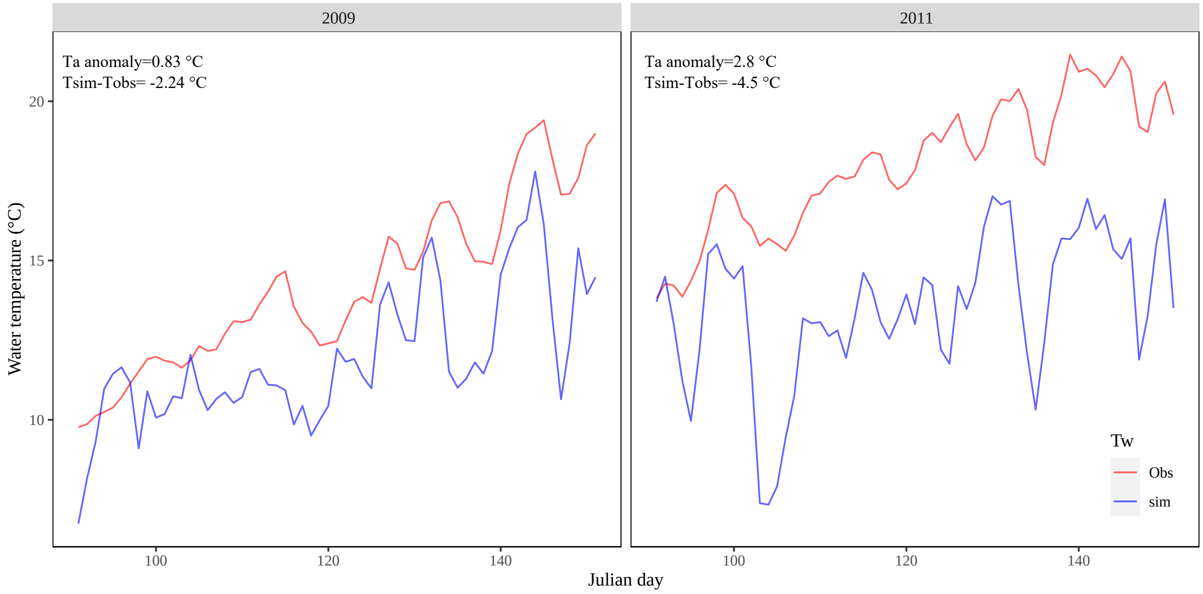

Figure 4.27: Difference between simulated (natural) and observed (influenced) Tw in spring in a hot year (2011) and in a cool (relatively) year (2009) at the station on Vincou stream, which is the most ponded station in the Vienne catchment. The numbers in the top left corner are showing spring Ta anomalies (with respect to the 1963–2019 period), and the mean difference between simulated (natural) and observed (influenced) Tw over spring.

Secondly, the heating effect signature at the stations with the longest available Tw data in the pond-like cluster (over the Loire River basin) is studied to see the evolution of Tw regimes under the impacts of ponds and the recent warming. We consider the whole basin at this step to have as many stations as possible. Note that the simulated Tw is used instead of Ta for calculating the heating effect (i.e., mean positive difference of daily observed (influenced) and simulated (natural) Tw from March–October). In section 3.2 (p. 54), Ta was used since data on the natural condition was not available then.

It is observed that across stations with the longest available Tw data and altered by ponds, as summer Ta anomalies is increasing with time (trend:1.11-2.04 °C/decade, but all non-significant), the heating effect is increasing as well (trend:0.46-1.23 °C/decade). The observed trend in heating effect at these stations is significant at the 88% confidence level. The most pronounced increase (1.23 °C/decade) occurs at the most ponded station (Ance du Nord at Saint-Julien-d'Ance; $f_{pond,catchment}$=0.38 %) for which the rate of increase is also significant at the 95% confidence level (see Figure 4.28). Note that the magnitude of trend is estimated by the non-parametric Theil–Sen estimator (Sen, 1968), and the significance level of detected trends is evaluated by the Mann-Kendall test (Mann, 1945). The Theil–Sen estimator and the Mann-Kendall test will be largely used in the next chapter for assessing past trends.

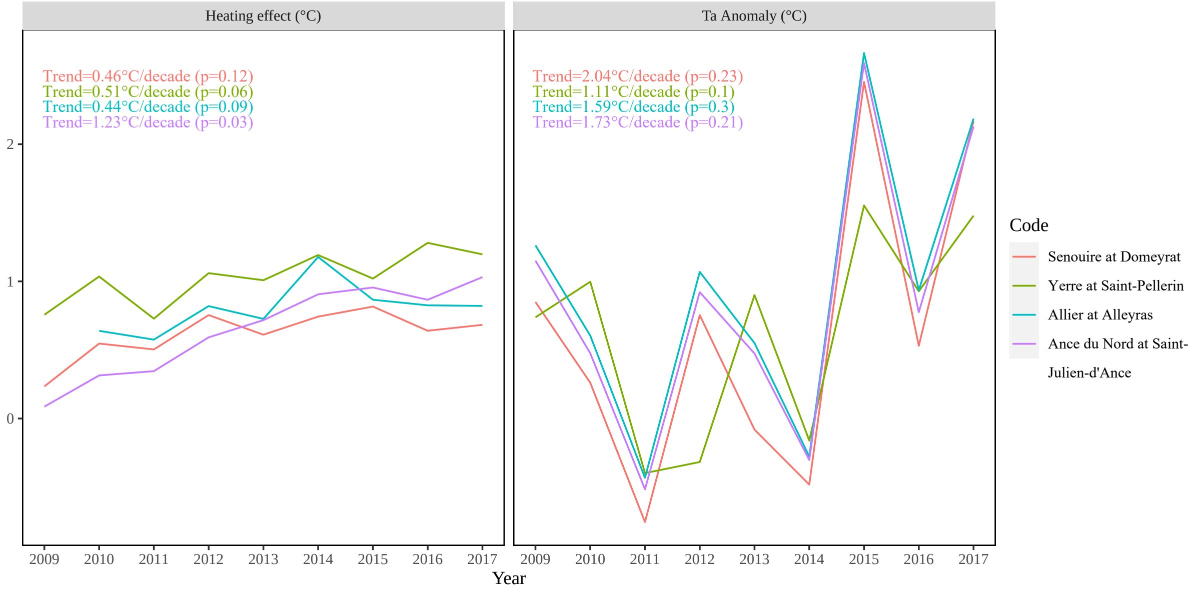

Figure 4.28: The evolution of the heating effect signature at the stations with the longest available Tw data in the pond-like cluster (over the Loire River basin). Ta anomalies (with respect to the 1963–2019 period) show summer anomalies. The numbers in the top left corner show trend values (Sen's slope) and corresponding significance level (evaluated by the Mann-Kendall test).

Dams

In Figure 3.6 (p. 60), Tw regimes altered by dams occurred in the upstream part of the Loire River basin where there is a considerable number of large dams (see right panel of Figure 2.1,right panel, p. 44). Figure 4.29 shows this part of the basin and the corresponding cluster of each Tw station in this region (obtained in section 3.3, p. 61). The dam thermal signatures, TS (daily JJA Tw-Ta linear regression slope), R^2 (JJA Tw-Ta coefficient of determination), and lag time (lag time between the annual peak in 30-days moving average Tw and Ta regimes) used to identify the influence of dams in the previous chapter (see Table 3.1, p. 58), are also presented here.

In this region, 20% of the stations belong to the pond-like cluster. Since this section aims at quantifying the influence of dams, pond-like stations are discarded here. The influence of dams on Tw regimes is clear in this region (Figure 4.29). For instance, the lowest R^2 (< 0.4), the lowest TS (< 0.2) and the greatest lag time (> 30 days) can be found at dam-like stations.

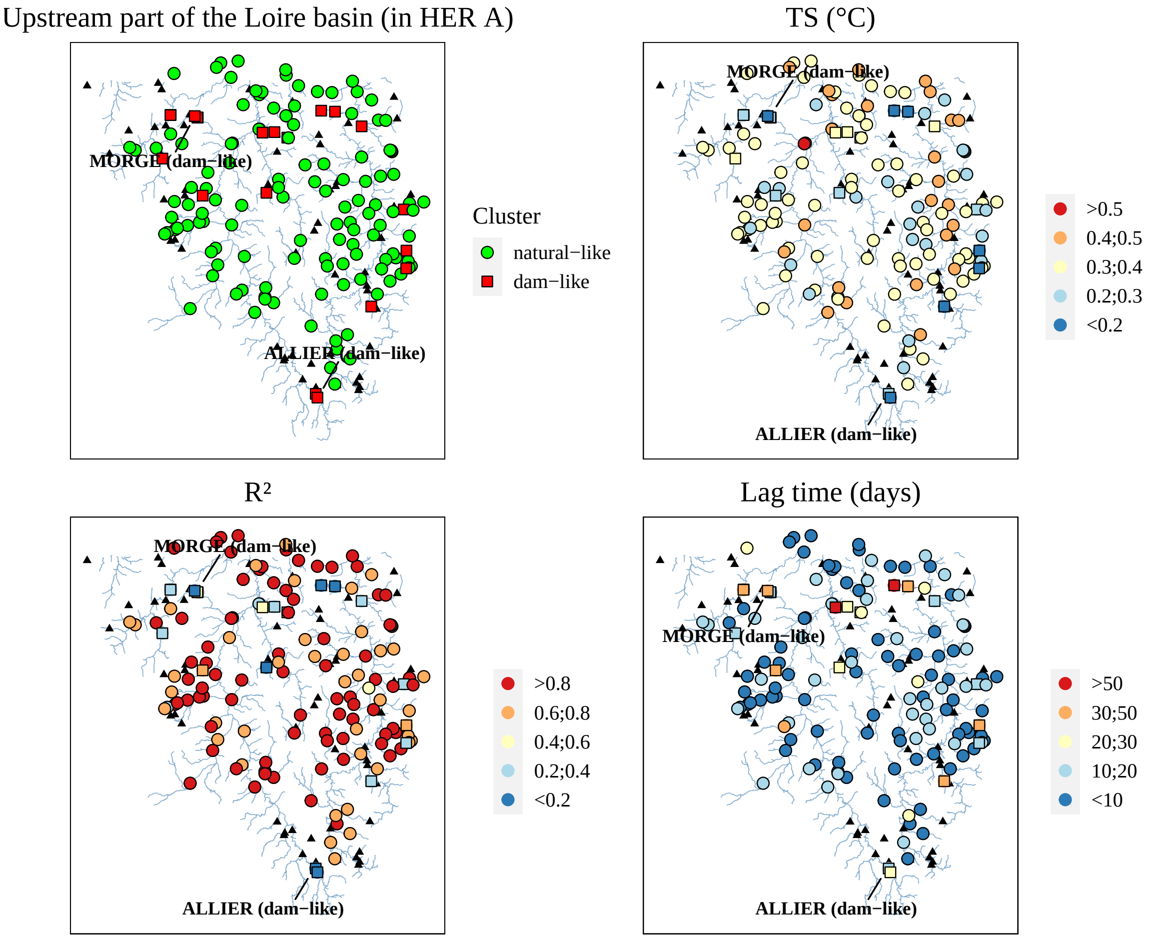

Figure 4.29: The upstream part of the Loire River basin with the stations identified as natural or influenced by dams (Figure 3.8, p. 62). The arrows are showing two stations influence by dams: 1) a station on Morge River downstream of la Sep dam (IRI=28.38%), 2) a station on the Allier River downstream of Naussac dam (IRI=61.41%). The dam thermal signatures, TS (daily JJA Tw-Ta linear regression slope), R^2 (JJA Tw-Ta coefficient of determination), and lag time (lag time between the annual peak in 30-days moving average Tw and Ta regimes) were used to identify the influence of dams in the previous chapter (see Table 3.1, p. 58). The shape of each point corresponds to the cluster of Tw station identified in the previous chapter.

To understand and quantify the relationship between the impacts of a dam in a hot year, the same method used above for ponds is adopted. Firstly, the difference between simulated (natural) and observed (influenced) Tw (i.e., T-NET bias) in two hot and cool years are compared at two different stations, which belong to dam-like cluster (section 3.3, p. 3.3). One of these stations shows the weakest R^2 (Tw-Ta correlation) among stations belonging to dam-like cluster (R^2=0.002). This station is on Morge River downstream of la Sep dam (IRI=28.38%) (see Figure 4.29). The other station has an upstream dam with the highest IRI among the stations partitioned into dam-like cluster. This station is on the Allier River downstream of Naussac dam (IRI=61.41%) (see Figure 4.29). Summarized information about these stations and the selected years are presented in Table 4.3. For the station on Morge River, the years 2015 and 2010 with summer Ta anomalies of 2.36°C and 0.28°C (with respect to the 1963–2019 period) are selected as the hot and cool (relatively) years, respectively. For the station on Allier River, the years 2015 and 2012 with summer Ta anomalies 2.45°C and 0.96°C (with respect to the 1963–2019 period) are selected as the hot and cool (relatively) years, respectively. The other reason for choosing these years is the availability of observed Tw data in these years at these stations.

Table 4.3: Ta anomalies (with respect to the 1963–2019 period) and difference between simulated (natural) and observed (influenced) Tw (i.e., T-NET bias) over summer at the two selected stations downstream of dams. One is on the Morge River downstream of la Sep dam (IRI=28.38%). The other one is on the Allier River downstream of Naussac dam (IRI=61.41%).

Stations	Morge River		Allier River	
	Hot year	Cool year	Hot year	Cool year
Selected years	2015	2010	2015	2012
Summer Ta anomalies (°C)	2.36	0.28	2.45	0.96
Bias (Tsim-Tobs) over summer (°C)	4.15	0.75	2.92	-0.22

The results reveal that for the Morge River, the bias between simulated and observed Tw over the summer in the hot year 2015 is 4.15 °C, which is approximately four times greater than the bias in the cool (relatively) year 2010 (0.75 °C) (Figure 4.30). At the station on the Allier River, the bias in the hot year 2015 is 2.92 °C over the summer, which is approximately three times the bias in the cool year 2012 (-0.92 °C). Consequently, both stations show that the impacts of dams are more critical in a hot year (with a 3-4 times greater decrease in summer Tw compared to a cool year).

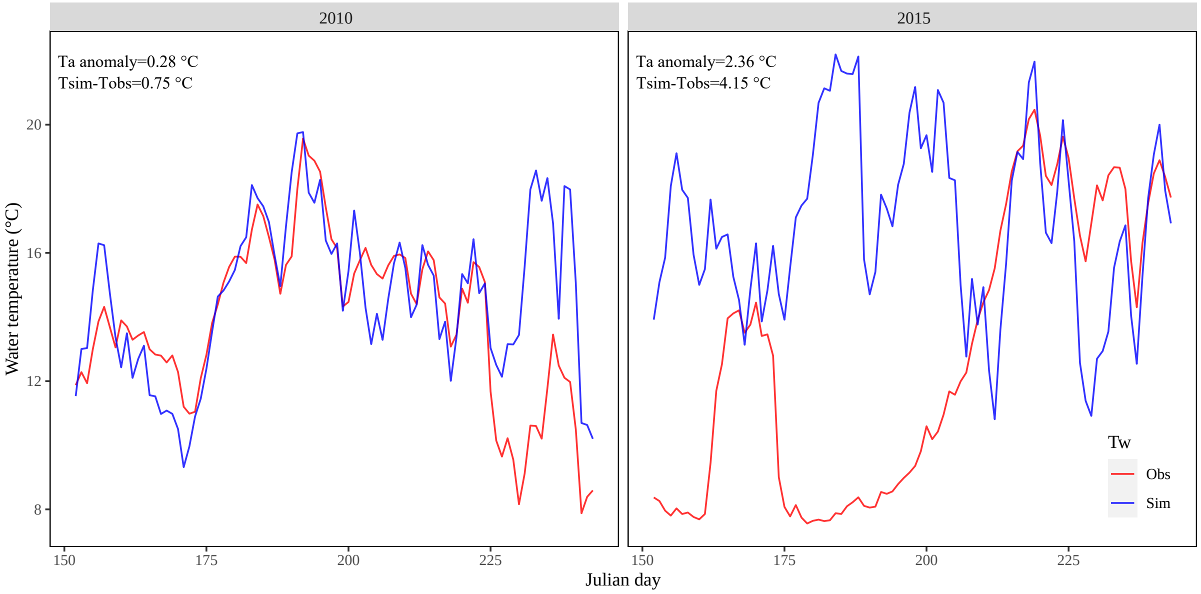

Figure 4.30: Difference between simulated (natural) and observed (influenced) Tw (i.e., T-NET bias) over summer at the station on the Morge River downstream of la Sep dam (IRI=28.38%). This station belongs to the dam-like cluster, and shows the weakest R^2 (Tw-Ta correlation) among the stations in the dam-like cluster (R^2=0.002) (see Figure 3.8, p. 62).

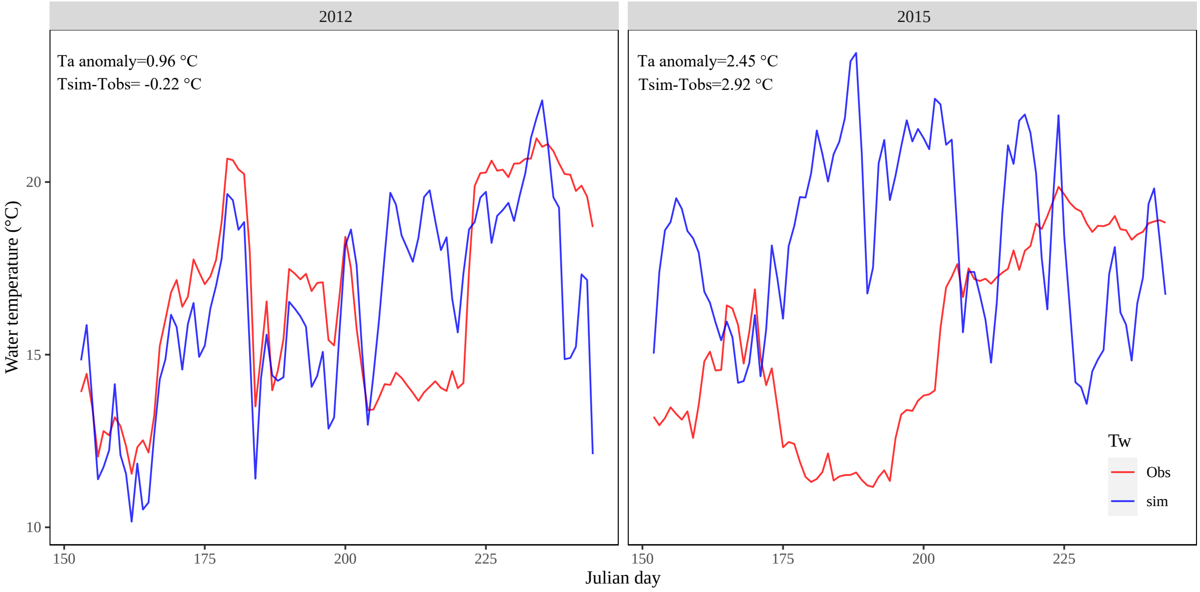

Figure 4.31: Difference between simulated (natural) and observed (influenced) Tw (i.e., T-NET bias) at the station on the Allier River downstream of Naussac dam (IRI=61.41%). This station belongs to dam-like cluster, and has an upstream dam with highest IRI among stations in the dam-like cluster (Figure 3.8, p. 62).

Secondly, the evolution of the difference between simulated (natural) and observed (influenced) Tw (i.e., T-NET bias), and Ta anomalies (with respect to the 1963–2019 period) over summer are compared at the dam-like stations with the available observed Tw data over a period of time. Unfortunately, unlike ponds (above) the Tw stations across the Loire River basin partitioned into the dam-like cluster, do not have long-term Tw data. Only four dam-like stations with continuous Tw data over the four years are available. Since for estimating trend magnitudes longer Tw data are needed, here, only the patterns of the evolution of biases and Ta anomalies over summer are compared. Indeed, it is expected that fluctuations in summer biases follow the fluctuations in summer Ta anomalies. For examples, it is expected that when summer Ta anomalies decrease, summer bias decreases as well. The indicator of bias over summer period is selected since this step can be complementary to the previous one expecting to see the highest summer biases for the years with the highest summer Ta anomalies.

The evolution of summer bias and summer Ta anomaly at four stations (across the Loire River basin) over the 2013–2016 period confirms the greater impact of dams on the summer thermal regimes in hot years (Figure 4.32). Indeed, with an increase of 3 °C in Ta anomaly from a cool year (2014) to a hot year (2015), the influence of dams gets 3-4 times greater across Tw stations influenced by an upstream dam.

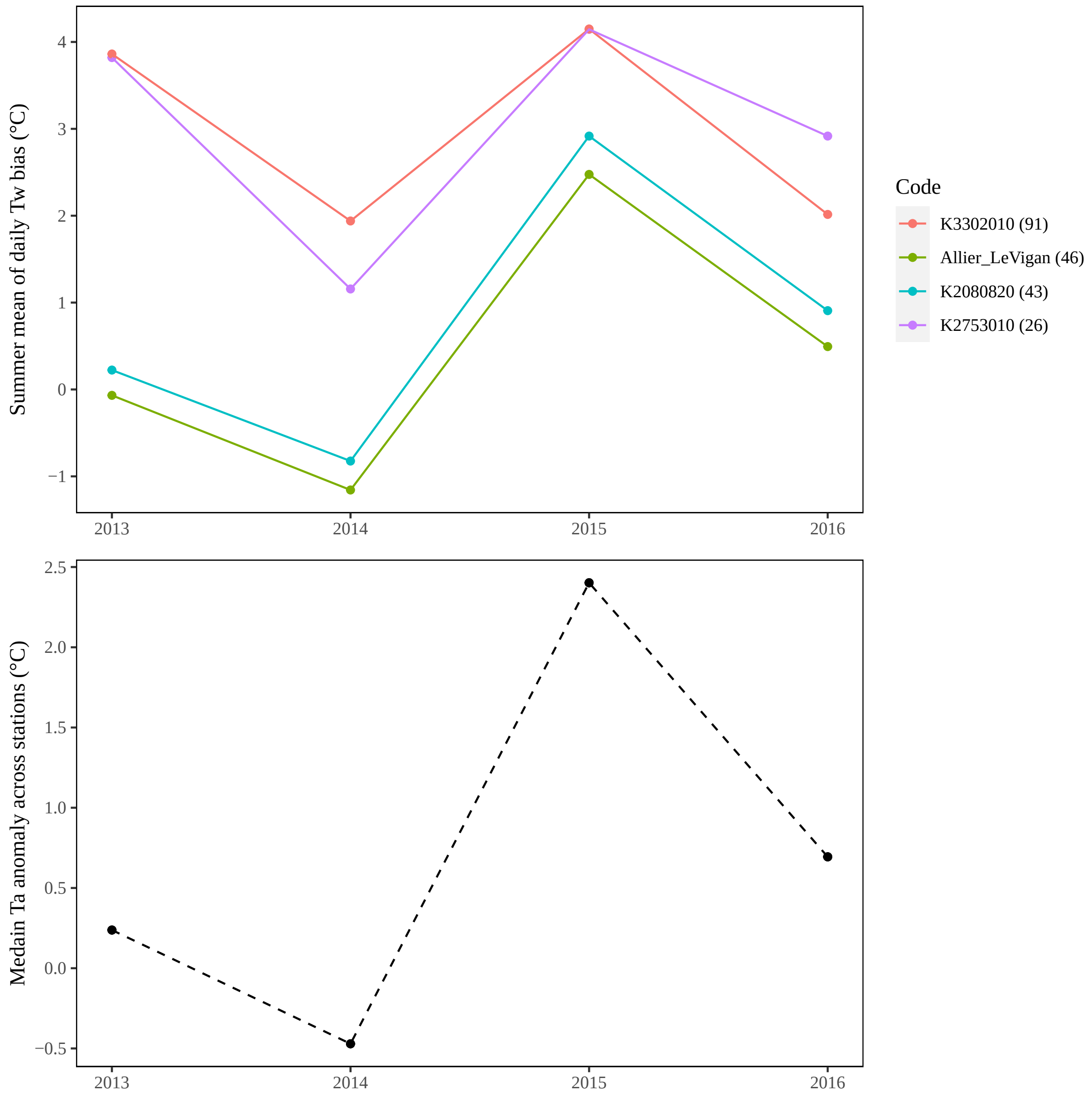

Figure 4.32: Evolution of (top) bias between simulated (natural) and observed (influenced) Tw, and (bottom) Ta anomalies (with respect to the 1963–2019 period) over summer. As summer Ta anomalies in each year has a very small variability from one station to another, the median Ta anomalies across stations is considered. The values in the parentheses next to the name of stations correspond to the distance of the station from the source (km).

4.5 Conclusion on regional modeling

In this chapter, the principles and input data of both the EROS hydrological model and the T-NET thermal model are detailed. Then the performance of both models are assessed at the near-natural stations. For assessing the performance of the T-NET model, the natural stations identified in the previous chapter are used.

At a majority of calibration (75 %) stations, and stations on the French Reference Hydrometric Network (83 %), the Nash-Sutcliffe efficiency of simulated daily Q is > 0.7 for Q, $\sqrt{Q}$ and $\ln Q$. Considering both calibration and RHN stations, the median relative bias (across stations) of the EROS model in simulating seasonal and annual Q ranges between -7.26 % and 37.7 % across seasons. The observed overestimation in summer and fall by the EROS model can be due to the fact that the EROS model does not consider the withdrawals and water abstractions.

For the T-NET model, the two hydraulic geometry models (ESTIMKART and Random Forest) and the two vegetation methods (constant and variable) are used and compared. The results show no significant difference between the two hydraulic geometry models in simulating daily Tw. However, new hydraulic geometry model (RF) predicts better daily Tw over winter months in small and medium rivers. On the other hand, dynamic riparian shading (variable method) as a function of tree height, river width, solar elevation angle, vegetation density, and phenology can improve the T-NET thermal model performance in simulating daily Tw compared to the constant method. The median bias (across stations) of the variable method is lower (up to 1.25 °C) than that of the constant method over the summer months in small and medium streams. Moreover, in these streams, the median RMSE for the variable method is lower (up to 0.5 °C) over the summer months compared to that for the constant method.

The T-NET model also performs well in simulating seasonal and annual Tw at 67 stations with continuous daily data (median range of RMSE= 0.2-1.11 °C across rivers and seasons). Indeed, 53-83% stations (resp. 50-100%) on small and medium (resp. large) rivers have RMSE$<$1 °C across seasons. Moreover, the T-NET model can capture the alterations resulting from groundwater inputs in Loire River basin. Indeed, along the longitudinal profile of Tw for the Loire River in 2003, a cooling at Saint-Laurent is observed for both simulated and observed Tw in spring, fall and summer compared to the Tw at Dampierre. This cooling effect from groundwater inputs is more pronounced in summer (1.8 °C decrease in Tw compared to Tw at Dampierre).

The bias between simulated (natural) and observed (influenced) Tw at the altered stations identified in the previous chapter is used here as a tool to quantify the influence of ponds and dams. It is highlighted that dam and pond impacts are more critical in a hot year. Indeed, the impacts of impoundments in a hot year can be 2-4 times greater than in a cool year. Moreover, there is an increasing trend in the heating effect of ponds in recent years

(2009–2017) at the four stations with the longest available Tw data in the pond-like cluster (trend:0.46-1.23 °C/decade, p-value$<$ 0.12). Among these stations, the most pronounced increase (1.23 °C/decade, p-value=0.05) occurs at the most ponded station.

Therefore, models like the T-NET can be used to assess the rate of change in Tw and to understand the heterogeneity in such changes in relation with hydroclimate changes and landscape at a large scale and a high spatial resolution over the past and future. Such models also provides a tool to understand Q and Tw changes under future projections. Hence, the next two chapters aim at assessing changes in Tw from past to future using the T-NET model over the Loire River basin.

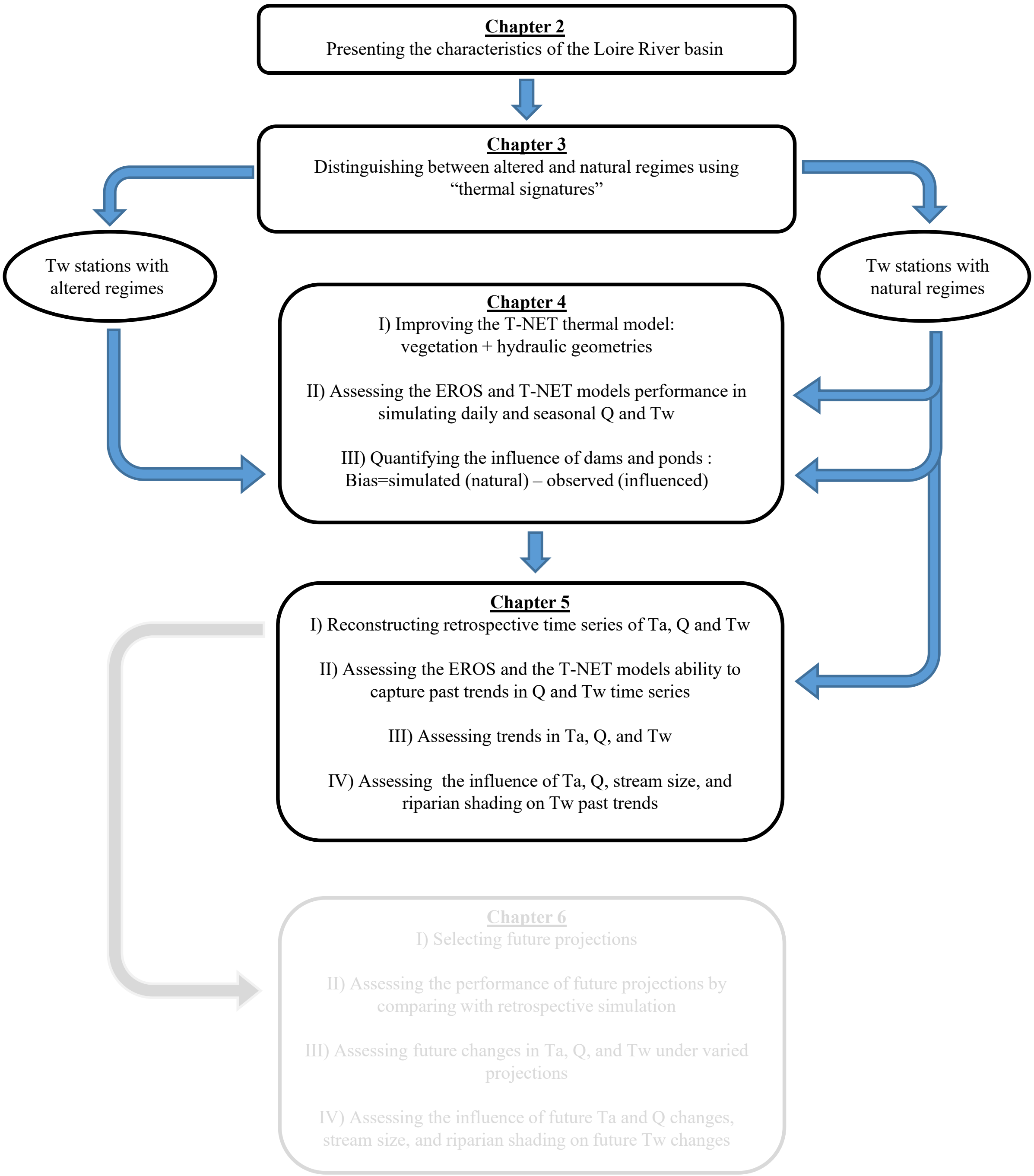

Schematic diagram illustrating thesis objectives.

CHAPTER 5

Regional, multi-decadal past trends in stream temperature

Stream temperature appears to be increasing globally (Hannah and Garner, 2015; Orr et al., 2015; Arora et al., 2016; Michel et al., 2020; Wilby and Johnson, 2020). This Tw warming may alter the spatial extent of habitat for cold-water species (Morales-Marín et al., 2019; Lee et al., 2020). However, the rate of Tw warming remains poorly understood at a large scale due to a paucity of long-term data (Webb, 1996; Arora et al., 2016), and difficulty in parsing the effects of hydroclimate and landscape variability. However, such a knowledge is helpful for integrated water resources management and for taking actions for attenuating the impacts of climate change.

Here, this issue is addressed by using the physical process-based T-NET thermal model coupled with the semi-distributed EROS hydrological model to reconstruct past daily Tw and Q at the scale of the entire Loire River basin (with 52 278 reaches). To understand how Tw has responded to recent climate change at a large scale, daily Q and Tw over the whole T-NET hydrographic network are first reconstructed over the past 57 years (1963–2019). Daily Ta over the past 57 years is also provided by the SAFRAN reanalysis data (see section 2.3.1). Then, the ability of both the T-NET and the EROS models to capture temporal trends are assessed against long-term continuous observed data over the Loire River basin (see Table 2.1, p. 48). The model outputs are then used to compute the magnitude of decadal trends in seasonal and annual Tw and Q over the past 57 years. Similar trends in seasonal and annual Ta are also computed. To understand the relative influence of Ta and Q (as the main hydroclimate drivers of Tw) on Tw, their trends, anomaly behaviors, and temporal patterns are compared. Finally, the diversity in Tw trends as a function of stream size, landscape diversity, and riparian shading is studied.

5.1 Spatial reconstruction of long-term trends

Many factors affect the spatio-temporal variability of Tw. In the current study, we consider Ta as a proxy for heat fluxes and meteorological variables, and Q as a proxy for thermal inertia and hydraulic geometries (which depends on Q, see Equ. 4.8).

Daily Q and Tw are reconstructed over the 57-yr period 1963–2019 using the EROS hydrological model and the T-NET thermal model. As mentioned in the previous chapter, although, meteorological variables are available over the 1958-2019 period, the first years are discarded from the analysis for the sake of EROS convergence (see Figure 4.3, p. 88). Thus, for each of the 52 278 reaches, daily time series of Ta (from the SAFRAN reanalysis data), Q (from the EROS model), and Tw (from the T-NET model) are reconstructed over the 1963–2019 period. Seasonal and annual averages of these 3 variables are considered in the trend assessment. The spatial maps of summer Tw in each year over the 1963–2019 period can be found in Appendix D. These maps that the high Tw (> 20 °C) are more frequent in the last decades compared to the first decades, highlighting stream warming as the result of recent climate change. Indeed, in the first decade, only 13.5 % of the reaches have Tw more than 17 °C whereas in the last decade, a considerable number of reaches (39.5 %) have Tw more than 17 °C (see Figure D.1).

The magnitude of trends in time series of these three variables (i.e., Tw, Ta and Q) is estimated by the non-parametric Theil–Sen estimator (Sen, 1968). The significance level of detected trends is evaluated by the Mann-Kendall test (Mann, 1945), commonly used in hydrological analyses (e.g., Giuntoli et al., 2013) but also thermal analyses (e.g., Kaushal et al., 2010; Arismendi et al., 2013a; Arevalo et al., 2020). This test is indeed robust to non-normal data, non-linear trends, and series with outliers and missing values. Trend magnitudes are reported in °C/decade for Ta and Tw, and in %/decade for Q, to help for comparisons across the basin.

In the following, the performance of both the EROS and T-NET models is first assessed at stations with long-term continuous daily data.

5.2 Model performance: trend assessment

5.2.1 The EROS model

To assess the EROS model ability to capture temporal trends, 44 RHN stations with long-term continuous daily data (see section 2.3.3, p. 48) are used. The performance of the EROS model in terms of bias and RMSE at these stations was also assessed in the previous chapter (see section 4.3.1, p. 102). As mentioned in the previous chapter (see section 4.1, p. 85), these RHN stations have long-term continuous daily data over the 1968-2019 period. The position of these stations (in red) can be found in Figure 2.1, right panel (p. 44).

Trends in observed and modeled Q at these 44 RHN stations over the 1968-2019 period are significantly correlated for all seasons with the exception of summer (Figure 5.1). The highest correlation across stations is observed in spring and fall (r= 0.69 and 0.71, p< 0.05), and the lowest correlation is observed in summer, which is also non-significant (r= 0.17, p= 0.26). Both modeled and observed Q are slightly decreasing (up to -11 %/decade) for the majority of stations across all seasons, but the trend is significant for a very few of them (and mostly at the annual scale), all located in HER A (and more precisely in the southern headwaters). Moreover, there are only a few discrepancies between estimates of trend significance in modeled and observed Q across seasons (11-18 % of stations).

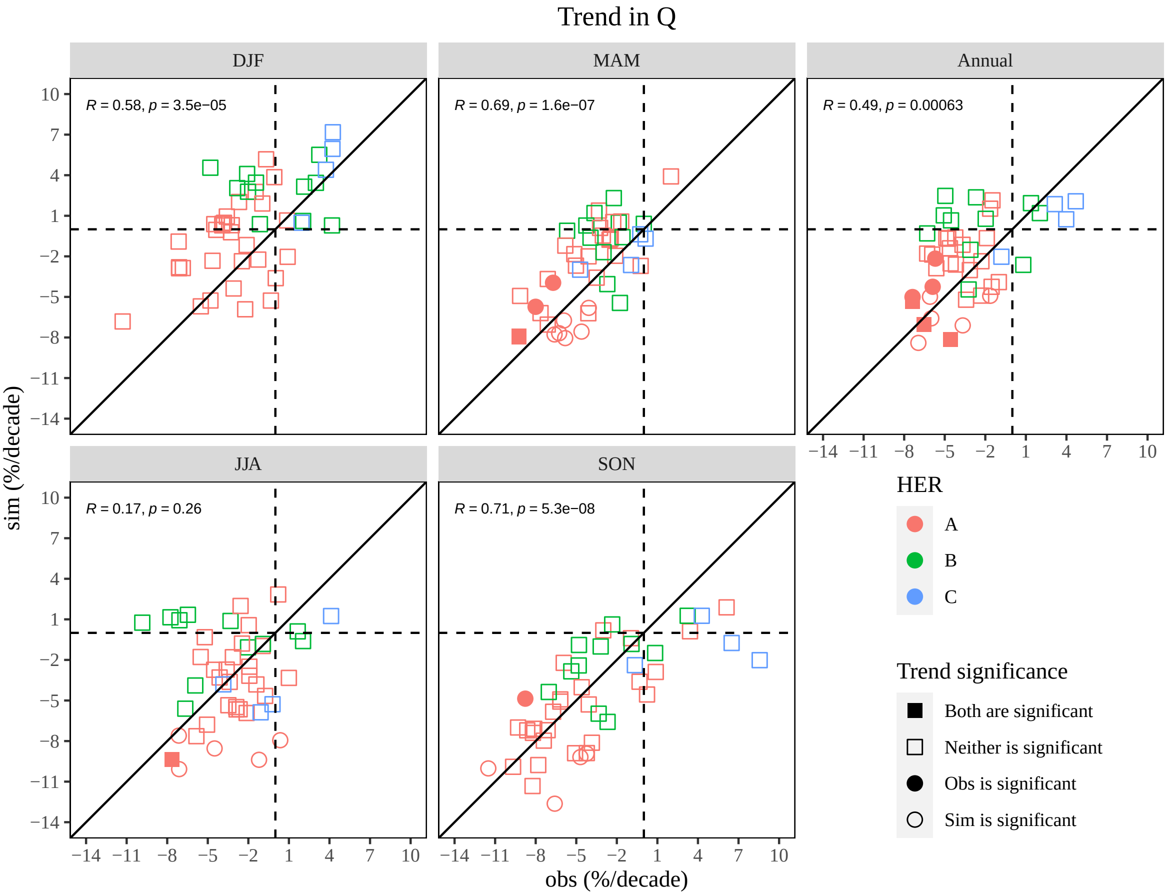

Figure 5.1: Relationships between long-term trends (1968–2019) in observed and simulated Q for 44 RHN stations, at the seasonal and annual scales. The magnitude of trends is estimated by Theil–Sen estimator. Point shapes indicate whether trends are significant or not at the 95% confidence level for observations and simulations according to the Mann-Kendall test. Colors refer to the Hydro-Ecoregion (HER) where the station is located. The position of these stations can be found in Figure 2.1, right panel (p. 44).

5.2.2 The T-NET model

Long-term continuous data are available at 14 Tw stations (see Table 2.1, p. 48). The position of these stations (in red) can be found in Figure 2.1, middle panel (p. 44). These stations were also identified with a near-natural thermal regime in Chapter 3 (see section 3.3, p. 61), and were used in the previous chapter (section 4.3, p. 102) for assessing the T-NET model performance in simulating daily and seasonal Tw. Of these 14 stations, 9 stations have 8-13 years of data and 5 stations have 20-40 years data (see Table 2.1, p. 48). These 14 near-natural stations with long-term continuous data compose the validation dataset for the seasonal and annual trend assessment. The long-term evolution of annual mean Tw at these 14 stations is presented in Figure 5.2, which clearly exhibits an increase in annual Tw over time. For large rivers, there is an increase of up to 2 °C between 1977 and 2019.

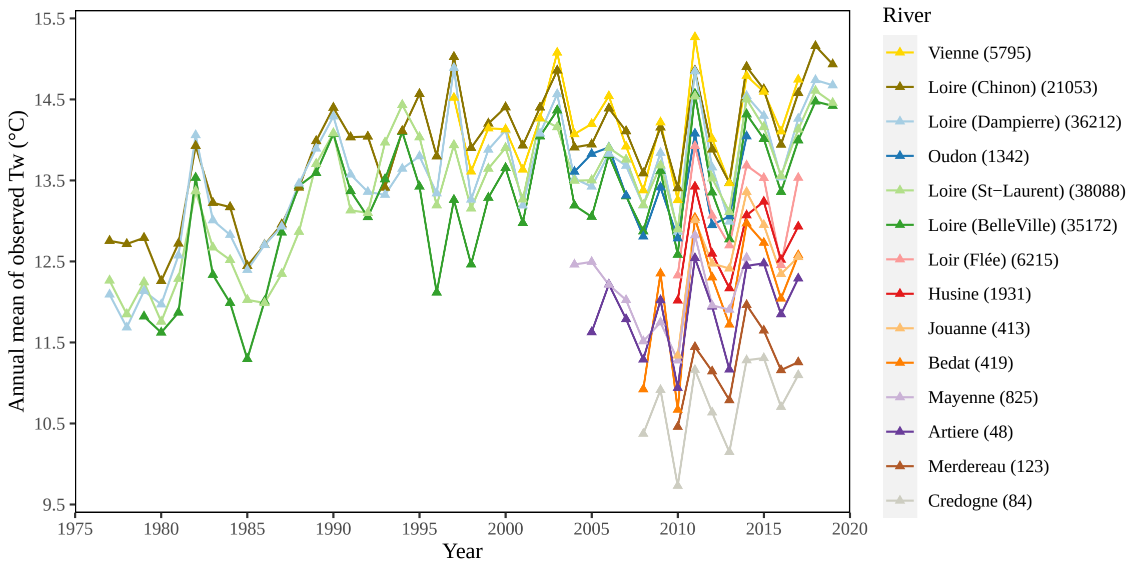

Figure 5.2: The annual mean of observed Tw at the 14 Tw stations with long-term data between 1977 and 2019 (see Table 2.1, p. 48). The numbers within parentheses denote the river catchment area (km^2).

Modeled and observed Tw trends are also correlated significantly (Figure 5.3) across seasons with the exception of fall. The highest correlation is observed in summer ($r = 0.94$, $p < 0.001$), and the lowest correlation is observed in fall, which is also non-significant ($r = 0.29$, $p = 0.32$). Contrasting with trends in Q, trends for Tw are rather increasing for most stations across seasons, but the very short period of record led mostly to non-significant trends. However, stations with long-term data show significant increasing trends for all seasons, with the exception of winter (Figure 5.3).

A visual comparison of observed and modeled Tw time series at stations with long-term data (> 20 years) indeed suggests a strong coherence and agreement between trends in observations and simulations for all seasons (Figure 5.4). Indeed, there is a very small difference between trend magnitudes in modeled and observed Tw across stations and seasons (up to 0.16 °C/decade). For the Loire river, on average over the 4 stations (Figure 5.4), the greatest increase occurs in spring – +0.61 (resp. +0.71) °C/decade in observations (resp. simulations) – and summer – +0.62 (resp. +0.58) °C/decade in observations (resp. simulations). The smallest

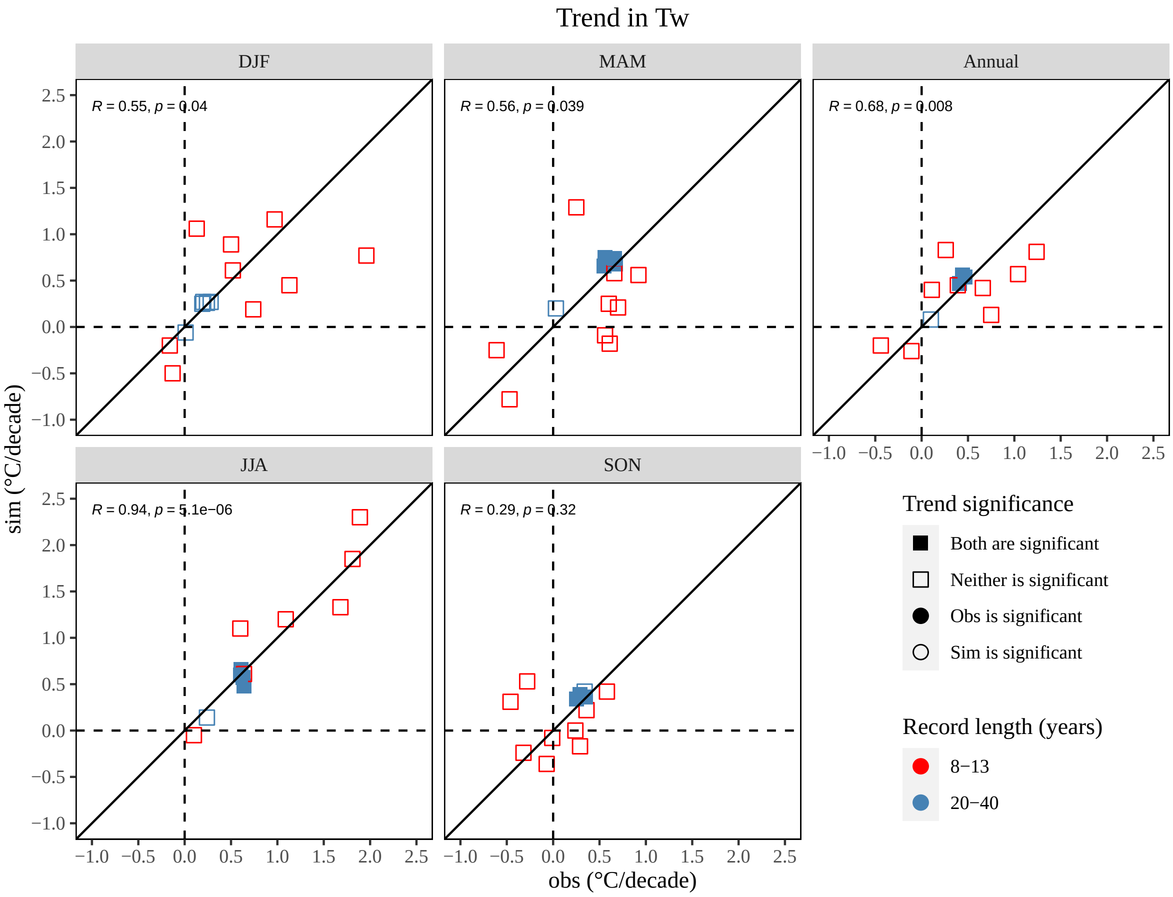

Figure 5.3: Relationships between trends in observed and simulated Tw for 14 stations, including 5 stations with long-term data (20-40 years, blue) and 9 stations with 8-13 years of data (red). The magnitude of trends is estimated by Theil–Sen estimator. Point shapes indicate whether trends are significant or not at the 95% confidence level for observations and simulations according to the Mann-Kendall test. Colors refer to total number of years with data. The position of these stations can be found in Figure 2.1, middle panel (p. 44).

increase was found in winter – +0.22 (resp. +0.28) °C/decade in observations (resp. simulations).

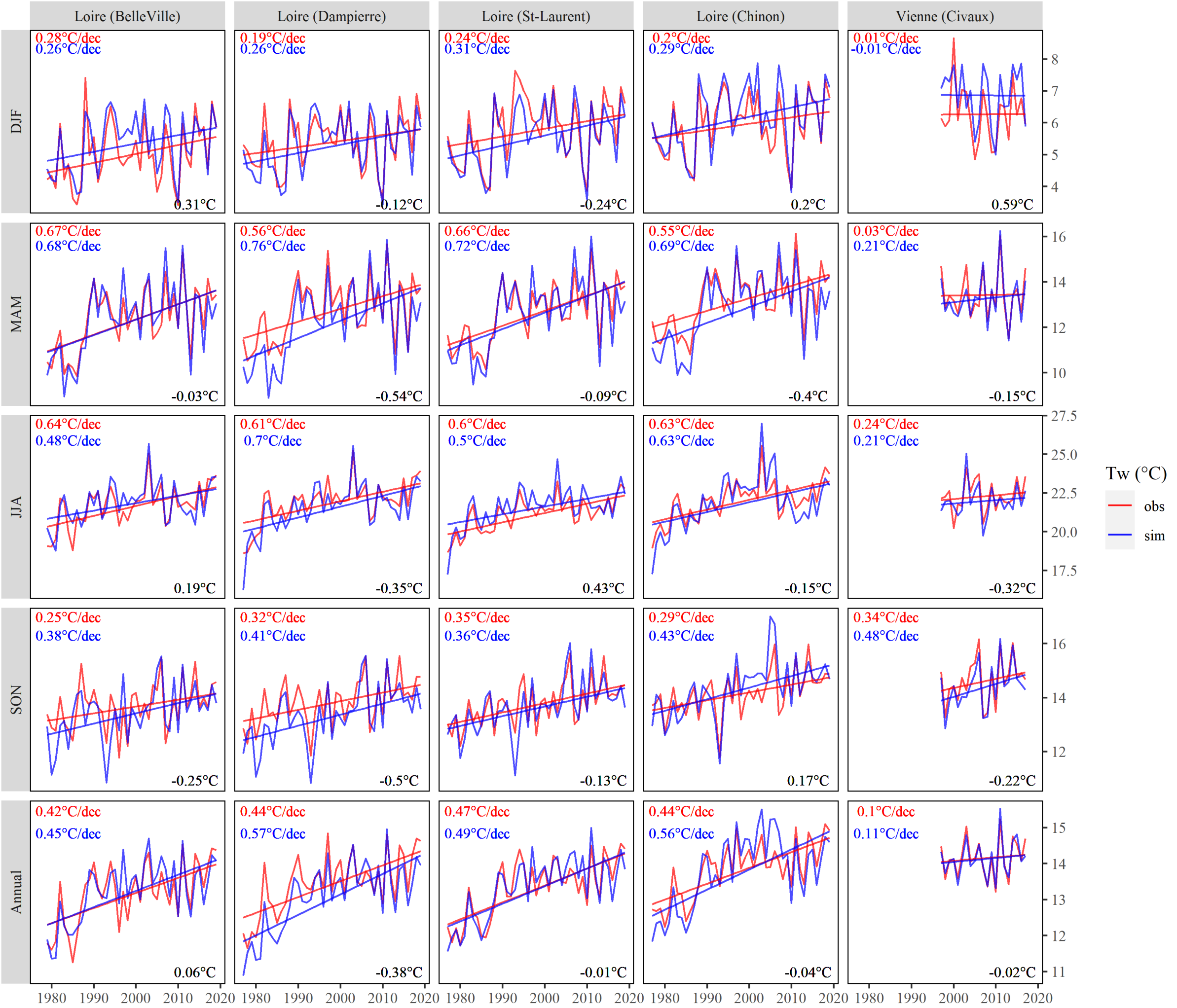

Figure 5.4: Seasonal and annual time series of observed and simulated Tw at stations with long-term continuous data (> 20 years) between 1977 and 2019 (see Table 2.1, p. 48). Numbers in red and blue in the top left corner of each graph show trend values (Sen's slope) in observed and simulated Tw. Numbers in black in the bottom right corner of each graph show the mean bias of the reconstruction.

5.3 Long-term trends in stream temperature, air temperature and streamflow over the 1963–2019 period

Here, the spatial variability of past trends in seasonal and annual Tw (simulated by the T-NET model), Ta (provided by SAFRAN) and Q (provided by the EROS model) over the 1963–2019 period for the whole Loire River basin (52 278 reaches) is presented to see visually whether there are spatial links between Tw and Ta and/Q.

Trends in Tw

Figure 5.5, left panel, shows an increase in simulated Tw in almost all reaches for all seasons, with trends that are everywhere – except some limited areas mainly in winter – statistically significant at the 95 % confidence level (Figure 5.6, left panel). Depending on the season considered, 62 % to 80 % of reaches show trends in the range of 0.2-0.4 °C/decade (i.e 1.14-2.28 °C over the whole 1963–2019 period; see Figure 5.7), with the exception of summer. Summer Tw trends are more spatially variable than in other seasons. The highest Tw trend values are found in summer (resp. spring), when 58 % (resp. 36 %) of reaches shows trend values higher than 0.4 °C/decade (Figure 5.7). In summer, such reaches are mainly located in the southern part of the basin, in HER A (see Figure 5.5, left). Spring Tw trends show a similar spatial pattern, but with lower trend values.

Trends in Ta

Figure 5.5, middle panel, shows increasing Ta trends for 99 % of all reaches across spring, summer, and the whole year. Such trends are all significant at the 95 % confidence level (Figure 5.6, middle panel). Depending on the season considered, for 64 % to 83 % of reaches, trends are mainly in the range of 0.2-0.4 °C/decade (Figure 5.7), with the exception of summer. The highest Ta trend values are found in summer (resp. spring), when 67 % (resp. 22 %) of reaches shows values higher than 0.4 °C/decade. Such reaches are mainly located in HER A, especially in summer. Non-significant trends are found over the whole basin in winter, and in the southern part of the basin in fall (Figure 5.6, middle panel).

Trends in Q

Figure 5.5, right panel, shows that trends in Q are contrasted across the basin and also across seasons, with upward and downward trends. Most of these trends are not significant at the 95 % confidence level (Figure 5.6, right panel). However, significant decreasing trends are found in the southern headwaters (HER A) in spring, summer, fall, and also when looking at the annual scale (Figure 5.6, right panel). Decreasing trends are observed for the majority of reaches across seasons (66-83% of reaches; see Figure 5.7), with the exception of winter (37% of reaches). Decreasing trends could have values higher than -5 % per decade, i.e. -28 % over the whole 1963–2019 period (19-36 % of reaches across seasons, with the exception of winter; see Figure 5.7).

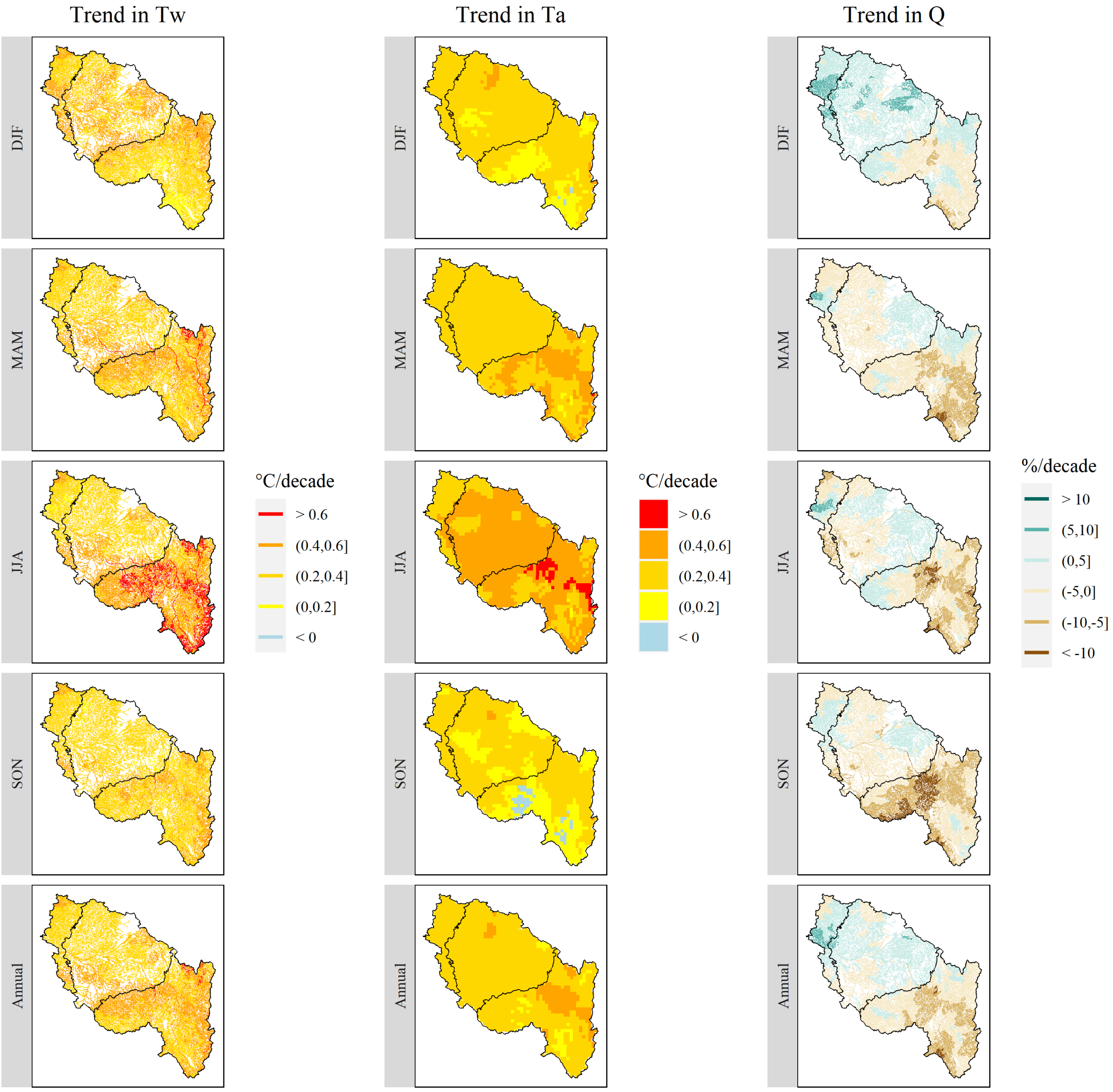

Figure 5.5: Spatial variability of trends in seasonal and annual Tw, Ta and Q over the 1963–2019 period, based on the Sen's Slope estimator. Solid black lines show the Hydro-Ecoregion (HER) delineation (see Figure 2.1, p. 44).

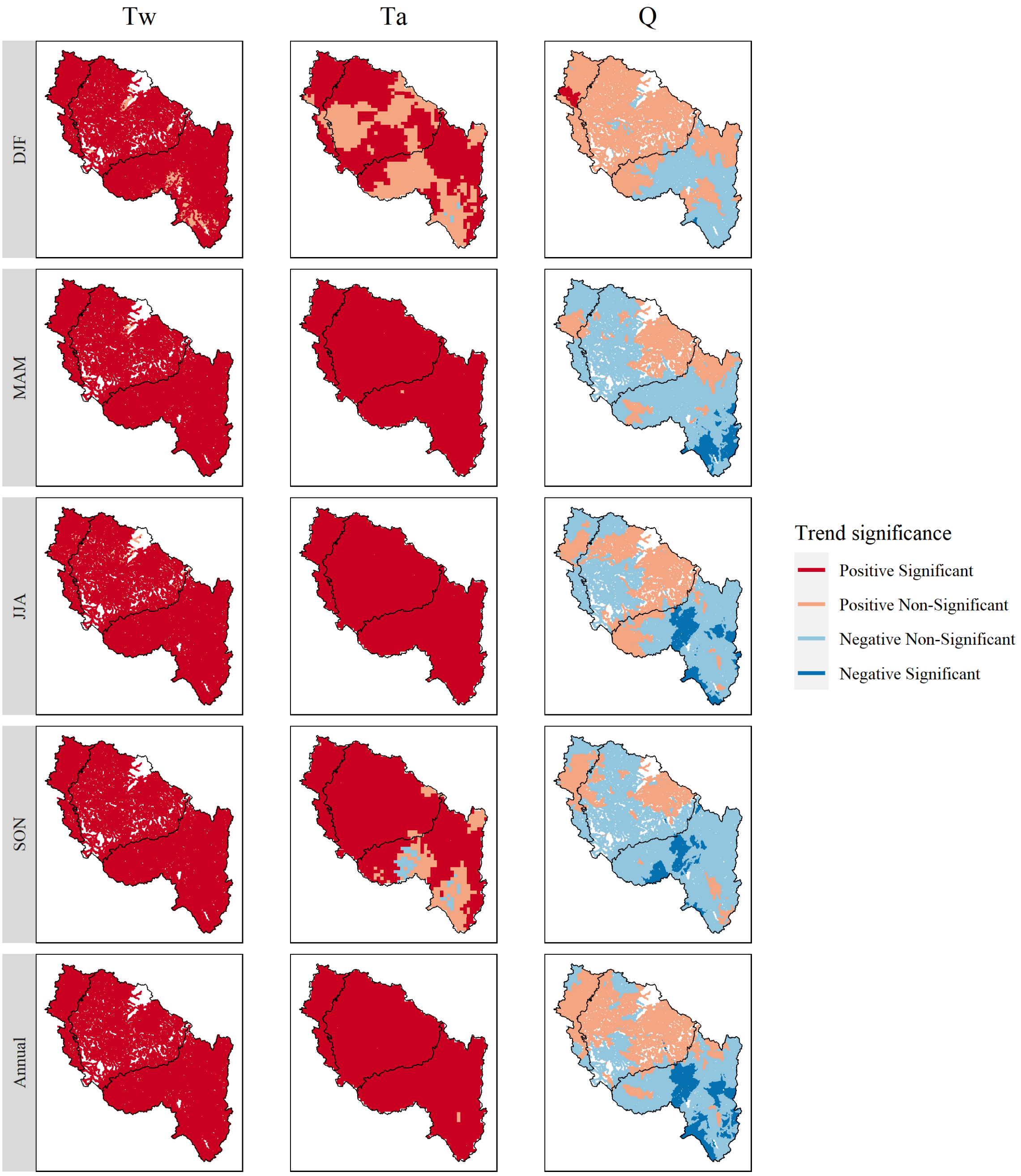

Figure 5.6: Spatial variability of the significance of trends in seasonal and annual Tw, Ta and Q over the 1963–2019 period, based on a Mann-Kendall test at the 95% confidence level. Solid black lines show the Hydro-Ecoregion delineation (see Figure 2.1, p. 44).

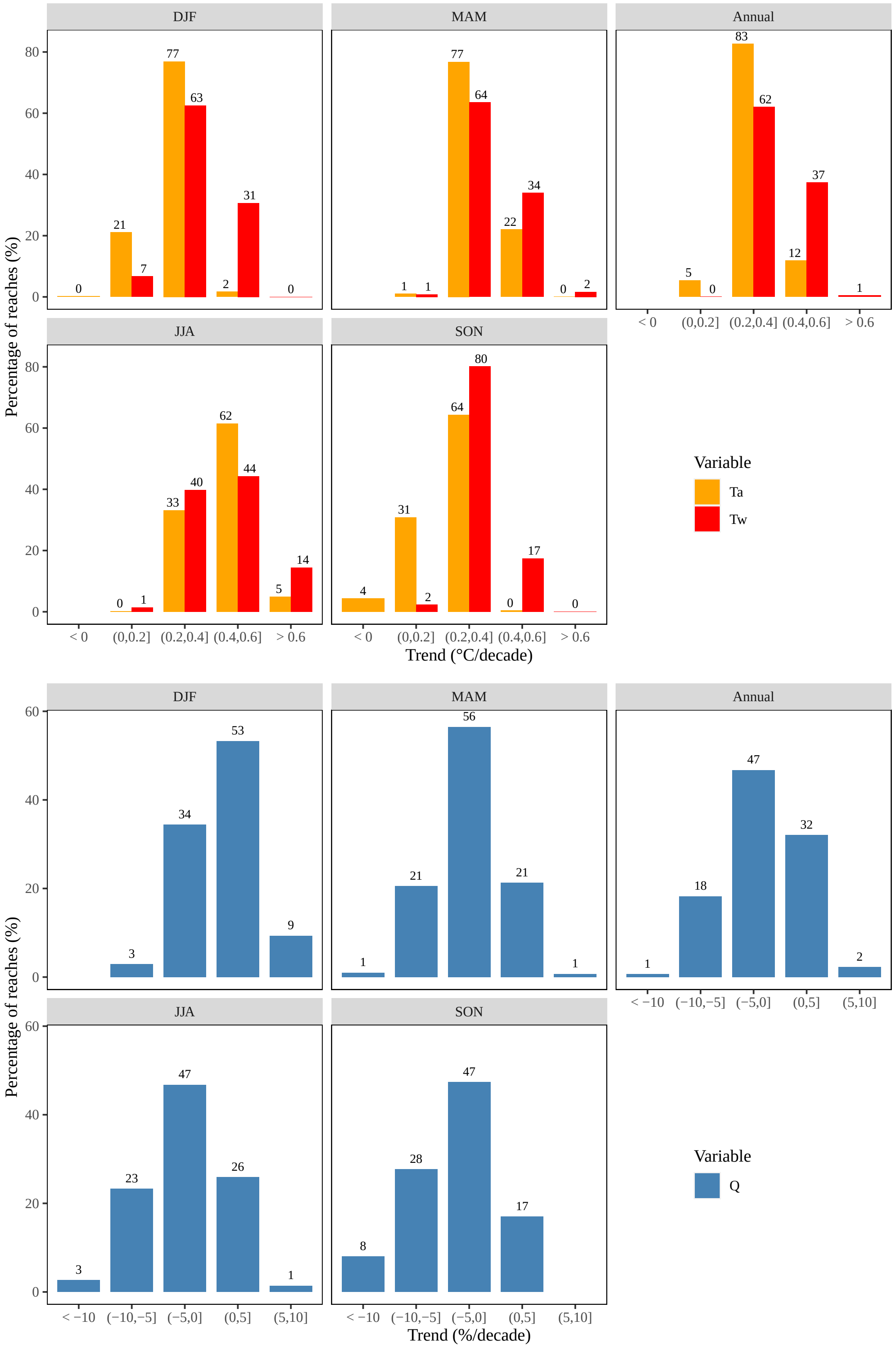

Figure 5.7: The range of the seasonal and annual (top) Tw, Ta, and (bottom) Q trends for all 52 278 reaches over the 1963–2019 period. This representation includes both significant and non-significant trends.

5.4 Hydroclimatic drivers of stream temperature trends

In the previous section, the spatial view of the variability in trends showed that more pronounced trends in Tw happened in HER A where increasing trends in Ta and decreasing trends in Q were observed as well. Therefore, there might be some spatial and temporal links between trends in Tw and trends in Ta and/or Q chosen as the main hydroclimate drivers of Tw in the current study. Moreover, it is hypothesized that other hydroclimate drivers (e.g., trend in Q) may be the responsible for the discrepancy between Tw trend and Ta trend. Therefore, to understand the relative influence of Ta and Q on Tw, in this section, we assess spatial coherence and temporal synchronicity between trends in Tw and trends in Ta and Q.

5.4.1 Stream temperature increases faster than air temperature

We first assess the spatial coherence between Tw and Ta or Q. In this regard, distributions of trends in Tw and Ta are first compared for the whole basin at the seasonal and annual scales using the non-parametric Wilcoxon signed rank test (Bauer, 1972) to determine whether Tw trends are greater than Ta trends. Then, the spatial coherence across reaches in terms of difference in trends between Tw and Ta on one hand, and sign of trend in Q on the other hand, is assessed to explain the discrepancy between Tw and Ta found in the previous step with respect to Q.

The median of Tw trends is higher than that of Ta trends for every season ($p<0.001$ according to the Wilcoxon signed rank test), except for summer when the median trend values for Tw and Ta are very similar, but more variable for Tw (+0.08 to +1.02 °C/decade) (Figure 5.8). The greatest increase in Tw is found in summer (+0.44 °C/decade). Overall, Tw trends are more spatially variable than Ta trends, suggesting the conditional influence of other factors like Q trends (Figure 5.8). Indeed, where Tw trends exceed Ta trends, decreasing Q trends occur coincidentally at the majority of reaches for all seasons (with the exception of winter) regardless of the significance level of these variables (Figure 5.9). If all significant and non-significant trends are considered, for 43-72 % of reaches across seasons (with the exception of winter), increase in Tw and Ta and decrease in Q occur coincidentally (Figure 5.9, top panel). The same can be found for 47-94% of reaches across seasons (with the exception of winter) when only significant events of all these variables are considered (Figure 5.9, bottom panel). Moreover, the difference between Tw and Ta trends could go up to 0.5 °C/decade (i.e. up to 2.8 °C/decade over the whole 1963–2019 period, see Figure 5.10) irrespective of whether all significant and non-significant trends are considered.

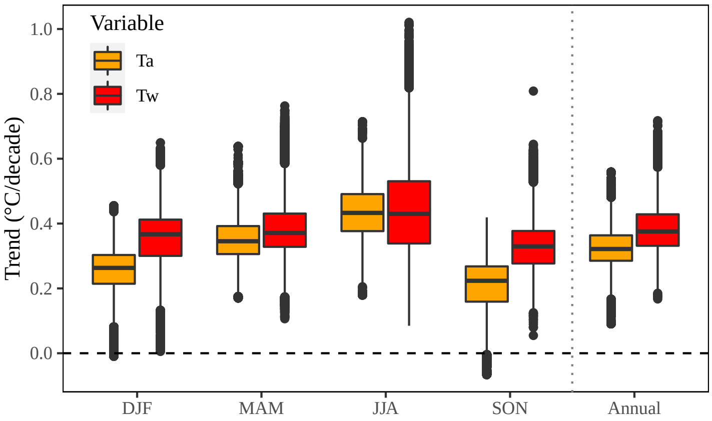

Figure 5.8: Distributions of seasonal and annual trends in Tw and Ta for all 52 278 reaches over the 1963–2019 period. Sen's slope is used as trend value estimate.

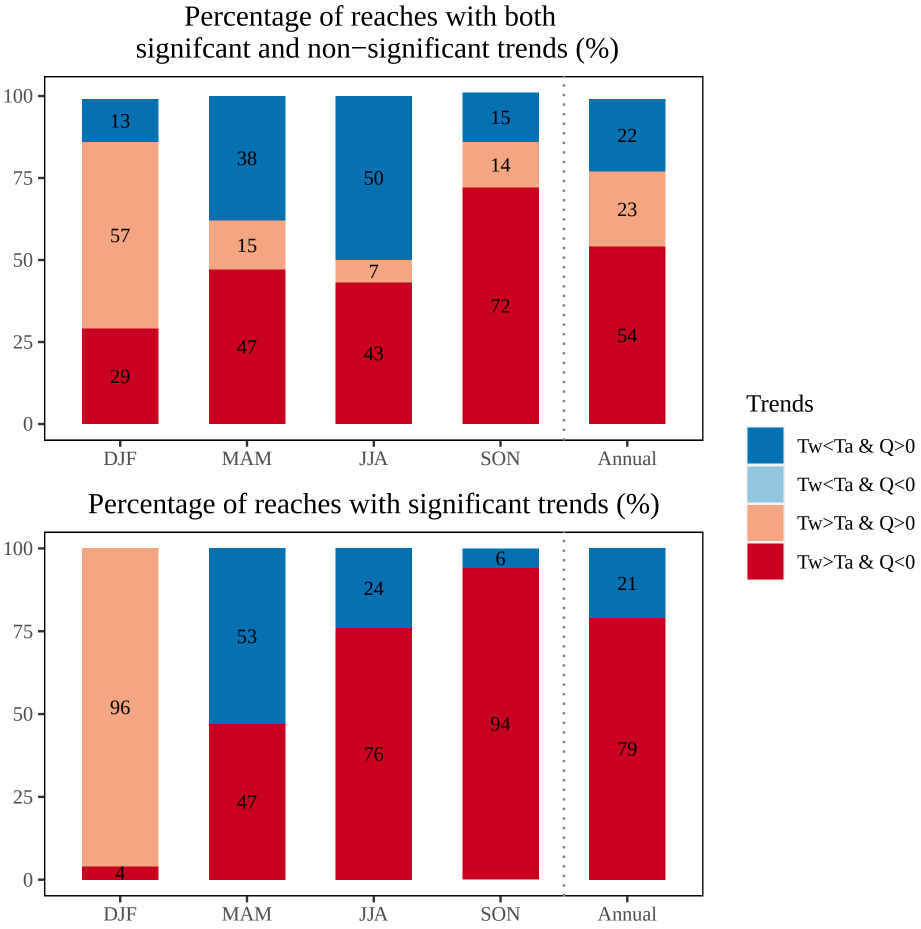

Figure 5.9: Percentage of reaches with consistent trends in Tw, Ta, and Q, categorised with respect to two criteria: (1) Tw trend>Ta trend, and (2) sign of Q trend for (top) all the significant and non-significant trends in Tw, Ta, and Q, and (bottom) only significant trends in Tw, Ta, and Q. Sen's slope is used as trend value estimate.

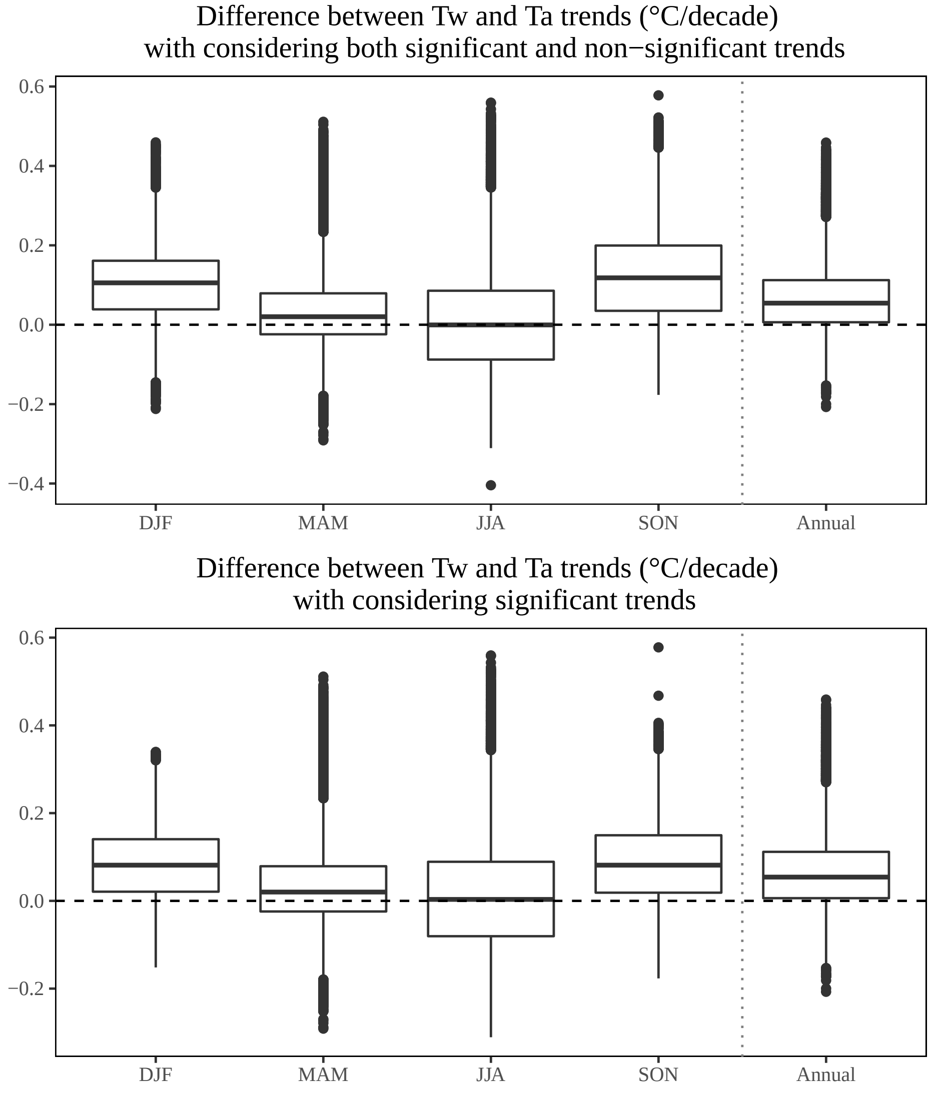

Figure 5.10: Difference between Tw and Ta trend at each reach in °C/decade for the whole 52 278 reaches

Of these specific reaches where all factors converge (trend in Tw higher than trend in Ta, and decreasing trend in Q), most are located in HER A regardless of considering all significant and non-significant trends (52-90 % of such reaches across seasons; see Figures 5.11, left panel and 5.12), or only significant events (100 % of such reaches across seasons; see Figure 5.11, right panel). Note that, in HER A, this convergence (trend in Tw higher than trend in Ta, and decreasing trend in Q) can be seen for all kind of rivers regardless of their size when both significant and non-significant events are considered (see Figure 5.13).

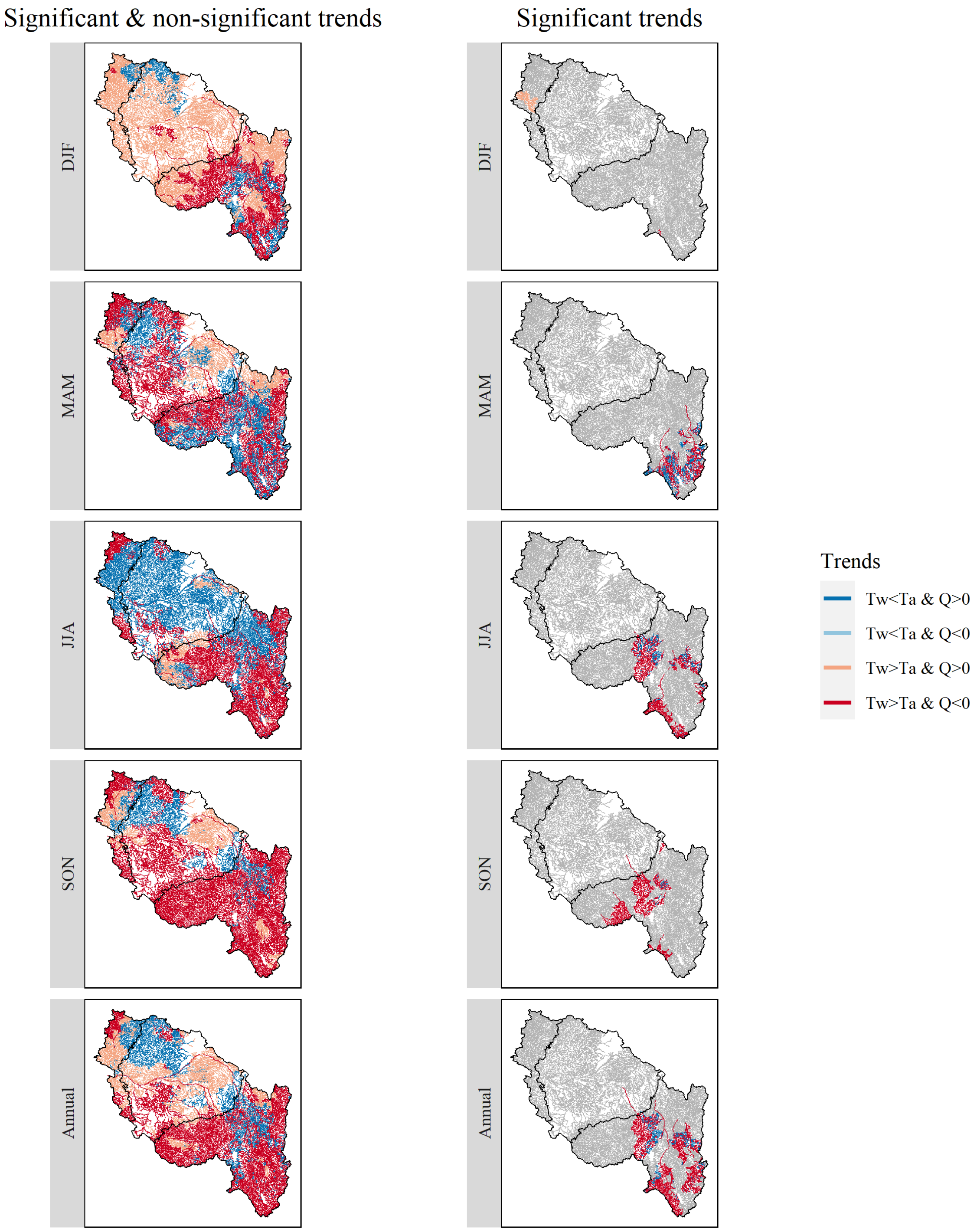

Figure 5.11: Map of reaches with consistent trends in Tw, Ta, and Q, categorised with respect to two criteria: (1) Tw trend>Ta trend, and (2) sign of Q trend. Sen's slope is used as trend value estimate. (left) All reaches with significant and non-significant trends in Tw, Ta and Q. (right) Only reaches with significant trends in Tw, Ta, and Q.

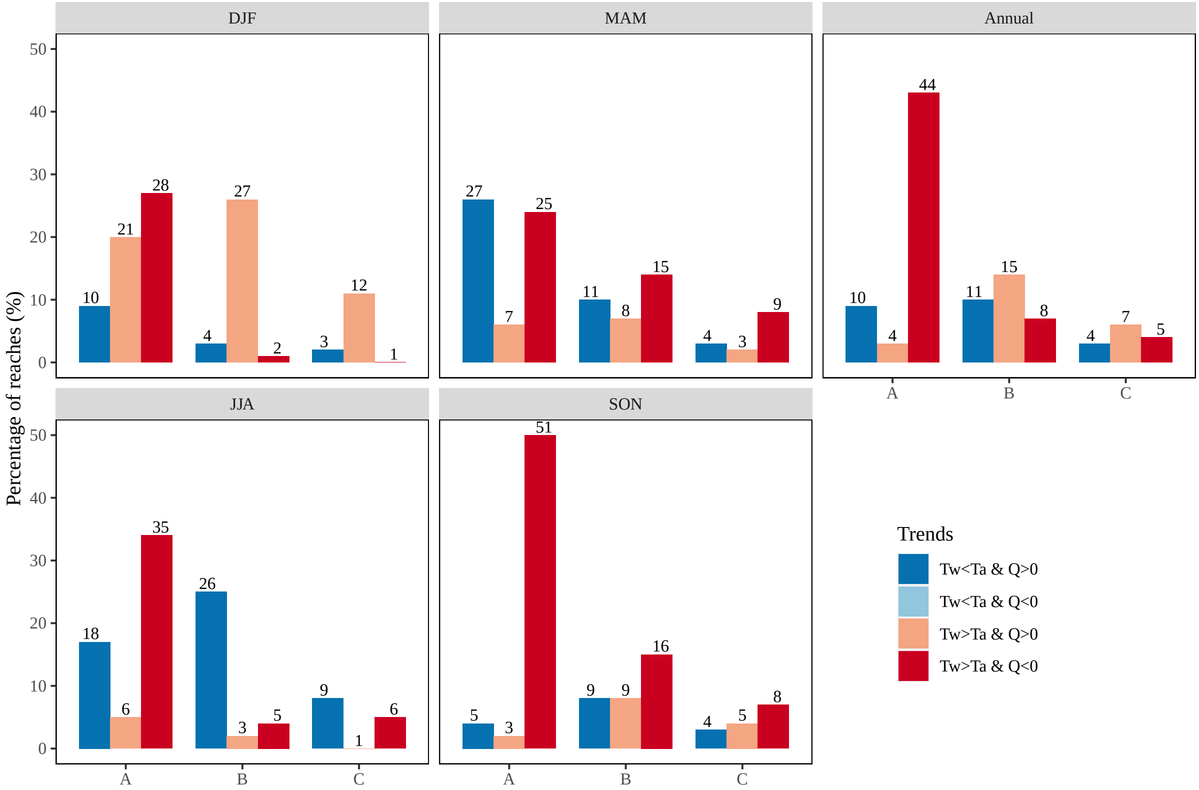

Figure 5.12: Percentage of reaches in each HER with consistent trends (significant and non-significant) in Tw, Ta, and Q, categorised with respect to two criteria: (1) Tw trend>Ta trend, and (2) sign of Q trend. Sen's slope is used as trend value estimate. Please note that the percentages are calculated with respect to the whole basin, which means that the sum of them in each season is equal to 100 %.

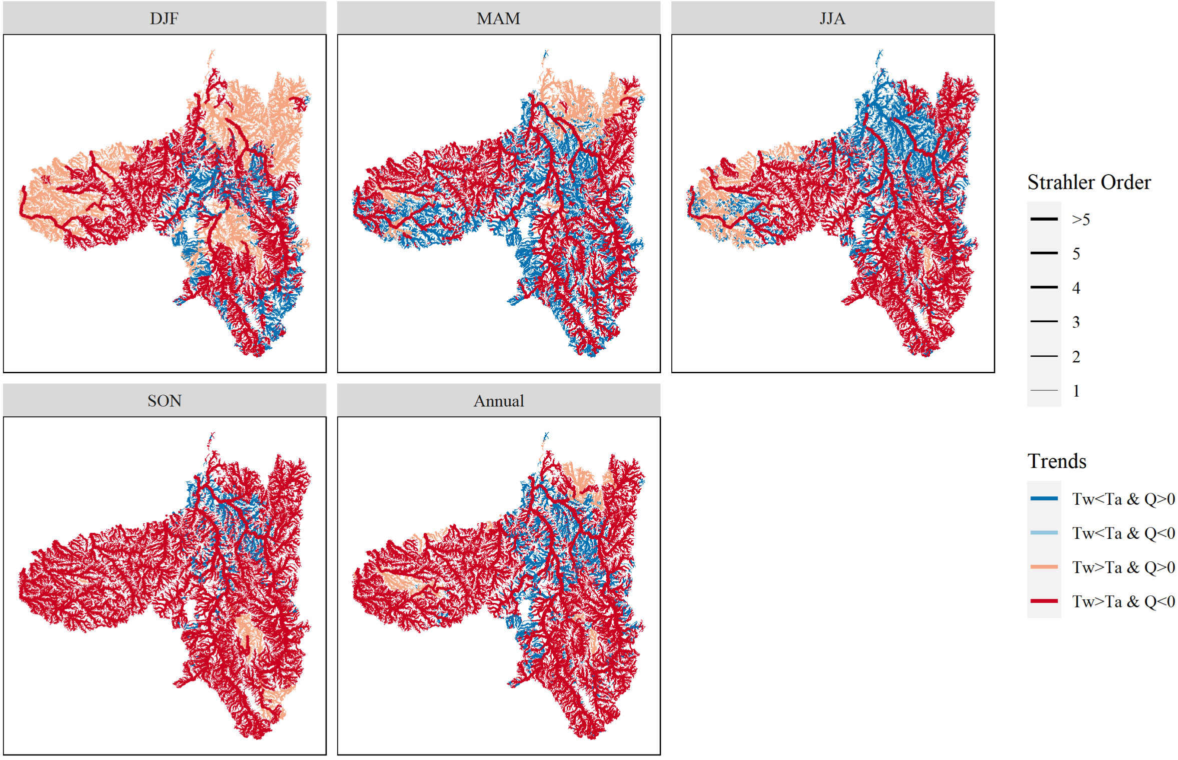

Figure 5.13: Map of reaches with consistent trends in Tw, Ta, and Q, categorised with respect two criteria in HER A: (1) Tw trend>Ta trend, and (2) sign of Q trend. Sen's slope is used as trend value estimate. All reaches with significant and non-significant trends in Tw, Ta and Q are considered. Note that size of the streams in the figure shows the reach Strahler Order.

5.4.2 Synchronicity of stream temperature anomalies with air temperature and streamflow anomalies

To assess the temporal link between Tw and Ta/Q, first, the Pearson correlation is computed for each reach between seasonal and annual means of (1) Tw and Ta, and (2) Tw and Q, to determine the strength and direction of the relationship between Tw and hydroclimatic drivers across reaches. Seasonal and annual anomalies of Tw, Ta, and Q – with respect to the 1963–2019 interannual mean – are then used to visually assess the synchronicity of extreme years.

Strong positive correlations between seasonal and annual averages of Tw and Ta are found across seasons (+0.72- +0.83; see Table 5.1). A negative correlation between summer Tw and Q time series is further observed (-0.40).

Table 5.1: Pearson correlation over the 1963–2019 period between seasonal and annual Tw and Ta and/or Q time series, averaged over all reaches. Percentages in brackets show the proportion of reaches with a significant correlation at the 95 % confidence level.

Season	Tw and Ta	Tw and Q
DJF	+0.73 (100%)	+0.52 (94%)
MAM	+0.78 (100%)	-0.02 (25%)
JJA	+0.82 (100%)	-0.40 (79%)
SON	+0.72 (99,6%)	-0.01 (19%)
Annual	+0.83 (100%)	-0.01 (22%)

The anomalies of Tw, Ta, and Q exhibit different patterns, with Tw and Ta generally increasing and Q remaining relatively stationary (Figure 5.14). Tw anomalies (with median anomaly form -3 to +3 °C across seasons) are generally more variable than Ta anomalies, especially in summer, but both time series appear to exhibit synchronous behaviors. Tw and Ta anomalies exhibit a clear negative-to-positive shift in the late 1980s at nearly all reaches, with median values shifting by approximately +2 °C after the change-point (Figure 5.14).

Critically, the largest summer Tw and Ta positive anomalies over the study period are observed in 1976, 1994, 1995, 2003, 2005, 2006, 2015, 2017, 2018 and 2019, which correspond to years with the largest negative anomalies in summer Q, with the exception of 1994 and 2018 (Figure 5.15). However, this signal is much less clear for the other seasons (Figure 5.16).

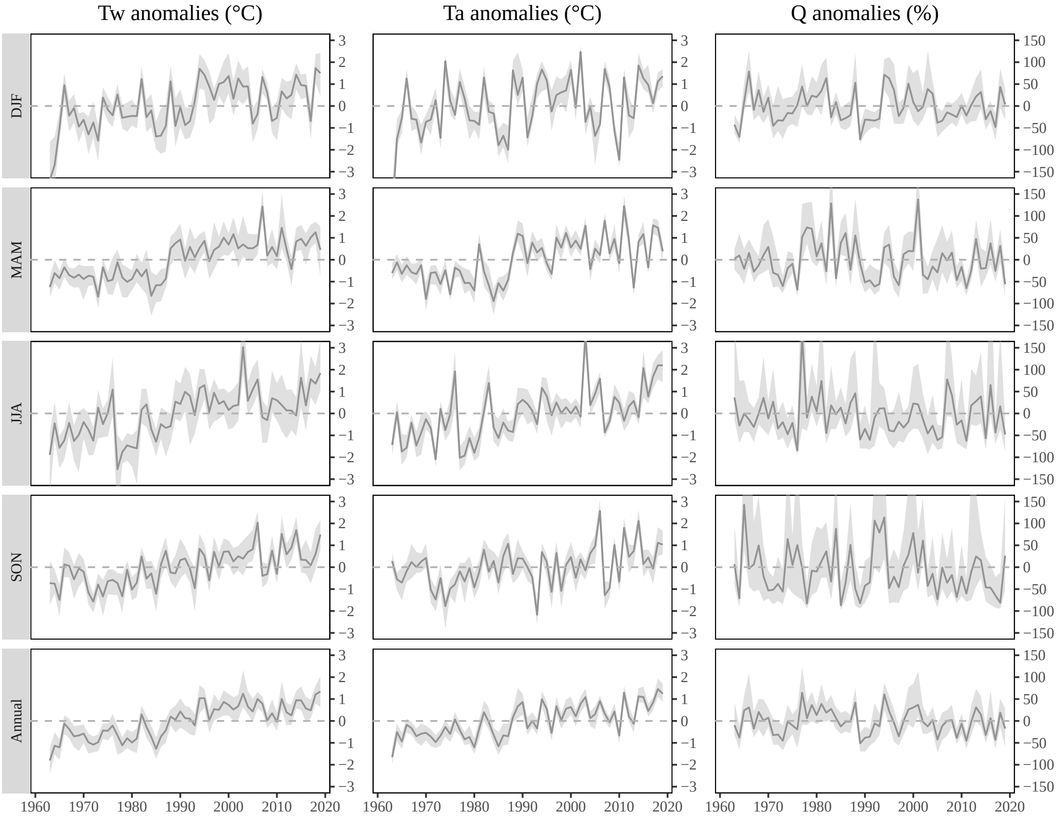

Figure 5.14: Seasonal and annual times series of anomalies in Tw (°C), Ta (°C) and relative Q (%) with respect to 1963–2019 average. Grey intervals show the 5th and 95th percentiles across reaches, and the solid grey line depicts the median value. Tw and Ta have the same scale.

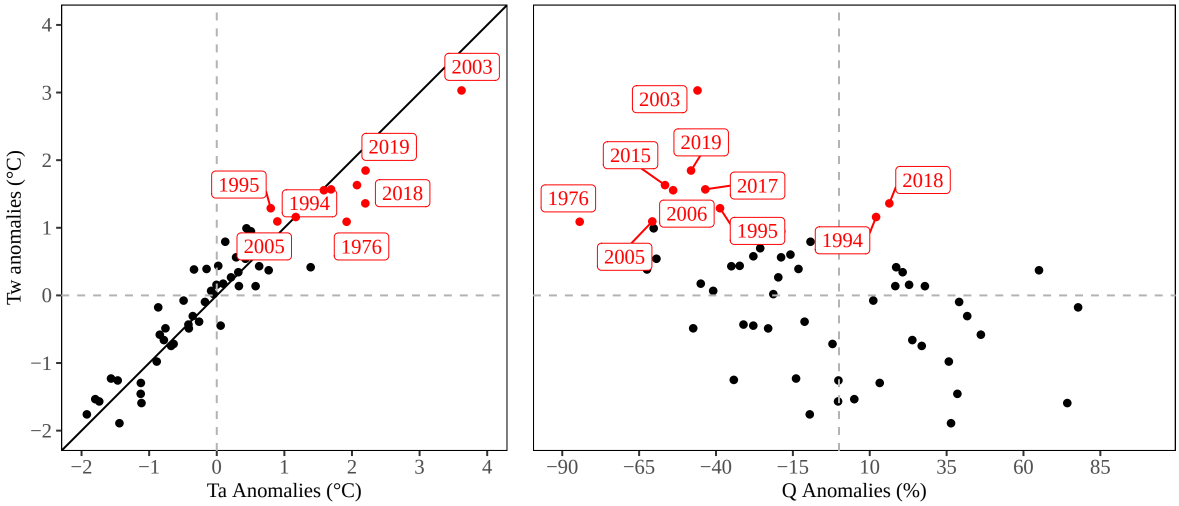

Figure 5.15: Relationship between Tw anomalies and Ta anomalies in summer on one side and Tw anomalies and Q anomalies in summer on the other side. Individual years are identified from their median anomaly across all reaches. Years with the highest anomalies in Tw (> 1 °C) are identified in red.

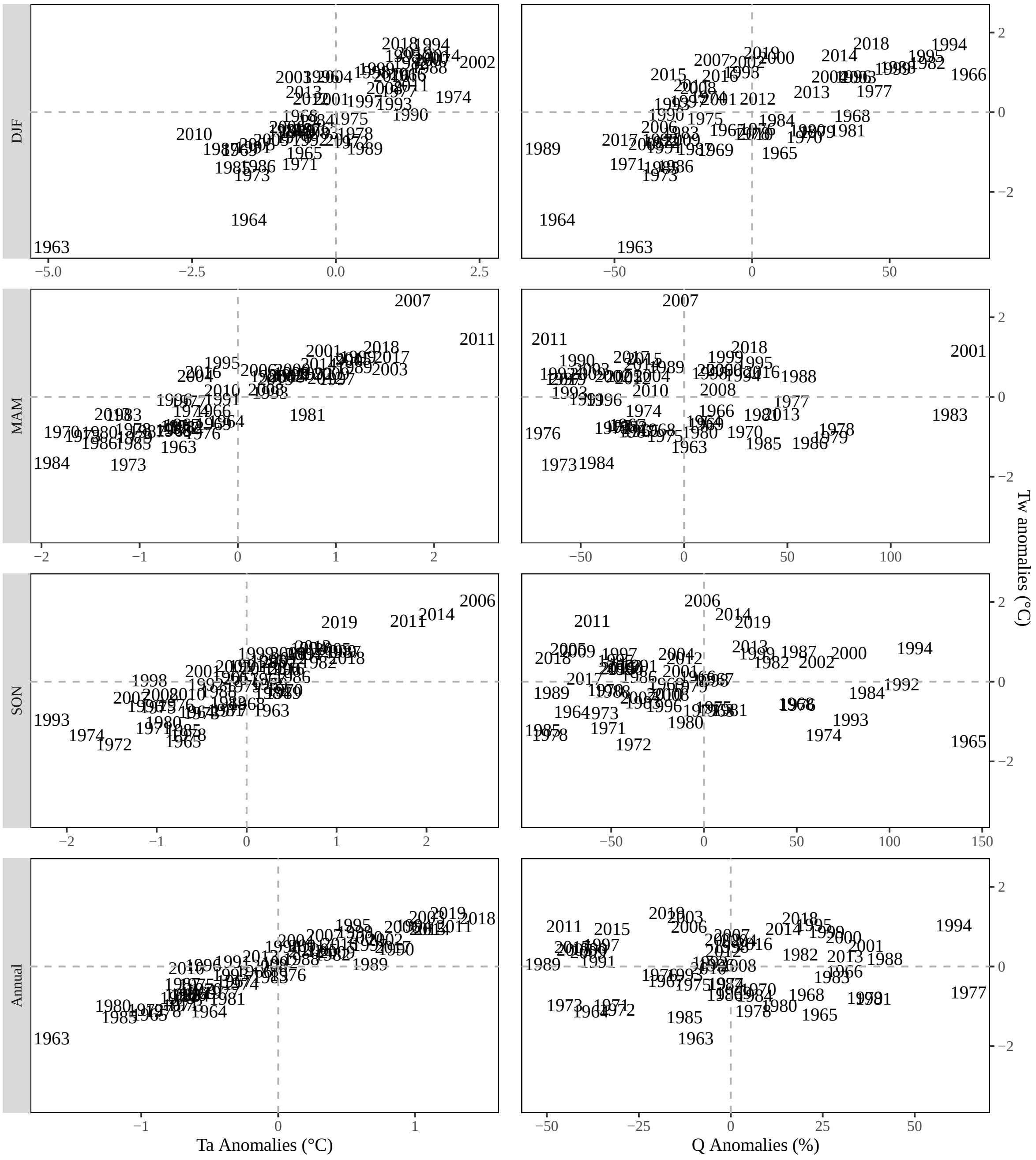

Figure 5.16: Relationship between Tw anomalies and Ta anomalies on one side and Tw anomalies and Q anomalies on the other side across seasons, with the exception of summer. The labels indicate the median anomalies of 52 278 reaches for each year. See Figure 5.15 for the summer period.

5.4.3 Change-point in stream temperature, air temperature and streamflow in the late 1980s

A clear negative-to-positive shift in the late 1980s at nearly all reaches for Tw and Ta anomalies was observed in the previous section (Figure 5.14), which was less visible for Q anomalies due to its high interannual variability. To see whether the change-points in Tw, Ta and Q occur around the same time, change-points in time series of anomalies of these variables at each reach are computed with the non-parametric Pettitt test. This test considers no change in the central tendency as a null hypothesis (Pettitt, 1979). Change points are reported at the 95 % confidence level.

The change-point analysis also support the previous visual observation, where change-points in seasonal and annual averages are largely coincident across these time series (Figure 5.17). These change points are observed in all seasons, but are most pronounced and synchronous around 1988 in spring and summer. The change-points detected in winter Tw and Ta time series are less concomitant, occurring mostly in the early 1990s (1992 and 1993) for Tw and in the late 1980s (1986-1989) for Ta. The fall change-points are distributed between 1980 and 1994 for both Tw and Ta. The significant change-points in seasonal Q time series are detected for a substantially smaller proportion of reaches, i.e. less than 40 % of reaches for spring and summer. The majority of these reaches are located in HER A across seasons (66-86 % of such reaches), with the exception of winter (49 %) (see Figure 5.18). In spring and summer, they occur in the late 1980s, similarly to Tw and Ta. Conversely, the significant change-points detected in other seasons are much more scattered in time, probably due to the high interannual variability of Q.

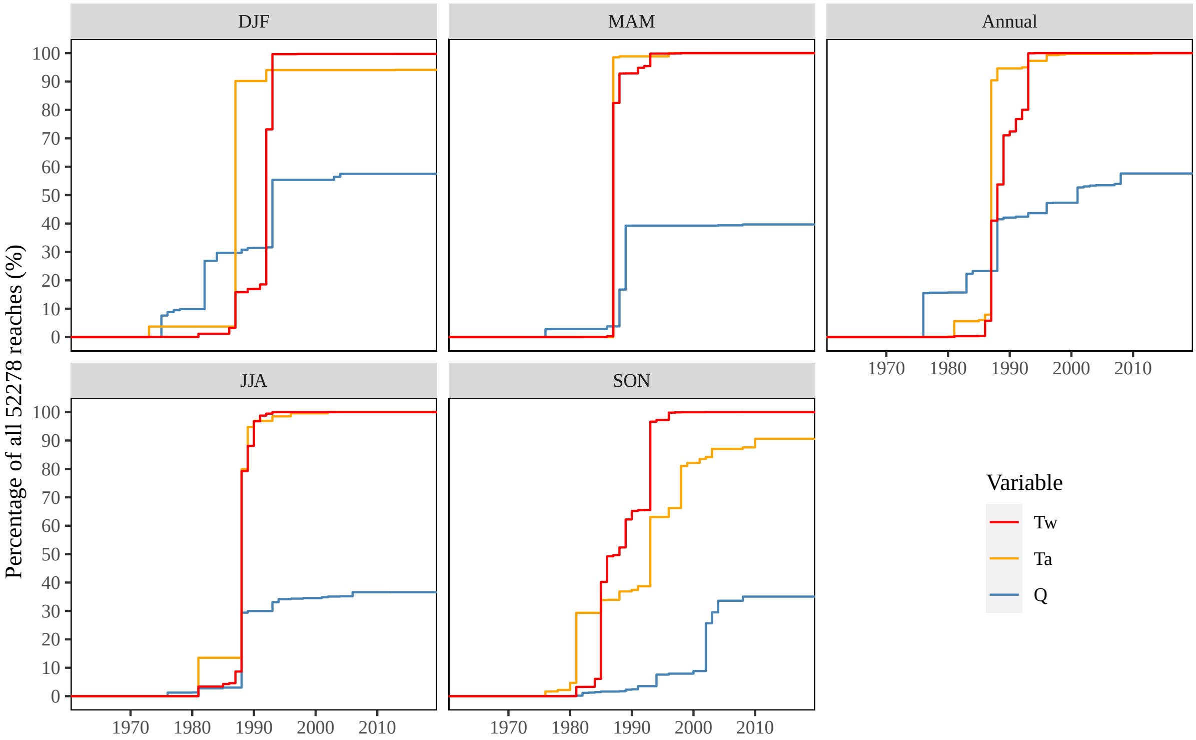

Figure 5.17: Change-points in Tw, Ta, and Q time series at the seasonal and annual scales, plotted as a proportion of reaches experiencing a shift in a given year. Only the first change-point detected at the 95% confidence level is considered, and non-significant change-points are removed, leading to curves not necessarily reaching 100 %.

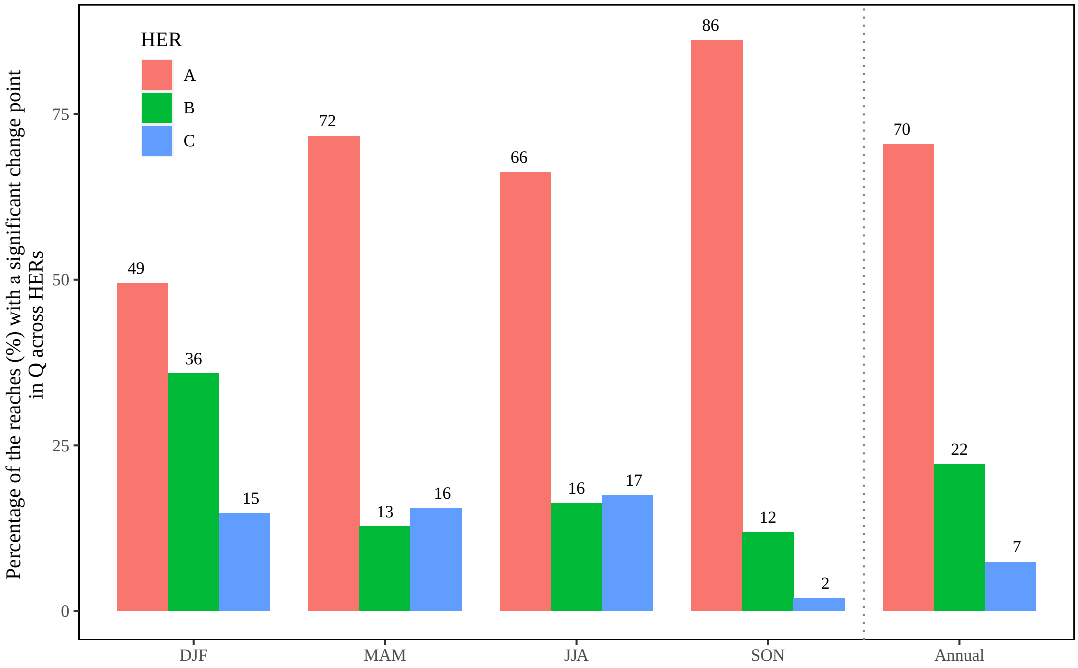

Figure 5.18: Percentage of reaches with a detected change-point in Q time series across HERs. Note that, in this figure, the percentage has been calculated over the reaches with a significant change-point, not over the whole 52 278 reaches.

5.5 Landscape drivers of stream temperature trends

Stream size, within individual large-scale homogeneous HERs, is selected as the first major potential landscape driver. The Strahler order of each reach is used as a proxy for stream size. Reaches with Strahler order 5–8 were combined into a single group termed "large rivers". The Spearman correlation is computed between decadal trends in Tw (i.e. across all reaches) and Strahler order. Such correlations are computed across HERs and at seasonal and annual scales to evaluate the spatial heterogeneity and seasonality. Finally, in order to better illustrate the relationship between trends in Tw and Strahler order, median Tw trends of each group of rivers with respect to Strahler order is presented.

5.5.1 Stream temperature increases faster in large rivers

The Strahler order of each reach is used here as a proxy for stream size. Reaches with Strahler order 5–8 are combined into a single group termed “large rivers”. The relationship between median decadal trends in Tw (i.e., median across all reaches) and Strahler order are assessed across HERs and at seasonal and annual scales to evaluate the spatial heterogeneity and seasonality.

Strahler order was strongly ($p < 0.001$) and positively correlated with Tw trends for all HERs in spring, and for HER A in summer and fall and at annual scale. HER A exhibited the highest positive correlations in spring ($r = +0.32$) and summer ($r = +0.15$) (see Figure 5.19). In other words, larger rivers tend to exhibit the largest increases in spring and summer Tw, especially for reaches located in the HER A. There, median trends in spring (resp. summer) ranges from +0.37 °C/decade (resp. +0.49 °C/decade) for small streams (Strahler order 1) to +0.55 °C/decade (resp. +0.64 °C/decade) for large streams (Strahler order ≥ 5).

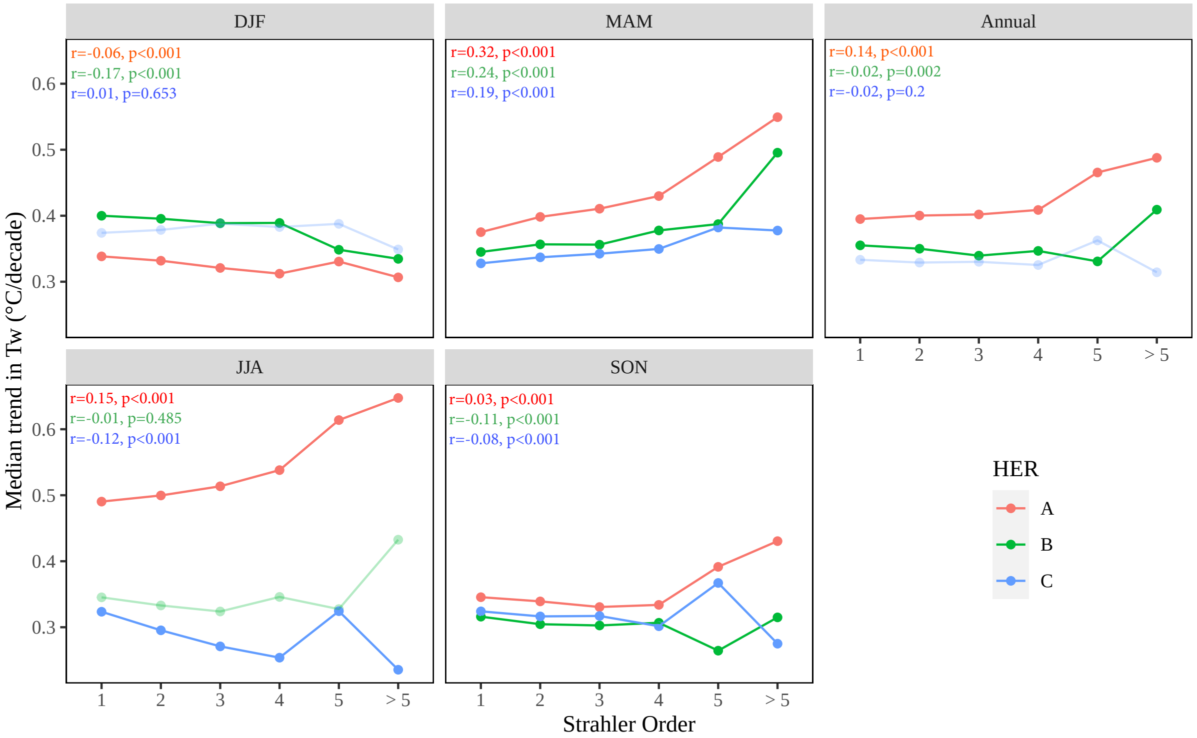

Figure 5.19: Relationships between reach size and median trends in Tw across reaches over the 1963–2019 period, by HER and by season. Correlations and associated p-values are shown on the top-right corner of each graph, and significant relationships at the 95% confidence level are identified by full solid lines

5.5.2 Stream temperature warming mitigated by riparian shading

Lastly, the influence of riparian vegetation shading on trends in Tw is assessed using the daily average of the riparian vegetation shading (SF for riparian shading factor) simulated by the T-NET model (see section 4.2.2.3, p. 97). Seasonal shading is computed as the average of the daily SF over each season. For this analysis, only low-order reaches – distance from the source < 30 km – are considered, based on previous observations that riparian shading primarily influences Tw at this scale (Moore et al., 2005; Loicq et al., 2018). Then, as the previous analysis for the influence of stream size, the relationship between median decadal Tw trends and five levels of riparian shading (<15 %; 15-25 %; 25-40 %; 40-60 %; >60 %) is assessed across HERs and seasons. The greatest SF (> 40 %) is found in summer (resp. spring) for 45 % (resp. 24 %) of reaches, which are mostly in HER A (61 % of such reaches). Finally, median Tw trends are compared for each level of riparian shading

For small streams, i.e. reaches located closer than 30 km from the source, the shading factor (SF) and trends in Tw are significantly ($p< 0.001$) and negatively correlated in HER A in all seasons, as well as in HER B and C in spring and in HER B in fall (Figure 5.20). Indeed, across seasons, the highest negative correlation is observed in HER A (r= -0.56 to -0.37 depending on the season). Unsurprisingly, the mitigating effect of shading on trends in Tw for small streams is observed for all HERs in spring, and only for HER A in summer and, to a lesser extent, in fall and winter. The median spring Tw trend in the HER A decreases by 0.12 °C/decade from sparsely shaded reaches (SF<15%) to highly shaded reaches (SF>40%). For summer Tw in HER A, the median trends decreases by 0.16 °C/decade from the lowest shaded reaches to highest shaded reaches.

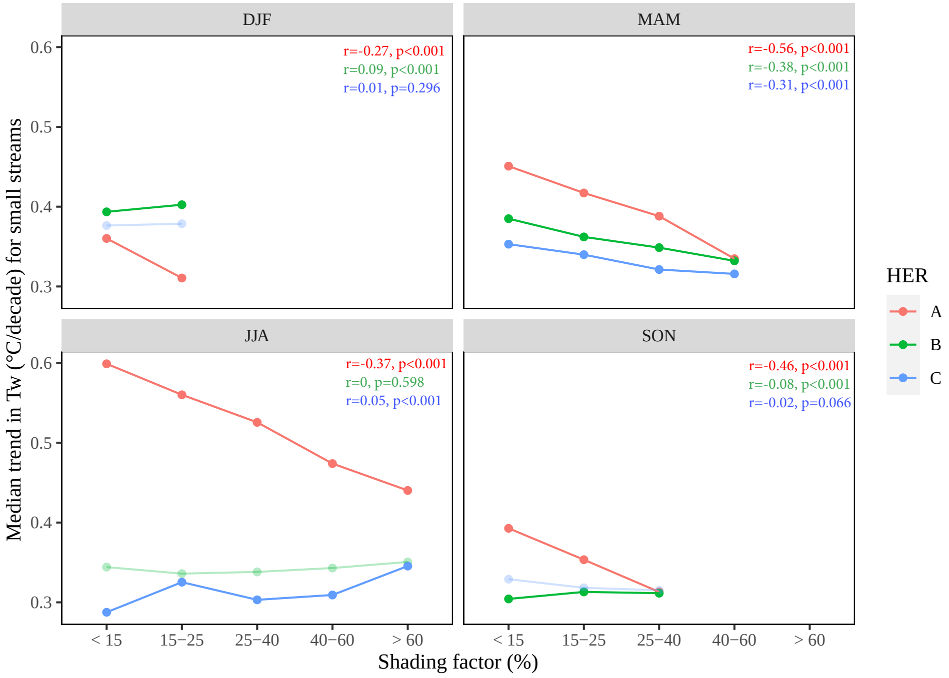

Figure 5.20: Relationships between shading factor and median trends in Tw over the 1963–2019 period for small streams, by HER and by season. Note that some shading factor classes are not observed in fall and winter.

5.6 Increase in stress on brown trout

An increase in Tw, especially in HER A, can increase the stress on cold-water fish species in this part of the basin. The brown trout, one of the common cold-water species in the Loire basin, especially in HER A, is selected here. Since lethal temperature for juvenile brown trout is 17 °C (Souchon and Tissot, 2012), the evolution of the number of days with Tw>17 °C ($N_{Tw} > 17$) is studied in rivers with a non-zero density (individual/100 m^2) for brown trout (see Figure 5.21 for density distribution over the 1994–2017 period). 80 % of such rivers are found in HER A. To do so, beforehand, the performance of the T-NET model in simulating this metric, $N_{Tw} > 17$, is assessed at 72 observed Tw stations with continuous daily data over the 2010–2014 period (see section 4.3.2.2, p. 113). Afterwards, the trend in $N_{Tw} > 17$ is computed over the 1963–2019 period for rivers with non-zero density of brown trout. Finally, the evolution of the brown trout vulnerability is calculated using adopted approach proposed by Lee et al. (2020) as following:

$$V = E \times S \tag{5.1}$$

V is vulnerability; E is the frequency of exposure time or the number of days with Tw> 17 °C , and S is the sensitivity score which is defined as following:

$$S = \frac{MIN - 17}{MAX - 17}, MIN = \begin{cases} 17 & \text{if Tw} < 17 \\ Tw & \text{otherwise} \end{cases} \tag{5.2}$$

with Tw, daily stream temperature at a specific day, and MAX is the maximum value of daily Tw found across all reaches with brown trout over the 1963–2019 period. This equation let scale Tw to 0 (17°C=lethal temperature for juvenile brown trout) and 1 (MAX).

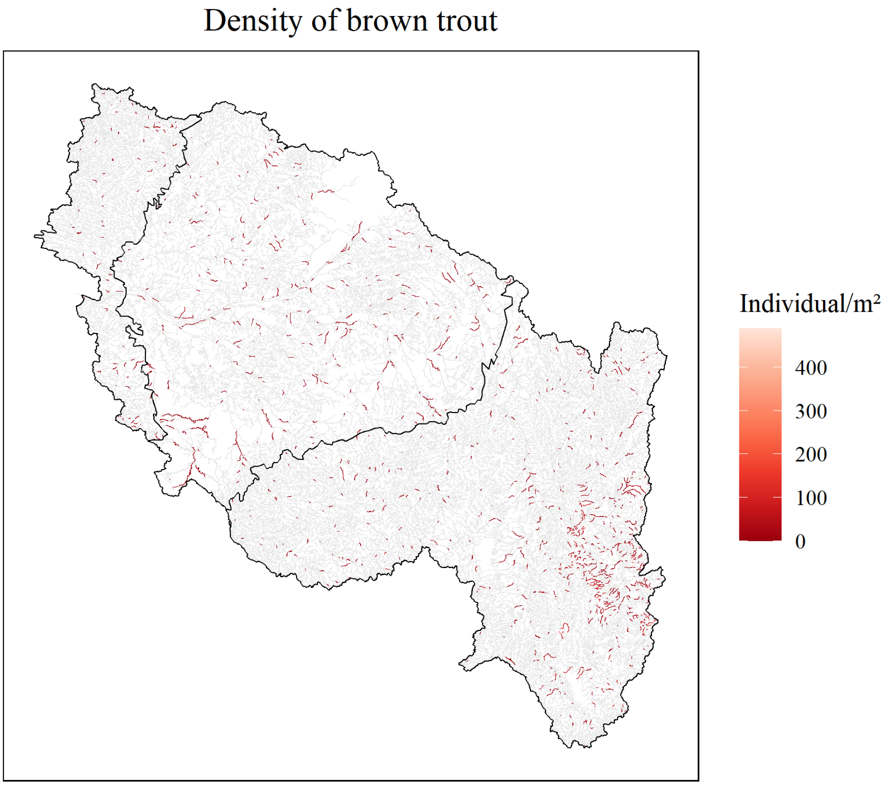

Figure 5.21: Map of brown trout density (over the 1994–2017 period, Poulet et al., 2011; Maire et al., 2017) across the basin. 80 % of rivers with non-zero density are located in HER A.

The T-NET model performs quite well in producing metric of $N_{Tw} > 17$ (median bias=1.5 days over the 2010-2014 period). In all HERs, there is an increasing trend (4 day/decade i.e. +22 days over the 1963–2019 period) in median of $N_{Tw} > 17$ across the rivers with non-zero density of brown trout (Figure 5.22). The years with greatest $N_{Tw} > 17$ correspond to years with the highest Tw anomalies (2003=65 days; 2006=45 days; 2017=42 days and 2019=39 days; and see Figure 5.15). Moreover, the vulnerability of brown trout increases 100 % over the 1963–2019 period (see Figure 5.23).

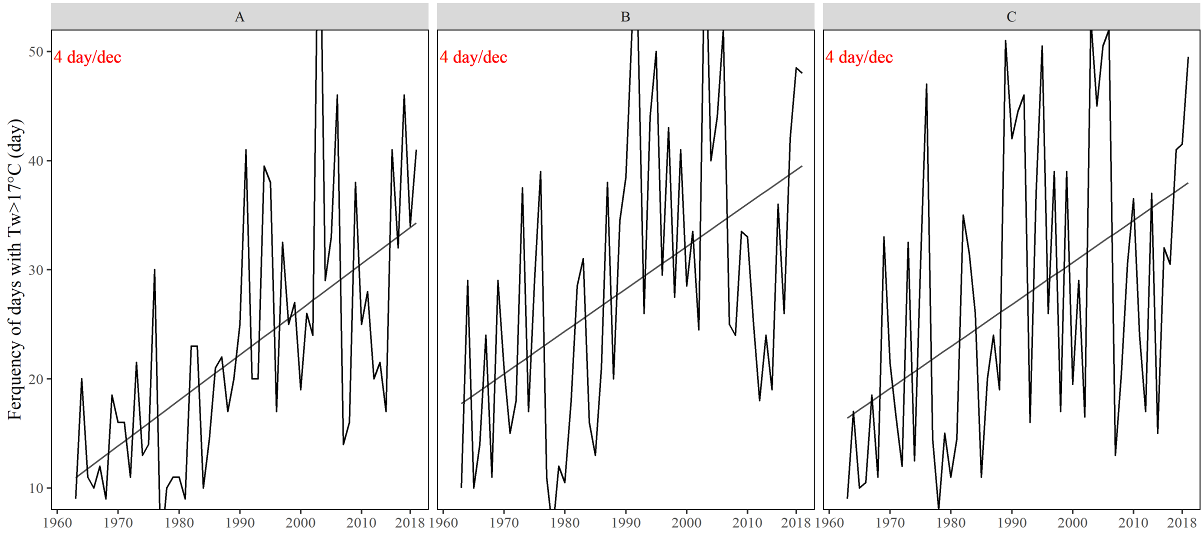

Figure 5.22: Evolution of the number of days with Tw>17 °C ($N_{Tw} > 17$) over the 1963–2019 period across HERs. For each HER, the median of $N_{Tw} > 17$ across rivers with non-zero density of brown trout (depicted in Figure 5.21) is used.

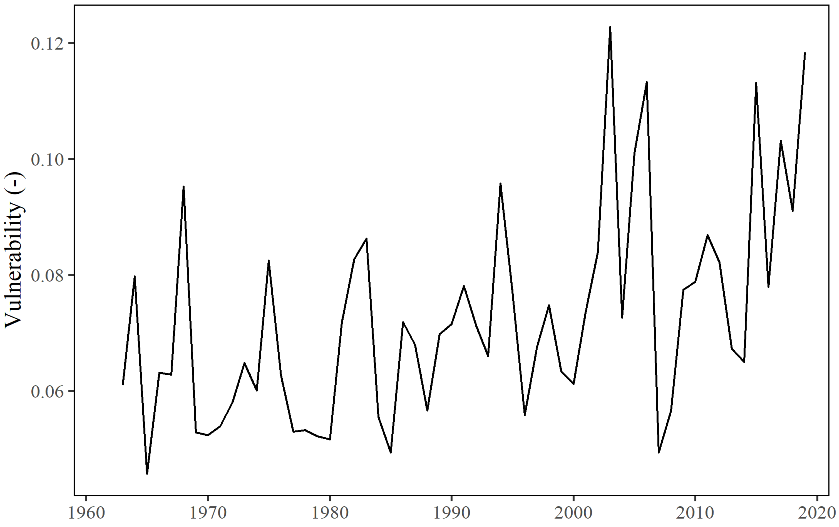

Figure 5.23: Evolution of vulnerability score of juvenile brown trout over the 1963–2019 period. The median value of the vulnerability score across the rivers with a non-zero density of brown trout is considered.

5.7 Discussion

5.7.1 Quality and suitability of simulated stream temperature and streamflow

Although some biases were observed for both Q and Tw in the previous chapter (see Figure 4.12, p. 103 and Figure 4.20, p. 114), we found significant correlations between modeled and observed trends in seasonal and annual Q, with the exception of summer (Figure 5.1), and Tw, with the exception of fall (Figure 5.3). The low correlation value found in summer Q (Figure 5.1) originated from poor simulation at very few stations all located in HER B. Two of these stations gauged catchments where numerous small ponds were found and the highly decreasing observed trends might be due to the increasing evaporation from these ponds which were obviously not included in the EROS hydrological model. This was also true in a lesser extent for the other hydrometric station, in which a canal followed a large part of the course of the river and might play a similar role with respect to summer evaporation trends. Apart from these specific stations, in summer, a coherence as good as in other seasons was found between trends in simulated and observed Q. Moreover, the spatial pattern in simulated Q trends, with significant decreases in the southern headwaters, was consistent with observations at the high-quality reference hydrometric stations (Giuntoli et al., 2013, their figure 5).

The low correlation between simulated and observed Tw trend found in fall (Figure 5.3) originated from two stations with 8-13 years Tw data while such correlation was really good at stations on the Loire and Vienne rivers with longer (20-40 years) Tw data. Therefore, poor correlation in fall could be due to insufficient Tw data at these two stations. Moreover, consistent with Moatar and Gailhard (2006) and Arevalo et al. (2020), we found no trend ($p > 0.05$) in both observation and simulation at Loire (Dampierre) in winter.

5.7.2 Agreement between trends in observed and simulated stream temperature

T-NET simulations over the 1963–2019 period show significantly increasing trends in Tw for almost all reaches over the Loire basin across seasons, with an increase of +0.38°C/decade on average at the annual scale. To the best of the authors' knowledge, the present study is one of the very few studies using modeled Tw to investigate past trends at a large scale (but see Van Vliet et al., 2011; Isaak et al., 2012, 2017; Wanders et al., 2019). Table 5.7.2, summarizing recently published findings based on observations over Europe, demonstrates that the present results are consistent with past trends observed in other European basins with clear increases in Tw over the recent decades. It also shows that the much larger scale and finer spatial resolution of the current study clearly stands out as unique. Although start year, end year and length of the study period can have a significant influence on trend estimates and trend detection (Arora et al., 2016), comparing trends with other studies conducted over different periods gives a comprehensive view upon the overall magnitude of changes in Tw and possible related drivers.

Global-scale stream temperature modelling suggests trends in annual averages (over the 1960–2014 period) ranging from +0.2 to +0.5 °C/decade over France (Wanders et al., 2019), which is consistent with our findings (mostly in the range of +0.2 to +0.4 °C/decade, Figure 5.7, top panel). The pronounced trends are in spring and summer, which was also found in other parts of Europe (e.g Kędra, 2020; Arora et al., 2016; Michel et al., 2020). Considerable discrepancies are also found between Tw and Ta trends across seasons for the majority of the reaches (see Figure 5.5, and 5.9), which is a common finding for other sites around the world (Arora et al., 2016; Wanders et al., 2019). This highlights that changes in Ta may not be the only driver of changes in natural Tw.

Table 5.2: Recent studies on Tw trends in Europe. A comprehensive review of the relevant literature published prior to 2016 can be found in Arora et al. (2016). Magnitudes with unspecified season are related to annual scale. Notice that except present study, the others used observed Tw.

Country	Sites	Period	Rate of change (°C/decade)	Reference
France	**52 278 reaches in the Loire basin**	**1963–2019**	**+0.17– +0.72 (Mean=+0.38)** **+0.01 to +0.65 (+0.35) in winter** **+0.11 to +0.76 (+0.38) in spring** **+0.08 to +1.02 (+0.44) in summer** **+0.05 to +0.81 (+0.33) in fall**	**Present study**
Austria	18 rivers	2010–2017	+1.9 to +3.2 in summer	Niedrist and Füreder (2021)
England	6148 sites	2000–2018	-0.4	Wilby and Johnson (2020)
Switzerland	31 rivers	1979–2018	+0.33 (±0.03) +0.6– +1.1 in summer	Michel et al. (2020)
Poland	5 Carpathian rivers	1984–2018	+0.33 to +0.92 +0.82 to +0.95 in spring +0.75 to +1.17 in summer +0.51 to +1.08 in fall +0.25 to +0.29 in winter	Kędra (2020)
France	11 stations on Loire, Vienne, Rhône, Seine, Meuse	1980-2015	+0.79 in spring	Maire et al. (2019)
Poland	6 stations on Warta River	1960–2009	+0.096 to +0.28	Ptak et al. (2019a)
Croatia	6 stations on Kupa River	1990–2017	+0.23 to +0.796	Zhu et al. (2019)
Switzerland	Rhine, Rhône, Aar, and Thur rivers	1983–2013	+0.27 (± 0.03)	Zobrist et al. (2018)

Table – continue

Country	Sites	Period	Rate of change (°C/decade)	Reference
Northern Germany	132 sites	1985–2010	+0.3 (±0.03)	Arora et al. (2016)
		1985–1995	+0.69 (±0.10) in spring +0.78 (±0.06) in summer +0.75 (±0.09) in fall +0.39 (±0.23) in winter +0.81 (±0.2)	
	475 sites	2000–2010	+0.9 (±0.07)	
England and Wales	2773 sites	1990–2006	+0.3 (±0.02)	Orr et al. (2015)
Poland	Coastal rivers (Rega, Parsęta, Słupia, Łupawa, Łeba)	1971–2015	+0.26 to +0.31 +0.46 in April (The month with the highest trend)	Ptak et al. (2016)
France	4 stations on Loire River	1976–2003	+0.61 to +0.71 +0.86 to +1.07 in spring and summer	Moatar and Gailhard (2006)

5.7.3 Drivers and spatial patterns

Consistent with our findings (see Figure 5.10), (Moatar and Gailhard, 2006) found Tw increased faster than Ta in spring and summer and at the annual scale for all 4 stations on the Loire River. (**?**) also found Tw trends $>$ Ta trends in summer. In Switzerland, (Michel et al., 2020) described an increase of $+0.33 \pm 0.03$ °C/decade in Tw, resulting from the joint effects of an increase in Ta ($+0.39 \pm 0.14$ °C/decade) and decreasing in Q (-10.1 ± 4.6%/decade) over the 1979–2018 period. In contrast with our results, they found Tw trends lower than Ta trends due to influence of snow melt and glacier melt in Alpine catchments. Consistent with their findings, (Orr et al., 2015) also found Tw trends $<$ Ta trends in UK. They suggested the such difference between Tw and Tw trends could be as a result of different processes driving Tw. In the current study, we found spatial coherence between trends in Tw and trends in Ta and Q. Indeed, the greatest increases in Tw (up to +1 °C/decade) were predominately located in the southern part of the basin, in HER A (Massif Central) where a greater increase in Ta (up to +0.71 °C/decade) and a greater decrease in Q (up to -16 %/decade) occurred jointly. We also found, at the majority of reaches where Tw trend $>$ Ta trend, decreasing Q trends occurred coincidentally for all seasons (with the exception of winter) (see Figure 5.9).

The decrease in Q could itself be due to a significant increase in potential evapotranspiration (PET) (up to +10 %) over the whole of basin and a decrease (mostly non-significant) in total precipitation (P) (up to -5 %/decade) (Figures 5.24 and 5.25). Such trends, computed here based on variables from the SAFRAN surface meteorological reanalysis (Vidal et al., 2010), are consistent with larger-scale studies (see e.g. Spinoni et al., 2017; Tramblay et al., 2020; Hobeichi et al., 2021). Moreover, Vicente-Serrano et al. (2019) attributed annual streamflow trends in southern France mostly to trends in precipitation and potential evapotranspiration, as opposed to irrigation and land-use changes that have additional strong effects e.g. in the Iberian peninsula. We also observed, for the majority of reaches where Tw increased less than Ta, an increase in Q occurred jointly suggesting that increase in Q or in other words increase in thermal inertia could also explain the discrepancy between Tw and Ta trends at these reaches (see Fig 5.9).

A strong synchronicity between Ta and Tw anomalies is observed in the present study in the warmest years, and these years are also among those with the largest negative Q anomalies (see Figures 5.15). Indeed, increase in summer Tw could be due to co-occurrence with the increase in summer Ta (average correlation: +0.82), and with decrease in summer Q (average correlation: -0.40). These findings are consistent with those of Michel et al. (2020): average Tw-Ta correlation: +0.61, and average Tw-Q correlation: -0.66. For the middle Loire river, Moatar and Gailhard (2006) found that the increase in Ta (resp. decrease in Q) explain 60 % (resp. 40 %) of the increase in Tw. Moreover, the significant change-point in Tw, Ta and Q time series in the late 1980s has also been found in other studies in Europe (Moatar and Gailhard,

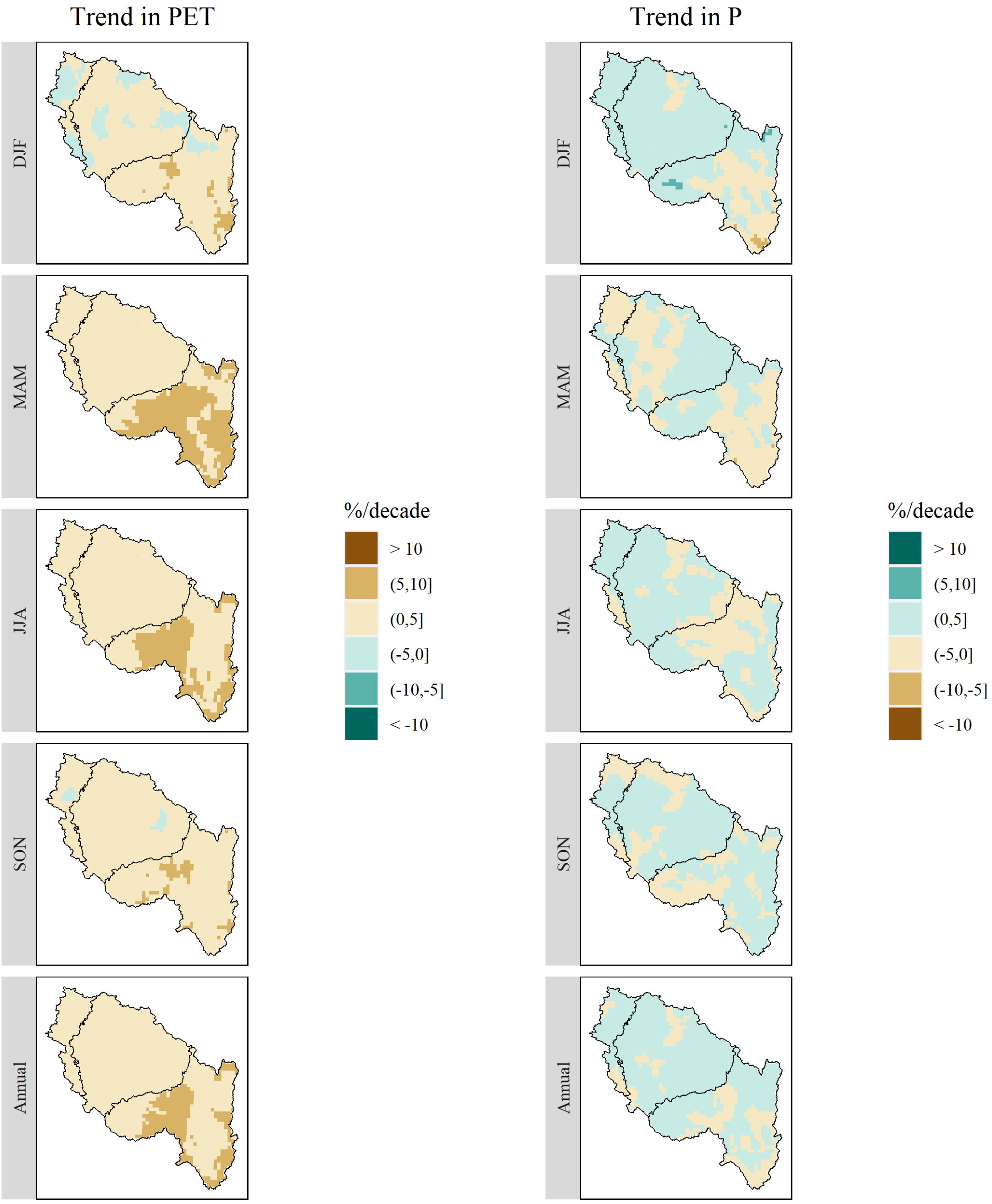

Figure 5.24: Spatial variability of trends in seasonal and annual potential evapotranspiration (PET) and total precipitation (P) over the 1963–2019 period. The solid black lines are showing the borders of HER (see Figure 2.1, p. 44).

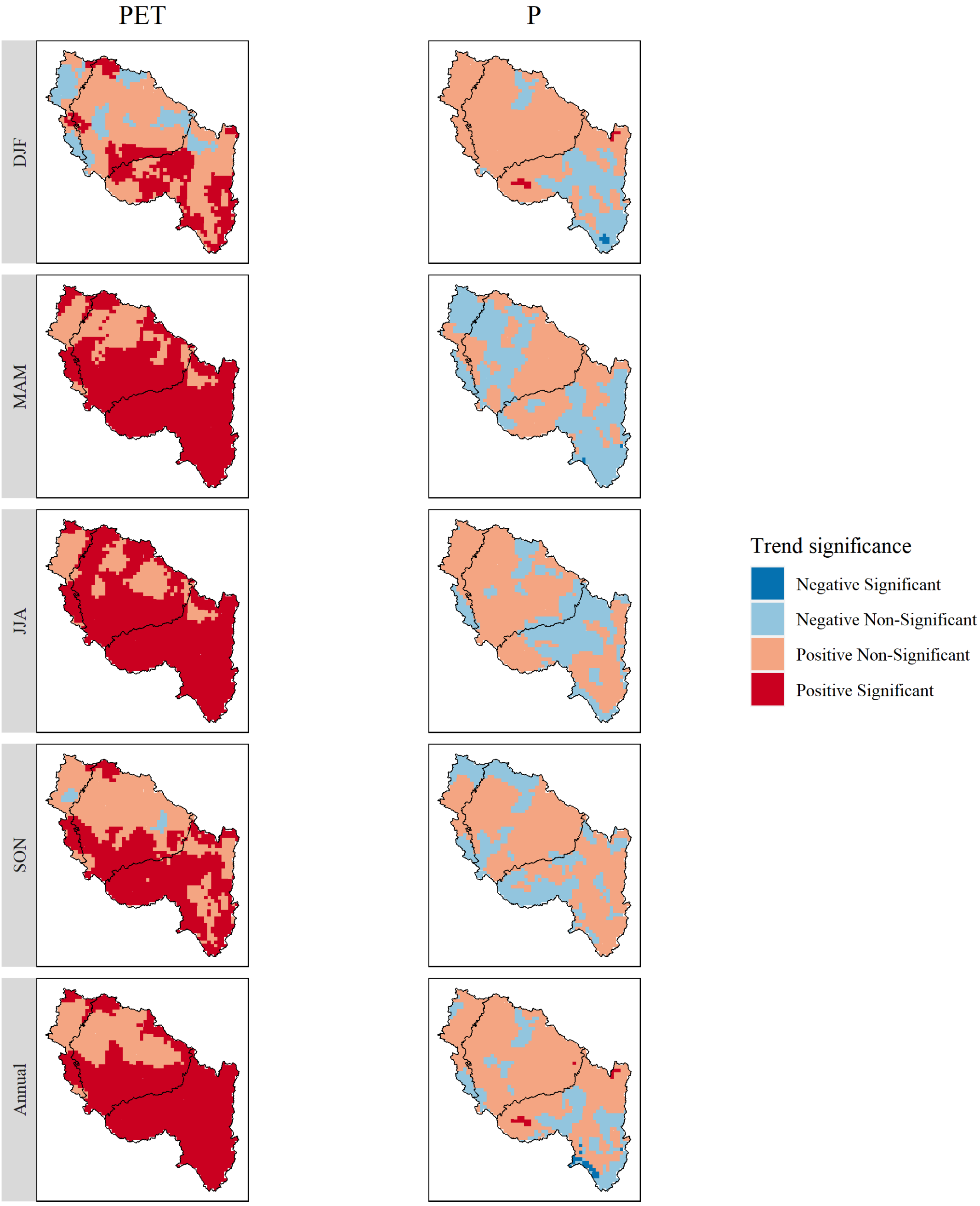

Figure 5.25: Spatial variability of the significance level of trends in seasonal and annual P and PET over the 1963–2019 period. The solid black lines are showing the borders of HERs (see Figure 2.1, p. 44).

2006; Arora et al., 2016; Zobrist et al., 2018; Ptak et al., 2019b; Michel et al., 2020). Long-term observational time series of the Loire at Dampierre also displays a similar change-point.

Trends in Tw might also be explained by trends in additional drivers, like shortwave radiation (Wanders et al., 2019), which is the dominant flux at the air-water interface, and is notably increasing over Europe (Sanchez-Lorenzo et al., 2015). This might explain discrepancies between Tw and Ta trends in spring and summer, when no decreasing trend in Q is found (see Figure 5.5).

The current study suggests that Ta and Q could exert a joint influence on Tw, based on an analysis of the spatial coherence and temporal synchronicity of these variables. Assessing causal influence of these factors on Tw trends is left for future research. In this regard, one could devise a formal attribution framework where one may e.g. remove trends in Q and trends in Ta alternatively in T-NET inputs.

5.7.4 Natural trends and anthropogenic influence on stream temperature

Natural Tw time series are used in the current study for detecting trends, as both the EROS and the T-NET models are used in a non-influenced set-up (see section 4.1, p. 85 and section 4.2, p. 89). However, anthropogenic impoundments (e.g., large dams, small reservoirs, and ponds) affect downstream Tw regimes in a diversity of ways that depend on their structure and position along the river continuum (see section 3.5; and Figure 3.18, p. 80). In this regard, on the one hand, large dams, by releasing cold hypolimnetic water in summer, can lower downstream Tw (Olden and Naiman, 2010, and see Figure 3.18, p. 80), and mitigate increasing trend in Tw (Cheng et al., 2020). Nevertheless, it is anticipated that a considerable proportion of streams regulated by large reservoirs may still warm with climate change (Null et al., 2013), and experience high temperatures and low flows under future climate change (Cheng et al., 2020). The mitigating influence of dams could be of importance for streams in the southern headwaters of the Loire basin since this area both experience the greatest Tw trends and gathers most of existing large dams (see Figure 2.1 (right panel), p. 44).

On the other hand, ponds and shallow reservoirs, by releasing warm water can increase downstream Tw (Zaidel et al. (2020); Chandesris et al. (2019); and see section 3.5 and Figure 3.18, p. 80) and exacerbate increasing trends in Tw (Wanders et al., 2019; Michel et al., 2020). The impacts of such reservoirs on Tw can be more pronounced than large dams (Sinokrot et al., 1995). In fact, given the potential climatic changes, the aquatic ecosystem downstream of such impoundments will experience higher Tw (Gooseff et al., 2005; Fang and Stefan, 2009; Ali et al., 2016). The warming effect of such surface waters in the current study seem more significant for streams located in lowlands in the middle and north of the Loire River basin where most of the shallow reservoirs are located (see Figure 2.1 (right panel), p. 44). In these streams, anthropogenically-induced trends in Tw may be greater than natural ones, and the warming process can get worse through the increasing demand for storing water in small reservoirs for irrigation. Nevertheless, the warming effect can be local, and unregulated streams being located close to such regulated streams may show limited to no warming (Wanders et al., 2019).

Note that although there are nuclear power plants in the Loire basin, their impacts on Tw is considered negligible according to Moatar and Gailhard (2006) and Bustillo et al. (2014). Moreover, it was observed in the current study that the Tw trend at Belleville located in upstream of power plants and consequently, not influenced by them, had the same trend magnitude as the other three stations located downstream (see Figure 5.4), showing a negligible influence of nuclear power plants on Tw trends.

5.7.5 Implications for river management and aquatic biota

The removal of riparian vegetation can increase Tw (Caissie, 2006), and changes in Tw can be even more sensitive to changes in riparian vegetation than to changes in Ta or Q (Wondzell et al., 2019). Here, in small streams, an increase of > 25 % of riparian shading (from < 15 % to > 40 %) can decrease the median trend in spring and summer Tw by up to 0.16 °C/decade (Figure 5.20). Spring and summer Tw trends are more pronounced in large rivers, especially in the south of the basin, with a difference in median Tw trends of up to +0.18 °C/decade (Figure 5.19), probably due to a decrease in Q (up to -2 %/decade, see Figure 5.26), a greater thermal sensitivity, and the absence of mitigating factors like riparian vegetation shading or groundwater inputs (Kelleher et al., 2012; Beaufort et al., 2020a).

Restoring riparian vegetation and shading can therefore substantially mitigate future increases in Tw. In addition, riparian restoration may lessen the impacts of climate change on flood damage to human infrastructure, on riparian biodiversity, on ecosystem vulnerability and on changes in Q (Palmer et al., 2009; Seavy et al., 2009; Perry et al., 2015). However, riparian restoration is not an easy task since the survival, persistence, growth rate of planted species as well as required time for thermal regime recovery under possibly severe future conditions should be studied beforehand (Perry et al., 2015). For instance, it may take between 5 and 15 years for rivers to recover their thermal regime following vegetation growth (Edmonds et al., 2000; Caissie, 2006). Moreover, the efficacy of riparian planting is also highly dependent upon the type and structure of forest stands (Dugdale et al., 2018), and this should also be considered in long-term projects.

Stream warming affects cold-water fish populations negatively at the warmer boundaries of their habitat (Hari et al., 2006). In the Loire basin, this issue may have a high importance in HER A with the most pronounced trends. In this regard, there is an increasing trend in the number of days with Tw higher than juvenile brown trout's lethal temperature (17 °C), in all HERs (trend=4 day/decade i.e. +22 day over the 1963–2019 period; see Figure 5.22) in rivers with a non-zero density of brow trout. Moreover, the vulnerability of this species double

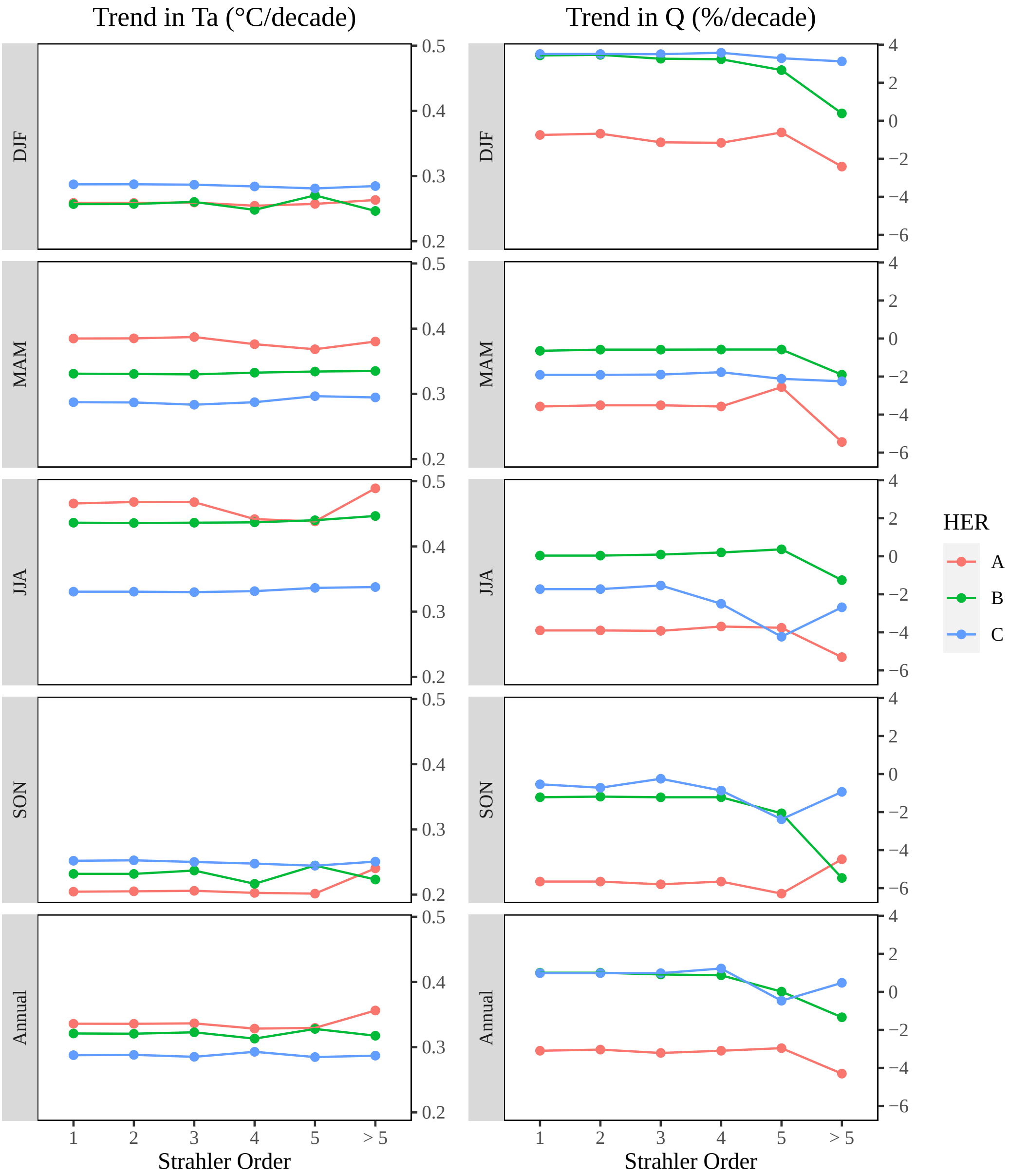

Figure 5.26: Relationships between median trends in Ta and Q over the period 1963—2019 and reach size (large rivers:Strahler order ⩾ 5).

over the 1963–2019 period. Furthermore, changes in spawning and migration timing (McCann et al., 2018; Arevalo et al., 2020), decreases in habitat availability and freshwater quality for organisms (Lennox et al., 2019), and shifts in species distribution (Comte et al., 2013) are already observed consequences of the long-term increase in Tw. Some major changes in fish density and community structure has already been reported in large rivers in France (Maire et al., 2019) for which we also found greater trends in Tw compared to small ones. Therefore, physical process-based thermal models like T-NET can also be used to assess the various stresses on freshwater habitat sustainability due to changes in Q and Tw (Morales-Marín et al., 2019).

5.8 Conclusion on past trends

Regional trends Tw at the reach resolution are detected and assessed by using the physical process-based T-NET model coupled with the semi-distributed EROS hydrological model over the Loire basin. Using model outputs across 52 278 reaches over the Loire basin, for 3 variables (Ta, Q, and Tw), and 5 time scales (4 seasons plus annual), consistent increasing Tw trends at the scale of the entire Loire River basin are found, regardless of the season (annual mean = +0.38 °C/decade). Increases are greatest in spring and summer with a median increase of +0.38 °C/decade (range=+0.11 to +0.76 °C/decade) and +0.44 °C/decade (+0.08 to +1.02 °C/decade), respectively. Critically, the rate of warming for stream temperature is in the majority of cases higher than the rate of atmospheric warming, suggesting a decoupling of thermal trajectories linked to decreasing Q, especially in the southern headwaters (the Massif central, HER A). Indeed, the results show that the greatest increase in Tw (up to 1 °C/decade) are in regions where the greatest increase in Ta (up to +0.71 °C/decade) and the greatest decreases in streamflow (up to -16 %/decade) occur coincidentally. Moreover, a significant change-point is detected in Tw, Ta and Q time series in the late 1980s.

The synchronicity of extreme events of low flows and high stream temperature in the southern headwaters will likely generate a double penalty for existing cold-water aquatic communities. However, riparian shading in small mountainous streams may mitigate such warming. In fact, an increase of $> 25\,\%$ of riparian shading (from $< 15\,\%$ to $> 40\,\%$) can decrease the median trend in spring and summer Tw by up to 0.16 °C/decade.

These findings underscore that Ta alone is likely not an adequate proxy to explain stresses and shifts experienced by aquatic communities over time and space, especially in regions with more pronounced stream warming, and thus there is a need to grow and maintain Tw sensor networks (see Figure 2.5 p. 47 showing a decline in number of Tw stations over the Loire River basin). This knowledge can help to develop appropriate management strategies to conserve thermal refugia and mitigate extreme thermal events induced by climate change.

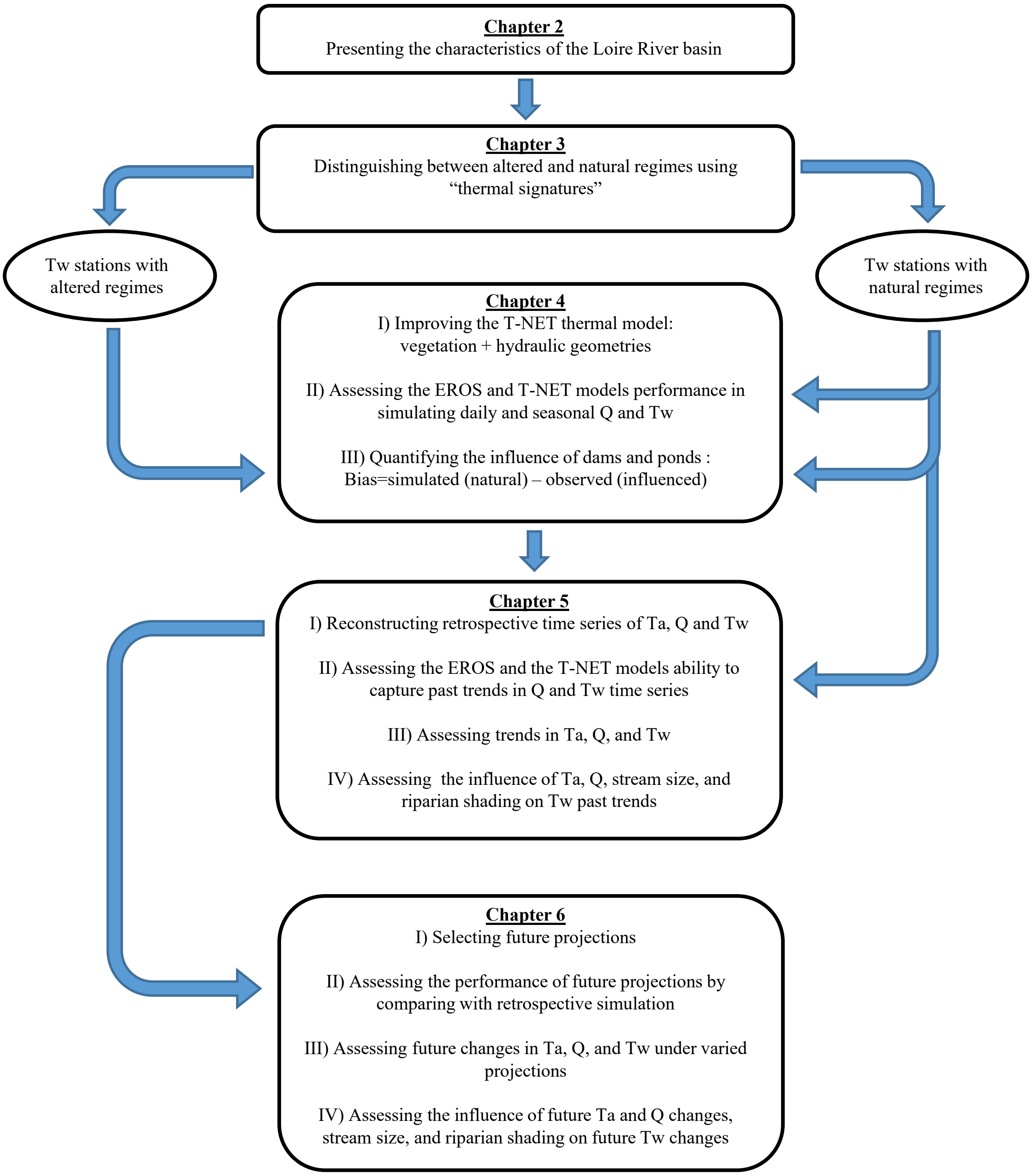

Schematic diagram illustrating thesis objectives.

CHAPTER 6

Future projections of stream temperature

In the previous chapter, it was observed that Tw increased for almost all reaches in all seasons over the past 57 years (1963–2019) with the greatest increase in spring and summer. Rates of Tw increases are greater than for Ta across seasons for the majority of reaches as a result of joint effects of the increase in Ta and decrease in Q, and possibly other factors. These findings raised a question concerning Tw changes in the future. Some studies already anticipated Tw warming will continue, and be more pronounced for the extreme scenarios and towards the end of the century (e.g., Mantua et al., 2010; van Vliet et al., 2013; Bustillo et al., 2014; Du et al., 2019; Michel et al., 2021). Nevertheless, so far, few studies assessed future Tw at a large scale and a high spatial resolution. Hence, there is still a weak understanding of the heterogeneity of magnitude of Tw changes under future climate change at a large scale and a high spatial resolution. Moreover, it is of high interest to understand such changes in Tw in relation to hydroclimate changes and landscape diversity in the future. Such knowledge underpins the mitigation and management strategies for preserving aquatic communities already under pressure.

To address this issue, scenarios of changes in the magnitude or Tw over the 21st century, and the influence of hydroclimate changes and landscape diversity on such changes are studied here at the scale of the Loire River basin and at the reach resolution. To do so, first, a subset of the new future climate projections over France (the DRIAS-2020 dataset, Soubeyroux et al., 2020) are selected. Note that this study is the first one using projections from the DRIAS-2020 dataset for hydrological and thermal projections. Then, the meteorological variables provided by these selected future projections are used in both the EROS hydrological model and the T-NET thermal model. The EROS model is first run to produce daily Q under varying selected future climate projections over the whole 21st century. Projected daily Q is then used in the T-NET thermal model to produce daily Tw under these climate and hydrological projections. The present-day performance of projections is assessed by comparing projections to the retrospective simulation obtained from the past analyses in the previous chapter over a recent historical period (section 5.3, p. 137). Model outputs are then used to compute the magnitude of changes in Ta, Q, and Tw under varying climate projections. To understand the relative influence of changes in Ta and Q on changes in Tw as the main hydro-climate drivers, their temporal patterns and spatial variability are compared. Afterward, future Tw as a function of stream size and riparian shading is studied. Finally, possible future stress on the brown trout, a common cold-water fish in the basin, is assessed as the result of changes in future Tw. In assessing future changes, the retrospective simulation obtained from the previous chapter is also used as a control for the past and present period, and as a reference for the future.

6.1 Selection of future climate projections

Changes in the concentration of greenhouse gases (GHG), are the main cause of observed current changes and future climatic conditions. The evolution of these GHG depends on a set of factors such as population growth, socio-economic and technological developments, and future policies choices (Soubeyroux et al., 2020). Since accurately predicting the evolution of these factors is not possible, climatologists use four Representative Concentration Pathways ("RCP") of GHG emissions corresponding to the fifth report of the Intergovernmental Panel on Climate Change (IPCC, 2014). The IPCC is the United Nations body for assessing the science related to climate change (https://www.ipcc.ch/). These four RCPs were selected from over 1000 available scenarios (Figure 6.1), and span between two extreme scenarios (RCP 2.6 and RCP 8.5) and two intermediate scenarios (RCP 4.5 and RCP 6.0). Each of them corresponds to a plausible representation of the future behavior of human societies. RCP 2.6 describes a world virtuous, very low in greenhouse gas emissions in which warming overall remains below 2 °C compared to pre-industrial temperatures. RCP 8.5 shows the situation when any politics of climate regulation are disregarded, leading to approximately 5 °C of global warming by the end of the century. RCP 4.5 and RCP 6.0 scenarios describe intermediate paths. RCP 6.0 continues to grow before the end of the century, then decreases at a higher rate than RCP 2.6. The RCP 4.5 also continues to grow for a few decades, then stabilizes before the end of the 21st century. An overview of these RCPs can be found in Van Vuuren et al. (2011).

The above RCPs are used as inputs of Global Climate Models (GCMs) for simulating the evolution of global climate. However, the resolution of GCMs is very coarse (between 150 and 200 km) leading to misrepresentation of the local meteorological phenomena and extreme events. To have a finer resolution of GCMs, Regional Climate Models (RCMs) are used. RCMs have a high spatial resolution (from 10 to 20 km), allowing to have a better representation of local climate (reliefs, land-sea contrasts, complex coastlines). In the current study, the DRIAS-2020 dataset is employed (Soubeyroux et al., 2020), which is based on simulations of regional climatic conditions at a high spatial resolution (DRIAS: http://www.drias-climat.fr/,

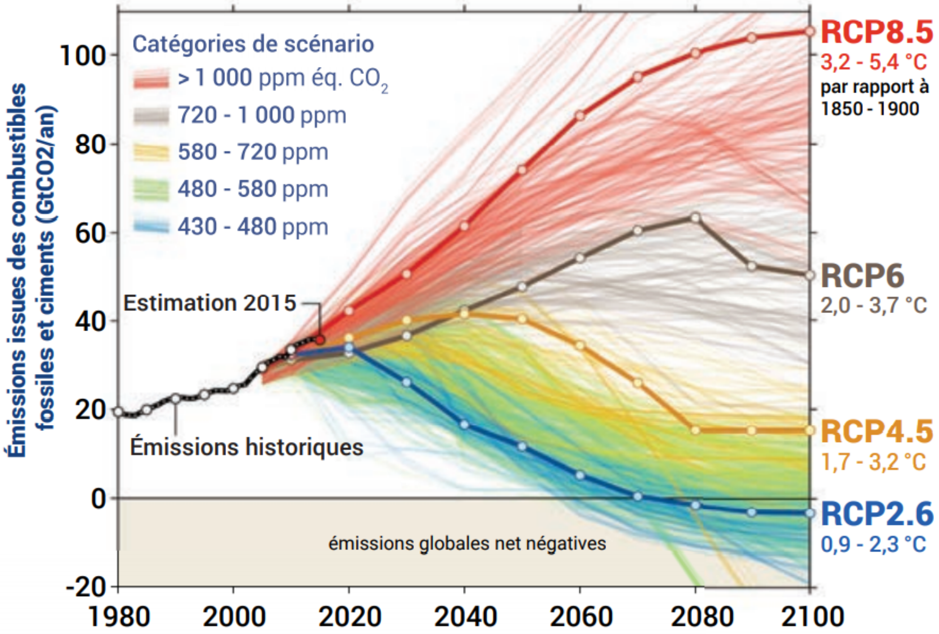

Données : CDIAC/GCP/IPCC/Fuss et al 2014

Figure 6.1: Evolution of emissions between 1980 and 2100 according to the different available scenarios. The four selected RCPs corresponding to the 5th report of IPCC (IPCC, 2014) are highlighted. Source: Global Carbon Project. This Figure is adopted from (Soubeyroux et al., 2020, see http://www.drias-climat.fr).

portail partenarial Météo-France, IPSL, Cerfacs.) from the Euro Cordex set corrected by a statistical bias correction method, ADAMONT (Verfaillie et al., 2017). The ADAMONT method allows correcting the distribution of simulated variables and making it consistent with the distribution of observed variables, using a climatology by season and other time periods. Therefore, the implementation of this method requires a set of reference observations for the current climate. The DRIAS-2020 dataset provides regionalized climate projections produced in French climate modeling laboratories (IPSL, CERFACS, CNRM) for the most recent RCPs presented in the fifth report of IPCC (IPCC, 2014).

For the DRIAS-2020 dataset, there are two periods of data: 1) the period with GCMs forced by historical observed concentrations in GHG between 1950 and 2005, and 2) the projection part using RCPs as forcings, which extends from 2006 to 2100. The 1976-2005 period is the reference period used to correct the biases of climate characteristics in projections with ADAMONT method (Verfaillie et al., 2017) with reference to the observed climate provided by the SAFRAN surface reanalysis (Quintana-Segui et al., 2008; Vidal et al., 2010, see section 2.3.1,p. 46 for more information about SAFRAN). The detailed information about different available GCM/RCMs and RCPs provided by the DRIAS-2020 dataset are presented in Table 6.1.

Table 6.1: The GCM/RCMs and RCPs provided by the DRIAS-2020 (Soubeyroux et al., 2020). The rows in green are showing the GCM/RCMs and RCPs used in this study. More information can be found in http://www.drias-climat.fr/. A review on RCPs can be found in Van Vuuren et al. (2011).

GCM	RCM	HISTO	RCP 2.6	RCP 4.5	RCP 8.5	Data period
CNRM-CM5	ALADIN63 V2	✓	✓	✓	✓	1951-2005; 2006-2100
Voldoire et al. (2013)	Colin et al. (2010); Bador et al. (2017)					
CNRM-CM5	Racmo22E V2	✓	✓	✓	✓	1950-2005; 2006-2100
Voldoire et al. (2013)	Van Meijgaard et al. (2012)					
IPSL-CM5-MIR	WRF381P	✓		✓	✓	1951-2005; 2006-2100
Dufresne et al. (2013); Hourdin et al. (2013)	Skamarock et al. (2008)					
IPSL-CM5-MIR	RCA4	✓		✓	✓	1970-2005; 2006-2100
Dufresne et al. (2013); Hourdin et al. (2013)	Kjellström and Ruosteenoja (2007) Kjellström et al. (2016)					
HadGEM2-ES	RegCM4-6	✓	✓		✓	1970-2005; 2006-2099
Jones et al. (2011)	Giorgi et al. (2012)					
HadGEM2-ES	CCLM4-8-17	✓		✓	✓	1950-2005; 2006-2099
Jones et al. (2011)	Keuler et al. (2016)					
EC-EARTH	Racmo22E V2	✓	✓	✓	✓	1950-2005; 2006-2100
Hazeleger et al. (2012, 2013)	Van Meijgaard et al. (2012)					
EC-EARTH	RCA4	✓	✓	✓	✓	1970-2005; 2006-2100
Hazeleger et al. (2012, 2013)	Kjellström and Ruosteenoja (2007) Kjellström et al. (2016)					
MPI-ESM-LR	CCLM4-8-17	✓	✓	✓	✓	1950-2005; 2006-2100
Stevens et al. (2013); Jungclaus et al. (2013)	Keuler et al. (2016)					
MPI-ESM-LR	REMO (2009)	✓	✓	✓	✓	1970-2005; 2006-2100
Stevens et al. (2013); Jungclaus et al. (2013)	Jacob et al. (2012)					
NorESM1-M	HIRHAM5 V3	✓		✓	✓	1951-2005; 2006-2100
Drange et al. (2012); Iversen et al. (2012)	Christensen et al. (1998)					
NorESM1-M	REMO (2015)	✓	✓		✓	1950-2005; 2006-2100
Drange et al. (2012); Iversen et al. (2012)	Jacob et al. (2012)					

For a given RCP, the simulated climate differs from one model to another, which reflects our imperfect understanding of the climate system. To take into account model uncertainty, and better represent the range of possible futures, it is, therefore, necessary to consider large sets of climate projections. In this regard, here, three different GCM/RCMs are selected, covering the dispersion of annual changes in P and Ta under RCP 8.5 over France at the end of the century. These GCM/RCMs include warm and wet (IPSL-CM5A/MRWRF381P), intermediate (CNRM-CM5-LR/ALADIN63), and hot and dry (HadGEM2/CCLM4-8-17) models to project future daily Q and Tw (see Figure 6.2). The detailed information about these selected GCM/RCMs can be found in Table 6.1 in green.

The selected GCM/RCMs are also among the "short list" of future climate models proposed by Météo-France for reducing the number of models and calculations time as there are many projections (total=30). This list contains GCM/RCMs that are representative of the dispersion of the other 12 GCM/RCMs of the DRIAS-2020 dataset. Moreover, these GCM/RCMs keep the dispersion of changes in P and Ta under RCP 8.5 at the end of the century as shown by Figure 6.2 on the annual basis. Such a representation of summer and winter periods are presented in Figures E.1 and E.2.

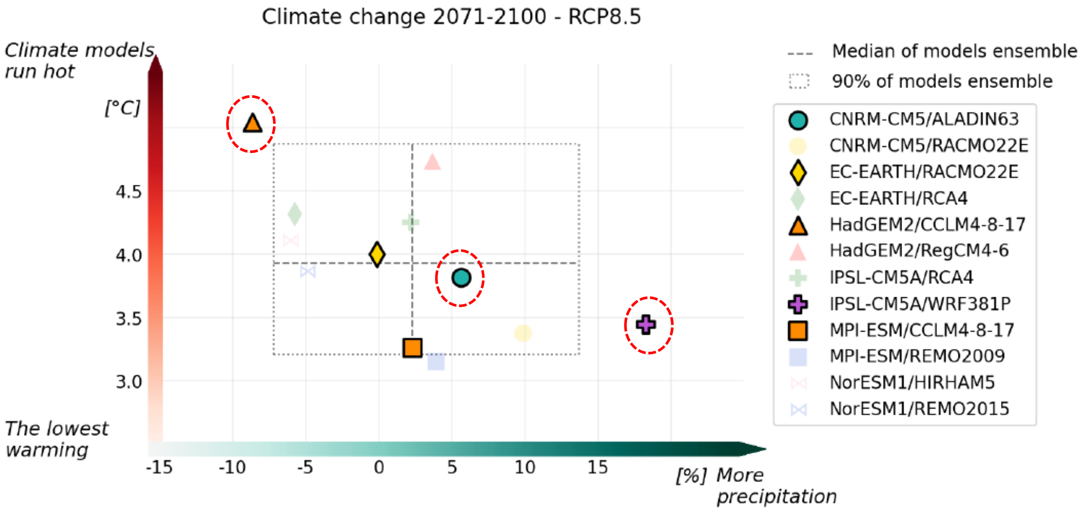

Figure 6.2: Annual changes in P (x-axis) and Ta (y-axis) over France at the end of the century (2071-2100) with respect to the 1976–2005 period (historical period) under RCP 8.5. The sharp points are the "short list" of future climate models proposed by Météo-France. The red dashed circles show the selected GCM/RCMs in the current study. This figure is adopted from DRIAS-2020 (Soubeyroux et al., 2020, http://www.drias-climat.fr).

Although there are several studies on the evolution of meteorological droughts and intense rainfall events in France as the result of climate change based on the fourth report of IPCC (see https://professionnels.ofb.fr/fr/node/43surf), this study is the first one that uses future climate projections provided by DRIAS-2020 based on the fifth report of IPCC for hydrological and thermal projections (but see Dayon et al., 2018, who used CMIP5 GCMs downscaled using another approach and not the DRIAS-2020 dataset).

6.2 Running the EROS and T-NET models under projections

The meteorological variables provided by the selected future climate models (green rows in Table 6.1) are integrated into both the EROS and T-NET models. Both the EROS and T-NET models are run under constant land cover/land use. The EROS model is first executed to produce daily Q under each projection (total= (2 GCM/RCMs × 2 RCP) + (1 GCM/RCM × 3 RCP)= 7 projections; see section 6.1) over the historical period (1950–2005) and the future (2006–2099). Indeed, for each projection, the EROS model is run from the 1950s to the 2100s while for RCPs of a GCM/RCM, the historical part (1950-2005) is the same. Note that calibrated parameters for the EROS model are kept as for the retrospective simulation. Then, future daily Q and meteorological variables provided by GCM/RCMs are used in the T-NET thermal model to produce daily Tw under these future climate projections over the whole century (1950–2099). Please note that, although selected GCM/RCMs have data from the 1950s, both hydrological and thermal models are used from the 1970s, onwards, when Q and Tw observations are available.

6.3 Performance of future projections

To see the performance of selected projections (7 in total), three main steps are defined:

1. Comparing meteorological variables in projections and in the SAFRAN reanalysis data over the 1976–2005 period;
2. Comparing absolute values of Tw in projections and in the retrospective simulation (driven by SAFRAN) over the 1976–2005 period;
3. Comparing recent trend magnitudes and significance levels of Tw in projections and in the retrospective simulation (driven by SAFRAN) over the whole 1976–2019 period.

Note that, in the following, for the sake of simplicity, figures including all GCM/RCMs, are presented from the wettest GCM/RCM (IPSL-CM5A/WRF381P) to the hottest one (HadGEM2/CCLM4-8-17) i.e. from left to right or top to bottom in a figure or a table. A similar approach is also considered for RCPs i.e. the figures are presented from RCP 8.5 to RCP 2.6.

6.3.1 Comparing meteorological variables in projections and in the SAFRAN reanalysis data over the 1976–2005 period

The meteorological variables (e.g., Ta, liquid and solid P, and PET) provided by three selected GCM/RCMs are compared with the corresponding variables provided by SAFRAN over the historical period 1976–2005. These variables are important since they are used as the inputs for both the hydrological model and the thermal model. The 1976–2005 period is selected since it was the reference period used to correct the biases of climate projections with respect to SAFRAN (Soubeyroux et al., 2020). In other words, with this correction, it is expected that all climate characteristics of each GCM/RCM should be close to those of SAFRAN over the 1976–2005 period.

Figure 6.3 shows that there is an excellent correlation between the interannual mean of meteorological variables averaged over each sub-catchment in projections and in retrospective simulation (cor>0.9) across variables and GCM/RCMs, with the exception of PET of all GCM/RCMs (cor=0.51-0.55 across GCM/RCMs). The observed weak correlation between PET in projections and in the retrospective simulations could be due to the difference in the PET formula used for SAFRAN and for downscaled projections. Indeed, PET of SAFRAN is computed with the full Penman-Monteith (PM) equation including radiation (Allen et al., 1998), which is biased (differently according to elevation) and non-homogeneous in time (see Le Moigne et al., 2020). However, PET in DRIAS-2020 is computed by a different PM equation using a proxy for radiation (calculated by maximum Ta (Tx) and minimum Ta (Tn)), in order to use neither GCM/RCMs radiation nor SAFRAN radiation for the bias correction (see http://www.drias-climat.fr/accompagnement/sections/310 for PET calculation in projections).

The map of biases (Figure 6.4) shows that for a considerable number of sub-basins ($\approx$50 %), across GCM/RCMs, there is an overestimation in PET (5-10 %) across the basin. There is also a slight underestimation in rainfall across sub-basins, mainly in HER (-5-0 %). For snow, the range of the bias is different from one GCM/RCM to another, but the majority of sub-basins (50-60 % depending on the GCM/RCM) show significant overestimation ($>$ 20%). Finally, a very small overestimation is observed for Ta across GCM/RCMs (mostly in the range of 0-0.5 °C).

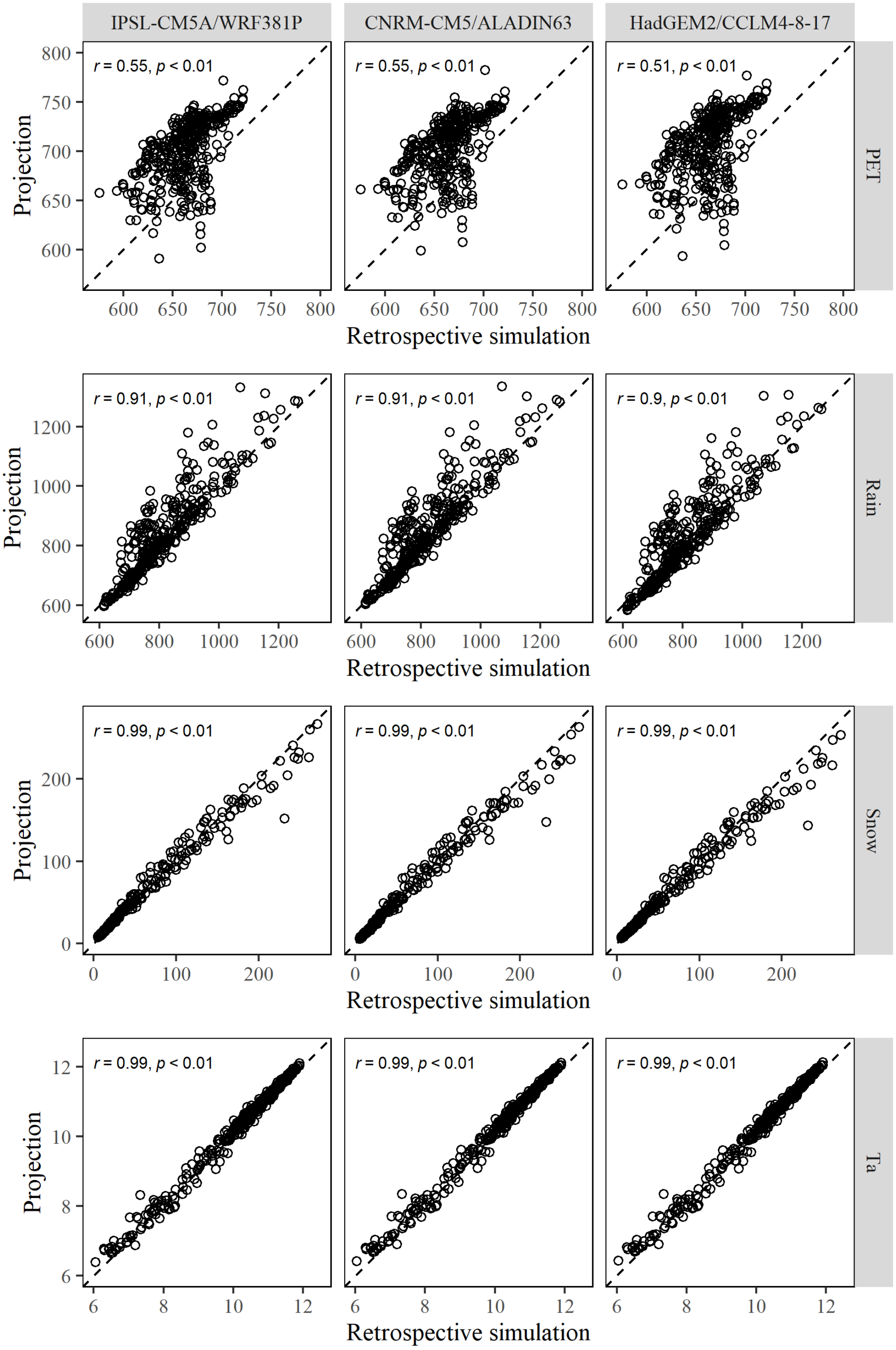

Figure 6.3: Comparing the interannual mean of meteorological variables (i.e., Ta (°C), liquid and solid P (mm), and PET (mm)) in projections and in the retrospective simulation (the SFARAN reanalysis data) for the 368 sub-basins over the 1976–2005 period. Each point is showing the average of the desired meteorological variable over the sub-basin. Pearson correlation and associated p-value are shown in the top left corner of each graph. The dashed line shows the 1:1 line in each graph.

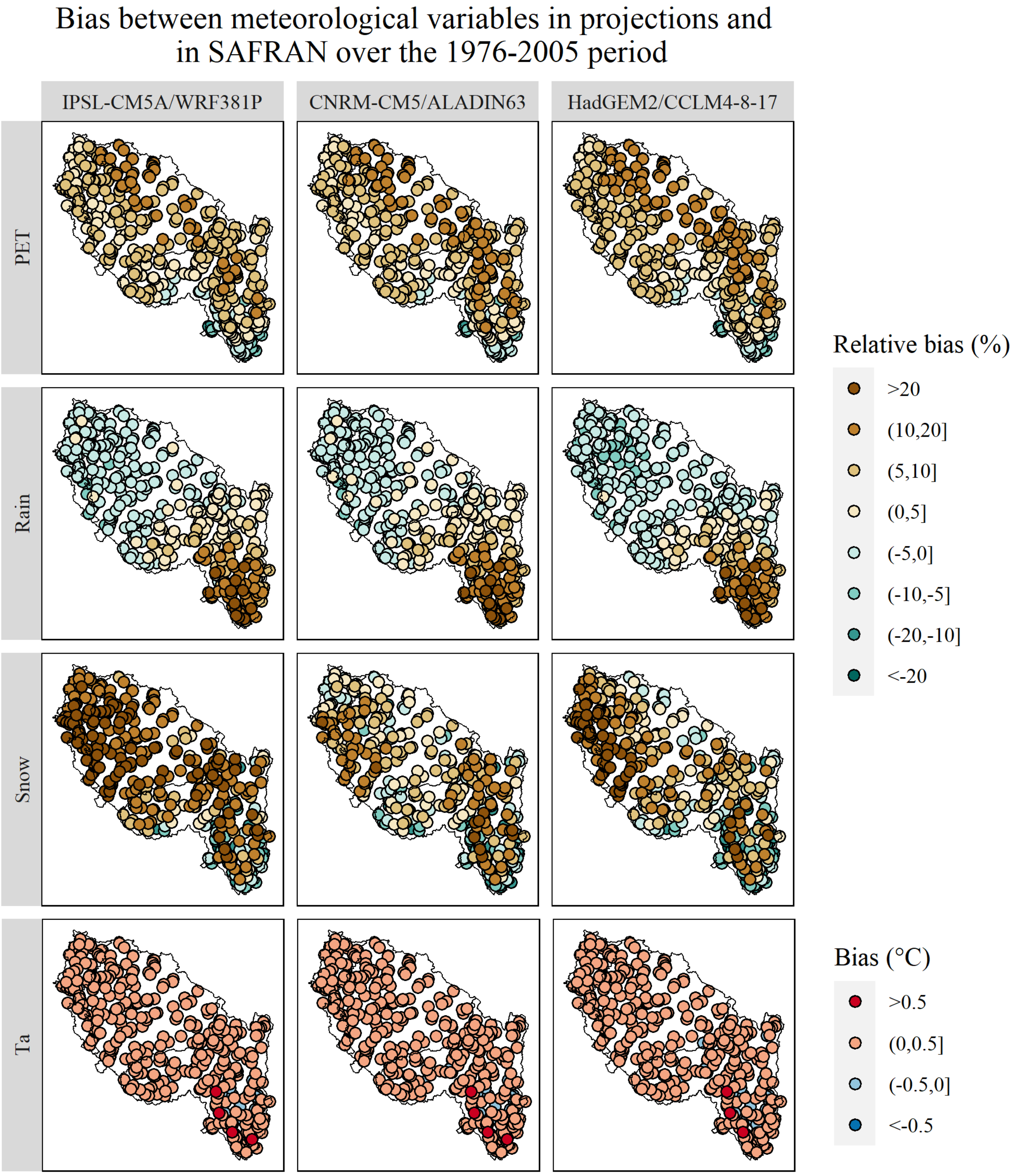

Figure 6.4: Map of relative bias or bias between the annual mean of meteorological variables in projections and in the SFARAN reanalysis data (the retrospective simulation) for the 368 sub-basins over the 1976–2005 period. For PET, liquid, and solid P, relative bias (%), and for Ta absolute bias (°C) are reported.

6.3.2 Comparing absolute values of stream temperature in projections and in the retrospective simulation over the 1976–2005 period

To assess whether projections are able to capture absolute values of Tw, the seasonal Tw in projections and in the retrospective simulation are compared over the 1976–2005 period. As the 1976–2005 period is a reference period for bias correction of future climate models, it is expected that Tw characteristics in projections and in the retrospective simulation would be close over this period. Note that retrospective Tw was simulated in the previous chapter by using meteorological variables from the SAFRAN reanalysis data.

Figure 6.5 shows that there is a slight overestimation in projected Tw across seasons and GCM/RCMs (median bias=0.13-0.43 °C). The Interquartile Range (IQR) remains small across GCM/RCMs and seasons (IQR=0.12-0.35 °C). The greatest biases across seasons and GCM/RCMs are in spring and summer (median bias=0.2-43 °C). Overall, the projections manage to get the right absolute values of Tw. The map of these biases reveals that, across GCM/RCMs, there are some positive biases ($0.5<\text{bias}<1$ °C) in winter in the higher altitudes of HER A (in the Massif Central), and in summer in the north part of HER A. The negative biases mostly occur in winter in HER B, and in summer in the higher altitudes of HER A for HadGEM2/CCLM4-8-17 (hot and dry) model (see Figure 6.6).

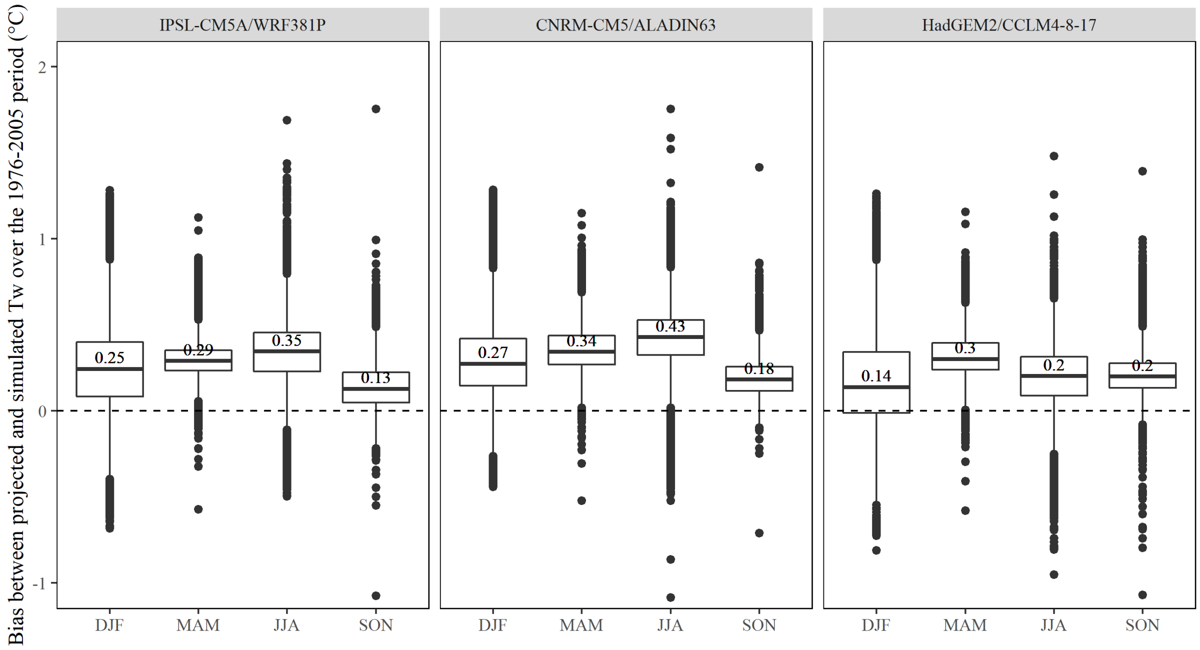

Figure 6.5: Bias between Tw absolute values in projections and in the retrospective simulation at the seasonal scale over the 1976–2005 period. Numbers denote the median bias over the 52 278 reaches.

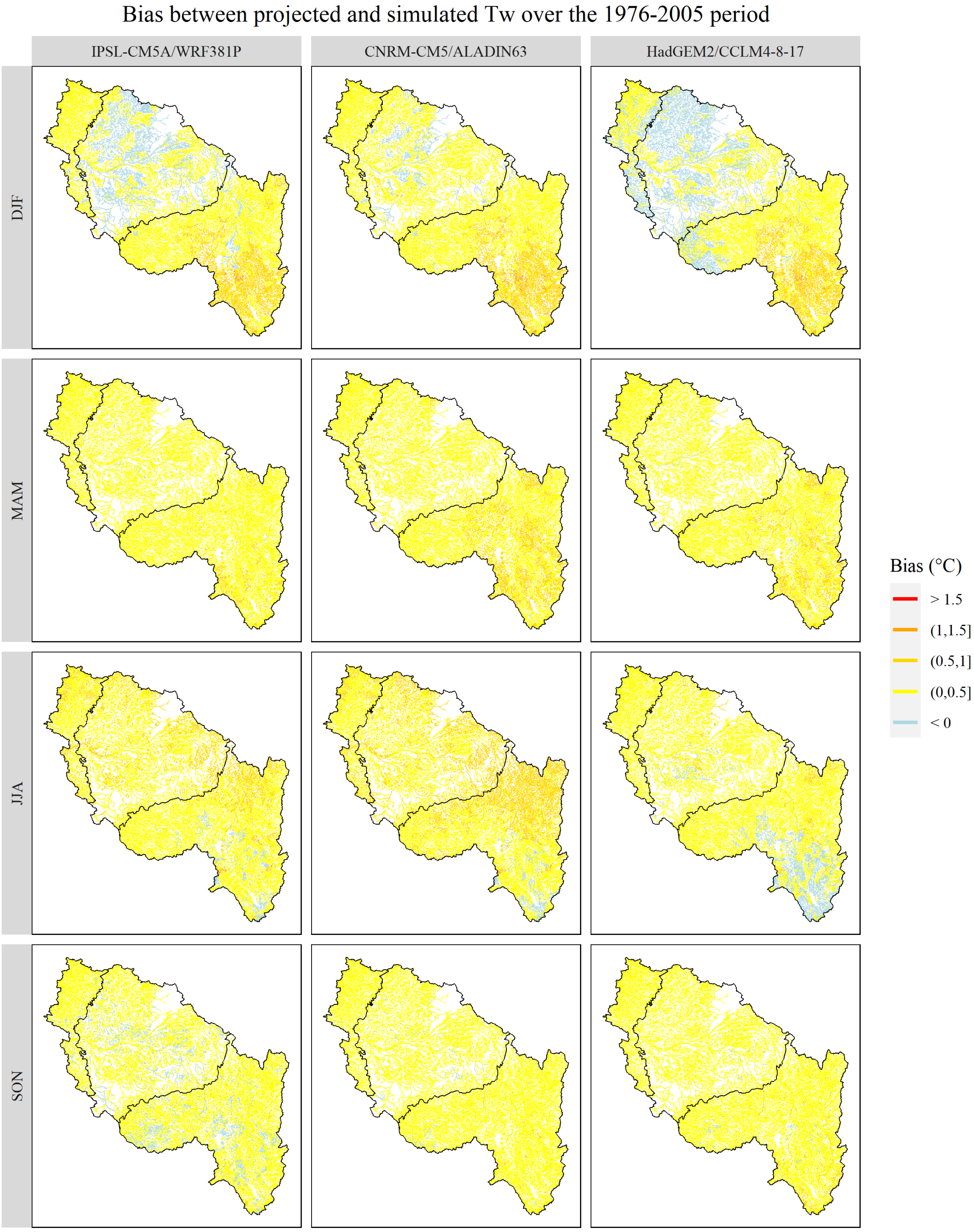

Figure 6.6: Map of biases between Tw absolutes values in projections and in the retrospective simulation at the seasonal scale over the 1976–2005 period.

6.3.3 Comparing recent trend magnitudes and significance levels of stream temperature in projections and in retrospective simulation over the whole 1976–2019 period

To assess whether projections can capture recent trend magnitudes, trends in Tw in projections and in the retrospective simulation are compared at the seasonal scale over the 1976–2019 period. The reasoning for choosing the 1976–2019 period at this step, is to have the longest possible historical period for the trend analyses. This period ends in 2019 since the retrospective simulation is available until 2019 as it was seen in the past trends analyses in the previous chapter (Figure 5.5, p. 139). Nevertheless, since the 1976–2019 period is longer than the historical period of projections (1976–2005) used in the above analyses for meteorological variables and Tw absolutes values, for each GCM/RCM and reach, the average of trend magnitudes over the RCPs is considered. To do so, first, the trend magnitude for each GCM/RCM and RCP (7 in total) is estimated with the non-parametric Theil–Sen estimator (Sen, 1968) used in detecting past trends in the previous chapter (section 5.1, p. 133). Then, the average of trend magnitudes over the RCPs for each GCM/RCM is used as the representative of the GCM/RCM. For instance, for the CNRM-CM5-LR/ALADIN63 model with 3 RCPs, the mean of trend magnitudes obtained from the 3 RCPs is used. Trends in Tw under different RCPs are not assessed here since the historical period over which RCPS are indeed different from each other, is small (2006–2019), and therefore, it is not appropriate for a trend assessment. Considering 1976–2019 period for such Tw trend assessment is also useless since, over a large part of this period (1976–2005), Tw under RCPs are not different from each other.

Figure 6.7 shows that there is an increasing trend in Tw at the majority of reaches over the 1976–2019 period for all GCM/RCMs and the retrospective simulation regardless of the season. A good seasonality can be seen only for the CNRM-CM5-LR/ALADIN63 model.

The map of Tw trend magnitudes in projections and in the retrospective simulation clearly exhibits that projections fail to get the right Tw trend magnitudes and their spatial variability (Figure 6.8). Indeed, projections cannot represent the signal of important trends in HER A. Nevertheless, like the retrospective simulation, the largest trends happen in summer for all GCM/RCMs, with the exception of the HadGEM2/CCLM4-8-17 (hot and dry) model for which the largest trends are mainly in fall. The spatial pattern of Tw trends of the IPSL-CM5A/WRF381P (warm and wet) model is the closest one to that of the retrospective simulation, especially in the summer period, but still, the difference between Tw trend magnitudes in this GCM/RCM and in the retrospective simulation remains considerable.

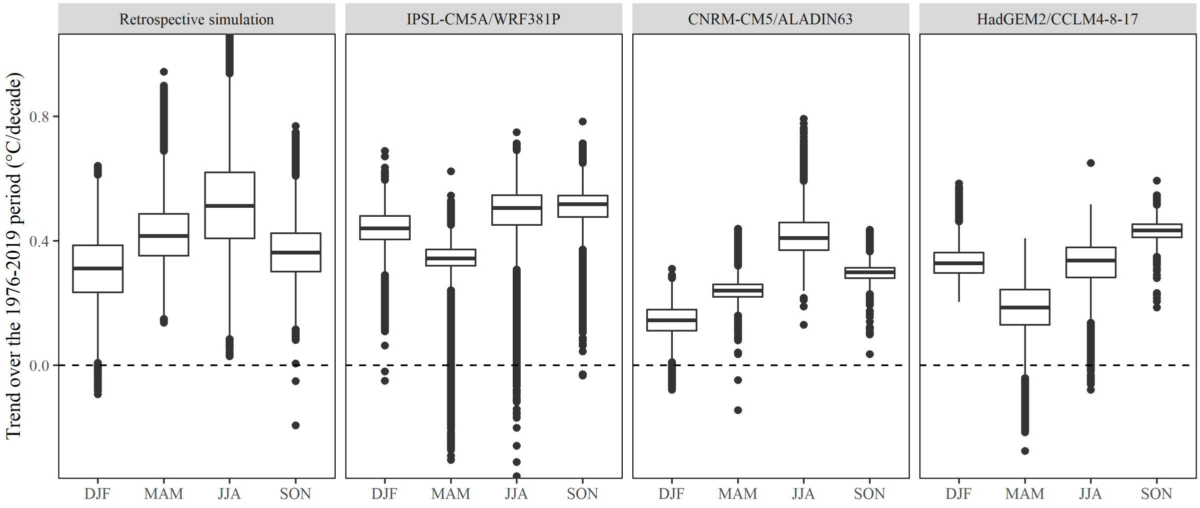

Figure 6.7: Trends in Tw in projections and in the retrospective simulation over the 1976–2019 period for the whole 52 278 reaches. Note that for each GCM/RCM, the average trend magnitudes over the RCPs are considered. The magnitude of the trend is estimated by Theil–Sen estimator.

At this step, after comparing Tw trends in projections and in the retrospective simulation, the significance level of such trends in projections and in the retrospective simulation are compared. To do so, as there is numerous possible combinations of GCM/RCMs and RCPs (7 in total), the following approach is taken to make the assessment simple:

1. For the GCM/RCM with three RCPs, the CNRM-CM5/ALADIN63 (intermediate) model, if two out of three RCPs have the same significance level as the retrospective simulation (i.e., both significant (p-value< 0.05) or non-significant), the significance level of both projection and simulation is considered “matched"; otherwise (i.e., one significant and the other one non-significant), it is considered “unmatched”.

2. For the two other GCM/RCMs with two RCPs (the IPSL-CM5A/WRF381P model and the HadGEM2/CCLM4-8-17 model), if both RCPs have the same significance level as the retrospective simulation, the significance level of both projection and the retrospective simulation is considered “matched”; otherwise it is considered “unmatched”.

Please note that similar to what was used in the past trend analyses (see section 5.1, p. 133), the significance levels of detected Tw trends are evaluated with the Mann-Kendall test (Mann, 1945).

In the majority of reaches across seasons (66-94% of reaches) for the IPSL-CM5A/WRF381P (warm and wet) model and the CNRM-CM5/ALADIN63 (intermediate) model, the significance level of Tw trends in projections and in the retrospective simulation are matched (Figure 6.9), with the exception of winter of the IPSL-CM5A/WRF381P (warm and wet) model (only 29% of reaches). The worst results belong to the HadGEM2/CCLM4-8-17 (hot and dry) model for which the majority of reaches across seasons (50-64% of reaches) have unmatched significance

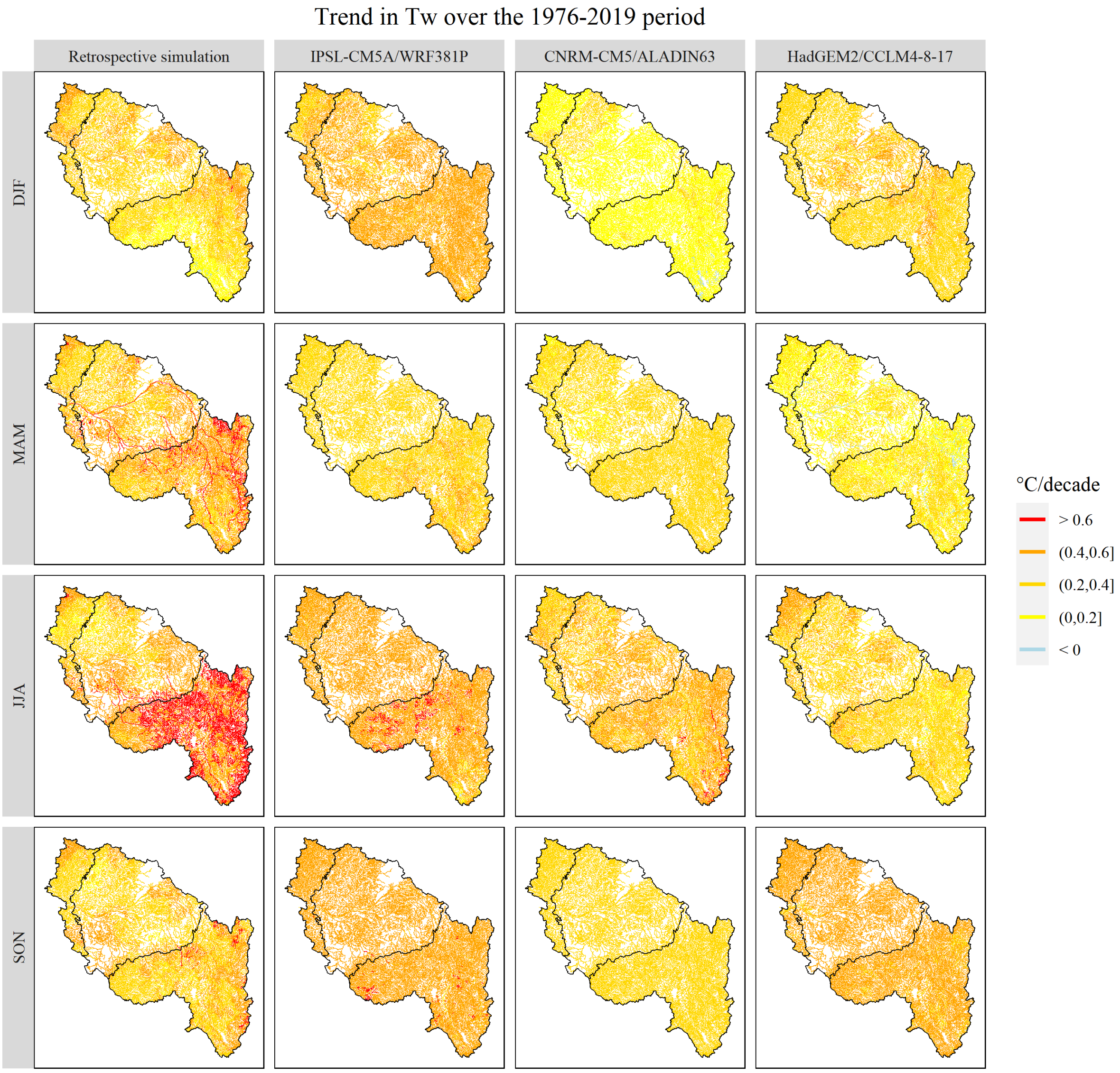

Figure 6.8: Spatial variability of seasonal trend in Tw based on the Sen's Slope estimator in projections and in the retrospective simulation over the 1976–2019 period. Note that for each GCM/RCM model, the average magnitude over RCPs is considered.

level between projections and the retrospective simulation, with the exception of fall (only 2% of reaches are unmatched). The majority of reaches with matched significance level between projections and the retrospective simulation show a significant trend (see light blues in Figures 6.9). The maps of the significance level of seasonal Tw trends over the 1976–2019 period in each GCM/RCM and RCP as well as in the retrospective simulation are provided in Figures E.3 (for RCP 8.5), E.4 (for RCP 4.5), and E.5 (for RCP 2.6). These maps also show mostly significant trends in projected Tw across GCM/RCMs, RCPs, seasons, and reaches.

Finally, the above results demonstrate that there is a significant increasing trend in Tw across

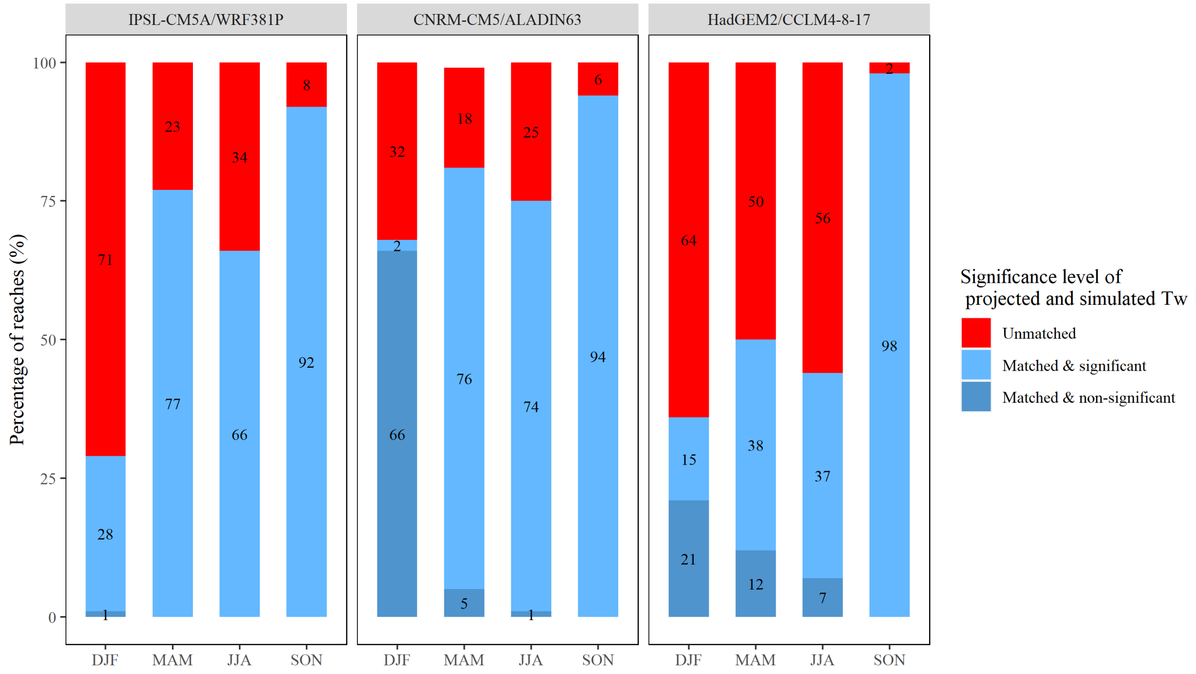

Figure 6.9: Percentage of reaches for which the significance levels of detected trends in Tw in projection and in the retrospective simulation are matched. Matched: Tw trend in both projection and the retrospective simulation is significant or non-significant; and Unmatched: one is significant and the other one is non-significant.

seasons (with the exception of winter) in projections like in the retrospective simulation over the 1976–2019 period.

6.4 Future changes in hydroclimate variables

In the previous section, it was found that the projections managed to get the right absolute values of Tw, but they failed to get the right magnitude of long-term Tw trends and their spatial variability over the recent decades. The results demonstrated that there was a significant increasing trend in Tw across seasons (with the exception of winter) in projections like in retrospective simulation over the 1976–2019 period. This raises a question concerning projected Tw in the future. Will Tw continue increasing in the future? If so, how much will it increase? Therefore, there is a need to understand future Tw changes and the influence of hydroclimate variables (e.g., Ta and Q) on such changes.

Here, future P and Ta, as part of hydroclimate variables, are first studied since Ta and P are the inputs of the EROS hydrological model, and Ta is also one of the important inputs in the T-NET thermal model. Moreover, in the first step in section 6.1, the GCM/RCMs were selected based on changes in Ta and P over France (Figure 6.2). Therefore, here, changes in P and Ta are studied at the scale of the Loire River basin.

To have an overview of future P, Ta, Q, and Tw, the magnitude of their changes with respect to a historical period is first calculated. To do so, first, time slices of 30-years are considered in the historical period and the future. It is assumed that 30 years will be enough to get the right variability in time series. For the future, two time slices are considered including the 2040–2069 period as the middle of the century, and the 2070–2099 period as the end of the century.

The 1990–2019 period is considered as the historical period instead of the 1976–2005 period, which is the reference period for bias correction of climate projections. The 1990–2019 is selected since it is assumed that a more recent period will be likely of high interest for stakeholders. In fact, changes with respect to an old period like 1976–2005 may have little meaning for stakeholders since Tw observations are hardly available for such an old period.

Consequently, in the following, first, the magnitude of changes in seasonal and annual P (computed for 368 sub-basins) and Ta (computed for DRIAS cells) over the Loire River basin are investigated in the middle (2040–2069) and at the end of the century (2070–2099) with respect to the historical period (1990–2019). Note that changes in P are presented for the sub-basins (instead of DRIAS cells) to be able to compare the spatial variability of P changes with that of Q changes. Then, changes in future Q (computed for 368 sub-basins) are studied in the same way. Changes in future Tw (computed for 52 278 reaches) are studied in detail in the next section. In the following, for simplicity, most of the time, only figures related to the most extreme scenario, RCP 8.5 are presented, and figures related to the other scenarios are presented in appendix E.

6.4.1 Changes in precipitation

The median changes (across sub-basins) in seasonal and annual P (Table. 6.2) show that the IPSL-CM5A/MRWRF381P (warm and wet) model for all RCPs projects mostly increases in P across seasons and time slices (median change up to +22 %), while the HadGEM2/CCLM4-8-17 (dry and hot) model projects mostly a decrease in P (median change up to -43 %). The CNRM-CM5-LR/ALADIN63 (intermediate) model projects both an increase and a decrease in P (median change up to +13 % increase and up to -9 % decrease). The greatest decrease in P is projected by the HadGEM2/CCLM4-8-17 (dry and hot) model under RCP 8.5 and 4.5 in summer at the end of the century (-43 % and -36 %, respectively) (Table. 6.2).

Considering RCP 8.5, there is a decrease in P across GCM/RCMs and time slices in spring and summer with the exception of summer of the CNRM-CM5-LR/ALADIN63 (intermediate) model in the middle of the century (median change=+5 %), and summer of the IPSL-CM5A/MRWRF381P (warm and wet) model at the end of the century (median change=+8 %) (Table. 6.2). In such a case, considering both spring and summer, the range of median changes in P across GCM/RCMs is [-29 % ; -1 %] over the 2040–2069 period, and [-43 % ; -1 %] over the 2070–2099 period (see Table. 6.2). Indeed, in such a case, a significant number of sub-basins (59-100 % across time slices) exhibit a decrease in P under RCP 8.5 (see Figure E.6). Under

Table 6.2: Median changes (across sub-basins) in seasonal and annual P under varied GCM/RCMs, and RCPs in the middle (2040–2069), and at the end of the century (2070–2099) with respect to the 1990–2019 period.

RCP	Model	2040–2069					2070–2099				
		DJF	MAM	JJA	SON	Annual	DJF	MAM	JJA	SON	Annual
4.5	IPSL-CM5A/WRF381P	+8	+1	+8	+4	+5	+15	0	+10	+6	+9
8.5	IPSL-CM5A/WRF381P	+22	-3	-3	+6	+8	+21	-1	+8	+21	+14
2.6	CNRM-CM5/ALADIN63	5	-1	-2	-1	0	+1	-9	-6	+1	-3
4.5	CNRM-CM5/ALADIN63	+4	-4	+1	-4	-1	+12	+1	-7	0	+2
8.5	CNRM-CM5/ALADIN63	+5	-4	+5	+3	+2	+13	-2	-9	+7	+3
4.5	HadGEM2/CCLM4-8-17	+3	-9	-30	-13	-11	+18	-3	-36	-10	-5
8.5	HadGEM2/CCLM4-8-17	+5	-1	-29	-10	-7	+21	-11	-43	-16	-10

RCP 8.5, only the HadGEM2/CCLM4-8-17 (dry and hot) model shows a decrease in P in fall at both the middle (median change=-10 %) and the end of the century (median change=-16 %). A large number of sub-basins with a decrease in P under RCP 8.5 in spring and summer (44-94 % of such sub-basins across time slices) are located in the upstream part of the basin in HER A, with the exception of the summer of the CNRM-CM5-LR/ALADIN63 (intermediate) model at the end of the century (Figures 6.10, 6.11, and E.6). Note that decreases in P under RCP 8.5 get stronger towards the end of the century (Figures 6.10, 6.11).

Considering RCP 4.5, like RCP 8.5, there is also a decrease in P across time slices in spring and summer in the CNRM-CM5-LR/ALADIN63 (intermediate) model and the HadGEM2/CCLM4-8-17 (dry and hot) model with the exception of summer of the CNRM-CM5-LR/ALADIN63 (intermediate) model in the middle of the century (median change=+1%), and the spring of the CNRM-CM5-LR/ALADIN63 (intermediate) model at the end of the century (median change=+1%) (Table 6.2). In such a case, considering both seasons, the range of median changes in P is [-30 % ; -4 %] over the 2040–2069 period, and [-36 % ; -3 %] over the 2070–2099 period (see Table 6.2). Indeed, in such a case, most of the sub-basins (60-100 %) exhibit a decreasing P. In such a case, a significant number of the sub-basins are located in the upstream part of the basin, HER A (41-100 % of such sub-basins) with the exception of summer of the CNRM-CM5-LR/ALADIN63 (intermediate) model (see Figures E.7, E.8, and E.6).

Under RCP 2.6, there is also a decrease in P across time slices in spring and summer (median change=-2 % over the 2040–2069 period; -9 and -6 % over the 2070–2099 period). In contrast to RCP 8.5 and RCP 4.5, a smaller proportion of the sub-basins with a decrease in P under RCP 2.6 (17-56 % of such sub-basins) are located in the upstream part of the basin, HER A (see Figures E.10, E.11, and E.12).

Across all GCM/RCMs and RCPs, P is increasing in winter in the middle of the century (median change=[+3 % ; +22 %]) and at the end of the century (median change=[+1 % ; +21 %]) (Table 6.2).

Regardless of GCM/RCM, season, time slice, and RCP, the majority of sub-basins with the

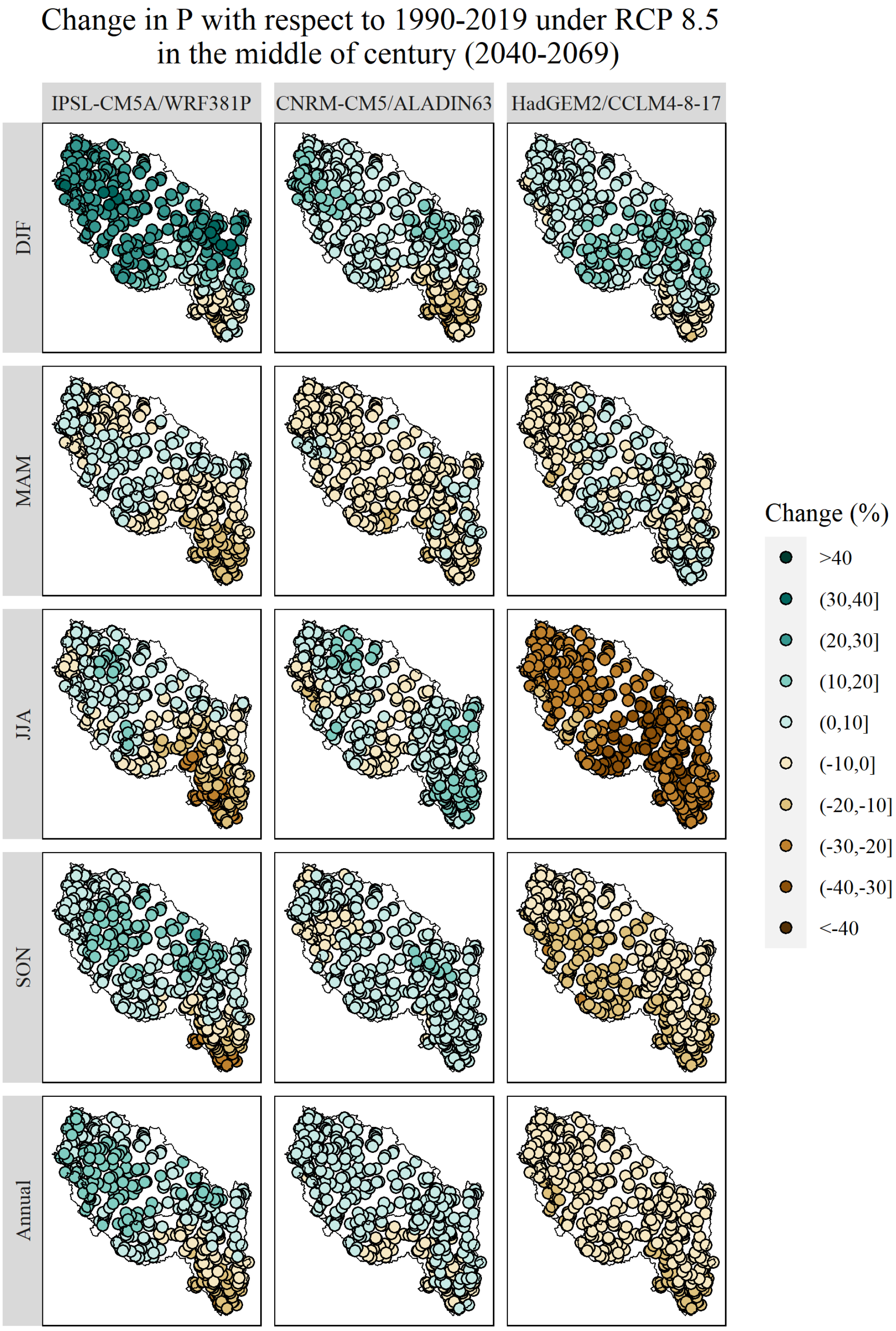

Figure 6.10: Map of changes in seasonal and annual P with respect to the 1990–2019 period under 3 varied GCM/RCMs and RCP 8.5 in the middle of the century (2040–2069) for the 368 sub-basins. The maps of changes in P under other RCPs over the sub-basins are provided in appendix E, section E.3.

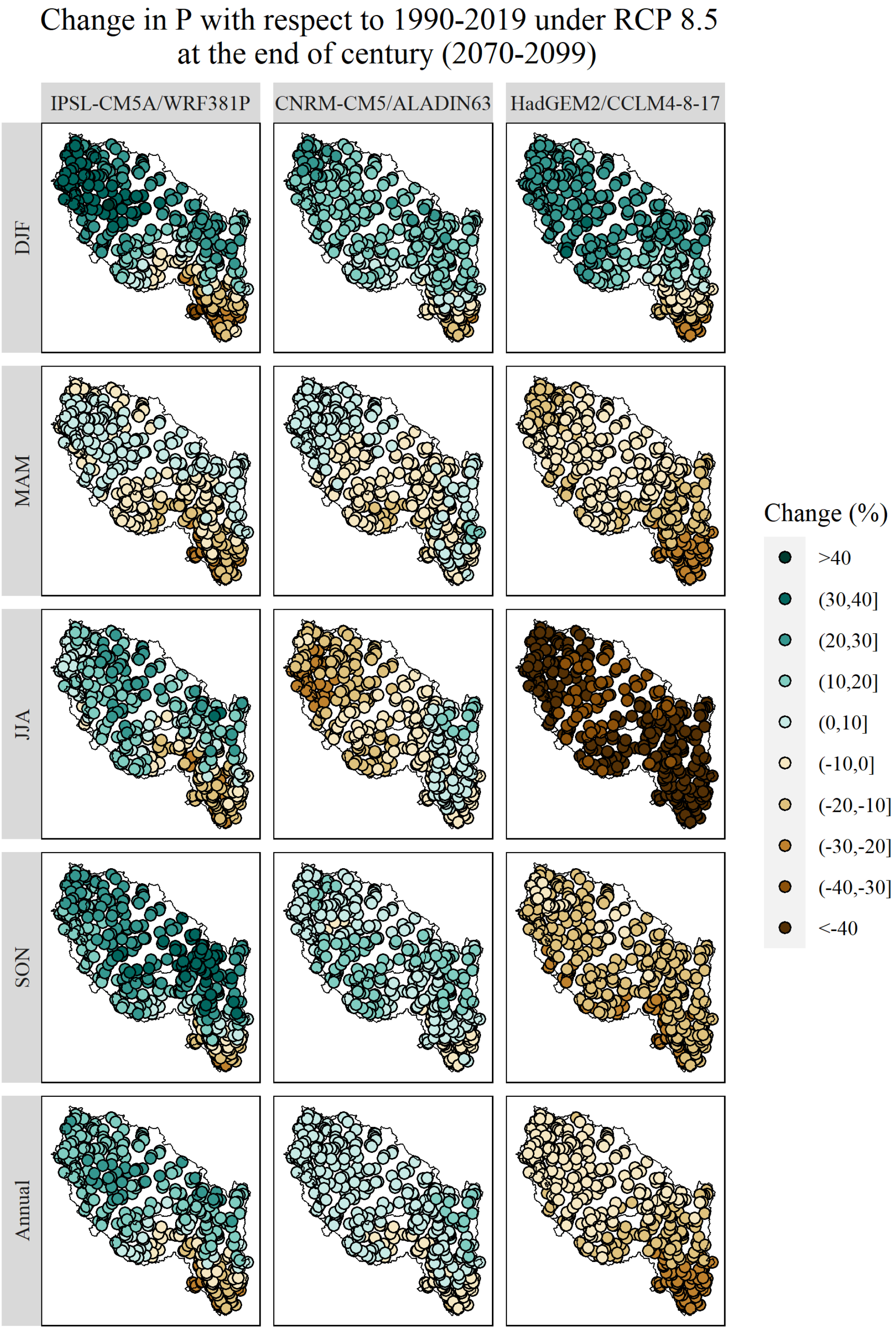

Figure 6.11: Map of changes in seasonal and annual P with respect to the 1990–2019 period under 3 GCM/RCMs and RCP 8.5 at the end of the century (2070–2099) for the 368 sub-basins. The maps of changes in P under other RCPs over the sub-basins are provided in appendix E, section E.3.

greatest decreases in P ([-50 % ; -40 %]) are found in the upstream part of the basin, in HER A (see Figures 6.10 and 6.11 for RCP 8.5).

Consequently, the median changes in P across sub-basins for the majority of combined GCM/RCMs and RCPs demonstrate that P is decreasing considerably in spring and summer in the middle of the century (median change up to -30 % depending on GCM/RCM, RCP, and season) with the exception of P changes under the IPSL-CM5A/WRF381P model and RCP 4.5 in spring and summer, and under the CNRM-CM5/ALADIN63 model and RCP 4.5 or 8.5 in summer. Such a decrease in P is also observed in spring and summer at the end of the century (median change up to -43 %) with the exception of P changes under the IPSL-CM5A/WRF381P model and RCP 4.5 or 8.5 in spring and summer, and under the CNRM-CM5/ALADIN63 model and RCP 4.5 in spring. 1In such a case, the majority of sub-basins with decreasing P (up to -50 %) are located in HER A for RCP 8.5 and 4.5. Note that a similar spatial variability in P changes is observed across seasons and GCM/RCMs (see Figures 6.10, 6.11, E.7, E.8, E.10 and E.11)

6.4.2 Changes in air temperature

The median changes (across the basin) in seasonal and annual Ta (Table 6.3) show a consistent increase in both time slices with respect to the 1990–2019 period regardless of the season, GCM/RCM, and RCP. Across seasons and GCM/RCMs, median changes in Ta ranges between [+0.5 °C ; +3.5 °C] in the middle of the century (Table 6.3). No considerable spatial variability in Ta changes under RCP 8.5 is observed across seasons in the middle of the century (Figure 6.12). In this time slice, most of the changes under RCP 8.5 are in the range of [+1 °C ; +2 °C] except for the winter of the IPSL-CM5A/MRWRF381P (warm and wet) model in HER A and a part of HER B, fall and annual of the HadGEM2/CCLM4-8-17 (dry and hot) model, and fall of the CNRM-CM5-LR/ALADIN63 (intermediate) model in HER A (range of changes=[+2 °C ; +3 °C]) (Figure 6.12). Moreover, across projections, the summer of the HadGEM2/CCLM4-8-17 model, and the spring and summer of the IPSL-CM5A/MRWRF381P model show the greatest (range=[+3 °C ; +4 °C]) and lowest (range=[0 °C ; +1 °C]) increase in Ta, respectively (see Figure 6.12). Relatively, RCP 4.5 has the same spatial pattern as RCP 8.5 in the middle of the century (see Figure E.13), but the lowest changes in Ta occur in the summer, fall, and annual of the IPSL-CM5A/MRWRF381P model and winter of the CNRM-CM5-LR/ALADIN63 (intermediate) model ([0 °C ; +1 °C]).

At the end of the century, median changes in Ta are mostly in the range of [+1.5 °C ; +6.3 °C] across seasons, GCM/RCMs, and RCPs (Table 6.3). In this time slice, again no considerable spatial variability in Ta changes under RCP 8.5 is observed across seasons (Figure 6.13). Most of changes under RCP 8.5 are in the range of [+3 °C ; +4 °C] except for the winter in the IPSL-CM5A/MRWRF381P (warm and wet) model in HER A, and summer, fall and annual of the

Table 6.3: Median changes (across the Loire River basin) in seasonal and annual Ta under different GCM/RCMs, and RCPs in the middle (2040–2069), and at the end of the century (2070–2099) with respect to the 1990–2019 period.

RCP	Model	2040–2069					2070–2099				
		DJF	MAM	JJA	SON	Annual	DJF	MAM	JJA	SON	Annual
4.5	IPSL-CM5A/WRF381P	+1.1	+1.0	+0.7	+0.8	+0.9	+1.8	+1.5	+0.2	+1.6	+1.3
8.5	IPSL-CM5A/WRF381P	+2.1	+0.9	+0.5	+1.5	+1.2	+4.0	+3.1	+1.0	+2.7	+2.7
2.6	CNRM-CM5/ALADIN63	+0.6	+0.9	+1.1	+1.5	+1.0	+0.3	+0.9	+0.9	+1.0	+0.8
4.5	CNRM-CM5/ALADIN63	+0.9	+1.2	+1.4	+1.4	+1.2	+1.6	+1.7	+1.5	+2.1	+1.7
8.5	CNRM-CM5/ALADIN63	+1.6	+1.6	+1.4	+2.0	+1.6	+3.1	+3.2	+3.7	+3.6	+3.4
4.5	HadGEM2/CCLM4-8-17	+2.0	+1.4	+3.0	+2.1	+2.1	+2.3	+1.7	+3.2	+2.9	+2.5
8.5	HadGEM2/CCLM4-8-17	+1.8	+1.7	+3.5	+2.8	+2.4	+3.6	+3.2	+6.3	+4.9	+4.5

HadGEM2/CCLM4-8-17 (dry and hot) model (>4 °C) (Figure 6.13). Across GCM/RCMs and seasons, summer of the IPSL-CM5A/MRWRF381P (warm and wet) model shows the lowest changes in Ta (range of changes=[0 °C ; +2 °C]). Relatively, RCP 4.5 has the same spatial pattern as RCP 8.5 at the end of the century, but to a lesser intensity (see Figure E.14) i.e. the majority of changes in Ta across GCM/RCMs are in range of [+1 °C ; +2 °C], with the exception of fall of the CNRM-CM5/ALADIN63 model, and winter, fall and annual of the HadGEM2/CCLM4-8-17 model ([+2 °C ; +3 °C]). Moreover the greatest changes in Ta under RCP 4.5 occurs on summer of the HadGEM2/CCLM4-8-17 (hot and dry) model ([+3 °C ; +4 °C]).

Under RCP 2.6, again, there is no considerable spatial variability in Ta changes. In both time slices, in the middle, and at the end of the century, changes in Ta remain < 2 °C (see Figures E.15 and E.16).

Consequently, the above results demonstrate that Ta is always increasing, and no spatial variability in Ta changes is observed regardless of the GCM/RCM, RCP, season, and time slice. Ta changes are mostly in range of [+1 °C ; +2 °C] in the middle of the century and in range of [+3 °C ; +4 °C] at the end of the century, with the exception of the HadGEM2/CCLM4-8-17 (dry and hot) model under which Ta changes are always greater than the other GCM/RCMs ([+2 °C ; +3 °C] in the middle of the century, and > 4 °C at the end of the century).

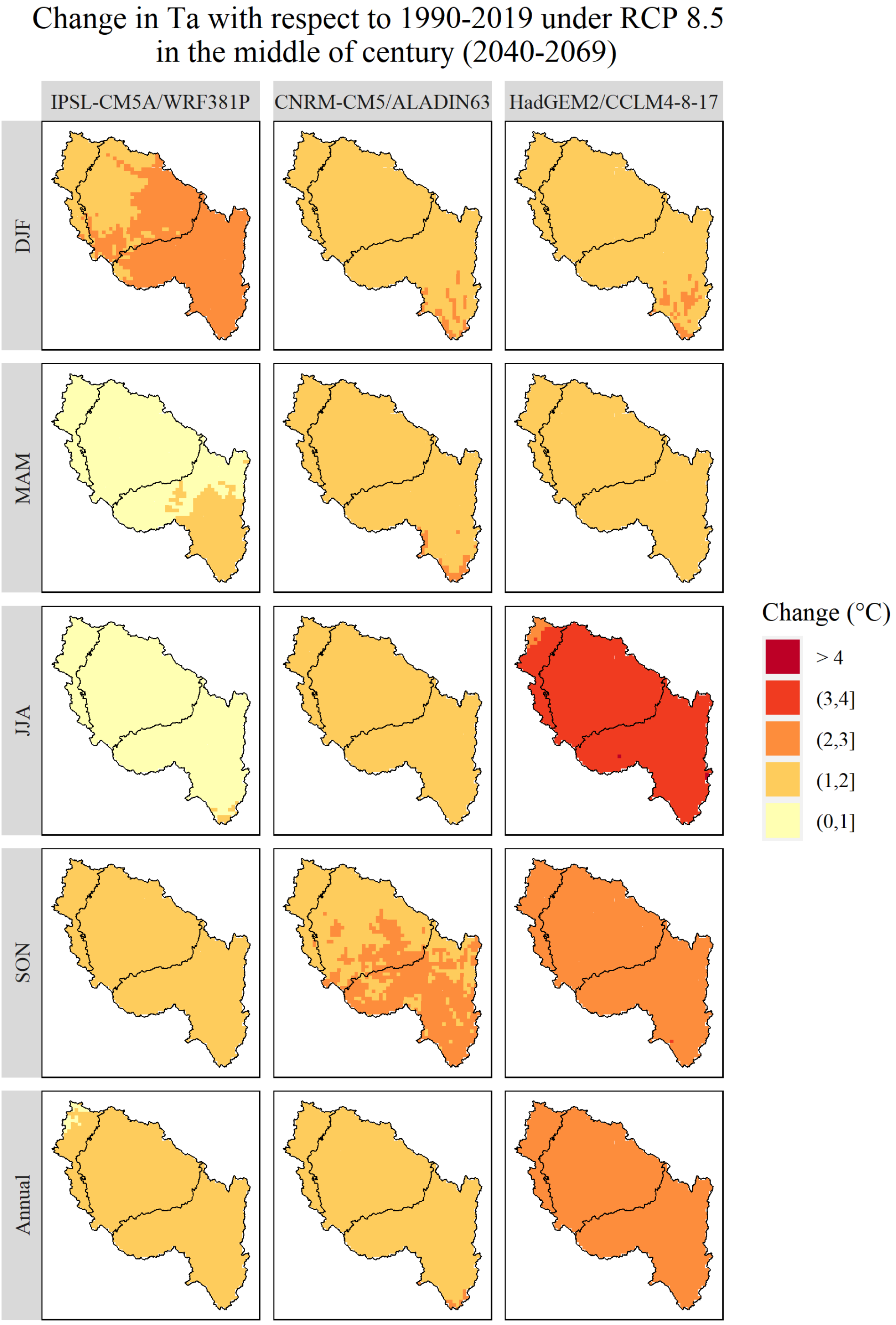

Figure 6.12: Map of changes in seasonal and annual Ta with respect to the 1990–2019 period under 3 varied GCM/RCMs and RCP 8.5 in the middle of the century (2040–2069). Solid black lines show the Hydro-Ecoregion (HER) delineation (see Figure 2.1). Maps of changes in Ta under other RCPs over the sub-basins are provided in appendix E, section E.4.

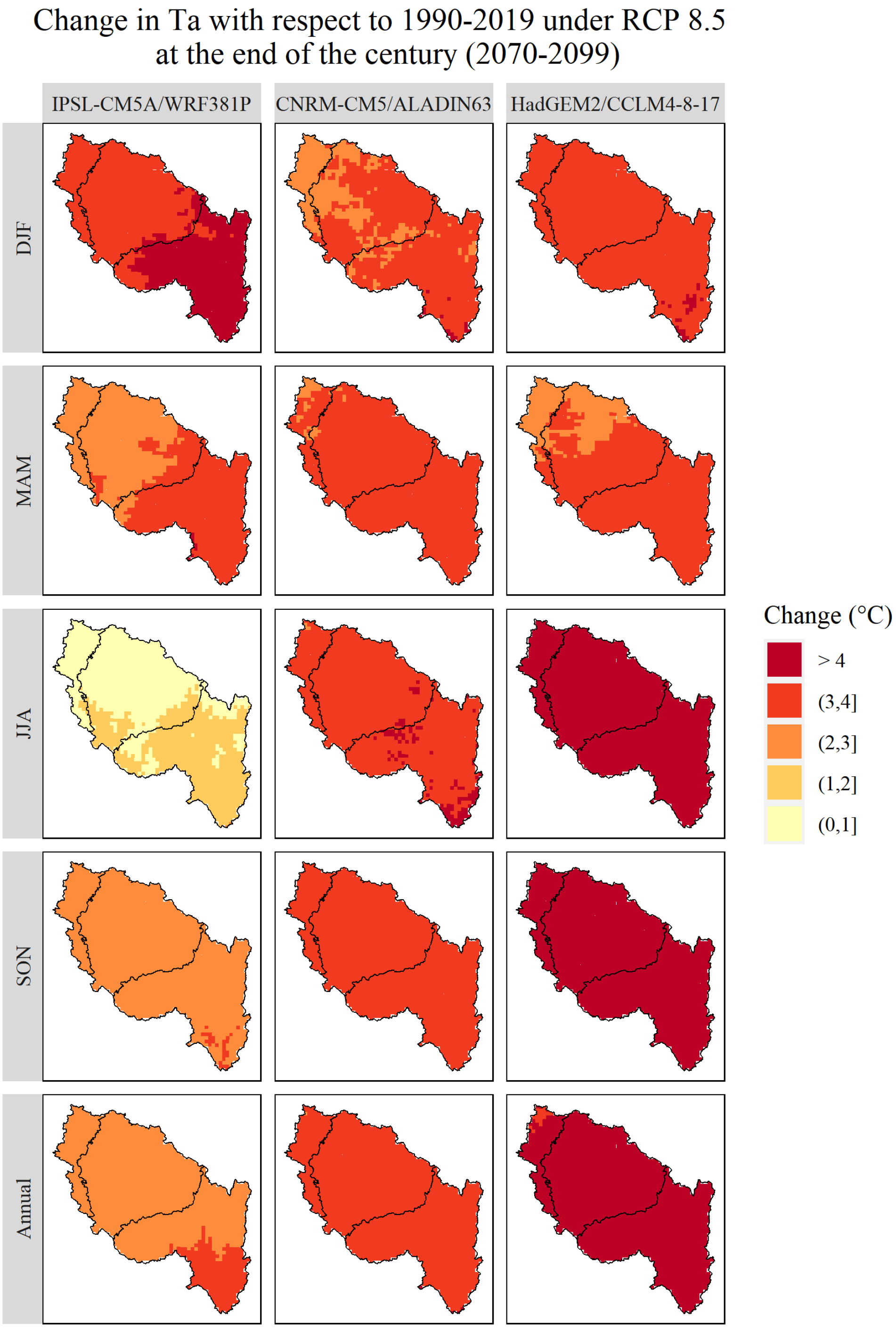

Figure 6.13: Map of changes in seasonal and annual Ta with respect to the 1990–2019 period under 3 varied GCM/RCMs and RCP 8.5 at the end of the century (2070–2099). Solid black lines show the Hydro-Ecoregion (HER) delineation (see Figure 2.1). The maps of changes in Ta under other RCPs over the sub-basins are provided in appendix E, section E.4.

6.4.3 Changes in streamflow

The above results demonstrated that across GCM/RCMs and RCPs, and time slices, there is a decrease in P in spring and summer (mostly in HER A). The HadGEM2/CCLM4-8-17 (dry and hot) model exhibited a decrease in P in fall as well. On the other hand, under all GCM/RCMs and RCPs in both time slices, an increase in Ta was observed regardless of the season. Nevertheless, there was less spatial variability in Ta changes compared to P changes. Hence, it is expected that such changes in P and Ta have an important influence on Q changes.

At this step, the magnitude of changes in seasonal and annual Q, and changes in the annual cycle of Q under future projections are investigated. Changes in low flows are also studied as well as seasonal values since the periods of low flows can have a critical influence on Tw. Here, the 10-quantile of Q over the desired period is considered as low flows, which was also used by van Vliet et al. (2013) for assessing future projections at a global scale.

The median changes (across sub-basins) in seasonal and annual Q (Table. 6.4) show that the IPSL-CM5A/MRWRF381P (warm and wet) model for all RCPs projects mostly an increase in Q across seasons and time slices (median change up to +52 %), while the HadGEM2/CCLM4-8-17 (dry and hot) model projects mostly decrease in Q (median change up to -55 %). The CNRM-CM5-LR/ALADIN63 (intermediate) model also projects mostly a decrease in median Q (median change up to -21 %). The greatest decrease in Q is projected by the HadGEM2/CCLM4-8-17 (dry and hot) model under RCP 8.5 and 4.5 in summer and fall of both time slices ([-55 % ; -28 %]) (Table 6.4). At the end of the century, regardless of GCM/RCM and RCP, a decrease in median Q is observed in summer.

Table 6.4: Median changes (across sub-basins) in seasonal and annual Q under varied GCM/RCMs and RCPs in the middle (2040–2069) and at the end of the century (2070–2099) with respect to the 1990–2019 period. Numbers in green and brown are showing the changes>10 % and <-10 %, respectively. These thresholds correspond to the ones used in Moatar et al. (2013) for assessing changes in Q under projections based on the 4th report of IPCC over the Loire River basin.

RCP	Model	2040–2069					2070–2099				
		DJF	MAM	JJA	SON	Annual	DJF	MAM	JJA	SON	Annual
4.5	IPSL-CM5A/WRF381P	+5	+10	+3	+14	+8	+16	+10	-1	+18	+13
8.5	IPSL-CM5A/WRF381P	+28	+6	-15	+19	+17	+24	-1	-11	+52	+22
2.6	CNRM-CM5/ALADIN63	+3	-6	-6	-7	-3	-5	-14	-11	+4	-7
4.5	CNRM-CM5/ALADIN63	-2	-12	-10	-7	-6	+10	-1	-1	+2	+4
8.5	CNRM-CM5/ALADIN63	-1	-7	-7	+11	-2	+12	-5	-21	-9	0
4.5	HadGEM2/CCLM4-8-17	-14	-21	-37	-38	-22	8	-7	-37	-45	-9
8.5	HadGEM2/CCLM4-8-17	-11	+5	-28	-40	-11	-7	-9	-43	-55	-18

Considering the extreme scenario, RCP 8.5, there is a considerable decrease in median changes in Q across GCM/RCMs and time slices in spring and summer. Considering both seasons, the range of decrease in median changes across GCM/RCMs is [-28 % ; -7 %] over the 2040–2069 period, and [-43 % ; -1 %] over the 2070–2099 period. Indeed, most of the sub-basins under RCP 8.5 (52-100 % across time slices) exhibit a decrease in Q in spring and summer across GCM/RCMs and time slices with the exception of spring of the IPSL-CM5A/WRF381P (warm and wet) model and the HadGEM2/CCLM4-8-17 (dry and hot) model in the middle of the century (see Figure E.17). A considerable number of the sub-basins with decreasing Q under RCP 8.5 in spring and summer (48-94% of such sub-basins across the time slices) are located in the upstream part of the basin, in HER A (Figures 6.14, 6.15, and E.17). Note that decreases in Q under RCP 8.5 get larger towards the end of the century (Figures 6.14). Such a spatial variability in Q changes is also observed for P, but to a lesser extent (Figures 6.10 and 6.11 for RCP 8.5).

A likely shift in low flows is projected by the HadGEM2/CCLM4-8-17 (dry and hot) model since a considerable decrease in median Q changes happens from summer to fall across time slices, especially under RCP 8.5 (from -28 % to -40 % over the 2040–2069 period, and from -43 to -55% over the 2070–2099; see Table. 6.4, and Figures 6.14, 6.15).

The median annual cycle of Q under RCP 8.5 at a sub-basin in the upstream part of the basin (Figure 6.16, right panel) shows a decrease in Q with respect to the historical period in the whole year for all GCM/RCMs, and time slices. For a sub-basin in the downstream part of the basin (Figure 6.16, left panel), such a decrease is less important with the exception of the HadGEM2/CCLM4-8-17 (dry and hot) model, especially during low flow periods. For the latter sub-basin, the IPSL-CM5A/WRF381P model projects an increase in Q in high flow periods. Moreover, the HadGEM2/CCLM4-8-17 (dry and hot) model shows a clear shift in the timing of low flows periods towards the end of the century in both sub-basins, which is expected as mentioned previously. Note that projected Q over the historical period (grey), compared to the retrospective simulation (black), shows important overestimation during high flows, especially for the sub-basin located upstream part of the Loire River basin (Figure 6.16), which is consistent with overestimation in precipitation found for sub-basins in the southern part of the basin (see Figure 6.4).

Across GCM/RCMs, RCPs, and time slices, a considerable decrease in low flows is also found (median change=[-58.46 % ; -2.05 %]; Figure 6.17). The smallest decrease in low flows occurs for the IPSL-CM5A/WRF381P (warm and wet) model under RCP 8.5 (median=-2.05 %), and the greatest decrease in low flows happens for the HadGEM2/CCLM4-8-17 (dry and hot) model under RCP 8.5 (median=-58.46 %). Indeed, most of the sub-basins (53-100 %) exhibit a decrease in low flows across GCM/RCMs and RCPs. Most of these sub-basins (48-77 % of such sub-basins) are located in the upstream part of the basin, HER A. The most pronounced decrease in low flows occurs towards the end of the century across GCM/RCMs, and RCPs with the exception of the IPSL-CM5A/WRF381P (warm and wet) model (see Figure 6.17).

Under RCP 4.5, like RCP 8.5, there is a decrease in Q across GCM/RCMs and time slices in

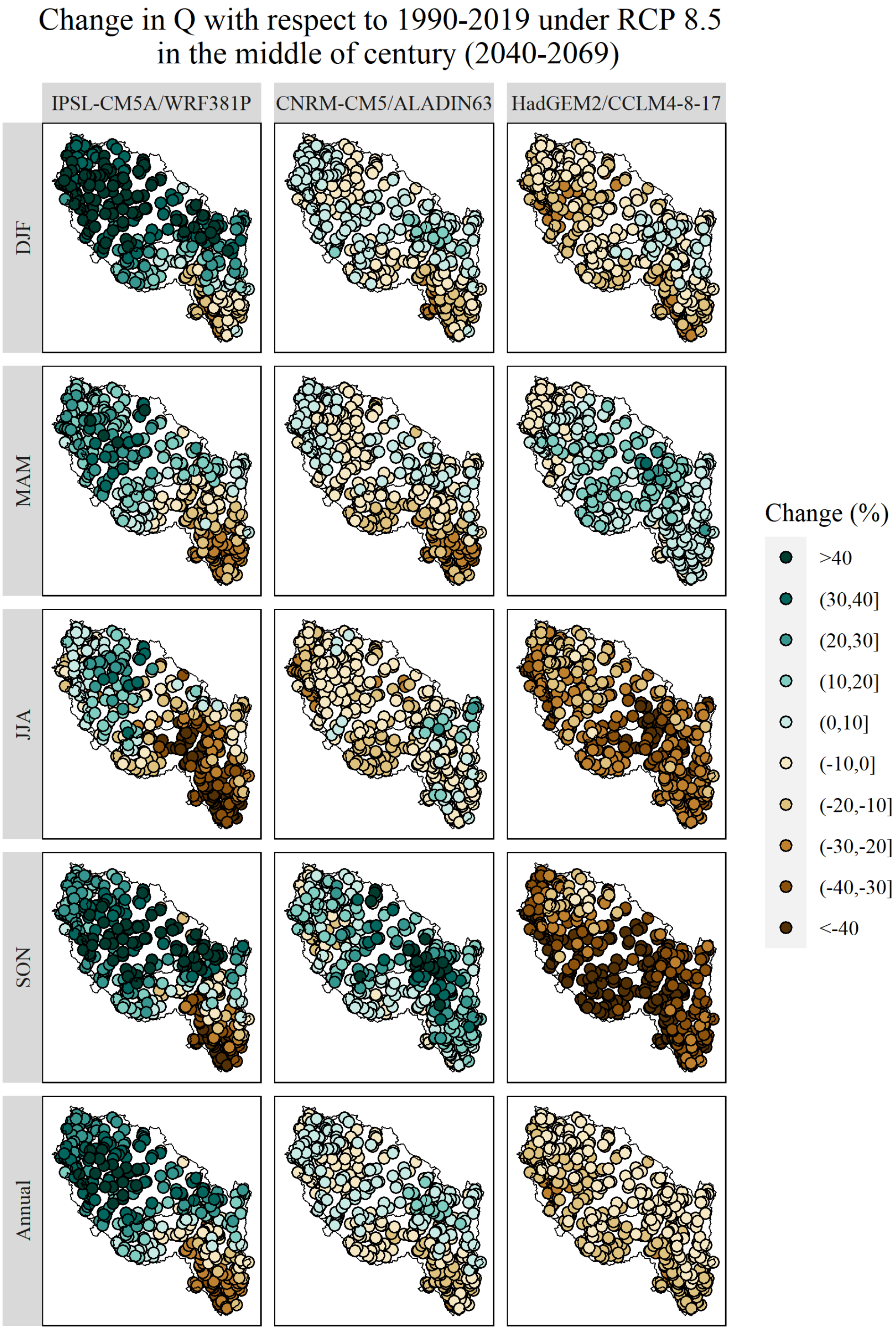

Figure 6.14: Map of changes in seasonal and annual Q with respect to the 1990–2019 period under 3 GCM/RCMs and RCP 8.5 in the middle of the century (2040–2069). The map of changes in Q under other RCPs over the sub-basins are provided in Appendix E, section E.5.

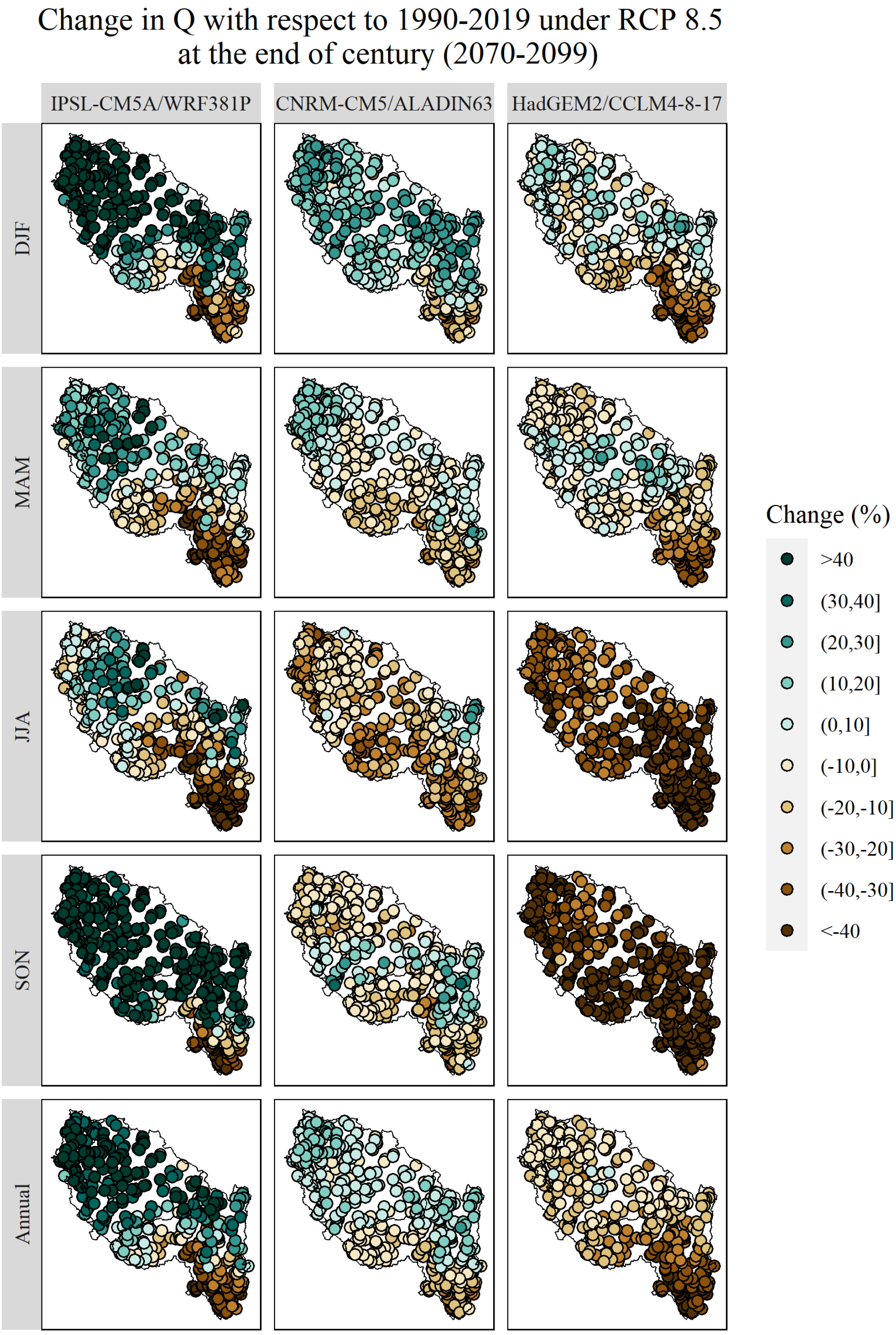

Figure 6.15: Map of changes in seasonal and annual Q with respect to the 1990–2019 period under 3 GCM/RCMs and RCP 8.5 at the end of the century (2070–2099). The map of changes in Q under other RCPs over the sub-basins are provided in Appendix E, section E.5.

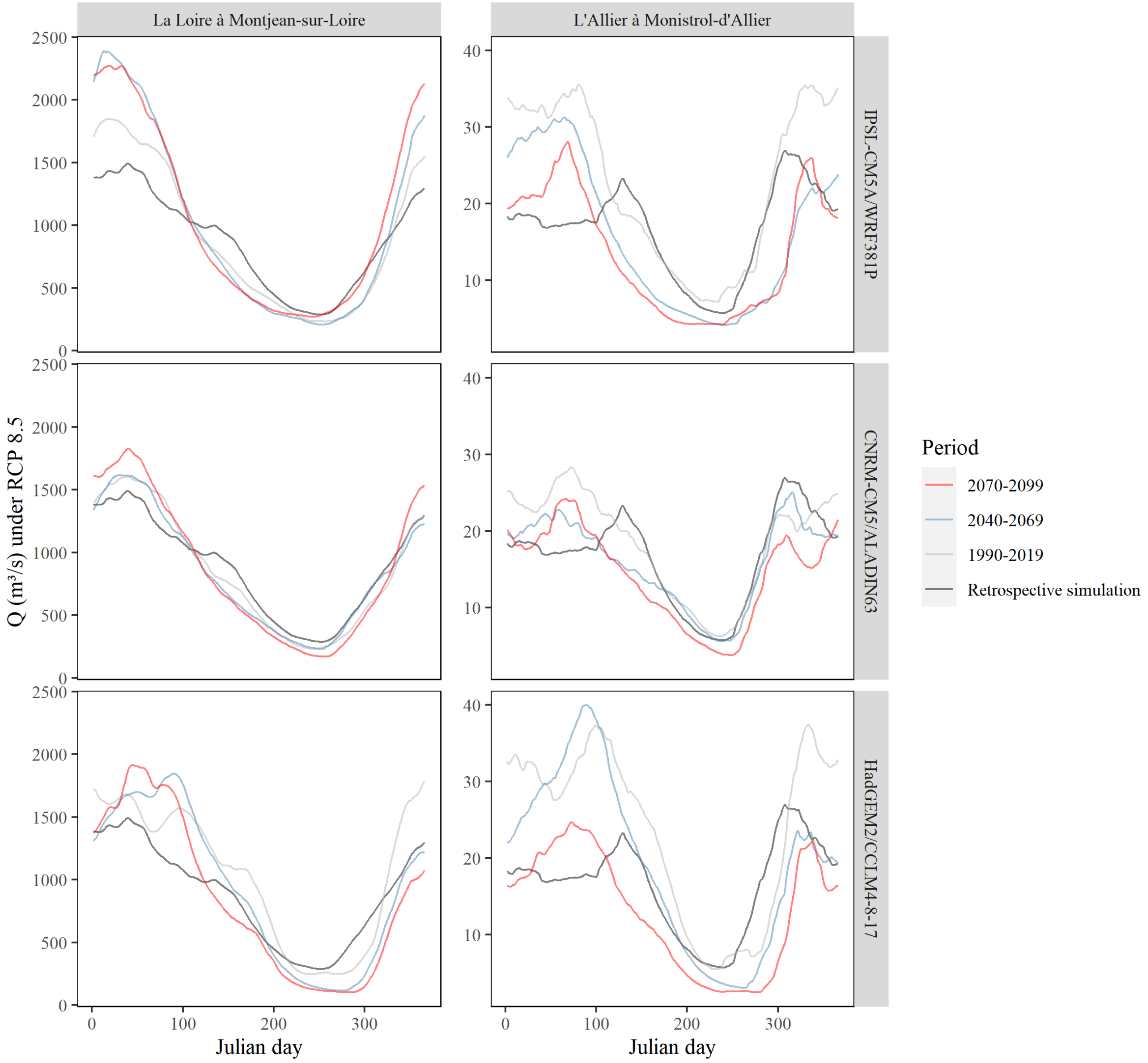

Figure 6.16: Median annual cycle of Q under three GCM/RCMs and RCP 8.5 in the historical period (1990–2019), in the middle (2040–2069), and at the end of the century (2070–2099) for two sub-basins: (right) in the upstream part (L'Allier à Monistrol-d'Allier), and (left) in the downstream part (La Loire à Montjean-sur-Loire) of the Loire River basin. For each cycle, average of Q over the desired time slice for each day is calculated then a 30-day moving average is applied on this daily cycle. The colors show different time slices.

spring and summer (considering the decrease in median change of both seasons: [-37 % ; -10 %] over the 2040–2069 period, and [-37 % ; -1 %] over the 2070–2099 period) with the exception of spring of the IPSL-CM5A/WRF381P (warm and wet) model in both time slices and summer of this model in the middle of the century (Table 6.4). Indeed, most of the sub-basins under RCP 4.5 (43-100 %) exhibit a decrease in Q in spring and summer across GCM/RCMs and time slices with the exception of spring of the IPSL-CM5A/WRF381P (warm and wet) model in both time slices. A significant number of sub-basins with a decrease in Q in spring and summer (49-100 %) are located in the upstream part of the basin in HER A with the exception of the summer of the CNRM-CM5-LR/ALADIN63 (intermediate) model in both time slices (see Figures E.18,

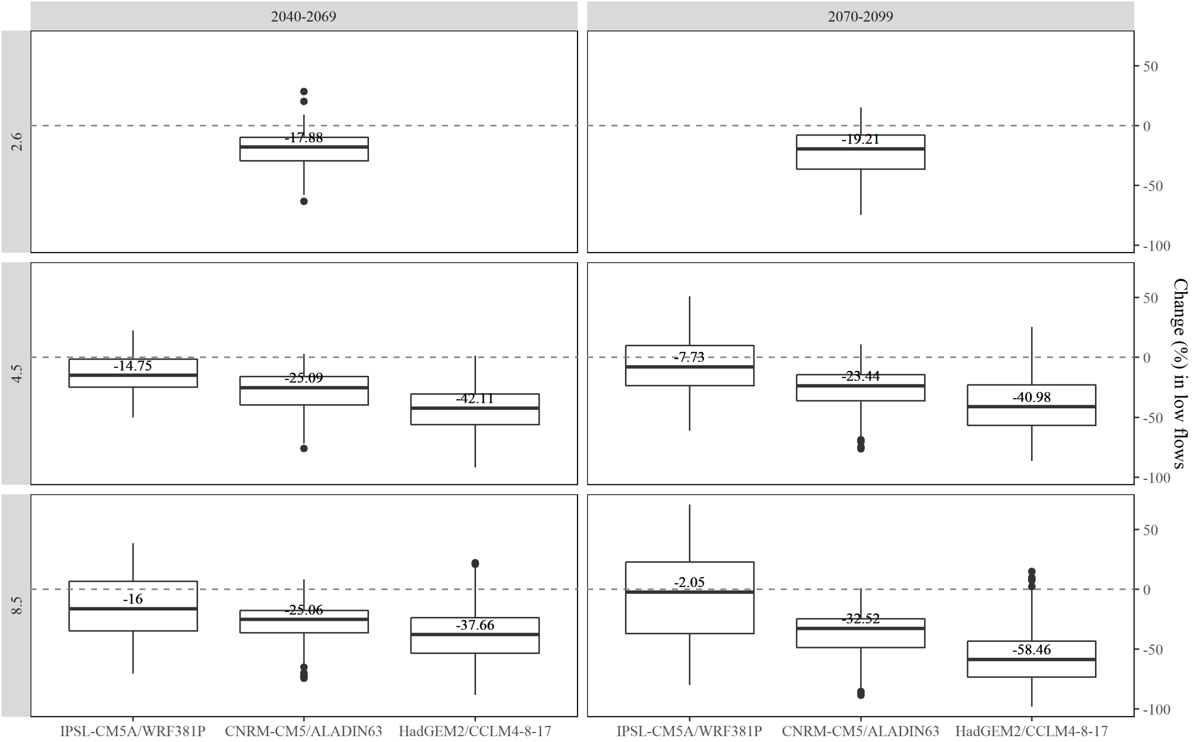

Figure 6.17: Changes in low flow values in different HERs under 3 GCM/RCMs and RCP 8.5 in the middle of the century (2040–2069) and at the end of the century (2070–2099) over the sub-basins. The low flow value is the 10-quantile of Q over the whole desired time slice.

E.19, and E.6).

Under RCP 2.6, there is also a decrease in Q across time slices in spring and summer (-6% over the 2040–2069 period; -14 and -11% over the 2070–2099 period) (Table 6.4). In contrast to RCP 8.5 and RCP 2.6, a lower proportion of sub-basins with a decrease in Q (30-52 % of such sub-basins) are located in the upstream part of the basin, HER A (see Figures E.21, E.22, and E.12).

Regardless of GCM/RCM, RCP, season, and time slice, the majority of pronounced decreases in Q ([-70 % ; -40 %]) are found in upstream part of the basin, in HER A (see Figures 6.14 and 6.15 for RCP 8.5).

Consequently, the median changes in Q across sub-basins demonstrate that Q is decreasing considerably in spring and summer in both the middle (median change up to -40 % depending on GCM/RCM, RCP, and season) and the end of the century (median change up to -55 %). In such a case, the majority of the sub-basins with decreasing Q (up to -76 %) are located in HER A for RCP 8.5 and 4.5. So, in contrast to the Ta changes with rather uniform spatial variability, there is considerable spatial variability in Q changes, which follow the spatial variability in P changes. Note that like changes in P, most of the sub-basins with increasing Q are found in HER B and C. Across GCM/RCMs, RCPs, and time slices, a considerable decrease in low flows is also observed (median change=-58.46 to -2.05 % depending on the GCM/RCM, RCP, and time slice). Moreover, the annual cycle of Q shows that there is a shift in low flows under the HadGEM2/CCLM4-8-17 (dry and hot) model.

6.5 Changes in stream temperature

The above results demonstrated a consistent increase in future Ta regardless of the season. Moreover, a significant decrease in future Q was found in spring and summer. Such changes in Ta and Q may have an influence on future Tw as well. Therefore, this question arises: what are the potential Tw changes in the future (?).

Figures 6.18 and 6.19 show a consistent increase in Tw for both the middle (2040-2069) and end of the century (2070-2099) across GCM/RCMs, RCPs, and seasons. In the middle of the century, the median (across reaches) Tw changes ranges between +0.72 °C and +2.68 °C across seasons, GCM/RCMs, and RCPs (see Figure 6.18). At the end of century, such range is [+0.47 °C ; +4.95 °C] (see Figure 6.19). Indeed, with the exception of the CNRM-CM5/ALADIN63 (intermediate) model under RCP 2.6, the increase in median Tw gets greater towards the end of the century for almost all GCM/RCMs, RCPs, and seasons.

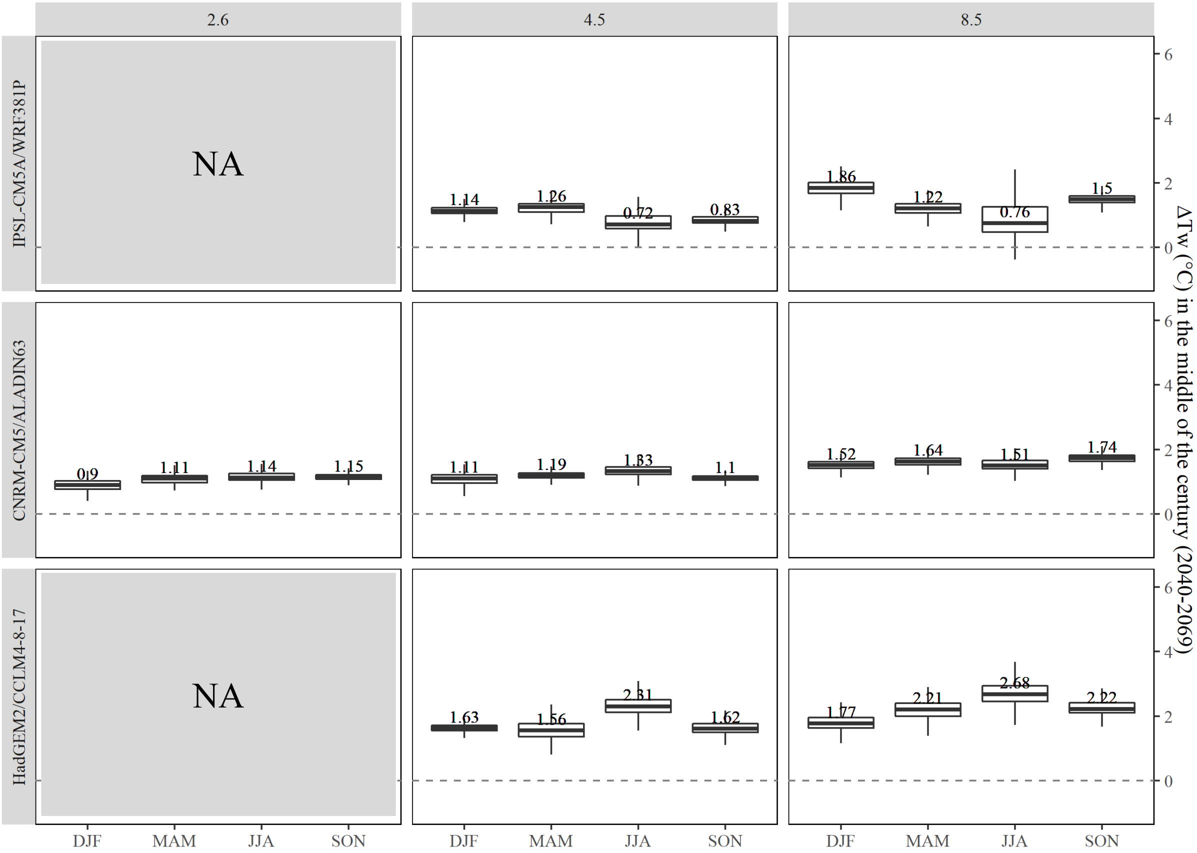

Figure 6.18: Changes in Tw under the 3 varied GCM/RCMs and 3 different RCPs in the middle of the century (2040–2069) with respect to the 1990–2019 period.

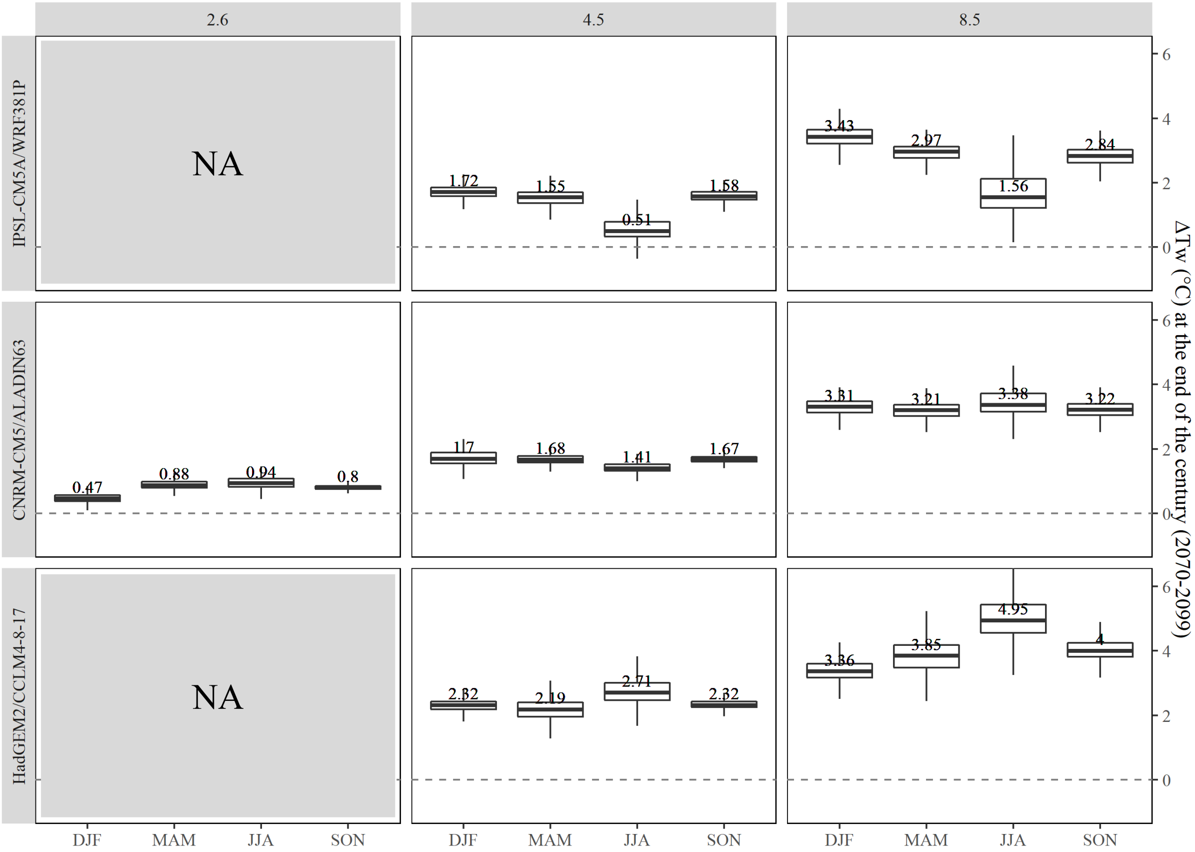

Figure 6.19: Changes in Tw under the 3 varied GCM/RCMs and 3 different RCPs at the end of the century (2070–2099) with respect to the 1990–2019 period.

There is no considerable spatial variability in Tw changes across GCM/RCMs, RCPs, and seasons. Compared to other RCPs, Tw changes under RCP 8.5 are more variable across GCM/RCMs (see Figures 6.18 and 6.19). However, the spatial variability in Tw changes under RCP 8.5 still remains small across seasons in both time slices (see Figures 6.20 and 6.21). In the middle of the century, most of changes are in the range of [+1 °C ; +2 °C] except for winter of the IPSL-CM5A/MRWRF381P model in HER B, and all seasons of the HadGEM2/CCLM4-8-17 model ([+2 °C ; +3 °C]) (see Figure 6.20). However, under this RCP, at the end of the century, there is spatial variability in Tw changes in summer for the IPSL-CM5A/MRWRF381P (warm and wet) model as well as in spring, summer, fall, and annual of the HadGEM2/CCLM4-8-17 (dry and hot) model (Figure 6.21). In this time slice, most of changes are in range of [+3 °C ; +4 °C] across seasons and GCM/RCMs under RCP 8.5 with the exception of spring, summer, fall and annual of the HadGEM2/CCLM4-8-17 (dry and hot) model. Changes in Tw projected by the IPSL-CM5A/MRWRF381P (warm and wet) model in the summer ranges between +1 °C and +2 °C in HER B. The northern part of HER A for the CNRM-CM5-LR/ALADIN63 (intermediate) model has changes$>$ 4 °C. Such changes are also found for the HadGEM2/CCLM4-8-17 (dry and hot) model in HER A in spring, summer, fall, and annual.

The map of changes in seasonal and annual Tw under other RCPs also shows that there is no significant spatial variability in Tw changes regardless of the season and the time slice (see Figure E.24, E.25, E.26, E.26). Such non-spatial variability in Tw changes is also observed for Ta (see for example Figures 6.12 and 6.13 for RCP 8.5). Although there is an increase in Q under RCP 8.5 in sub-basins in HER B and C (see Figures 6.14 and 6.15), there is a consistent increase in Tw across the basin, which may be due to an increase in Ta found over the whole basin.

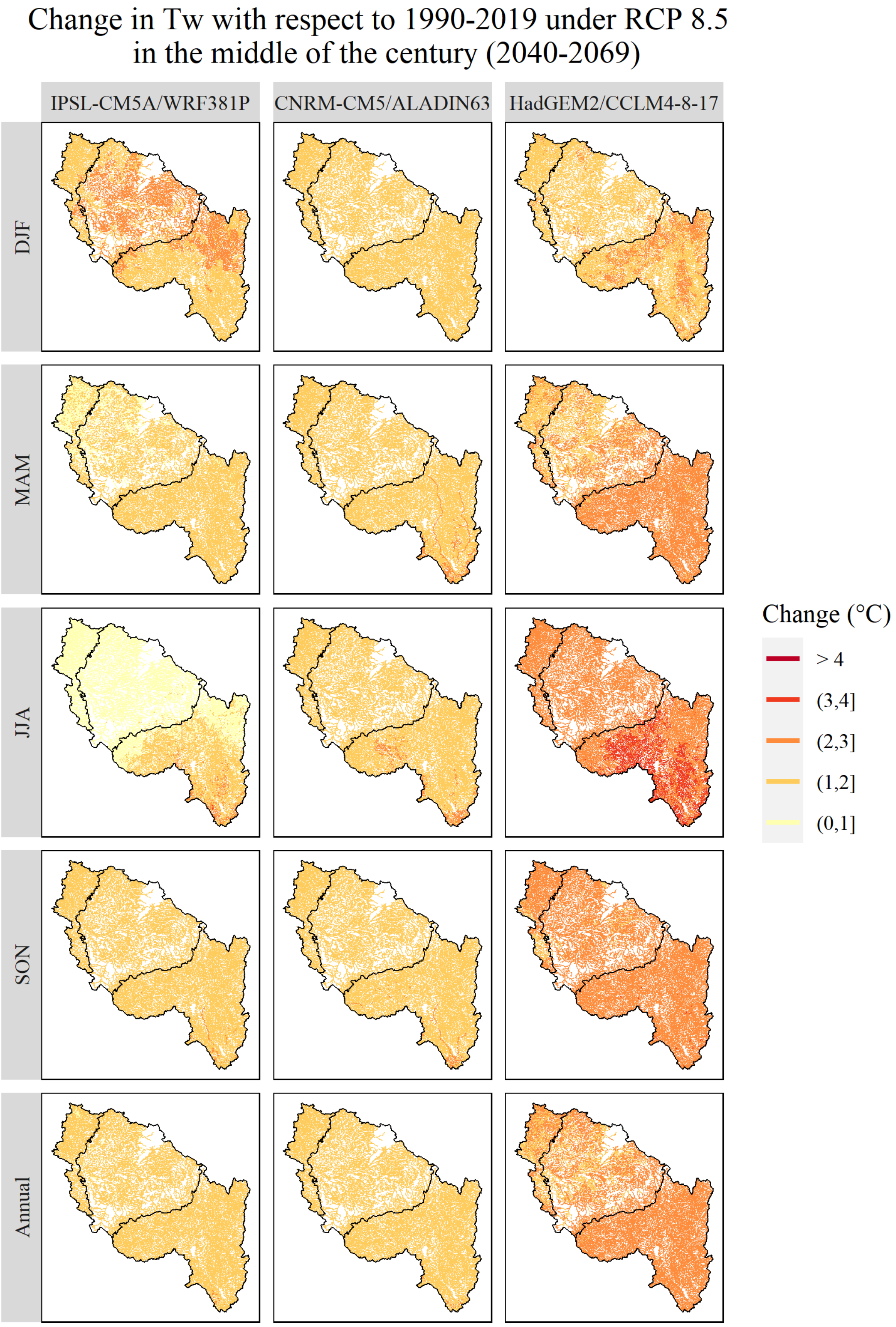

Figure 6.20: Map of changes in seasonal and annual Tw with respect to the 1990–2019 period under 3 GCM/RCMs and RCP 8.5 in the middle of the century (2040–2069). Solid black lines show the Hydro-Ecoregion (HER) delineation (see Figure 2.1).

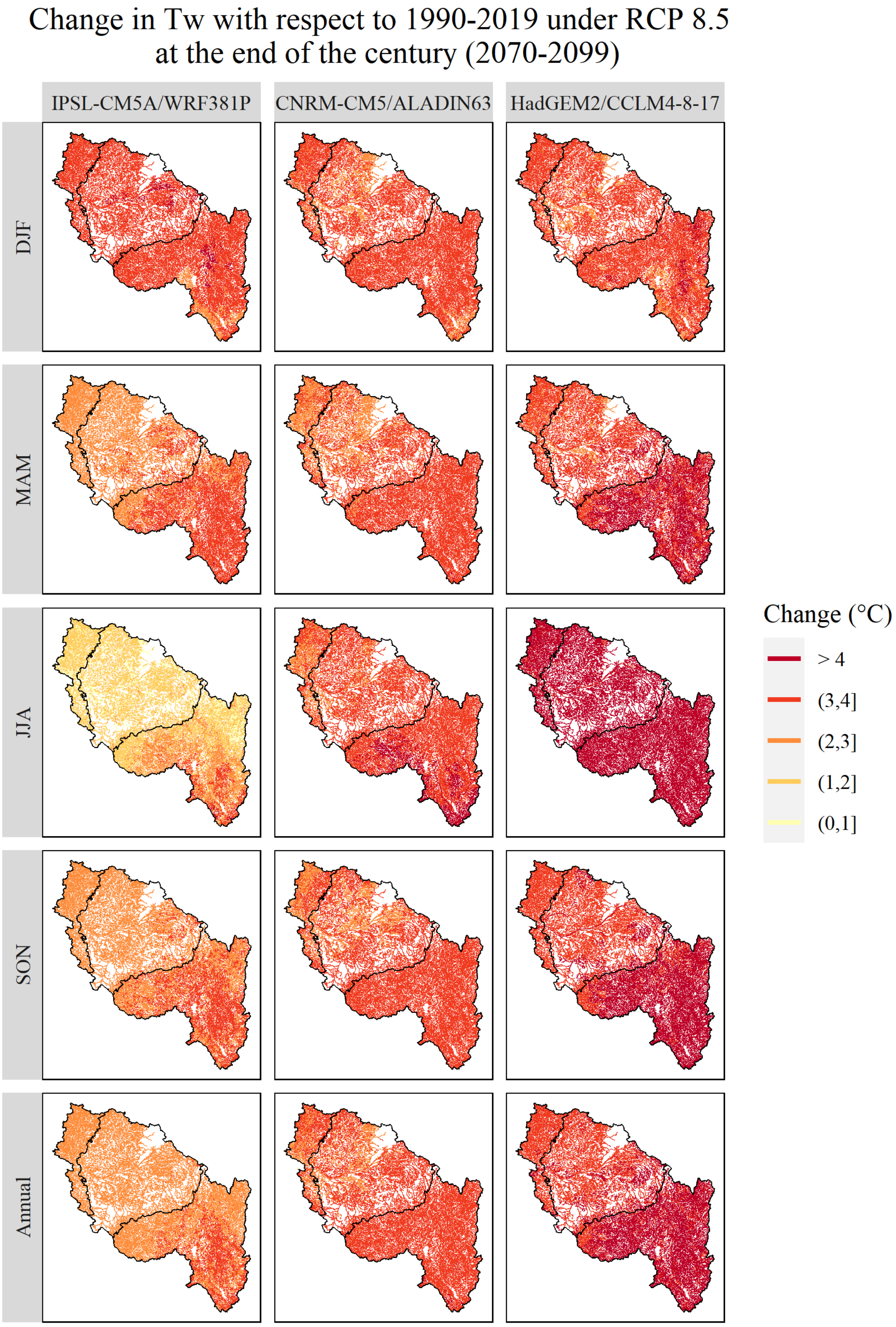

Figure 6.21: Map of changes in seasonal and annual Tw with respect to the 1990–2019 period under 3 GCM/RCMs and RCP 8.5 at the end of the century (2070–2099). Solid black lines show the Hydro-Ecoregion (HER) delineation (see Figure 2.1).

Across GCM/RCMs and RCPs, the projected Tw changes are not considerably different from one season to another in the middle of the century (see Figure 6.18). However, such difference between the seasons gets larger towards the end of the century (see Figure 6.19). Nevertheless, across GCM/RCMs and RCPs, the greatest median changes in Tw are in spring and summer of both time slices with the exception of the IPSL-CM5A/MRWRF381P (warm and wet) model, and the CNRM-CM5/ALADIN63 (intermediate) model under RCP 4.5 at the end of the century (Figures 6.18 and 6.19). In such a case, the median change in Tw is in range of [+1.14 °C ; +2.68 °C] in the middle of century, and [+0.88 °C ; +4.95 °C] at the end of the century. However, for the IPSL-CM5A/MRWRF381P (warm and wet) model, the greatest changes are in winter ([+1.14 °C ; +3.43 °C] across time slices and RCPs).

In the previous chapter, the maps of summer Tw in the retrospective simulation (over the 1963–2019) showed that the high Tw ($>$ 20 °C) are getting frequent in the last decades (2000-2019), especially in 2003, 2017, and 2019 compared to the first decade (1963–1970) (see Appendix D). Here, the maps of mean summer Tw over the middle and end of the century demonstrate that, under all GCM/RCMs, such increase in the frequency of the high Tw ($>$ 20 °C) continues towards the end of the century, and it is the highest for the HadGEM2/CCLM4-8-17 (dry and hot) model across GCM/RCMs, and under RCP 8.5 across RCPs (Figures 6.22 and 6.23). Moreover, the largest mean summer Tw ($>$ 23 °C) occurs in large rivers regardless of the GCM/RCM and RCP.

The above results demonstrate that projected Tw changes are to a large extent sensitive to the selected RCP and GCM/RCM. To better understand the influence of the selected RCP on projected Tw changes, Tw changes are assessed for one GCM/RCM under all RCPs (the CNRM-CM5/ALADIN63 (intermediate) model). Moreover, to address the influence of the selected GCM/RCM on Tw changes, Tw changes are assessed for all selected GCM/RCMs in the current study under one important RCP, which is here RCP 8.5 based on the pronounced Tw changes projected under this RCP (see Figures 6.18, 6.19, 6.22 and 6.23).

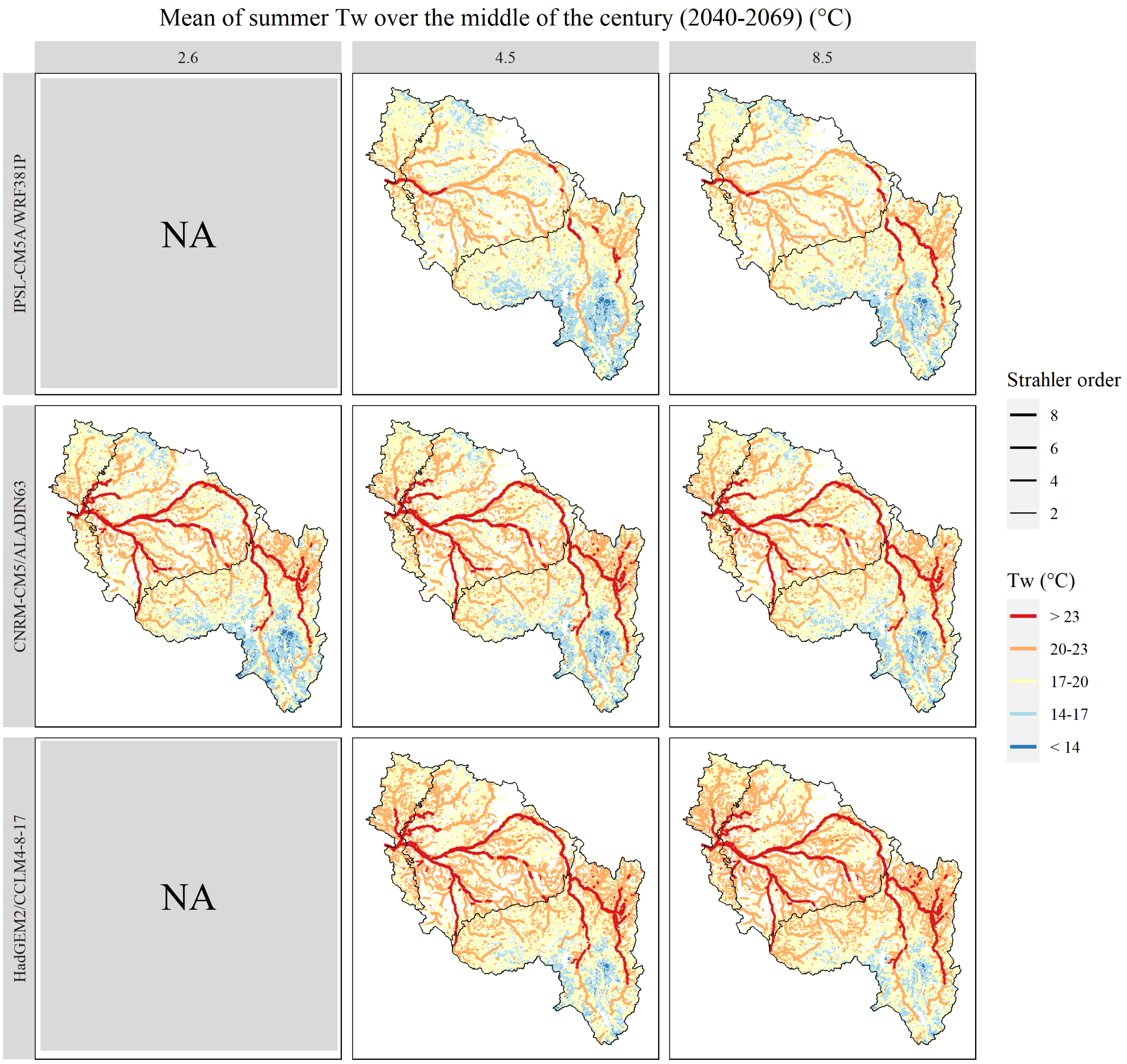

Figure 6.22: Map of mean summer Tw under 3 varied GCM/RCMs and 3 different RCPs over the middle of the century (2040–2069). Solid black lines show the Hydro-Ecoregion (HER) delineation (see Figure 2.1, p. 44).

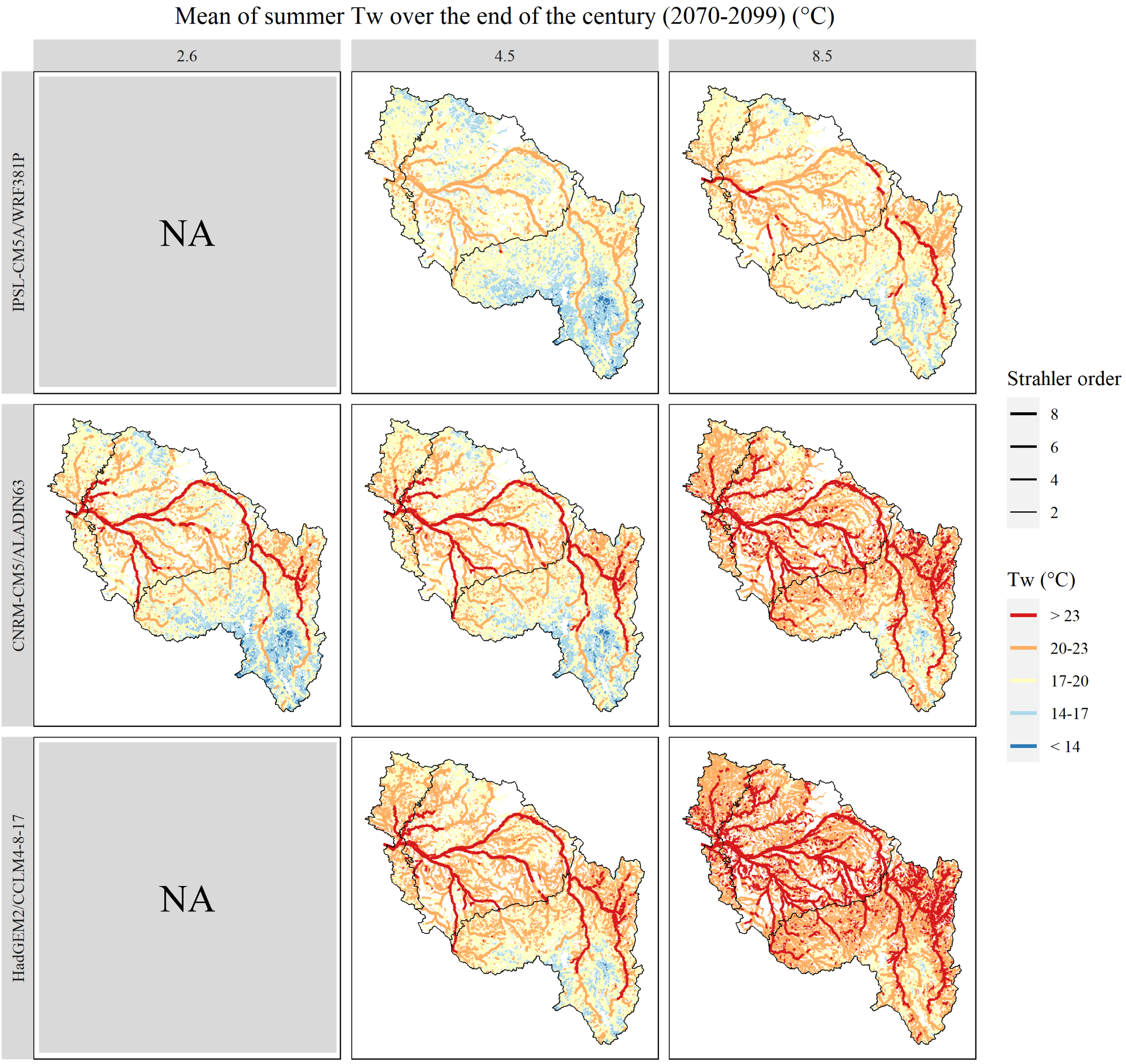

Figure 6.23: Map of mean summer Tw under 3 varied GCM/RCMs and 3 different RCPs over the end of the century (2070–2099). Solid black lines show the Hydro-Ecoregion (HER) delineation (see Figure 2.1, p. 44).

6.5.1 Uncertainty of emission scenarios (RCPs)

Here, Tw changes under the CNRM-CM5/ALADIN63 (intermediate) model and 3 RCPs are studied to assess the RCPs uncertainty. To understand the difference between the 3 RCPs, in addition to seasonal Tw changes, we compare the annual cycle of Tw and seasonal Tw anomalies – with respect to the 1990–2019 interannual mean – under these 3 RCPs. Finally, the longitudinal profile of summer Tw for the Loire River is compared under these RCPs.

Seasonal changes in stream temperature

Changes in Tw under RCP 4.5 are larger than those under RCP 2.6, with the exception of fall in the middle of the century (see Figure 6.24). But, changes in Tw under RCP 4.5 are lower than those under RCP 8.5. Median changes in Tw (across the reaches) under different RCPs are more important towards the end of the century except for RCP 2.6 with a median change of [+0.9 °C ; +1.15 °C] across seasons in the middle of the century, and median change of [+0.47 °C ; +0.94 °C] across seasons at the end of the century. Such behavior for RCP 2.6 seems compatible with the representation of the future behavior of emissions evolution under RCP 2.6 (Figure 6.1). Moreover, the difference between RCPs in projecting Tw changes gets greater towards the end of the century. The small difference between RCPs in the middle of the century can also be seen in Figure 6.22, middle panel. Regardless of the RCP, the median of Tw changes is not significantly different from one season to another. This could be due to the nature of the CNRM-CM5/ALADIN63 (intermediate) model, which shows a small difference between seasons in terms of Tw changes compared to the other two GCM/RCMs in both time slices (see Figures 6.18 and 6.19). Nevertheless, even for the other two GCM/RCMs, such a difference between seasons is larger at the end of the century.

The greatest median Tw changes across time slices, and seasons belong to RCP 8.5 with range of [+1.51 °C ; +1.74 °C] across seasons in the middle of century (vs [+0.91 °C ; +1.33 °C] for the other two RCPs together), and range of [+3.21 °C ; +3.38 °C] across seasons at the end of century (vs [+0.47 °C ; +1.70 °C] for the other two RCPs together). Under this RCP, the high summer Tw ($>$ 20 °C) are more frequent over the basin compared to two other RCPs (see Figures 6.22 and 6.23, middle panel). Indeed, for RCP 2.6 and 4.5, the spatial variability of mean summer Tw in the middle of the century is not much different from that at the end of the century. The greatest median change in Tw is under RCP 8.5 in summer at the end of the century (+3.38 °C). Moreover, more variability in Tw changes under RCP 8.5 is observed in summer at the end of the century ([-0.06 °C ; +5.56 °C]; and see Figures 6.22 and 6.23).

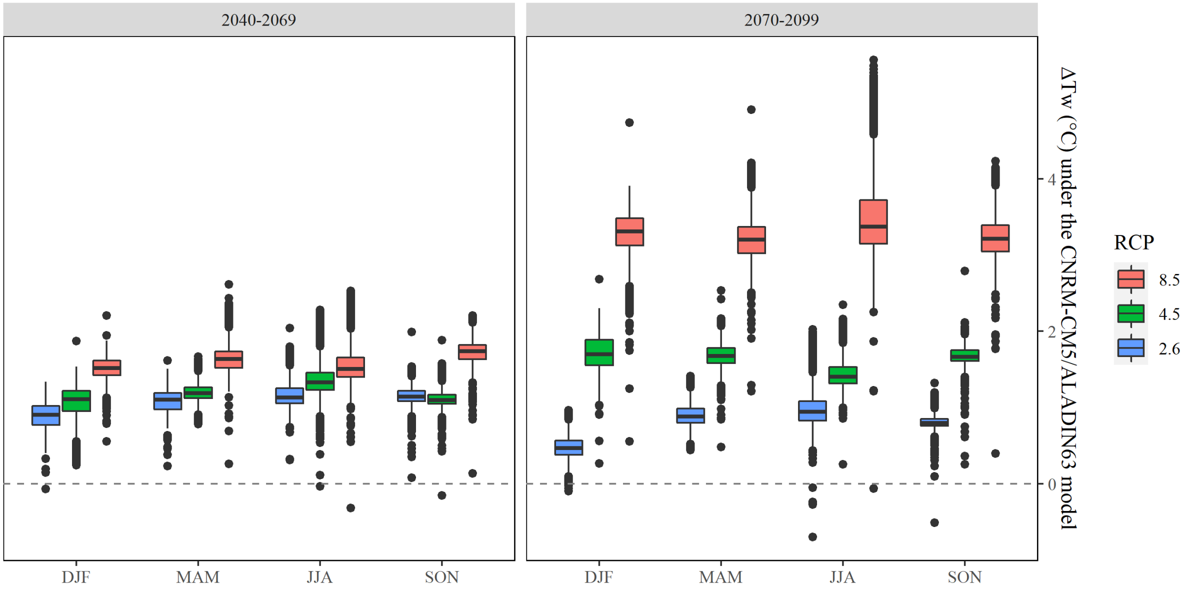

Figure 6.24: Changes in Tw under the CNRM-CM5-LR/ALADIN63 (intermediate) model and 3 different RCPs in the middle (2040–2069) and at the end of the century (2070–2099) with respect to the 1990–2019 period.

Annual cycle of stream temperature

There is a good agreement between the median (across reaches) annual cycle of Tw in projections (grey line) and in the retrospective simulation (black line) (Figure 6.25). There is a very small difference between the annual cycle of Tw in the middle of the century and at the end of the century for RCP 2.6 and 4.5. Compared to the historical period, they are shifted up by up to +2 °C over the summer (Figure 6.25). For RCP 8.5, compared to the historical period, there is a clear upward shift over the whole year in the middle of the century (up to +2.16 °C), and at the end of the century (up to +3.90 °C). For all RCPs, there is no shift in the timing of the maximum value of Tw (horizontal shift).

Seasonal anomalies of stream temperature

The median anomalies (across reaches) of Tw with respect to the 1990–2019 period under all 3 different RCPs exhibit a clear increase in Tw in the middle and at the end of the century (Figure 6.26). The range of anomalies under different RCPs is not really different from one season to another. Across seasons, the range of Tw anomalies under RCP 2.6, and under RCP 4.5 are close ([-1.88 °C ; +3.92 °C] depending on the RCP, and season). Across RCPs, the greatest positive anomalies across seasons occur under RCP 8.5 (≈+5 °C).

For RCP 2.6 and 4.5, an increase in Tw anomalies is observed from the past until the middle of the century. However, under these RCPs, such an increase in Tw is more moderate at the end of the century compared to that for RCP 8.5. Indeed, under RCP 8.5, such an increase in Tw continues toward the end of the century at the same rate as in the middle of the century.

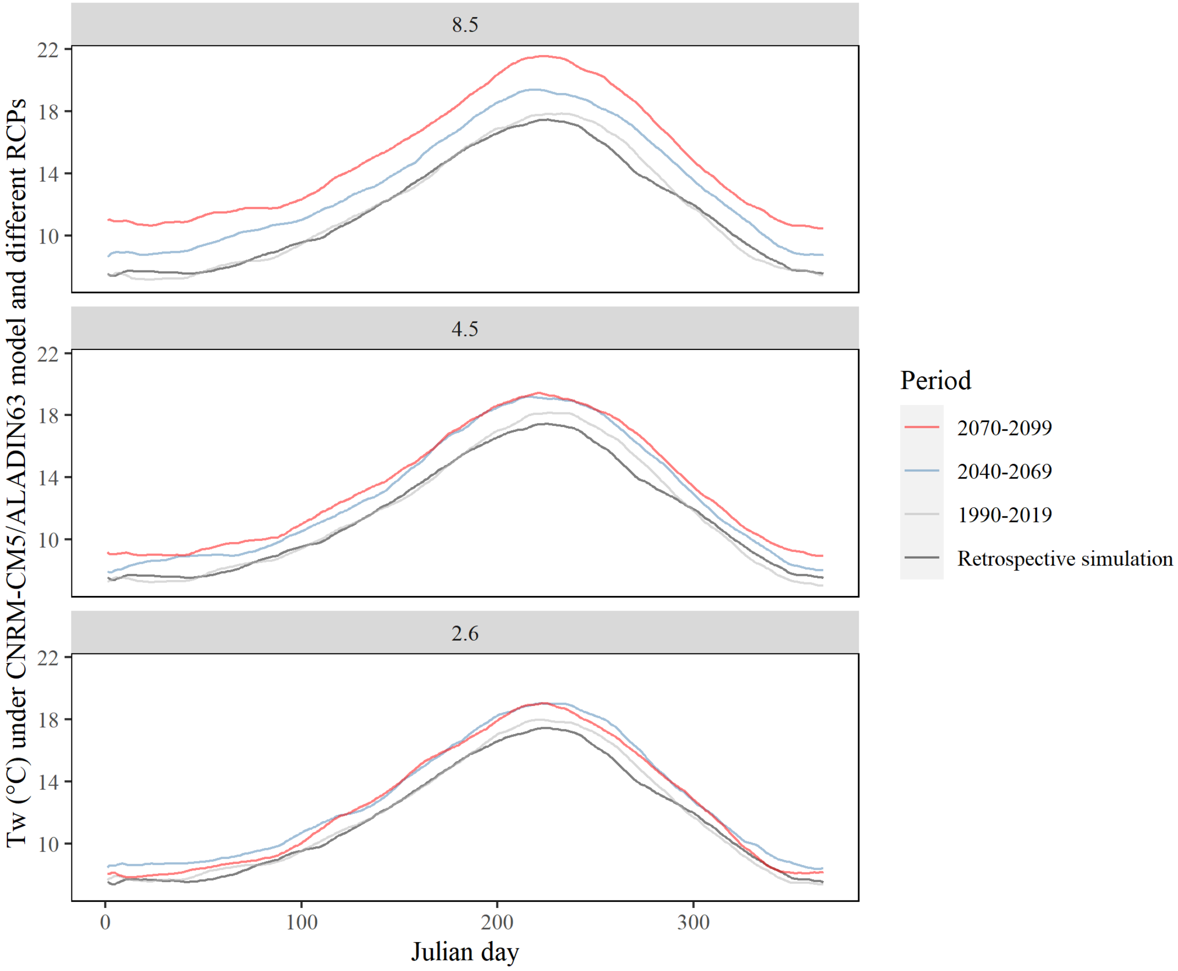

Figure 6.25: Median (across reaches) annual cycle of Tw under the CNRM-CM5-LR/ALADIN63 (intermediate) model, and 3 different RCPs in the historical period (1990–2019), in the middle (2040–2069) and at the end of the century (2070–2099). The black line shows the median annual cycle of Tw over the historical period (1990–2019) in the retrospective simulation. For each cycle, the average of Tw over the time slice for each day is calculated; then the 30-day moving average is applied to this daily cycle. The colors show different time slices.

Longitudinal profile of stream temperature for the Loire River

There is also a good agreement between the longitudinal profile of summer Tw for the Loire River in the retrospective simulation (black line) and in observation at four Tw stations along the river (in point) across RCPs (Figure 6.27). Note that there are Tw data over the 1990–2019 period at these four stations (see Table 2.1, p. 48). Compared to the longitudinal profile in the retrospective simulation (black line), an overestimation (up to +0.9 °C) in projections (grey line) is observed in the middle and at the end of the profile for all RCPs. Such a longitudinal profile of summer Tw was seen before in Figure 4.22 (p. 116) for the Loire River in 2003, and in Figure 1.4 (p. 34).

The longitudinal profile in projections and in the retrospective simulation mimics the same pattern. Like what was observed for the annual cycle of Tw (Figure 6.25), the longitudinal

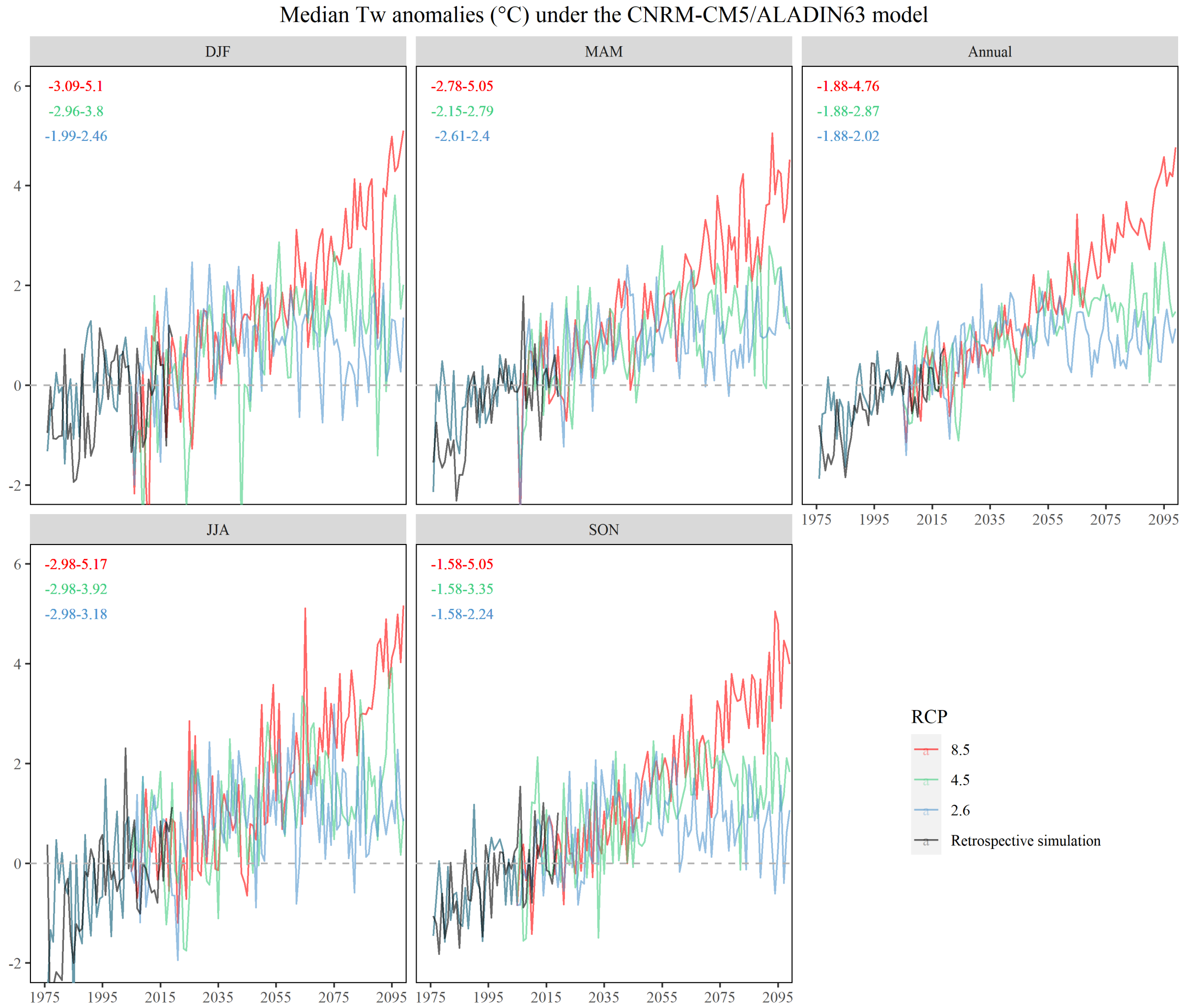

Figure 6.26: Comparing median anomalies of Tw (across reaches) with respect to the 1990–2019 period at the seasonal and annual scale under the CNRM-CM5-LR/ALADIN63 (intermediate) model, and 3 different RCPs. Colors are showing different RCPs. Numbers in colors in the top left corner of each graph show the range of median anomalies. The black line is showing median anomalies of Tw (across reaches) in the retrospective simulation with respect to the 1990–2019 period.

profile of summer Tw in the middle and at the end of the century almost overlaps for RCP 2.6 and 4.5. They are shifted up (by [+1.3 °C ; +2 °C] depending on RCP) compared to the historical period. The magnitude of this upward shift is almost the same all along with the longitudinal profile. For RCP 8.5, compared to the historical period, there is a clear upward shift in the middle of the century (up to +2 °C), and at the end of the century (up to +4.5 °C).

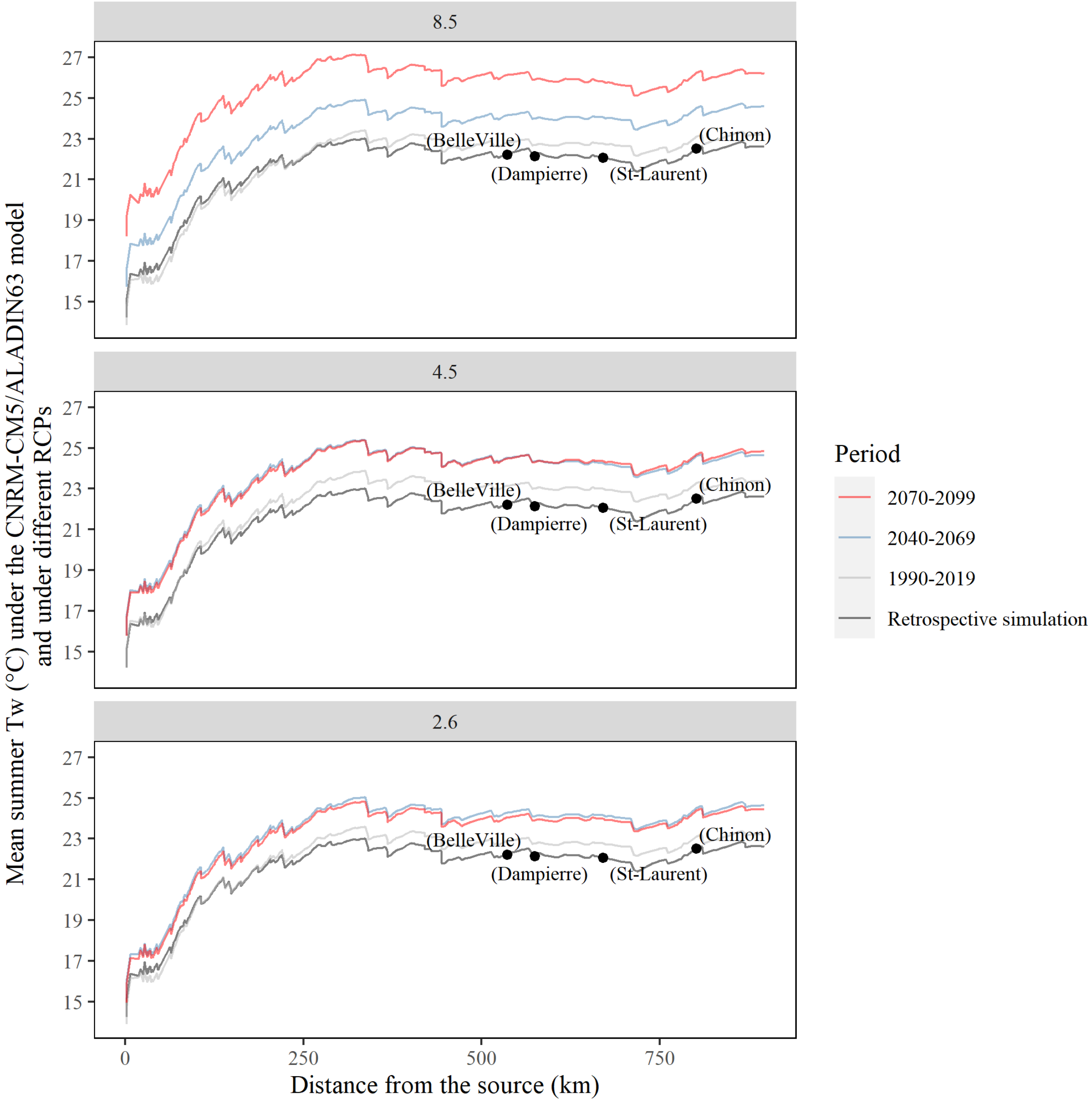

Figure 6.27: The longitudinal profile of summer Tw for the Loire River under the CNRM-CM5-LR/ALADIN63 (intermediate) model, and 3 different RCPs in the historical period (1990–2019), in the middle (2040–2069) and at the end of the century (2070–2099). The black line shows the longitudinal profile of summer Tw over the historical period (1990–2019) in the retrospective simulation. The points are showing observed Tw (see Table 2.1, p. 48 about these stations). The colors show different time slices.

6.5.2 Uncertainty of climate modeling

At this step, to show the uncertainty among the different GCM/RCMs in a more simple way, the analyses will focus on all selected GCM/RCMs in the current study under one RCP. Here RCP 8.5 is selected since it projects more important changes based on the above results (see section 6.5.1). Like what was done in the section 6.5.1 for assessing RCPs uncertainty, here, in addition to seasonal Tw changes, we compare the annual cycle of Tw for three different

GCM/RCMs under RCP 8.5. The longitudinal profile of summer Tw for the Loire River across these various GCM/RCMs are also compared.

Seasonal changes in stream temperature

For all GCM/RCMs under RCP 8.5, median Tw changes (across reaches) show an increase in Tw regardless of season and time slice ([+0.76 °C ; +4.95 °C]) (Figure 6.28). Such an increase in median Tw gets greater towards the end of the century for all GCM/RCMs. Consequently, the frequency of the high summer Tw ($>$ 20 °C) increases towards the end of the century with the worst case for the HadGEM2/CCLM4-8-17 (dry and hot) model with an increase in the frequency of summer Tw $>$ 23 °C (see Figures 6.22 and 6.23). In winter, median Tw changes under all models are close unlike in summer when median Tw changes is considerably different from one model to another.

Across GCM/RCMs, the greatest changes in median Tw (across reaches) are in the spring and summer of both time slices with the exception of the IPSL-CM5A/MRWRF381P (warm and wet) model (Figure 6.28). In such a case, the median change in Tw is in range of [+1.64 °C ; +2.68 °C] in the middle of century, and [+3.21 °C ; +4.95 °C] at the end of the century. For the IPSL-CM5A/MRWRF381P (warm and wet) model, the greatest changes are in winter with a median change of [+1.86 °C ; +3.83 °C] , respectively, in the middle and at the end of the century.

Annual cycle of stream temperature

Like Figure 6.25 for RCPs, there is a good agreement between the median annual cycle of Tw in retrospective simulation (black line) and in projections (grey line) over the historical period across GCM/RCMs under RCP 8.5. Compared to the historical period, across GCM/RCMs under RCP 8.5, the annual cycle of Tw is shifted up over the whole year in the middle of the century (by up to +2.8 °C), and at the end of the century (by up to +5.17 °C at the end of the century), with the exception of the IPSL-CM5A/MRWRF381P (warm and wet) model for which such a shift is less clear during summer (Figure 6.29). The greatest shift in the annual cycle of Tw in both time slices happens under the HadGEM2/CCLM4-8-17 (dry and hot) model. For all GCM/RCMs, there is no shift in the timing of the maximum value of Tw (horizontal shift) like what was observed across RCPs in Figure 6.25.

Longitudinal profile of stream temperature for the Loire River

There is also a good agreement between the longitudinal profile of summer Tw for the Loire River in retrospective simulation (black line) and in observation at four Tw stations (in point) across GCM/RCMs (Figure 6.30). There is a similarly good agreement in projections (grey line) and in the retrospective simulation (black line) (Figure 6.30) across different GCM/RCMs,

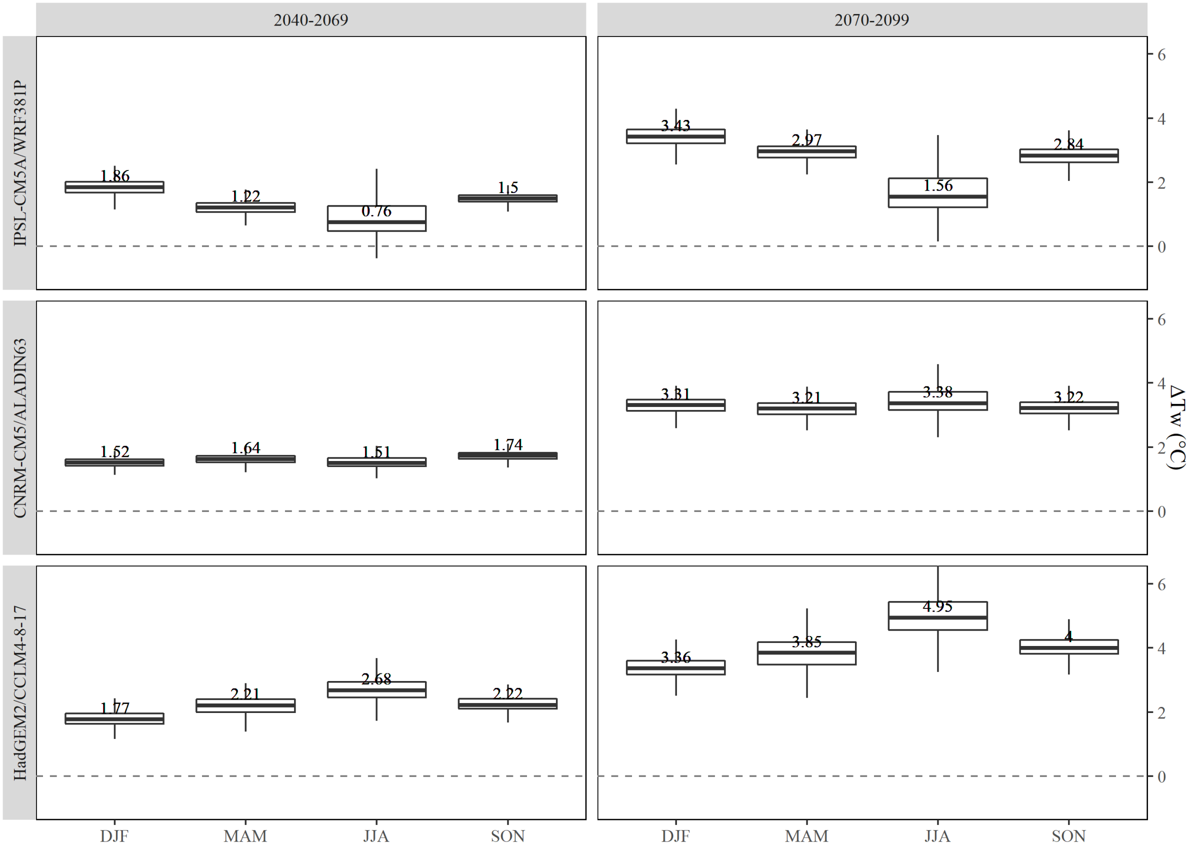

Figure 6.28: Seasonal changes in Tw under different GCM/RCMs and RCP 8.5 with respect to the 1990–2019 period in the middle of the century (2040–2069) and at the end of the century (2070–2099). The numbers are showing median Tw changes across reaches.

except for the HadGEM2/CCLM4-8-17 (dry and hot) model in the lower distances from the source (up to 1 °C underestimation), and for the two other GCM/RCMs at the end of the profile (up to 1 °C overestimation).

Across GCM/RCMs, the longitudinal profile of summer Tw in projections and in the retrospective simulation mimic the same pattern as across RCPs in Figure 6.27. Compared to the historical period, across GCM/RCMs and time slices, the longitudinal profile of summer Tw has an upward shift (Figure 6.30), except for the IPSL-CM5A/MRWRF381P (warm and wet) model in the middle and at the end of the longitudinal profile at the end of the century. In such a case, in the middle of the century, the maximum upward shift along the profile ranges between +1.64 °C and +3.2 °C depending on the GCM/RCM. Such range at the end of the century is [+2.5 °C ; +5.7 °C].

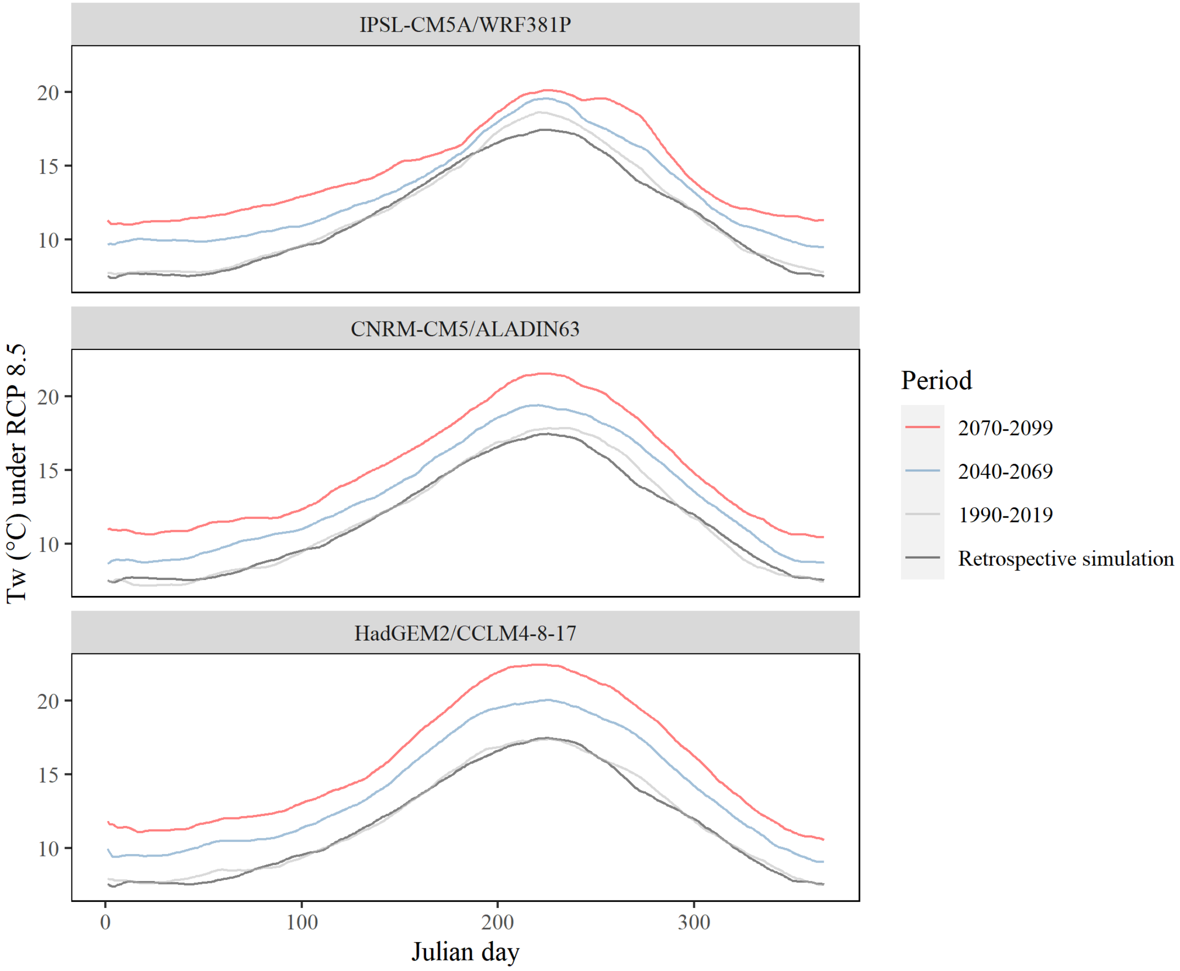

Figure 6.29: Median (across reaches) annual cycle of Tw under three GCM/RCMs and RCP 8.5 in the historical period (1990–2019), in the middle (2040–2069) and at the end of the century (2070–2100). The black line shows the median annual cycle of Tw over the historical period (1990–2019) in the retrospective simulation. For each cycle, the average of Tw over the desired time slice for each day is calculated then the 30-day moving average is applied to this daily cycle. The colors show different time slices.

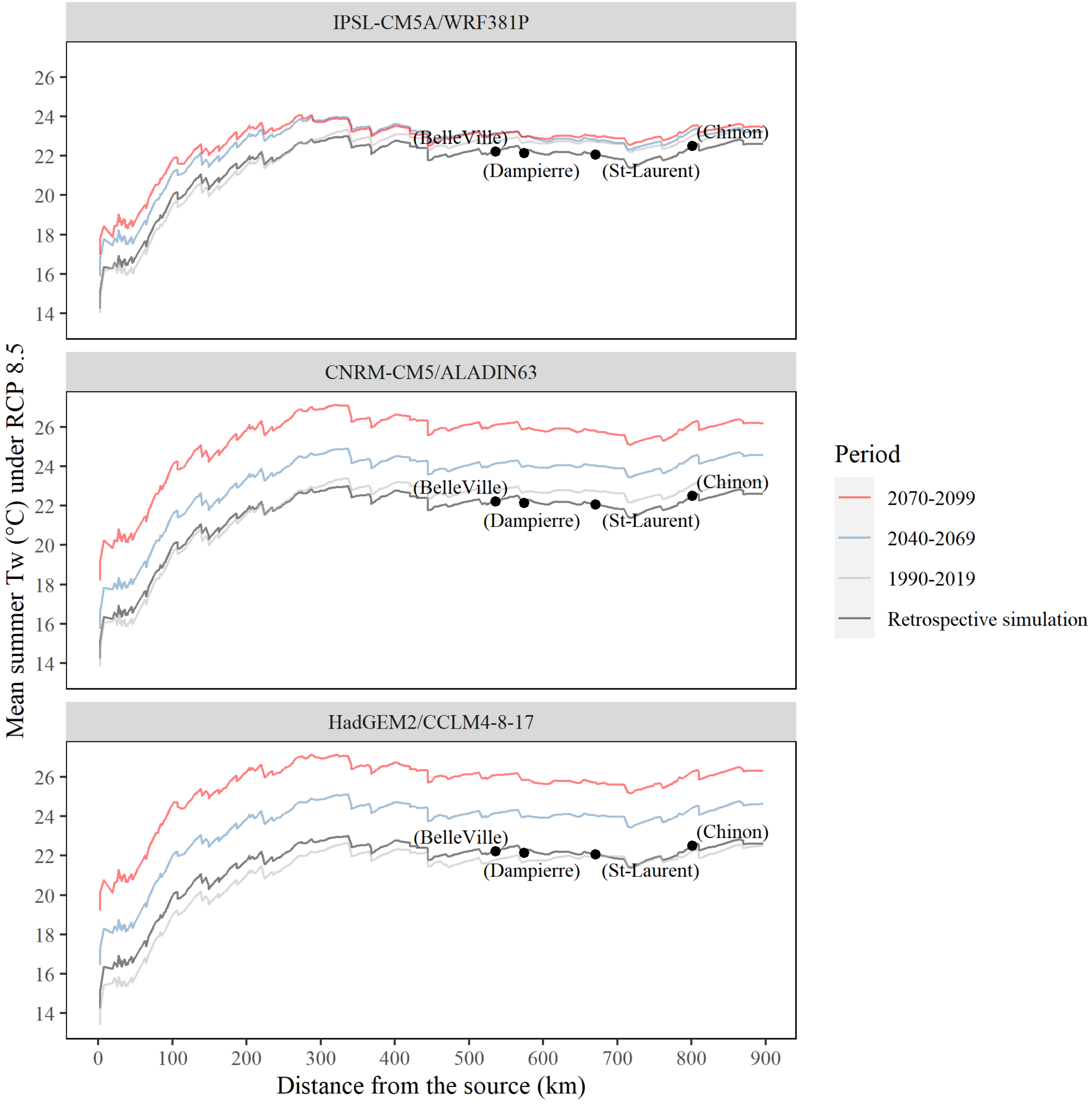

Figure 6.30: The longitudinal profile of summer Tw for 3 GCM/RCMs under RCP 8.5 for the Loire River in the historical period (1990–2019), in the middle (2040–2069) and at the end of the century (2070–2099). The black line shows the longitudinal profile of summer Tw over the historical period (1990–2019) in the retrospective simulation. The colors show different time slices.

6.5.3 Evolution of summer stream temperature over two centuries (1880-2099) for the Loire River

Figure 6.31 presents the evolution of summer Tw anomalies with respect to the 1976–2005 period over two centuries at Dampierre on the Loire River, a Tw station with long-term observed data (see Table 2.1, p. 48 for more information about this station). In fact, to have this type of information, different types of Tw data are combined as follows:

- Reconstructed Tw over the 1880-2003 period adopted from Moatar and Gailhard (2006) (referred as reconstruction (Moatar and Gailhard, 2006) here). Moatar and Gailhard (2006) reconstructed Tw over this period by developing a statistical link between Tw, Ta and Q.
- Retrospective simulation over the 1963-2019 period provided by the T-NET thermal model (referred as retrospective simulation (T-NET) here). This simulation was done in the current study in the previous chapter (see section 5.3, p. 137).
- Projected Tw under different GCM/RCMs, and RCPs over the 1976–2100 period.
- Finally, observed Tw (over the 1977-2019 period) is added to this combination of Tw data to have a control over the past and present, and a reference for the future. The agreement between observation and the retrospective simulation (T-NET) for seasonal Tw was already seen at this station in Figure 5.4 (p. 137).

Since all of these different Tw data have data over the 1976–2005 period, and there is also an agreement between Tw absolute values in projections and in the retrospective simulation over this period (see Figure 6.5), the Tw anomalies are considered with respect to the 1976–2005 period.

Figure 6.31, first of all, reveals a great increase in Tw in the 1890s. Devers et al. (2021) showed a negative anomaly in P over France in the 1890s, and this resulted in a negative anomaly in Q over the Loire river basin (see Figure 5.1 of Devers, 2019). The other great increase in Tw is observed in the 1940s. Moatar and Gailhard (2006) explained such increase due to a great decrease in Q. Devers (2019) (see Figure 5.16, p. 212) also observed such a decrease in Q in the 1940s as a result of an increase in Ta. In other words, this period was hot and dry, which had impacts on Tw.

A difference between the reconstruction and the retrospective simulation (< 0.67 °C) can be seen. This difference may originate from the fact that the reconstruction is based on a statistical link between Tw, Ta, and Q, and does not consider the influence of other drivers, while the retrospective simulation considers other drivers as well as their physical relationship (see Equ. 4.6, p. 93).

Across GCM/RCMs, the largest summer Tw anomalies belong to projections under RCP 8.5, with the exception of the IPSL-CM5A/MRWRF381P (warm and wet) model. The increase in Tw started in the late 1980s, which was previously seen in the past trend analyses (see Figure 5.14, p. 150). Such an increase in Tw anomalies in summer will continue towards the end of the century, and can reach up to [+2 °C ; +5 °C] depending on the GCM/RCM and RCP.

Finally, for RCP 2.6 and 4.5 across GCM/RCMs, the rate of an increase in the summer Tw anomaly between 1980 and 2030 is higher than that at the end of the century. In other words, changes in summer Tw anomalies under RCP 2.6 and 4.5 get more moderate at the end of the century, which is compatible with the representation of future behavior of emissions evolution under these RCPs (see Figure 6.1, and observed Tw anomalies across these RCPs in Figure 6.26)

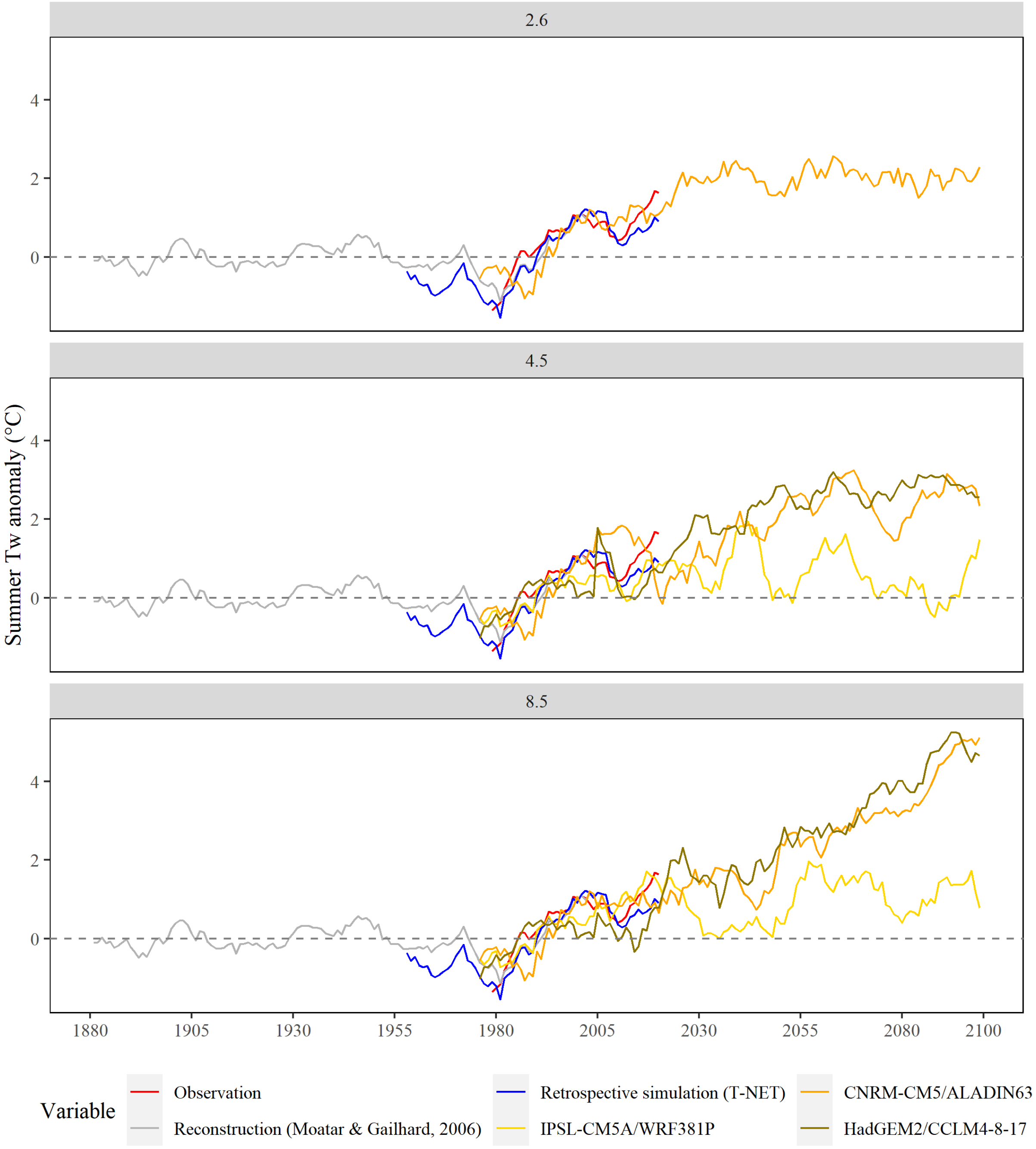

Figure 6.31: The anomalies of the 10-year moving average of Tw in summer with respect to the 1976–2005 period over the two centuries at Dampierre on the Loire River (see Table 2.1, p. 48 for more information about this station). Different types of Tw data are combined to produce this figure including reconstruction (1880-2003) adopted form Moatar and Gailhard (2006), the retrospective simulation (1963-2019) (from the previous chapter, Chapter 5), observation (1977-2019), and projections (1976–2099). Colors show different types of Tw data.

6.6 Hydroclimate drivers of changes in future stream temperature

Since Tw changes under RCP 8.5 are the most important ones across RCPs based on the above results, we decide to focus the next analyses on this RCP. This also makes assessments simpler.

In Chapter 5, spatial and temporal links between past trends in Tw, Ta, and Q were found (see section 5.4, p. 142). This arises a question, which is whether such spatial and temporal links between changes in these variables are also observed in the future. To answer this question, first, anomalies of these variables – with respect to the 1990–2019 interannual mean – are computed for different seasons and GCM/RCMs under RCP 8.5 over the 1976–2099 period. The anomalies of Tw, Ta, and Q are reported in °C, °C, and %, respectively, with respect to the 1990–2019 period. Then, the median anomalies of these variables across reaches are compared to investigate whether the greatest Tw anomalies, Ta anomalies, and Q anomalies are concomitant or not (i.e., whether there is a temporal link between Tw, Ta, and Q). Finally, to determine the spatial links, jointly positive Tw changes, negative Q changes, and positive Ta changes under all GCM/RCMs and RCP 8.5 are identified for all 52 278 reaches across seasons.

6.6.1 Synchronicity of stream temperature anomalies with air temperature and streamflow anomalies in future

Ta anomalies (°C) are always increasing across seasons and GCM/RCMs (Figure 6.32). The same was observed for the Ta anomalies in the retrospective simulation (see Figure 5.14, p. 150). The greatest positive median of Ta anomaly (across reaches) is in summer (up to 10 °C) under the HadGEM2/CCLM4-8-17 (dry and hot) model at the end of the century. Across GCM/RCMs and seasons, the negative anomalies are mainly before the middle of the century.

On the other hand, Q anomalies are relatively decreasing (Figure 6.33). Across GCM/RCMs and seasons, the median of Q anomalies are negative (up to -97%) for the majority of the years over the 1976–2099 period, with the exception of median anomalies of the IPSL-CM5A/MRWRF381P (warm and wet) model. The lowest median of Q anomalies is projected by the HadGEM2/CCLM4-8-17 (dry and hot) model in fall (up to -97%).

Tw anomalies (°C), like Ta anomalies, are always increasing across seasons and GCM/RCMs (Figure 6.34). Tw anomalies are more variable across the basin than Ta anomalies. The same feature was already observed for the Tw anomalies in the retrospective simulation (see Figure 5.14, p. 150). Moreover, compared to Ta anomalies, the range of Tw anomalies is smaller across GCM/RCMs and seasons. The greatest median of Tw anomalies is observed in summer (up to 7 °C) under the HadGEM2/CCLM4-8-17 (dry and hot) model.

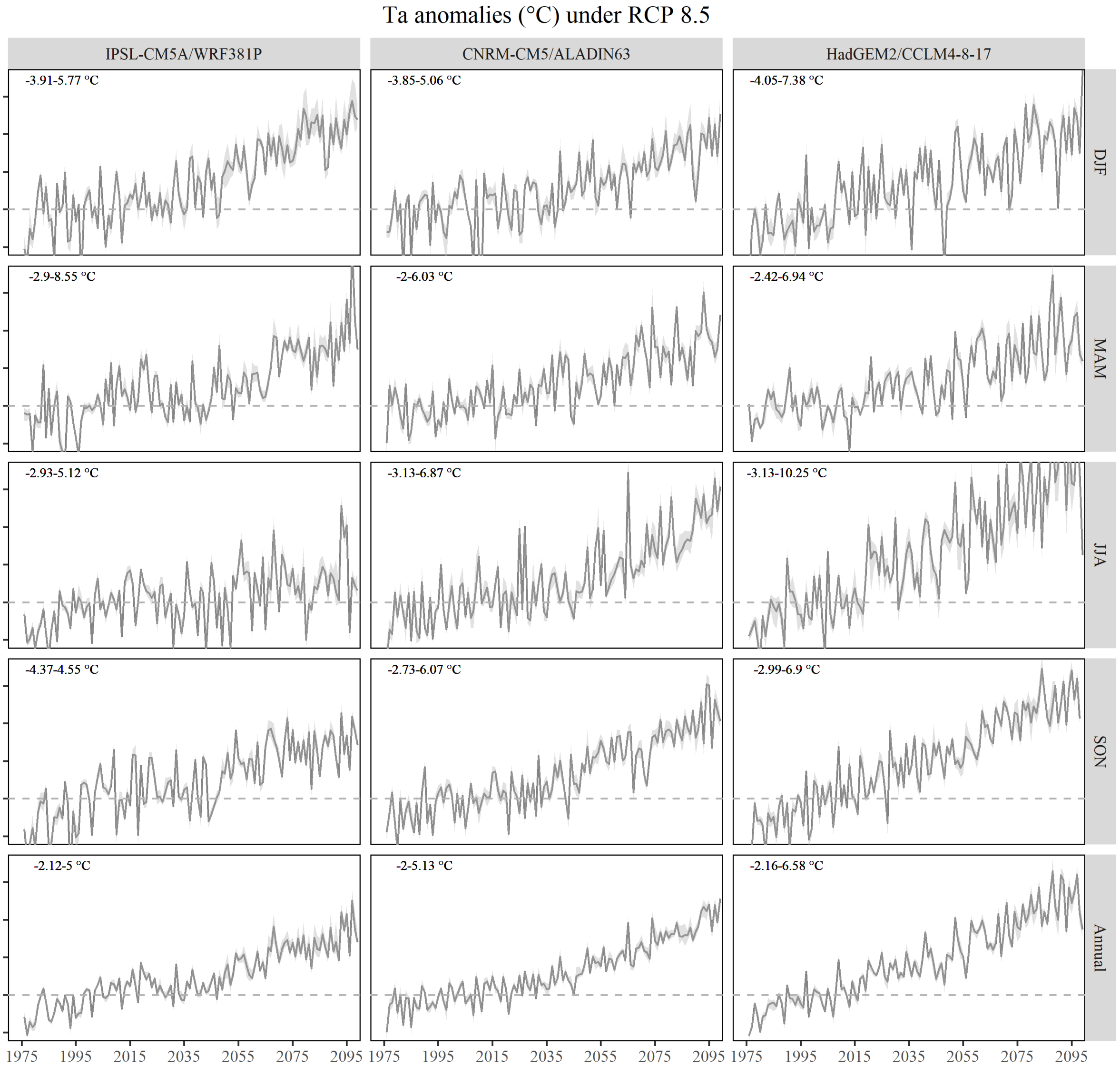

Figure 6.32: Seasonal and annual anomalies of Ta with respect to the 1990–2019 period for different GCM/RCMs under RCP 8.5. Numbers in black in the top left corner of each graph show the range (minimum and maximum) of median anomalies. The solid line shows the median anomaly across reaches.

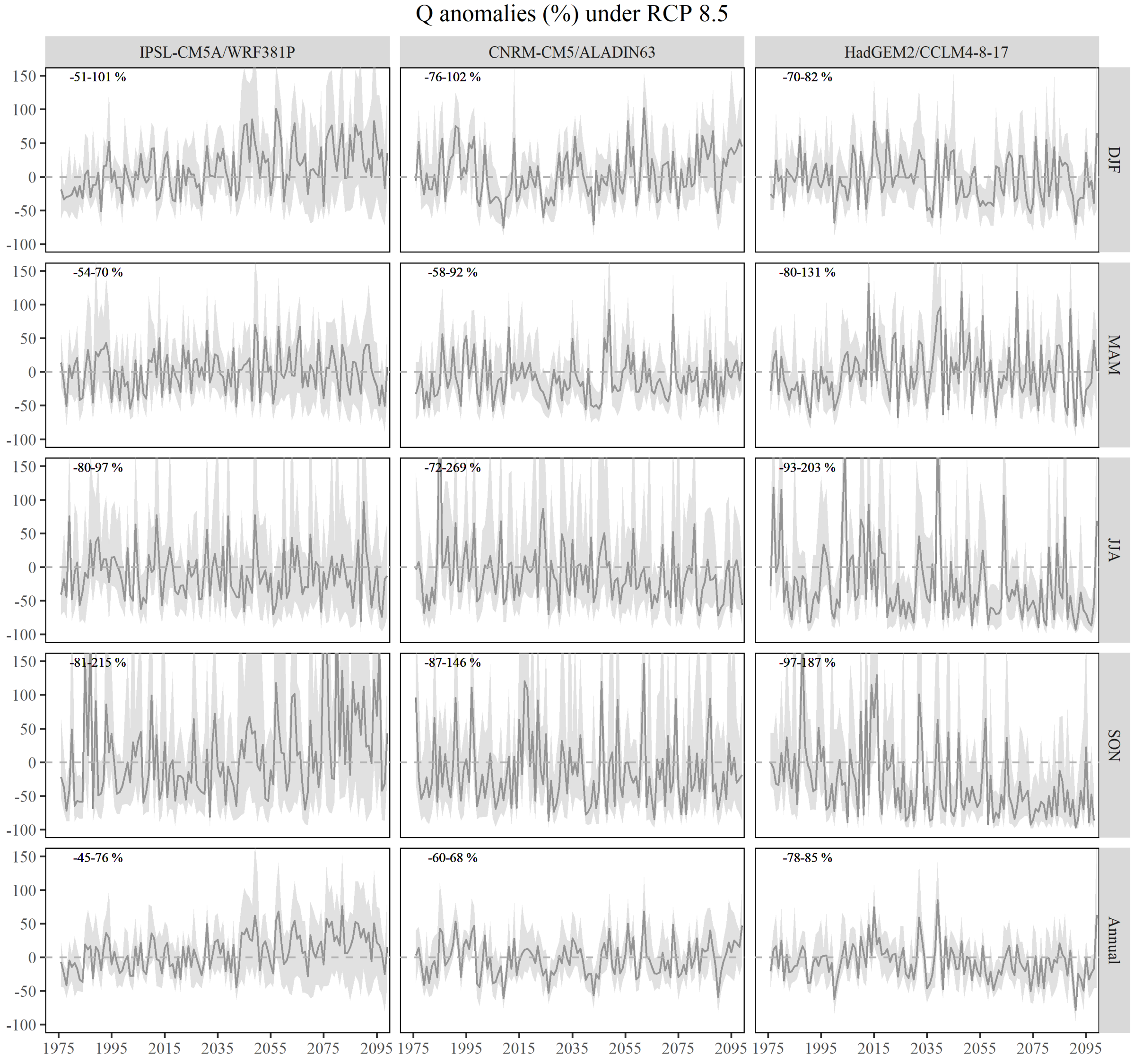

Figure 6.33: Seasonal and annual anomalies of Q with respect to the 1990–2019 period for different GCM/RCMs under RCP 8.5. Numbers in black in the top left corner of each graph show the range of median anomalies. The solid line shows the median anomaly across reaches.

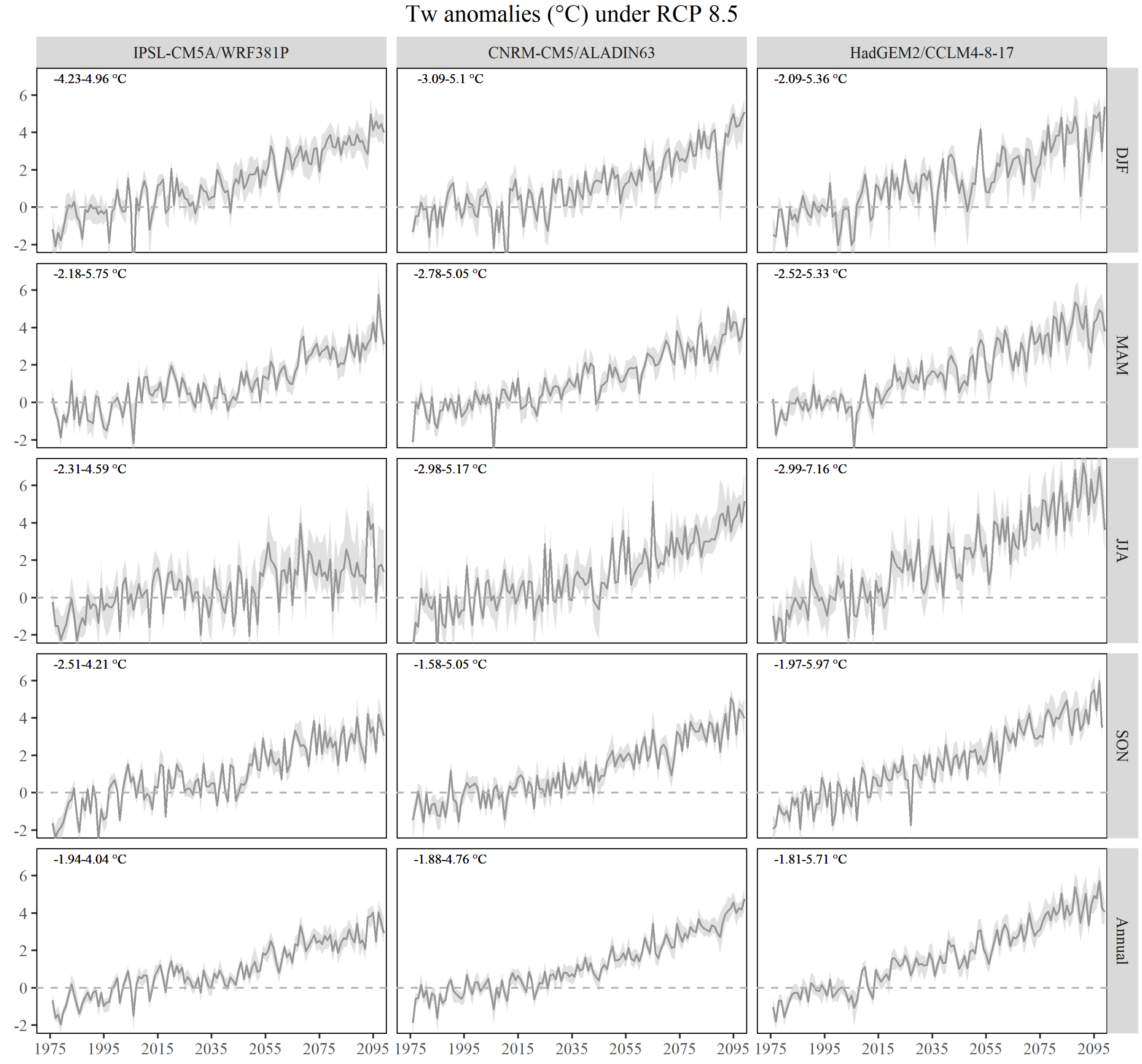

Figure 6.34: Seasonal and annual anomalies of Tw with respect to the 1990–2019 period for different GCM/RCMs under RCP 8.5. Numbers in black in the top left corner of each graph show the range of median anomalies. The solid line shows the median anomaly across reaches. This figure has the same scale as the Ta anomalies (Figure 6.32).

Anomalies of Ta and Tw (Figures 6.32 and 6.34) are generally increasing while both decreasing and increasing Q anomalies is observed (Figure 6.33). To understand the temporal links between anomalies of Tw and Q in one hand, and anomalies of Tw and Ta in the other hand, the median of such anomalies across the reaches are compared together (see Figure 6.35).

Figure 6.35 depicts that the majority of negative median Tw anomalies across seasons and GCM/RCMs occur before the middle of the century (>80% of such anomalies). These negative Tw anomalies happen when there are either negative Ta anomalies or positive Q anomalies or both conditions (Figure 6.35). Moreover, a larger dispersion in future anomalies (cross and triangle shapes) is observed compared to the recent period anomalies (circles) (see Figure 6.35).

To test whether the greatest values of positive median Tw anomalies can be due to co-occurrence of increase in Ta and decrease in Q, which are the main hydro-climate drives of Tw, first, a threshold for spotting the greatest Tw anomalies is selected. Here, the median of Tw anomalies over the basin in the summer of 2003 in the retrospective simulation is used. The summer of 2003 is selected since it is the most important hot summer in the recent period (Moatar and Gailhard, 2006; Bustillo et al., 2014). For the retrospective simulation, the median of summer Tw anomalies across all reaches with respect to the 1990–2019 period is 2.3 °C. Afterward, the median Ta and Q anomalies corresponding to these largest median Tw anomalies (> +2.3 °C=anomaly of summer 2003) are investigated. Such an assessment can also help to understand whether hot years like the hot summer of 2003 will be experienced again in the future or not.

Across seasons and GCM/RCMs, 30 to 55 years (over the 1976–2099 period) have a Tw anomaly> +2.3 °C (anomaly of summer 2003), with the exception of spring, summer and annual of the IPSL-CM5A/MRWRF381P (warm and wet) model (7-27 years) (Figure 6.35). As mentioned before, the majority of positive Tw anomalies occur before the middle of the century, meaning that the years with the largest Tw anomalies occur mainly over the 2040–2099 period. Therefore, years like the hot summer of 2003 will be experienced frequently in the middle and at the end of the century (50-80 % of the years over the 2040-2099 period) regardless of the season.

For a considerable number of the years (41-92 %) with Tw anomaly>+2.3 °C, across seasons and GCM/RCMs, both a positive Ta anomaly (> 2 °C), and a negative Q anomaly (< -10%) occur jointly, with the exception of fall of the IPSL-CM5A/MRWRF381P (warm and wet) model, and winter of all models (5-30 % of years) (Figure 6.35), showing that the greatest values of positive median Tw anomalies can be due to co-occurrence of increase in Ta and decrease in Q.

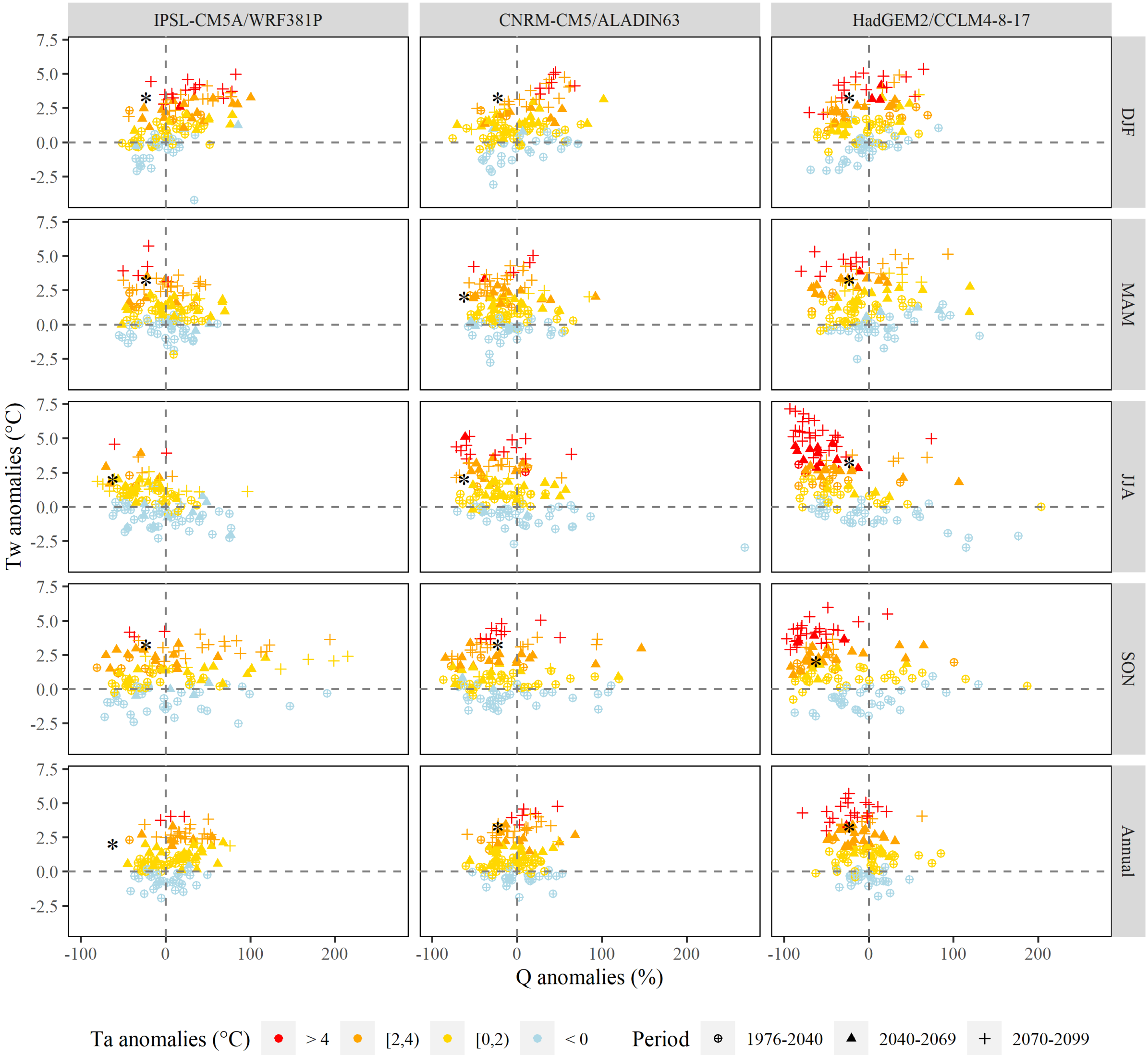

Figure 6.35: Relationship between Tw anomalies and Ta anomalies (with respect to the 1990–2019 period) in one hand, and Tw anomalies and Q anomalies in the other hand under different GCM/RCMs and RCP 8.5 in different seasons. Points are individual years identified from median anomaly values across all reaches. Colors and shape points are showing Ta anomalies and corresponding time slice, respectively. The grey dashed lines correspond to zero Q and Ta anomalies. The symbol "*" in black corresponds to the median of Tw anomaly (across reaches) in the summer of 2003 in the retrospective simulation over the 1990–2019 period (+2.3 °C).

6.6.2 Synchronicity of extreme changes in stream and air temperature, and streamflow across reaches

In the previous section, temporal links between Tw and Ta and/or Q were found. Here, the spatial links between these variables are assessed at the reach scale. To do so, the percentage of reaches with jointly positive Tw changes, positive Ta changes, and negative Q changes is computed for each season, time slice, and GCM/RCM under RCP 8.5.

Positive Tw changes, positive Ta changes, and negative Q changes occur coincidentally at the majority of reaches (55-100 %) across GCM/RCMs under RCP 8.5, seasons, and time slices (Figure 6.36), with the exception of winter of the IPSL-CM5A/MRWRF381P (warm and wet) model and the CNRM-CM5-LR/ALADIN63 (intermediate) model in both time slices, spring and fall of the IPSL-CM5A/MRWRF381P (warm and wet) model in both time slices, and spring of the HadGEM2/CCLM4-8-17 (dry and hot) model in the middle of the century (12-43% of reaches, considering all these exceptions). In both time slices, the majority of such joining conditions (60-100 % of such reaches) are in HER A (see Figures E.28 and E.29).

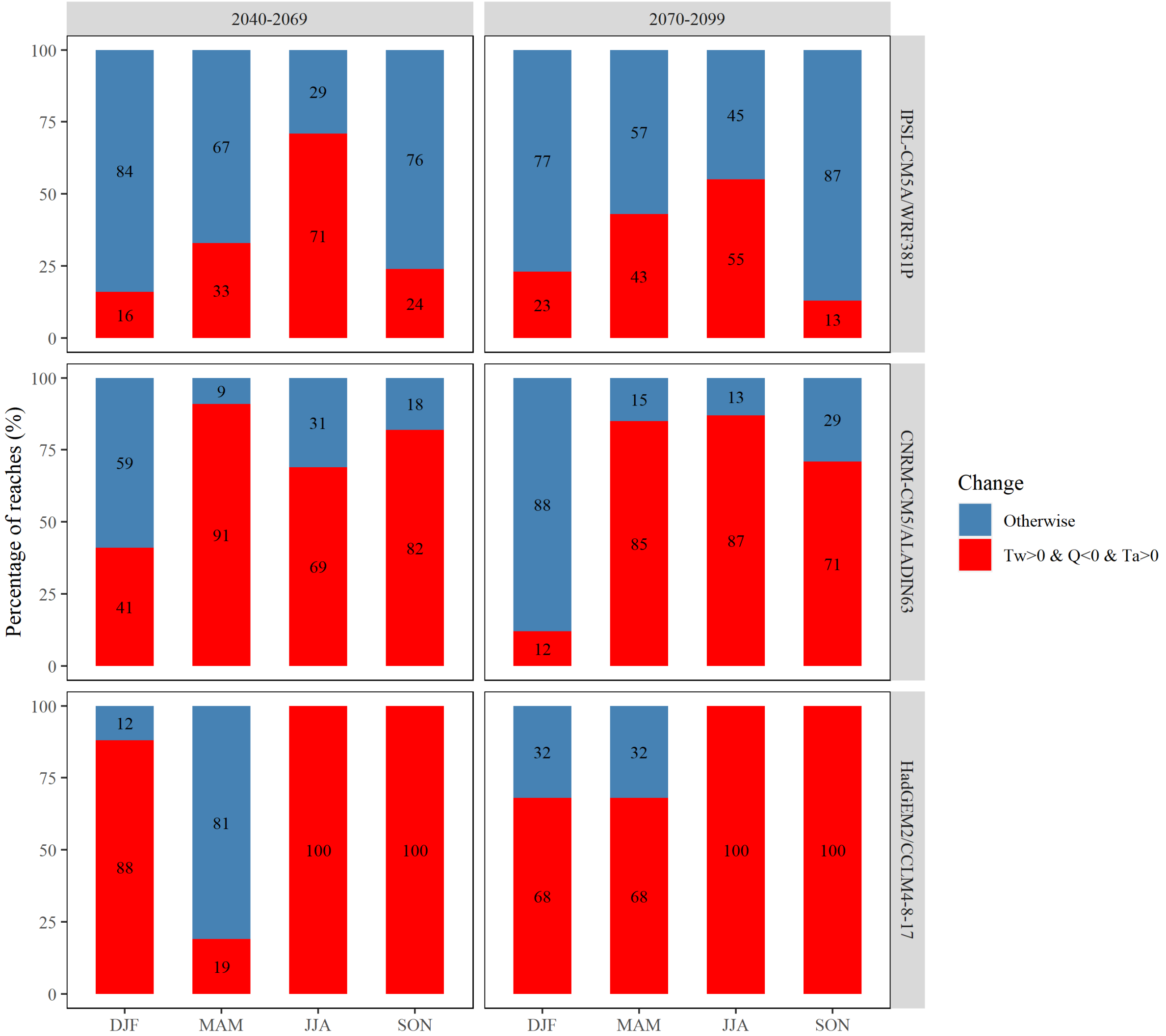

Figure 6.36: Percentage of reaches with consistent changes in Tw, Ta and Q categorised with respect to sign of change in Tw, Ta, and Q for different GCM/RCMs under RCP 8.5, seasons, and time slices. The changes are calculated with respect to the 1990–2019 period.

6.7 Landscape drivers of stream temperature

6.7.1 Influence of stream size

In Chapter 5, stream size, HER and riparian shading factor (SF) were identified as the major potential landscape drivers, especially in the summer period (see Figures 5.19, p. 155, and 5.20, p. 156). To evaluate the influence of such drivers on future Tw over the summer, a similar approach to Chapter 5 (see section 5.5, p. 154) is used. To do so, first, the mean summer Tw over the different time slices including the 1990–2019, 2040–2069 and 2070–2099 periods is computed for all reaches, and for all GCM/RCMs under RCP 8.5. The same indicator is also calculated by using the retrospective simulation over the 1990–2019 period to use it as a control for the past and a reference for the future. Then, to see the influence of reach size on interannual means, the Strahler order of each reach is used as a proxy for stream size. Reaches with Strahler order 5–8 are combined into a single group termed "large rivers". Finally, the relationship between the median of summer Tw (i.e., median across all reaches) and Strahler order is assessed across HERs, time slices, and GCM/RCMs.

The evolution of median summer Tw and reach size in projections along with that in the retrospective simulation over the historical period 1990–2019 across HERs (see Figure 6.37). Across GCM/RCMs under RCP 8.5, HERs, and time slices, Strahler order is positively correlated with median summer Tw (Figures 6.37). Indeed, across GCM/RCMs, and HERs, median summer Tw in large rivers (Strahler order ≥ 5) is greater (by [+5 °C ; +6.7 °C]) than that in small streams (Strahler order 1) in both time slices. Overall, there is [+5 °C ; +7 °C] difference between median summer Tw in large rivers and in small streams across GCM/RCMs, HERs, and time slices including the historical period.

6.7.2 Influence of riparian shading

At this step, the relationship between summer Tw and riparian shading is assessed. To do so, similarly to what was done for assessing the influence of stream size on summer Tw in the previous section, first, the mean summer Tw over the different time slices including the historical period is computed for all reaches, and for all GCM/RCMs under RCP 8.5. Then, five levels of riparian shading (<15 %; 15-25 %; 25-40 %; 40-60 %; >60 %) for small streams (distance from the source <30 km) are considered like in the past trend analysis in the previous chapter (section 5.5, p. 154). Then, the relationship between median of summer Tw (i.e., median across all reaches) and levels of riparian shading is assessed across HERs, time slices, and GCM/RCMs.

The relationship between median summer Tw and riparian shading in projections along with that in the retrospective simulation over the historical period 1990–2019 across HERs as

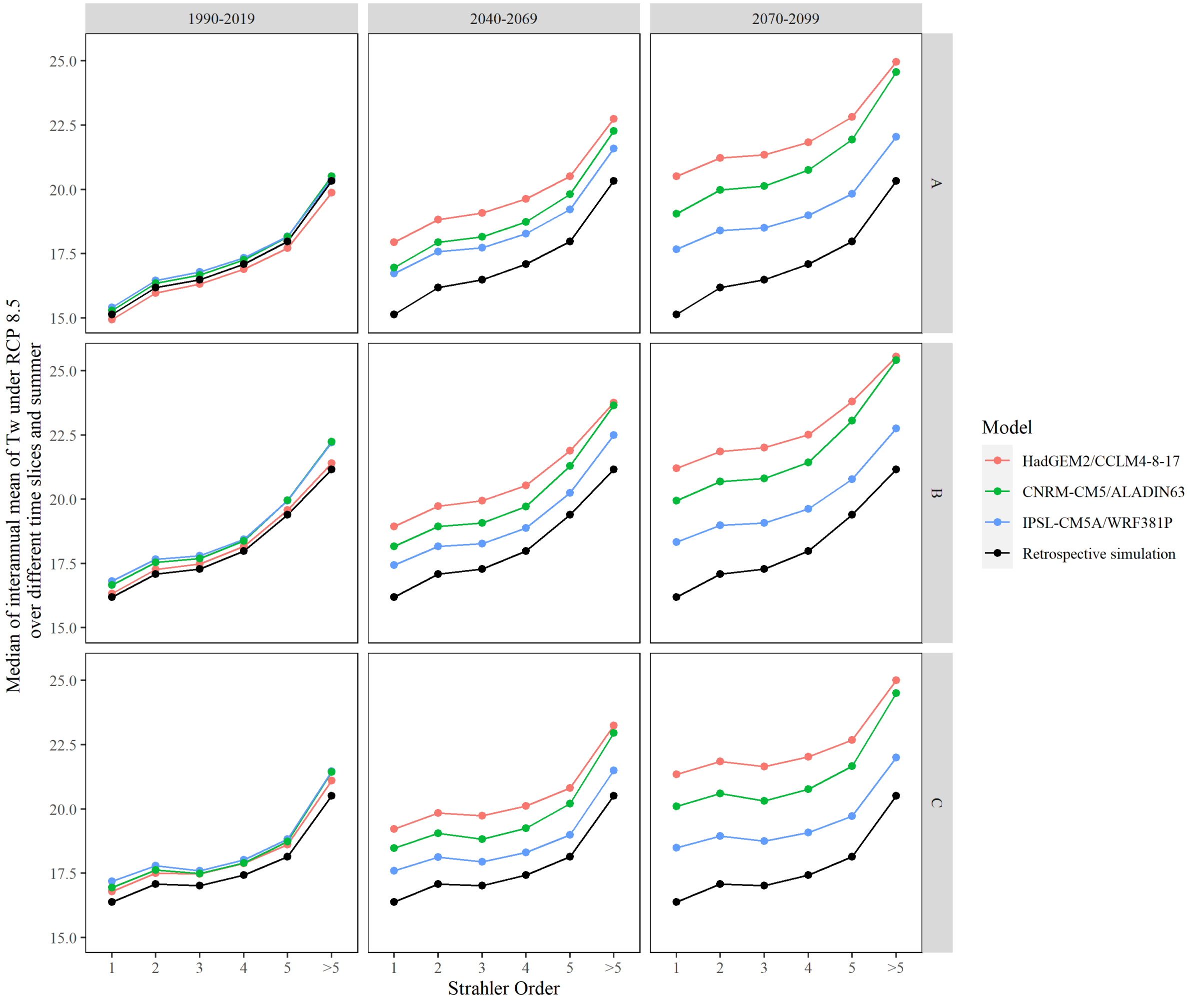

Figure 6.37: Relationships between reach size, and median summer Tw across reaches for different HERs and GCM/RCMs under RCP 8.5 in the middle (2040–2069) and at the end of the century (2070–2099). The colors show different GCM/RCM. The black line shows the median summer Tw in the retrospective simulation.

shown in Figure 6.38. There is an important mitigation effect of shading on summer Tw for small streams for all GCM/RCMs and HERs (Figures 6.38). The median summer Tw, across GCM/RCMs and HERs, is [+3.5 °C ; +4.5 °C] lower in the middle and at end of the century in sparsely shaded reaches ($SF < 15\%$) with respect to highly shaded reaches ($SF > 40\%$). Overall, there is [+3.3 °C ; +4.6 °C] difference between median summer Tw in sparsely shaded reaches ($SF < 15\%$) and in highly shaded reaches ($SF > 40\%$) across GCM/RCMs, HERs and time slices including the historical period.

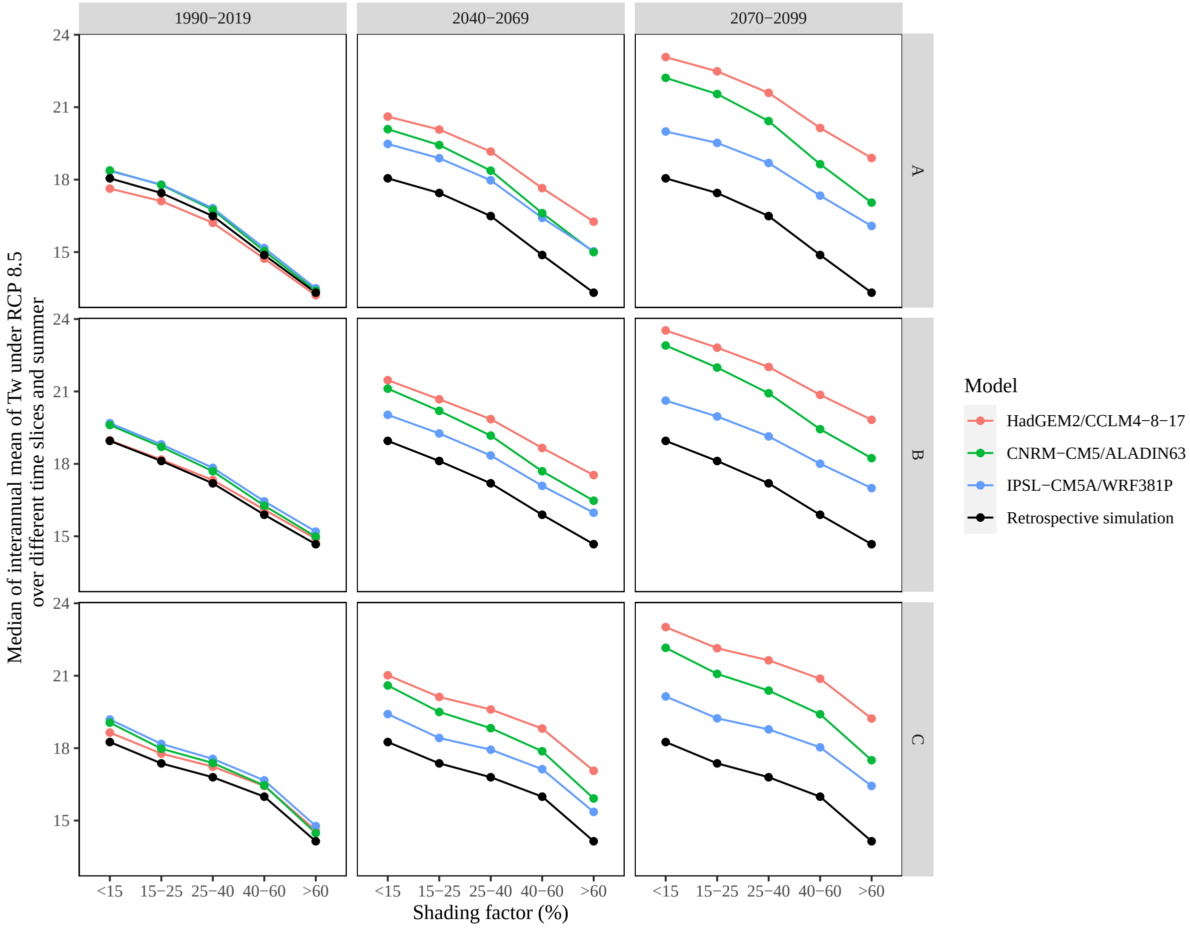

Figure 6.38: Relationships between riparian shading factor (SF) and median summer Tw across small reaches (distance from the source < 30 km) for different HERs and GCM/RCMs under RCP 8.5 in the middle (2040–2069) and at the end of the century (2070–2099). The colors show different GCM/RCM. The black line shows the median summer Tw in the retrospective simulation.

6.8 Increase in stress on brown trout in the future

In the past trend analyses, the evolution of the number of days with Tw>17 °C ($N_{Tw} > 17$=the lethal temperature of juvenile brown trout) was studied in rivers with non-zero density (individual/100 m^2) for brown trout (see section 5.6, p. 156). It was observed that there was an increase in $N_{Tw} > 17$ metric over the recent period. This section aims at determining the evolution of this metric under future projections. To do so, the mean of $N_{Tw} > 17$ over different time slices and the historical period is calculated for all GCM/RCMs under RCP 8.5. The $N_{Tw} > 17$ is also calculated through the retrospective simulation over the 1990–2019 period. Note that, like section 5.6 (p. 156), only rivers with non-zero density for brown trout are considered.

There is a quite good agreement between the median of $N_{Tw} > 17$ (across reaches) in projections (25-35 days, depending on the GCM/RCMs) and in the retrospective simulation (27 days) over the historical period 1990–2019 (Figure 6.39). Median of $N_{Tw} > 17$ increases from the his-

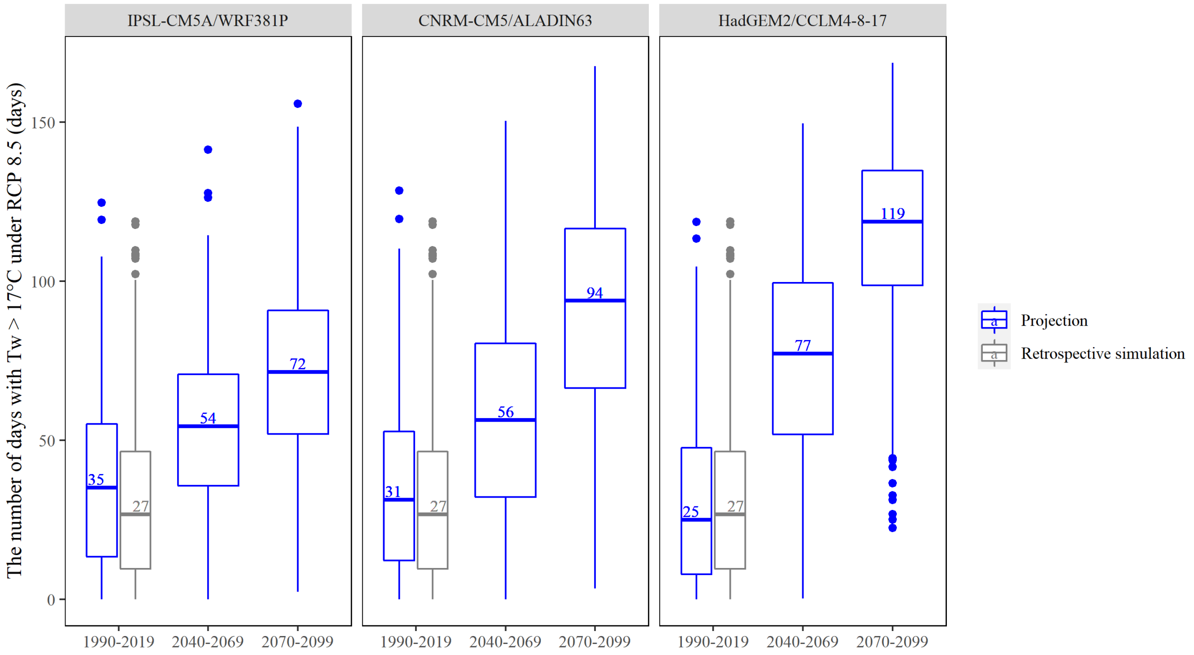

Figure 6.39: The evolution of the number of days with Tw>17 °C for different GCM/RCMs under RCP 8.5 over the historical period (1990–2019), in the middle (2040–2069) and the end of the century (2070–2099). The grey boxplots are showing results in the retrospective simulation over the 1990–2019 period. Only rivers with non-zero density for brown trout depicted in Figure 5.21 (p. 157) are used. The numbers are showing median values across reaches.

torical period to the end of the century for all GCM/RCMs. In the middle of the century, median $N_{Tw} > 17$ increases by 50-200 % with respect to the 1990–2019 period across GCM/RCMs. At the end of the century, such an increase seems more critical (by 100-300 %, depending on the GCM/RCM).

6.9 Summary of findings

6.9.1 Performance of future projections

There is a good correlation (r> 0.9) between meteorological variables in projections and in the retrospective simulation (provided by the SAFRAN reanalysis data), with the exception of PET of all models (cor=0.51-0.55 across GCM/RCMs) (see Figure 6.3). As mentioned before, such a bias can be due to different formulas used in SFARAN and in GCM/RCMs to calculate PET. Nevertheless, there is a small bias between Tw absolute values in projections and in the retrospective simulation (see Figures 6.5 and 6.6). In fact, projections can get the right absolute values of Tw (median bias=0.13-0.43 across seasons, and GCM/RCMs), but they fail to reach the right magnitude of trends and their spatial variability (see Figure 6.7 and 6.8). However, like in the retrospective simulation, projections show a significant increasing trend in Tw over the recent period (1976–2019) (Figure 6.9). Moreover, in different assessments, a good agreement between the projections and the retrospective simulation or even observations was found (e.g., see Figures 6.25, 6.26, 6.27, 6.29, 6.30, 6.31, 6.37, 6.38 and 6.31).

6.9.2 Uncertainty of projections

As expected, projected Tw changes are different from one RCP to another (section 6.5.1), and from GCM/RCM to another (section 6.5.2). In the current study, to assess the RCPs uncertainty, the Tw changes projected by one GCM/RCM under different RCPs are studied and compared (see section 6.5.1). In the current study, the 3 RCPs are available for the CNRM-CM5/ALADIN63 (intermediate) model. As this GCM/RCM is the intermediate one, the uncertainty resulting from the GCM/RCM itself is lower compared to the other selected GCM/RCMs, which are either warm and wet or hot and dry.

Under the CNRM-CM5/ALADIN63 (intermediate) model, the difference between RCPs in projecting Tw changes is not significant in the middle of the century, but it gets larger towards the end of the century (see Figure 6.24). The largest median changes in Tw across time slices, and seasons belongs to RCP 8.5 with a range of [+1.51 °C ; +1.74 °C] across seasons in the middle of century (vs [+0.91 °C ; +1.33 °C] for the two other RCPs), and range of +3.21 ; +3.38 °C across seasons at the end of century (vs [+0.47 °C ; +1.70 °C] for the two other RCPs) (see Figure 6.24).

Compatible with the representation of future behavior of emission evolution under RCP 2.6 (Figure 6.1), the median changes in Tw under this RCP across seasons is smaller at the end of the century compared to the middle of the century ([+0.9 °C ; +1.15 °C] vs [+0.47 °C ; +0.94 °C]; and see Figure 6.24). Moreover, compared to the historical period, the median annual cycle of Tw under RCP 2.6 and 4.5 is shifted up in the middle of the century (up to +2 °C), but there is no upward shift at the end of the century under these RCPs. In contrast to that, under RCP 8.5, an important upward shift over the whole year is found in the median annual cycle of Tw for both the middle (up to +2.16 °C) and the end of the century (up to +3.9 °C). The median Tw anomalies under RCP 2.6 and 4.5 across seasons also show that Tw changes get moderate at the end of the century in contrast with median Tw anomalies under RCP 8.5 for which an increase in Tw continues toward the end of the century with the same rate of increase in the middle of the century. The longitudinal profile of summer Tw for the Loire River also reveals such a moderate behavior for RCP 2.6 and 4.5 at the end of the century all along with the profile.

In addition to RCP uncertainty, there is climate modeling uncertainty. In fact, Tw changes projected by the three selected GCM/RCMs in the current study can vary significantly from one GCM/RCM to another (see section 6.5.2). For instance, under RCP 8.5, in the middle of the century (resp. at the end of the century), the range of median Tw changes across seasons is [+0.76 °C ; +1.86 °C] (resp. [+1.56 °C ; +3.43 °C]) for the warm and wet (IPSL-

CM5A/MRWRF381P) model whereas for the hot and dry (HadGEM2/CCLM4-8-17) model, this range is larger, [+1.77 °C ; +2.68 °C] (resp. [+3.36 °C ; +4.95 °C]) (see Figure 6.28). Such a difference can also be seen in the median annual cycle of Tw under these two GCM/RCMs (see Figure 6.29).

Moreover, depending on the GCM/RCMs, the season with the largest projected Tw changes is different. For instance, this season for the warm and wet (IPSL-CM5A/MRWRF381P) model is winter whereas for the two other models is spring and summer (see Figure 6.28). For the intermediate (CNRM-CM5-LR/ALADIN63) model, projected Tw changes across seasons do not vary so much in contrast to the other GCM/RCMs. The median annual cycle of Tw confirms such seasonal differences between GCM/RCMs. Indeed, the median annual cycle of Tw is shifted up over the whole year in the middle of the century (by up to +2.8 °C), and at the end of the century (by up to +5.17 °C at the end of the century) for all GCM/RCMs with the exception of the warm and wet (IPSL-CM5A/MRWRF381P) model for which this shift is less clear during summer (Figure 6.29).

The longitudinal profile of summer Tw for the Loire River also shows that there is an increase in Tw until 400 km distance from the source for the warm and wet (IPSL-CM5A/MRWRF381P) model for both time slices (see Figure 6.30). In contrast to this GCM/RCM, for the other two GCM/RCMs, such an increase in summer Tw occurs all along the profile for both time slices. Surely, the magnitude of increase in summer Tw is different from GCM/RCM to another.

The difference between GCM/RCMs can also be seen in projected Q changes. For instance, under the hot and dry (HadGEM2/CCLM4-8-17) model, there is a shift towards the fall in the timing of low flows whereas such shifts are less visible for the other GCM/RCMs (see Figure 6.16).

Finally, these uncertainties in projections should be considered in river management projects. The more GCM/RCMs and RCPs considered, the better would be our understanding of plausible futures, and the more reliable actions can be taken for adapting to the impacts of climate change.

6.10 Discussion

6.10.1 Worldwide increase in future stream temperature

The large scale and high spatial resolution assessment of future Tw changes in the current study shows a consistent increase in Tw (with respect to the 1990–2019 period) in the middle (2040–2069) and at the end of the century (2070–2099). Such important changes in Tw can also be found in other climate change impact studies on future Tw around the world, which used RCPs of the fifth IPCC (IPCC, 2014). These studies are summarized in Table 6.10.1. As seen in this

Table, the large scale and fine spatial resolution of the current study clearly stands out as unique as well as being among very few studies conducted in Europe. Although the reference period and future time slices considered in these future studies may be different, comparisons with them gives a comprehensive view of the overall future Tw changes all around the world.

In the current study, the median Tw change (across reaches) ranges between +0.72 °C and +2.68 °C across GCM/RCMs, RCPs, and seasons in the middle of the century. Other future studies also found an increase in Tw up to +3.8 °C in the middle of the century, with the exception of the study of Carlson et al. (2017), which found more increase in Tw (up to +6.8 °C) in surface-runoff dominated systems (see Table 6.10.1).

At the end of century, the range of median Tw change is [+0.47 °C ; +4.95 °C] across GCM/RCMs, RCPs, and seasons. Along with our findings, other future studies anticipated up to +7 °C increase in Tw at the end of the century. In Europe, Michel et al. (2021) recently found [+0.9 °C ; +3.5 °C] increase in Tw at the end of the century (over 12 catchment across Switzerland), which is in accordance with our findings over the Loire River basin in France.

Table 6.5: Recent studies on impact of climate change on future Tw, which used projections under RCPs of Van Vuuren et al. (2011).

Country	Study area	The middle of the century (°C)	The end of the century (°C)	Reference
France	**52278 reaches in the Loire basin**	**+0.9 ; +1.15** °C **(depending on the season) under RCP 2.6** **+0.72-+2.31** °C **(depending on the season) under RCP 4.5** **+0.76 ; +2.68** °C **(depending on the season) under RCP 8.5**	**+0.47 ; +0.94** °C **(depending on the season) under RCP 2.6** **+0.51 ; +2.71** °C **(depending on the season) under RCP 4.5** **+1.56 ; +4.95** °C **(depending on the season) under RCP 8.5**	**Present study**
US and Poland	5 rivers combined	+1 ; +2	+2 ; +3	Piotrowski et al. (2021)
Switzerland	12 catchments		+0.9 ; +3.5	Michel et al. (2021)
US	2 rivers		interquartile range of maximum daily summer temperature: +0.5 to +6.4	Lee et al. (2020)
Western Canada	Athabasca River Basin	+0.8 ; +1.1	+1.6 ; +3.1	Du et al. (2019)
Lithuania	Five catchments		+4.0 ; +5.1	Kriaučiūnienė et al. (2019)
US	Eel River basin		+1.20 ; +2.40 in summer under RCP 8.5 +0.58 ; +3.46 in winter under RCP 8.5	Liu et al. (2018)
US	The Chehalis River Basin		Up to +7	Seixas et al. (2018)

Table – continue

Country	Study area	The middle of the century (°C)	The end of the century (°C)	Reference
US	Michigan	+0.1 ; +3.8 in groundwater-dominated streams +0.2 ; +6.8 in surface-runoff dominated systems		Carlson et al. (2017)
Canada	the Fourchue River		+0.2 ; +0.7 in June and September	Kwak et al. (2017)
In the central Spain	14 mountain rivers		Up to 4.0	Santiago et al. (2017)
US	The upper Shavers Fork sub-watershed	+0.2 ; +1.2	Merriam et al. (2017)	
US	three northern Wisconsin streams		+1.1 ; +3.2	Selbig (2015)

6.10.2 Implications for aquatic biota

Both Q, and Tw are the key factors affecting the suitability of instream habitats (Benda et al., 2004). Therefore, the worldwide increase in Tw (see Table 6.10.1) can have an important impact on cold-water habitats. For instance, Lee et al. (2020) found that stream warming may limit particular species and life stages in the future. They found that vulnerability scores would increase by more than 50% for both life stages of all species during August, and the vulnerability was more important for adults than juveniles. In the Loire River basin (current study), the pronounced increase (up to 300% at the end of the century) in the number of days exceeding the upper tolerance temperature of juvenile brown trout may pose a potential threat to this species (see Figure 6.39).

The evolution of summer Tw anomalies – with respect to the 1990–2019 period – over two centuries (at Dampierre) also demonstrates a fast increase after 1980, which was also seen in the past trend analyses (see Figure 5.17, p. 5.17). Nevertheless, depending on GCM/RCM and RCP such an increase can continue or get moderate at the end of the century compared to the middle of the century (summer Tw anomaly at the end of the century=[+2 °C ; +5 °C]). These observed changes in Tw can alter habitat availability and freshwater quality for organisms. Indeed, the organisms may not be able to adapt to such changes.

Here, in addition to increasing in Tw, a pronounced decrease (median change up to -43 %) in Q, especially in spring and summer was found across GCM/RCMS, RCPs, and time slices (Table 6.4; Figures 6.24 and 6.28). The synchronicity of a decrease in Q and an increase in Tw can affect the persistence of specialized aquatic organisms (e.g., for cold-water biota, Arismendi et al., 2013b) and the completion of their life cycle (e.g., for diadromous fish, Arevalo et al., 2020). Here, findings show that the largest median Tw anomaly (>+2.3 °C=summer Tw anomaly in 2003), and the greatest positive median Ta anomaly (>+2 °C), and the largest negative median Q anomaly (< -10%) occur jointly in the future (see Figure 6.35). Such events can double the problem for cold-water aquatic species. Importantly, such events are mainly in the upstream part of the basin (HER A), where mostly cold-water aquatic communities are present.

Therefore, thermal model outputs (like T-NET outputs) can also be used to assess the various stresses on freshwater habitat sustainability due to changes in Q and Tw in the future, and their synchronicity. Such future assessments are critical for developing effective management responses to climate change.

6.10.3 Sensitivity of results to the selected historical period 1990–2019

The 1990–2019 period selected as the historical period here, seems a risky choice since Tw warming has already occurred during this period (+2 °C increase compared to the 1963–1990 period; see Figures 5.14, p. 150, Figure 6.31). To see the sensitivity of reported Tw changes to this selected historical period, another historical period (1976–2005) is tested. This period was also used as the reference period to correct biases of climate models (see section 6.3.1). A large proportion of the years over this selected period (1976–2005), has negative anomalies with respect to the 1963–2019 period (see Figure 5.14, p. 150).

There is a slight difference between median (across reaches) changes in Tw with respect to the 1990–2019 period and those with respect to the 1976–2005 period. The largest changes in Tw with respect to the 1976–2005 period, like the 1990–2019 period, are in spring and summer across GCM/RCMs and time slices except for the IPSL-CM5A/MRWRF381P (warm and wet) model (Figure 6.40). In these seasons, median Tw changes with respect to the 1976–2005 period (resp. the 1990–2019 period) is [+1.95 °C ; +3.07 °C] (resp. [+1.64 °C ; +2.68 °C]) in the middle of the century, and [+3.51 °C ; +5.35 °C] (resp. [+3.21 °C ; +4.95 °C]) at the end of the century (Figure 6.40). Note that for these two historical periods, a similar variability is observed for Tw change (see Figure 6.40). Comparing median (across reaches) Tw anomalies with respect to the 1990–2019 period to that with respect to the 1976–2005 period also exhibits a very small difference across seasons and GCM/RCMs under RCP 8.5 (range difference=[-0.7 °C ; +7 °C]; see Figure 6.41).

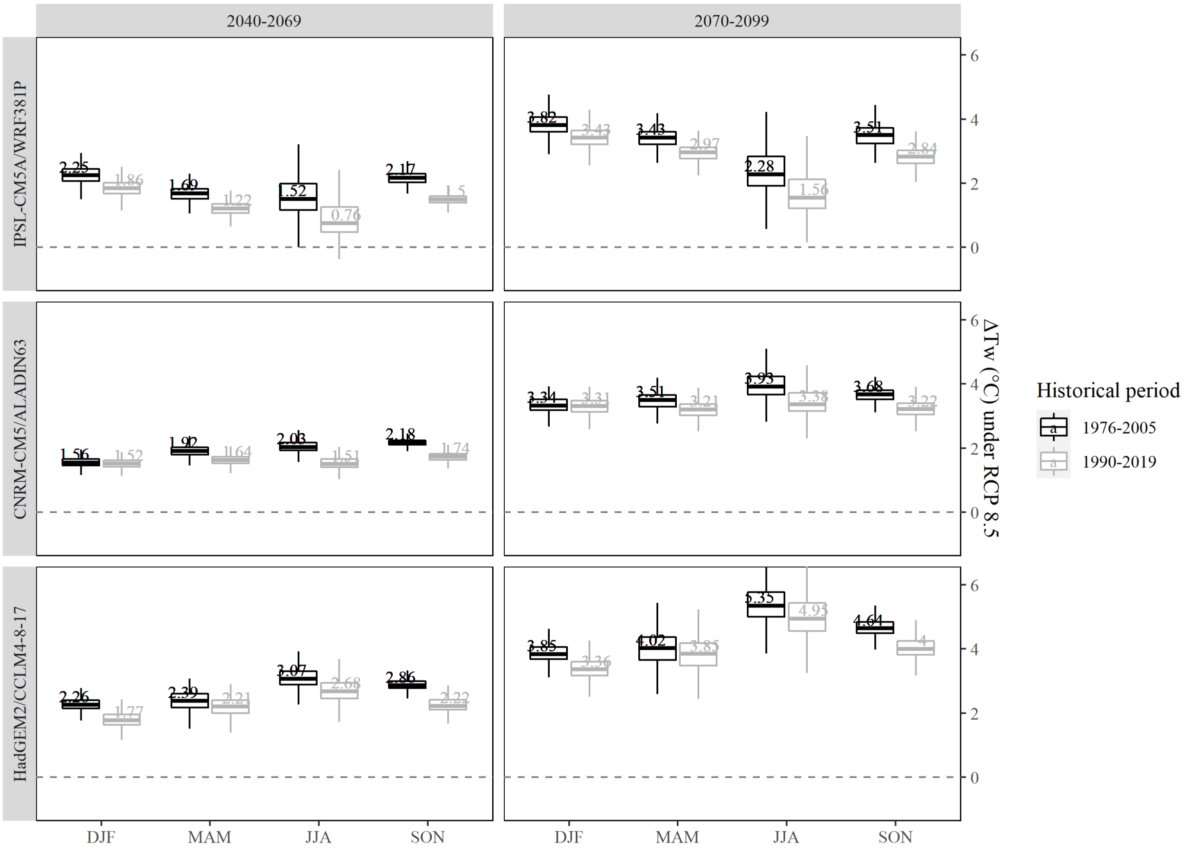

Figure 6.40: Comparing seasonal changes in Tw with respect to the 1990–2019 period (grey) to that with respect to the 1976–2005 period (black) for different GCM/RCMs under RCP 8.5 and seasons.

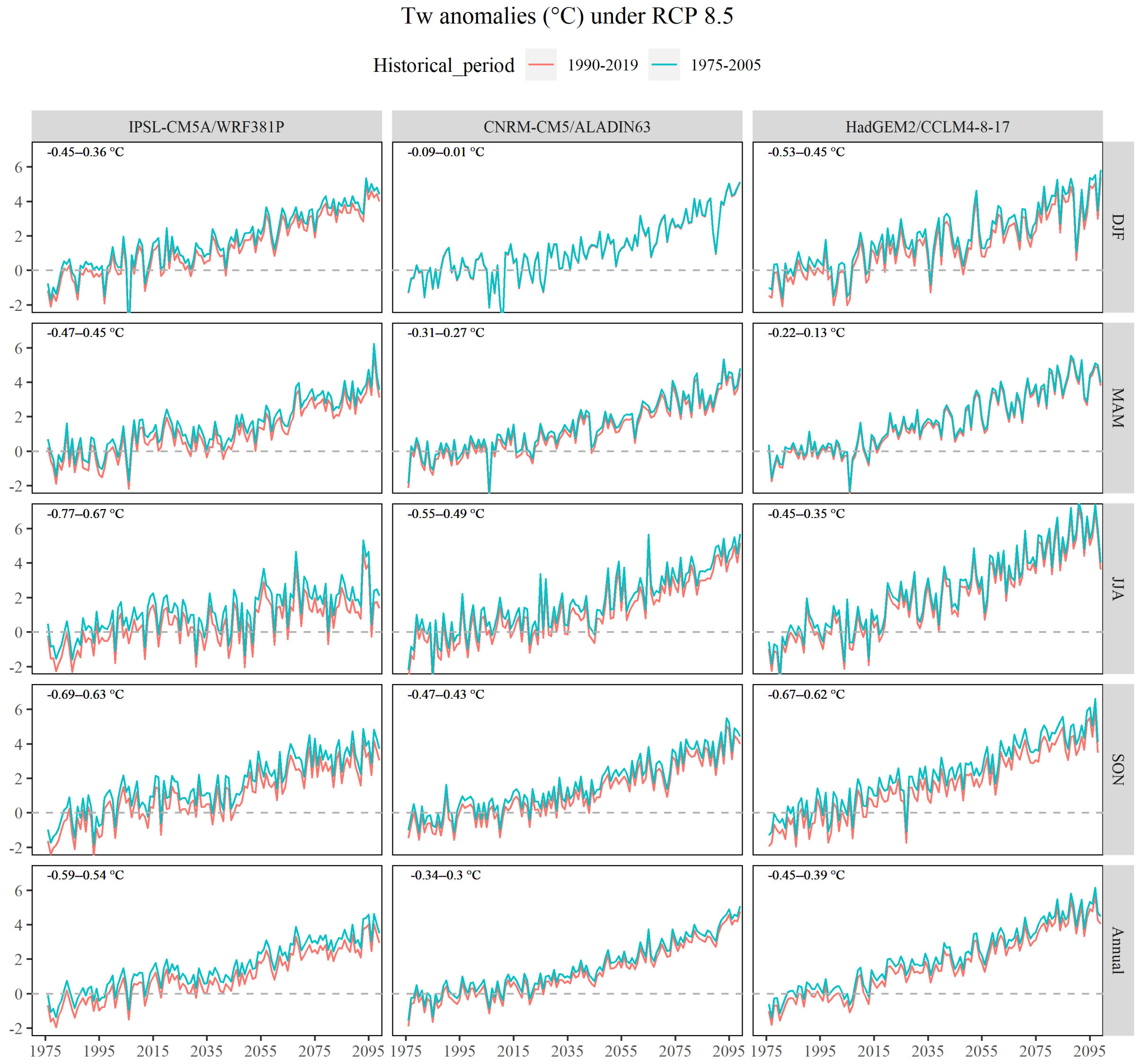

Figure 6.41: Comparing median (across reaches) anomalies of Tw with respect to the 1990–2019 period to that with respect to the 1976–2005 period for different GCM/RCMs under RCP 8.5 at the seasonal scale. The values in the top left corner show the range of difference between two anomalies with different historical period.

6.10.4 Riparian vegetation under climate change

For future projections, an increase of riparian shading, higher than 25 % , could mitigate the increase in the mean summer Tw by [+3.3 °C ; +4.6 °C] in small streams (see Figure 6.38). Along with this result, Seixas et al. (2018) found that, in some small mountain streams, the riparian landscape explains the low sensitivity of projected Tw to projected Ta. Such mitigation impacts of riparian shading were also seen for Tw past trends in the previous chapter (see Figure 5.20, p. 156). Nevertheless, here, the T-NET model is ran under constant land use/land cover (see section 6.2), and hence no changes in riparian vegetation under climate change is considered while the survival of certain plants and vegetation cover may be also threatened by recent climate change (Zarei et al., 2020).

As Ta increases due to climate change, a shift in the spatial distribution of vegetation can occur. This shift mainly occurs toward the upslopes where the climate would be more favorable under climate change (Breshears et al., 2008; Feeley et al., 2011). Moreover, decreases in species abundance, competition, and change in the available plant are observed due to climate change (Breshears et al., 2008). It is thus important to understand how vegetation cover relates to climate change. Such knowledge underlies mitigation impacts of vegetation cover for stream warming.

Some management scenarios related to vegetation cover such as a decrease or increase in current vegetation cover like the study of Wondzell et al. (2019), can be considered to understand the impacts of changes in vegetation cover on future Tw changes with respect to the influence of hydroclimate changes. However, to have a wider perspective, in addition to such scenarios, as pointed out in the previous chapter (see section 5.7.5), the survival, persistence, growth rate of planted species, required time for thermal regime recovery under possibly severe future conditions, and the efficacy of riparian planting (e.g., the type and structure of forest stands) (Caissie, 2006; Dugdale et al., 2018) should be also considered in management strategies.

6.11 Conclusion on future changes

Future seasonal and annual Tw changes at the reach resolution are assessed by using the physical process-based T-NET model coupled with the semi-distributed EROS hydrological model over the Loire basin. This study is the first one uses the DRIAS-2020 climate projections for hydrological and thermal projections. Assessing the performance of the selected projections demonstrate that they are able to get the right values of meteorological variables and seasonal Tw absolute values, but they fail to reach the observed magnitude of recent trends in Tw. Nevertheless, an increasing trend in Tw in the recent period (1976–2019) is found in projections like in the retrospective simulation.

Using model outputs across 52 278 reaches over the Loire basin, a consistent increase in Tw (with respect to the 1990–2019 period) is found in the middle (2040–2069) and at the end of the century (2070–2099). The median Tw change ranges between +0.72 °C and +2.68 °C across GCM/RCMs, RCPs, and seasons in the middle of the century. Such range is [+0.47 °C ; +4.95 °C] at the end of the century. Moreover, two centuries of summer Tw anomalies for the Loire River – with respect to the 1990–2019 period – show a fast increase in the late 1980s. Nevertheless, depending on the GCM/RCM and RCP such an increase can continue or get moderate at the end of the century compared to the middle of the century (summer Tw anomaly at the end of the century=[+2 °C ; +5 °C]).

The greatest changes in Tw happen in spring and summer, especially at the end of the century. Moreover, in these seasons, the majority of sub-basins show a decrease in Q in the middle (median change up to -40 %) and at the end of the century (median change up to -43 %), most of which are located in HER A. Although there is an increase in Q under RCP 8.5 in sub-basins in HER B and C, the influence of the increase in Ta (anomalies up to 10 °C with respect to the 1990–2019 period) on Tw changes is more pronounced as a consistent increase in Tw across the basin is found.

Results show that the largest median (across reaches) Tw anomalies ($>$+2.3 °C=summer Tw anomaly in 2003), and the largest positive median Ta anomalies ($>$+2 °C), and the largest negative Q anomalies ($<$ -10%) occur jointly regardless of the season in the future (see Figure 6.35) except for the winter. This also highlights that hot years like that of the summer of 2003 will be experienced frequently in the middle and at the end of the century regardless of the season.

Moreover, for the majority of reaches with positive Tw changes, positive Ta changes and negative Q changes (with respect to the 1990–2019 period) are concomitant, most of which are located in the upstream part of the basin, HER A. This will likely generate a double penalty for existing cold-water aquatic communities. However, riparian shading in small mountainous streams may mitigate such warming. In fact, an increase of $>$ 25 % of riparian shading (from $<$ 15 % to $>$ 40 %) can mitigate the increase in future summer Tw by [+3.3 °C ; +4.6 °C].

These findings highlight that both future Tw and Q are required to be used to explain stresses and shifts experienced by aquatic communities in the future, and using future Ta is not sufficient. This knowledge is imperative to implement effective management measures to lower the impacts of climate change and to assess future needs for increasing thermal resilience for aquatic communities.

CHAPTER 7

Final conclusions and perspectives

7.1 Conclusions

Stream temperature is a key factor for water quality, aquatic communities and socio-economic activities (Poole and Berman, 2001; Ducharne, 2008; Caissie, 2006; Ouellet et al., 2020). There is an emerging concern about the cumulative effects of impoundments and recent climate change on thermal regimes at a large scale and a high spatial resolution. The main objective of this doctoral project was to address these issues at a scale of the Loire River basin, one of the largest European basin (10^5 km^2) by using a physical process-based thermal (T-NET) (Beaufort et al., 2016b; Loicq et al., 2018) coupled with a semi-distributed hydrological model (EROS) (Thiéry, 1988; Thiéry and Moutzopoulos, 1995; Thiéry, 2018).

Identifying the influence of impoundments

To address the influence of impoundments, two challenges were encountered. Firstly, the T-NET thermal model does not take into account impoundments, and thus could only produce "natural" thermal regimes. Therefore, it could not be used at this step. Secondly, we lacked Tw data for both upstream and downstream parts of impoundments, and thus the impacts of impoundments could not be evaluated by using upstream reference conditions – a traditional practice favored in the literature (Webb and Walling, 1993, 1996, 1997; Lowney, 2000; Preece and Jones, 2002; Casado et al., 2013; Maheu et al., 2016c; Chandesris et al., 2019). Consequently, the first objective of this doctoral project was to distinguish between altered and natural thermal regimes and identify the influence of impoundments without a prior information on the source of modification or upstream water temperature conditions, using observed Tw data at the scale of the Loire River basin. To do so, analogous to "hydrological signatures" (Gupta et al., 2008), we defined the novel "thermal signatures" based on observed stream-air temperature linear regression and seasonality analysis at 330 Tw stations on medium and small streams (i.e., regimes sensitive to anthropogenic alterations) scattered over the Loire River basin (see Figure 3.5, p. 58 and Table 3.1, p. 58).

Thermal signatures were designed to identify two dominant modes of thermal alteration induced by dams and ponds in the Loire River basin. Indeed, thermal signatures enabled a rapid and clear evaluation of the cumulative impacts of human impoundments, and helped distinguishing between altered and natural regimes and identifying the influence of dams and ponds (see section 3.4, p. 63). Results indicated that large dams, at local scales, decreased summer stream temperature and delayed the annual stream temperature peak relative to the natural regimes (see Figure 3.18, p. 80). Moreover, very large dams (IRI>20%) completely erased the stream-air temperature correlation (see Figure 3.15, p. 74). In contrast, the cumulative effects of upstream ponds increased summer stream temperature and increased synchronicity with the air temperature regime (see Figure 3.18, p. 80).

Improving the hydraulic geometry and riparian shading in T-NET

The second objective of this work was to make some modifications to the T-NET thermal model to improve hydraulic geometry and riparian shading, using natural stations identified through the thermal signatures in the first objective. In this regard, firstly, a new hydraulic geometry model developed through a Random Forest approach (Morel et al., 2020) was used and could better predict river width and river depth compared to the previous hydraulic geometry model, ESTIMKART (Lamouroux et al., 2010). It slightly improved the model performance in simulating daily Tw over winter months in small and medium rivers compared to the ESTIMKART model (see Figure 4.16, p. 109). Secondly, dynamic riparian shading as a function of tree height, river width, solar elevation angle, vegetation density, and phenology (Li et al., 2012; Loicq et al., 2018) was implemented instead of considering a constant riparian shading, which also improved T-NET performance over the summer months in small and medium streams (see Figure 4.17, p. 111).

Quantifying the influence of impoundments by T-NET bias

After improving the T-NET thermal model, the third objective was to use its outputs to infer and quantify the impacts of dams and ponds at the altered stations identified through the thermal signatures in the first objective. Comparison between T-NET model bias – i.e. difference between simulated (natural) and observed (influenced) Tw – in hot and in cool years at stations in a region with a lots of ponds (the Vienne basin and its surroundings), and in another region with several large dams (the upstream part in HER A) helped to quantify impacts of impoundments in a hot year with respect to a cool year (see Figures 4.27, p. 122 and 4.30, p. 125 and 4.31, p. 126). Moreover, a significant increase in the heating effect of ponds – i.e. mean positive difference of daily observed (influenced) and simulated (natural) Tw from March–October – was found in recent years over the 2009–2017 period with the most pronounced increase at the most ponded station (see Figure 4.28, p. 123).

Assessing regional, multi-decadal past trends in natural Tw

The fourth objective was to reconstruct Tw over the 1963–2019 period, using the T-NET thermal model outputs to estimate the magnitude of past trends in simulated Tw (at the seasonal and annual scales) and assess the variation in such trends in relation with hydroclimate changes (i.e., Ta and Q), stream size, landscape diversity (different HERs) and riparian shading (extracted from the T-NET model).

We found consistent increasing Tw trends at the scale of the entire Loire River basin, regardless of the season (see Figures 5.8, p. 143 and 5.5, p. 139). Such results were consistent with past trends observed in other European basin with clear increases in Tw over the recent decades (see Table 5.7.2, p. 162). Critically, the rate of warming for stream temperature in the current study was in the majority of cases higher than the rate of atmospheric warming (see Figure 5.8, p. 143), suggesting a decoupling of thermal trajectories linked to other factors like decreasing Q, especially in the southern headwaters (see Figures 5.9 143 and 5.11, p. 146 and 5.12, p. 147). Indeed, spring and summer stream temperature, air temperature, and streamflow time series exhibited common change-points occurring in the late 1980s, suggesting a temporal coherence between changes in the hydroclimatic drivers and a rapid stream temperature response (see Figure 5.17, p. 153). Moreover, Tw trends in all seasons except winter were greater in rivers with Strahler order > 5 (see Figure 5.19, p. 155), which we attributed to lack of the mitigation effect of riparian shading for large rivers. There was also a synchronicity of years with extreme low flows and high stream temperature in the southern headwaters, doubling the problem for cold-water aquatic communities (see Figure 5.5, p. 139). However, riparian shading in small mountainous streams mitigated this warming (see Figure 5.20, p. 156).

The current study suggested that Ta and Q could exert a joint influence on Tw, based on an analysis of the spatial coherence and temporal synchronicity of these variables. Assessing causal influence of these factors on Tw trends was left for future research. In this regard, one could devise a formal attribution framework where one may e.g. remove trends in Q and trends in Ta alternatively in T-NET inputs.

Assessing regional changes in natural Tw over the 21st century

Finally, the last objective was to understand the magnitude of Tw changes under a few future climate projections (provided by DRIAS-2020 over France, Soubeyroux et al., 2020) and effects of hydroclimate changes (i.e., Ta and Q), stream size, landscape diversity (different HERs) and riparian shading on such Tw changes at a large scale and a high spatial resolution.

First of all, seven carefully contrasted projections managed to get the right values of meteorological variables and seasonal Tw absolute values over the recent period, but they failed to reach the observed magnitude of recent trends in Tw and their spatial variability (see Figures 6.3 p. 179 and 6.5 p. 181 and 6.7 p. 184). Projected Tw showed a consistent increase in future Tw towards the end of the century over the whole Loire River basin across projections and seasons (see Figure 6.18, p. 201 and 6.19, p. 202). Nevertheless, depending on the RCP, the magnitude of this increase would continue or become moderate at the end of the century compared to the middle of the century (see Figure 6.26, p. 212 and Figure 6.31, p. 220). Such important changes in future Tw were also found in other climate change impact studies, which used RCPs of the fifth report of IPCC like the current study (IPCC, 2014). But, the large scale and fine spatial resolution of the current study is unique as well as being among the very few studies conducted in Europe or even over the world (see Table 6.10.1, p. 237).

In addition to positive Tw changes, a considerable decrease in future Q especially in spring and summer, was found (see Table 6.4). The majority of the sub-basins with a decrease in Q were located in the upstream part of the basin, HER A. Indeed, like in the past trend analysis, the largest Tw anomalies synchronized with the negatives Q anomalies, suggesting a decoupling of thermal trajectories linked to decreasing Q (see Figure 6.35, p. 226). Moreover, the positive Tw changes, positive Ta changes and negative Q changes (with respect to the 1990–2019 period) were concomitant at the majority of the reaches (see Figure 6.36, p. 228) especially in upstream part of the Loire River basin, in HER A (see Figures E.28 and E.29). Like in the past trend analysis, such joint effects would likely generate a double penalty for existing cold-water aquatic communities in the mountain streams. Nevertheless, riparian vegetation shading could mitigate future increase in the summer Tw for small streams (see Figure 6.38, p. 231). Moreover, an increase in Q in sub-basins in HER B and C was found; however the influence of the increase in Ta (see Figure 6.12, p. 194) on Tw changes was more pronounced as a consistent increase in Tw across the basin was found (see Figure 6.20, p. 204).

Natural Tw and the influence of impoundments

It should be noted that natural Tw time series were used in the current study for detecting trends over the past and assessing changes in future Tw as both the EROS and the T-NET models do not consider the influence of impoundments (see section 4.1, p. 85 and section 4.2, p. 89). However, dams and ponds can alter these natural downstream Tw regimes in a diversity of ways (see Figure 3.18, p. 80). For instance, large dams, by releasing cold hypolimnetic water in summer (like what was found through first objective) can lower downstream Tw and mitigate the increasing trend in Tw, which could be important for streams in southern headwaters (HER A) since this area experience the largest past Tw trends (see Figure 5.5, p. 139), and gathers most of existing large dams (see Figure 2.1, right panel, p. 44).

In contrast to large dams, the cumulative effects of upstream ponds can exacerbate increasing trends in Tw (which was also found in the first objective). In this regard, an increase in the heating effect of ponds on Tw over recent years (2009–2017) was found here (through third objective) (see Figure 4.28, p. 123). The warming effect of such surface waters in the current study may be more significant for streams located in lowlands in the middle and north of the Loire River basin where most of the shallow reservoirs are located (see Figure 2.1 (right panel), p. 44).

Moreover, the impacts of dams and ponds can be exacerbated in hot years, which were projected here to be more frequent in future (Figure 6.35, p. 226). In this regard, using T-NET natural simulations at altered stations revealed that the impacts of impoundments in a hot year could be 2-4 times larger than in a cool year.

7.2 Perspectives

The perspectives of this dissertation are multiple and they are explained in different sections.

Applications of thermal signatures

The proposed thermal signatures approach can be applied to the other regions impacted by anthropogenic impoundments to identify highly influenced reaches and hotspots, and trace systematic thermal alterations at a large scale. Our thermal signatures were designed to identify two dominant modes of thermal alteration induced by dams and ponds in the Loire River basin, but they may reveal other modes of operation in other regions, and other thermal signatures may be needed there. They can also be used in regions with the available data for both the upstream and downstream parts of impoundments to validate this thermal signature approach by comparing altered regimes identified through observations – a traditional practice favored by existing literature. Other thermal signatures can also be added to proposed ones. For instance, signatures like the amplitude and phase of paired annual air and stream temperature can be used to identify the influence of shallow groundwater inputs, which show a high vulnerability to climate change (Hare et al., 2021). Moreover, the synthesis of thermal signatures and hydrological signatures could be applicable to analyze fish and macroinvertebrate communities or to identifying the influence of groundwater inputs.

Critically, by identifying near natural thermal regimes, and distinguishing between natural and altered regimes, thermal signatures provide some important information to managers on reference conditions and strategic Tw measurement networks. Managers may synthesize and collect data along spatial gradients of identified alterations. For instance, such signatures underscore a need to grow and maintain Tw sensor networks over the Loire basin as well as at the national scale. Figure 2.5 (p. 47) however shows a strong decrease in Tw measurements in the last years over the Loire River basin.

In the current study we lacked data on the depth of the pond/shallow reservoirs at this scale, preventing us from using the residence time, which is an important descriptor of alterations induced by ponds (Maheu et al., 2016c; Chandesris et al., 2019). The relationship between this descriptor and alterations induced by ponds can be assessed once such data are available or when proposed thermal signatures are applied to other regions with available data on the depth of ponds/shallow reservoirs.

Ultimately, these signatures can be used to differentiate natural regimes from altered ones to develop a reference-condition model based on identified natural regimes (Hill et al., 2013). Then, this natural model can be used at the identified altered stations to quantify the influence of impoundments like what was done in the current study in the third objective (using T-NET thermal model). They can also be used in conjunction with thermal models like in the current study to identify biases, leading to improve the performance of the thermal model.

Improving the thermal model

At the level of the thermal model, further modifications can be applied to improve its performance. Such modifications or improvements can be considered in other thermal models as well. For instance, shading resulting from topography has been neglected in the T-NET thermal model of the current study. However, this can be high of importance especially for reaches in high altitudes in HER A in the Loire River basin. Therefore, a routine for computing topography shading (e.g., Moore et al., 2014; Sun et al., 2015) can be inserted in the T-NET model.

Moreover, the estimated tree height and vegetation density in the routine used for computing riparian shading (the so-called variable method) can be improved using LiDAR data. In the future, when LiDAR data are available at a large scale (e.g., at the scale of the Loire River basin), such data can be used to improve the performance of the model following Loicq et al. (2018). Note that changes in land-use between the time of extraction and usage of the data may lead to some uncertainties in the results.

Further, a routine for snow melt can be considered in the thermal model. For instance, here, the EROS hydrological model coupled with the T-NET thermal model does not provide data on snow melt. However, solid precipitation can have a significant influence on Q and Tw of rivers at high altitudes. Recently Yan et al. (2021) showed that the thermal regime of snowmelt-fed rivers are more vulnerable to a warming climate, showing the importance of considering snow melt in thermal models for future assessments.

Models like T-NET can be transferred to regions with an available connected hydrographic network, available hourly meteorological variables, and modeled stream flows. In this regard, the T-NET thermal model coupled with the J2000 hydrological model (instead of the EROS hyrological model) is going to be used over the Saône basin (29 000 km^2). The J2000 hydrological model was originally developed at Friedrich-Schiller University in Jena (Germany) to meet the challenges of the Water Framework Directive (Krause et al., 2006), and has been co-developed at INRAE, Riverly since 2011. This hydrological model has been implemented over the Rhône basin (J2000-Rhône) since 2013 (Cipriani et al., 2014; Branger et al., 2016). A significant improvement to the underground part of this model (classification of the lithology and parameterization) was reached (Branger et al., 2020), allowing a better representation of the underground contribution to flows, especially on the Saône basin.

The J2000 hydrological model is indeed a fully distributed process-based hydrological model, based on the Hydrological Response Unit (HRU) concept. The units are homogeneous in terms of topography, geology, land use and soil properties. In contrast to the hydrological model of the current study (EROS), J2000- Rhône can have a finer spatial resolution, and it considers the impact of impoundments. As J2000 can provide regulated streamflows, a routine for considering the influence of impoundments can be added to the thermal model. Consequently, this thermal model can be applied to assess different management scenarios. For instance, they can be executed with and without considering the influence of impoundments, and obtained thermal regimes from these execution can be compared to quantify and infer the influence of impoundments on the thermal regime. Quantifying the impact of impoundments may provide managers with required knowledge and materials to take proper actions against the negative impacts of impoundments. This quantification is similar to what was done in Chapter 4 of the current study at the altered stations identified through thermal signatures. Moreover, scenarios of impoundments management and future projections can be combined to assess the influence of impoundments in the context of climate change and to have a better understanding of plausible futures.

Further exploration on stream temperature under climate change

In the current study, three varied GCM/RCMs and RCPs, and seven projections in total provided by DRIAS-2020 (Soubeyroux et al., 2020) were used. These projections were selected from the 30 projections provided by DRIAS-2020 and further a subset of five from DRIAS-2020 projections suggested by Météo-France (see section 6.1). Therefore, in future assessments, more projections e.g. all 30 DRIAS-2020 projections can be used in both EROS and T-NET models. Indeed, the more GCM/RCMs and RCPs, the better would be our understanding of plausible futures and climate model uncertainty. Additionally, we tried to describe the future projections and assessed performance of projections with the available observed data. We described the projections; however, there is still a need to understand better propagation of uncertainties coming from the hydrological and hydraulic geometry models on the thermal model.

Moreover, a national project called “EXPLORE2” is going to publish a collection of projected streamflows from multiple hydrological models under the DRIAS-2020 projections over France between 2022 and 2023 (https://professionnels.ofb.fr/fr/node/1244). In fact, the objective of this project is to evaluate the impacts of climate change on water resources over France for the 21st century. Such hydrological projections can be used to project Q, which can be used in T-NET model to project Tw. Projected Q and Tw by these hydrological projections can be compared with those projected by EROS. This can help assessing the differences between projected stream temperatures across different hydrological projections and to have better understating of uncertainties across different hydrological models. Additionally, EXPLORE2 is going to provide new climate projections on top of DRIAS-2020 (Soubeyroux et al., 2020). These new projections can also be used to project Q and Tw in the future in addition to DRIAS-2020 projections.

In the current study, both EROS and T-NET were run under constant land use/land cover (see section 6.2, p. 177), therefore no change in vegetation cover due to current and future climate change was considered. However, the perspectives of beyond EXPLORE2 is to provide land use/land cover scenarios in hydrological models. Once they will be available, they can be used in the hydrolgoical model(s) forcing T-NET. However, riparian shading itself is an important regulator for Tw, and scenarios of changes in riparian vegetation may be implemented directly in the thermal model like the study of Wondzell et al. (2019). All these scenarios may help understanding the impacts of reduction/increase in vegetation cover induced by climate change on future stream temperature and assess the mitigation impacts of planting trees along rivers.

Integrating the impacts of impoundments in both hydrological and thermal models

As mentioned several times in the text, the EROS hydrological model and consequently, the T-NET thermal do not take into account the influence of impoundments. Therefore, another improvement to T-NET or thermal models like T-NET (which produce natural regimes) would be to consider the impact of impoundments on thermal regimes. For this aim, first of all, a hydrological model, which considers such impacts is required. Nevertheless, other information and data on top of regulated Q by impoundments may be required since, for instance, large dams may affect thermal regimes not only through Q regulation, but also through modifying the components of heat budget as a results of a reservoir thermal stratification. The literature also shows that although there are a few distributed thermal models (e.g., Yearsley, 2009; Wu et al., 2012; Yearsley, 2012; Li et al., 2015), they do not include reserevoir thermal stratification (Niemeyer et al., 2018). In fact, these thermal models mainly increase the river cell to increase the travel time at the site of the reservoir, which could successfully simulate Tw downstream of impoundments with a relatively short residence time (e.g., Yearsley, 2012; Li et al., 2015, and see Niemeyer et al. (2018), Table 1). However, such a representation decreased model performance at locations of large dams. In this regard, Niemeyer et al. (2018) developed a new component to represent the effects of stratification on reservoir, and used this component to their thermal model to simulate Tw. Their proposed module could decrease the bias in simulating downstream Tw. Therefore, combination of these approaches for different types of anthropogenic impoundments can be taken into account in a thermal model provided that the information on dam mode-of-operation, is available.

Using thermal models outputs in ecological settings

The current study mainly used seasonal and annual Tw metrics to present and explain the impacts of past and future climate changes. These metrics explain the magnitude components of a thermal regime; nevertheless, many other Tw metrics including ecologically important Tw metrics (see Verneaux et al., 1977; Buisson et al., 2008; Steel et al., 2017) can be used. Note that the T-NET performance in simulating the desired metric should be assessed before hand. For instance, the model can simulate quite well the maximum monthly Tw at 67 stations with continuous daily data over the 2010–2014 period (median bias=0.5°C).

Finally, outputs of thermal models like the T-NET model can be applied in many ecological settings. Indeed, such implications are already in progress over the Loire River basin by using outputs of both EROS and T-NET models. For instance, the current study was defined in parallel with a doctoral project related to the spatial organization of aquatic communities at a large scale. In this project, in the first step, using the EROS and T-NET outputs and extensive biological monitoring data, the influence of fine scale modeled Tw and Q (extracted from the T-NET model) on the spatial organization of aquatic communities at a large scale (Loire basin) over the period 1990–2010, is assessed. The contents of this assessment were already submitted and the manuscript is under review. In the second step, the spatial distribution of (contemporary) fish and macroinvertebrates communities at the reach scale is going to be modeled by using biological abundance data and environmental and landscape variables (e.g., vegetation cover, slope, stream temperature, streamflow, air temperature river depth and width extracted from the T-NET model) over the period 2007-2017. Ultimately, the potential impacts of climate change on the future aquatic communities using species distribution models developed by the same approach in the second step will be assessed.

Moreover, Recently, Arevalo et al. (2020) proposed an approach to study impacts of joint temporal trends in Tw and Q on migratory fish. They have tested this methodological framework on more than 30 years (1976–2019) of Tw and Q data for 6 large French rivers (the Garonne, Dordogne, Rhône, Rhine, Loire and Vienne rivers in France), and found influences of joint temporal trends on species migrating. This study is going to continue at the scale of the Loire River basin using T-NET and EROS outputs.

Conclusions finales et perspectives

Conclusion

La température des cours d'eau est un facteur clé pour la qualité de l'eau, les communautés aquatiques et les activités socio-économiques (Poole and Berman, 2001; Ducharne, 2008; Caissie, 2006; Ouellet et al., 2020). Il existe une inquiétude émergente concernant les effets cumulatifs des retenues et des changements climatiques récents sur les régimes thermiques à grande échelle et à haute résolution. L'objectif principal de ce projet doctoral était d'aborder ces questions à l'échelle du bassin de la Loire, l'un des plus grands bassins européens (10^5 km^2) en utilisant un procédé physique thermique (T-NET) (Beaufort et al., 2016b; Loicq et al., 2018) couplé à un modèle hydrologique semi-distribué (EROS) (Thiéry, 1988; Thiéry and Moutzopoulos, 1995; Thiéry, 2018).

Identifier l'influence des retenues

Pour contrer l'influence des retenues, deux défis ont été rencontrés. Premièrement, le modèle thermique T-NET ne prend pas en compte les retenues, et ne pourrait donc produire que des régimes thermiques « naturels ». Par conséquent, il n'a pas pu être utilisé à cette étape. Deuxièmement, nous manquions de données Tw pour les parties amont et aval des retenues, et donc les impacts des retenues n'ont pas pu être évalués en utilisant des conditions de référence en amont – une pratique traditionnelle privilégiée dans la littérature (Webb and Walling, 1993, 1996, 1997; Lowney, 2000; Preece and Jones, 2002; Casado et al., 2013; Maheu et al., 2016c; Chandesris et al., 2019). Par conséquent, le premier objectif de ce projet doctoral était de distinguer les régimes thermiques altérés et naturels et d'identifier l'influence des retenues sans information préalable sur la source de modification ou les conditions de température de l'eau en amont, à partir des données Tw observées à l'échelle de la Loire bassin. Pour ce faire, de manière analogue aux « signatures hydrologiques » (Gupta et al., 2008), nous avons défini les nouvelles « signatures thermiques » sur la base de la régression linéaire de Tw-Ta observée et de l'analyse de la saisonnalité à 330 stations Tw sur des cours d'eau moyens et petits (c'est-à-dire, des régimes sensibles aux altérations anthropiques) dispersées sur le bassin de la Loire (voir

Figure 3.5, p. 58 et Tableau 3.1, p. 58). Les signatures thermiques ont mis en évidence deux modes dominants d'altération thermique induits par les barrages et les étangs du bassin de la Loire. En effet, les signatures thermiques ont permis une évaluation rapide et claire des impacts cumulatifs des retenues humaines, et ont aidé à faire la distinction entre les régimes altérés et naturels. Ils pourraient aider à distinguer les régimes altérés des régimes naturels et à identifier l'influence des barrages et des étangs (voir section 3.4, p. 63). Les résultats ont indiqué que les grands barrages, à l'échelle locale, diminuaient la température estivale des cours d'eau et retardaient le pic annuel de température des cours d'eau par rapport aux régimes naturels. De plus, les très grands barrages (IRI>20%) ont complètement effacé la corrélation entre Tw et Ta. En revanche, les effets cumulatifs des étangs en amont ont augmenté la température estivale des cours d'eau et augmenté la synchronisation avec le régime de température de l'air.

Amélioration de la géométrie hydraulique et de l'ombrage riverain dans T-NET

Le deuxième objectif de ce travail était d'apporter quelques modifications au modèle thermique T-NET pour améliorer la géométrie hydraulique et l'ombrage riverain en utilisant des stations naturelles identifiées grâce aux signatures thermiques du premier objectif. À cet égard, tout d'abord, un nouveau modèle de géométrie hydraulique développé grâce à une approche de forêt aléatoire (Morel et al., 2020) a été utilisé et pourrait mieux prédire la largeur et la profondeur de la rivière par rapport au modèle de géométrie hydraulique précédent, ESTIMKART (Lamouroux et al., 2010). Il a légèrement amélioré les performances du modèle en simulant la Tw quotidienne au cours des mois d'hiver dans les petites et moyennes rivières par rapport au modèle ESTIMKART (voir Figure 4.16, p. 109). Deuxièmement, un ombrage riverain dynamique en fonction de la hauteur des arbres, de la largeur de la rivière, de l'angle d'élévation solaire, de la densité de la végétation et de la phénologie (Li et al., 2012; Loicq et al., 2018) a été mis en œuvre au lieu de considérer un ombrage riverain constant, qui a également amélioré les performances du T-NET au cours des mois d'été dans les petits et moyens cours d'eau (voir Figure 4.17, p. 111).

Quantification de l'influence des retenues par biais T-NET

Après avoir amélioré le modèle thermique T-NET, le troisième objectif était d'utiliser ses résultats pour déduire et quantifier les impacts des barrages et des étangs aux stations modifiées qui ont été identifiées grâce aux signatures thermiques du premier objectif. Comparaison entre le biais du modèle T-NET – c'est-à-dire la différence entre la Tw simulée (naturelle) et observée (influencée) – pendant les années chaudes et fraîche aux stations d'une région avec beaucoup d'étangs (le bassin de la Vienne et ses environs), et dans une autre région avec plusieurs grands barrages (la partie amont dans HER A) a permis de quantifier les impacts des retenues en année chaude par rapport à une année fraîche (voir Figures 4.27, p. 122 et 4.30, p. 125 et 4.31, p. 126). De plus, une augmentation significative de l'effet de chauffage des étangs - c'est-à-dire une différence positive moyenne de la Tw quotidienne observée (influencée) et simulée (naturelle) de mars à octobre - a été trouvée ces dernières années sur la période 2009-2017 avec l'augmentation la plus prononcée à la station la plus étangée (voir Figure 4.28, p. 123).

Évaluer les tendances passées de la Tw naturelle à l'échelle régionale

Le quatrième objectif était de reconstruire Tw sur la période 1963–2019, en utilisant les sorties du modèle thermique T-NET pour estimer l'ampleur des tendances passées de la Tw simulée (aux échelles saisonnières et annuelles) et évaluer la variation de ces tendances en relation avec les changements hydroclimatiques (c'est à dire Ta et Q), la taille des cours d'eau, différentes HERs et l'ombrage riverain (extrait du modèle T-NET). Nous avons trouvé des tendances à la hausse cohérentes de Tw à l'échelle de l'ensemble du bassin de la Loire, quelle que soit la saison (voir Figures 5.8, p. 143 et 5.5 , p. 139). Ces résultats étaient cohérents avec les tendances passées observées dans d'autres bassins européens avec une nette augmentation de Tw au cours des dernières décennies (voir Tableau 5.7.2, p. 162). De manière critique, le taux de réchauffement de la température du cours d'eau dans l'étude actuelle était dans la majorité des cas supérieur au taux de réchauffement atmosphérique (voir Figure 5.8, p. 143), suggérant un découplage des trajectoires thermiques lié à d'autres facteurs comme la diminution de Q, en particulier dans les eaux d'amont sud (voir Figures 5.9 143 et 5.11, p. 146 et 5.12, p. 147). En effet, les séries temporelles de la température des cours d'eau au printemps et en été, de la température de l'air et des débits ont montré des points de changement communs survenant à la fin des années 1980, suggérant une cohérence temporelle entre les changements dans les facteurs hydroclimatiques et une réponse rapide de la température des cours d'eau (voir la Figure 5.17, p. 153). De plus, les tendances Tw en toutes saisons sauf en hiver étaient plus importantes dans les rivières avec un ordre Strahler > 5 (voir Figure 5.19, p. 155), ce que nous avons attribué au manque d'atténuation effet de l'ombrage riverain pour les grandes rivières. Il y avait également une synchronicité d'années avec des débits extrêmement faibles et une température élevée des cours d'eau dans les eaux d'amont sud, doublant le problème pour les communautés aquatiques d'eau froide (voir Figure 5.5, p. 139). Cependant, l'ombrage riverain dans les petits ruisseaux de montagne a atténué ce réchauffement (voir Figure 5.20, p. 156).

Évaluer les changements de Tw naturel au cours du 21e siècle à l'échelle régionale

Enfin, le dernier objectif était de comprendre l'ampleur des changements de Tw sous quelques projections climatiques futures (fournies par DRIAS-2020 sur la France, Soubeyroux et al., 2020) et les effets des changements hydroclimatiques (Notamment Ta et Q), cours d'eau la taille, la diversité du paysage (différentes HER) et l'ombrage riverain sur de tels Tw changent à grande échelle et à haute résolution spatiale. Tout d'abord, sept projections soigneusement contrastées ont pu obtenir les bonnes valeurs des variables météorologiques et des valeurs absolues saisonnières de Tw sur la période récente, mais elles n'ont pas réussi à reproduire l'ampleur observée des tendances récentes de Tw et leur variabilité spatiale (voir les Figures Figures 6.3 p. 179 et 6.5 p. 181 et 6.7 p. 184).

Les scénarios de Tw projetée a montré une augmentation constante de la Tw future vers la fin du siècle sur l'ensemble du bassin de la Loire à travers les projections et les saisons (voir Figures 6.18, p. 201 et 6.19, p. 202). Néanmoins, selon les RCP, l'ampleur de cette augmentation se poursuivrait ou deviendrait modérée à la fin du siècle par rapport au milieu du siècle (voir Figure 6.26, p. 212 et Figure 6.31, p. 220). Des changements aussi importants dans le futur Tw ont également été trouvés dans d'autres études d'impact sur le changement climatique, qui ont utilisé les RCP du cinquième rapport du IPCC comme l'étude actuelle (IPCC, 2014). Mais, la grande échelle et la résolution spatiale fine de l'étude actuelle est unique et fait partie des très rares études menées en Europe ou même dans le monde (voir Tableau 6.10.1, p. 237).

En plus des changements positifs de Tw, une diminution considérable du futur Q, en particulier au printemps et en été, associée aux scénarios simulés (voir le tableau 6.4). La majorité des sous-bassins avec une diminution de Q sont situés dans la partie amont du bassin, HER A. En effet, comme dans l'analyse de tendance passée, les plus grandes anomalies Tw se synchronisent avec les anomalies Q négatives, suggérant un découplage des trajectoires liées à la diminution de Q (voir Figure 6.35, p. 226). De plus, les changements positifs de Tw, les changements positifs de Ta et les changements négatifs de Q (par rapport à la période 1990-2019) sont concomitants à la majorité des biefs (voir Figure 6.36, p. 228) en particulier dans la partie amont du bassin de la Loire, dans HER A (voir Figures E.28 et E.29). Comme dans l'analyse des tendances passées, de tels effets conjoints engendreraient probablement une double pénalité pour les communautés aquatiques d'eau froide existantes dans les ruisseaux de montagne. Néanmoins, l'ombrage de la végétation riveraine pourrait atténuer l'augmentation future de la Tw estivale pour les petits ruisseaux (voir Figure 6.38, p. 231). De plus, une augmentation de Q dans les sous-bassins de HER B et C a été trouvée; cependant, l'influence de l'augmentation de Ta (voir Figure 6.12, p. 194) sur les changements de Tw pourrait plus prononcée car une augmentation cohérente de Tw dans ces HERs a été trouvée (voir Figure 6.20, p. 204).

Natural Tw et l'influence des retenues

Il convient de noter que les séries temporelles naturelles de Tw ont été utilisées dans la présente étude pour détecter les tendances dans le passé et évaluer les changements dans le futur Tw, car les modèles EROS et T-NET ne tiennent pas compte de l'influence des retenues (voir la section 4.1, p. 85 et section 4.2, p. 89). Cependant, les barrages et les étangs peuvent modifier ces régimes Tw naturels en aval de diverses manières (voir Figure 3.18, p. 80). Par exemple, les grands barrages, en libérant de l'eau hypolimnétique froide en été (comme ce qui a été trouvé dans le premier objectif) peuvent abaisser Tw en aval et atténuer la tendance à la hausse de Tw, ce qui pourrait être important pour les cours d'eau des sources sud (HER A) puisque cette zone connaît les plus grandes tendances passées Tw, et rassemble la plupart des grands barrages existants (voir Figure 2.1, panneau de droite, p. 44).

De plus, les impacts des barrages et des étangs peuvent être exacerbés lors des années chaudes, qui devaient ici être plus fréquentes à l'avenir (Figure 6.35, p. 226). À cet égard, l'utilisation de simulations naturelles T-NET dans des stations modifiées a révélé que les impacts des retenues pendant une année chaude peuvent être 2 à 4 fois plus importants que pendant une année froide.

Perspectives

Les perspectives de cette thèse sont multiples et elles sont expliquées dans différentes sections.

Applications des signatures thermiques

L'approche des signatures thermiques proposée peut être appliquée aux autres régions touchées par les retenues anthropiques pour identifier les tronçons et les points chauds fortement influencés, et tracer les altérations thermiques systématiques à grande échelle. Nos signatures thermiques ont mis en évidence deux modes dominants d'altération thermique induite par les barrages et étangs du bassin de la Loire, mais elles peuvent révéler d'autres modes de fonctionnement dans d'autres régions, et d'autres signatures thermiques peuvent y être nécessaires. Ils peuvent également être utilisés dans les régions disposant des données disponibles pour les parties amont et aval des retenues afin de valider cette approche de signature thermique en comparant les régimes modifiés qui ont été identifiés grâce aux observations - une pratique traditionnelle favorisée par la littérature existante. D'autres signatures thermiques peuvent également être ajoutées à celles proposées. Par exemple, des signatures telles que l'amplitude et la phase de la température annuelle appariée de l'air et du cours d'eau peuvent être utilisées pour identifier l'influence des apports d'eaux souterraines peu profondes, qui montrent une grande vulnérabilité au changement climatique (Hare et al., 2021). De plus, la synthèse des signatures thermiques et des signatures hydrologiques pourrait être applicable pour analyser les communautés de poissons et de macroinvertébrés ou pour identifier l'influence des apports d'eau souterraine.

De manière critique, en identifiant les régimes thermiques naturels et en distinguant les régimes naturels des régimes altérés, les signatures thermiques fournissent des informations importantes aux gestionnaires sur les conditions de référence et les réseaux stratégiques de mesure Tw. Les gestionnaires peuvent synthétiser et collecter des données le long de gradients spatiaux d'altérations identifiées. Par exemple, de telles signatures soulignent un besoin de développer et de maintenir des réseaux de capteurs Tw sur le bassin de la Loire ainsi qu'à l'échelle nationale. La Figure 2.5 (p. 47) montre cependant une forte diminution des mesures de Tw ces dernières années sur le bassin de la Loire.

Dans la présente étude, nous manquions de données sur la profondeur des étangs/réservoirs peu profonds à cette échelle, nous empêchant d'utiliser le temps de résidence, qui est un descripteur important des altérations induites par les étangs (Maheu et al., 2016c; Chandesris et al., 2019). La relation entre ce descripteur et les altérations induites par les étangs peut être évaluée une fois que ces données sont disponibles ou lorsque les signatures thermiques proposées sont appliquées à d'autres régions avec des données disponibles sur la profondeur des étangs/réservoirs peu profonds.

En fin de compte, ces signatures peuvent être utilisées pour différencier les régimes naturels des régimes altérés afin de développer un modèle de conditions de référence basé sur des régimes naturels identifiés (Hill et al., 2013). Ils peuvent également être utilisés en conjonction avec des modèles thermiques comme dans l'étude actuelle pour identifier les biais, conduisant à améliorer les performances du modèle thermique.

Amélioration du modèle thermique

Au niveau du modèle thermique, d'autres modifications peuvent être apportées pour améliorer ses performances. De telles modifications ou améliorations peuvent également être envisagées dans d'autres modèles thermiques. Par exemple, l'ombrage résultant de la topographie a été négligé dans le modèle thermique T-NET de la présente étude. Cependant, cela peut être d'une grande importance en particulier pour les tronçons en haute altitude dans HER A dans le bassin de la Loire. Par conséquent, une routine de calcul de l'ombrage de la topographie (e.g., Moore et al., 2014; Sun et al., 2015) peut être insérée dans le modèle T-NET.

De plus, l'estimation de la hauteur des arbres et de la densité de végétation dans la routine utilisée pour calculer l'ombrage riverain (la méthode dite variable) peut être améliorée à l'aide des données LiDAR. À l'avenir, lorsque les données LiDAR seront disponibles à grande échelle (par exemple, à l'échelle du bassin de la Loire), ces données pourront être utilisées pour améliorer les performances du modèle en suivant Loicq et al. (2018). Il est à noter que les changements dans l'utilisation des terres entre le moment de l'extraction et l'utilisation des données peuvent entraîner certaines incertitudes dans les résultats.

De plus, une routine pour la fonte des neiges peut être considérée dans le modèle thermique. Par exemple, ici, le modèle hydrologique EROS couplé au modèle thermique T-NET ne fournit pas de données sur la fonte des neiges. Cependant, les précipitations solides peuvent avoir une influence significative sur Q et Tw des rivières à haute altitude. Récemment, Yan et al. (2021) a montré que le régime thermique des rivières alimentées par la fonte des neiges est plus vulnérable au réchauffement climatique, montrant l'importance de prendre en compte la fonte des neiges dans les modèles thermiques pour les évaluations futures.

Des modèles tels que T-NET peuvent être transférés dans des régions disposant d'un réseau hydrographique connecté disponible, de variables météorologiques horaires disponibles et de débits de cours d'eau modélisés. A cet égard, le modèle thermique T-NET couplé au modèle hydrologique J2000 (en lieu et place du modèle hydrologique EROS) va être utilisé sur le bassin de la Saône (29 000 km^2). Le modèle hydrologique J2000 a été initialement développé à l'Université Friedrich-Schiller d'Iéna (Allemagne) pour répondre aux défis de la Directive Cadre sur l'Eau (Krause et al., 2006), et a été co-développé à l'INRAE, Riverly depuis 2011. Ce modèle hydrologique a été implantée sur le bassin du Rhône (J2000-Rhône) depuis 2013 (Cipriani et al., 2014; Branger et al., 2016). Une amélioration significative de la partie souterraine de ce modèle (classification de la lithologie et paramétrage) a été atteinte (Branger et al., 2020), permettant une meilleure représentation de la contribution souterraine aux écoulements, notamment sur le bassin de la Saône.

Le modèle hydrologique J2000 est en effet un modèle hydrologique entièrement distribué basé sur les processus, et sur le concept d'unité de réponse hydrologique (HRU). Les unités sont homogènes en termes de topographie, de géologie, d'occupation du sol et de propriétés du sol. Contrairement au modèle hydrologique de l'étude actuelle (EROS), J2000-Rhône peut avoir une résolution spatiale plus fine, et il considère l'impact des retenues. Comme J2000 peut fournir des débits régulés, une routine pour considérer l'influence des retenues peut être ajoutée au modèle thermique. Par conséquent, ce modèle thermique peut être appliqué pour évaluer différents scénarios de gestion. Par exemple, ils peuvent être exécutés avec et sans tenir compte de l'influence des retenues, et les régimes thermiques obtenus à partir de ces exécutions peuvent être comparés pour quantifier et déduire l'influence des retenues sur le régime thermique. La quantification de l'impact des retenues peut fournir aux gestionnaires les connaissances et le matériel nécessaires pour prendre les mesures appropriées contre les impacts négatifs des retenues. Cette quantification est similaire à ce qui a été fait dans le chapitre 4 de la présente étude aux stations altérées identifiées par les signatures thermiques. De plus, des scénarios de gestion des retenues et des projections futures peuvent être combinés pour évaluer l'influence des retenues dans le contexte du changement climatique et avoir une meilleure compréhension des futurs plausibles.

Exploration plus poussée sur la température des cours d'eau sous le changement climatique

Dans la présente étude, trois GCM/RCM et RCP variés, et sept projections au total fournies par DRIAS-2020 (Soubeyroux et al., 2020) ont été utilisées. Ces projections ont été sélectionnées parmi les 30 projections fournies par DRIAS-2020 et en outre un sous-ensemble de cinq projections de DRIAS-2020 suggérées par Météo-France (voir section 6.1). Par conséquent, dans les évaluations futures, davantage de projections, par exemple les 30 projections DRIAS-2020 peuvent être utilisées dans les modèles EROS et T-NET. En effet, plus il y aura de GCM/RCM et de RCP, meilleure sera notre compréhension des futurs plausibles et de l'incertitude des modèles climatiques.

De plus, un projet national appelé « EXPLORER2 » va publier entre 2022 et 2023 une collection de débits projetés à partir de plusieurs modèles hydrologiques sous les projections DRIAS-2020 sur la France (https://professionnels.ofb.fr /fr/noeud/1244). En effet, l'objectif de ce projet est d'évaluer les impacts du changement climatique sur les ressources en eau de la France pour le 21ème siècle. De telles projections hydrologiques peuvent être utilisées pour projeter Q, qui peut être utilisée dans le modèle T-NET pour projeter Tw. Q et Tw projetés par ces projections hydrologiques peuvent être comparés à ceux projetés par EROS. Cela peut aider à évaluer les différences entre les températures projetées des cours d'eau dans différentes projections hydrologiques et à diminuer les incertitudes dans les différents modèles hydrologiques. De plus, EXPLORE2 fournira de nouvelles projections climatiques en plus de DRIAS-2020 (Soubeyroux et al., 2020). Ces nouvelles projections peuvent également être utilisées pour projeter Q et Tw dans le futur en plus des projections DRIAS-2020.

Dans la présente étude, EROS et T-NET ont été exécutés sous une utilisation/couverture des terres constante (voir la section 6.2), donc aucun changement dans la couverture végétale dû au changement climatique actuel et futur n'a été pris en compte. Cependant, les perspectives d'au-delà d'EXPLORER2 sont de fournir des scénarios d'utilisation des terres/d'occupation des terres dans les modèles hydrologiques. Une fois disponibles, ils pourront être utilisés dans le(s) modèle(s) hydrologique(s) forçant T-NET. Cependant, l'ombrage riverain lui-même est un régulateur important pour Tw, et des scénarios de changements dans la végétation riveraine peuvent être mis en œuvre directement dans le modèle thermique comme l'étude de Wondzell et al. (2019). Tous ces scénarios peuvent aider à comprendre les impacts de la réduction/augmentation de la couverture végétale induite par le changement climatique sur la température future des cours d'eau et à évaluer les impacts d'atténuation de la plantation d'arbres le long des rivières.

Intégrer les impacts des retenues dans les modèles hydrologiques et thermiques

Comme mentionné à plusieurs reprises dans le texte, le modèle hydrologique EROS et par conséquent, le modèle thermique T-NET ne prennent pas en compte l'influence des retenues. Par conséquent, une autre amélioration du T-NET ou des modèles thermiques comme le T-NET (qui produisent des régimes naturels) serait de considérer l'impact des retenues sur les régimes thermiques. Pour ce faire, tout d'abord, un modèle hydrologique, qui considère de tels impacts est nécessaire. Néanmoins, d'autres informations et données en plus du Q régulé par les retenues peuvent être nécessaires car, par exemple, les grands barrages peuvent affecter les régimes thermiques non seulement par la régulation du Q, mais aussi en modifiant les composants du bilan thermique en raison d'une stratification thermique du réservoir. La littérature montre également que bien qu'il existe quelques modèles thermiques distribués (e.g., Yearsley, 2009; Wu et al., 2012; Yearsley, 2012; Li et al., 2015), ils n'incluent pas la stratification thermique du réservoir (Niemeyer et al., 2018). En fait, ces modèles thermiques augmentent principalement la cellule de la rivière pour augmenter le temps de trajet sur le site du réservoir, ce qui pourrait simuler avec succès Tw en aval des retenues avec un temps de séjour relativement court (eg, Yearsley, 2012; Li et al., 2015, et voir Niemeyer et al. (2018), Tableau 1). Cependant, une telle représentation a diminué les performances du modèle aux emplacements des grands barrages. À cet égard, Niemeyer et al. (2018) a développé un nouveau composant pour représenter les effets de la stratification sur le réservoir, et a utilisé ce composant dans son modèle thermique pour simuler Tw. Leur module proposé pourrait diminuer le biais dans la simulation de Tw en aval. Par conséquent, la combinaison de ces approches pour différents types de retenues anthropiques peut être prise en compte dans un modèle thermique à condition que les informations sur le mode de fonctionnement des barrages soient disponibles.

Utilisation des sorties de modèles thermiques dans des contextes écologiques

La présente étude a principalement utilisé des métriques Tw saisonnières et annuelles pour présenter et expliquer les impacts des changements climatiques passés et futurs. Ces métriques expliquent les composantes de magnitude d'un régime thermique ; néanmoins, de nombreuses autres métriques Tw qui sont écologiquement importantes (voir Verneaux et al., 1977; Buisson et al., 2008; Steel et al., 2017) peuvent être utilisées. Notez que les performances de T-NET dans la simulation de la métrique souhaitée doivent être évaluées au préalable. Par exemple, le modèle peut assez bien simuler la Tw mensuelle maximale à 67 stations avec des données continues à long terme sur la période 2010-2014 (biais médian=0,5°C).

Enfin, les sorties de modèles thermiques comme le modèle T-NET peuvent être appliquées dans de nombreux contextes écologiques. En effet, de telles implications sont déjà en cours sur le bassin de la Loire en utilisant les sorties du modèle thermique T-NET. Par exemple, la présente étude a été définie en parallèle d'un projet de doctorat portant sur l'organisation spatiale des communautés aquatiques à grande échelle. Dans ce projet, dans la première étape, en utilisant les sorties T-NET et des données de surveillance biologique étendues, l'influence de Tw et Q modélisés (extraits du modèle T-NET) sur l'organisation spatiale des communautés aquatiques à grande échelle (bassin de la Loire) sur la période 1990-2010, est évalué. Le contenu de cette évaluation a déjà été soumis et est en cours de révision. Dans la deuxième étape, la distribution spatiale des communautés (contemporaines) de poissons et de macroinvertébrés à l'échelle du tronçon en utilisant des données d'abondance biologique et des variables environnementales et paysagères (par exemple, la couverture végétale, la pente, la température du cours d'eau, le débit, la température de l'air, la profondeur et la largeur de la rivière extraites du modèle T-NET) sur la période 2007-2017 va être modélisé. À terme, les impacts potentiels du changement climatique sur les futures communautés aquatiques à l'aide de modèles de distribution d'espèces développés par la même approche dans la deuxième étape seront évalués.

De plus, Arevalo et al. (2020) a récemment proposé une approche pour étudier les impacts des tendances temporelles conjointes de Tw et Q sur les poissons migrateurs. Ils ont testé ce cadre méthodologique sur plus de 30 ans (1976-2019) de données Tw et Q pour 6 grands fleuves français (Garonne, Dordogne, Rhône, Rhin, Loire et Vienne en France), et ont trouvé des influences de tendances temporelles conjointes sur les espèces migratrices. Cette étude va se poursuivre à l'échelle du bassin de la Loire à l'aide des sorties T-NET et EROS.

Bibliography

Ali, S., Mishra, P., Islam, A., and Alam, N. (2016). Simulation of water temperature in a small pond using parametric statistical models: Implications of climate warming. *Journal of Environmental Engineering*, 142(3):04015085.

Allaby, M. (2019). *A Dictionary of Plant Sciences*. Oxford University Press.

Allen, R. G., Pereira, L. S., Raes, D., and Smith, M. (1998). Crop Evapotranspiration – Guidelines for computing crop water requirements. FAO Irrigation and Drainage Paper 56, FAO.

Anderson, E. P., Jenkins, C. N., Heilpern, S., Maldonado-Ocampo, J. A., Carvajal-Vallejos, F. M., Encalada, A. C., Rivadeneira, J. F., Hidalgo, M., Cañas, C. M., Ortega, H., et al. (2018). Fragmentation of andes-to-amazon connectivity by hydropower dams. *Science advances*, 4(1):eaao1642.

Arevalo, E., Lassalle, G., Tétard, S., Maire, A., Sauquet, E., Lambert, P., Paumier, A., Villeneuve, B., and Drouineau, H. (2020). An innovative bivariate approach to detect joint temporal trends in environmental conditions: Application to large french rivers and diadromous fish. *Science of the Total Environment*, 748:141260.

Arismendi, I., Johnson, S. L., Dunham, J. B., and Haggerty, R. (2013a). Descriptors of natural thermal regimes in streams and their responsiveness to change in the pacific northwest of north america. *Freshwater Biology*, 58(5):880–894.

Arismendi, I., Johnson, S. L., Dunham, J. B., Haggerty, R., and Hockman-Wert, D. (2012). The paradox of cooling streams in a warming world: regional climate trends do not parallel variable local trends in stream temperature in the pacific continental united states. *Geophysical Research Letters*, 39(10).

Arismendi, I., Safeeq, M., Dunham, J. B., and Johnson, S. L. (2014). Can air temperature be used to project influences of climate change on stream temperature? *Environmental Research Letters*, 9(8):084015.

Arismendi, I., Safeeq, M., Johnson, S. L., Dunham, J. B., and Haggerty, R. (2013b). Increasing synchrony of high temperature and low flow in western north american streams: double trouble for coldwater biota? *Hydrobiologia*, 712(1):61–70.

Arora, R., Tockner, K., and Venohr, M. (2016). Changing river temperatures in northern germany: trends and drivers of change. *Hydrological Processes*, 30(17):3084–3096.

Aulinger, T., Mette, T., Papathanassion, K., Hajnsek, I., Heurich, M., and Krzystek, P. (2005). Validation of heights from interferometric sar and lidar over the temperate forest site“nationalpark bayerischer wald”. In *ESA Special Publication*, volume 586, page 11.

Bador, M., Terray, L., Boe, J., Somot, S., Alias, A., Gibelin, A.-L., and Dubuisson, B. (2017). Future summer mega-heatwave and record-breaking temperatures in a warmer france climate. *Environmental Research Letters*, 12(7):074025.

Bae, M.-J., Merciai, R., Benejam, L., Sabater, S., and García-Berthou, E. (2016). Small weirs, big effects: disruption of water temperature regimes with hydrological alteration in a mediterranean stream. *River Research and Applications*, 32(3):309–319.

Batalla, R. J., Gomez, C. M., and Kondolf, G. M. (2004). Reservoir-induced hydrological changes in the ebro river basin (ne spain). *Journal of hydrology*, 290(1-2):117–136.

Bauer, D. F. (1972). Constructing confidence sets using rank statistics. *Journal of the American Statistical Association*, 67(339):687–690.

Beaufort, A. (2015). *Modélisation physique de la température des cours d’eau à l’échelle régionale: application au bassin versant de la Loire*. PhD thesis, Tours.

Beaufort, A., Curie, F., Moatar, F., Ducharne, A., Melin, E., and Thiéry, D. (2016a). T-net, a dynamic model for simulating daily stream temperature at the regional scale based on a network topology. *Hydrological Processes*, 30(13):2196–2210.

Beaufort, A., Moatar, F., Curie, F., Ducharne, A., Bustillo, V., and Thiéry, D. (2016b). River temperature modelling by strahler order at the regional scale in the loire river basin, france. *River Research and Applications*, 32(4):597–609.

Beaufort, A., Moatar, F., Sauquet, E., Loicq, P., and Hannah, D. M. (2020a). Influence of landscape and hydrological factors on stream–air temperature relationships at regional scale. *Hydrological Processes*, 34(3):583–597.

Beaufort, A., Moatar, F., Sauquet, E., and Magand, C. (2020b). Thermie en rivière : Analyse géostatistique et description de régime : Application à l’échelle de la France. Research report, INRAE.

Benda, L., Poff, N. L., Miller, D., Dunne, T., Reeves, G., Pess, G., and Pollock, M. (2004). The network dynamics hypothesis: how channel networks structure riverine habitats. *BioScience*, 54(5):413–427.

Benyahya, L., Caissie, D., St-Hilaire, A., Ouarda, T. B., and Bobée, B. (2007). A review of statistical water temperature models. *Canadian Water Resources Journal*, 32(3):179–192.

Berhanu, B., Seleshi, Y., Demisse, S., and Melesse, A. (2015). Flow regime classification and hydrological characterization: a case study of ethiopian rivers. *Water*, 7(6):3149–3165.

Blöschl, G., Hall, J., Viglione, A., Perdigão, R. A., Parajka, J., Merz, B., Lun, D., Arheimer, B., Aronica, G. T., Bilibashi, A., et al. (2019). Changing climate both increases and decreases european river floods. *Nature*, 573(7772):108–111.

Boon, P. and Shires, S. (1976). Temperature studies on a river system in north-east england. *Freshwater Biology*, 6(1):23–32.

Bourges, B. (1985). Improvement in solar declination computation. *Solar Energy*, 35(4):367–369.

Branger, F., Gouttevin, I., Tilmant, F., Cipriani, T., Barachet, C., Montginoul, M., Le Gros, C., Sauquet, E., Braud, I., and Leblois, E. (2016). *Modélisation hydrologique distribuée du Rhône*. PhD thesis, irstea.

Branger, F., Horner, I., Marçais, J., Caballero, Y., and Braud, I. (2020). Diagnostic of a regional distributed hydrological model through hydrological signatures. In *EGU General Assembly*.

Branger, F. and McMillan, H. (2019). Deriving hydrological signatures from soil moisture data. *Hydrological Processes*.

Breshears, D. D., Huxman, T. E., Adams, H. D., Zou, C. B., and Davison, J. E. (2008). Vegetation synchronously leans upslope as climate warms. *Proceedings of the National Academy of Sciences*, 105(33):11591–11592.

Briggs, M. A., Lane, J. W., Snyder, C. D., White, E. A., Johnson, Z. C., Nelms, D. L., and Hitt, N. P. (2018). Shallow bedrock limits groundwater seepage-based headwater climate refugia. *Limnologica*, 68:142–156.

Bruno, D., Belmar, O., Maire, A., Morel, A., Dumont, B., and Datry, T. (2019). Structural and functional responses of invertebrate communities to climate change and flow regulation in alpine catchments. *Global change biology*, 25(5):1612–1628.

Brutsaert, W. and Stricker, H. (1979). An advection-aridity approach to estimate actual regional evapotranspiration. *Water resources research*, 15(2):443–450.

Buendía, C., Sabater, S., Palau, A., Batalla, R., and Marcé, R. (2015). Using equilibrium temperature to assess thermal disturbances in rivers. *Hydrological Processes*, 29(19):4350–4360.

Buisson, L., Blanc, L., and Grenouillet, G. (2008). Modelling stream fish species distribution in a river network: the relative effects of temperature versus physical factors. *Ecology of Freshwater Fish*, 17(2):244–257.

Buisson, L. and Grenouillet, G. (2009). Contrasted impacts of climate change on stream fish assemblages along an environmental gradient. *Diversity and Distributions*, 15(4):613–626.

Bustillo, V., Moatar, F., Ducharne, A., Thiéry, D., and Poirel, A. (2014). A multimodel comparison for assessing water temperatures under changing climate conditions via the equilibrium temperature concept: case study of the middle loire river, france. *Hydrological Processes*, 28(3):1507–1524.

Caissie, D. (2006). The thermal regime of rivers: a review. *Freshwater biology*, 51(8):1389–1406.

Caissie, D., Satish, M. G., and El-Jabi, N. (2007). Predicting water temperatures using a deterministic model: Application on miramichi river catchments (new brunswick, canada). *Journal of Hydrology*, 336(3-4):303–315.

Caissie, D., St-Hilaire, A., and El-Jabi, N. (2004). Prediction of water temperatures using regression and stochastic models. *57th Canadian Water Resources Association Annual Congress*, 6.

Carlson, A. K., Taylor, W. W., Hartikainen, K. M., Infante, D. M., Beard, T. D., and Lynch, A. J. (2017). Comparing stream-specific to generalized temperature models to guide salmonid management in a changing climate. *Reviews in Fish Biology and Fisheries*, 27(2):443–462.

Casado, A., Hannah, D. M., Peiry, J.-L., and Campo, A. M. (2013). Influence of dam-induced hydrological regulation on summer water temperature: Sauce grande river, argentina. *Ecohydrology*, 6(4):523–535.

Chandesris, A. and Pella, H. (2006). *Constitution d'une base d'information spatialisée «barrages, retenues et plans d'eau» au niveau national en vue d'évaluer les modifications hydromorphologiques*. PhD thesis, irstea.

Chandesris, A., Van Looy, K., Diamond, J. S., and Souchon, Y. (2019). Small dams alter thermal regimes of downstream water. *Hydrology & Earth System Sciences*, 23(11).

Charrad, M., Ghazzali, N., Boiteau, V., Niknafs, A., and Charrad, M. M. (2014). Package 'nbclust'. *Journal of statistical software*, 61:1–36.

Cheng, Y., Voisin, N., Yearsley, J. R., and Nijssen, B. (2020). Reservoirs modify river thermal regime sensitivity to climate change: a case study in the southeastern united states. *Water Resources Research*, 56(6):e2019WR025784.

Christensen, O. B., Christensen, J. H., Machenhauer, B., and Botzet, M. (1998). Very high-resolution regional climate simulations over scandinavia—present climate. *Journal of Climate*, 11(12):3204–3229.

Chu, C., Jones, N. E., Mandrak, N. E., Piggott, A. R., and Minns, C. K. (2008). The influence of air temperature, groundwater discharge, and climate change on the thermal diversity of stream fishes in southern ontario watersheds. *canadian Journal of Fisheries and aquatic sciences*, 65(2):297–308.

Cipriani, T., Tilmant, F., Le Gros, C., Barachet, C., Branger, F., Sauquet, E., Braud, I., Leblois, E., and Gouttevin, I. (2014). *Modélisation hydrologique distribuée du Rhône. Rapport d'avancement 2014-version finale*. PhD thesis, irstea.

Colin, J., Déqué, M., Radu, R., and Somot, S. (2010). Sensitivity study of heavy precipitation in limited area model climate simulations: influence of the size of the domain and the use of the spectral nudging technique. *Tellus A: Dynamic Meteorology and Oceanography*, 62(5):591–604.

Comte, L., Buisson, L., Daufresne, M., and Grenouillet, G. (2013). Climate-induced changes in the distribution of freshwater fish: observed and predicted trends. *Freshwater Biology*, 58(4):625–639.

Cox, T. J. and Rutherford, J. C. (2000). Predicting the effects of time-varying temperatures on stream invertebrate mortality. *New Zealand Journal of Marine and Freshwater Research*, 34(2):209–215.

Daniels, M. E. and Danner, E. M. (2020). The drivers of river temperatures below a large dam. *Water Resources Research*, 56(5):e2019WR026751.

Dayon, G., Boe, J., Martin, E., and Gailhard, J. (2018). Impacts of climate change on the hydrological cycle over france and associated uncertainties. *Comptes Rendus Geoscience*, 350(4):141–153.

Devers, A. (2019). *Vers une réanalyse hydrométéorologique à l'échelle de la France sur les 150 dernières années par assimilation de données dans des reconstructions ensemblistes*. Theses, Université Grenoble Alpes.

Devers, A., Vidal, J.-P., Lauvernet, C., and Vannier, O. (2021). Fyre climate: A high-resolution reanalysis of daily precipitation and temperature in france from 1871 to 2012. *Climate of the Past*, 17(5):1857–1879.

Domisch, S., Araújo, M. B., Bonada, N., Pauls, S. U., Jähnig, S. C., and Haase, P. (2013). Modelling distribution in e uropean stream macroinvertebrates under future climates. *Global Change Biology*, 19(3):752–762.

Drange, H., Roelandt, C., Seierstad, I., Hoose, C., and Kristjnsson, J. (2012). The norwegian earth system model, noresm1-m part 1: description and basic evaluation. *Geosci Model Dev Discuss*, 5(3):28432931Bollasina.

Dripps, W. and Granger, S. R. (2013). The impact of artificially impounded, residential headwater lakes on downstream water temperature. *Environmental earth sciences*, 68(8):2399–2407.

Du, X., Shrestha, N. K., and Wang, J. (2019). Assessing climate change impacts on stream temperature in the athabasca river basin using swat equilibrium temperature model and its potential impacts on stream ecosystem. *Science of the Total Environment*, 650:1872–1881.

Ducharne, A. (2008). Importance of stream temperature to climate change impact on water quality. *Hydrology and Earth System Sciences*, 12(3):797–810.

Ducharne, A., Sauquet, E., Habets, F., Déqué, M., Gascoin, S., Hachour, A., Martin, E., Oudin, L., Pagé, C., Terray, L., et al. (2011). Evolution potentielle du régime des crues de la seine sous changement climatique. *La Houille Blanche*, (1):51–57.

Dufresne, J.-L., Foujols, M.-A., Denvil, S., Caubel, A., Marti, O., Aumont, O., Balkanski, Y., Bekki, S., Bellenger, H., Benshila, R., et al. (2013). Climate change projections using the ipsl-cm5 earth system model: from cmip3 to cmip5. *Climate dynamics*, 40(9):2123–2165.

Dugdale, S. J., Hannah, D. M., and Malcolm, I. A. (2017). River temperature modelling: A review of process-based approaches and future directions. *Earth-Science Reviews*, 175:97–113.

Dugdale, S. J., Malcolm, I. A., Kantola, K., and Hannah, D. M. (2018). Stream temperature under contrasting riparian forest cover: Understanding thermal dynamics and heat exchange processes. *Science of The Total Environment*, 610:1375–1389.

Edinger, J. E., Duttweiler, D. W., and Geyer, J. C. (1968). The response of water temperatures to meteorological conditions. *Water Resources Research*, 4(5):1137–1143.

Edmonds, R., Murray, G., and Marra, J. (2000). Influence of partial harvesting on stream temperatures, chemistry, and turbidity in forests on the western olympic peninsula, washington. *WSU Press*.

Elliott, J. and Elliott, J. (2010). Temperature requirements of atlantic salmon salmo salar, brown trout salmo trutta and arctic charr salvelinus alpinus: predicting the effects of climate change. *Journal of fish biology*, 77(8):1793–1817.

Erickson, T. R. and Stefan, H. G. (2000). Linear air/water temperature correlations for streams during open water periods. *Journal of Hydrologic Engineering*, 5(3):317–321.

Fang, X. and Stefan, H. G. (2009). Simulations of climate effects on water temperature, dissolved oxygen, and ice and snow covers in lakes of the contiguous us under past and future climate scenarios. *Limnology and Oceanography*, 54(6part2):2359–2370.

Feeley, K. J., Silman, M. R., Bush, M. B., Farfan, W., Cabrera, K. G., Malhi, Y., Meir, P., Revilla, N. S., Quisiyupanqui, M. N. R., and Saatchi, S. (2011). Upslope migration of andean trees. *Journal of Biogeography*, 38(4):783–791.

Floury, M., Usseglio-Polatera, P., Ferreol, M., Delattre, C., and Souchon, Y. (2013). Global climate change in large e uropean rivers: long-term effects on macroinvertebrate communities and potential local confounding factors. *Global change biology*, 19(4):1085–1099.

Fraley, J. J. (1979). Effects of elevated stream temperatures below a shallow reservoir on a cold water macroinvertebrate fauna. In *The ecology of regulated streams*, pages 257–272. Springer.

Garcia, F., Folton, N., and Oudin, L. (2017). Which objective function to calibrate rainfall–runoff models for low-flow index simulations? *Hydrological sciences journal*, 62(7):1149–1166.

Garg, H. and Datta, G. (1993). Fundamentals and characteristics of solar radiation. *Renewable energy*, 3(4-5):305–319.

Garner, G., Hannah, D. M., Sadler, J. P., and Orr, H. G. (2014). River temperature regimes of england and wales: spatial patterns, inter-annual variability and climatic sensitivity. *Hydrological Processes*, 28(22):5583–5598.

Garner, G., Malcolm, I. A., Sadler, J. P., and Hannah, D. M. (2017). The role of riparian vegetation density, channel orientation and water velocity in determining river temperature dynamics. *Journal of Hydrology*, 553:471–485.

Giorgi, F., Coppola, E., Solmon, F., Mariotti, L., Sylla, M., Bi, X., Elguindi, N., Diro, G., Nair, V., Giuliani, G., et al. (2012). Regcm4: model description and preliminary tests over multiple cordex domains. *Climate Research*, 52:7–29.

Giuntoli, I., Renard, B., Vidal, J.-P., and Bard, A. (2013). Low flows in france and their relationship to large-scale climate indices. *Journal of Hydrology*, 482:105–118.

Gomi, T., Moore, R. D., and Dhakal, A. S. (2006). Headwater stream temperature response to clear-cut harvesting with different riparian treatments, coastal british columbia, canada. *Water Resources Research*, 42(8).

Gooseff, M. N., Strzepek, K., and Chapra, S. C. (2005). Modeling the potential effects of climate change on water temperature downstream of a shallow reservoir, lower madison river, mt. *Climatic Change*, 68(3):331–353.

Grantz, E. M., Haggard, B. E., and Scott, J. T. (2014). Stoichiometric imbalance in rates of nitrogen and phosphorus retention, storage, and recycling can perpetuate nitrogen deficiency in highly-productive reservoirs. *Limnology and Oceanography*, 59(6):2203–2216.

Gunawardhana, L. N., Kazama, S., and Kawagoe, S. (2011). Impact of urbanization and climate change on aquifer thermal regimes. *Water resources management*, 25(13):3247–3276.

Gupta, H. V., Wagener, T., and Liu, Y. (2008). Reconciling theory with observations: elements of a diagnostic approach to model evaluation. *Hydrological Processes: An International Journal*, 22(18):3802–3813.

Habets, F., Boé, J., Déqué, M., Ducharne, A., Gascoin, S., Hachour, A., Martin, E., Pagé, C., Sauquet, E., Terray, L., et al. (2013). Impact of climate change on the hydrogeology of two basins in northern france. *Climatic change*, 121(4):771–785.

Habets, F., Molénat, J., Carluer, N., Douez, O., and Leenhardt, D. (2018). The cumulative impacts of small reservoirs on hydrology: A review. *Science of the Total Environment*, 643:850–867.

Handcock, R., Gillespie, A., Cherkauer, K., Kay, J., Burges, S., and Kampf, S. (2006). Accuracy and uncertainty of thermal-infrared remote sensing of stream temperatures at multiple spatial scales. *Remote Sensing of Environment*, 100(4):427–440.

Handcock, R. N., Torgersen, C. E., Cherkauer, K. A., Gillespie, A. R., Tockner, K., Faux, R. N., Tan, J., and Carbonneau, P. (2012). Thermal infrared remote sensing of water temperature in riverine landscapes. *Fluvial remote sensing for science and management*, 1(2012):85–113.

Hannah, D. M. and Garner, G. (2015). River water temperature in the united kingdom: changes over the 20th century and possible changes over the 21st century. *Progress in Physical Geography*, 39(1):68–92.

Hannah, D. M., Malcolm, I. A., and Bradley, C. (2009). Seasonal hyporheic temperature dynamics over riffle bedforms. *Hydrological Processes: An International Journal*, 23(15):2178–2194.

Hannah, D. M., Malcolm, I. A., Soulsby, C., and Youngson, A. F. (2004). Heat exchanges and temperatures within a salmon spawning stream in the cairngorms, scotland: seasonal and sub-seasonal dynamics. *River Research and Applications*, 20(6):635–652.

Hannah, D. M., Malcolm, I. A., Soulsby, C., and Youngson, A. F. (2008). A comparison of forest and moorland stream microclimate, heat exchanges and thermal dynamics. *Hydrological Processes: An International Journal*, 22(7):919–940.

Hare, D. K., Helton, A. M., Johnson, Z. C., Lane, J. W., and Briggs, M. A. (2021). Continental-scale analysis of shallow and deep groundwater contributions to streams. *Nature communications*, 12(1):1–10.

Hari, R. E., Livingstone, D. M., Siber, R., BURKHARDT-HOLM, P., and Guettinger, H. (2006). Consequences of climatic change for water temperature and brown trout populations in alpine rivers and streams. *Global Change Biology*, 12(1):10–26.

Harrison, J. A., Maranger, R. J., Alexander, R. B., Giblin, A. E., Jacinthe, P.-A., Mayorga, E., Seitzinger, S. P., Sobota, D. J., and Wollheim, W. M. (2009). The regional and global significance of nitrogen removal in lakes and reservoirs. *Biogeochemistry*, 93(1-2):143–157.

Hazeleger, W., Guemas, V., Wouters, B., Corti, S., Andreu-Burillo, I., Doblas-Reyes, F. J., Wyser, K., and Caian, M. (2013). Multiyear climate predictions using two initialization strategies. *Geophysical Research Letters*, 40(9):1794–1798.

Hazeleger, W., Wang, X., Severijns, C., Ştefănescu, S., Bintanja, R., Sterl, A., Wyser, K., Semmler, T., Yang, S., Van den Hurk, B., et al. (2012). Ec-earth v2. 2: description and validation of a new seamless earth system prediction model. *Climate dynamics*, 39(11):2611–2629.

Hill, R. A., Hawkins, C. P., and Carlisle, D. M. (2013). Predicting thermal reference conditions for usa streams and rivers. *Freshwater Science*, 32(1):39–55.

Hobeichi, S., Abramowitz, G., and Evans, J. P. (2021). Robust historical evapotranspiration trends across climate regimes. *Hydrology and Earth System Sciences*, 25(7):3855–3874.

Horner, I., Branger, F., McMillan, H., Vannier, O., and Braud, I. (2020). Information content of snow hydrological signatures based on streamflow, precipitation and air temperature. *Hydrological Processes*, 34(12):2763–2779.

Hourdin, F., Foujols, M.-A., Codron, F., Guemas, V., Dufresne, J.-L., Bony, S., Denvil, S., Guez, L., Lott, F., Ghattas, J., et al. (2013). Impact of the lmdz atmospheric grid configuration on the climate and sensitivity of the ipsl-cm5a coupled model. *Climate Dynamics*, 40(9-10):2167–2192.

Huntington, T. G. (2006). Evidence for intensification of the global water cycle: review and synthesis. *Journal of Hydrology*, 319(1-4):83–95.

Hutchison, B. A. and Matt, D. R. (1977). The distribution of solar radiation within a deciduous forest. *Ecological Monographs*, 47(2):185–207.

ICOLD (2011). International commission on large dam.

IGN (2006). Descriptif technique bd carthage.

IGN (2008). Descriptif technique bd topo. Technical report, Institut Gógraphique National.

IGN (2011). Descriptif technique bd alti. Technical report, Institut Gógraphique National.

Imdadullah, M., Aslam, M., and Altaf, S. (2016). Mctest: An r package for detection of collinearity among regressors. *The R Journal*, 8(2):495–505.

Imholt, C., Gibbins, C., Malcolm, I., Langan, S., and Soulsby, C. (2010). Influence of riparian cover on stream temperatures and the growth of the mayfly baetis rhodani in an upland stream. *Aquatic Ecology*, 44(4):669–678.

IPCC (2014). *Climate change 2014: synthesis report. Contribution of Working Groups I, II and III to the fifth assessment report of the Intergovernmental Panel on Climate Change*.

Isaak, D., Wollrab, S., Horan, D., and Chandler, G. (2012). Climate change effects on stream and river temperatures across the northwest us from 1980–2009 and implications for salmonid fishes. *Climatic change*, 113(2):499–524.

Isaak, D. J., Wenger, S. J., Peterson, E. E., Ver Hoef, J. M., Nagel, D. E., Luce, C. H., Hostetler, S. W., Dunham, J. B., Roper, B. B., Wollrab, S. P., et al. (2017). The norwest summer stream temperature model and scenarios for the western us: A crowd-sourced database and new geospatial tools foster a user community and predict broad climate warming of rivers and streams. *Water Resources Research*, 53(11):9181–9205.

Iversen, T., Bentsen, M., Bethke, I., Debernard, J., Kirkevåg, A., Seland, Ø., Drange, H., Kristjánsson, J., Medhaug, I., Sand, M., et al. (2012). The norwegian earth system model, noresm1-m–part 2: Climate response and scenario projections. *Geosci. Model Dev. Discuss*, 5(3):2933–2998.

Jackson, F., Hannah, D. M., Fryer, R., Millar, C., and Malcolm, I. (2017). Development of spatial regression models for predicting summer river temperatures from landscape characteristics: Implications for land and fisheries management. *Hydrological processes*, 31(6):1225–1238.

Jackson, F., Malcolm, I., and Hannah, D. M. (2016). A novel approach for designing large-scale river temperature monitoring networks. *Hydrology Research*, 47(3):569–590.

Jackson, F. L., Fryer, R. J., Hannah, D. M., Millar, C. P., and Malcolm, I. A. (2018). A spatio-temporal statistical model of maximum daily river temperatures to inform the management of scotland's atlantic salmon rivers under climate change. *Science of the Total Environment*, 612:1543–1558.

Jacob, D., Elizalde, A., Haensler, A., Hagemann, S., Kumar, P., Podzun, R., Rechid, D., Remedio, A. R., Saeed, F., Sieck, K., et al. (2012). Assessing the transferability of the regional climate model remo to different coordinated regional climate downscaling experiment (cordex) regions. *Atmosphere*, 3(1):181–199.

Johnson, M. F. and Wilby, R. L. (2015). Seeing the landscape for the trees: metrics to guide riparian shade management in river catchments. *Water Resources Research*, 51(5):3754–3769.

Johnson, S. L. (2004). Factors influencing stream temperatures in small streams: substrate effects and a shading experiment. *Canadian Journal of Fisheries and Aquatic Sciences*, 61(6):913–923.

Johnson, S. L. and Jones, J. A. (2000). Stream temperature responses to forest harvest and debris flows in western cascades, oregon. *Canadian Journal of Fisheries and Aquatic Sciences*, 57(S2):30–39.

Jones, C., Hughes, J., Bellouin, N., Hardiman, S., Jones, G., Knight, J., Liddicoat, S., O'connor, F., Andres, R. J., Bell, C., et al. (2011). The hadgem2-es implementation of cmip5 centennial simulations. *Geoscientific Model Development*, 4(3):543–570.

Jungclaus, J., Fischer, N., Haak, H., Lohmann, K., Marotzke, J., Matei, D., Mikolajewicz, U., Notz, D., and Von Storch, J. (2013). Characteristics of the ocean simulations in the max planck institute ocean model (mpiom) the ocean component of the mpi-earth system model. *Journal of Advances in Modeling Earth Systems*, 5(2):422–446.

Kaushal, S. S., Likens, G. E., Jaworski, N. A., Pace, M. L., Sides, A. M., Seekell, D., Belt, K. T., Secor, D. H., and Wingate, R. L. (2010). Rising stream and river temperatures in the united states. *Frontiers in Ecology and the Environment*, 8(9):461–466.

Kędra, M. (2020). Regional response to global warming: Water temperature trends in semi-natural mountain river systems. *Water*, 12(1):283.

Kędra, M. and Wiejaczka, Ł. (2018). Climatic and dam-induced impacts on river water temperature: Assessment and management implications. *Science of the Total Environment*, 626:1474–1483.

Kelleher, C., Wagener, T., Gooseff, M., McGlynn, B., McGuire, K., and Marshall, L. (2012). Investigating controls on the thermal sensitivity of pennsylvania streams. *Hydrological Processes*, 26(5):771–785.

Keuler, K., Radtke, K., Kotlarski, S., and Lüthi, D. (2016). Regional climate change over europe in cosmo-clm: Influence of emission scenario and driving global model. *Meteorologische Zeitschrift*, 25(2):121–136.

Kinouchi, T., Yagi, H., and Miyamoto, M. (2007). Increase in stream temperature related to anthropogenic heat input from urban wastewater. *Journal of Hydrology*, 335(1-2):78–88.

Kirk, M. A. and Rahel, F. J. (2021). Air temperatures overpredict changes to stream fish assemblages with climate warming compared to water temperatures. *Ecological Applications*, page e02465.

Kjellström, E., Bärring, L., Nikulin, G., Nilsson, C., Persson, G., and Strandberg, G. (2016). Production and use of regional climate model projections–a swedish perspective on building climate services. *Climate services*, 2:15–29.

Kjellström, E. and Ruosteenoja, K. (2007). Present-day and future precipitation in the baltic sea region as simulated in a suite of regional climate models. *Climatic Change*, 81(1):281–291.

Krause, P., Bäse, F., Bende-Michl, U., Fink, M., Flügel, W., and Pfennig, B. (2006). Multi-scale investigations in a mesoscale catchment–hydrological modelling in the gera catchment. *Advances in Geosciences*, 9:53–61.

Kriaučiūnienė, J., Virbickas, T., Šarauskienė, D., Jakimavičius, D., Kažys, J., Bukantis, A., Kesminas, V., Povilaitis, A., Dainys, J., Akstinas, V., et al. (2019). Fish assemblages under climate change in lithuanian rivers. *Science of The Total Environment*, 661:563–574.

Kurylyk, B. L., Bourque, C.-A., and MacQuarrie, K. T. (2013). Potential surface temperature and shallow groundwater temperature response to climate change: an example from a small forested catchment in east-central new brunswick (canada). *Hydrology and Earth System Sciences*, 17(7):2701–2716.

Kurylyk, B. L., MacQuarrie, K. T., Caissie, D., and McKenzie, J. M. (2015). Shallow groundwater thermal sensitivity to climate change and land cover disturbances: derivation of analytical expressions and implications for stream temperature modeling. *Hydrology and Earth System Sciences*, 19(5):2469–2489.

Kurylyk, B. L., MacQuarrie, K. T., and Voss, C. I. (2014). Climate change impacts on the temperature and magnitude of groundwater discharge from shallow, unconfined aquifers. *Water Resources Research*, 50(4):3253–3274.

Kwak, J., St-Hilaire, A., Chebana, F., and Kim, G. (2017). Summer season water temperature modeling under the climate change: case study for fourchue river, quebec, canada. *Water*, 9(5):346.

Lalot, E., Curie, F., Wawrzyniak, V., Baratelli, F., Schomburgk, S., Flipo, N., Piégay, H., and Moatar, F. (2015). Quantification of the contribution of the beauce groundwater aquifer to the discharge of the loire river using thermal infrared satellite imaging. *Hydrology and Earth System Sciences*, 19(11):4479–4492.

Lamouroux, N., Pella, H., Vanderbecq, A., Sauquet, E., and Lejot, J. (2010). Estimkart 2.0: Une plate-forme de modèles écohydrologiques pour contribuer à la gestion des cours d'eau à l'échelle des bassins français. *Version provisoire. Cemagref, Agence de l'Eau Rhône-Méditerranée-Corse, Onema, Lyon (45 pp.).*

Le Moal, M., Gascuel-Odoux, C., Ménesguen, A., Souchon, Y., Étrillard, C., Levain, A., Moatar, F., Pannard, A., Souchu, P., Lefebvre, A., et al. (2019). Eutrophication: A new wine in an old bottle? *Science of the total environment*, 651:1–11.

Le Moigne, P., Besson, F., Martin, E., Boé, J., Boone, A., Decharme, B., Etchevers, P., Faroux, S., Habets, F., Lafaysse, M., et al. (2020). The latest improvements with surfex v8. 0 of the safran–isba–modcou hydrometeorological model for france. *Geoscientific Model Development*, 13(9):3925–3946.

LeBlanc, R. T., Brown, R. D., and FitzGibbon, J. E. (1997). Modeling the effects of land use change on the water temperature in unregulated urban streams. *Journal of Environmental Management*, 49(4):445–469.

Lee, S.-Y., Fullerton, A. H., Sun, N., and Torgersen, C. E. (2020). Projecting spatiotemporally explicit effects of climate change on stream temperature: A model comparison and implications for coldwater fishes. *Journal of Hydrology*, 588:125066.

Lehner, B., Liermann, C. R., Revenga, C., Vörösmarty, C., Fekete, B., Crouzet, P., Döll, P., Endejan, M., Frenken, K., Magome, J., et al. (2011). High-resolution mapping of the world's reservoirs and dams for sustainable river-flow management. *Frontiers in Ecology and the Environment*, 9(9):494–502.

Lennox, R. J., Crook, D. A., Moyle, P. B., Struthers, D. P., and Cooke, S. J. (2019). Toward a better understanding of freshwater fish responses to an increasingly drought-stricken world. *Reviews in fish biology and fisheries*, 29(1):71–92.

Lessard, J. L. and Hayes, D. B. (2003). Effects of elevated water temperature on fish and macroinvertebrate communities below small dams. *River research and applications*, 19(7):721–732.

Li, G. (2006). *Stream temperature and dissolved oxygen modeling in the lower Flint River basin, GA*. PhD thesis, University of Georgia.

Li, G., Jackson, C. R., and Kraseski, K. A. (2012). Modeled riparian stream shading: Agreement with field measurements and sensitivity to riparian conditions. *Journal of hydrology*, 428:142–151.

Li, H.-Y., Leung, L. R., Tesfa, T., Voisin, N., Hejazi, M., Liu, L., Liu, Y., Rice, J., Wu, H., and Yang, X. (2015). Modeling stream temperature in the anthropocene: An earth system modeling approach. *Journal of Advances in Modeling Earth Systems*, 7(4):1661–1679.

Liu, D., Xu, Y., Guo, S., Xiong, L., Liu, P., and Zhao, Q. (2018). Stream temperature response to climate change and water diversion activities. *Stochastic Environmental Research and Risk Assessment*, 32(5):1397–1413.

Loicq, P. (2018). *Caractérisation et modélisation de la température des rivières sur le bassin de la Maine: influence de la végétation rivulaire et des échanges nappe-rivière*. PhD thesis, Tours.

Loicq, P., Moatar, F., Jullian, Y., Dugdale, S. J., and Hannah, D. M. (2018). Improving representation of riparian vegetation shading in a regional stream temperature model using lidar data. *Science of the total environment*, 624:480–490.

Lowney, C. L. (2000). Stream temperature variation in regulated rivers: Evidence for a spatial pattern in daily minimum and maximum magnitudes. *Water Resources Research*, 36(10):2947–2955.

Maheu, A., Poff, N., and St-Hilaire, A. (2016a). A classification of stream water temperature regimes in the conterminous usa. *River Research and Applications*, 32(5):896–906.

Maheu, A., St-Hilaire, A., Caissie, D., and El-Jabi, N. (2016b). Understanding the thermal regime of rivers influenced by small and medium size dams in eastern canada. *River research and applications*, 32(10):2032–2044.

Maheu, A., St-Hilaire, A., Caissie, D., El-Jabi, N., Bourque, G., and Boisclair, D. (2016c). A regional analysis of the impact of dams on water temperature in medium-size rivers in eastern canada. *Canadian Journal of Fisheries and Aquatic Sciences*, 73(12):1885–1897.

Maire, A., Laffaille, P., Maire, J.-F., and Buisson, L. (2017). Identification of priority areas for the conservation of stream fish assemblages: implications for river management in france. *River research and applications*, 33(4):524–537.

Maire, A., Thierry, E., Viechtbauer, W., and Daufresne, M. (2019). Poleward shift in large-river fish communities detected with a novel meta-analysis framework. *Freshwater Biology*, 64(6):1143–1156.

Majdi, N., Uthoff, J., Traunspurger, W., Laffaille, P., and Maire, A. (2020). Effect of water warming on the structure of biofilm-dwelling communities. *Ecological Indicators*, 117:106622.

Mann, H. B. (1945). Nonparametric tests against trend. *Econometrica: Journal of the econometric society*, pages 245–259.

Mantua, N., Tohver, I., and Hamlet, A. (2010). Climate change impacts on streamflow extremes and summertime stream temperature and their possible consequences for freshwater salmon habitat in washington state. *Climatic Change*, 102(1-2):187–223.

Maxted, J. R., McCready, C. H., and Scarsbrook, M. R. (2005). Effects of small ponds on stream water quality and macroinvertebrate communities. *New Zealand Journal of Marine and Freshwater Research*, 39(5):1069–1084.

Mayer, T. D. (2012). Controls of summer stream temperature in the pacific northwest. *Journal of Hydrology*, 475:323–335.

Mbaka, J. G. and Wanjiru Mwaniki, M. (2015). A global review of the downstream effects of small impoundments on stream habitat conditions and macroinvertebrates. *Environmental Reviews*, 23(3):257–262.

McCann, E. L., Johnson, N. S., and Pangle, K. L. (2018). Corresponding long-term shifts in stream temperature and invasive fish migration. *Canadian Journal of Fisheries and Aquatic Sciences*, 75(5):772–778.

McMillan, H., Westerberg, I., and Branger, F. (2017). Five guidelines for selecting hydrological signatures. *Hydrological Processes*.

Meisner, J. D. (1990). Potential loss of thermal habitat for brook trout, due to climatic warming, in two southern ontario streams. *Transactions of the American Fisheries Society*, 119(2):282–291.

Merriam, E. R., Fernandez, R., Petty, J. T., and Zegre, N. (2017). Can brook trout survive climate change in large rivers? if it rains. *Science of the Total Environment*, 607:1225–1236.

Michel, A., Brauchli, T., Lehning, M., Schaefli, B., and Huwald, H. (2020). Stream temperature and discharge evolution in switzerland over the last 50 years: annual and seasonal behaviour. *Hydrology & Earth System Sciences*, 24(1).

Michel, A., Schaefli, B., Wever, N., Zekollari, H., Lehning, M., and Huwald, H. (2021). Future water temperature of rivers in switzerland under climate change investigated with physics-based models. *Hydrology and Earth System Sciences Discussions*, pages 1–45.

Minaudo, C., Curie, F., Jullian, Y., Gassama, N., and Moatar, F. (2018). Qual-net, a high temporal-resolution eutrophication model for large hydrographic networks. *Biogeosciences*, 15(7):2251–2269.

Moatar, F., Bustillo, V., Ducharne, A., Billen, G., Garnier, J., Silvestre, M., Callens, J., Thiery, D., Sauquet, E., and Vidal, J.-P. (2013). Impact du changement climatique sur l'hydrosystème loire: Hydrologie, régime thermique, qualité-icc-hydroqual. In *14ème Carrefour des gestions locales de l'eau*, page 22.

Moatar, F. and Dupont, N. (2016). *La Loire fluviale et estuarienne: un milieu en évolution*. Editions Quae.

Moatar, F. and Gailhard, J. (2006). Water temperature behaviour in the river loire since 1976 and 1881. *Comptes Rendus Geoscience*, 338(5):319–328.

Mohseni, O., Erickson, T. R., and Stefan, H. G. (1999). Sensitivity of stream temperatures in the united states to air temperatures projected under a global warming scenario. *Water Resources Research*, 35(12):3723–3733.

Mohseni, O. and Stefan, H. (1999). Stream temperature/air temperature relationship: a physical interpretation. *Journal of hydrology*, 218(3-4):128–141.

Moore, R., Leach, J., and Knudson, J. (2014). Geometric calculation of view factors for stream surface radiation modelling in the presence of riparian forest. *Hydrological Processes*, 28(6):2975–2986.

Moore, R., Spittlehouse, D., and Story, A. (2005). Riparian microclimate and stream temperature response to forest harvesting: A review. *JAWRA Journal of the American Water Resources Association*, 41(4):813–834.

Morales-Marín, L., Rokaya, P., Sanyal, P., Sereda, J., and Lindenschmidt, K. (2019). Changes in streamflow and water temperature affect fish habitat in the athabasca river basin in the context of climate change. *Ecological Modelling*, 407:108718.

Morel, M., Booker, D. J., Gob, F., and Lamouroux, N. (2020). Intercontinental predictions of river hydraulic geometry from catchment physical characteristics. *Journal of Hydrology*, 582:124292.

Nash, J. E. and Sutcliffe, J. V. (1970). River Flow Forecasting Through Conceptual Models. Part 1: A Discussion of Principles. *Journal of Hydrology*, 10(3):282–290.

Nelson, K. C. and Palmer, M. A. (2007). Stream temperature surges under urbanization and climate change: data, models, and responses 1. *JAWRA Journal of the American Water Resources Association*, 43(2):440–452.

Niedrist, G. H. and Füreder, L. (2021). Real-time warming of alpine streams:(re) defining invertebrates' temperature preferences. *River Research and Applications*, 37(2):283–293.

Niemeyer, R. J., Cheng, Y., Mao, Y., Yearsley, J. R., and Nijssen, B. (2018). A thermally stratified reservoir module for large-scale distributed stream temperature models with application in the tennessee river basin. *Water Resources Research*, 54(10):8103–8119.

Null, S. E., Ligare, S. T., and Viers, J. H. (2013). A method to consider whether dams mitigate climate change effects on stream temperatures. *JAWRA Journal of the American Water Resources Association*, 49(6):1456–1472.

O'Gorman, E. J., Pichler, D. E., Adams, G., Benstead, J. P., Cohen, H., Craig, N., Cross, W. F., Demars, B. O., Friberg, N., Gislason, G. M., et al. (2012). Impacts of warming on the structure and functioning of aquatic communities: individual-to ecosystem-level responses. *Advances in ecological research*, 47:81–176.

Olden, J. D. and Naiman, R. J. (2010). Incorporating thermal regimes into environmental flows assessments: modifying dam operations to restore freshwater ecosystem integrity. *Freshwater Biology*, 55(1):86–107.

Orr, H. G., Simpson, G. L., des Clers, S., Watts, G., Hughes, M., Hannaford, J., Dunbar, M. J., Laizé, C. L., Wilby, R. L., Battarbee, R. W., et al. (2015). Detecting changing river temperatures in england and wales. *Hydrological Processes*, 29(5):752–766.

Otto, H.-J. (1998). *Ecologie forestière*. Forêt privée française.

Oudin, L., Andréassian, V., Mathevet, T., Perrin, C., and Michel, C. (2006). Dynamic averaging of rainfall-runoff model simulations from complementary model parameterizations. *Water Resources Research*, 42(7).

Ouellet, V., St-Hilaire, A., Dugdale, S. J., Hannah, D. M., Krause, S., and Proulx-Ouellet, S. (2020). River temperature research and practice: Recent challenges and emerging opportunities for managing thermal habitat conditions in stream ecosystems. *Science of the Total Environment*, 736:139679.

O'Driscoll, M. A. and DeWalle, D. R. (2006). Stream–air temperature relations to classify stream–ground water interactions in a karst setting, central pennsylvania, usa. *Journal of Hydrology*, 329(1-2):140–153.

Palmer, M. A., Lettenmaier, D. P., Poff, N. L., Postel, S. L., Richter, B., and Warner, R. (2009). Climate change and river ecosystems: protection and adaptation options. *Environmental management*, 44(6):1053–1068.

Pella, H., Lejot, J., Lamouroux, N., and Snelder, T. (2012). Le réseau hydrographique théorique (rht) français et ses attributs environnementaux. *Géomorphologie: relief, processus, environnement*, 18(3):317–336.

Perry, L. G., Reynolds, L. V., Beechie, T. J., Collins, M. J., and Shafroth, P. B. (2015). Incorporating climate change projections into riparian restoration planning and design. *Ecohydrology*, 8(5):863–879.

Pettitt, A. N. (1979). A non-parametric approach to the change-point problem. *Applied Statistics*, 28(2):126–135.

Petts, G. E. and Gurnell, A. M. (2005). Dams and geomorphology: research progress and future directions. *Geomorphology*, 71(1-2):27–47.

Pilgrim, J. M., Fang, X., and Stefan, H. G. (1998). Stream temperature correlations with air temperatures in minnesota: Implications for climate warming 1. *JAWRA Journal of the American Water Resources Association*, 34(5):1109–1121.

Piotrowski, A. P., Osuch, M., and Napiorkowski, J. J. (2021). Influence of the choice of stream temperature model on the projections of water temperature in rivers. *Journal of Hydrology*, 601:126629.

Poole, G. C. and Berman, C. H. (2001). An ecological perspective on in-stream temperature: natural heat dynamics and mechanisms of human-causedthermal degradation. *Environmental management*, 27(6):787–802.

Poulet, N., Beaulaton, L., and Dembski, S. (2011). Time trends in fish populations in metropolitan france: insights from national monitoring data. *Journal of Fish Biology*, 79(6):1436–1452.

Poulin, M. (1980). *MODELISATION DU COMPORTEMENT THERMIQUE DES COURS D'EAU: APPLICATION AU RHIN*. PhD thesis.

Prats, J., Val, R., Dolz, J., and Armengol, J. (2012). Water temperature modeling in the lower ebro river (spain): Heat fluxes, equilibrium temperature, and magnitude of alteration caused by reservoirs and thermal effluent. *Water Resources Research*, 48(5).

Preece, R. M. and Jones, H. A. (2002). The effect of keepit dam on the temperature regime of the namoi river, australia. *River Research and Applications*, 18(4):397–414.

Prudhomme, C., Giuntoli, I., Robinson, E. L., Clark, D. B., Arnell, N. W., Dankers, R., Fekete, B. M., Franssen, W., Gerten, D., Gosling, S. N., et al. (2014). Hydrological droughts in the 21st century, hotspots and uncertainties from a global multimodel ensemble experiment. *Proceedings of the National Academy of Sciences*, 111(9):3262–3267.

Ptak, M., Choiński, A., and Kirviel, J. (2016). Long-term water temperature fluctuations in coastal rivers (southern baltic) in poland. *Bulletin of Geography. Physical Geography Series*, 11(1):35–42.

Ptak, M., Sojka, M., Kałuża, T., Choiński, A., and Nowak, B. (2019a). Long-term water temperature trends of the warta river in the years 1960–2009. *Ecohydrology & Hydrobiology*, 19(3):441–451.

Ptak, M., Sojka, M., and Kozłowski, M. (2019b). The increasing of maximum lake water temperature in lowland lakes of central europe: case study of the polish lakeland. In *Annales de Limnologie-International Journal of Limnology*, volume 55, page 6. EDP Sciences.

Quintana-Segui, P., Le Moigne, P., Durand, Y., Martin, E., Habets, F., Baillon, M., Canellas, C., Franchisteguy, L., and Morel, S. (2008). Analysis of near-surface atmospheric variables: Validation of the safran analysis over france. *Journal of applied meteorology and climatology*, 47(1):92–107.

R Core Team (2013). *R: A Language and Environment for Statistical Computing*. R Foundation for Statistical Computing, Vienna, Austria.

Romaní, A. M., Boulêtreau, S., Villanueva, V. D., Garabetian, F., Marxsen, J., Norf, H., Pohlon, E., Weitere, M., et al. (2016). Microbes in aquatic biofilms under the effect of changing climate. *Climate change and microbial ecology: Current research and future trends*, pages 83–96.

Sanchez-Lorenzo, A., Wild, M., Brunetti, M., Guijarro, J. A., Hakuba, M. Z., Calbó, J., Mystakidis, S., and Bartok, B. (2015). Reassessment and update of long-term trends in downward surface shortwave radiation over europe (1939–2012). *Journal of Geophysical Research: Atmospheres*, 120(18):9555–9569.

Santiago, J. M., Muñoz-Mas, R., Solana-Gutiérrez, J., García de Jalón, D., Alonso, C., Martínez-Capel, F., Pórtoles, J., Monjo, R., and Ribalaygua, J. (2017). Waning habitats due to climate change: the effects of changes in streamflow and temperature at the rear edge of the distribution of a cold-water fish. *Hydrology and Earth System Sciences*, 21(8):4073–4101.

Sauquet, E. and Catalogne, C. (2011). Comparison of catchment grouping methods for flow duration curve estimation at ungauged sites in france. *Hydrology and Earth System Sciences*.

Sauquet, E., Krasovskaia, I., and Leblois, E. (2000). Mapping mean monthly runoff pattern using eof analysis. *Hydrology and Earth System Sciences*.

Scheffers, B. R., De Meester, L., Bridge, T. C., Hoffmann, A. A., Pandolfi, J. M., Corlett, R. T., Butchart, S. H., Pearce-Kelly, P., Kovacs, K. M., Dudgeon, D., et al. (2016). The broad footprint of climate change from genes to biomes to people. *Science*, 354(6313).

Schmadel, N. M., Harvey, J. W., Alexander, R. B., Schwarz, G. E., Moore, R. B., Eng, K., Gomez-Velez, J. D., Boyer, E. W., and Scott, D. (2018). Thresholds of lake and reservoir connectivity in river networks control nitrogen removal. *Nature communications*, 9(1):1–10.

Seavy, N. E., Gardali, T., Golet, G. H., Griggs, F. T., Howell, C. A., Kelsey, R., Small, S. L., Viers, J. H., and Weigand, J. F. (2009). Why climate change makes riparian restoration more important than ever: recommendations for practice and research. *Ecological Restoration*, 27(3):330–338.

Seixas, G. B., Beechie, T. J., Fogel, C., and Kiffney, P. M. (2018). Historical and future stream temperature change predicted by a lidar-based assessment of riparian condition and channel width. *JAWRA Journal of the American Water Resources Association*, 54(4):974–991.

Selbig, W. R. (2015). Simulating the effect of climate change on stream temperature in the trout lake watershed, wisconsin. *Science of the Total Environment*, 521:11–18.

Sen, P. K. (1968). Estimates of the regression coefficient based on kendall's tau. *Journal of the American statistical association*, 63(324):1379–1389.

Sinokrot, B., Stefan, H., McCormick, J., and Eaton, J. (1995). Modeling of climate change effects on stream temperatures and fish habitats below dams and near groundwater inputs. *Climatic Change*, 30(2):181–200.

Sinokrot, B. A. and Stefan, H. G. (1993). Stream temperature dynamics: measurements and modeling. *Water resources research*, 29(7):2299–2312.

Skamarock, W. C., Klemp, J. B., Dudhia, J., Gill, D. O., Barker, D. M., Wang, W., and Powers, J. G. (2008). A description of the advanced research wrf version 3. ncar technical note-475+ str.

Smith, K. and Lavis, M. (1975). Environmental influences on the temperature of a small upland stream. *Oikos*, pages 228–236.

Soubeyroux, J.-M. et al. (2020). Les nouvelles projections climatiques de rÉfÉrence drias 2020 pour la mÉtropole. Technical report, METEO FRANCE.

Souchon, Y. and Tissot, L. (2012). Synthesis of thermal tolerances of the common freshwater fish species in large western europe rivers. *Knowledge and Management of Aquatic Ecosystems*, (405):03.

Spinoni, J., Naumann, G., and Vogt, J. V. (2017). Pan-european seasonal trends and recent changes of drought frequency and severity. *Global and Planetary Change*, 148:113–130.

Sridhar, V., Sansone, A. L., LaMarche, J., Dubin, T., and Lettenmaier, D. P. (2004). Prediction of stream temperature in forested watersheds 1. *JAWRA Journal of the American Water Resources Association*, 40(1):197–213.

Steel, E. A., Beechie, T. J., Torgersen, C. E., and Fullerton, A. H. (2017). Envisioning, quantifying, and managing thermal regimes on river networks. *BioScience*, 67(6):506–522.

Steel, E. A. and Lange, I. A. (2007). Using wavelet analysis to detect changes in water temperature regimes at multiple scales: Effects of multi-purpose dams in the willamette river basin. *River Research and Applications*, 23(4):351–359.

Stefan, H. G. and Preud'homme, E. B. (1993). Stream temperature estimation from air temperature 1. *JAWRA Journal of the American Water Resources Association*, 29(1):27–45.

Stefani, F., Schiavon, A., Tirozzi, P., Gomarasca, S., and Marziali, L. (2020). Functional response of fish communities in a multistressed freshwater world. *Science of The Total Environment*, 740:139902.

Stevens, B., Giorgetta, M., Esch, M., Mauritsen, T., Crueger, T., Rast, S., Salzmann, M., Schmidt, H., Bader, J., Block, K., et al. (2013). Atmospheric component of the mpi-m earth system model: Echam6. *Journal of Advances in Modeling Earth Systems*, 5(2):146–172.

Sun, N., Yearsley, J., Voisin, N., and Lettenmaier, D. P. (2015). A spatially distributed model for the assessment of land use impacts on stream temperature in small urban watersheds. *Hydrological Processes*, 29(10):2331–2345.

Taylor, C. A. and Stefan, H. G. (2009). Shallow groundwater temperature response to climate change and urbanization. *Journal of Hydrology*, 375(3-4):601–612.

Thiéry, D. (1988). Forecast of changes in piezometric levels by a lumped hydrological model. *Journal of Hydrology*, 97(1-2):129–148.

Thiéry, D. (2018). Logiciel éros version 7.1. guide d'utilisation. In *Rapport BRGM/RP-67704-FR*.

Thiéry, D. and Moutzopoulos, C. (1995). Un modèle hydrologique spatialisé pour la simulation de très grands bassins: le modèle eros formé de grappes de modèles globaux élémentaires. *VIIIèmes journées hydrologiques de l'ORSTOM" Régionalisation en hydrologie, application au développement", Le Barbé et E. Servat (Eds.)*, pages 285–295.

Tisseuil, C., Vrac, M., Grenouillet, G., Wade, A. J., Gevrey, M., Oberdorff, T., Grodwohl, J.-B., and Lek, S. (2012). Strengthening the link between climate, hydrological and species distribution modeling to assess the impacts of climate change on freshwater biodiversity. *Science of the total environment*, 424:193–201.

Todd, D. K. and Mays, L. W. (2004). *Groundwater hydrology*. John Wiley & Sons.

Tramblay, Y., Koutroulis, A., Samaniego, L., Vicente-Serrano, S. M., Volaire, F., Boone, A., Le Page, M., Llasat, M. C., Albergel, C., Burak, S., Cailleret, M., Cindrić Kalin, K., Davi, H., Dupuy, J.-L., Greve, P., Grillakis, M., Hanich, L., Jarlan, L., Martin-StPaul, N., Martínez-Vilalta, J., Mouillot, F., Pulido-Velazquez, D., Quintana-Seguí, P., Renard, D., Turco, M., Türkeş, M., Trigo, R., Vidal, J.-P., Vilagrosa, A., Zribi, M., and Polcher, J. (2020). Challenges for drought assessment in the mediterranean region under future climate scenarios. *Earth-Science Reviews*, 210:103348.

Uppala, S. M., Kållberg, P., Simmons, A. J., Andrae, U., Bechtold, V. D. C., Fiorino, M., Gibson, J., Haseler, J., Hernandez, A., Kelly, G., et al. (2005). The era-40 re-analysis. *Quarterly Journal of the Royal Meteorological Society: A journal of the atmospheric sciences, applied meteorology and physical oceanography*, 131(612):2961–3012.

Valette, L., Piffady, J., Chandesris, A., and Souchon, Y. (2012). Syrah-ce: description des données et modélisation du risque d'altération hydromorphologique des cours d'eau pour l'état des lieux dce. *Rapport Technique Onema-Irstea*.

Valverde, L., Jugé, P., and Handfus, T. (2013). Résultats granulométriques et localisation des points dures en loire. rapport infosed 2.

van Looy, K. and Tormos, T. (2013). Indicateurs spatialisés du fonctionnement des corridors rivulaires. Technical report, Irstea.

Van Meijgaard, E., Van Ulft, L., Lenderink, G., De Roode, S., Wipfler, E. L., Boers, R., and van Timmermans, R. (2012). *Refinement and application of a regional atmospheric model for climate scenario calculations of Western Europe*. Number KVR 054/12. KVR.

Van Vliet, M., Ludwig, F., Zwolsman, J., Weedon, G., and Kabat, P. (2011). Global river temperatures and sensitivity to atmospheric warming and changes in river flow. *Water Resources Research*, 47(2).

Van Vliet, M., Yearsley, J., Franssen, W., Ludwig, F., Haddeland, I., Lettenmaier, D., and Kabat, P. (2012a). Coupled daily streamflow and water temperature modelling in large river basins. *Hydrology and Earth System Sciences*, 16(11):4303–4321.

van Vliet, M. T., Franssen, W. H., Yearsley, J. R., Ludwig, F., Haddeland, I., Lettenmaier, D. P., and Kabat, P. (2013). Global river discharge and water temperature under climate change. *Global Environmental Change*, 23(2):450–464.

Van Vliet, M. T., Yearsley, J. R., Ludwig, F., Vögele, S., Lettenmaier, D. P., and Kabat, P. (2012b). Vulnerability of us and european electricity supply to climate change. *Nature Climate Change*, 2(9):676–681.

Van Vuuren, D. P., Edmonds, J., Kainuma, M., Riahi, K., Thomson, A., Hibbard, K., Hurtt, G. C., Kram, T., Krey, V., Lamarque, J.-F., et al. (2011). The representative concentration pathways: an overview. *Climatic change*, 109(1):5–31.

Venables, W. and Ripley, B. (2002). Random and mixed effects. In *Modern applied statistics with S*, pages 271–300. Springer.

Verfaillie, D., Déqué, M., Morin, S., and Lafaysse, M. (2017). The method adamont v1. 0 for statistical adjustment of climate projections applicable to energy balance land surface models. *Geoscientific Model Development*, 10(11):4257–4283.

Verneaux, J. et al. (1977). Biotypologie de l'ecosysteme" eau courante". determinisme approche de la structure biotypologique.

Vicente-Serrano, S., Hannaford, J., Murphy, C., Peña Gallardo, M., Lorenzo-Lacruz, J., Domínguez-Castro, F., López Moreno, J. I., Beguería, S., Noguear, I., Harrigan, S., and Vidal, J.-P. (2019). Climate, irrigation, and land-cover change explain streamflow trends in countries bordering the northeast atlantic. *Geophysical Research Letters*, 46(19):10821–10833.

Vidal, J.-P., Martin, E., Franchistéguy, L., Baillon, M., and Soubeyroux, J.-M. (2010). A 50-year high-resolution atmospheric reanalysis over france with the safran system. *International Journal of Climatology*, 30(11):1627–1644.

Voldoire, A., Sanchez-Gomez, E., y Mélia, D. S., Decharme, B., Cassou, C., Sénési, S., Valcke, S., Beau, I., Alias, A., Chevallier, M., et al. (2013). The cnrm-cm5. 1 global climate model: description and basic evaluation. *Climate dynamics*, 40(9):2091–2121.

Vörösmarty, C. J., Meybeck, M., Fekete, B., Sharma, K., Green, P., and Syvitski, J. P. (2003). Anthropogenic sediment retention: major global impact from registered river impoundments. *Global and planetary change*, 39(1-2):169–190.

Wanders, N., van Vliet, M. T., Wada, Y., Bierkens, M. F., and van Beek, L. P. (2019). High-resolution global water temperature modeling. *Water Resources Research*, 55(4):2760–2778.

Ward, J. (1985). Thermal characteristics of running waters. In *Perspectives in southern hemisphere limnology*, pages 31–46. Springer.

Wasson, J.-G., Chandesris, A., Pella, H., and Blanc, L. (2002). Typology and reference conditions for surface water bodies in france: the hydro-ecoregion approach. *TemaNord*, 566:37–41.

Webb, B. (1996). Trends in stream and river temperature. *Hydrological processes*, 10(2):205–226.

Webb, B. and Nobilis, F. (1995). Long term water temperature trends in austrian rivers. *Hydrological Sciences Journal*, 40(1):83–96.

Webb, B. and Walling, D. (1993). Temporal variability in the impact of river regulation on thermal regime and some biological implications. *Freshwater Biology*, 29(1):167–182.

Webb, B. and Walling, D. (1996). Long-term variability in the thermal impact of river impoundment and regulation. *Applied Geography*, 16(3):211–223.

Webb, B. and Walling, D. (1997). Complex summer water temperature behaviour below a uk regulating reservoir. *Regulated Rivers: Research & Management: An International Journal Devoted to River Research and Management*, 13(5):463–477.

Webb, B. and Zhang, Y. (1997). Spatial and seasonal variability in the components of the river heat budget. *Hydrological processes*, 11(1):79–101.

Webb, B. W., Hannah, D. M., Moore, D. R., Brown, L. E., and Nobilis, F. (2008). Recent advances in stream and river temperature research. *Hydrological Processes: An International Journal*, 22(7):902–918.

Wilby, R. and Johnson, M. (2020). Climate variability and implications for keeping rivers cool in england. *Climate Risk Management*, 30:100259.

Wondzell, S. M., Diabat, M., and Haggerty, R. (2019). What matters most: are future stream temperatures more sensitive to changing air temperatures, discharge, or riparian vegetation? *JAWRA Journal of the American Water Resources Association*, 55(1):116–132.

Woodward, G., Perkins, D. M., and Brown, L. E. (2010). Climate change and freshwater ecosystems: impacts across multiple levels of organization. *Philosophical Transactions of the Royal Society B: Biological Sciences*, 365(1549):2093–2106.

Wu, H., Kimball, J. S., Li, H., Huang, M., Leung, L. R., and Adler, R. F. (2012). A new global river network database for macroscale hydrologic modeling. *Water resources research*, 48(9).

Yan, H., Sun, N., Fullerton, A., and Baerwalde, M. (2021). Greater vulnerability of snowmelt-fed river thermal regimes to a warming climate. *Environmental Research Letters*, 16(5):054006.

Yearsley, J. (2012). A grid-based approach for simulating stream temperature. *Water Resources Research*, 48(3).

Yearsley, J. R. (2009). A semi-lagrangian water temperature model for advection-dominated river systems. *Water Resources Research*, 45(12).

Yearsley, J. R., Sun, N., Baptiste, M., and Nijssen, B. (2019). Assessing the impacts of hydrologic and land use alterations on water temperature in the farmington river basin in connecticut. *Hydrology and Earth System Sciences*, 23(11):4491–4508.

Zaidel, P. A., Roy, A. H., Houle, K. M., Lambert, B., Letcher, B. H., Nislow, K. H., and Smith, C. (2020). Impacts of small dams on stream temperature. *Ecological Indicators*, 120:106878.

Zarei, A., Asadi, E., Ebrahimi, A., Jafari, M., Malekian, A., Nasrabadi, H. M., Chemura, A., and Maskell, G. (2020). Prediction of future grassland vegetation cover fluctuation under climate change scenarios. *Ecological Indicators*, 119:106858.

Zhao, F., Zhan, X., Xu, H., Zhu, G., Zou, W., Zhu, M., Kang, L., Guo, Y., Zhao, X., Wang, Z., et al. (2022). New insights into eutrophication management: Importance of temperature and water residence time. *Journal of Environmental Sciences*, 111:229–239.

Zhu, S., Bonacci, O., Oskoruš, D., Hadzima-Nyarko, M., and Wu, S. (2019). Long term variations of river temperature and the influence of air temperature and river discharge: case study of kupa river watershed in croatia. *Journal of Hydrology and Hydromechanics*, 67(4):305–313.

Zobrist, J., Schoenenberger, U., Figura, S., and Hug, S. J. (2018). Long-term trends in swiss rivers sampled continuously over 39 years reflect changes in geochemical processes and pollution. *Environmental Science and Pollution Research*, 25(17):16788–16809.

Appendices

APPENDIX **A**

List of hydrometric stations

A.1 Calibration stations

Table A.1: Hydrometric stations used for calibrating the EROS model. The coordinate system is Lambert 93.

Code	X	Y	Code	X	Y	Code	X	Y
K0030010	782951.5	6414192.53	K2994010	736672.91	6540594.87	L5323010	545858.81	6574379.22
K0100020	772656.16	6421130.17	K3030810	735469.79	6551442.81	L5401810	541026.08	6577325.24
K0114020	782012.53	6425971.35	K3060310	736668.98	6557845.24	L5411810	536388.26	6593688.03
K0120020	772342.34	6433586.37	K3074010	734989.94	6559798.81	L5511910	566061.64	6601927.25
K0214010	777234.49	6435320.18	K3153010	727642.86	6580048.82	L5561910	553958.69	6609399.05
K0253010	771322.79	6440119.92	K3222010	688282.05	6525966.37	L5623010	566129.59	6585376.24
K0260020	771122.62	6441373.46	K3273010	677001.58	6531871.31	L5733020	545749.08	6600837.33
K0274010	775767.88	6440265.03	K3292020	684155.16	6541572.7	L5741910	541210.53	6616557.38
K0323010	764733.08	6463225.53	K3302010	692376.4	6547771.09	L6020710	525254.72	6648032.12
K0333010	769051.99	6456732.82	K3322010	707289.97	6557394.06	L6202030	534042.26	6647476.55
K0433010	793328.79	6452049.75	K3373010	717470.43	6573726.36	L6216920	534804.39	6655744.8
K0454020	804549.45	6458743.05	K3382010	722819.39	6578859.87	L7024030	512558.18	6674243.89
K0513010	769765.95	6475999.17	K3400810	724449.11	6589153.6	L7123001	494104.55	6674771.59
K0550010	787629.76	6466827.68	K3450810	724945.61	6606875.99	L8000010	478654.44	6683523.68
K0567530	806852.21	6467648.28	K3464010	722732.58	6609889.92	L8000020	465026.76	6691030.66
K0614010	798209.5	6492243.69	K3533010	711630.41	6615778.6	L8102120	449468.79	6620233.71
K0624510	792741.2	6486346.52	K3553010	711291.92	6620523.47	L8134020	456571.82	6635375.61
K0643110	788306.28	6488474.34	K3570810	702854.72	6630134.65	L8134030	454221.47	6630380.96
K0663310	818834.02	6504313.2	K3603010	700318.51	6624148.77	L8142110	460974.38	6647372.85
K0690010	795444.71	6505606.35	K3650810	705312.18	6649600.15	L8213010	456845.66	6651016.08
K0700010	794011.24	6516916.61	K4000010	705478.14	6657309.81	L8222110	457351.54	6655168.68
K0704510	800844.99	6509017.36	K4013010	694860.63	6643833.83	L8343010	445025.5	6660677.07
K0733220	767468.69	6511172.29	K4073110	692174.97	6685604.64	L8503010	470917.08	6645472.99
K0744010	775055.52	6517711.39	K4080010	689932.68	6693437.73	L8523010	465646.45	6670831.16
K0753210	777764.72	6516595.07	K4094010	699774.98	6695047.52	L8602110	466404.46	6684947.45
K0773210	789867.36	6514831.69	K4180001	671170.55	6731766.36	L8700010	434438.96	6708084.56
K0813020	777866.55	6526232.8	K4350010	620421.84	6755955.81	L9113020	472674.57	6705504.14
K0910010	783495.88	6548195.42	K4383110	619581.93	6750919.04	L9213010	456751.85	6711149.44
K0943010	803043.67	6543369.82	K4414010	601734.76	6745208.3	M0014110	511124.95	6830559.2
K0974010	791941.72	6540145.1	K4470010	567715.82	6711930.06	M0050620	476191.8	6813716.45
K0983010	786635.94	6542928.86	K4672210	582000.2	6715910.7	M0064310	474030.15	6816704.98
K1063010	789033.35	6561789.47	K4793010	568727.89	6712260.08	M0104010	471084.96	6812816.82
K1173210	780716.65	6584764.08	K4800010	563737.76	6711029.54	M0114910	466609.04	6807989.92
K1180010	775416.87	6598045.25	K4843010	567279.26	6717758.14	M0124010	470175.53	6803608.36
K1211810	805741.33	6668125.12	K4853000	546701.73	6705808.19	M0134010	474407.73	6800822.25
K1243010	807709.22	6658665.57	K4856020	548382.99	6708030.58	M0153010	492525.81	6804453.09
K1251810	800395.36	6656379.63	K4873110	541692.62	6718434.37	M0250610	492076.05	6780273.93
K1273110	795640	6655320.94	K4900030	522757.55	6701739.51	M0301510	519962.6	6821670.61
K1314010	796369.69	6641255.62	K4923030	523091.01	6708333.55	M0361510	537960.4	6804263.49
K1321810	790857.92	6639718.73	K5083010	667880.44	6563896.54	M0365010	538447.41	6803460.97
K1363010	801601.89	6614847.57	K5090910	665099.49	6564156	M0401510	524785.82	6787488.02
K1414010	772221.98	6591042.11	K5143110	644188.08	6567616.83	M0421510	506671.93	6774450.03
K1440010	758704.68	6604553.88	K5210910	669411.79	6579236.14	M0424810	506092.38	6770111.79
K1503010	752595.8	6558819.46	K5220910	669548.89	6588291.52	M0434010	498419.79	6774479.36
K1524010	751666.96	6566505.43	K5333110	692450.33	6600889.29	M0500610	486747.44	6760780.35

Table – continued from previous page

Code	X	Y	Code	X	Y	Code	X	Y
K1533010	749768.8	6569862.16	K5336010	669263.45	6591861.1	M0504510	490897.76	6763220.33
K1533020	748477.97	6574001.65	K5343210	681138.37	6579271.36	M0514010	487154.66	6757938.95
K1563010	751628.12	6600038.56	K5363210	686719.93	6589600.12	M0525210	482025.47	6762082.49
K1713010	748787.77	6662603.36	K5383010	675020.6	6603279.23	M0535010	472687.35	6760559.71
K1753110	751861.52	6638555.88	K5383020	677965.98	6600877.38	M0556030	460428.43	6757116.3
K1764020	749737.8	6646177.95	K5400920	661103.5	6625234.75	M0583020	458486.1	6759214.86
K1773010	743874.58	6639242.04	K5424010	676883.18	6626098.63	M0613010	452888.25	6786541.34
K1775510	741035.94	6646341.56	K5433020	671240.68	6625260.44	M0624010	450428.1	6763632.24
K1810310	741012.7	6619277.05	K5490910	628944.68	6680176.26	M0633010	448822.96	6760568.59
K1833010	732963.62	6631860.24	K5543010	668077.37	6656775.46	M0653110	447343.66	6757373
K1900010	719237.65	6648564.3	K5552300	667365.24	6661087.75	M0680610	446696.74	6749682.71
K1914510	725491.38	6651469.17	K5574100	656041.58	6669124.65	M1021610	579516.95	6789386.02
K1930010	712538.91	6653662.98	K5623010	673373.21	6633957.63	M1024810	580451.65	6796363.89
K1943010	715762.14	6670786.66	K6102420	636675.4	6639122	M1025510	581897.5	6794662.95
K1954010	719177.03	6670488.02	K6192410	626433.44	6673961.09	M1034020	577257.18	6791139
K1963010	715420.36	6662497.85	K6220910	587480.35	6686733.37	M1041610	582396.96	6784692.43
K2064010	768036.92	6403973.02	K6332520	644267.59	6718465.63	M1073010	583350.4	6780367.07
K2070810	770083.71	6399656.73	K6334010	657517.29	6710286.25	M1114011	570170.99	6770401.64
K2090810	758148.9	6415950.36	K6373020	647624.24	6705374.95	M1124810	573547.14	6766372.66
K2134010	759282.77	6403083.65	K6402510	620801.04	6699709.72	M1151610	541989.11	6741998.37
K2143020	756470.79	6407837.48	K6593010	583594.56	6685964.02	M1214010	539428.53	6774705.01
K2163110	750376.37	6410166.94	K6720910	510073.62	6696866.37	M1233040	535834.49	6755628.4
K2173010	758159.03	6415730.36	K6888888	504041.49	6694278.9	M1244010	531409.95	6756250.32
K2210810	750948.31	6430038.27	K7202610	610704.55	6627512.79	M1254010	525400.73	6747168.55
K2223020	749804.25	6422237.32	K7207510	600095.52	6637984.3	M1313010	515673.46	6746916.44
K2223030	749311.88	6424262.58	K7424010	564519.64	6677363.99	M1324010	517754.69	6748807.85
K2233020	750199.11	6430049.61	K7433030	555863.05	6677229.2	M1341610	511637.74	6738259.97
K2240810	747038.82	6436626.23	K7542610	502619.83	6690088.81	M1424410	490523.01	6722732.01
K2254010	743424.21	6430371.73	L0050630	603177.5	6515649.78	M1463020	482667.09	6738625.62
K2283110	741942.66	6441592.78	L0093010	587609.27	6519590.89	M1531610	456567.93	6734782.88
K2300810	738585.41	6446506.65	L0123030	604380.98	6525491.5	M1534510	458785.53	6740138.78
K2316210	734438.48	6449249.22	L0140610	576145.81	6532951	M3014010	453612.63	6820615.89
K2330810	732040.25	6462428.39	L0201510	618636.04	6532588.99	M3020910	452174.43	6825773.09
K2335510	728022.81	6460287.35	L0231510	610747.58	6544738.61	M3040910	447668.6	6828522.79
K2363020	739462.55	6456890.63	L0244510	600487.85	6545634.7	M3060910	434868.21	6822130.27
K2383110	739912.58	6461547.54	L0321510	575843.52	6533490.79	M3103010	430255.32	6838319.86
K2430810	727435.69	6476843.28	L0400610	570147.12	6530328.32	M3133010	428554.3	6828213.29
K2450810	726195.18	6481053.92	L0513010	570349.3	6515621.48	M3213010	418513.95	6822516.47
K2514020	694743.48	6458879.82	L0700610	552429.56	6528656.45	M3223010	428711.63	6813063.8
K2534010	714375.85	6460229.81	L0914010	534207.87	6530397.57	M3230910	430888.44	6804093.78
K2544010	715468.34	6461353.55	L0920610	529943.29	6532328.48	M3230920	434588.61	6811582.43
K2623010	714870.72	6481211.54	L0940610	519849.45	6548569.75	M3253110	431126.77	6802693.75
K2644010	727901.38	6502651.18	L1400610	523453.59	6591969.92	M3313010	408122.91	6806599.73
K2654010	708674.33	6494591.89	L2103020	488108.96	6587342.19	M3340910	421176.35	6774584.46
K2674010	708164.13	6498657.58	L2201610	488630.6	6587674.22	M3403010	441603.26	6789384.4
K2680810	715735.12	6506906.31	L2253010	481675	6596691.33	M3504010	418107.23	6772123.37
K2680820	716477.96	6501759.58	L2313050	491289.01	6596307.13	M3600910	423731.17	6752857.52
K2698210	710133.51	6510984.05	L2321610	491719.94	6596952.98	M3630910	423426.88	6737493.86
K2714010	721763.96	6523835.51	L2334010	495969.1	6609112.42	M3711810	406840.23	6766673.64
K2724220	713392.14	6521811.04	L2341620	496739.53	6611765.37	M3771810	406013.34	6748828.88
K2753010	704428.32	6547200.87	L2404030	491240.93	6612485.33	M3774010	401606.08	6750125.13
K2763110	708494.65	6525024.99	L2501610	503121.22	6625741.29	M3813010	394514.86	6741073.7
K2773120	723923.21	6534263.06	L3100610	512198.52	6637247.61	M3823010	403638.95	6738341.8
K2774020	717395.71	6532278.12	L3123010	511933.5	6637334.43	M3834030	409826.02	6734380.84
K2783010	723969.22	6534304.3	L3200610	514769.47	6645514.6	M3851810	410467.31	6738856.38
K2784510	725208.73	6535865.96	L4110710	624824.04	6558635.88	M3861810	417514.43	6736439.21
K2790810	734729.01	6541118.88	L4210710	616674.31	6569122.11	M3910910	428330.25	6721795.82
K2821910	758348.62	6476155.94	L4523010	593324.14	6587527.46	M4101921	432023.02	6713951.14
K2834010	749296.63	6483211.34	L4530710	593549.12	6595922.69	M4114010	428242.6	6716846.14
K2851910	756980.86	6494073.44	L4653010	595016.65	6619337.52	M5014220	435287.67	6703144.21
K2884010	746234.72	6511569.07	L4710710	569129.59	6616131.21	M5124310	436601	6686179.05
K2944010	742758.8	6517314.35	L5301810	541790.51	6566963.28	M5214020	426482.73	6695431.4
K2981910	737043.05	6532500.7	L5301811	581228.04	6559554.67	M5300010	408857.48	6706221.26

A.2 Hydrometric stations on the Reference Hydrometric Network

Table A.2: Hydrometric stations with long-term continuous daily data located on the Reference Hydrometric Network. The coordinate system is Lambert 93.

Code	X	Y	Code	X	Y	Code	X	Y
K0010010	791375.44	6408562.73	K2871910	747510.65	6510159.49	L2443010	490191.09	6617355.1
K0403010	802401.56	6440678.06	K3264010	674712.2	6530166.07	L4220710	598477.39	6587347.52
K0454010	795337.61	6458003.17	K3374710	715272.82	6571544.75	L4321710	623221.41	6584565.78
K0523010	773565.84	6468033.13	K4443010	599274.27	6739425.6	L4411710	599253.63	6588169.36
K0567520	798002.01	6469025.4	K5183010	655710.56	6565553.43	L5034010	583787.34	6556316.2
K0673310	807203.23	6501839.54	K5200910	664208.83	664208.83	L5101810	578997.01	6558306.51
K1284810	790906.06	6656780.1	K5653010	655005.78	6660896.66	L5134010	556619.25	6562905.24
K1341810	779283.4	6604359.27	K6492510	587732.21	6687266.69	L5223020	546585.47	6562341.84
K1383010	783354.72	6597220.43	K7312610	557740.57	6659092.39	L7000610	513799.08	6664712.54
K1724210	758122.06	6645915.05	K7414010	566649.23	6672109.22	M0243010	492217.25	6788044.53
K2363010	740999.39	6455503.89	K7514010	535046.72	6685285.32	M1213010	537414.42	6770526.61
K2514010	700546.24	6448347.57	L0314010	589894.82	6540597.58	M1354020	510446.79	6725644.89
K2523010	702148.01	6451101.5	L0563010	563206.59	6518987.08	M3323010	419385.98	6791915.44
K2593010	720781.8	6476056.23	L0813010	538441.77	6536959.68	M3423010	423967.87	6776825.99
M3423010	423967.87	6776825.98	M5102010	444579.08	6682426.15	M5222010	425705.89	6696960.64

A.3 Naturalized hydrometric stations

Table A.3: List of hydrometric stations influenced by dams. The time series of these stations are naturalized by French Electricity (EDF).

Code	Location
K0100020	La Loire at Goudet
K0120020	La Loire at Coubon
K0260020	La Loire at Chadrac
K0550010	La Loire at Bas-en-Basset
K0690010	La Loire at Montrond-les-Bains
K0700010	La Loire at Feurs
K0910010	La Loire at Villerest
K1180010	La Loire at Digoin
K1440010	La Loire at Gilly-sur-Loire
K1900010	La Loire at Imphy
K1930010	La Loire at Nevers
K2240810	L'Allier at Prades
K2300810	L'Allier at Langeac
K2330810	L'Allier at Vieille-Brioude
K2430810	L'Allier at Agnat
K2680810	L'Allier at Vic-le-Comte
K2790810	L'Allier at Limons
K3030810	L'Allier at Saint-Yorre
K3400810	L'Allier at Chatel-de-Neuvre
K3450810	L'Allier at Moulins
K3570810	L'Allier at Livry
K3650810	L'Allier at Cuffy
K4000010	La Loire at Cours-les-Barres
K4080010	La Loire at Saint-Satur
K4180010	La Loire at Gien

APPENDIX B

List of stream temperature stations

B.1 330 Tw stations used for identifying the influence of dams and pond in chapter 3

Table B.1: 330 Tw stations used for identifying the influence of dams and pond in chapter 3 and their corresponding cluster (see section 3.8, p. 62).

Code	X	Y	Cluster	Code	X	Y	Cluster
4033300	705720.51	6546511.87	1.dam-like	4110700	513471.06	6839787.44	3.natural-like
Allier–LeVigan	764853.23	6408536.13	1.dam-like	4113050	462449.51	6801814.76	3.natural-like
Arbiche–Pont–de–la–Roue	808819.29	6500577.25	1.dam-like	4115580	539815.59	6811654.7	3.natural-like
Arnon–2	649712.98	6602886.75	1.dam-like	4115675	542431.46	6813629.81	3.natural-like
Brugere–aval	740221.22	6508901.85	1.dam-like	4119220	467550.61	6773677.77	3.natural-like
Credogne–Chez–Cottard	738262.27	6538935.58	1.dam-like	4119750	449760.49	6781304.86	3.natural-like
Credogne–la–Poncette	744224.98	6539192.33	1.dam-like	4124985	431549.11	6802740.45	3.natural-like
Credogne–Le–Bessière	750678.68	6536423.25	1.dam-like	4125500	407481	6810460.44	3.natural-like
Furan–Jardins–du–Bernay	810155.53	6480042.68	1.dam-like	Aigre–Romilly	573328.31	6766316.68	3.natural-like
Gand–Amont–confl–Rhins	787770.37	6542061.42	1.dam-like	Aix–Les–Sigauds	787745.17	6526749.95	3.natural-like
K2080820	765703.68	6406653.53	1.dam-like	Ance–Pontempeyrat	770634.03	6472338.5	3.natural-like
K2753010	704416.33	6547181.78	1.dam-like	AnceNord–Moulas	778715.16	6463049.91	3.natural-like
K3222010	688258.38	6525974.84	1.dam-like	ANDELOT–a–Brout–Vernet	722527.23	6566502.77	3.natural-like
K3302010	692395.48	6547777.84	1.dam-like	Andrable–Cacharat	778486.46	6473447.73	3.natural-like
Lignon–Versilhac	792592.37	6452113.66	1.dam-like	Andrable–Jamillard	776741.26	6485606.63	3.natural-like
Monne–Pont–de–la–Monne	708383.07	6507477.43	1.dam-like	Anzon–La–Rivalsupt	759531.05	6522835.44	3.natural-like
Morge–Montcel	705912.94	6546415.47	1.dam-like	Anzon–Memos	768923.3	6523301.84	3.natural-like
Renaison–Avalbarrage	767589.28	6549879.12	1.dam-like	Ardillère–amont	505244.86	6719130.93	3.natural-like
Renaison–Les–Berands	774457.7	6549404.76	1.dam-like	Ardillère–aval	499138.31	6723525.85	3.natural-like
Semene–Les–Plats	810038.81	6471193.1	1.dam-like	Arnon–1	648499.64	6598505.2	3.natural-like
Sioule–Chateauneuf	692297.36	6547681.35	1.dam-like	Arnon–3	651824.73	6613147.41	3.natural-like
4015050	797039.92	6570610.36	2.pond-like	Arnon–4	647937.51	6622504.9	3.natural-like
4017000	791142.7	6645947.97	2.pond-like	ARNON–a–Viplaix	650085.13	6596289.72	3.natural-like
4017250	801851.19	6638870.5	2.pond-like	Arzon–Coutarel	767766.31	6458264.6	3.natural-like
4023000	752029.15	6600455.09	2.pond-like	Auron–4	665939.15	6646369.65	3.natural-like
4023130	767377.35	6624305.71	2.pond-like	Auze–Torsiac	715908.23	6472910.58	3.natural-like
4023450	778429.98	6633673.96	2.pond-like	Auzon–Bourg	729201.73	6477124.42	3.natural-like
4023680	749654.87	6646136.86	2.pond-like	Auzon–Chanonat	702751.48	6511567.46	3.natural-like
4023700	743907.11	6639148.1	2.pond-like	Barangeon–1	642142.48	6685751.33	3.natural-like
4025100	716009.55	6657911.1	2.pond-like	BARBENAN–aval–a–Arfeuilles	756260.64	6562357.03	3.natural-like
4027210	758933.59	6400303.82	2.pond-like	BESBRE–a–St–Clement	754226.59	6552246.37	3.natural-like
4028450	692889.56	6464672.26	2.pond-like	BESBRE–a–St–Prix	749864.47	6570286.9	3.natural-like
4028500	701134.87	6449170.66	2.pond-like	Bonson–Chavas	793695.14	6487832.39	3.natural-like
4036300	758324.79	6476175.7	2.pond-like	Bonson–Fournier	785171	6478216.56	3.natural-like
4037900	749010.77	6508578.66	2.pond-like	Bonson–Les Littes	797017.88	6492669.21	3.natural-like
4051125	628780.58	6746274.75	2.pond-like	Bonsonnet–Fougerols	783455.54	6483100.17	3.natural-like
4062000	675012.72	6603312.99	2.pond-like	Borne–StVidal	762537	6442387.4	3.natural-like
4082740	476016.11	6599895.3	2.pond-like	BOUBLE–amont–a–Echassieres	694063.88	6568458.1	3.natural-like
4086320	510349.21	6638271.95	2.pond-like	Céroux–MoulinPoudrière	725206.8	6458361.57	3.natural-like
4088000	616737.01	6569477.08	2.pond-like	Charlet–Authezat	714746.52	6505371.55	3.natural-like

Table – continued from previous page

Code	X	Y	Cluster	Code	X	Y	Cluster
4091250	595800.36	6621533.91	2.pond-like	choisille–beaumont–amont	524869.9	6720603.73	3.natural-like
4093500	571631.18	6558876.63	2.pond-like	choisille–beaumont–aval	526047.55	6714216.33	3.natural-like
4094200	562498.33	6547415.4	2.pond-like	choisille–chenusson–amont	528909.89	6719752.85	3.natural-like
4096430	553949.24	6609409.42	2.pond-like	choisille–sembançay–amont	518181.81	6713665.11	3.natural-like
4099960	457550.74	6651854.93	2.pond-like	choisille–sembançay–aval	522228.28	6706594.77	3.natural-like
4104200	455563.92	6710920.78	2.pond-like	Coise–Moulin–Trunel	811669.85	6503644.36	3.natural-like
4105800	578908.83	6780129.73	2.pond-like	Coise–Pont–des–Romains	803471.68	6499487.82	3.natural-like
4106000	572674.59	6775523.16	2.pond-like	Cotatay–Pre–Farost	811005.95	6474769.13	3.natural-like
4111000	486696.56	6818875.16	2.pond-like	Couze–Ardes–Riviere–l–eveque	712688.7	6479404.68	3.natural-like
4114500	493921.16	6790698.11	2.pond-like	Couze–Pavin–no–kill	694641.65	6490518.83	3.natural-like
4116800	527295.91	6794532.15	2.pond-like	Couze–Pavin–Parc	690684.41	6489026.71	3.natural-like
4123750	434920.95	6822095.59	2.pond-like	Couze–Pavin–St–Pierre–Colamine	695764.43	6491244.39	3.natural-like
4123800	430911.06	6820578.81	2.pond-like	Couze–Pavin–Tete-de–Lion	706758.97	6494148.96	3.natural-like
4130500	406878.04	6766726.35	2.pond-like	Couze–Pavin–Villetour	689415.91	6488324.31	3.natural-like
Alagnon–Auzat	723317.47	6482523.93	2.pond-like	Couzon–Aubusson	746288.14	6515630.34	3.natural-like
Allagnon–Babory	714547.05	6467878.59	2.pond-like	Couzon–Cote–ratier	813440.51	6500195.76	3.natural-like
Allagnon–Chambezon	719441.74	6474799.73	2.pond-like	Credogne–sources	751193.48	6536335.72	3.natural-like
Allier–Vabres	753189.97	6422534.35	2.pond-like	Credogne–STEP	736483.95	6540656.66	3.natural-like
AnceNord–LeRodier	771947.89	6468219.95	2.pond-like	Curraize–Le–Garet–de–la–Cote	782072.47	6494147.13	3.natural-like
AnceNord–LeTheil	782558.73	6464187.98	2.pond-like	Curraize–Les–Jaquets	791378.88	6498627.34	3.natural-like
Arquejols–LaPinède	764721.93	6410376.88	2.pond-like	deme–aval	523303.77	6730564.65	3.natural-like
Arzon–Beaune	764230.44	6464397.13	2.pond-like	Dore–Masselebre	757204.55	6485129.94	3.natural-like
AUMANCE–a–Meaulne	671654.72	6607690.13	2.pond-like	Dore–Procureur	754171.61	6476163.71	3.natural-like
Champdieu–Le–Moulin–Chandy	771500.09	6475259.4	2.pond-like	Dunière–Vaubarlet	795613.41	6458298.94	3.natural-like
CHER–a–Lavault–Ste–Anne	669027.46	6578948.39	2.pond-like	Egrenne 764 2012-2018	424525.35	6849863.25	3.natural-like
choisille–sembançay–median	519312.81	6713241.37	2.pond-like	Egvonne–Patte–de–mouton	566989.12	6766920.57	3.natural-like
Conie–amont	588431.74	6780008.18	2.pond-like	escotais–amont	516644.79	6720758.13	3.natural-like
Couzon–Pont–Du–Megain	744774.98	6515958.07	2.pond-like	escotais–aval	510977.94	6727511.62	3.natural-like
Dore–Brugeailles	757496.4	6489132.04	2.pond-like	Fouragettes–Goudet	772290.96	6421570.79	3.natural-like
Dore–Chauttes	756094.81	6501539.33	2.pond-like	Foussarde–Vieuvicq	566559.92	6796490.94	3.natural-like
E5831–TE1–H1	596822.08	6737144.45	2.pond-like	Gampille–Chazeau	799835.63	6475606.15	3.natural-like
Furan–Amont–confl–Loire	797573.19	6492480.13	2.pond-like	Gand–Bois–Corcy	802599.49	6530001.02	3.natural-like
Furan–La–Porchere	804807.56	6487872.66	2.pond-like	Gand–Chez–Chabout	802902.07	6529393.71	3.natural-like
Furan–Le–Pont–Blanc	801046.4	6490517.42	2.pond-like	Gand–Le–Rey	801959.72	6530198.3	3.natural-like
Grande–Sauldre–2	659889.94	6717369.05	2.pond-like	Gazeille–LaBesseyre	781979.77	6425986.65	3.natural-like
Grande–Sauldre–3	647641.57	6718565.73	2.pond-like	Grande–Sauldre–1	677562.27	6691235.82	3.natural-like
Guette	646023.14	6691583.55	2.pond-like	GRAVERON–a–Sorbier	748887.9	6585186.47	3.natural-like
K0100020	772781.2	6421537.19	2.pond-like	Huisne–amont	539403.19	6807209.88	3.natural-like
K0403030	797861.36	6433169.49	2.pond-like	Huisne–aval–au–dessus–du–vannage	537854.58	6804024.84	3.natural-like
K2070810	767908.95	6404314.24	2.pond-like	Huisne–aval–confluence–Ronne	537806.59	6803925.3	3.natural-like
K2123010	755239.77	6397009.31	2.pond-like	Huisne–aval–Le–Radray	535170.56	6802570.9	3.natural-like
K2134010	759802.76	6403075.84	2.pond-like	Ionne–4	670035.76	6705583.79	3.natural-like
K2514020	694739.24	6458900.83	2.pond-like	Jarnossin–Marpin	792775.66	6555226.46	3.natural-like
K2593010	720761	6476047.35	2.pond-like	Jarnossin–Rajasse	785566.65	6559374.2	3.natural-like
K2674040	694559.37	6496837.4	2.pond-like	Joyeuse	646226.62	6598539.74	3.natural-like
K2851910	756989.54	6494064.86	2.pond-like	K2316210	734412.72	6449213.87	3.natural-like
K3030810	735498.32	6551455.77	2.pond-like	K2335510	728014.8	6460293.98	3.natural-like
Lignon–Bathelane	800862.36	6447517.08	2.pond-like	K2363020	739481.26	6456900.29	3.natural-like
Lignon–LesBuffets	797834.78	6434182.77	2.pond-like	K2365510	739522.27	6455843.93	3.natural-like
Lignon–Vendets	792164.91	6458806.64	2.pond-like	K2383110	739886.87	6461522.71	3.natural-like
Loir–median–Station–St–Maur	582338.66	6784617.22	2.pond-like	K2523010	702130.96	6451091.3	3.natural-like
Loir–moyen–Alluyes	579775.2	6792287.22	2.pond-like	K2623010	714851.05	6481233.59	3.natural-like
Loire–LeBrignon	771524.19	6425471.83	2.pond-like	K2630310	722888.46	6492841.21	3.natural-like
Loire–Salettes	776280.42	6418129.96	2.pond-like	K2644010	727902.37	6502636.2	3.natural-like
Loire–Vallet	779078.47	6417128.45	2.pond-like	K2654010	708659.24	6494582.52	3.natural-like
M0583020	458443.7	6759212.92	2.pond-like	K2674010	708162.46	6498633.14	3.natural-like
M3060910	434920.97	6822096.98	2.pond-like	K2674030	692875.91	6496678.74	3.natural-like
M3423010	423929.43	6776858.87	2.pond-like	K2698210	710185.63	6511025.36	3.natural-like
M5222210	425703.6	6696977.04	2.pond-like	K2714010	721738.22	6523821.57	3.natural-like
OEIL–a–Malicorne	681171.1	6579915.07	2.pond-like	K2724210	710982.96	6519098.12	3.natural-like
Ondaine–Le–Pertuiset	797741.38	6479758.63	2.pond-like	K2773120	722677.81	6533379.85	3.natural-like
Onzon–Le–Moulin–Picon	808445.06	6487841.7	2.pond-like	K2774010	697993.68	6533409.89	3.natural-like
Oudon–Sonde–1	404507.89	6751213.19	2.pond-like	K2884010	746240.44	6511549.54	3.natural-like
Oudon–Sonde–2	404203.01	6751407.96	2.pond-like	K2994010	736684.07	6540613.75	3.natural-like
Oudon–Sonde–3	403608.02	6751417.36	2.pond-like	K3053100	749980.34	6547336.55	3.natural-like
Oudon–Sonde–4	403315.45	6751976.88	2.pond-like	K3060310	736638.83	6557852.94	3.natural-like
Ozanne–Trizay	577245.44	6791130.91	2.pond-like	K3074010	734972.03	6559803.15	3.natural-like
Petite–sauldre–2	653436.25	6703338.83	2.pond-like	K3153010	726089.87	6574665.81	3.natural-like
Rhins–Ile–Berthier	785784.86	6550478.17	2.pond-like	K3264010	674697.42	6530180.8	3.natural-like
Senouire–Domeyrat	739268.76	6461303.54	2.pond-like	K3374710	715272.17	6571519.72	3.natural-like
Seuge–Longeval	742502.52	6426291.87	2.pond-like	K3464010	722189.87	6608779.21	3.natural-like
Sinaise	638665.02	6622644.25	2.pond-like	K7022620	621819.43	6611663.7	3.natural-like
Suissesse–Adiac	775346.95	6447431.5	2.pond-like	Laussonne–LaTerrasse	775485.13	6430874.64	3.natural-like
Thironne–montigny	562381.81	6800173.31	2.pond-like	Lignon–Alpomb	778598.21	6515471.39	3.natural-like
Vernon–1	662338.38	6689913.09	2.pond-like	Lignon–Amont–pt–Neuf	769826.03	6509777.54	3.natural-like

Table – continued from previous page

Code	X	Y	Cluster	Code	X	Y	Cluster
Virlange–LaBrugère	742239.76	6422164.81	2.pond-like	Lignon–Le–Sagnat	764366.56	6514393.27	3.natural-like
Yerre–moyen–Arrou	559850.17	6778032.48	2.pond-like	Loir–amont–Illiers–Combray	569466.08	6801913.12	3.natural-like
4003645	769715.89	6475994.58	3.natural-like	Loise–La–Vieille–Cure	803799.46	6518110.1	3.natural-like
4003900	787335.09	6465763.17	3.natural-like	Loise–Mayoliere	797237.85	6517215.29	3.natural-like
4009050	818827.2	6504302.71	3.natural-like	long–amont	521637.59	6720802.99	3.natural-like
4021250	768551.46	6582925.45	3.natural-like	long–aval	514399.15	6730530.6	3.natural-like
4022210	750110.42	6567622.41	3.natural-like	M0613010	452902.68	6786526.66	3.natural-like
4024060	742853.03	6601451.83	3.natural-like	M1313010	515645.14	6746930.17	3.natural-like
4029700	700821.64	6492596.86	3.natural-like	M1463010	489334.84	6741419.85	3.natural-like
4034650	723225.85	6533704.96	3.natural-like	M3313010	408492.24	6804335.56	3.natural-like
4040150	750076.45	6547335.74	3.natural-like	Magnore–RD535	774902.86	6434985.64	3.natural-like
4040355	737980.7	6559209.67	3.natural-like	Mare–Aval–double	794690.71	6502945.34	3.natural-like
4041700	685177.11	6531178.62	3.natural-like	Mare–Le–Moulin	775439.77	6493299.75	3.natural-like
4041760	671971.84	6531570.21	3.natural-like	Mare–Molley	783867	6490448.55	3.natural-like
4042100	717421.83	6573732.71	3.natural-like	Mazure–Combres	558890.61	6801833.14	3.natural-like
4043800	716195.96	6604025.33	3.natural-like	Méjeanne–Montbel	774379.89	6413400.6	3.natural-like
4044400	700335.81	6622069.6	3.natural-like	Monne–Chabannes	701201.46	6503038.04	3.natural-like
4046960	699738.19	6695043.78	3.natural-like	Morge–Manzat	692382.27	6538253.19	3.natural-like
4048550	672642.83	6718155.67	3.natural-like	Ondaine–Chambon–Feugerolles	803445.29	6478445.16	3.natural-like
4049625	649245.79	6740290.73	3.natural-like	Onzon–Bramefain	811549.56	6487290.82	3.natural-like
4051650	608980.02	6746970.07	3.natural-like	Ouatier	665579.87	6669602.31	3.natural-like
4060900	686607.74	6599111.86	3.natural-like	Portefeuille–1	645388.45	6620117.93	3.natural-like
4061400	686432.76	6591216.48	3.natural-like	Rau–Charlottier–Amont	748495.81	6506760.64	3.natural-like
4066500	657055.09	6660039.87	3.natural-like	Renaison–Roanne	782821.3	6548457.94	3.natural-like
4068550	647604.68	6705375.59	3.natural-like	Rhins–Gai–sejour	799801.88	6545039.97	3.natural-like
4070211	599934.81	6680759.42	3.natural-like	rorthe–aval	520456.47	6734067.1	3.natural-like
4070215	582832.08	6657534.84	3.natural-like	Salereine–1	678132	6702991.42	3.natural-like
4072150	499262.06	6695992.46	3.natural-like	SARMON–a–Brugheas	728599.9	6552859.57	3.natural-like
4075700	628112.91	6510868.98	3.natural-like	Semene–Croquet	807438.4	6468339.39	3.natural-like
4076000	578911.93	6530471.28	3.natural-like	Semene–Le–Mas	812546.33	6472340.79	3.natural-like
4076100	624889.34	6522762.4	3.natural-like	Semene–Le–Sapt	811414.85	6471456.15	3.natural-like
4079750	554680.26	6520904.5	3.natural-like	Semène–PontSalomon	797747.22	6470868.83	3.natural-like
4080830	548462.97	6538387.01	3.natural-like	Semène–Vial	801965.11	6464794.32	3.natural-like
4080950	536025.59	6529242.83	3.natural-like	Senouire–Mazerat	743821.78	6454021.64	3.natural-like
4082375	524610.48	6585432.09	3.natural-like	Sianne–Ferrière	713354.23	6467476.7	3.natural-like
4082550	489936.27	6584120.9	3.natural-like	SICHON–a–Arronnes	743844.85	6551166.62	3.natural-like
4082930	493477.1	6611191.93	3.natural-like	SICHON–a–Lavoine	753791.63	6542914.22	3.natural-like
4086060	524079.4	6624818.57	3.natural-like	St–Suzanne–Ferchaux	554815.66	6789239.01	3.natural-like
4093800	556575.39	6562898.73	3.natural-like	Sumène–Eynac	780683.73	6438067.66	3.natural-like
4095190	545886.04	6574265.1	3.natural-like	Teyssonne–Aval–Saint–Forgeux	772934.78	6558914.58	3.natural-like
4096360	555218.49	6593584.66	3.natural-like	Teyssonne–Montely	783201.98	6564589.88	3.natural-like
4097050	532298.28	6662471.02	3.natural-like	Teyssonne–Pt–du–Moulin–Pinay	765698.34	6559413.54	3.natural-like
4099400	458246.01	6634869.56	3.natural-like	Trambouze–La–Tombee	796161.92	6545177.28	3.natural-like
4101400	439304.37	6656651.58	3.natural-like	Valcherie–Bois–de–la–Montat	804888.18	6476441.36	3.natural-like
4105680	560905.88	6791165.29	3.natural-like	Veyre–Pontavat	694264.35	6504535.02	3.natural-like
4108050	547228.15	6747565.35	3.natural-like	Vizezy–Bullieu	786148.4	6505085.3	3.natural-like
4108290	530437.48	6772101.34	3.natural-like	Vizezy–La–Guillanche	779427.13	6501776.3	3.natural-like
4108425	522514.35	6758807.33	3.natural-like	Vizezy–Vizezy	789749.18	6514600.24	3.natural-like
4108440	529290.63	6744809.07	3.natural-like	Yerre–amont	548898.86	6782924.3	3.natural-like
4108736	489343.68	6741419.78	3.natural-like	Yerre–aval	570066.31	6771675.47	3.natural-like

B.2 67 stations with continuous daily Tw over the 2010–2014 period

Table B.2: 67 stations with continuous daily Tw over the 2010–2014 period. Only 53 stations are presented here. The rest of the stations with the long-term time series are presented in Table 2.1.

Code	X	Y	Code	X	Y	Code	X	Y
4021250	768551.46	6582925.45	4108425	522514.35	6758807.33	K3264010	674697.42	6530180.8
4022210	750110.42	6567622.41	4110700	513471.06	6839787.44	K3374710	715272.17	6571519.72
4024060	742853.03	6601451.83	Ance–Pontempeyrat	770634.03	6472338.5	Lignon–Amont–pt–Neuf	769826.03	6509777.54
4040150	750076.45	6547335.74	Andrable–Cacharat	778486.46	6473447.73	Lignon–Le–Sagnat	764366.56	6514393.27
4042100	717421.83	6573732.71	Andrable–Jamillard	776741.26	6485606.63	Loir–amont–Illiers–Combray	569466.08	6801913.12
4043100	723856.48	6582328.33	Anzon–La–Rivalsupt	759531.05	6522835.44	Loise–La–Vieille–Cure	803799.46	6518110.1
4043800	716195.96	6604025.33	Anzon–Memos	768923.3	6523301.84	Loise–Mayoliere	797237.85	6517215.29
4044400	700335.81	6622069.6	Bonson–Fournier	785171	6478216.56	4046800	690032.61	6693063.16
Coise–Moulin–Trunel	811669.85	6503644.36	4048550	672642.83	6718155.67	Cotatay–Pre–Farost	811005.95	6474769.13
Mare–Aval–double	794690.71	6502945.34	4049625	649245.79	6740290.73	Couzon–Cote–ratier	813440.51	6500195.76
Mare–Le–Moulin	775439.77	6493299.75	4060500	670482.64	6603987.08	Curraize–Les–Jaquets	791378.88	6498627.34
Mare–Molley	783867	6490448.55	4060900	686607.74	6599111.86	Jarnossin–Marpin	792775.66	6555226.46
Semene–Croquet	807438.4	6468339.39	4061400	686432.76	6591216.48	Jarnossin–Rajasse	785566.65	6559374.2
Semene–Le–Mas	812546.33	6472340.79	4065000	635690.14	6674511.28	K2365510	739522.27	6455843.93
St–Suzanne–Ferchaux	554815.66	6789239.01	4075700	628112.91	6510868.98	K2383110	739886.87	6461522.71
Trambouze–La–Tombee	796161.92	6545177.28	4082550	489936.27	6584120.9	Valcherie–Bois–de–la–Montat	804888.18	6476441.36
4086060	524079.4	6624818.57	Vizezy–Bullieu	786148.4	6505085.3	4091400	576556.7	6616444.39
Vizezy–Vizezy	789749.18	6514600.24	Yerre–amont	548898.86	6782924.30			

APPENDIX C

Annual regime of simulated and observed stream temperature at 67 stations with continuous daily data.

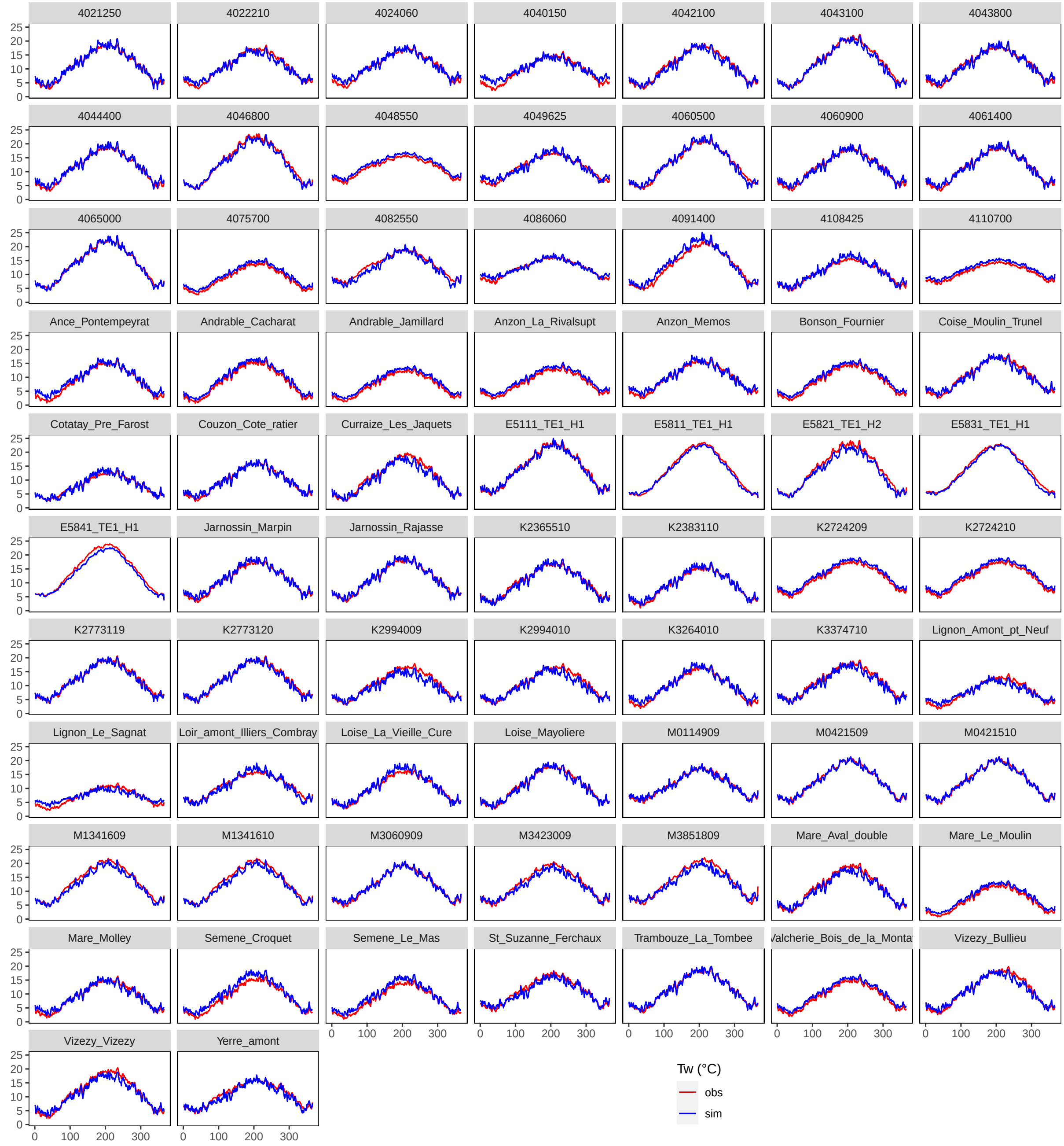

Figure C.1: The annual regime of simulated and observed Tw at 67 stations with continuous daily data over the 2010-214 period.

APPENDIX D

Map of summer stream temperature over the 1963–2019 period

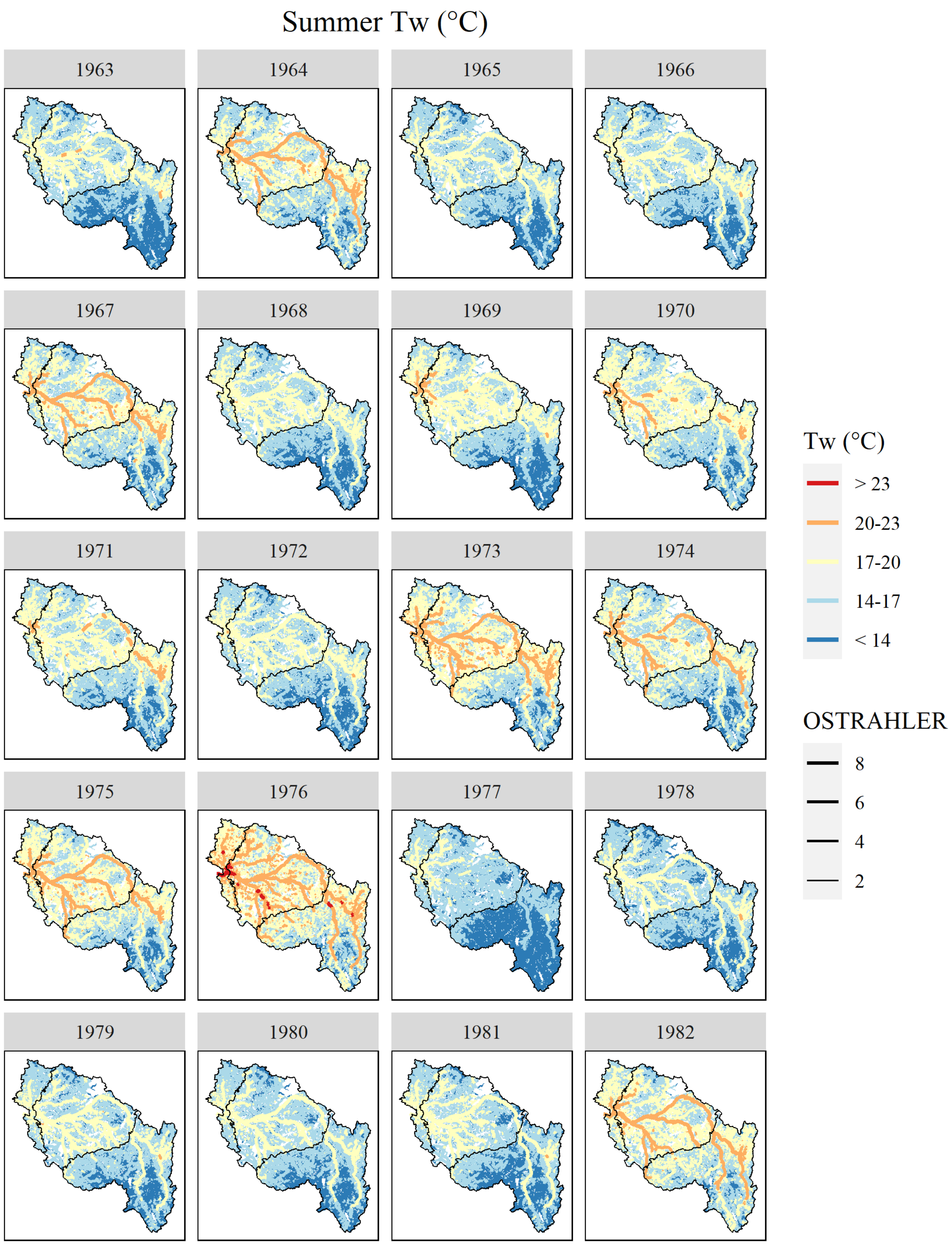
Summer Tw (°C)
1963
1964
1965
1966
1967
1968
1969
1970
1971
1972
1973
1974
1975
1976
1977
1978
1979
1980
1981
1982
Tw (°C)
> 23
20-23
17-20
14-17
< 14
OSTRAHLER
8
6
4
2

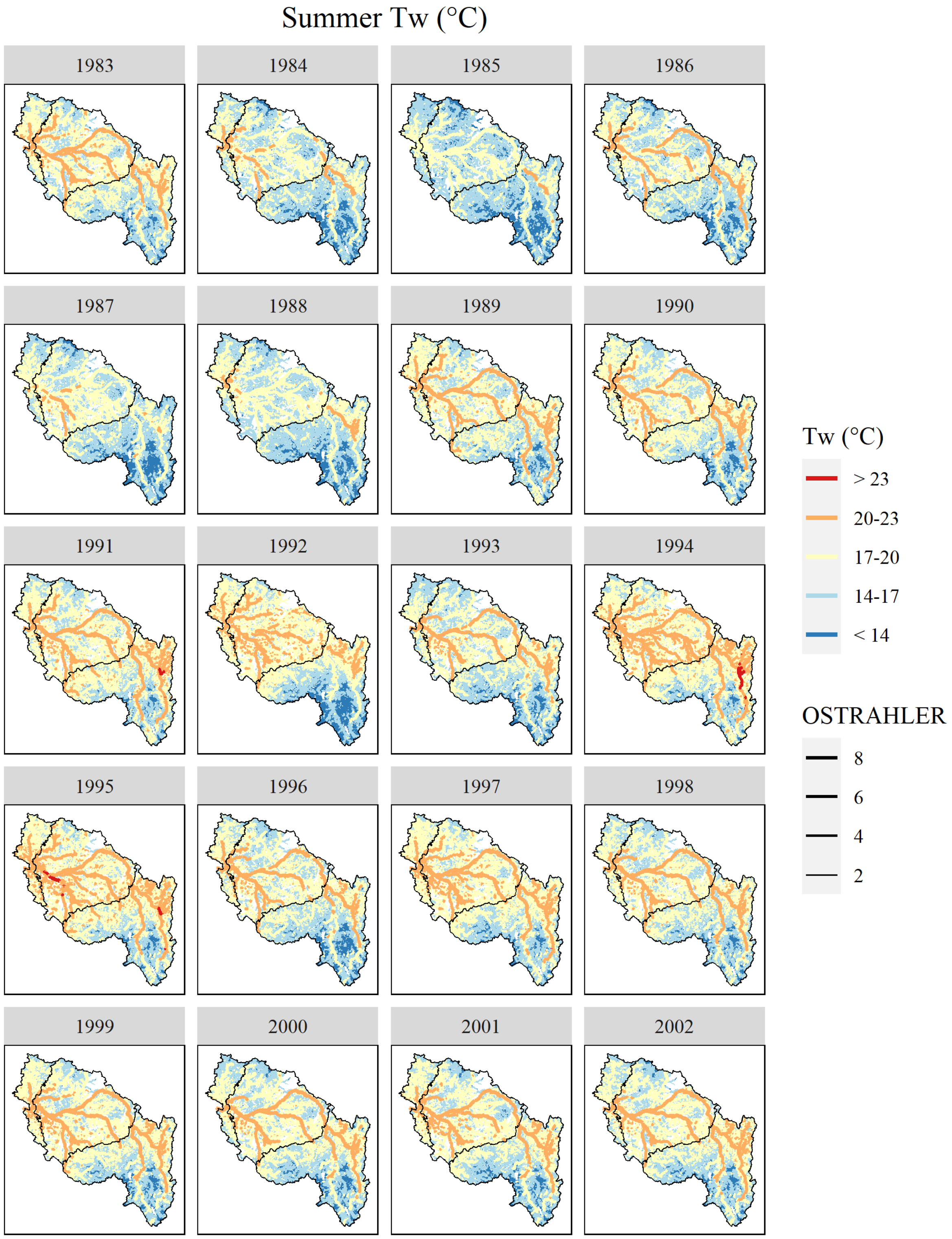
Summer Tw (°C)
1983
1984
1985
1986
1987
1988
1989
1990
1991
1992
1993
1994
1995
1996
1997
1998
1999
2000
2001
2002
Tw (°C)
> 23
20-23
17-20
14-17
< 14
OSTRAHLER
8
6
4
2

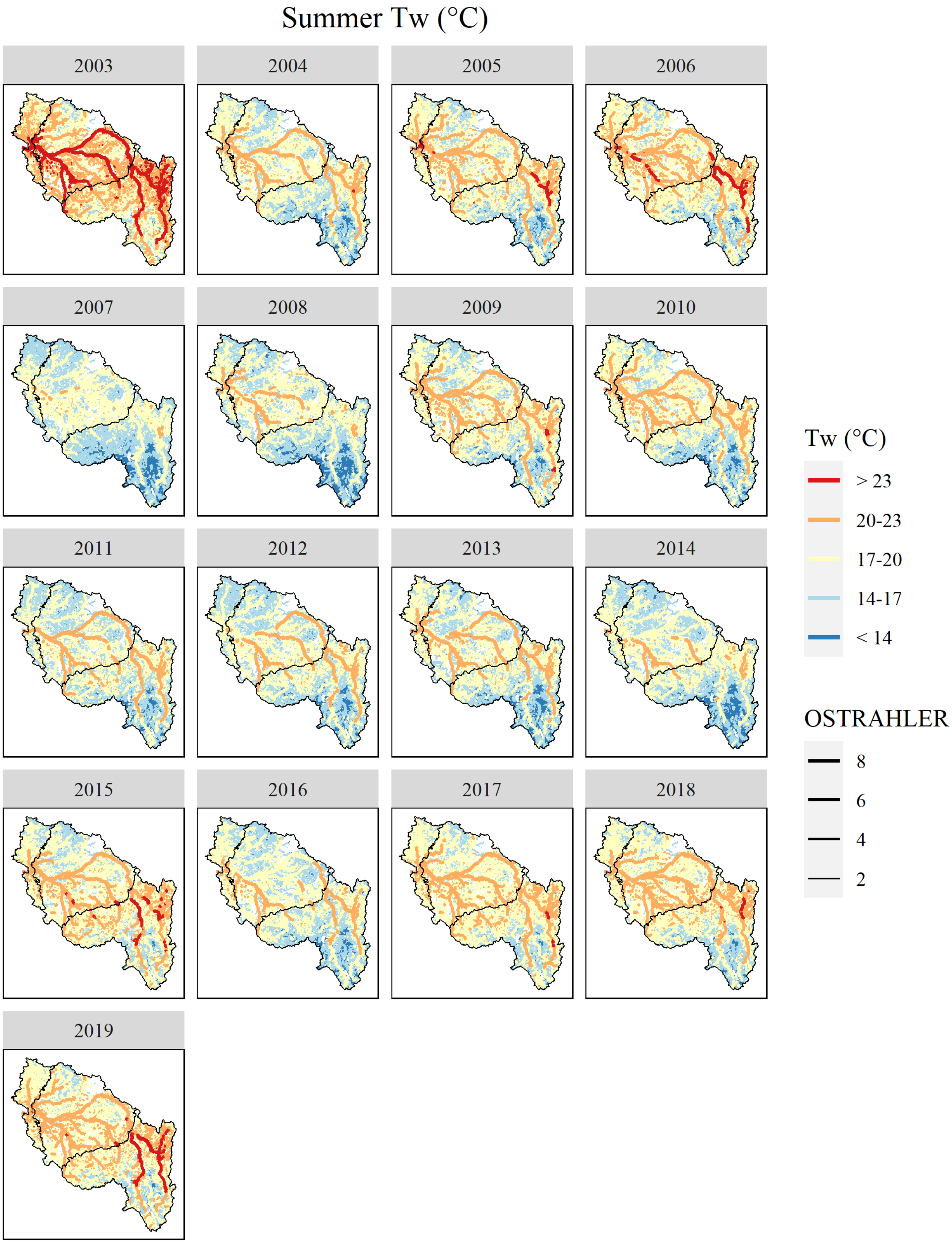
Summer Tw (°C)
2003
2004
2005
2006
2007
2008
2009
2010
2011
2012
2013
2014
2015
2016
2017
2018
2019
Tw (°C)
> 23
20-23
17-20
14-17
< 14
OSTRAHLER
8
6
4
2

Figure D.1: Frequency of Tw intervals shown in spatial maps of Appendix D for different decades over the 1963–2019 period.

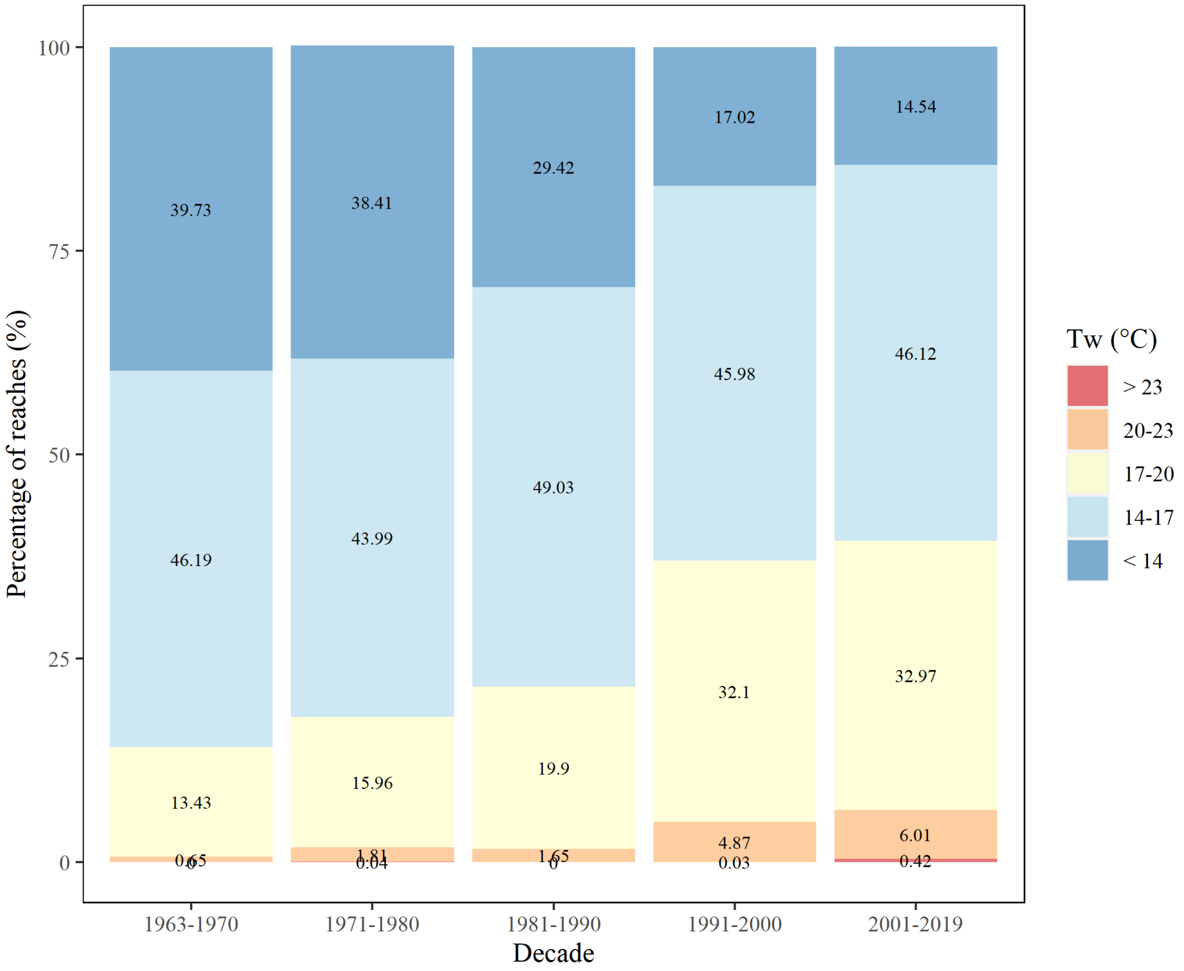

APPENDIX E

Future climate projections

E.1 Changes in precipitation and air temperature under varied climate models

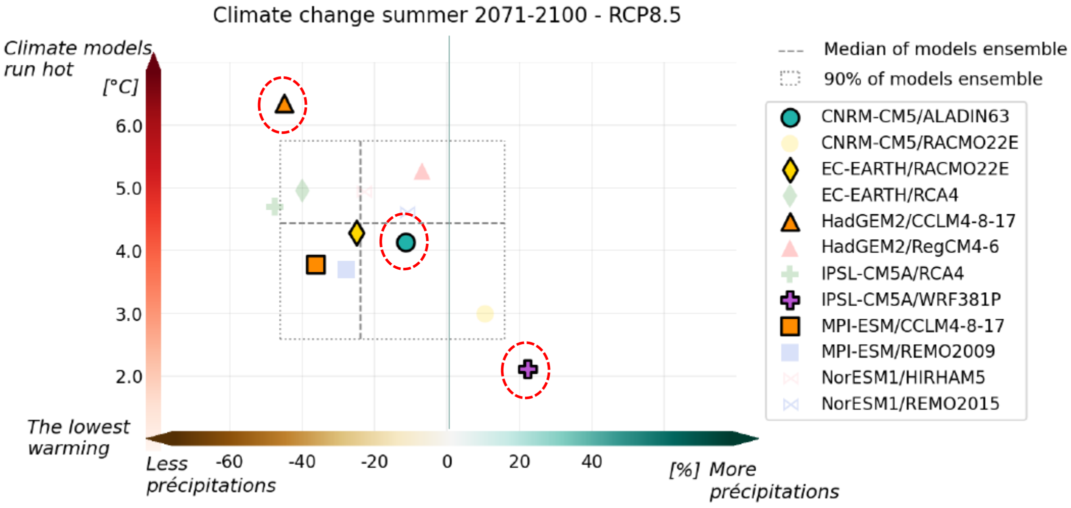

Figure E.1: Summer changes in P (x-axis) and Ta (y-axis) over France at the end of the century (2071-2100) with respect to the 1976-2005 period (historical period) under RCP 8.5. The sharp points are the "short list" of future climate models proposed by Météo-France. The red dashed circles show the selected GCM/RCMs in the current study. This figure is adopted from DRIAS-2020 (Soubeyroux et al. (2020); see http://www.drias-climat.fr/).

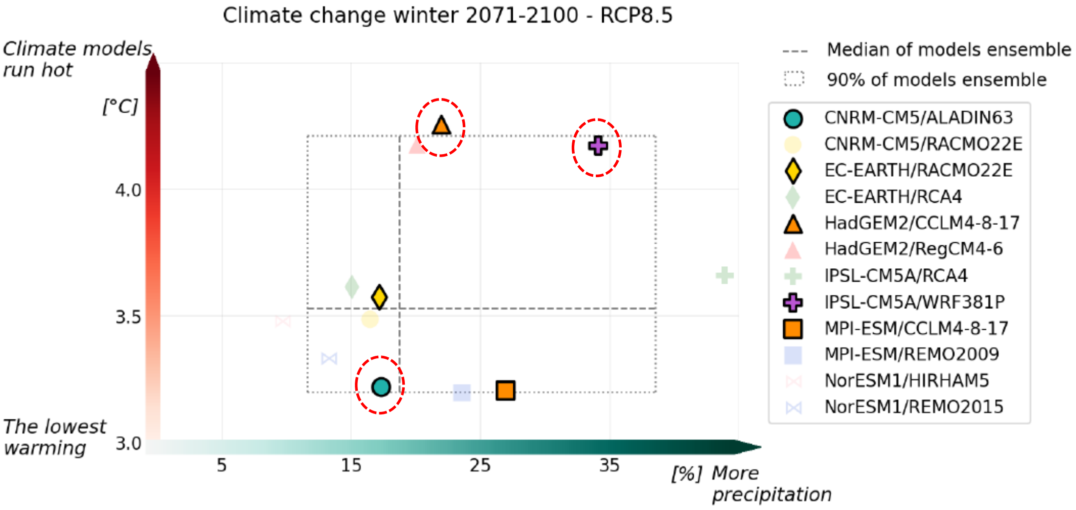

Figure E.2: Winter changes in P (x-axis) and Ta (y-axis) over France at the end of the century (2071-2100) with respect to the 1976-2005 period (historical period) under RCP 8.5. The sharp points are the "short list" of future climate models proposed by Météo-France. The red dashed circles show the selected GCM/RCMs in the current study. This figure is adopted from DRIAS-2020 (Soubeyroux et al. (2020); see http://www.drias-climat.fr/).

E.2 Maps of significance levels of trends in stream temperature

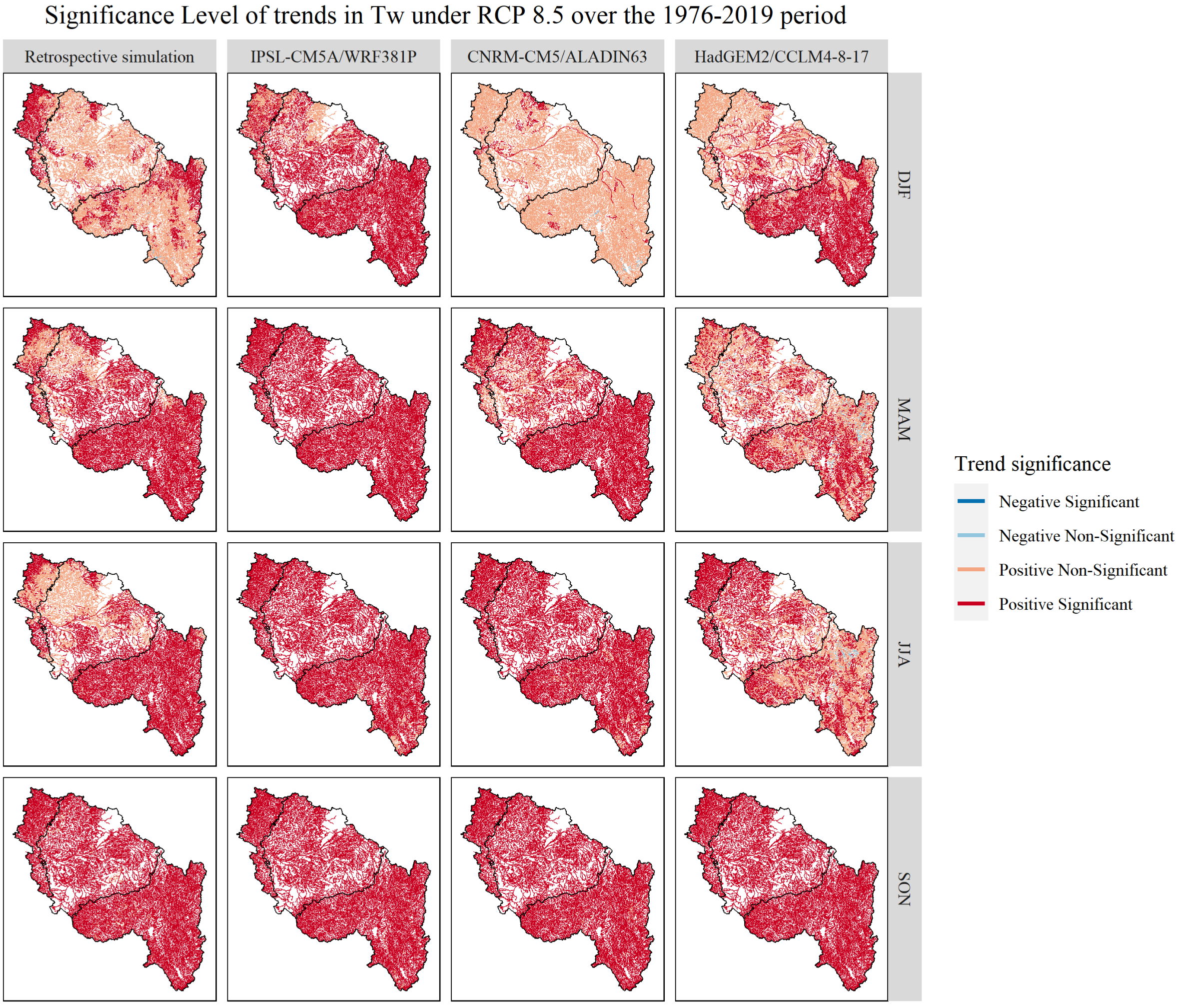

Figure E.3: Spatial variability of the significance of trends in seasonal Tw for different GCM/RCMs under RCP 8.5, and retrospective simulation over the 1976–2019 period, based on a Mann-Kendall test at the 95% confidence level. Solid black lines show the Hydro-Ecoregion delineation (see Figure 2.1).

Figure E.4: Spatial variability of the significance of trends in seasonal Tw for different GCM/RCMs under RCP 4.5, and retrospective simulation over the 1976–2019 period, based on a Mann-Kendall test at the 95% confidence level. Solid black lines show the Hydro-Ecoregion delineation (see Figure 2.1).

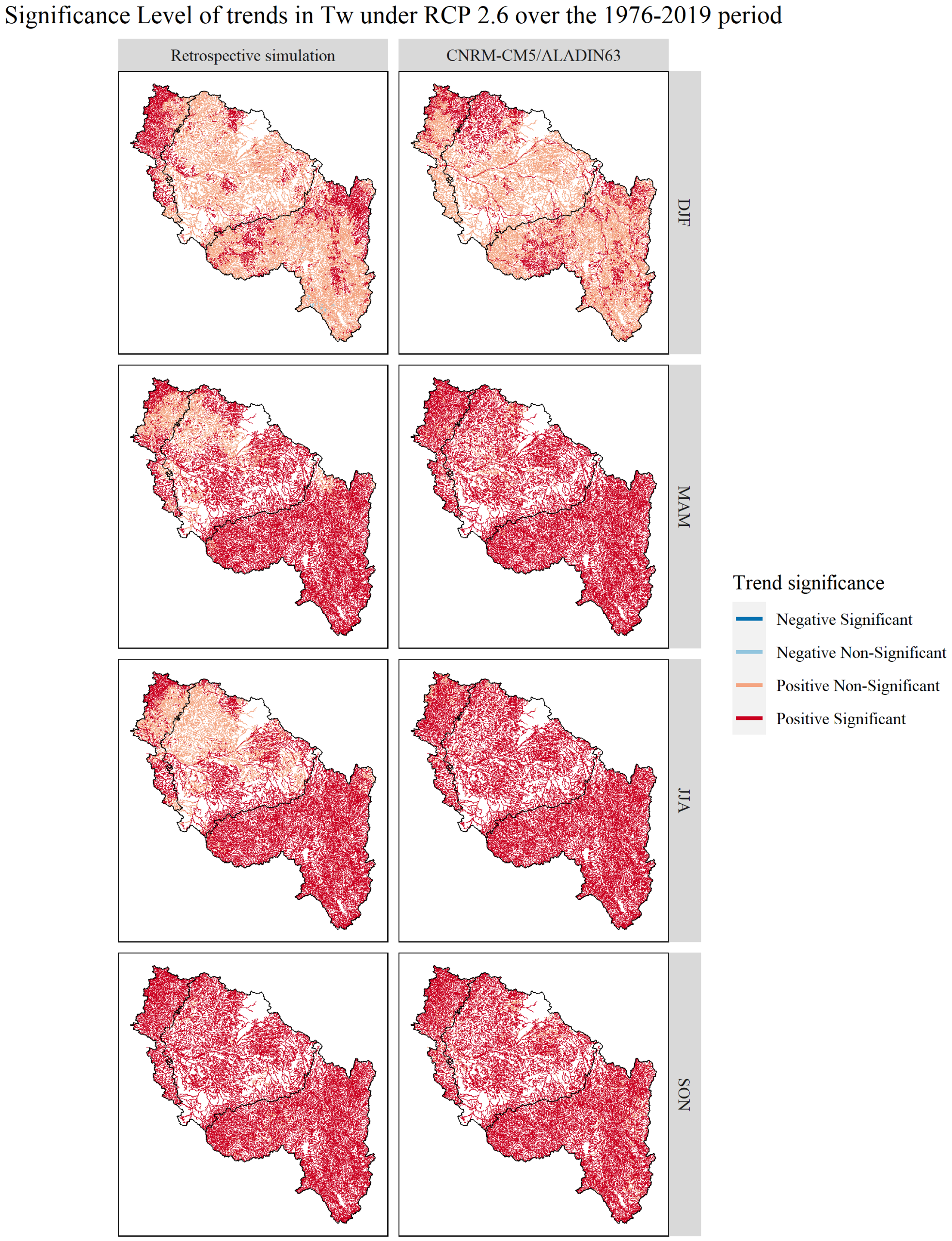

Figure E.5: Spatial variability of the significance of trends in seasonal Tw for CNRM-CM5-LR/ALADIN63 model under RCP 2.6, and retrospective simulation over the 1976–2019 period, based on a Mann-Kendall test at the 95% confidence level. Solid black lines show the Hydro-Ecoregion delineation (see Figure 2.1).

E.3 Maps of future changes in precipitation

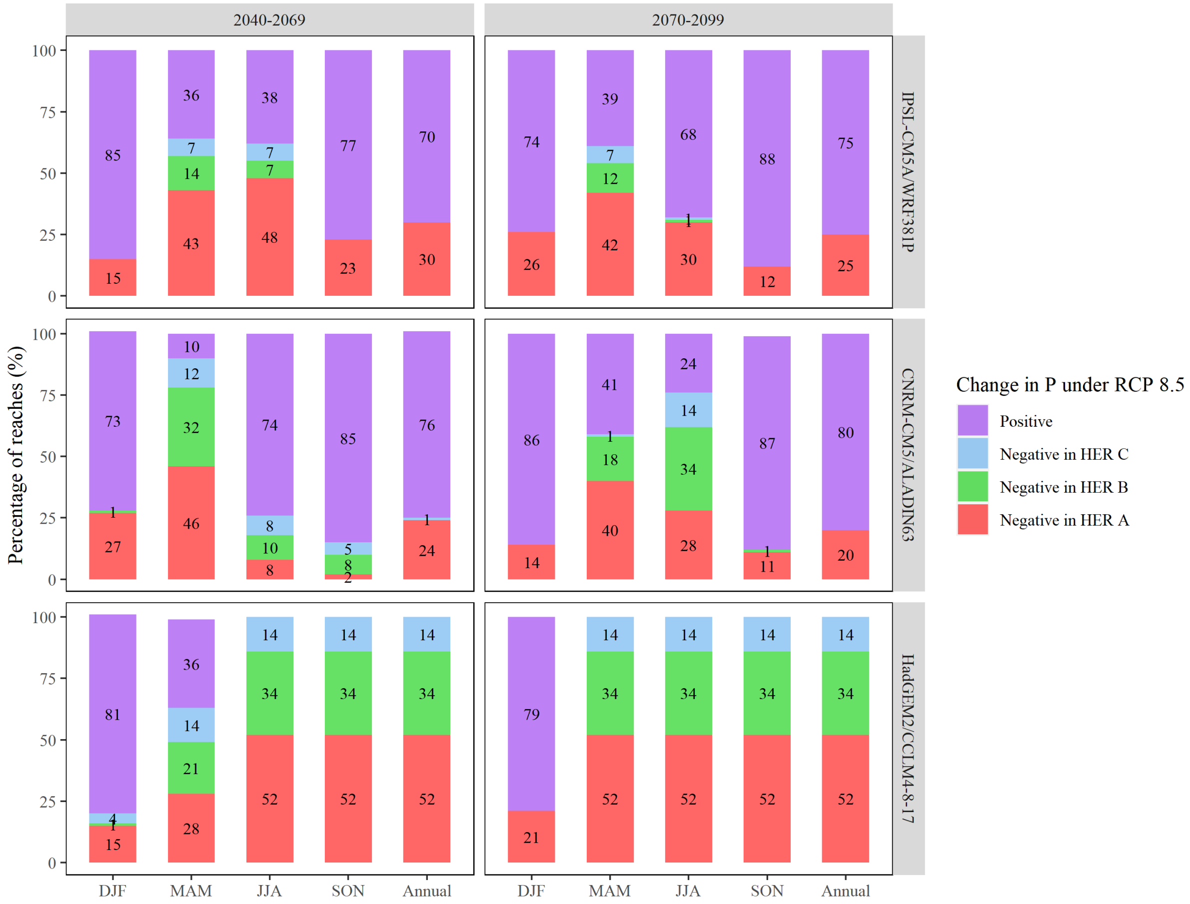

Figure E.6: Percentage of reaches with positive and negative changes in P under different GCM/RCM and RCP 8.5 for different seasons, and time slices. The proportion of reaches with negative changes in P in each HER is specified to trace the position of decreasing changes in P.

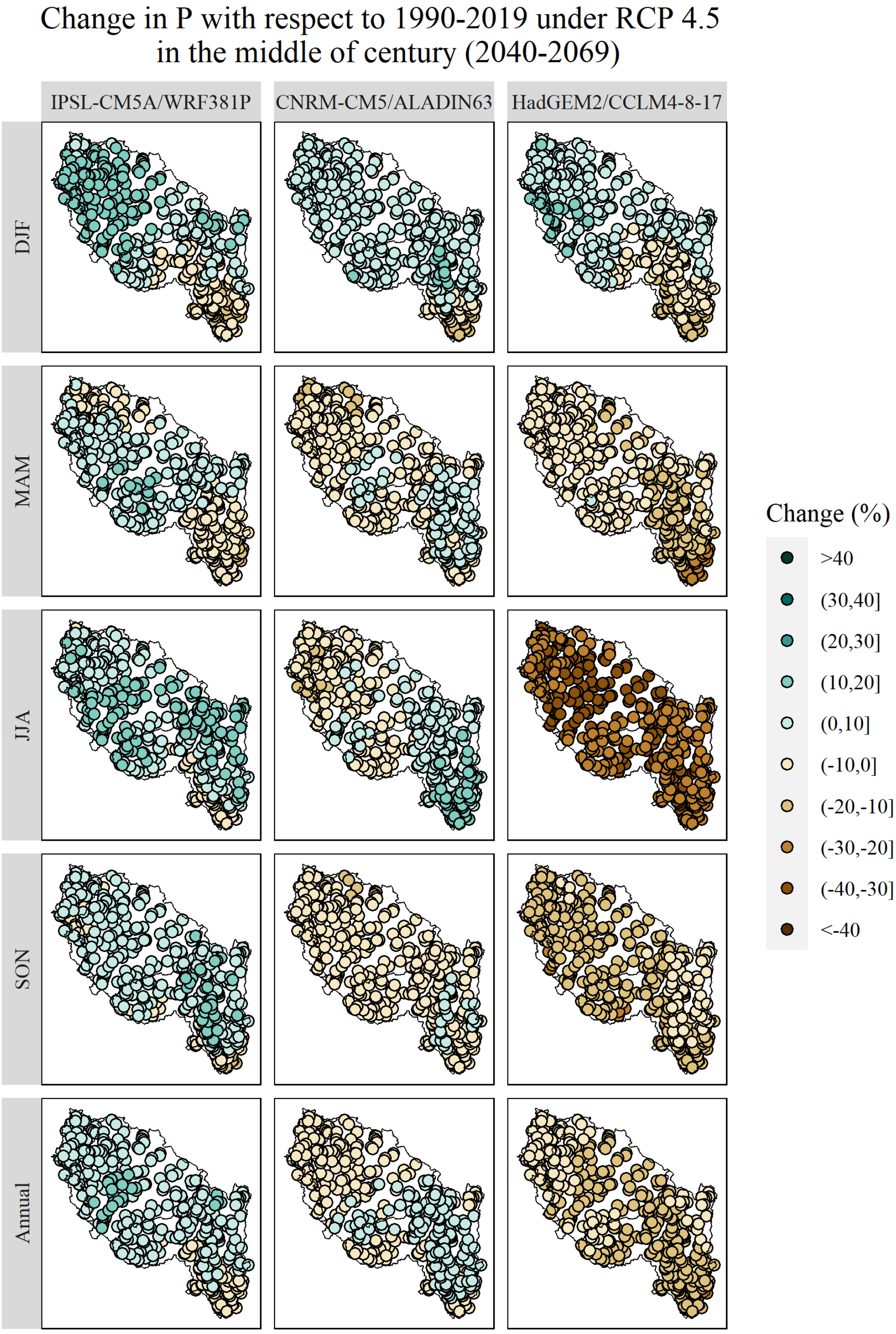

Figure E.7: Map of changes in seasonal and annual P with respect to the 1990-2019 period under 3 GCM/RCMs and RCP 4.5 in the middle of century (2040-2069).

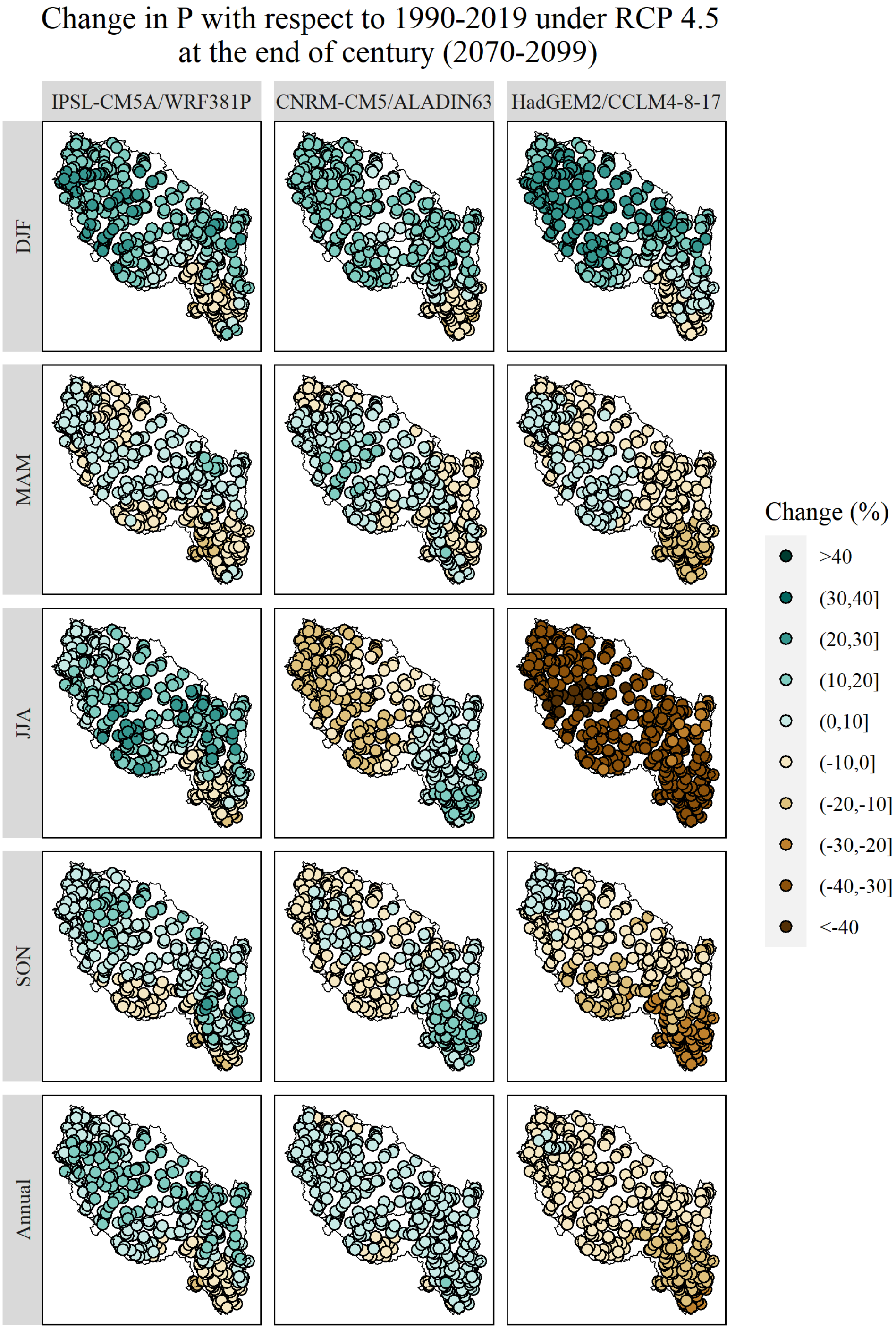

Figure E.8: Map of changes in seasonal and annual P with respect to the 1990-2019 period under 3 GCM/RCMs and RCP 4.5 at the end of the century (2070-2099).

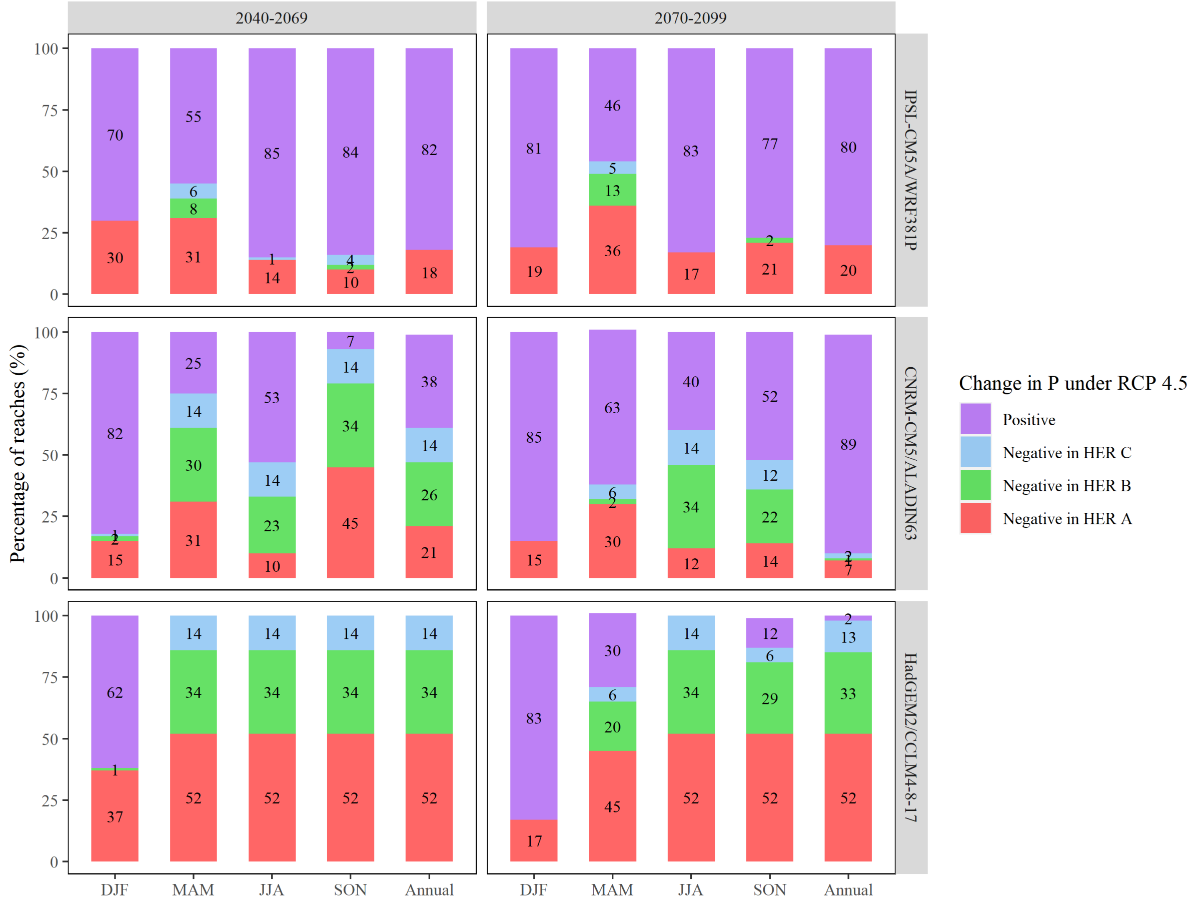

Figure E.9: Percentage of reaches with positive and negative changes in P under different GCM/RCM and RCP 4.5 for different seasons, and time slices. The proportion of reaches with negative changes in P in each HER is specified to trace the position of decreasing changes in P.

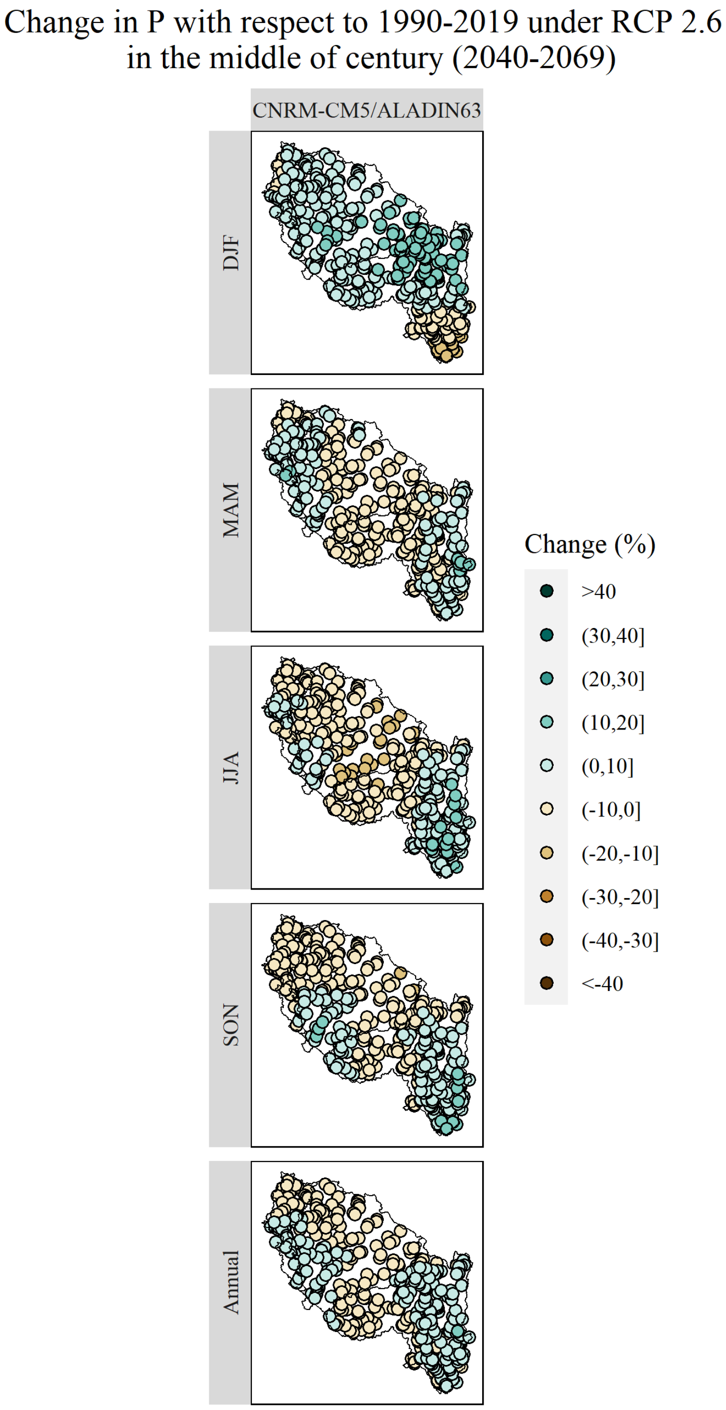

Figure E.10: Map of changes in seasonal and annual P with respect to the 1990-2019 period under the CNRM-CM5-LR/ALADIN63 model and RCP 2.6 in the middle of century (2040-2069).

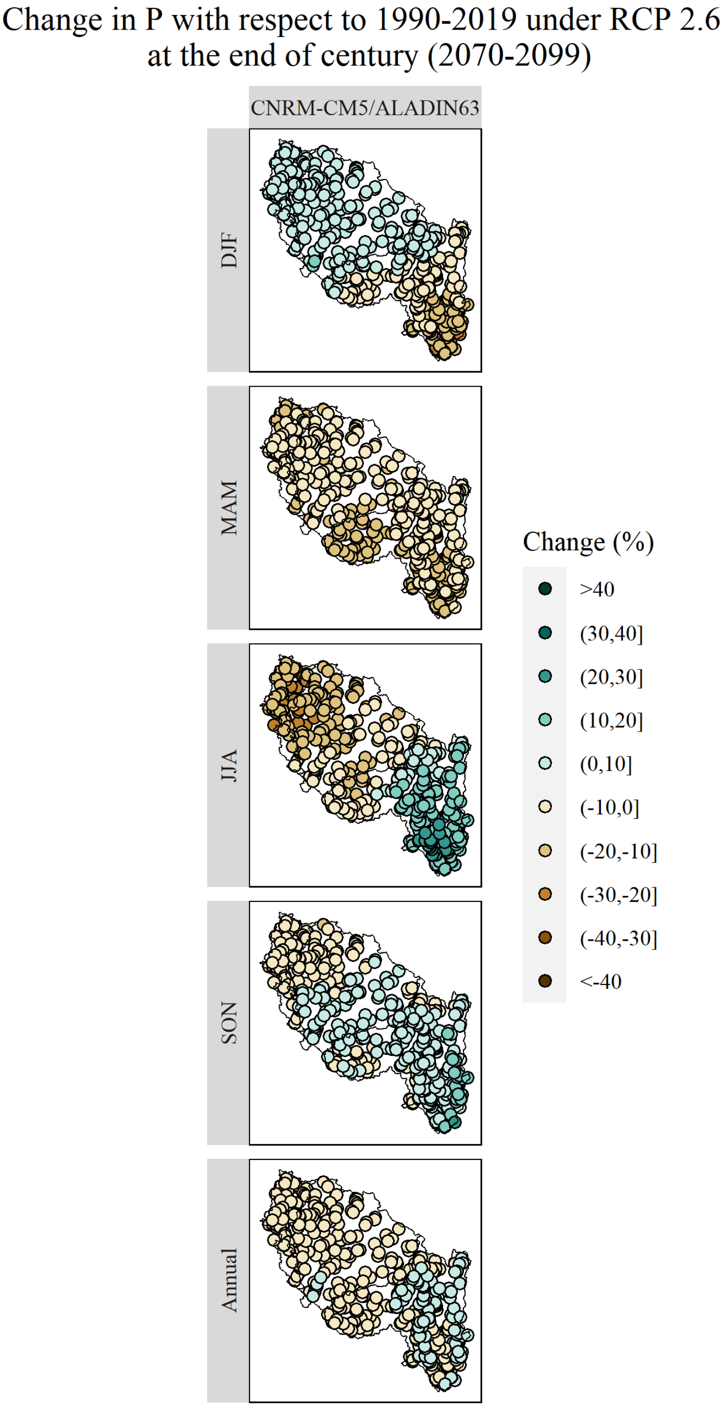

Figure E.11: Map of changes in seasonal and annual P with respect to the 1990-2019 period under the CNRM-CM5-LR/ALADIN63 model and RCP 2.6 at the end of the century (2070-2099).

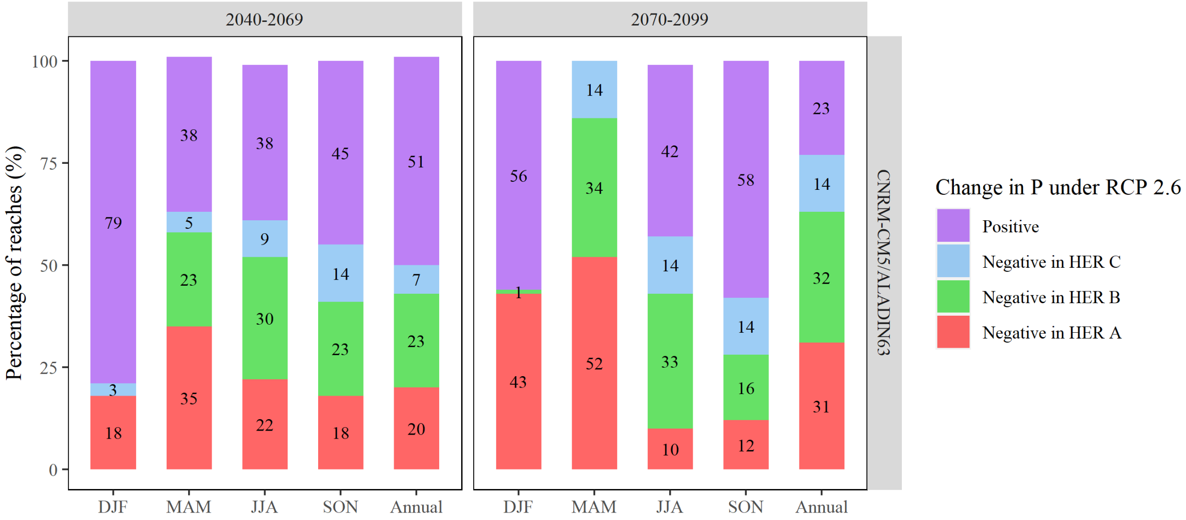

Figure E.12: Percentage of reaches with positive and negative changes in P under the CNRM-CM5-LR/ALADIN63 model and RCP 2.6 for different seasons, and time slices. The proportion of reaches with negative changes in P in each HER is specified to trace the position of decreasing changes in P.

E.4 Maps of future changes in air temperature

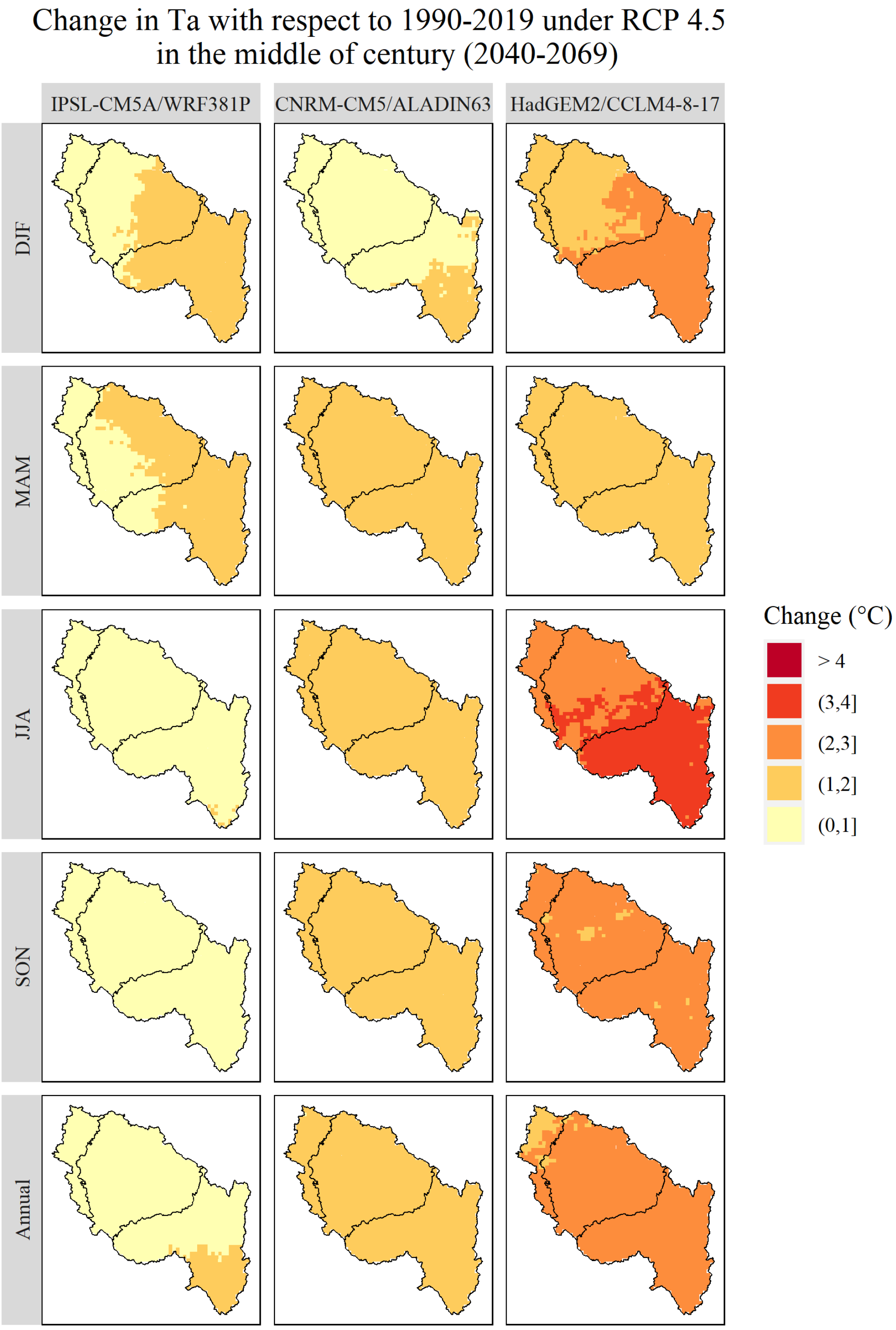

Figure E.13: Map of changes in seasonal and annual Ta with respect to the 1990-2019 period under 3 GCM/RCMs and RCP 4.5 in the middle of century (2040-2069). Solid black lines show the Hydro-Ecoregion (HER) delineation (see Figure 2.1).

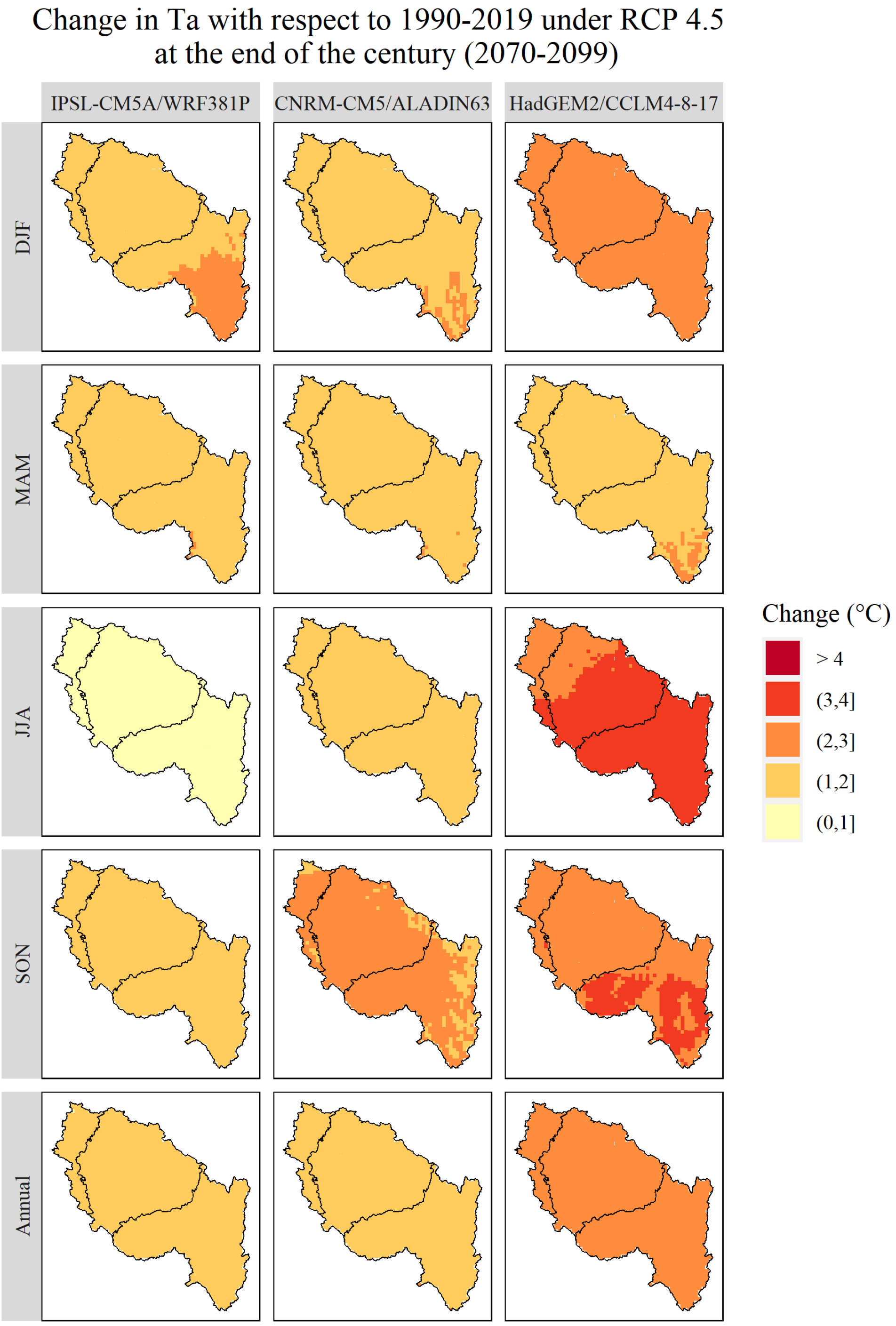

Figure E.14: Map of changes in seasonal and annual Ta with respect to the 1990-2019 period under 3 GCM/RCMs and RCP 4.5 at the end of the century (2070-2099). Solid black lines show the Hydro-Ecoregion (HER) delineation (see Figure 2.1).

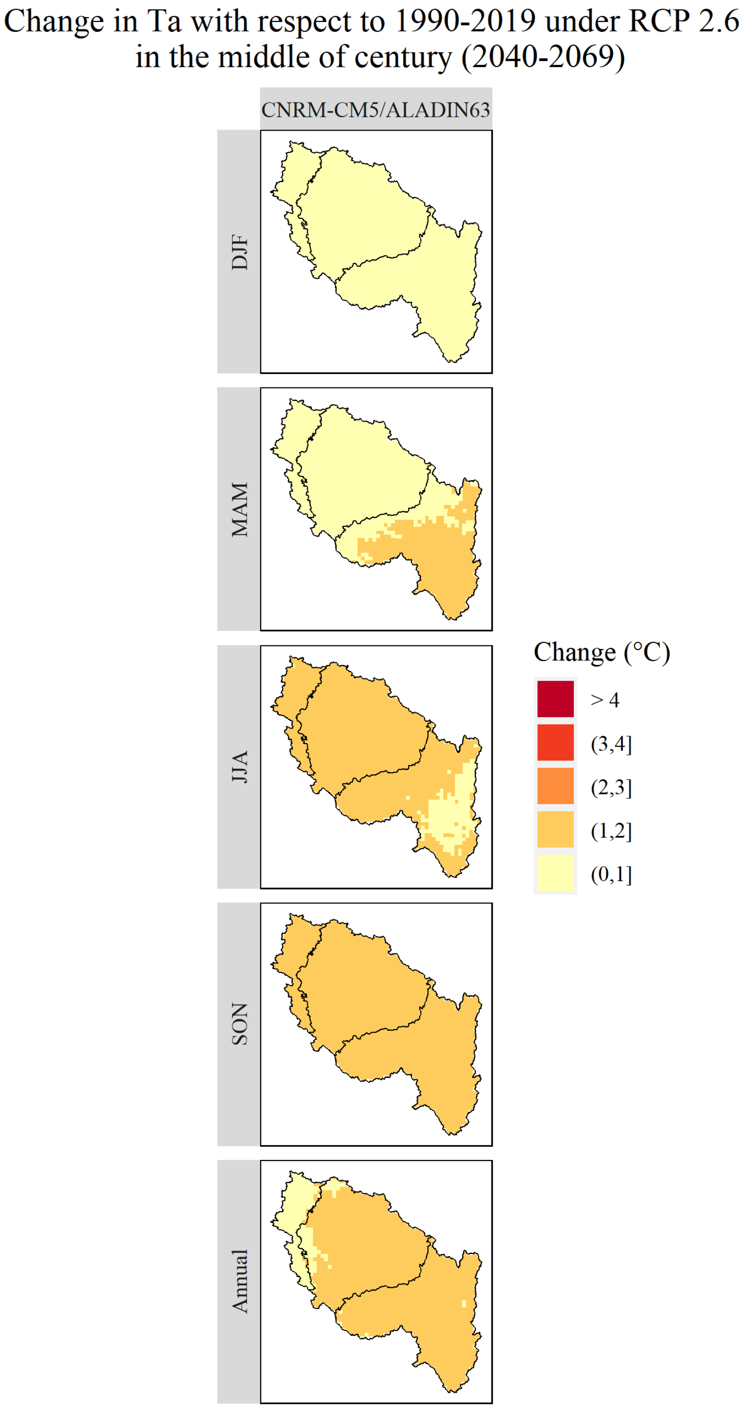

Figure E.15: Map of changes in seasonal and annual Ta with respect to the 1990-2019 period under the CNRM-CM5-LR/ALADIN63 model and RCP 2.6 in the middle of century (2040-2069). Solid black lines show the Hydro-Ecoregion (HER) delineation (see Figure 2.1).

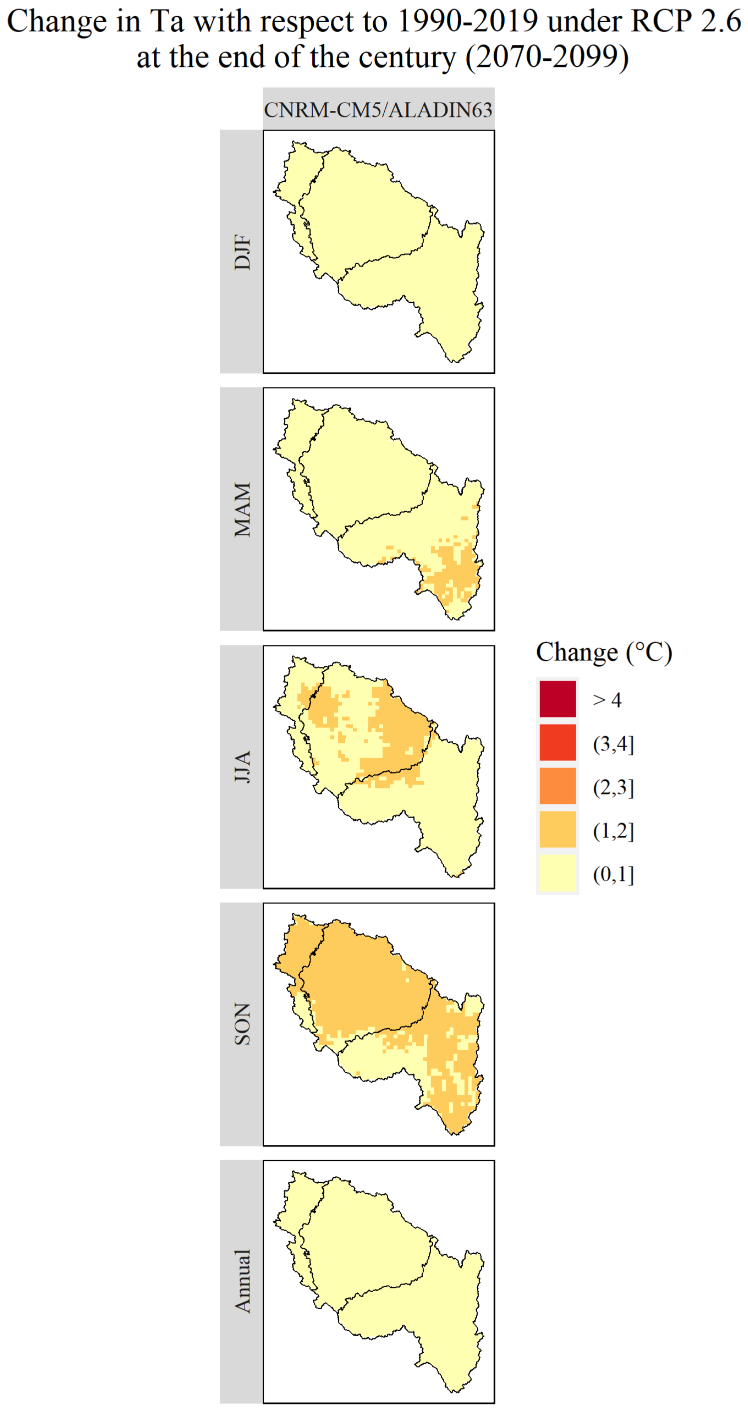

Figure E.16: Map of changes in seasonal and annual Ta with respect to the 1990-2019 period under 3 GCM/RCMs and RCP 2.6 at the end of the century (2070-2099). Solid black lines show the Hydro-Ecoregion (HER) delineation (see Figure 2.1).

E.5 Maps of future changes in streamflow

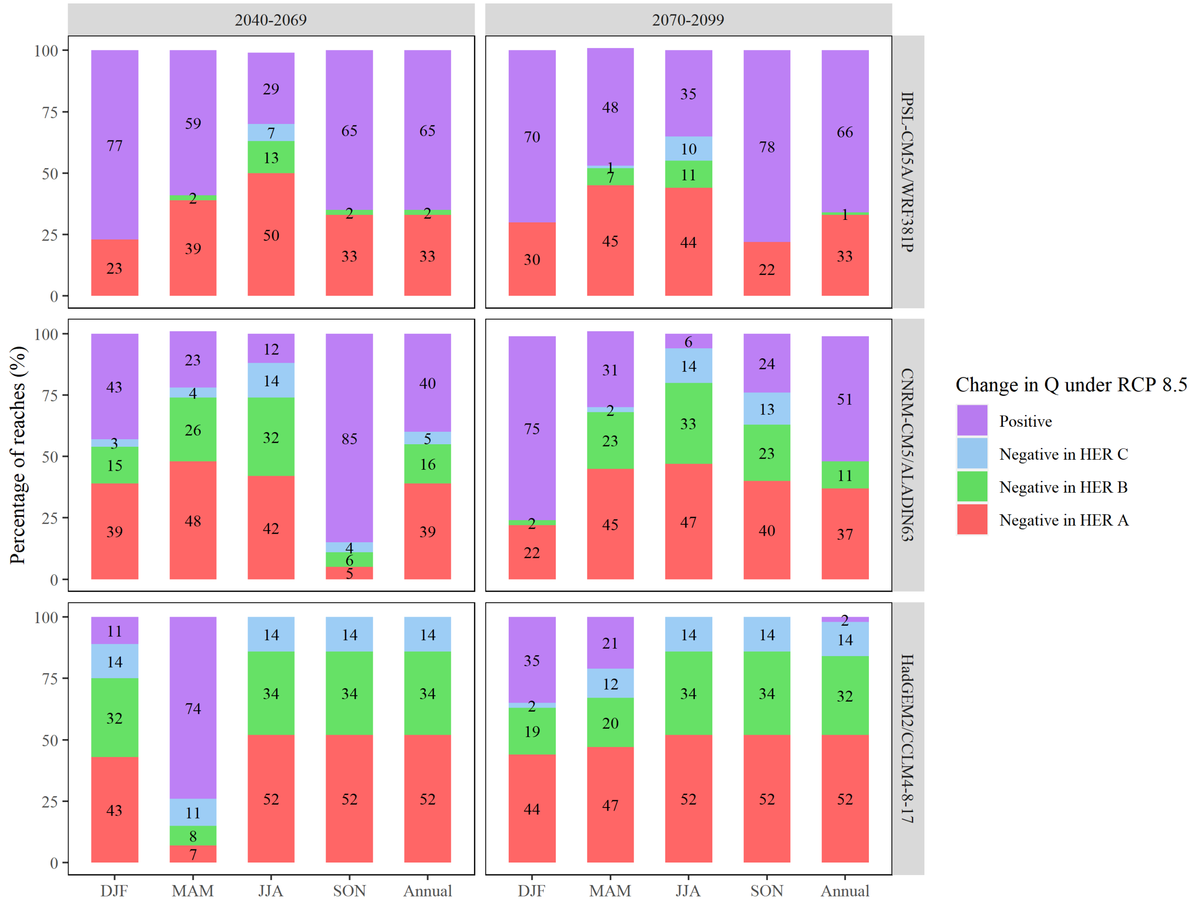

Figure E.17: Percentage of reaches with positive and negative changes in Q under different GCM/RCM and RCP 8.5 for different seasons, and time slices. The proportion of reaches with negative changes in Q in each HER is specified to trace the position of decreasing changes in Q.

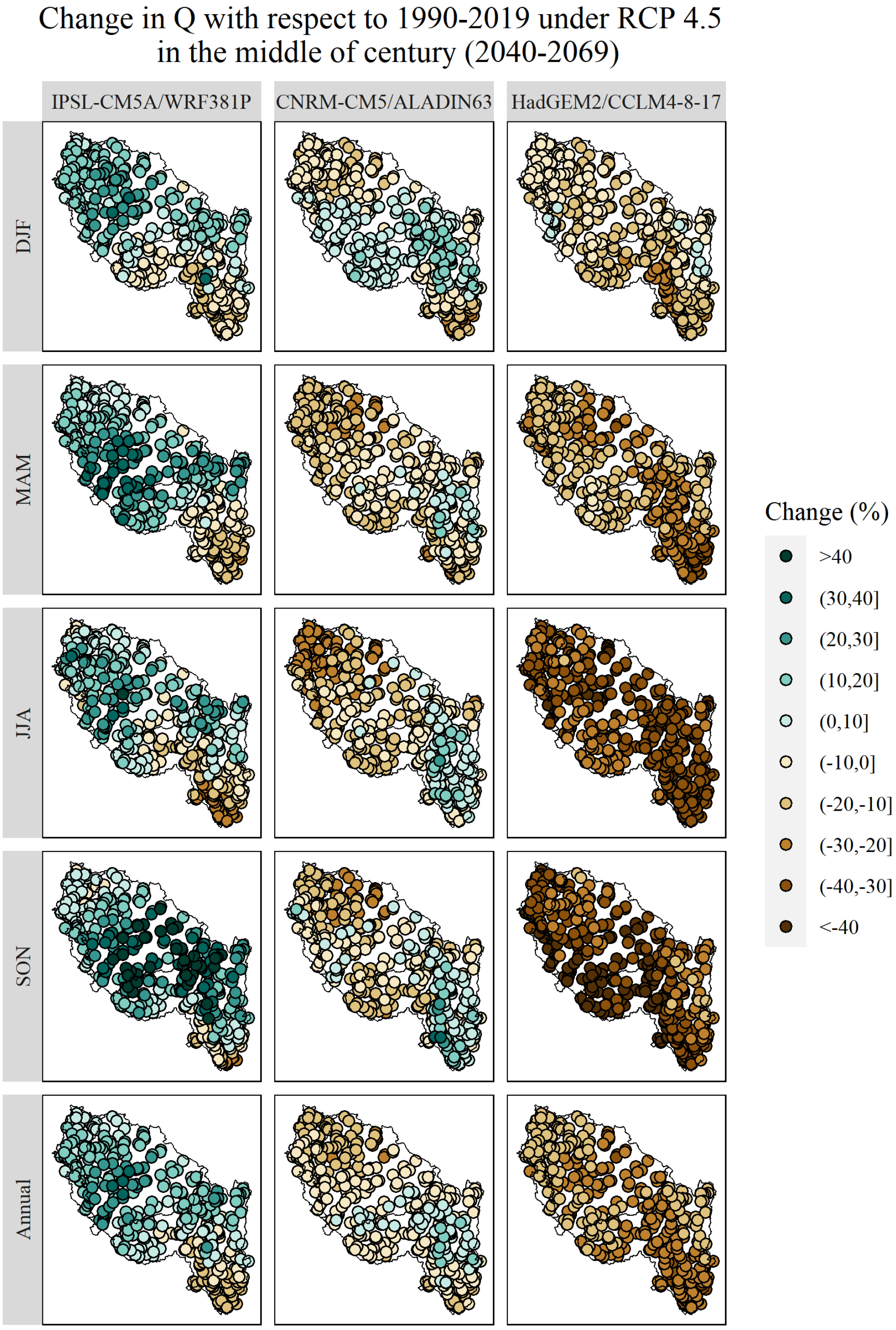

Figure E.18: Map of changes in seasonal and annual Q with respect to the 1990-2019 period under 3 GCM/RCMs and RCP 4.5 in the middle of century (2040-2069).

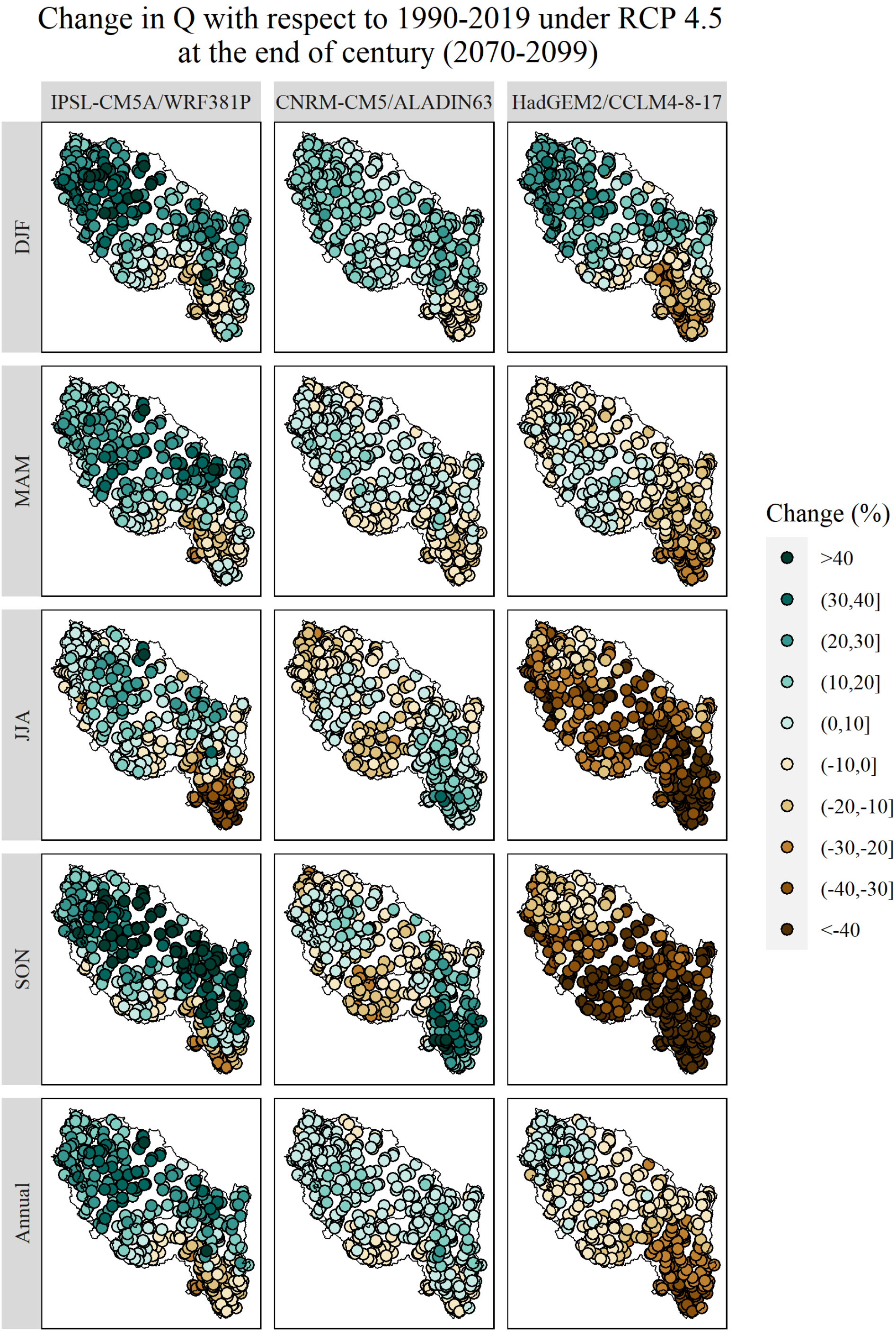

Figure E.19: Map of changes in seasonal and annual Q with respect to the 1990-2019 period under 3 GCM/RCMs and RCP 4.5 at the end of the century (2070-2099).

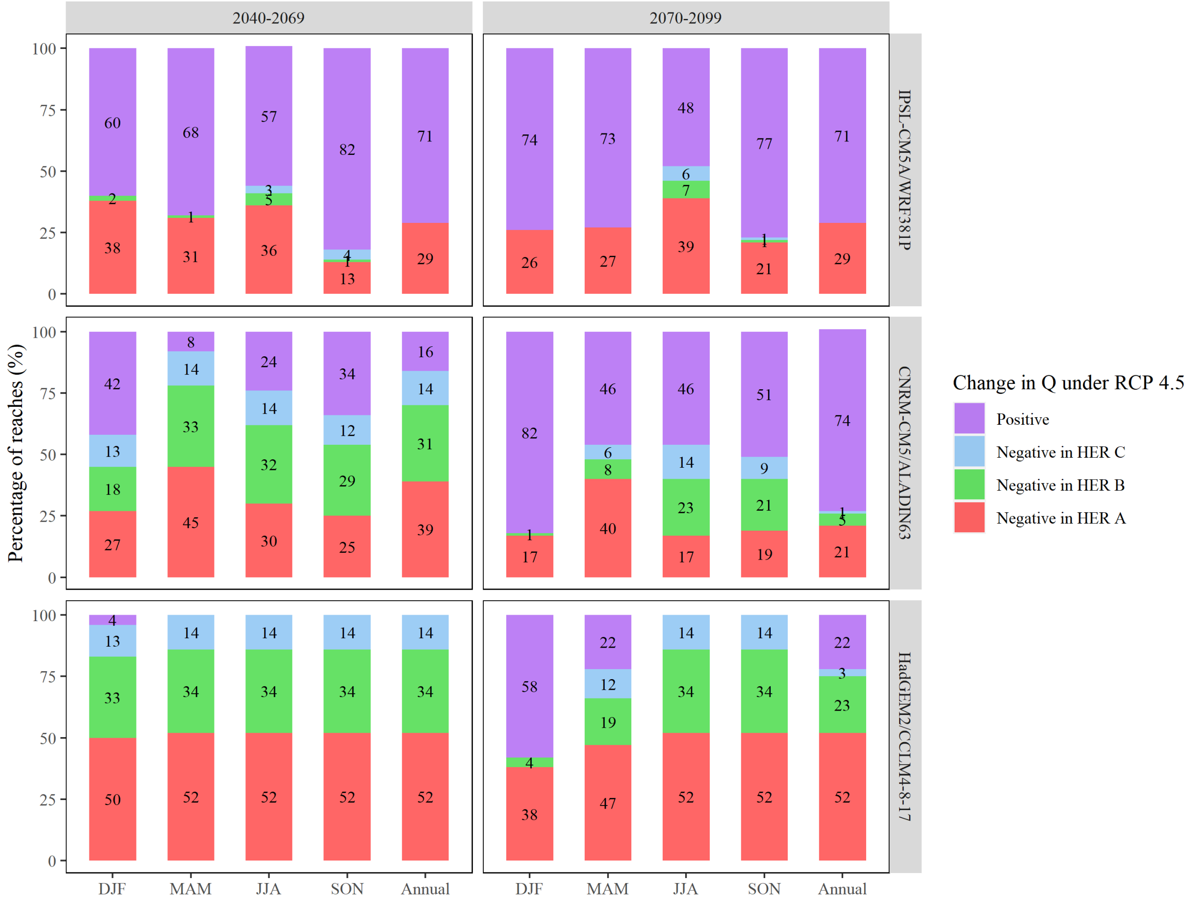

Figure E.20: Percentage of reaches with positive and negative changes in Q under different GCM/RCM and RCP 4.5 for different seasons, and time slices. The proportion of reaches with negative changes in Q in each HER is specified to trace the position of decreasing changes in Q.

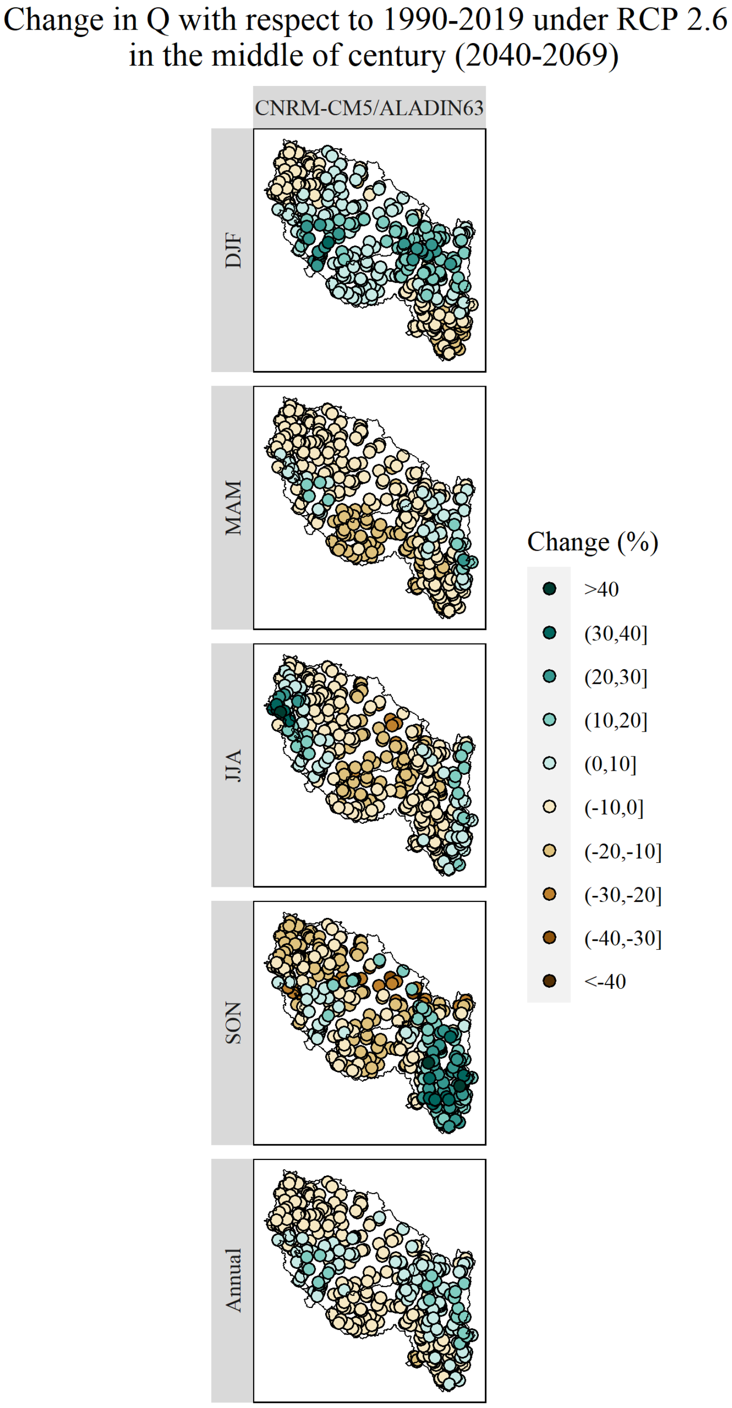

Figure E.21: Map of changes in seasonal and annual Q with respect to the 1990-2019 period under the CNRM-CM5-LR/ALADIN63 model and RCP 2.6 in the middle of century (2040-2069).

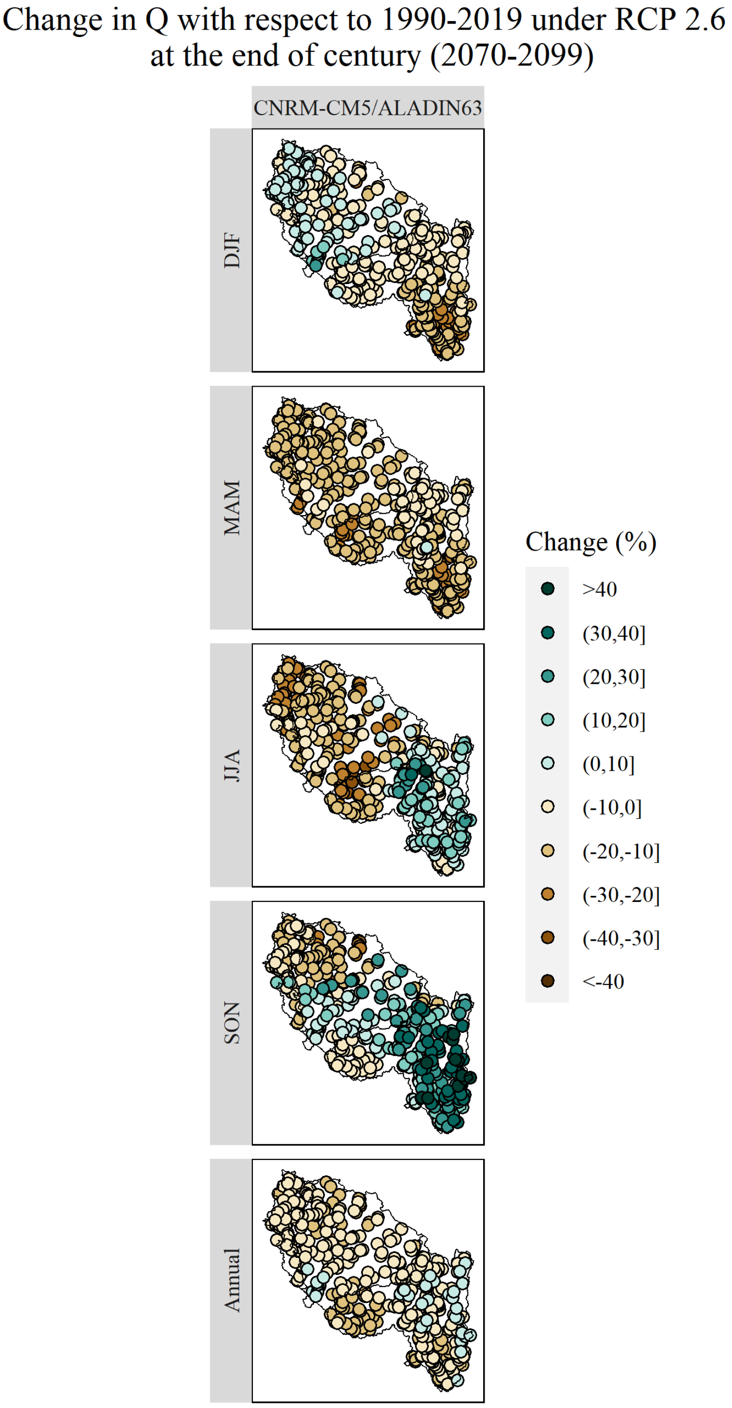

Figure E.22: Map of changes in seasonal and annual Q with respect to the 1990-2019 period under the CNRM-CM5-LR/ALADIN63 model and RCP 2.6 at the end of the century (2070-2099).

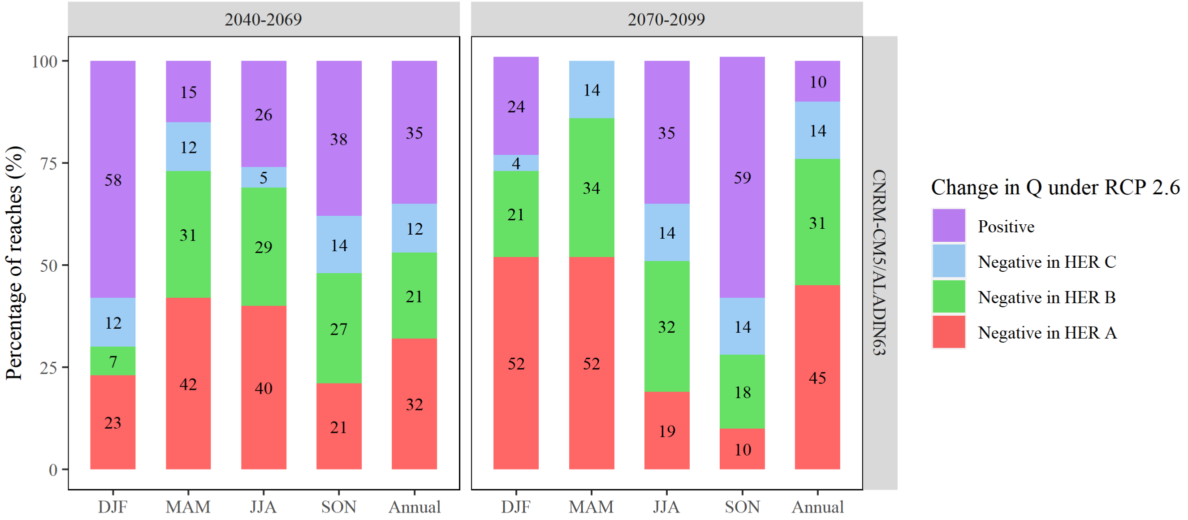

Figure E.23: Percentage of reaches with positive and negative changes in Q under the CNRM-CM5-LR/ALADIN63 model and RCP 2.6 for different seasons, and time slices. The proportion of reaches with negative changes in Q in each HER is specified to trace the position of decreasing changes in Q.

E.6 Maps of future changes in stream temperature

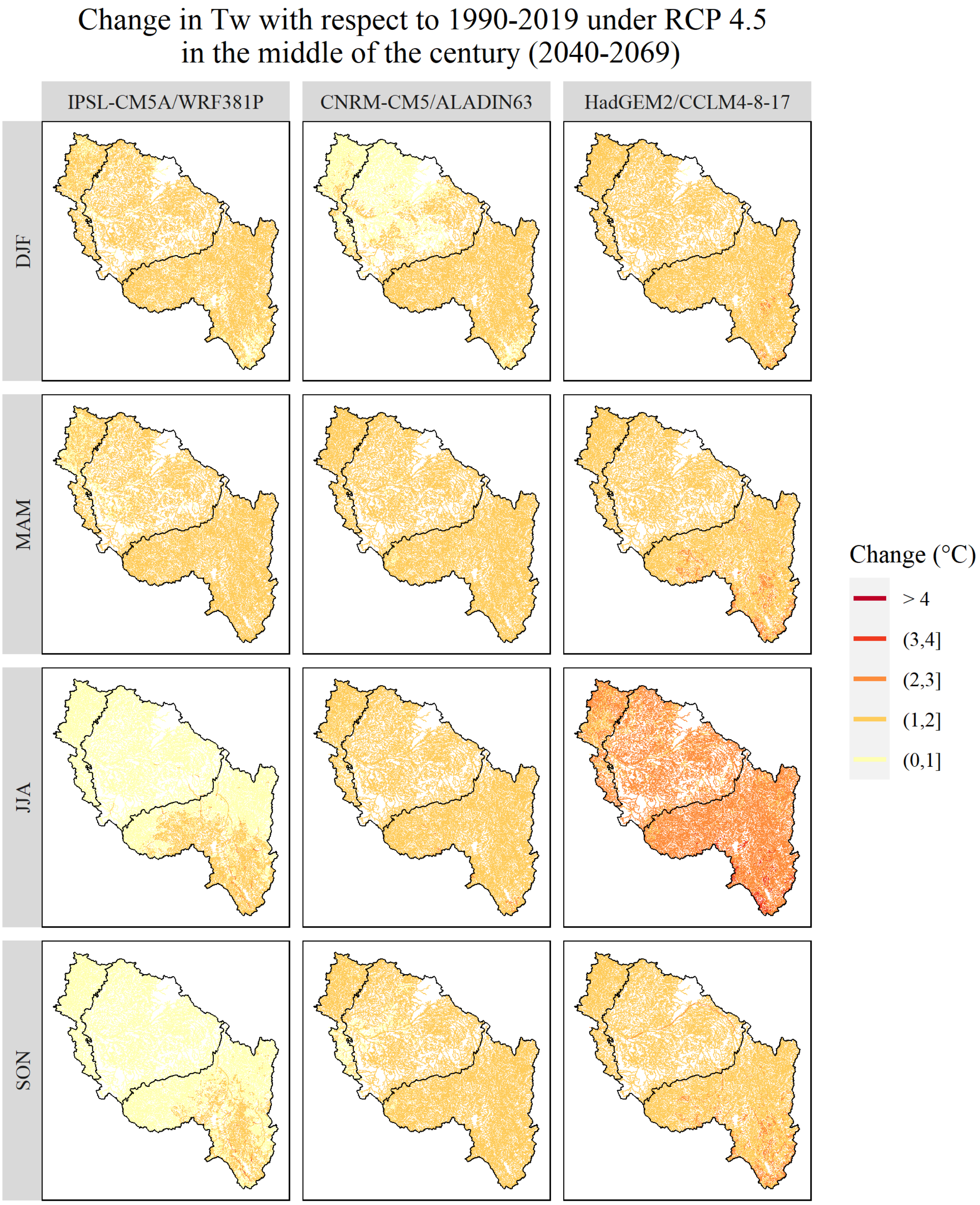

Figure E.24: Map of changes in seasonal and annual Tw with respect to the 1990–2019 period under 3 GCM/RCMs and RCP 4.5 in the middle of the century (2040–2069). Solid black lines show the Hydro-Ecoregion (HER) delineation (see Figure 2.1).

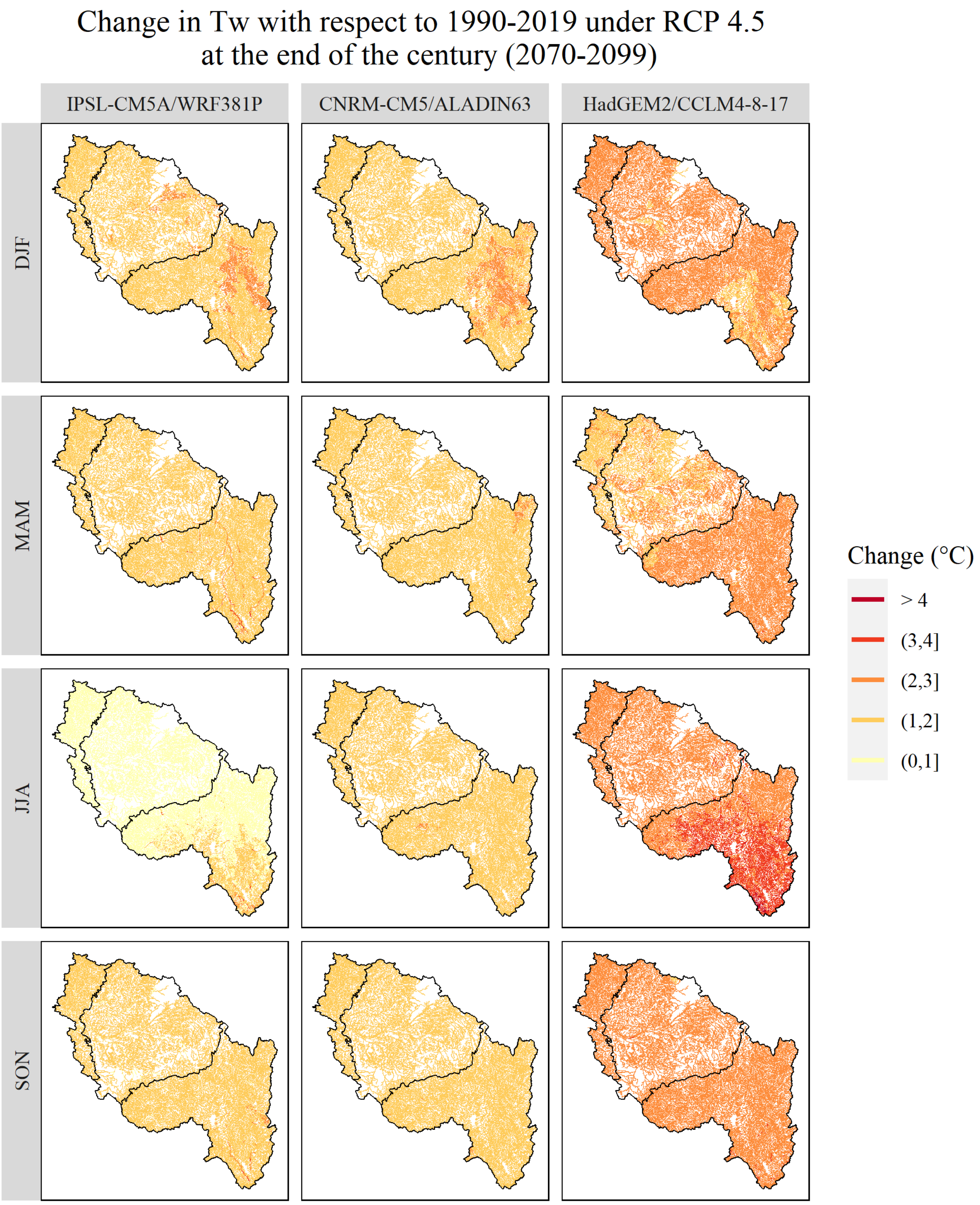

Figure E.25: Map of changes in seasonal and annual Tw with respect to the 1990–2019 period under 3 GCM/RCMs and RCP 4.5 at the end of the century (2070–2099). Solid black lines show the Hydro-Ecoregion (HER) delineation (see Figure 2.1).

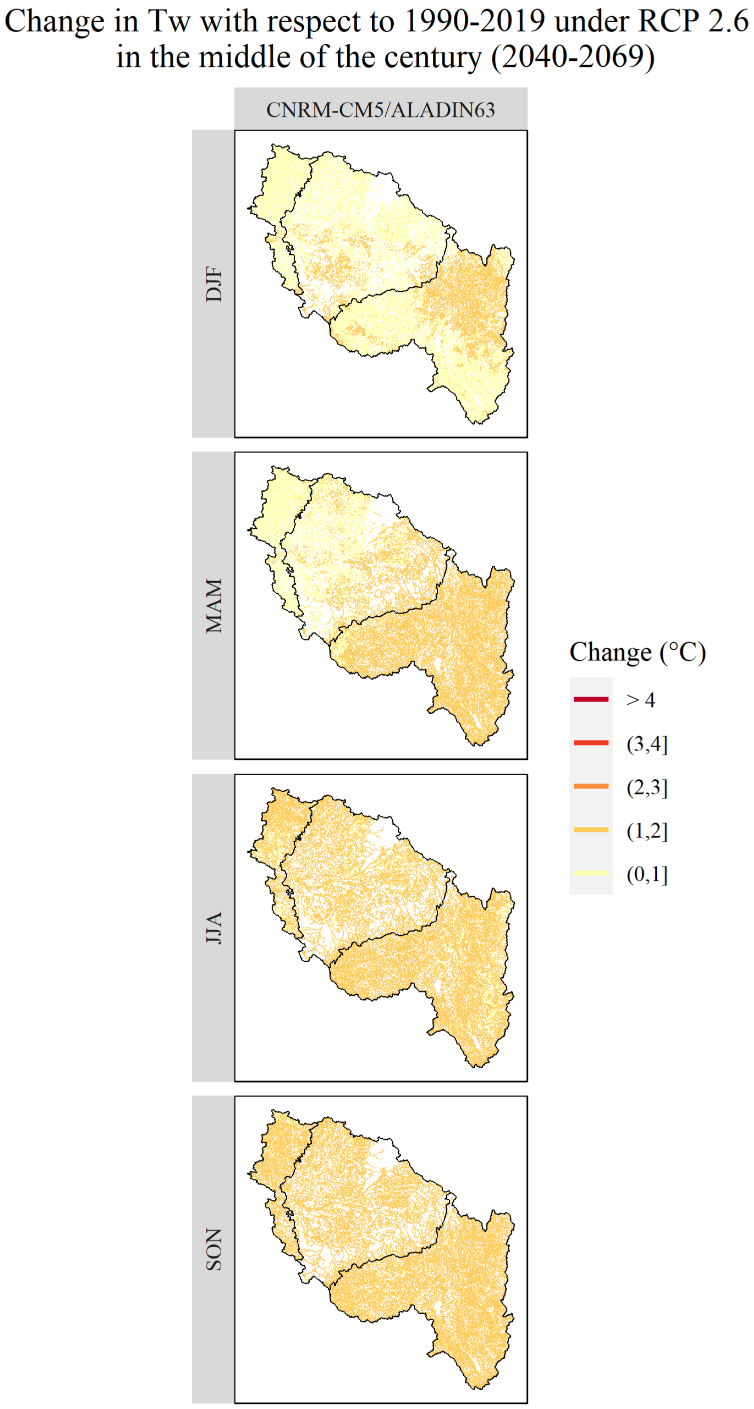

Figure E.26: Map of changes in seasonal and annual Tw with respect to the 1990–2019 period he CNRM-CM5-LR/ALADIN63 model and RCP 2.6 in the middle of the century (2040–2069). Solid black lines show the Hydro-Ecoregion (HER) delineation (see Figure 2.1).

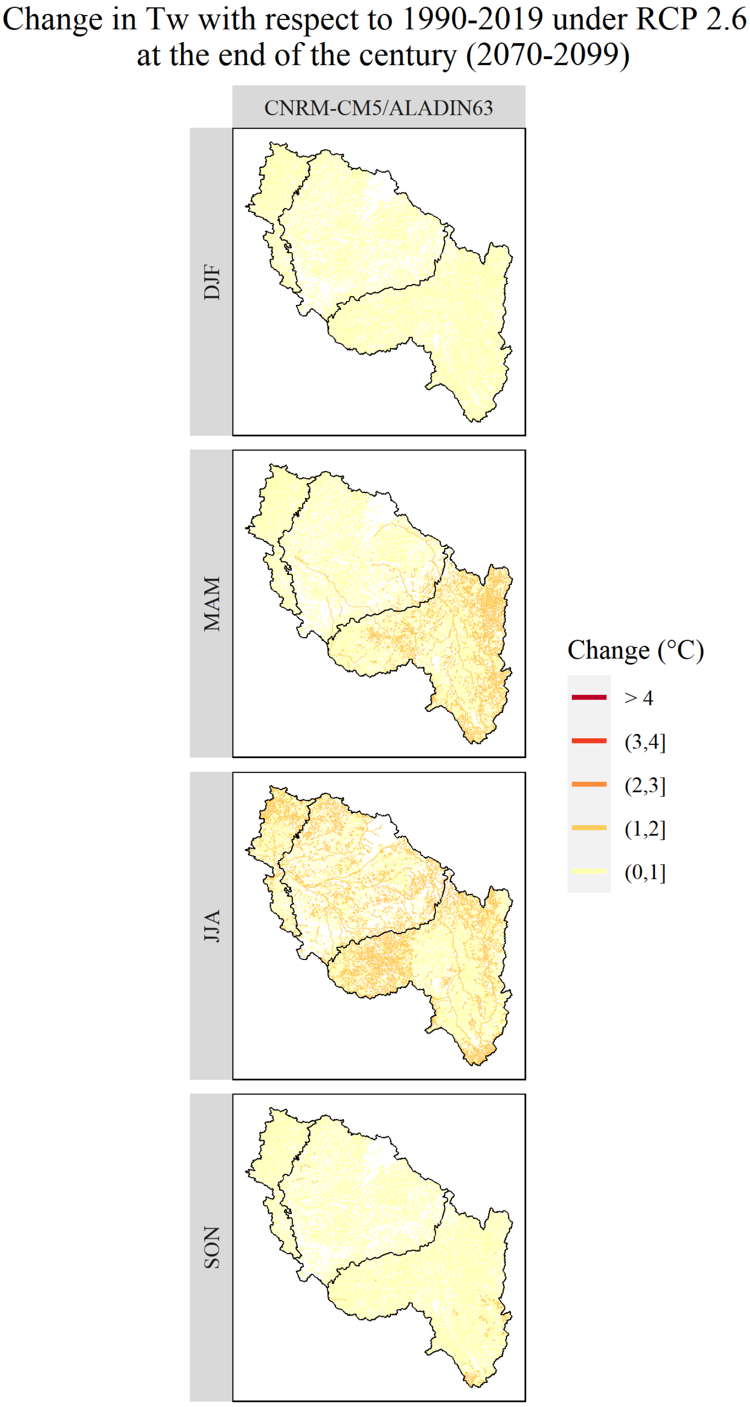

Figure E.27: Map of changes in seasonal and annual Tw with respect to the 1990–2019 period he CNRM-CM5-LR/ALADIN63 model and RCP 2.6 at the end of the century (2070–2099). Solid black lines show the Hydro-Ecoregion (HER) delineation (see Figure 2.1).

E.7 Synchronicity of extreme changes in stream and air temperature, and streamflow across reaches

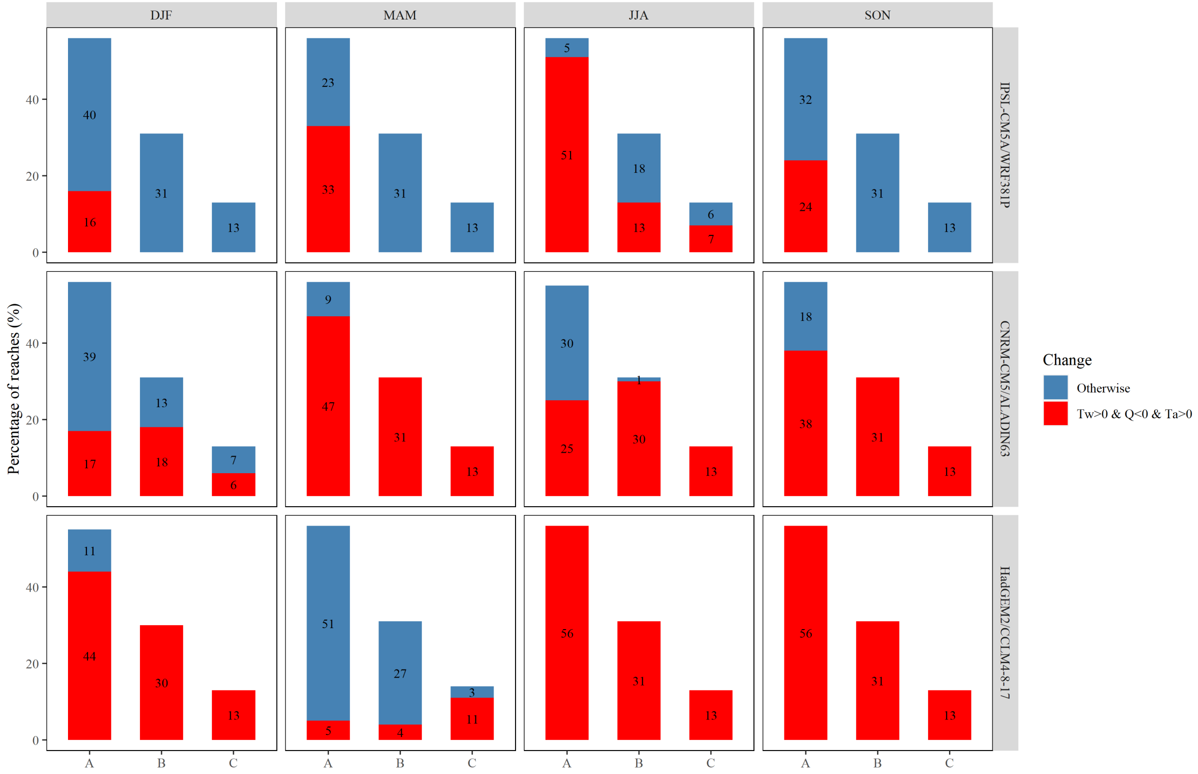

Figure E.28: Percentage of reaches with consistent changes in Tw, Q and Ta in the middle of the century (2040–2069), categorised with respect to sign of change in Tw and Q for different GCM/RCMs, seasons and HERs under RCP 8.5. The changes are calculated with respect to the 1990-2019 period.

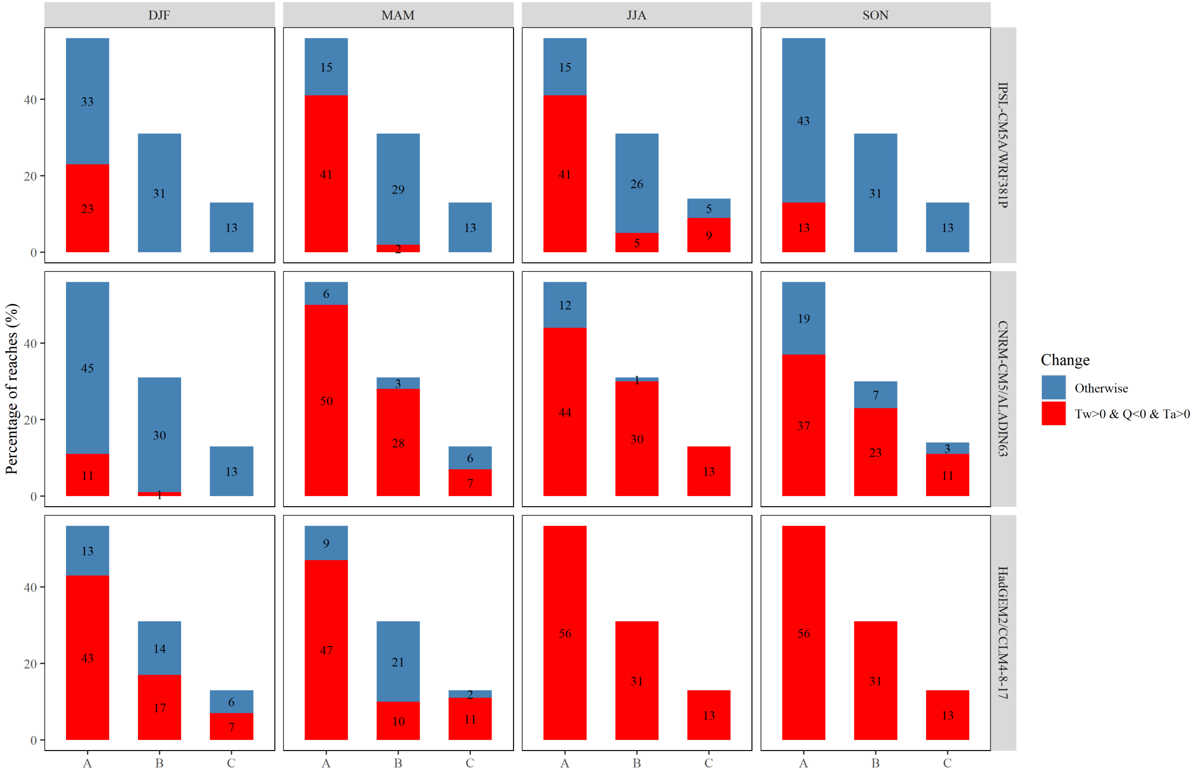

Figure E.29: Percentage of reaches with consistent changes in Tw, Q and Ta at the end of the century (2070-2099), categorised with respect to sign of change in Tw and Q for different GCM/RCMs, seasons and HERs under RCP 8.5. The changes are calculated with respect to the 1990-2019 period.

Hanieh Seyedhashemi

Influence des retenues d'eau et du changement climatique sur la température des cours d’eau :

modélisation à haute résolution et application au bassin de la Loire

Résumé

La température du cours d'eau (Tw) est un paramètre critique affectant la qualité de l'eau et la répartition des communautés aquatiques, mais notre compréhension de sa variabilité spatio-temporelle induite par les retenues d’eau (par exemple, barrages, petits réservoirs et étangs) à grande échelle est limitée. De plus, l'ampleur des changements de température des cours d'eau dans le passé et dans le futur reste mal documentée en raison d'un manque de données à long terme et de la difficulté à analyser les effets de la variabilité hydroclimatique et des caractéristiques des bassins versants. Par conséquent, dans ce projet de doctorat, ces questions sont abordées en utilisant à la fois les données de température des cours d'eau observées et les sorties du modèle thermique basé sur les processus physiques T-NET (Temperature-NETwork) couplé au modèle hydrologique semi-distribué EROS à l'échelle d’un grand bassin de la Loire (10^5 km^2 avec 52278 tronçons modélisés). Les résultats montrent que les grands barrages diminuent la température estivale de 2°C et retardent le pic annuel de la Tw de 23 jours par rapport aux régimes naturels. En revanche, les effets cumulatifs des étangs augmentent la température estivale de 2,3°C et augmentent la synchronicité avec les régimes de température de l'air. De plus, Tw a augmenté pour presque tous les biefs en toutes saisons (jusqu’à 5.7°C) sur la période 1963-2019 et va se poursuivre dans le futur [+0,72°C ; +2,68°C] suivant les projections climatiques au milieu du siècle (2040-2069). Ces augmentations sont liées au réchauffement atmosphérique (jusqu’à 4°C) et à la diminution des débits (jusqu'à -70%), principalement dans la partie amont du bassin.

Mots-clefs : Régime thermique, Barrages et étangs, Analyses statistiques, Tendances à long terme, Scénarios climatiques, Projections futures

Résumé en anglais

Stream temperature is a critical parameter affecting water quality and the distribution of aquatic communities, but our understanding of its spatio-temporal variability induced by anthropogenic impoundments (e.g., large dams, small reservoirs, and ponds) at a large scale is limited. Moreover, the magnitude of changes in stream temperature over both the past and future remains poorly constrained due to a paucity of long-term data and difficulty in parsing effects of hydroclimate and landscape variability. Hence, in this doctoral project, these issues are addressed using both observed stream temperature data and the outputs of the T-NET (Temperature-NETwork) physical process-based thermal model coupled with the EROS semi-distributed hydrological model at the scale of the entire Loire River basin in France, a large European basin (10^5 km^2 with 52278 reaches). Results show that large dams decrease summer Tw by 2°C and delay the annual Tw peak by 23 days relative to the natural regimes. In contrast, the cumulative effects of upstream ponds increase summer Tw by 2.3°C and increase the synchronicity with air temperature regimes. Moreover, Tw increased for almost all reaches in all seasons (up to +5.7°C) over the 1963-2019 period, and will continue in the future according to climate projections in the middle of the century, 2040-2069 ([+ 0.72° C; + 2.68°C] depending on season and projection). These increases are linked to atmospheric warming (up to +4°C) and the decrease in flows (up to -70%), mainly in the upstream part of the basin.

Key words: Thermal regime, Dams and ponds, Statistical analyses, Long-term trends, Climate scenarios, Future projections